“Understanding metallogeny around Loch Tay, Scotland: insights from isotope geochemistry and petrographic studies”

Shane Patrick David Webb

Submitted in accordance with the requirements

for the degree of Doctor of Philosophy

THE UNIVERSITY OF LEEDS

SCHOOL OF EARTH AND ENVIRONMENT

INSTITUTE OF APPLIED GEOSCIENCE

April 2024

I confirm that the work submitted is my own, except where work which has formed part of jointly authored publications is included. My contribution and the other authors to this work has been explicitly indicated below. I confirm that appropriate credit has been given within the thesis where reference has been made to the work of others. The following jointly authored publications have been used to generate some parts of this thesis:

Webb, S., Torvela, T., Chapman, R. and Savastano, L. 2024a. Textural mapping and building a paragenetic interpretation of hydrothermal veins. *Geological Society, London, Special Publications*, **541**(1), https://doi.org/10.1144/SP541-2023-17

Webb, S., Torvela, T., Chapman, R., Selby, D. and Gooday, R. 2024b. A reinterpretation of the mineralisation processes involved in the formation of the Tomnadashan sulphide deposit, Loch Tay. *Scottish Journal of Geology*, **60**, https://doi.org/10.1144/sjg2023-023

The paragenetic interpretations of Tomnadashan and the Glen Almond Vein presented in these papers have been replicated in Chapters 5 and 6. Furthermore, passages from Webb *et al.* 2024a have been paraphrased to describe the methodology and limitations of characterising the paragenesis of a hydrothermal vein, as well as in Chapter 7, where a passage regarding the implications of the paragenetic interpretation of the Glen Almond Vein has been adapted from the source material. The contributions of the various co-authors of these publications are as follows:

Webb *et al.* 2024a

Shane Webb: conceptualization (equal), data curation (equal), formal analysis (equal), visualization (supporting), writing – original draft (equal), writing – review & editing (supporting); *Taija Torvela*: conceptualization (equal), data curation (equal), formal analysis (supporting), supervision (lead), visualization (lead), writing – original draft (equal), writing – review & editing (lead); *Rob Chapman*: conceptualization (supporting), data curation (supporting), formal analysis (equal), visualization (supporting), writing – original draft (supporting), writing – review & editing (supporting); *Lucia Savastano*: data curation (supporting), formal analysis (equal), writing – review & editing (supporting).

Webb *et al.* 2024b

Shane Webb: conceptualization (lead), data curation (equal), formal analysis (equal), visualisation (equal), writing – original draft (lead), review & editing (lead); *Taija Torvela*; conceptualisation (supporting), data curation (equal), formal analysis (equal), visualisation (equal), writing – original draft (equal), review & editing (supporting), supervision (lead); Rob Chapman; data curation (supporting), formal analysis (equal), visualisation (supporting), writing – original draft (supporting), review & editing (supporting); *Bob Gooday*; data curation (supporting), formal analysis (equal), visualisation (supporting), writing – original draft (supporting), review & editing (supporting); David Selby; formal analysis (equal), writing – original draft (supporting), review & editing (supporting)

Acknowledgements

Thanks go to my primary supervisor, Dr Taija Torvela, and my other supervisors, Dr Rob Chapman, Dr Jason Harvey, and Dr Daniel Morgan, who have been of invaluable assistance in my aim of getting a PhD. Thanks to Dr Bob Jamieson for helping with the sulphur isotope analyses, and Lucia Savastano for her contributions in writing the paragenesis paper. Thanks to Dr Richard Walshaw for training me on the SEM, and Harri Wyn Williams for helping with the preparation of thin sections. I also want to thank the NERC Panorama DTP for funding my studentship over the last 3.5 years.

Thanks to the staff at the British Geological Survey and the Scottish Universities Environmental Research Consortium (Dr Matt Horstwood, Dr Simon Tapster, Dr Vanessa Pashley, Professor Adrian Boyce, Mr Andrew Tait, Dr Rona McGill, and Dr Laura Hepburn) for their contributions to the analyses in this PhD, which were awarded under NEIF grant 2649.0423. Thanks to the various members of staff at National Museums Scotland (Dr Rachel Walcott, Dr Bob Gooday, Peder Aspen, and others) and the National Museum of Wales (Andrew Haycock and Tom Cotterell) for providing samples. Thanks to Professor David Selby for his support with the Re-Os dating. Thanks to Green Glen Minerals for allowing access to the field. Special thanks go to Dr Stephen Moreton for providing a sample of molybdenite from Tomnadashan and Nature Scotland for allowing me to sample there.

Lastly, I want to thank the School of Earth and Environment at the University of Leeds for providing me with a supportive environment in which to conduct my research. Thanks to the various people who have been influential in my academic career; Professor Dick White and Dr Nick Gardiner at the University of St Andrews, as well as my MSc dissertation supervisor, Dr John Cunningham, from Birkbeck College London. Thanks to Dr Paul Anderson, my undergraduate dissertation supervisor at the University of Birmingham, a project that ultimately inspired me to pursue economic geology.

I want to thank my family, in particular my mother, Mary Anne Webb, for supporting my academic endeavours.

Abstract

The southern margin of Loch Tay, which encompasses a 100 km^2 portion of the Scottish Grampians, hosts several polymetallic veins that consistently trend 120-140 ° and were initiated contemporaneously during the Caledonian Orogeny. At Lead Trial and Tomnadashan, the veins crosscut granitoids, whereas several other veins throughout the region are hosted in metasediments. To characterise some aspects of the mineral system (the ages of mineralisation and magmatism, and potential sources of mineralising fluids), an integrated approach involving geochronology (Re-Os, U-Pb), isotope geochemistry ($\delta^{34}S$, Pb) and petrography was implemented.

Petrographic characterisation has enabled the construction of novel parageneses for Lead Trial, Tomnadashan, and the Glen Almond Vein. The paragenesis of Tomnadashan demonstrated that molybdenite occurs in the second paragenetic stage out of six, indicating that the Re-Os dates (c. 425-417 Ma) pertain to the initial mineralisation processes at this locality. CA-ID-TIMS U-Pb dates of zircons from four granitoids throughout the Loch Tay region yielded ages of c. 420-418 Ma. These datasets demonstrate that mineralisation and magmatism around Loch Tay are coeval. This interpretation is supported by the $\delta^{34}S$ values and Pb isotope ratios recorded from the mineralisation at Lead Trial and Tomnadashan, which are typical of magmatic-hydrothermal processes. However, the $\delta^{34}S$ and Pb datasets also indicate a crustal contribution to the mineralising fluids associated with the metasediment-hosted veins.

The results have been used to interpret a metallogenic model for Loch Tay; mineralisation around Lead Trial and Tomnadashan involved a fluid that was derived from I-type granites. However, the genesis of the metasediment-hosted veins was linked to a fluid that developed as a result of mixing between magmatic and crustal sources of sulphur (e.g. the Dalradian Supergroup). The isotope datasets are indicative of at least two mineralisation events around Loch Tay, although the age of the metasediment-hosted veins remains unknown.

Table of Contents

List of Tables

List of Figures

Abbreviations

(aq)	Aqueous
BGS	British Geological Survey
BSE	Backscatter electron
BSR	Bacterial Sulphate Reduction
CDR	Controlled dissolution reaction
CL	Cathodoluminescence
CSF	Crustal-scale Fault
CUB	Calliachar-Urlar Burns
$D_{(1-4)}$	Deformation events
EDS	Energy Dispersive Spectroscopy
EDX	Energy-dispersive X-ray analysis
EMPA	Electron Microprobe Analyses
FA	Forearc
FT1	Fluid Type 1
FT2	Fluid Type 2
(g)	Gaseous
g/t	Grams per tonne
Ga	Gigaannum
GAV	Glen Almond Vein
GGM	Green Glen Minerals
kbar	Kilobar
km	Kilometre
LA-ICP-MS	Laser Ablation Inductively Coupled Plasma Mass Spectrometry
ln	Natural logarithm
LTVS	Loch Tay Vein System
LTF	Loch Tay Fault
M	Molarity
m	Metre
Ma	Million years
mbar	Millibar
MC-ICP-MS	Multi Collector Inductively Coupled Plasma Mass Spectrometry
mol	Mole
mol/kg	Mole per kilogramme
mol %	Mole percent
Moz	Million ounces

MSA	Mineral Systems Approach
MSWD	Mean square of weighted distributions
MVT	Mississippi Valley Type deposit
Nd: YAG	Neodymium-doped yttrium aluminium garnet
NMS	National Museums Scotland
NMW	National Museum of Wales
OGD	Orogenic Gold Deposit
P	Pressure
PGE	Platinum Group Element
ppb	Parts per billion
ppm	Parts per million
p(x^2)	p chi squared
RLM	Reflected Light Microscopy
rpm	Revolutions per minute
SD	Standard Deviation
SEDEX	Sedimentary exhalative deposit
SEM	Scanning Electron Microscopy
SHOG	Sediment-hosted Orogenic Gold
SIMS	Secondary Ion Mass Spectrometry
SLTD	Syn- to Late Tectonic Dispersed
SUERC	Scottish Universities Environmental Research Centre
TIMS	Thermal Ion Mass Spectrometry
TSR	Thermomechanical sulphate reduction
V-CDT	Vienna-Canyon Diablo Troilite
wt %	Weight percent
‰	Per mille
α	Isotopic fractionation factor
Δ	Change/difference
κ	Kappa
μ	Mu
μg/kg	Microgram per kilogram
μl/min	Microlitre per minute
μm	Micrometre
ω	Omega
σ	Sigma

Mineral abbreviations and formulas

In tables and figures, mineral names have been shortened to International Mineralogical Association abbreviations (Warr, 2021). * indicates an abbreviation unique to this thesis.

Mineral	Abbreviation
Actinolite	Act
Adularia*	Adl
Albite	Ab
Alunite	Alu
Ankerite	Ank
Apatite	Ap
Arsenopyrite	Apy
Azurite	Azu
Barytes	Brt
Bismuth telluride	BiTe
Bornite	Bn
Calcite	Cal
Carbonate*	Carb
Chlorite	Chl
Covellite	Cv
Chalcocite	Cc
Chalcopyrite	Ccp
Cubanite	Cbn
Diopside	Di
Dolomite	Dol
Electrum*	El
Enargite	Eng
Epidote	Ep
Freiburgite	Fb
Fuchsite*	Fch
Garnet	Grt
Galena	Gn
Hematite	Hem
Hessite	Hes
Hornfels*	Hnf

Illite	Ilt
Ilmenite	Ilm
Jasper*	Jasp
Kaolinite	Kln
K-feldspar	Kfs
Limonite*	Lm
Luzonite	Luz
Magnetite	Mag
Malachite	Mlc
Mca	Mica
Millerite	Mlr
Molybdenite	Mol
Monazite	Mnz
Pentlandite	Pn
Pyrite	Py
Pyrophyllite	Prl
Pyrrhotite	Pyh
Olivine	Ol
Quartz	Qz
Rutile	Rt
Sericite*	Ser
Serpentine group	Srp
Siderite	Sd
Silicate*	Sil
Sphalerite	Sp
Sphene*	Ttn
Smectite	Sme
Sulfosalts*	Ss
Sylvanite	Syv
Talc	Tlc
Tennantite	Tnt
Tetrahedrite	Ttr
Zircon	Zrn

Chapter 1: Introduction

The southern margin of Loch Tay (Fig. 1.1.), which is located in the Perthshire region of Scotland, hosts several gold and base metal deposits (herein referred to as the 'Study Area'; Fig. 1.1.b.). These occurrences of mineralisation have been exploited by artisanal miners over the past few hundred years (Ordernheimer, 1840; Thost, 1860; Henwood, 1871). Tomnadashan and Coire Buidhe were worked for copper and silver during the 19th century (Pattrick, 1984), whilst around the town of Aberfeldy (Foss; Fig. 1.1.b.), barytes has been mined from a Neoproterozoic sedimentary exhalative (SEDEX) deposit since the 1970s (Moles *et al.*, 2014). Lead excavation occurred at the locality known as 'Lead Trial' (Fig. 1.1.b.) in the 19th century (Ordernheimer, 1840). However, the auriferous potential of this prospect is currently being investigated by Green Glen Minerals (formerly Erris Gold Resources), who have reported gold grades of 4.44 g/t over an interval of drill core measuring 1.65 m (Green Glen Minerals, 2021). The Calliachar Burn and the Urlar Burn (collectively referred to as the 'Calliachar-Urlar Burns', or CUB; Fig. 1.1.b.) both contain auriferous quartz veins that were explored by Colby Gold plc in the 1980s and 1990s (Ixer *et al.*, 1997). Several other localities throughout the Study Area have also been the focus of commercial gold exploration; some examples include Tombuie (Corkhill *et al.*, 2010), Invergeldie, and Fortingall (Naden *et al.*, 2010).

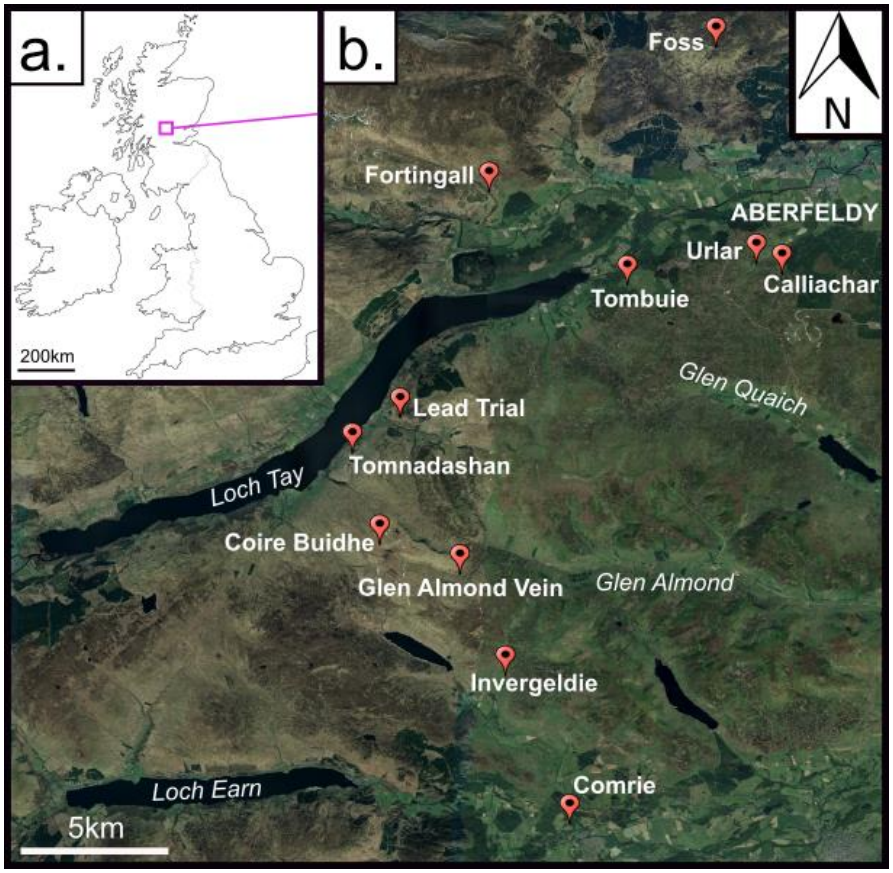

Figure 1.1. Maps of the Study Area. **a.** Outline map of the UK (Ordnance Survey, 2016) depicting the location of Loch Tay (purple box) and **b.** Localities of interest (Google Earth, 2023).

Around Loch Tay, mineralisation is hosted within the Dalradian Supergroup of the Grampian Terrane. There are other occurrences of auriferous veins in this terrane, some of which have been mined in recent years (Cavanacaw and Cononish; Parker and Pearson, 2012; Scotgold, 2022; 2023) or are awaiting the results of a planning application (Curraghinalt; Dalradian Resources, 2018). Geochronological analyses have confirmed an association between these localities and the Caledonian Orogeny (Rice *et al.,* 2012; 2016). Despite commercial interest in the mineralisation around Loch Tay, further exploration is hampered by a lack of understanding regarding the genetic relationships between the different mineral deposits, the potential role of magmatism in the mineralisation processes, and the temporal evolution of the metallogenic system locally. Veins throughout the Study Area (collectively termed the 'Loch Tay Vein System', or LTVS) consistently trend NW-SE (120-140 °; Corkhill *et al.*, 2010) and are typically hosted in structures (e.g. joints) associated with the Loch Tay Fault (LTF), potentially indicating contemporaneous initiation during the same dilatational episode. However, there are no published geochronological ages for mineralisation at any of the localities within the LTVS. Furthermore, it is possible that later mineralisation events may have affected some structures but not others. The Siluro-Devonian granitoids, which are cross-cut by the NW-SE trending suite of veins at Lead Trial and Tomnadashan, have also never been dated and it is therefore unknown whether any of them are coeval with the mineralisation.

Previous research has suggested that the formation of auriferous veins throughout the Grampian Terrane of Scotland (which encompasses the LTVS) is linked to processes associated with the Caledonian Orogeny (Simpson *et al.*, 1989; Ixer *et al.*, 1997; Corkhill *et al.*, 2010; Tanner, 2014a; Rice *et al.*, 2018). Whilst gold deposits are known to form during orogenic cycles, the source of the mineralising fluids is a point of contention at many auriferous veins hosted in orogenic belts globally, with magmatic and metamorphic ('orogenic') sources being postulated in the search for a unifying genetic model (Goldfarb and Groves, 2015; Mortensen *et al.*, 2022; Goldfarb and Pitcairn, 2023). This debate extends to Loch Tay, where previous research has described magmatic (Pattrick, 1984; Corkhill *et al.*, 2010) and 'orogenic' mineralising fluids (Ixer *et al.*, 1997).

1.1. Background and rationale

This study has sought to resolve the previously outlined genetic uncertainties of the LTVS through an integrated approach involving geochronology and stable isotope geochemistry. Furthermore, context for these analyses has been provided by undertaking detailed petrographic characterisation. Whilst the results of this study are likely to assist in the formulation of superior exploration strategies locally, the approach itself may provide a template for resolving similar metallogenic issues in other geological settings. A superior understanding of the metallogeny around Loch Tay (including the gold mineralisation processes that have occurred at recently discovered localities, such as Lead Trial and the GAV) has been developed by completing the following aims:

- To create paragenetic interpretations for several localities in the Study Area.
- To determine the age of some of the mineralisation in the LTVS.
- To develop an understanding of the age of magmatism around Loch Tay.
- To evaluate the source and conditions of the mineralising fluids involved in episodes of gold mineralisation throughout the LTVS.

These aims, as well as the research questions and hypotheses they pertain to, are explored further in Section 3.7., following an in-depth review of pre-existing studies that are relevant to the LTVS.

1.2. Structure of the PhD thesis

The following section provides an executive summary of the content of each chapter in the thesis.

Chapter 2 – Genetic models for gold mineralisation

Many occurrences of gold mineralisation around the world have well-established genetic models, some of which may be relevant to the Study Area. Here, a detailed review of the characteristics and genetic models of orogenic, porphyry, and epithermal deposits is provided. Typical processes involving the transportation and deposition of auriferous mineralising fluids are also summarised. Furthermore, the theoretical principles behind the application of the different isotope systems (U-Pb, Re-Os, $\delta^{34}S$, and Pb) in this study are explored.

Chapter 3 – Geological background of the Study Area

Loch Tay is situated within the Grampian Terrane, which was shaped to a large extent by the Caledonian Orogeny. This event is directly responsible for many occurrences of gold mineralisation throughout Scotland and Ireland. In this chapter, the major depositional, magmatic, and structural episodes of the Grampian Terrane are described, with particular attention given to the Caledonian Orogeny itself. The

chapter ends with a discussion of the research questions, hypotheses, and aims of this study, which are all contextualised by the literature review that comprises the first three chapters of the thesis.

Chapter 4 – Methodologies

The nature of this research is multidisciplinary, combining techniques from different aspects of geoscience to better understand the mineralisation processes locally. The methodical approach towards characterising the paragenesis of hydrothermal veins (Webb *et al.*, 2024a) is summarised, as are the procedures that were used to conduct the isotope analyses in this study. Limitations and uncertainties regarding these procedures are outlined in a separate section at the end of the chapter.

Chapter 5 – Observations and results

This chapter begins by outlining the results of the geological field campaigns that were conducted in 2021 and 2022. In this chapter, the observations from the petrographic studies on the granitoids and veins are presented. Quantitative data from the Re-Os, U-Pb, $\delta^{34}S$, and Pb analyses are also provided.

Chapter 6 – Interpretation

The results from the previous chapter are directly followed with an interpretation of the data. This includes the presentation of charts showing the paragenesis of mineralisation at Tomnadashan, Lead Trial, and the Glen Almond Vein (GAV).

Chapter 7 – Discussion

In this chapter, the implications of the results are discussed within their wider geological context, which was introduced in Chapters 2 and 3. The results have particular relevance for establishing the source and nature of the mineralising fluids involved in the formation of the LTVS. A detailed discussion regarding the implications of the ages of mineralisation and magmatism locally, as well as the parageneses of the different veins, is also provided. This information is synthesised to produce a preliminary genetic model for the mineralisation processes in the LTVS.

Chapter 8 – Conclusions

The main findings of this study are summarised, along with recommendations for further research.

Chapter 2: Genetic models for gold mineralisation

2.1. Introduction

Given that the genetic model for the LTVS is unknown, it is necessary to provide an overview of the processes that form gold deposits in similar tectonic settings (some of which are shown in Fig. 2.1.), as well as the relevant mechanisms for the transportation and deposition of mineralising fluids.

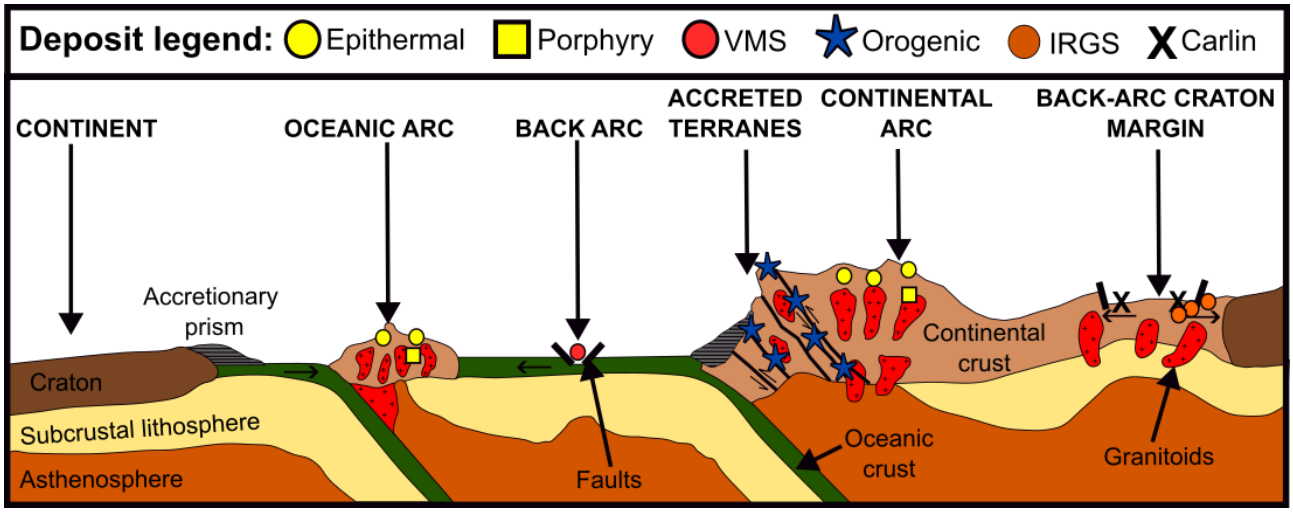

Figure 2.1. Examples of the tectonic settings in which gold deposits form (Groves *et al.*, 2003). VMS = Volcanogenic Massive Sulphide, IRGS = Intrusion Related Gold Systems.

The conceptualisation of the formation of ore deposits has evolved over time. Historically, deposit classification involved describing styles of mineralisation according to their mineralogy, host rocks, and geographic location, which resulted in over ninety categories of ore deposits being recognised (Cox and Singer, 1986). In the 20th century, researchers began to relate the precipitation of metalliferous minerals to specific environments, and classified ore deposits according to pressure, temperature, and depth (Lindgren, 1933). Names such as 'mesothermal' (emplaced at depths of 1.5-3 km) and 'hypothermal' (mineralisation at depths of >3 km) were applied to various deposits (Lindgren, 1933). In recent years, there has been an emphasis on the 'Mineral Systems Approach' (MSA); this concept postulates that ore deposits are not isolated phenomena and instead represent the result of geological processes operating over various spatial and temporal scales (McCuaig *et al.*, 2010; McCuaig and Hronsky, 2014; Joly *et al.*, 2015). For this reason, it is necessary to conceptualise ore deposits in terms of their fluid characteristics, transportation pathways, and trap-scale processes that result in metal precipitation; collectively, this information is required to establish genetic relationships and therefore determine whether there is a single mineral system (or multiple overprinting mineral systems) in a given area.

2.2. Genetic models for gold mineralisation in orogenic belts

Features	**Orogenic** (Ridley and Diamond, 2000; Goldfarb *et al.*, 2001)	**Porphyry** (Berger *et al.*, 2008; Sillitoe, 2000; 2010; Prokofiev and Naumov, 2022)	**High sulphidation epithermal** (Simmons *et al.*, 2005)	**Low sulphidation epithermal** (Simmons *et al.*, 2005)
Description	Qz ± Carb veins in deformed metamorphic terranes	Qz ± Carb veinlets/disseminations in igneous intrusions, along with sulphide mineralisation	Open-space filling in breccias, mineralisation with an irregular geometry	Disseminated mineralisation in subvertical fractures
Geological setting	Accretionary orogens	During or after oceanic lithosphere subduction	Magmatic arcs under neutral to mildly extensional stress	Post collisional rifting of a magmatic arc
Structural controls	Lower-order crustal scale structures associated with transcrustal faults	Pre-existing structural controls are not an essential prerequisite for porphyry formation	Control may be structural, lithological, or hydrothermal	Mainly structural; lithological or hydrothermal controls are less important
Mineralisation	Apy, Py, Pyh	Hypogene ore; Ccp, Mol, Cc, Bn, Py, Gn, Tnt, Trt, Eng, native gold	Py, Eng, Luz, Cv	Apy, Pyh, Sp, Py, Gn, El
Mineralising fluids	Low salinity (3-7 wt % NaCl), CO_2 rich (8-60 mol %), neutral pH	Oxidised, hypersaline (>0.1-88 wt % NaCl, average salinity is 29 wt % NaCl)	Reduced, acidic pH values, salinity is relatively high (< 5-20 wt % NaCl)	Oxidised, neutral pH values, low salinity (< 5 wt % NaCl)
Alteration	Ser + Ab + Carb + Chl (dependent on host lithology)	Varied; potassic, phyllic, sericitic and propylitic alteration haloes	Alu + Prl + Di + Kln	Qz + Adl + Carb + Ilt
Temperature	250-350 °C	350-700 °C	200-300 °C	100-200 °C

Table 2.1. Typical characteristics of various genetic models that may be relevant to the mineralisation around Loch Tay. The mineral abbreviations are from Warr (2021) and are listed in full on Pg. xxvii.

Around Loch Tay, previous research has referred to the following genetic models; orogenic (Ixer *et al.*, 1997), porphyry (Pattrick, 1984), and epithermal processes (Corkhill *et al.*, 2010). A review of the literature describing these genetic models (Table 2.1.) is therefore necessary. The composition of mineralising fluids associated with orogenic, epithermal and porphyry mineralisation has been characterised by fluid inclusion studies on ore deposits globally; the typical fluid composition of each deposit style is shown in Fig. 2.2.

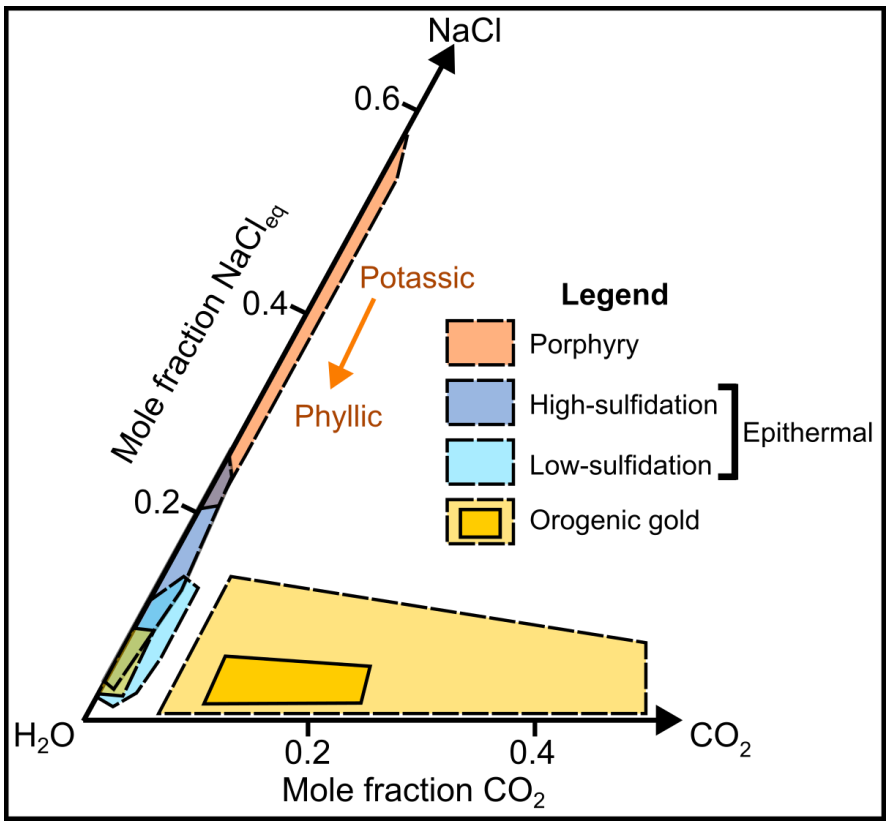

Figure 2.2. Compositional characteristics of mineralising fluids from different gold deposit styles that may be present around Loch Tay (adapted from Ridley and Diamond, 2000). Data for porphyry and epithermal mineralisation were reproduced from Hedenquist and Lowenstern (1994). Regarding 'Orogenic gold', the solid line represents the compositions that are considered by Ridley and Diamond (2000) to be typical of this deposit style, whilst the dashed line encompasses occurrences of orogenic gold from outside of this range.

2.2.1. ‘Orogenic’ gold

The term ‘orogenic gold deposit’ (OGD) is used to describe auriferous veins that are hosted by geological structures within deformed metamorphic terranes (Table 2.1.). Whilst the typical tectonic settings of OGDs are depicted in Fig. 2.1., OGDs may also form within back-arc metamorphic settings (Goldfarb *et al.*, 2001; Goldfarb and Pitcairn, 2023) during compressional inversion (i.e. the reverse reactivation of extensional normal faults due to crustal shortening; Ziegler, 1987). OGD mineralisation has occurred throughout the breadth of geological time, although most commercially viable deposits are Archean in age (Groves *et al.*, 1998; Goldfarb *et al.*, 2001). The youngest OGDs date to the Cenozoic (e.g. Pingfengshan, Taiwan; Craw *et al.*, 2010). A wide range of vein textures (comb, cockade, crustiform, and colloform) may be associated with OGDs (Groves *et al.*, 1998; Goldfarb *et al.*, 2001; Goldfarb *et al.*, 2015), with mineralisation occurring at depths of 3 to 20 km (Fig. 2.3.).

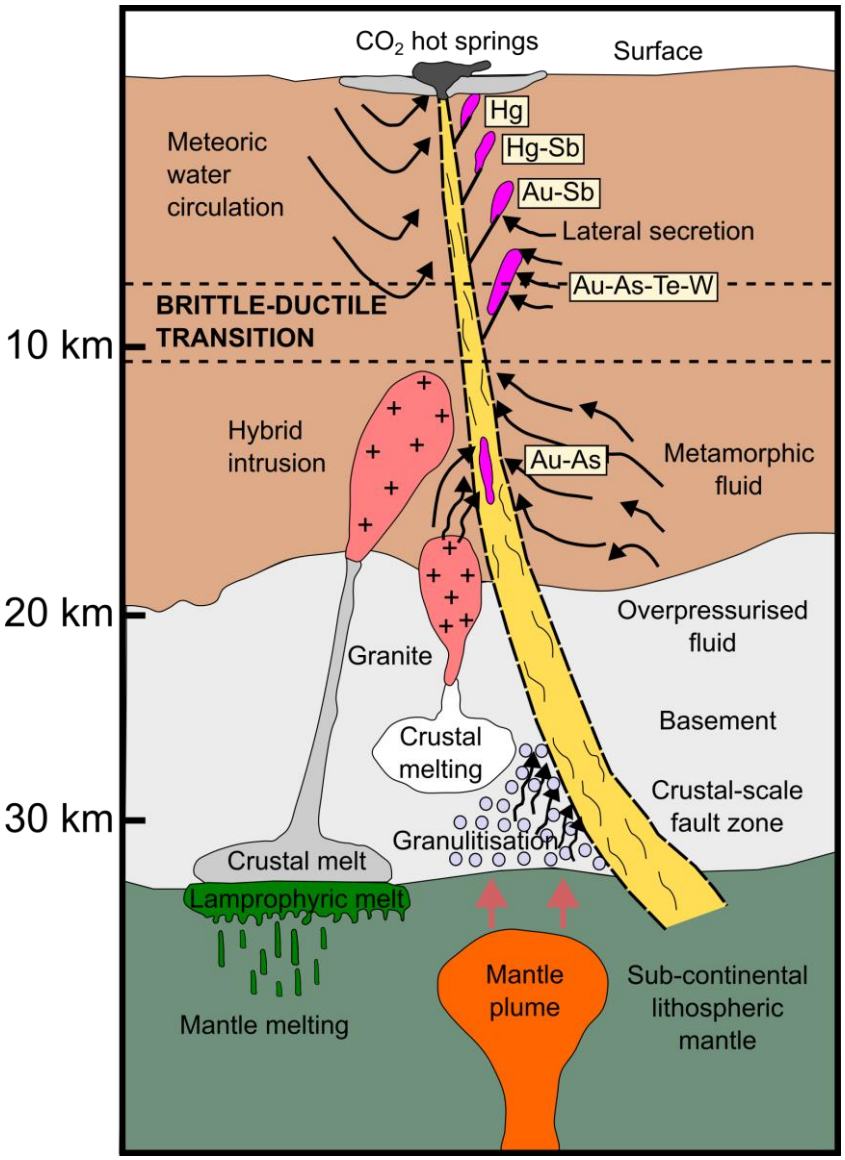

Figure 2.3. The crustal continuum model, which shows the proposed fluid sources for OGDs at different depths in the continental crust (Groves, 1993; Goldfarb *et al.*, 2005).

As shown in Fig. 2.3., several fluid sources have been suggested for OGDs; however, it is consistently advocated that the mineralising fluids are not predominantly magmatic (Tomkins, 2013; Goldfarb and Groves, 2015; Gaboury, 2019) and are therefore different from porphyry deposits in this regard (Goldfarb and Pitcairn, 2023). A detailed discussion regarding the potential fluid sources of OGDs is undertaken in Section 2.3. Regardless, fluid inclusions are important for understanding the characteristics of mineralising fluids associated with OGDs; in the following paragraphs, the results of previous studies on fluid inclusions from OGDs are summarised.

In terms of composition, OGD mineralising fluids are mostly comprised of H_2O, NaCl, and CO_2; fluid inclusions typically indicate low salinities and near neutral pH values (Table 2.1.; Fig. 2.2.; Garofalo *et al.*, 2014; Goldfarb and Groves, 2015). Regarding salinity, Na is usually the most abundant cation, followed by K, which occurs in higher concentrations relative to both Mg and Ca (Goldfarb and Groves, 2015). However, K is usually saturated in the fluid to a greater extent than Na; the precipitation of muscovite and potassium feldspar is therefore more typical than albite (Kerrich and Fyfe, 1981; Goldfarb and Groves, 2015). The pH of mineralising fluids associated with OGDs is usually between 5.5 and 7 (Neall and Phillips, 1987; Gibert *et al.*, 1992; Ridley and Diamond, 2000). Furthermore, fluid inclusions from OGDs consistently record elevated CO_2 concentrations of >5 mol %, with typical $\delta^{18}O$ values being +8-10 ‰ (Groves *et al.*, 1998; Goldfarb *et al.*, 2001). Several publications have estimated the H_2S contents of orogenic fluids as encompassing a range of between 0.01 and 0.36 mol % (Bottrell and Miller, 1989; Goldfarb *et al.*, 1989; Yardley *et al.*, 1993; Mernagh and Bastrakov, 2013), which is similar to the quantities of H_2S that have been measured from fluid inclusions within quartz veins in the Alps of Europe (0.006 to 0.18 mol %; Rauchenstein-Martinek *et al.*, 2014; Goldfarb and Groves, 2015). The oxygen fugacity of orogenic fluids is typically below the hematite-magnetite buffer (Phillips, 1993; Phillips and Powell, 1993; Phillips and Evans, 2004; Goldfarb and Groves, 2015). Orogenic fluids may also contain a wide range of hydrocarbons (e.g. C_2H_4 or HCO_3^-; Channer and Spooner, 1994; Goldfarb *et al.*, 1989; Guha *et al.*, 1990; Gaboury, 2013), although the presence of hydrocarbons in orogenic fluids may be the result of reactions between volatiles (C-, O-, and H-) during rapid uplift (Tsunogae and Dubessy, 2009; Goldfarb and Groves, 2015).

The characteristics of fluid inclusions from OGDs (Table 2.1.; Fig. 2.2.) have remained relatively consistent over geological time (Ridley and Diamond, 2000; Garofalo *et al.*, 2014; Goldfarb and Groves, 2015; Hodgson and MacGeehan, 1982; McCuaig and Kerrich, 1998; Ridley and Diamond, 2000). However, it is important to emphasise that there is some variability regarding the H_2O, CO_2, and CH_4 contents of the mineralising fluids (Fig. 2.2.; Ridley and Diamond, 2000; Fu *et al.*, 2012; Lawrence *et al.*, 2013; Goldfarb and Groves, 2015). The variations in composition are usually explained in the context of pressure decreases that occur during the transportation of hydrothermal fluids (see Section 2.6.). For example, depressurisation and unmixing of an aqueous carbonic fluid may cause phase separation and the development of a vapour phase comprised of 70 % CO_2 (or even pure CO_2; White *et al.*, 2015; Goldfarb and Groves, 2015). Unmixing associated with

pressure decreases can also increase the salinity of mineralising fluids (due to the loss of the vapour phase; Neumayr and Hagemann, 2002). Furthermore, some of the variations in mineralising fluids associated with OGDs are related to the age of the deposit; for example, the CO_2 content of mineralising fluids involved in the formation of Phanerozoic OGDs may be slightly higher than the values recorded from fluids associated with Precambrian OGDs (Ridley and Diamond, 2000; Goldfarb and Groves, 2015). In addition, Prokofiev *et al.* 2020a reviewed fluid inclusions from 275 OGDs and noted that Precambrian deposits recorded median salinities of 6.1 wt % NaCl, whilst Phanerozoic OGDs are typified by values of 3.8 wt % NaCl (Prokofiev *et al.*, 2020a). Fluid inclusions from Precambrian OGDs also typically documented higher pressures (1680 bar) relative to the Phanerozoic iterations (1305 bar), indicating that older OGDs may have formed at greater depths in the crust (Prokofiev *et al.*, 2020a).

Regarding the relevance of Archean OGD genetic models to the LTVS, it is important to note that the physiochemical conditions on the Precambrian Earth were significantly different from those in the Phanerozoic (Mortensen *et al.*, 2022). For example, the 'single lid' tectonic regime that was active throughout the Archean (Stern, 2020) is not comparable to Phanerozoic plate tectonics (Mortensen *et al.*, 2022). Furthermore, the Great Oxygenation Event at c. 2400 Ma had yet to occur and the oxidation state of the oceans was lower, meaning that the Au concentration of seawater in the Archean was higher than it was throughout the Phanerozoic (Large *et al.*, 2015). The combination of different global tectonic regimes and ocean chemistry means that the conditions of sediment deposition were different in the Precambrian Earth (Mortensen *et al.*, 2022); Archean oceans experienced more volcaniclastic input and there was no carbonate precipitation or accumulation of organic carbon on continental shelves (Gaboury, 2019). In light of the previously outlined differences between OGDs from the Precambrian and Phanerozoic, genetic models of OGD mineralisation pertaining to the former are judged to be of limited relevance to the Grampian Terrane. Instead, the focus of this review is on Phanerozoic occurrences of 'orogenic' gold mineralisation.

2.2.1.a. Phanerozoic OGDs

The concept of a distinct Phanerozoic classification of OGD is controversial, given that the same generic principles of physics and chemistry should apply to OGDs of all ages (Mortensen *et al.*, 2022). Nonetheless, based on contemporary tectonic settings, 4 subtypes of Phanerozoic OGDs were proposed by Mortensen *et al.* 2022; crustal-scale fault (CSF), sediment hosted orogenic gold (SHOG), forearc (FA), and syn- and late tectonic dispersed (SLTD). The characteristics of these subtypes are summarised in Table 2.2. However, all Phanerozoic OGD subtypes may display a close spatial association with graphitic units (unlike Precambrian OGDs), which may in some cases act as a reductant for the mineralising fluids (Cox *et al.*, 1995; Craw *et al.*, 1999; Bierlein *et al.*, 2001; Hu *et al.*, 2015; Gaboury, 2019).

Subtype	CSF (crustal-scale fault)	SHOG (sediment-hosted orogenic gold)	FA (Forearc)	SLTD (syn- and late-tectonic dispersed)
Style	Ribbon-banded Qz ± Carb veins	Qz ± Carb saddle reefs, vein faults/breccias, disseminated	Ribbon-banded Qz ± Carb veins, Qz fissure veins, mineralised shear zones with low grade disseminated haloes	Qz ± Carb fissure veins; less abundant fault veins, large quantities of alluvial gold
Host rocks	Variable, depending on the location along major fault zones	Thick sequences of fine-grained, variably carbonaceous, thin-bedded clastic rocks	Fine to medium-grained, non-carbonaceous and carbonaceous metaclastic rocks	Variable: gold grades may be correlated with specific reactive lithologies
Structural controls	Transcurrent faults at crustal, secondary, and tertiary scales	Saddle reefs, wing veins in anticlinal folds; fault veins, breccias in high angle faults; disseminated mineralisation	Extensional fault arrays; brittle–ductile shear zones (tens to hundreds of metres thick)	Extensional fracture arrays through the brittle portions of the crust
Tectonic setting	Active orogenic belts, transpressive terrane sutures	Uncertain; back-arc and syn- to late-tectonic settings recognised	Active forearcs	Active collisional and transpressional orogens
Relative timing	Syn- to late-tectonic	Associated with discrete periods of deformation and metamorphism	Form in foreland complexes during subduction, ridge subduction events	Syn- to late-tectonic; late contractional deformation events
Alteration	Ank in chloritic hosts; Fch in serpentinite hosts	Widespread Fe-Carb ‘spotting’, localised Ser adjacent to veins	Ank at shallower levels (c. 5 km); shallow veins have cm-scale Sil	Minor (cm-m); Ank alteration of chloritic hosts; Ser and Py in wallrock next to veins
Examples	Newfoundland, Sierra Nevada, Caborca	Sukhoi Log, Meguma, South Cariboo	Hillgrove, Chugach	Klondike, Taiwan, potentially the Scottish Grampian

Table 2.2. Principal features of the different Phanerozoic OGD subtypes (adapted from Mortensen *et al.*, 2022). Mineral abbreviations are from Warr (2021) and are listed on Pg. xxvii.

The subtypes described by Mortensen *et al.* 2022 (Table 2.2.) provide a useful overview and context in which to consider the Grampian occurrences of gold mineralisation. The SLTD subtype is the most common style of Phanerozoic OGD globally (Mortensen *et al.*, 2022). Despite their high grades, SLTD OGDs are often too small in size to be commercially viable (Mortensen *et al.*, 2022). Instead, the CSF or SHOG subtypes are more likely to host gold deposits with economic potential (due to their larger sizes; Mortensen *et al.*, 2022). The FA subtype is considered to be the rarest form of Phanerozoic OGD because of the uncommon tectonic setting it represents (potentially sitting on top of a subducting, spreading ridge; Mortensen *et al.*, 2022).

However, it is important to emphasise that Mortensen *et al.* 2022 also recognised several Phanerozoic OGDs that did not fall into any subtype; Jiaodong has several genetic differences with other Phanerozoic OGDs (e.g. the mineralising fluids were derived from a metasomatised mantle wedge). Coffee (Yukon, Canada) is also challenging to classify within the scheme (Table 2.2.) because it displays characteristics of both the SLTD and CSF subtypes (Mortensen *et al.*, 2022); for example, Coffee is spatially associated with a regional strike-slip fault (Allan *et al.*, 2013; Sánchez *et al.*, 2014), as envisioned in the CSF subtype (Table 2.2.). However, gold mineralisation at Coffee is also disseminated throughout the host rocks (MacKenzie *et al.*, 2015; MacWilliam, 2018), which is not typical of CSF deposits (Table 2.2.). Furthermore, Mortensen *et al.* 2022 expressed uncertainty over the relevance of their classification scheme to gold deposits in the Grampian Terrane and suggested that they may not even have any 'orogenic' affinities whatsoever (given the potential link between gold mineralisation and magmatism in Scotland; see Section 3.5.). These examples demonstrate the limitations of attempting to classify Phanerozoic OGDs. Furthermore, Mortensen *et al.* 2022 also noted that it is theoretically possible for several of these subtypes to develop within the same orogenic cycle, meaning that a given geographic location (e.g. the Cariboo Gold District in British Columbia, Canada) can host multiple subtypes as a result of overprinting mineralisation episodes.

2.2.2. Porphyries

Porphyry deposits, which are defined as large volumes of hydrothermally altered rocks associated with the emplacement of porphyry stocks (Sillitoe, 1972; 1973; 2010), are typical features of magmatic arcs that overlie subduction zones (Richards, 2003). However, it is important to make a distinction between porphyry-style mineralisation and the term 'porphyry' as it pertains to igneous rocks (i.e. a rock with porphyritic texture; Sillitoe, 2010). A relatively large list of criteria is required to distinguish porphyry deposits from other magmatic processes that can result in mineralisation. In addition to the characteristics outlined in Table 2.3., porphyry mineralisation is also accompanied by other distinctive textures; for example, mineralisation can be disseminated or occur as stockworks (i.e. a dense collection of randomly oriented veins; Gustafson and Hunt, 1975; Westra and Keith, 1981; Sillitoe, 2010). Furthermore, quartz from porphyry veinlets often shows patterns of concentric zonation in cathodoluminescence (CL) (Penniston-Dorland, 2001).

Feature	Description
1	Cu-bearing sulphides hosted within (or disseminated around) stockworks in upright-vertical cylindrical stocks and/or dyke complexes
2	Typical mineralisation depths of 1-4 km (although some may form at depths of up to 15 km in rarer cases; Sillitoe, 2010)
3	A direct relationship with the emplacement of intermediate to silicic magmas generated in magmatic arcs above a subduction zone
4	Zones of phyllic, argillic and propylitic alteration surrounding a potassic core (although the alteration assemblages can be variable, with some of these haloes being absent)

Table 2.3. Modified list of the features that a mineral deposit must have in order for it to be classified as a porphyry (Berger *et al.* 2008).

In terms of the genetic model for porphyry deposits (Fig. 2.4.), this has been relatively well-constrained by previous studies, and is briefly summarised here. The sources of metals in porphyry deposits are sulphides that formed in VMS and SEDEX deposits within oceanic basins and mid-ocean ridges (Sillitoe, 1972; 1997; 2008; Qu *et al.*, 2004; Butterworth *et al.*, 2016). When the oceanic crust that hosts these VMS sulphides is subducted, metasomatism and partial melting of the mantle wedge occurs, resulting in hydrous, oxidised magmas with the ability to transport metals and sulphur (Richards, 2003).

At the deposit-scale, large volumes of fluid are released from the crystallising pluton to facilitate efficient metal and ligand circulation (Fig. 2.4.b.). The outer 'skin' of the magma touches the country rock first and cools faster, forming a solidified carapace around the central mush (Candela, 1991). Volatiles exist in the interior as bubbles; high degrees of connectivity between the bubbles enables their collective ascent towards the carapace (Wilson *et al.*, 2003). Crystallisation results in vapour pressure that exerts a tensile stress on the carapace, creating fractures through which volatiles migrate and mineralisation occurs (Burnham, 1985). The emplacement of magmatic bodies with temperatures higher than the host rocks may cause thermal disequilibrium and the development of metal zonation (Sillitoe and Thompson, 1998). However, the shallow emplacement depths mean that porphyries are susceptible to removal by erosion (Kesler and Wilkinson, 2008). For this reason, most commercially viable porphyries formed during the Cenozoic (Kesler and Wilkinson, 2008). Numerical modelling and high-precision geochronology indicate that the mineralisation intervals of porphyry mineralisation are typically between 50 and 100 kyr (Ingebritsen and Manning, 2010; von Quadt *et al.*, 2011).

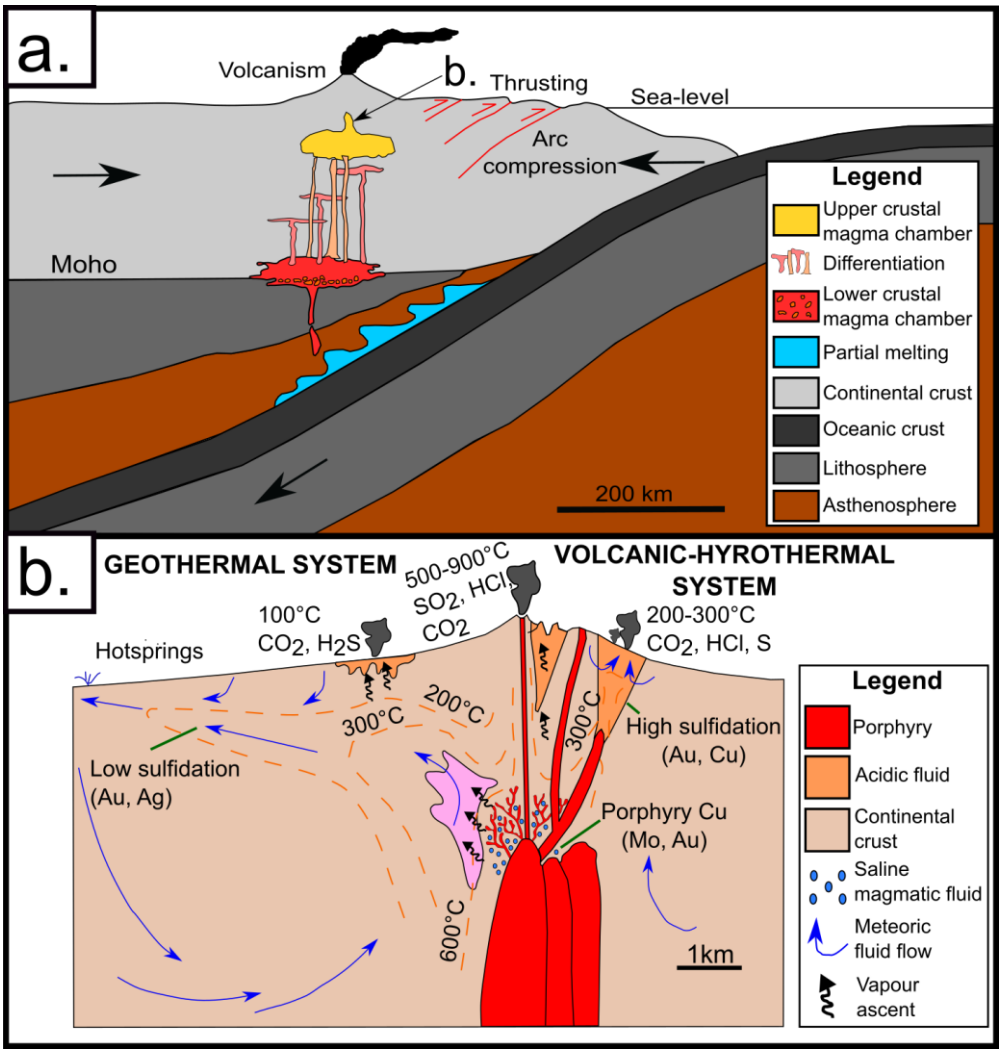

Figure 2.4. Porphyry mineralisation processes**. a.** Geodynamic setting (Park *et al.*, 2021) **b.** Deposit-scale genetic model for porphyry and epithermal deposits (Hedenquist and Lowenstern, 1994).

In terms of fertility, Sillitoe (1998) described the following conditions as being favourable for porphyry formation: inhibited plutonic ascension through the overriding plate, formation of a voluminous magma chamber at shallow depths, high degrees (>95 %) of fractional crystallisation (increasing the likelihood of volatile saturation), inhibited development of multiple stocks (resulting in the concentration of mineralising fluids into a smaller space), and rapid uplift. Wilkinson (2013) suggested that the inhibited ascension of andesitic magmas between 4 and 10 km meant they resided at depths where they could continually be rejuvenated by new magmatic influxes. This in turn increases the likelihood of sulphide saturation, resulting in the production of regions in the magma chamber with high metal concentrations that can be exploited by later aqueous fluids (Wilkinson, 2013). Regarding the role of rapid uplift in generating porphyries, this process is often coincident with stress relaxation and may stimulate the large-scale migration of mineralising fluids (Tosdal and Richards, 2001; Richards, 2003; Gow and Walshe, 2005). Furthermore, rapid uplift and shallow emplacement depths can increase the likelihood of mixing between the mineralising and meteoric fluids, which commonly results in fluid cooling and metal precipitation (Li *et al.*, 2019; Li *et al.*, 2022b). This process is described in more detail in Section 2.7.1.

2.2.3. Epithermal gold deposits

Epithermal mineralisation displays a spatial association with porphyries (Fig. 2.4.b.); deposits often form in back-arc basins and extensional rifts behind the main orogenic belt (Simmons *et al.*, 2005; Tosdal *et al.*, 2009). Epithermal deposits are typically classified as high, intermediate, or low sulphidation, depending on their diagnostic mineralogies and textures (Simmons *et al.*, 2005; Table 2.1.). A wide range of textural features are associated with epithermal gold mineralisation, such as bladed calcite, quartz pseudomorphs and rhombic adularia (Keith and Muffler, 1978; Dong and Morrison, 1995); these textures are produced by fluid boiling (Taylor, 2007).

High sulphidation epithermal deposits form as a result of mineralising fluids migrating away from porphyries (Hedenquist *et al.*, 1994; 1998); these fluids, which have a pH of <2 (Stoffregen, 1987; Hedenquist and Aoki, 1991; Hedenquist and Lowenstern, 1994), cause dissolution and leaching of soluble components (e.g. feldspars) from the host rocks (Heinrich, 2004), leaving a porous silica residue (Stoffregen, 1987; Hedenquist and Lowenstern, 1994). This creation of space may be conducive for the later deposition of Au and Cu-bearing ores (Hedenquist and Lowenstern, 1994). The mineralogy of high sulphidation deposits is characterised by pyrite, enargite, luzonite, covellite, digenite, famatinite, and orpiment (Giggenbach, 1997; Carman, 2003; Einaudi *et al.*, 2003; Table 2.1.). Coarse-grained alunite is also common (Taylor, 2007).

The mineralising fluids associated with high sulphidation epithermal mineralisation, despite being generated in close proximity to porphyry deposits (Arribas *et al.*, 1995; Fig. 2.4.b.), differ compositionally from the fluids involved in porphyry mineralisation. For example, the salinity of fluid inclusions from high sulphidation mineralisation is normally recorded as 5-20 wt % NaCl, whereas values of >20 wt % are more typical of porphyry deposits (Table 2.1.). One explanation for this phenomenon is that the hypersaline brine associated with porphyry mineralisation is too dense to ascend into the shallower zone of epithermal mineralisation (Fig. 2.4.b.; Hedenquist and Lowenstern, 1994). Various fluid inclusion and stable isotope studies have compared the mineralising fluids associated with high sulphidation mineralisation to magmatic vapours (Giggenbach, 1992; Rye, 1993; Albinson *et al.*, 2001; Cooke and Simmons, 2000; Hedenquist *et al.*, 1994).

Low sulphidation deposits, on the other hand, form at greater distances from the volcanic edifice (Fig. 2.4.b.); magmatic fluids only contribute <10 % of the H_2O to the resulting mineralising fluid (Hedenquist and Lowenstern, 1994; Simmons *et al.*, 2005). The fluids involved in the mineralisation processes have low salinities (~5 wt % NaCl; Table 2.1.), near-neutral pH values and contain reduced sulphur (H_2S; Hedenquist and Lowenstern, 1994). These compositional differences (relative to high sulphidation epithermal deposits) may reflect the greater amount of mixing with meteoric water that ensues during transportation over larger distances (Fig. 2.4.b.); meteoric fluids have more neutral pH values and the effects of dilution

potentially act to reduce salinity (i.e. as a result of decreases in ligand availability; Cooke and Simmons, 2000; Einaudi *et al.*, 2003; Simmons *et al.*, 2005). The low salinities are not conducive to the transportation of copper in the CuCl ligand; for this reason, low sulphidation epithermal mineralisation is not typically associated with economic quantities of copper (Hedenquist and Lowenstern, 1994; Hedenquist, 2000; Taylor, 2007). The mineralogical assemblages of low sulphidation deposits may contain arsenopyrite, loellingite, pyrrhotite, sphalerite, galena, and pyrite (Giggenbach, 1997; Einaudi *et al.*, 2003; 2005; Table 2.1.). Alunite in low sulphidation deposits is much finer grained relative to high sulphidation environments (Taylor, 2007). The preservation of carbonates is a key feature that distinguishes low sulphidation deposits from mineralisation of the high sulphidation variety, in which the acidic environment dissolves carbonate minerals (Simmons *et al.*, 2005).

2.2.4. Alteration styles

A wide range of hydrothermal alteration styles (i.e. the alteration of rocks and phases during reactions with hydrothermal fluids; Schwartz, 1959; Burnham, 1962; Giggenbach, 1984) have been described from the different genetic models presented in Section 2.1.; however, they are not necessarily mutually exclusive. For this reason, a collective review of the different hydrothermal alteration processes is provided in this subsection.

OGDs are impacted by a wide variety of hydrothermal alteration styles (Table 2.2.); the alteration processes associated with this genetic model typically involve the exchange of CO_2, K, and S between the wallrock and mineralising fluid (Phillips *et al.*, 1987; Ridley and Diamond, 2000). The alteration assemblage is dependent upon the mineralisation depth, host rock, composition of the hydrothermal fluid, fluid/rock ratio, and number of mineralisation events (Evans, 2010; Li *et al.*, 2022a). For example, OGD mineralisation at epizonal depths (Fig. 2.3.) is likely to involve mixing between a variety of fluid sources of different temperatures (e.g. mixing between metamorphic and meteoric fluids), resulting in disequilibrium between the mineralising fluids and host rocks (Craw *et al.*, 2009). Where disequilibrium occurs, the alteration assemblage may differ from the host rock (Craw *et al.*, 2009; Eilu and Groves, 2001); this is because conditions of disequilibrium are conducive to the dissolution and replacement of pre-existing minerals (Morse and Arvidson, 2002; Craw *et al.*, 2009). In greenschist facies rocks, disequilibrium often involves the replacement of chlorite by ankeritic carbonate (Craw *et al.*, 2009). Sometimes, the type of host rock itself may determine the type of hydrothermal alteration that takes place; iron-rich sedimentary host rocks have a composition that is more conducive to wallrock sulphidation (see Section 2.7.2.) and the formation of pyrite during hydrothermal alteration, whereas in iron-poor carbonaceous rocks, the host rock composition is less favourable (Petrella *et al.*, 2021). Furthermore, the formation of OGDs is likely to take place over several million years and involve multiple mineralisation events, leading to the overprinting of previous alteration assemblages (Goldfarb and Groves, 2015; Li *et al.*, 2022a; Mortensen *et al.*, 2022).

The well-established spatial relationship between alteration haloes (Fig. 2.5.) and porphyries has been exploited as a vector towards economic mineralisation (Sillitoe, 2010). Shortly after emplacement, K^+ metasomatism of upper crustal rocks (at temperatures of 400-600 °C and neutral pH conditions) causes potassic alteration around the porphyry carapace (i.e. the dissolution of preexisting phases and the precipitation of phases with high K contents; Sillitoe, 2010), resulting in an assemblage dominated by alkali feldspar, biotite, and quartz veins (Sillitoe, 2010; Watanabe *et al.*, 2018). Sericite is also common in the potassic alteration zone; furthermore, andalusite has occasionally been documented from the potassic assemblages in some porphyry systems, such as El Salvador (Chile; Gustafon and Hunt, 1975; Proffett, 2009). When the fluids initially involved in the hydrothermal alteration contain high concentrations of Ca^+ or Na^+ ions, sodic or calcic alteration occurs in the zone typically occupied by the potassic halo (e.g. the Yerington Batholith, Nevada) (Duan *et al.*, 2021).

Regarding phyllic alteration, this process is defined as the hydrolysis of aluminous minerals to micaceous phyllosilicates (Wallace and Maher, 2019) and is typically expressed as the quartz-sericite-pyrite assemblage peripheral to the potassic halo (i.e. in the upper levels of the porphyry system; Fig. 2.5.). The transition in alteration style is the result of fluids becoming cooler and more acidic (Seedorff *et al.*, 2005) during the increasing involvement of meteoric fluids at shallower crustal depths (Harris and Golding, 2002).

In terms of the propylitic halo, this assemblage has many similarities with the minerals produced during greenschist metamorphism (Xiao *et al.*, 2018) and often demarcates the most distant reaches of the magmatic-hydrothermal system (Lowell and Guilbert, 1970). Propylitic alteration occurs at temperatures of 200-350 °C in regions where the fluid/rock ratio is lower. Historically, deposit models assumed that propylitic alteration was an isochemical process stimulated by heated meteoric waters (Taylor, 1974), resulting in assemblages dominated by epidote and chlorite. Actinolite and calcite may also be present (Norman *et al.*, 1991). However, propylitic assemblages can also result from the removal of elements in the potassic core (Ca, Fe, and Co) and subsequent addition of these elements to minerals undergoing propylitic alteration (Pacey *et al.*, 2016). In these interpretations, propylitic alteration is more likely to be the result of lateral and upward migrating magmatic fluids equilibrating with the country rock during decreasing fluid/rock ratios as the fluid cools through an interval of 350-200 °C (Norman *et al.*, 1991; Pacey *et al.*, 2016).

Around the volcanic edifice of a porphyry, there is normally an alteration assemblage dominated by kaolinite, dickite, pyrophyllite and alunite (Reed, 1997). This assemblage is termed ‘argillic alteration’ and is subdivided into distinct categories depending on the extent of host mineral breakdown (Meyer and Hemley, 1967; Sillitoe, 2010). The advanced argillic iteration involves the removal of alkali elements from the rocks by acidic fluids with a high fluid to rock ratio (Reed, 1997). Advanced argillic processes are typically the hallmark of high sulphidation deposits (see Section 2.2.3.) and occur directly above the region

of porphyry emplacement. At temperatures <250 °C, the ordinary form of argillic alteration can occur over larger areas surrounding the pluton; this process involves H^+ ion metasomatism (Reed, 1997). This assemblage is characterised by kaolinite, smectite, and illite (Parry *et al.*, 2002; Sillitoe, 2010; Hedenquist and Arribas, 2022).

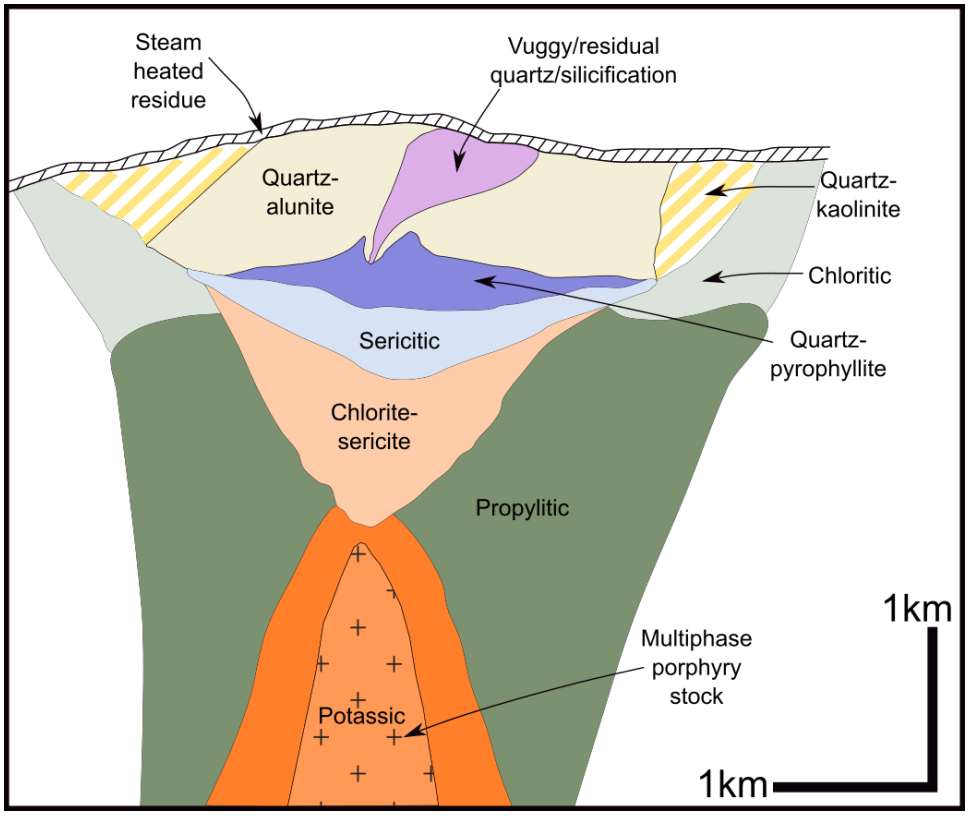

Figure 2.5. Schematic cross-section depicting the different alteration haloes and mineral assemblages associated with the emplacement of a porphyry (Sillitoe, 2010).

2.3. Sources of mineralising fluids in orogenic belts

As depicted in Fig. 2.3., a variety of fluid sources have been proposed for OGDs. However, several researchers have suggested that the OGDs are not predominantly sourced from magmatic fluids, with metamorphic fluids being the most typical fluid source instead (Goldfarb *et al.*, 2001; Phillips and Powell, 2010; Goldfarb and Groves, 2015; Goldfarb and Pitcairn, 2023). Furthermore, OGDs are frequently characterised as 'gold-only', whereas magmatic-hydrothermal deposits are 'gold-plus' and contain high concentrations of other metals (e.g. Cu, Zn, Pb; Table 2.1.; Goldfarb *et al.*, 2005; Richards, 2009; Tomkins, 2013; Goldfarb and Pitcairn, 2023). Nonetheless, magmatic-hydrothermal fluid sources have been postulated at multiple Phanerozoic OGDs globally (Boehlke and Kistler, 1986; Sillitoe and Thompson, 1998; Slobodník *et al.*, 2008; Zachariáš *et al.*, 2013; Goldfarb and Pitcairn, 2023). Given this disagreement in the literature, it is necessary to provide an overview of the potential fluid sources in OGDs. For simplicity, fluid sources associated with OGDs are presented separately from magmatic-hydrothermal fluid sources, which are briefly summarised in the paragraph below.

Whilst it is commonly assumed that porphyry and epithermal deposits have a magmatic fluid source (Fig. 2.4.), the exact nature of this may vary. Hedenquist and Lowenstern (1994) suggested that metals can enter the magmas associated with porphyry and epithermal mineralisation via mantle melting, mass transfer from the subducting slab, and melting of the crust. In Section 2.2.2., the genetic model presented for porphyries assumed that the source of metals may ultimately be pre-existing VMS and SEDEX mineralisation in the oceanic crust, which is broken down and remobilised during subduction (Sillitoe, 1972; Qu *et al.*, 2004; Butterworth *et al.*, 2016). However, there are also other possible metal sources. For example, siderophile elements (Au, Sn, Mo, and PGEs) are typically hosted within the Fe-Ni sulphides that occur in the upper mantle (Lorand, 1990). The process of subduction may stimulate partial melting of the mantle, causing these elements to be released into the newly generated magma (Sillitoe, 1972; Hedenquist and Lowenstern, 1994; Kesler *et al.*, 2002; Tosdal *et al.*, 2009). Alternatively, the crust through which the pluton ascends may also contain high concentrations of metals; assimilation of this material could increase the likelihood of commercially viable deposits forming (Mathur *et al.,* 2000; Chiaradia *et al.*, 2004; Qiu *et al.*, 2017).

2.3.1. Potential sources of mineralising fluids in OGDs

As noted above, whilst a range of fluid sources may be involved in the processes associated with the formation of OGDs, they are not necessarily distinct; it may be possible for OGDs to form from a mixture of different fluids (e.g. mixtures of metamorphic and magmatic fluids; Large *et al.*, 2011; Lawrence *et al.*, 2013; Meyer, 2023). In this subsection, the various interpretations regarding the sources of fluids in OGDs are summarised.

2.3.1.a. Metamorphic fluids

Out of all the different fluid sources depicted in Fig. 2.3., genetic models involving metamorphic fluids are favoured at a majority of OGDs worldwide (Henley *et al.*, 1976; Phillips and Groves, 1983; Goldfarb *et al.*, 2005; Phillips and Powell, 2010; Goldfarb and Groves, 2015; Goldfarb and Pitcairn, 2023). The most commonly postulated model of OGD formation suggests that a mineralising fluid develops during orogenic compression and metamorphic devolatisation processes at the greenschist-amphibolite facies boundary between temperatures of 440 and 520 °C (Equation 1). The reaction outlined in Equation 1 leads to the release of water, which is speculated to scavenge H_2O, CO_2, S, and Au from the sediment pile; this process ultimately results in the formation of a mineralising fluid (Phillips and Powell, 2010).

Chlorite + epidote + ankerite – dolomite + albite + quartz = amphibole + plagioclase + water

Equation 1. Metamorphic reactions during the greenschist-amphibolite transition (Phillips and Powell, 2010).

An alternative model focuses on the role of the pyrite-pyrrhotite reaction (Phillips and Powell, 2010), which occurs during prograde metamorphism under greenschist facies (before the amphibolite transition takes place); this reaction results in the formation of hydrogen bisulphide (Equation 2), which could form metal-ligand complexes with the gold in the metasediment pile. Assuming that the pyrite contains As and Au, the breakdown of this pyrite may release these elements into the solution (Kogan *et al.*, 1994; Tom *et al.*, 1997; Large *et al.*, 2011). OGDs that form from the process described in Equation 2 usually display an association with As (Phillips and Powell, 2010).

$$FeS_2 + H_2O = FeS + H_2S + 0.5O_2$$

Equation 2. The metamorphic reaction involving the transition of pyrite to pyrrhotite (Phillips and Powell, 2010).

Evidence to support this theoretical scenario of 'orogenic' gold mineralisation (Fig. 2.3.; Equations 1 and 2) mostly comes in the form of stable isotope and fluid inclusion data (Goldfarb *et al.*, 2001; Phillips and Powell, 2010; Goldfarb and Groves, 2015; Goldfarb and Pitcairn, 2023). There are several reasons as to why the reactions outlined in Equation 1 are favourable to the generation of the mineralising fluids associated with OGDs (Fig. 2.2). For example, the minerals shown in Equation 1 do not have chlorine in their mineral structures, meaning that the fluids released during metamorphic devolatisation may have low salinities (Phillips and Powell, 2010). Furthermore, the breakdown of ankerite and dolomite (Equation 1) is likely to release a carbonic fluid (Fyfe and Henley, 1973; Norris and Henley, 1976; Phillips and Powell, 2010). However, it should be noted that in a scenario involving the devolatisation of a pelitic sediment pile without the chlorite-bearing assemblages shown in Equation 1, a fluid with lower H_2O and CO_2 quantities is likely to be released (Phillips and Powell, 2010). Lithological variations in orogenic belts globally may therefore explain some of the diversity in the composition of orogenic fluids shown in Fig. 2.2. Altogether, whilst fluid inclusion studies may implicate the involvement of 'orogenic' fluids (Fig. 2.2) in the formation of

OGDs, there are caveats regarding their interpretation. For example, given the long transportation pathways of the mineralising fluids associated with OGDs, the composition of the fluid may change as a result of mixing with different lithologies encountered along the flow path (Ridley and Diamond, 2000; Goldfarb and Groves, 2015).

However, there are several problems with genetic models for OGDs that invoke metamorphic fluids. For example, geochronological evidence demonstrates that many OGDs formed >50 Ma after peak metamorphism (Campbell and Hill, 1988; Jamielita *et al.*, 1990; Nesbitt, 1991; Yardley and Cleverley, 2013; Doublier *et al.*, 2014). In such instances, a metamorphic fluid source for OGDs would require for the fluids to be retained in the crust for tens of millions of years prior to the release of mineralising fluids, which given the low storativities and porosities of metamorphic rocks, may not feasible (Yardley and Cleverley, 2013). Furthermore, rates of heating during regional metamorphism are very slow (5-20 °C per Ma; England and Thompson, 1984; Carlson *et al.*, 1995; Janots *et al.*, 2009), which should theoretically make the release of orogenic fluids (and OGD mineralisation) a protracted event. In addition, metamorphic devolatisation reactions are endothermic (Yardley, 1977; Fisher, 1978; Walther and Orville, 1982; Carlson *et al.*, 1995); they consume heat, which ultimately restricts the rate of metamorphic reactions. Metamorphic reactions are therefore potentially unlikely to generate a mineralising fluid rapidly (Yardley and Cleverley, 2013). However, in several instances, geochronological evidence is inconsistent with the concept of OGD formation being a protracted event; for example, $^{40}Ar/^{39}Ar$ radiometric dates taken across five OGD vein swarms within the Juneau Gold Belt (Alaska, USA) revealed mineralisation timeframes of <1 Ma (Goldfarb *et al.*, 1988; 1991). This may suggest that the formation of OGDs is a geologically rapid process (Ridley and Diamond, 2000; Yardley and Cleverley, 2013; Wyman *et al.*, 2016).

Despite conceptual problems with a metamorphic fluid source for OGDs, fluid inclusions with gold concentrations of up to 6,000 ppm have been recorded from quartz veins in the Kola super-deep borehole at depths of 9.5 to 11 km (Prokofiev *et al.*, 2020b). This is evidence that deeper mineralising fluids with a probable metamorphic origin (Fig. 2.3.) are capable of transporting large quantities of gold. Furthermore, there are examples of hydrothermal systems where magmatism is absent, yet OGDs have been able to form (e.g. Taiwan; Craw *et al.,* 2010). The following paragraphs describe geological scenarios in which metamorphic fluids may have the potential to form OGDs.

The favoured defence for a metamorphic origin of auriferous mineralising fluids is the ‘deep-late’ model (Stüwe *et al.* 1993; Stüwe; 1998), which seeks to explain the temporal discrepancy between OGD mineralisation and peak metamorphism (~50 Ma) that is frequently documented worldwide (Goldfarb and Groves, 2015). The ‘deep-late’ model suggests that during prograde cycles of Barrovian-type metamorphism, deeper levels of the crust experience peak metamorphism (and fluid production) up to tens of millions of years after the lithologies at shallower levels (i.e. greenschist facies) reached their peak

metamorphic conditions (Stüwe *et al.*, 1993; Stüwe, 1998). It is then assumed that the fluids from the later and deeper metamorphic event migrate upwards into greenschist facies rocks (which are now on a retrograde path). Stüwe *et al.* 1993 argued that the time difference between prograde metamorphism at shallow and deep levels may be as large as 50 Ma, explaining the temporal discrepancy between OGD mineralisation and peak metamorphism that is commonly observed (Stüwe, 1998). However, 'deep-late' scenarios are not typical of all tectonic settings or orogenic cycles (Stüwe *et al.*, 1993; Stüwe, 1998). For example, Stüwe (1998) described how in metamorphic terranes that experience heating from below, 'deep-earlier' metamorphism occurs, in which the deeper crustal levels are metamorphosed before the shallower layers. Under these conditions, any veins that formed from metamorphic fluids are likely to have been remobilised when the shallower levels underwent prograde metamorphism (Stüwe, 1998).

As described previously, OGD formation is often rapid (<1 Ma), yet metamorphic heating is very slow. However, Yardley and Cleverley (2013) also outlined some scenarios in which metamorphic fluids could be involved in rapid OGD formation. For example, decarbonation reactions during metamorphism may increase the likelihood of metamorphic fluids being involved in the formation of OGDs (Yardley and Cleverley, 2013). These reactions (e.g. the conversion of calcite and quartz into wollastonite, or dolomite and quartz into diopside; Baker *et al.*, 2004; Meinert *et al.*, 2005; Grammatikopoulos *et al.*, 2006) are typical of skarn-related processes and result in the development of porosity within metamorphic rocks (Yardley, 2009); specifically, decarbonation reactions can cause the solid volume to decrease, which ultimately augments the permeability (Balashov and Yardley, 1998; Yardley and Cleverley, 2013). Decarbonation processes usually occur at higher temperatures (e.g. >400 °C; Meinert *et al.*, 2005), where the water content is very low (Yardley and Cleverley, 2013). However, in sedimentary piles, carbonates and pelites are commonly interbedded (Yardley and Cleverley, 2013). The injection of water from the pelites into the carbonates may decrease the temperature required for equilibrium, meaning the decarbonation reactions can proceed without a further source of heat (Yardley and Cleverley, 2013). The pelites could theoretically equilibrate with the carbonates once the decarbonation reactions have finished, preventing further temperature decreases (Yardley and Cleverley, 2013). The increase in porosity and permeability as a result of decarbonation reactions may assist in channelling fluid flow in large enough quantities to result in the formation of OGDs over short timescales (i.e. < 1 Ma; Yardley *et al.*, 1991; Yardley and Cleverley, 2013).

Another mechanism that may enable metamorphic fluids to flow rapidly and in large quantities sufficient to form OGDs over timescales <1 Ma is rapid uplift (and the rheological changes induced by this process; Yardley and Cleverley, 2013). This is because rapidly uplifted rocks are likely to contain a pervasive fluid phase during exhumation; hydrofracturing associated with rapid uplift can result in permeability increases (Sibson, 2000; 2004). Furthermore, the pressure decreases that are stimulated by rapid uplift may also trigger metamorphic dehydration reactions at a much earlier stage in the overall evolution of the orogen, meaning the mineralising fluids can be generated over short timescales (Yardley and Cleverley, 2013).

2.3.1.b. Meteoric fluids

As shown in Fig. 2.3., meteoric water circulation has been suggested as a mechanism for OGD formation at depths of <10 km in the crust. However, the consistent occurrence of fluid inclusions with high concentrations of non-aqueous volatiles at OGDs (Kerrich, 1989; Ridley and Diamond, 2000; Gaboury *et al.*, 2021) shows that the fluid responsible for introducing the metals into the zone of mineralisation are unlikely to have a meteoric origin (given that meteoric waters are usually depleted in these constituents; Goldfarb and Groves, 2015). Furthermore, the fluid inclusion data that has been interpreted by several researchers as representing a meteoric contribution to OGDs is usually sourced from bulk analyses in highly deformed quartz veins, which are not represent of episode involving metallic mineralisation (Goldfarb and Groves, 2015).

Nonetheless, genetic models for OGDs involving meteoric fluids tend to invoke the scavenging and transportation of gold from previously formed occurrences of mineralisation by infiltrating meteoric waters (Ramsay *et al.*, 1998; Vallance *et al.*, 2004; Menzies *et al.*, 2014; Wen *et al.*, 2015). In the Otago Schist Belt of New Zealand, meteoric fluids are thought to have circulated throughout large regions of the continental crust; the steep topographic profile of the region (a byproduct of rapid uplift) was favourable to the influx of meteoric water along deeply penetrating faults (Pitcairn *et al.*, 2006). It has also been suggested that the composition of the meteoric water involved in OGD formation changes during interactions with the host metamorphic rocks (Jenkin *et al.*, 1994); in the Alpine Schist Belt (New Zealand), fluid inclusions from quartz veins interpreted to have a meteoric origin record temperatures of 200-350 °C (Jenkin *et al.*, 1994). These hotter meteoric fluids may have the ability to remobilise gold from pre-existing occurrences of gold mineralisation, resulting in another episode of gold precipitation (Pitcairn *et al.*, 2006).

Whilst meteoric fluids are unlikely to represent a source of ore-forming fluids in OGDs, the influx of surficial waters may trigger gold precipitation, potentially as a result of cooling or dilution during fluid mixing (Beaudoin and Chiaradia, 2016). This topic is discussed more in Section 2.7.1.

2.3.1.c. Magmatic-hydrothermal fluids

In light of the previously outlined problems of OGD genetic models involving metamorphic fluids (Section 2.3.1.a.), magmatic-hydrothermal fluid sources are increasingly being postulated for OGDs (Goldfarb and Pitcairn, 2023). Such interpretations have been made for OGDs that postdate metamorphism by tens of millions of years and are coeval with a magmatic intrusion in the nearby vicinity (Goldfarb and Groves, 2015; Goldfarb and Pitcairn, 2023). Magmatic-hydrothermal fluid sources may also be invoked based on the geochemical characteristics of the OGD; for example, at Zarmitan (Uzbekistan), where auriferous veins are hosted in granitoids, elevated W, Bi, and Sb concentrations associated with the gold mineralisation and Au concentrations of <300 ppb in dykes that crosscut the host rock were considered to be indicative of a

magmatic origin (Abzalov, 2007; Goldfarb and Pitcairn, 2023). Sulphur isotope data has also been used to identify a magmatic-hydrothermal source for some OGDs; at Bakyrchik (Kazahkstan) and East Sayan (Russia), $\delta^{34}S$ values of ~0 ‰ have been interpreted as evidence of a magmatic-hydrothermal mineralising fluid (Soloviev *et al.*, 2020; Damdinov *et al.*, 2021; Goldfarb and Pitcairn, 2023). As shown on Fig. 2.3., various magmatic sources have been suggested for OGDs, and in this subsection, the different interpretations (with relevance to Phanerozoic OGDs) are summarised.

There is debate over whether some OGDs (e.g. Pogo, Alaska; Rhys *et al.*, 2003; Goldfarb *et al.*, 2004; 2005) are related to IRGS (Fig. 2.1.), i.e. derived as a result of mineralising fluids released by reduced intrusions (Sillitoe and Thompson, 1998; Thompson *et al.*, 1999). For example, some researchers have classified Pogo as an IRGS (Thompson and Newberry, 2000). In contrast to oxidised magmatic-hydrothermal systems (Fig. 2.4.), gold deposits associated with IRGS form at depths of 3-6 km in the roof zones of reduced plutons (Thompson *et al.*, 1999). IRGS mineralising fluids are aqueous-carbonic (McCoy *et al.*, 1997; Maloof *et al.*, 2001) as a result of the assimilation of carbonaceous host rocks during plutonic ascent and may therefore resemble the fluids associated with OGDs (Fig. 2.2.; Goldfarb and Pitcairn, 2023). Other similarities between OGDs and IRGS include very low sulphide contents, comparable alteration assemblages (i.e. similar to the OGD assemblage shown in Table 2.1.), and high concentrations of the same elements (e.g. As and Sb; Goldfarb and Pitcairn, 2023). Whilst there are several characteristics that can be used to identify and distinguish IRGS from OGDs (coeval episodes of mineralisation and reduced magmatism, concentric metal zonation, scheelite-rich hydrothermal systems; Hart, 2007), the deposit style is an important example of how magmatic mineralising fluids may resemble the fluids associated with OGDs (Fig. 2.2.; Hart, 2007).

Regarding other magmatic fluid sources, some deposits classified as OGDs are suggested to have a genetic link to fluids emanating from oxidised intrusions (Fig. 2.3.; Goldfarb and Pitcairn, 2023). However, Goldfarb and Pitcairn (2023) have noted the constraints with such interpretations. Generally speaking, until ascending magmatic bodies reach depths of 4 to 6 km (or <2 kbar; Fig. 2.6.a.), large amounts of volatile degassing does not occur (Lowenstern *et al.*, 1991; Rasmussen *et al.*, 2022). A similar situation can be inferred from models of ascending basaltic melts, in which degassing cannot give rise to an aqueous carbonic fluid until even shallower depths (<1 kbar; Fig. 2.6.b.). For this reason, Goldfarb and Pitcairn (2023) suggested that magmatic-hydrothermal fluids were only plausible sources of OGDs that formed at shallow depths (i.e. low pressures) of <3-4 km and maintained that deeper (>6 km) OGDs are genetically linked to metamorphic fluids. However, given that many OGDs record evidence of magmatic-hydrothermal fluids, Goldfarb and Pitcairn (2023) also suggested that overprinting of previously formed OGDs by later magmatic-hydrothermal fluids may be involved in redistributing the material and contributing to the overall formation of an economically viable deposit.

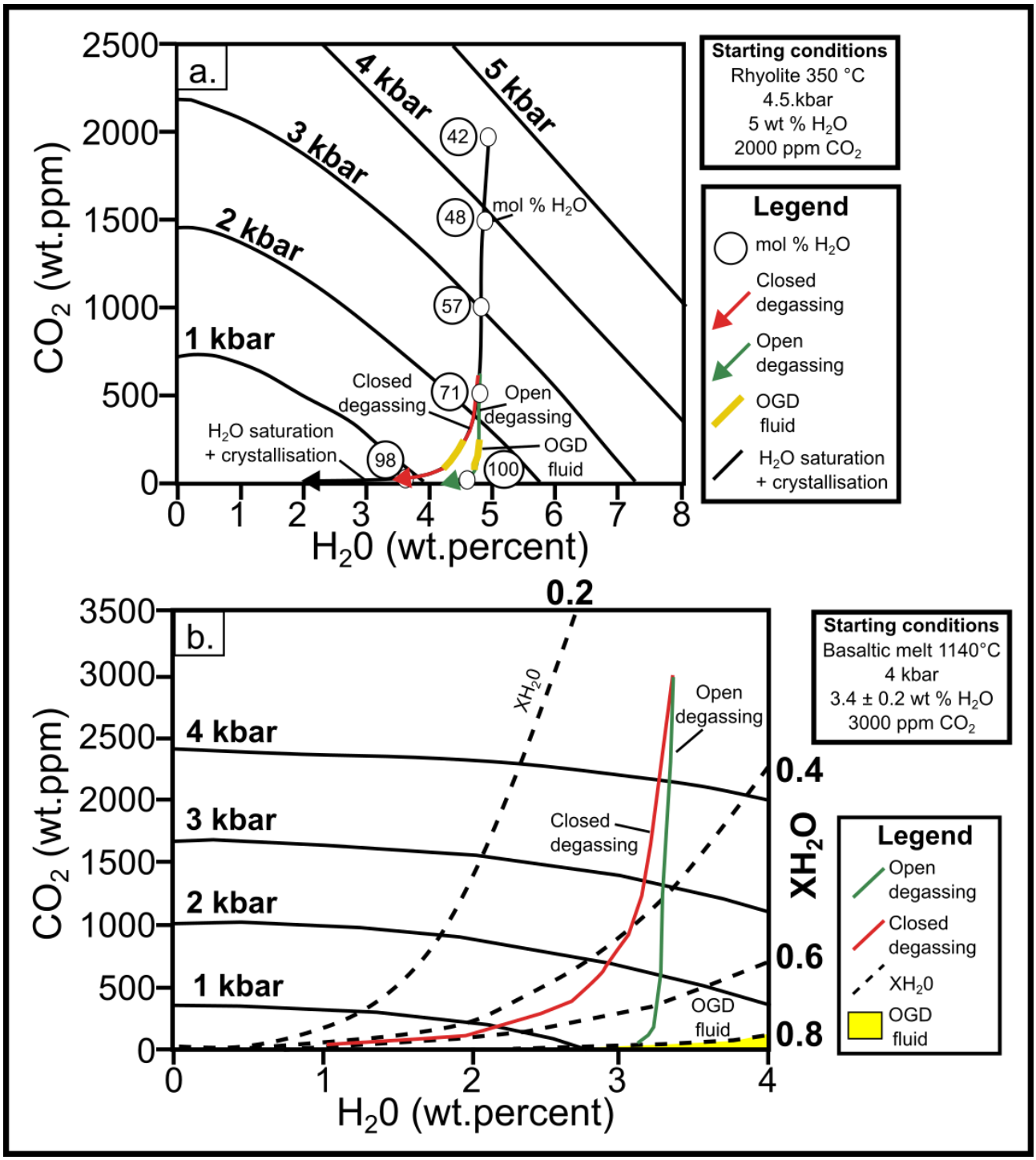

Figure 2.6. Magma degassing diagrams illustrating the conditions under which OGD mineralising fluids can develop (adapted from Goldfarb and Pitcairn, 2023). **a.** Magmatic degassing of a rhyolite initially comprised of 5 wt % H_2O and 0.2 wt % CO_2 ascending from a depth of 17 km (Lowenstern, 1991). Large quantities of CO_2 are lost from the melt before the release of H_2O between 3 and 5 km for an open system versus a closed system. The volatile compositions typical of OGDs do not arise until the magma reaches depths of approximately 5 km from the surface. Numbers in circles pertain to the H_2O contents of the aqueous-carbonic phase. **b.** Magmatic degassing for a basaltic melt with an initial composition of 3.4 wt % H_2O and 0.3 wt % CO_2 ascending from 15 km (Spilliaert *et al.*, 2006; Audétat and Simon, 2012). Significant release of fluids with compositions typical of OGDs (XH_2O = 80-95 %) do not occur until very shallow depths and pressures. The dashed lines represent XH_2O with mole ratios from 0.2 to 0.8.

2.3.4.d. Mantle-derived fluids

Some researchers have suggested that the mineralising fluids associated with OGDs are derived from the mantle (Goldfarb *et al.*, 2001; Hronsky *et al.*, 2012; Goldfarb and Groves, 2015; Wang *et al.*, 2022; Zhao *et al.*, 2022b). However, it should be noted that the only Phanerozoic OGD with a confirmed link to the mantle is Jiaodong (see Section 2.2.1.a.), which as previously discussed, is potentially an outlier relative to other Phanerozoic subtypes (Goldfarb and Santosh, 2014; Groves *et al.*, 2020a, b; Mortensen *et al.*, 2022). At Jiaodong, the gold mineralisation is both disseminated and vein-hosted (Groves and Santosh, 2016). However, the ore deposits in this region have several characteristics of OGDs (Table 2.1.); for example, the veins are structurally controlled by NE trending faults (Groves and Santosh, 2016). However, Groves and Santosh (2016) ruled out genetic processes solely involving metamorphic devolatisation (Phillips and Powell, 2010; Section 2.3.1.a.) because metamorphism of the host rocks at Jiaodong occurred over 2 Ga after peak metamorphism in this geological setting. A magmatic-hydrothermal fluid source is considered to be an insufficient explanation for the features at Jiaodong because the mineralisation does not show a close spatial association with granitoids that are coeval with the mineralisation events (Groves and Santosh, 2016). The fluid inclusion populations from the gold deposits of Jiaodong were also noted to display characteristics of both 'orogenic' and magmatic mineralising fluids (Fig. 2.1.; Goldfarb and Santosh, 2014). Furthermore, several fluid inclusion and stable isotope studies have highlighted commonalities between the ore-forming fluids at Jiaodong and mantle-derived fluids (Mao *et al.*, 2008; Wang *et al.*, 2022; 2024). A mantle source for the mineralising fluids in OGDs would require high concentrations of gold, sulphur, and other metals within the upper mantle, in addition to the presence of long lived transcrustal structures capable of tapping the fluid source (Groves *et al.*, 2020a, b; Mortensen *et al.*, 2022).

In this paragraph, the genetic model postulated for mantle derived OGDs (Groves and Santosh, 2015; 2016) is summarised. The mineralising processes associated with a subcrustal fluid source are interpreted to have a genetic link with devolatisation of a subducting slab and the overlying oceanic crust at a convergent margin (Groves and Santosh, 2015; Fig. 2.7.); the subduction process stimulates extensive fluid flow in an upwards direction along the boundary between the slab and mantle (Fig. 2.7.; Sibson, 2004; Peacock *et al.*, 2011). The breakdown of pyrite to pyrrhotite in the oceanic sediments during subduction releases a fluid with high concentrations in Au, As, Sb, and Te (Large *et al.*, 2009; 2011; Steadman *et al.*, 2013). The slab-mantle boundary, experiencing overpressure (Sibson, 2013), channels the devolatised fluids into crustal-scale fault zones (Fig. 2.7.). This process ultimately results in fertilisation of a slab of the mantle, which can be subsequently exploited during later mineralisation events (Groves and Santosh, 2016; Groves *et al.*, 2020a). The release of fluids from the slab may be more likely to occur following subduction or during a switch from compression to transpression (Seno and Kirby, 2014). Under these conditions, fluid flow may be the result of the increased shearing and fracture creation (i.e. increased permeability) that is often associated with transpressional stress (Groves *et al.*, 2020a, b). Later episodes of uplift and relaxation may

be conducive to the movement of mineralising fluids retained within the mantle (Zhang *et al.*, 2024). OGD formation eventually takes place along second and third order structures (Breeding and Ague, 2002; Hyndman *et al.*, 2015).

As mentioned previously, the literature is in agreement with the suggestion that Jiaodong formed as a result of a mantle-derived mineralising fluid (Groves and Santosh, 2016; Groves *et al.*, 2020a, b; Wang *et al.*, 2022). However, the general applicability of these models (Fig. 2.7.) to other Phanerozoic OGDs remains uncertain (Mortensen *et al.*, 2022), although Groves *et al.* 2020a suggested that the mantle is likely to have a consistent geochemical signature and can therefore explain the 'orogenic' fluid commonly documented at OGDs globally (as by fluid inclusions; Fig. 2.2.). It is important to emphasise that in contrast to the more generic subcrustal model postulated by Groves *et al.* 2020a (Fig. 2.7.), mineralisation at Jiaodong is linked to a subducting slab that stalled (Qiu *et al.*, 2020); Mortensen *et al.* 2022 considered this to be an atypical tectonic setting that contrasts with those associated with the Phanerozoic OGD subtypes (Table 2.2.).

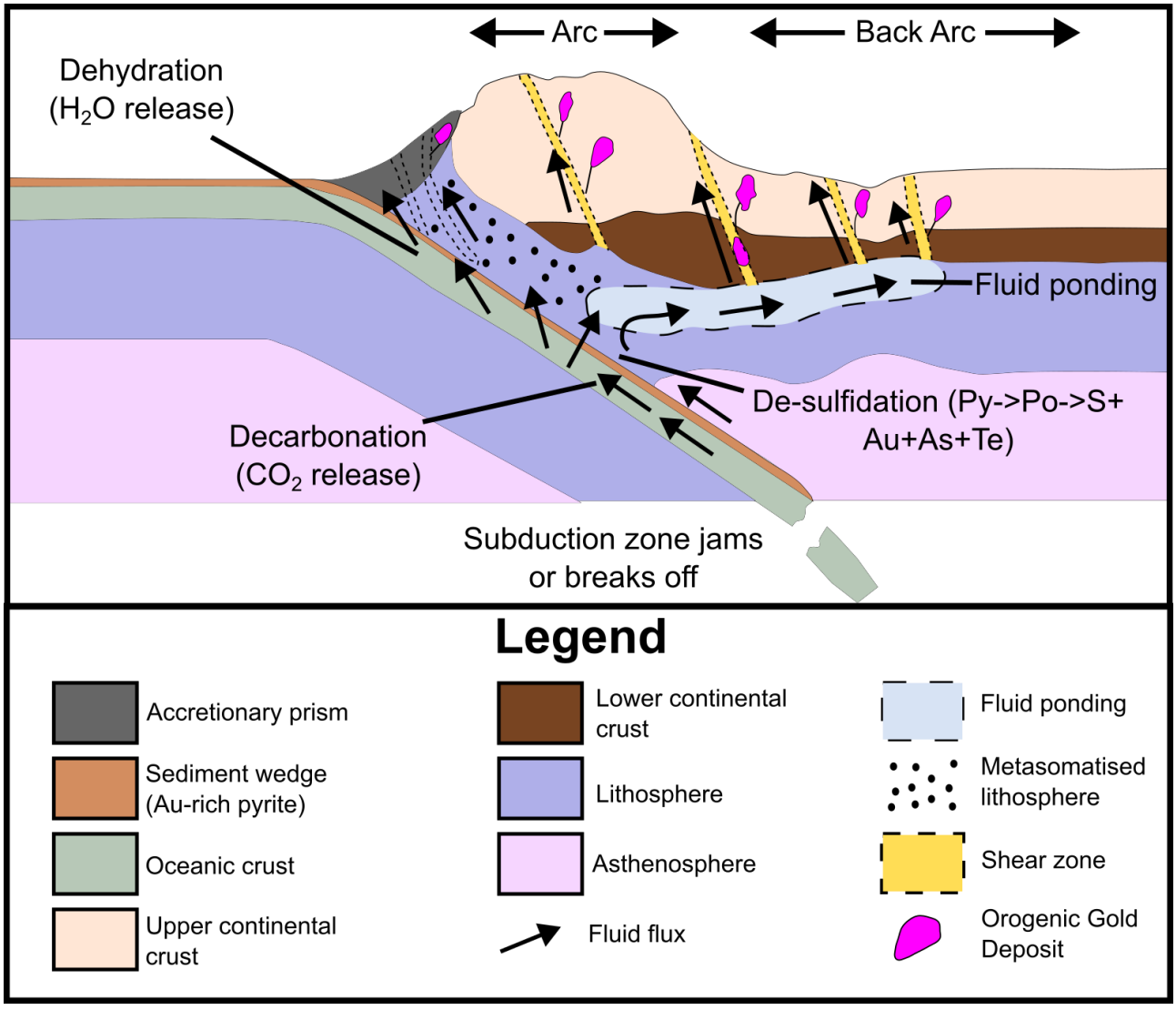

Figure 2.7. Genetic model for OGD formation involving fluid flux from a subducting slab (adapted from Wyman *et al.*, 2008; Goldfarb and Groves, 2015; Groves *et al.* 2020a, b).

2.4. Geochemical behaviour of gold

The purpose of this section is to describe the behaviour of gold within hydrothermal solutions, which provides a context in which to consider the processes of metal transportation and precipitation.

2.4.1. Metal-ligand complexing

In the context of hydrothermal solutions, solubility can be defined as the amount of dissolved metal that can be transported by the fluid (Wood and Samson, 1998). However, unless the solution contains other components that the metals can bond with, the solubility of most metals in a fluid is negligible (Holland, 1972; Wood and Samson, 1998). In hydrothermal solutions, metals commonly form bonds with ligands; some of the typical bonds involved in metal transportation are shown in Fig. 2.8. The 'hard metals' have positive charges and small atomic radii; they are naturally attracted to 'hard ligands', which are also characterised by negative electronic charges (Pearson, 1963). Hard metals and hard ligands readily form coordinate or ionic bonds to achieve electronic stability (Pearson, 1963). This concept is known as 'Pearson's Principle' (Pearson, 1963).

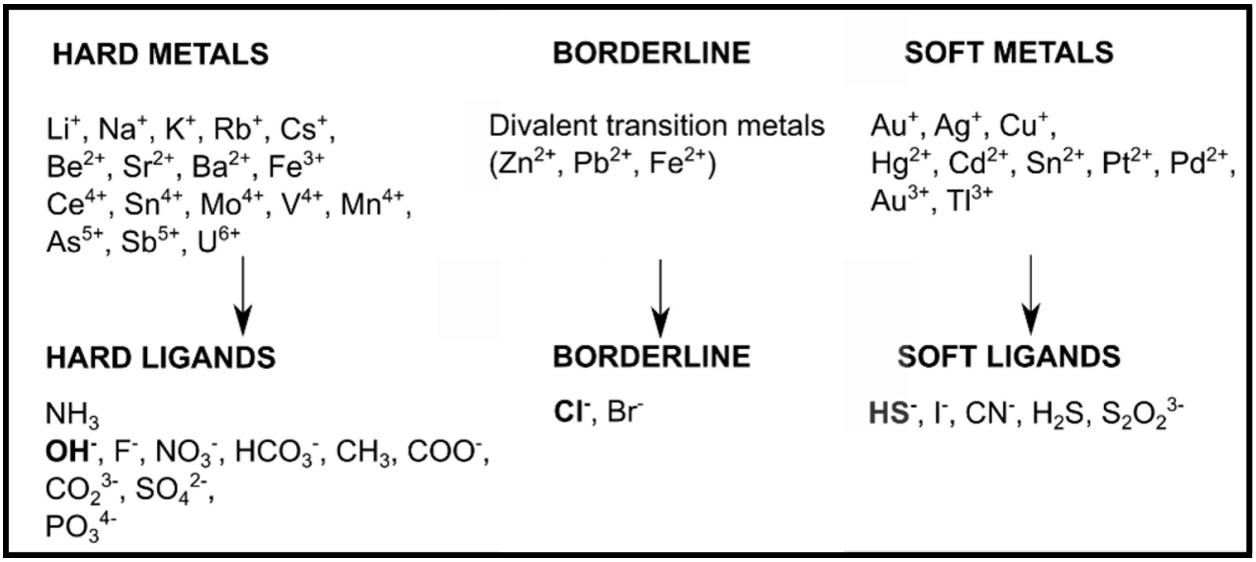

Figure 2.8. Pearson's metal-ligand classification scheme (adapted from Pearson, 1963). Ligands common in hydrothermal solutions are in bold.

As depicted in Fig. 2.8., gold is one of the softest metals (due to the large size of the ion and low charge; Pearson, 1963; Wood and Sansom, 1998), meaning that it generally forms bonds with soft ligands, such as the bisulphide ion. The solubility and type of metal-ligand complex that forms are also controlled by changes in HS^- activity, fO_2, and pH (Stefánsson and Seward, 2003; 2004; Phillips and Powell, 2010). An example of this relationship is shown in Equation 3, in which acidic conditions favour the AuHS metal-ligand complex; on the other hand, alkaline environments may favour the formation of $Au(HS)_2^-$.

$$Au(s) + H_2S + HS^- = Au(HS)_2^- + 0.5H_2$$

$$K(Au(HS)_2^- = [H_2]^{0.5} \times [Au(HS)_2^-/([H_2S] \times [HS^-]$$

Equation 3. Metal-ligand complexing that occurs between gold and the bisulphide complex within aqueous sulphide-bearing fluids up to temperatures of 500 °C (adapted from: Stefánsson and Seward, 2004; Phillips and Powell, 2010).

Generally speaking, the solubility of metal-ligand complexes involving gold in aqueous fluids is temperature dependent (Fig. 2.9.a.; Seward, 1973; Barnes, 1979; Schenberger and Barnes, 1989; Zotov *et al.*, 1991; Johnson *et al.*, 1992; Benning and Seward, 1996). There are several factors that explain the trends depicted on Fig. 2.9.a.; at temperatures >500 °C, the concentration of H_2S in equilibrium with Fe-bearing phases is normally much greater (e.g. 10^{-5} mol/kg at 150 °C, 0.5 mol/kg at 500 °C; Pokrovski *et al.*, 2014). For this reason, the fluid is often supersaturated with respect to H_2S, meaning that precipitation is more likely (Pokrovski *et al.*, 2014). Furthermore, temperatures of >400 °C are more favourable to the formation of bonds between metals and hard ligands (e.g. chloride; Brimhall and Crerar, 1987; Kouzmanov and Pokrovski, 2012). This is because the AuCl bond is relatively stronger, under most conditions, than the AuH_2S bond; at higher temperatures, weaker bonds tend to be broken more easily (Pokrovski *et al.*, 2009; 2014; 2015). The $Au[HS]_2^-$ complex Is most stable at temperatures of 400-250 °C (Phillips and Powell, 2010; Pokrovski *et al.*, 2014).

It may be possible to make predictions about the likely metal-ligand complexes within a hydrothermal solution when a variety of ligands are present (Stefánsson and Seward, 2003; 2004). For example, Au is a soft metal; it preferentially forms complexes with the bisulphide ion, provided there is an availability of bisulphide in the mineralising fluids (Equation 3; H_2S) (Garofalo *et al.*, 2014). In highly oxidising environments with temperatures >350 °C (such as those associated with porphyry or epithermal deposits), there is a usually a preponderance of Cl relative to H_2S (Liu *et al.*, 2014); for this reason, AuCl complexes are more typically associated with porphyry and epithermal mineralisation processes (Gammons and William-Jones, 1997; Migdisov *et al.*, 2014; Hurtig and William-Jones, 2015).

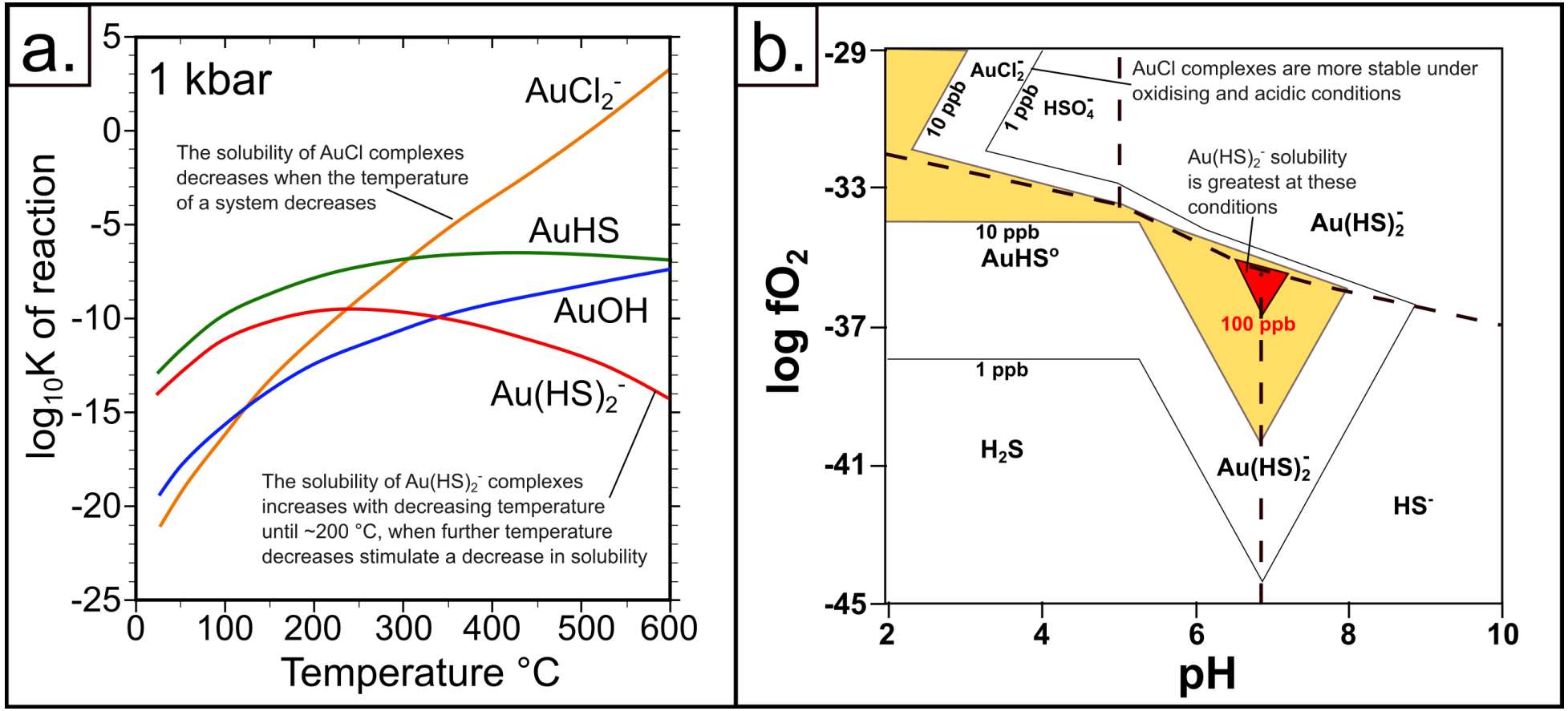

Figure 2.9. Diagrams depicting the solubility of metal-ligand complexes involving gold. **a.** Thermodynamic equilibrium constants of the formation reactions of different ligand complexes involving gold (assuming pressures of 1 kbar). These models also assume buffering of oxygen and sulphur fugacity by pyrite-pyrrhotite-magnetite and pyrite-magnetite-hematite. Adapted from Pokrovski *et al.* 2014. **b.** Eh-pH diagram demonstrating the stability of different metal-ligand complexes for gold at 500 bar and 250 °C (adapted from Stefánsson and Seward, 2003; 2004).

2.4.2. Colloidal gold

In recent years, the role of metal-ligand complexes in the formation of high-grade gold deposits has been debated. In contemporary epithermal environments, Au concentrations of 16 ppb (Ladolam, Papua New Guinea; Simmons *et al.*, 2016) and 1 to >1000 µg/kg (North Island, New Zealand; Simmons *et al.*, 2016) have been recorded from geothermal waters. Assuming gold concentrations of <16 ppb, $>10^{10}$ l of mineralising fluid would be required to form a bonanza gold deposit (>6 Moz Au) at a solubility this low, provided that 100 % of Au is precipitated at the trap (Petrella *et al.*, 2020). This is not a realistic scenario for gold mineralisation in the natural world (Petrella *et al.*, 2020). One potential solution to this problem involves a model in which gold particles are transported as colloids (Saunders, 1990; Herrington and Wilkinson, 1993; Hough *et al.*, 2011; Petrella *et al.*, 2020). In this scenario, multiple Si and Au nanoparticles nucleate when the hydrothermal fluid becomes supersaturated in these components (Saunders and Schoenly, 1995). Colloidal gold has traditionally been associated with epithermal models of gold mineralisation (McLeish *et al.*, 2018; Petrella *et al.*, 2020). However, Petrella *et al.* 2020 identified nanoparticles indicative of colloidal processes at Callie, an Archean OGD in Western Australia.

Hydrothermal fluids may become supersaturated with colloids in response to boiling associated with pressure decreases (Gartman *et al.*, 2018). These processes are often caused by the creation of space during dilation or fracturing (Herrington and Wilkinson, 1993). Fluid boiling also increases the frequency of collisions between negatively charged colloids (i.e. they would normally repel one another), meaning that colloidal aggregation is feasible (Frondel, 1938; Saunders, 1990). However, boiling-induced supersaturation normally leads to the rapid precipitation of crystalline phases from the oversaturated fluid. Provided that Si colloids are suspended in the mineralising fluid, the gold colloids can avoid being precipitated, should they coagulate with Si (Petrella *et al.*, 2020); this is because Si colloids are stable in hydrothermal solutions (until a temperature threshold of 350 °C is exceeded; Frondel, 1938; Liu *et al.*, 2019; Petrella *et al.*, 2020).

2.5. Gold remobilisation

Whilst OGDs tend to record several mineralisation events (Groves *et al.*, 2003; Goldfarb *et al.*, 2005; Hastie *et al.*, 2020), each one may not pertain to the injection of a distinct auriferous fluid; rather, it is possible for gold remobilisation (i.e. the breakdown, transportation and reprecipitation of preexisting gold mineralisation; LaFlamme *et al.*, 2018; Wagner *et al.*, 2016; Wu *et al.*, 2019; Hastie *et al.*, 2020; 2021) to create paragenetically later generations of gold mineralisation, some of which may be bonanza grade (Hastie *et al.*, 2020). The common observation of post-mineralisation fractures hosting gold across several deposit styles (Robert, 2001; Goldfarb *et al.*, 2005) means that gold remobilisation may be a relatively common ore-forming process (Hastie *et al.*, 2020; 2021).

In practice, gold remobilisation is likely to be detectable where contemporaneous sulphide and gold mineralisation has taken place, followed by sulphide dissolution and subsequent release and transportation of the gold nanoparticles. An example of the controlled dissolution reaction (CDR) textures produced by this process is shown in Fig. 2.10.; such textures would be recognisable during petrographic characterisation. Hastie *et al.* 2020 described two processes with the potential to cause gold remobilisation: fluid-mediated remobilisation (Fougerouse *et al.*, 2016) and partial melting (Frost *et al.*, 2002; Tomkins *et al.*, 2007), which can result in CDR textures (Fig. 2.10.). Fluid-mediated remobilisation occurs when a new fluid encroaching on a pre-existing vein contains components less soluble than the local mineralogy, triggering dissolution and replacement of the sulphide hosting the gold (Hastie *et al.*, 2021). During dissolution, gold is released into the new hydrothermal fluid before undergoing transportation. Gold remobilisation by partial melting is a slight variation of the previously described fluid-mediated processes; as the sulphides dissolve, they may release chalcophile elements with low melting points (e.g. Bi and Te). This causes the melting point of the sulphides to decrease (Hastie *et al.*, 2020; 2021), potentially to the point where dissolution can continue under the pressure and temperature conditions associated with greenschist and amphibolite facies.

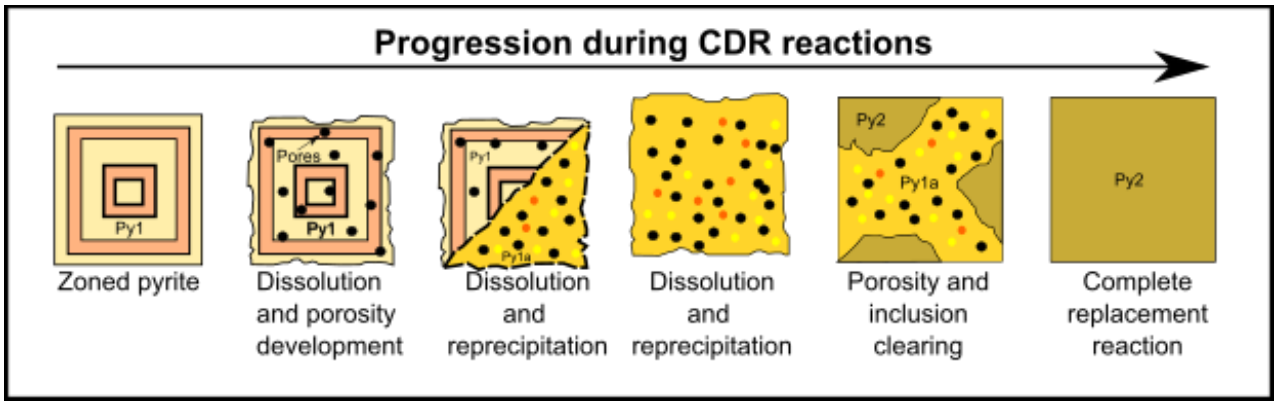

Figure 2.10. Textural evidence for gold remobilisation (Hastie *et al.*, 2020; 2021).

2.6. Transportation of mineralising fluids

Following the genesis of an auriferous fluid, transportation usually occurs over several kilometres prior to metal precipitation (Fig. 2.11.). In this subsection, the migration of mineralising fluids throughout the crust is explored. Regarding Fig. 2.11., this schematic pertains to scenarios of OGD mineralisation in which a fluid is generated at a single locality prior to large-scale migration and metal scavenging (Cox, 2005); however, it is important to note that Phillips and Powell (2010) favoured a model involving the generation of a mineralising fluid at the site of metamorphism. There are therefore several interpretations regarding the exact processes involved in the transportation of mineralising fluids associated with OGDs, although most models emphasise the need for large quantities of the mineralising fluids to be focused by structural channels (Cox, 2005; Phillips and Powell, 2010; Gaboury, 2019; Fig. 2.11.).

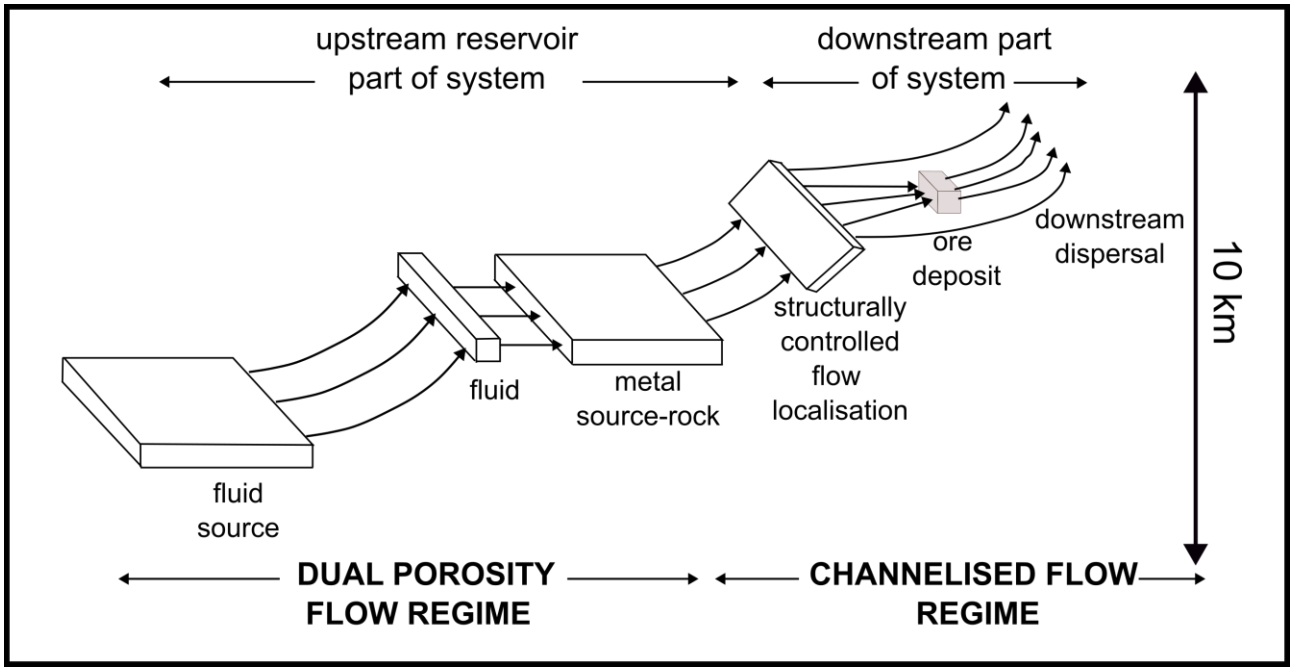

Figure 2.11. Schematic overview of the structure of a fracture-controlled hydrothermal system involving a single fluid source in which metals are scavenged from the surrounding rocks (Cox, 2005).

In scenarios of OGD formation, the deterioration of hydrous minerals as a result of metamorphism during reactions with adjacent grains (e.g. carbonates or silicates) leads to the production of a fluid bordering these grains (Etheridge *et al.*, 1983). However, there is considerable uncertainty regarding the migration of these fluids away from the source (which may already have high metal concentrations; Phillips and Powell, 2010). Cox (2005) emphasised the importance of strain, which may increase the permeability of the rock mass. Mineral precipitation from the migrating fluids can destroy this permeability, meaning that strain must continually be applied for fluid movements to continue (Cox, 2005).

However, the previously described inter-grain boundary flow of auriferous fluids upon generation is unlikely to be applicable to settings in which the metamorphic rocks have very low porosities and

permeabilities (Cox, 2005). In these situations, which could arise at greater depths in the crust (i.e. below the brittle-ductile transition; Fig. 2.3.), the movement of the auriferous fluids is likely to occur in fractures (Cox, 2005, Hodkiewicz *et al.*, 2005). However, an increase in pore fluid pressure may result in fracturing, as demonstrated by the Mohr circle (i.e. a diagram used to visualise the transformation of stresses in a two-dimensional object experiencing shear stress; Chen and Nur, 1992) in Fig. 2.12. The original principles of the effects of pore fluid pressure on rock failure were originally described by Terzaghi (1923) and can be summarised as follows; the increase in fluid pressure pushes the grains within a rock apart, resulting in a decreased effective normal stress. This causes the Mohr circle to shift to the left (Fig. 2.12.) and intersect with the Mohr-Coulomb failure envelope (i.e. a line connecting a series of points representing combinations of normal and shear stresses that cause the rock to fail; Labuz and Zang, 2014); at this point, fractures develop in the rock (Fig. 2.12.). The increase in pore fluid pressure during metamorphic devolatisation may therefore facilitate the development of excess permeability at depth, enabling fluid migration (Phillips and Powell, 2010).

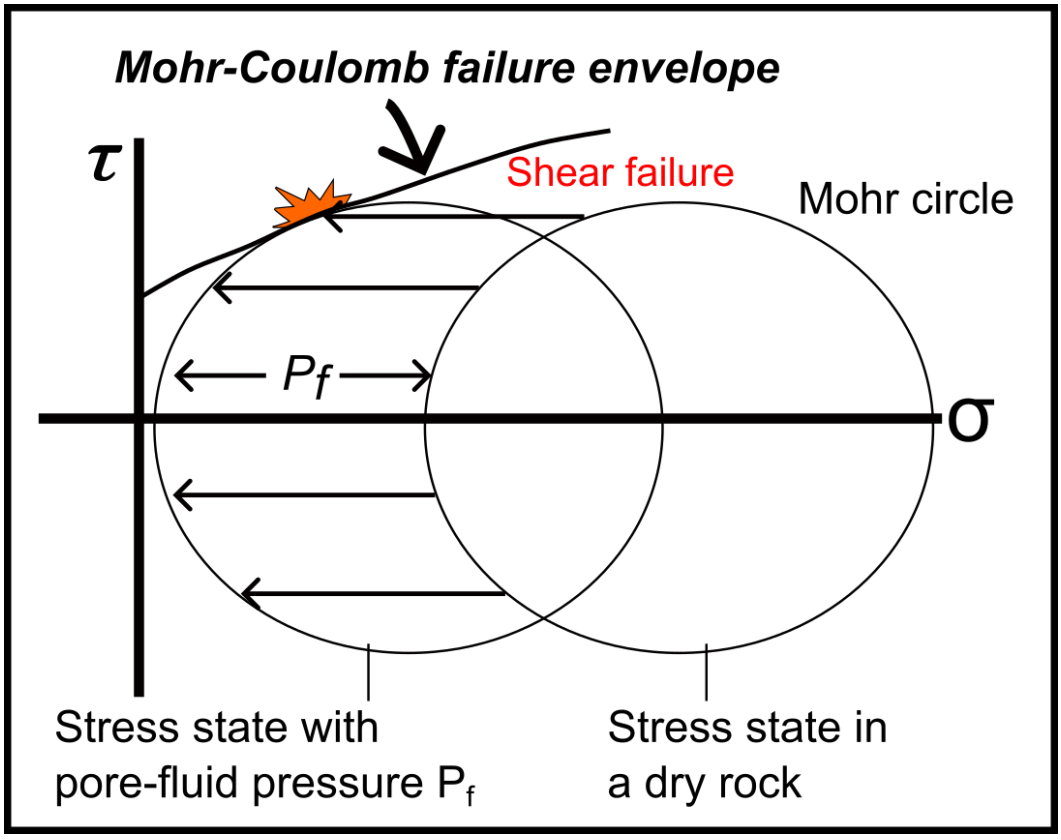

Figure 2.12. Example diagram depicting the impact of an increase of pore fluid pressure on a dry rock using Mohr circles (σ = normal stress, τ = shear stress). An increase in pore fluid pressure causes the Mohr circle to shift to the left and intersect with the failure envelope, resulting in fracturing. Adapted using the principles in Brace (1961) and Chen and Nur (1992).

Deformation-induced stress may enable a percolation threshold to be achieved (this process is also applicable to pores at the microscale; Fig. 2.13.a.). In the initial stages of deformation, pores or fractures are usually isolated (Cox, 2005); there may be a 'backbone' network of pores or fractures along which flow is initially concentrated (Fig. 2.13.). However, experimental evidence indicates that with further strain and deformation, the pores or fractures may increase in size and begin forming connections with one another, resulting in the development of a fracture percolation network (Zhang *et al.*, 1994; Cox, 1999; Fig. 2.13.b.). Ultimately, the increasing degree of connectivity causes a percolation threshold (i.e. the fluids are able to migrate throughout the entire fracture percolation network; Sahimi, 1994; Cox, 2005) to be exceeded. There are several geological scenarios in which this process may occur; for example, the gradual linkage of several very large structures may be sufficient (Xiong *et al.*, 2023). Alternatively, interconnections between many small structures or pores may also result in the percolation threshold being exceeded (Fig. 2.13.; Xiong *et al.*, 2023). Regardless of the mechanisms by which this process occurs, traversing the threshold is often the point at which crustal-scale flow begins (Cox, 1999). Furthermore, the onset of the percolation threshold (Fig. 2.13.b.) often coincides with a decrease in pressure, which can ultimately stimulate phase separation (Section 2.7.1.) and an increase in metal solubility; this process may assist in the formation of high-grade ore deposits (Xiong *et al.*, 2023). During fieldwork, it may be possible to infer that a percolation threshold has not been exceeded on the basis that observed or mapped fractures are likely to be small and display poor degrees of interconnectedness (Roberts *et al.*, 1988).

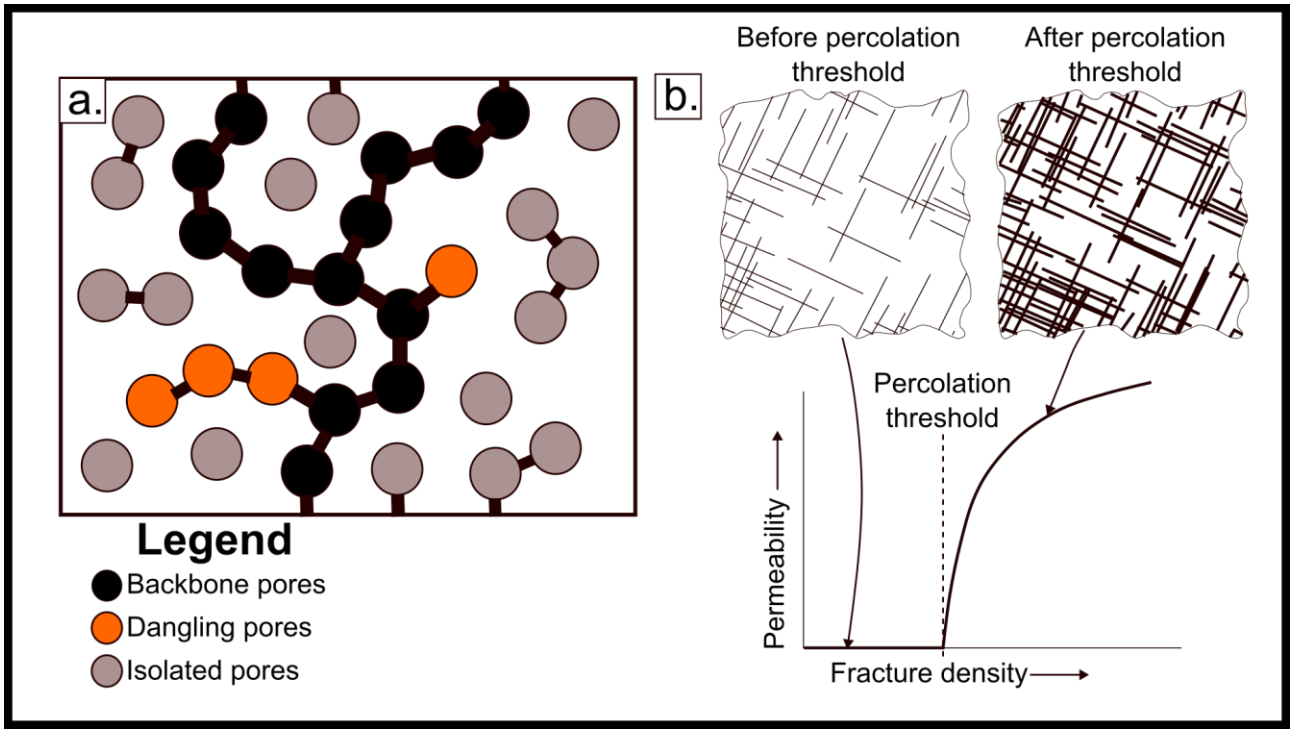

Figure 2.13. Connectivity of pores during fracturing and increased fluid pressure (adapted from; Odling, 1997; Cox, 2005; Robb, 2005; Grimshaw, 2018). **a.** Connection of the dangling pores enables a percolation threshold to be reached. **b.** Percolation threshold plotted as a function of fracture density and connectivity.

For further fluid migration towards sites of potential OGD formation (Fig. 2.11.), there must be flow paths with geometries capable of focusing the fluid flow, as well as conduits undergoing active deformation (which results in elevated permeability; Sibson *et al.*, 1975; 1988; Sibson, 1996). The mineralising fluids may travel between 3 and 10 km prior to gold mineralisation (Phillips and Powell, 2010; Fig. 2.11.). Upon moving into the structural conduits required for transportation towards the 'downstream' regions of mineralisation (Fig. 2.11), further movements of the mineralising fluids may proceed via the 'fault valve' model (Sibson *et al.*, 1988; Fig. 2.14.). It should be emphasised that the fault-valve model is not exclusive to OGDs and also has the potential to be relevant to fluids with a magmatic source, potentially at shallower depths in the crust (Sibson *et al.*, 1988; Fig. 2.14.). Whilst Sibson (1975; 1987; 1988; 2004) originally developed the fault valve model using New Zealand as a case study (i.e. a compressional regime), it is also applicable to extensional regimes (Sibson, 1992; 1994; Curzi *et al.*, 2023). The most important component of the fault valve model (Fig. 2.5.) is the build-up of fluid pressure, which is not necessarily restricted to compressional settings.

Stage	Name	Description
1	Prefailure	Fluid pressure below the impermeable brittle deformation zone increases beyond lithostatic values; subhorizontal extensional veins (termed flats) open
2	Seismogenic Fault Failure	Accumulating shear stress causes the fault to fail at the bottom of the brittle deformation zone, creating a seismic rupture that propagates along the dip of the fault to the surface; shear and deviatoric stresses decrease
3	Postfailure Discharge	The low deviatoric stress causes the fluids to migrate along the rupture zone and into the flats; the decrease in pressure may trigger mineral precipitation (Section 2.7.).
4	Self-sealing	Precipitation of phases blocks further fluid motions along the rupture (permeability decreases)
5	Repetition	Fluid pressure begins to increase; Stages 1-4 are repeated

Table 2.4. Stages of the fault valve model (Sibson *et al.* 1988).

Reactivation as described by the fault valve model (Table 2.4.) may impact a fault of any angle provided that the pore fluid pressure is sufficiently high (i.e. it exceeds lithostatic load; Lisle and Srivastava, 2004). In a compressional setting, shallow dipping faults (<45 °) are more likely to be reactivated, whilst faults with high dip angles (>45 °) are more difficult to reactivate and hence require a greater amount of fluid pressure before movements can be initiated (Célérier, 1995; Lisle and Srivastava, 2004; del Ventisette *et al.*, 2006). Furthermore, reactivation is favoured under regional compression where the principal stresses are oriented at a high angle to the strike of the faults (Etheridge, 1986). This is not the case in other stress regimes; for example, in a transcurrent setting, subvertical faults are more likely to be reactivated (Sibson *et al.*, 1988;

Richard and Krantz, 1991). On the other hand, normal faults are reactivated at high angles to the principal stresses in an extensional setting (Morley *et al.*, 2004).

In extensional settings, veins with multiple quartz generations have also been observed (Hulin, 1929; Sibson, 1981), which has led to the interpretation that, as with compressional stresses (Fig. 2.14.a.), the transportation of mineralising fluids under these conditions is also associated with earthquake rupture processes (Sibson, 1987). Extensional settings commonly host epithermal gold mineralisation (Section 2.2.3.), i.e. in dilatational fault jogs (Sibson, 1987; Fig. 2.14.b.). The deposition of the veins typically occurred during episodes of boiling, brecciation, and recementation (Hulin, 1929; Henley, 1985). Collectively, these observations led Sibson (1987) to propose the 'suction pump' model for epithermal mineralisation at depths <1 km. In many active strike-slip fault systems (e.g. the San Andreas Fault; Sibson, 1987), dilatational jogs >1 m wide typically form in regions impacted by earthquakes; the jogs may continue to depths of <10 km (Sibson, 1987), preventing further rupturing of the strike-slip faults on either side of the jog (Sibson, 1985; 1987). Instead, aftershocks may propagate alongside the jogs themselves and the faults transfer slip to one another through the jogs (Sibson, 1987). The creation of space at shallow depths is accompanied by pressure decrease and fluid flow. Ultimately, the formation of space may promote boiling (Sibson, 1987) and the mechanical energy released by this process typically causes further fracturing. In this scenario, the previously outlined concept of the percolation threshold (Fig. 2.13.) is once again relevant; further fracturing may augment permeability of the fault system (Sibson, 1987).

The fault valve model is supported by contemporary geophysical evidence (e.g. seismic studies demonstrating simultaneous variations in fault slip and pore fluid pressure in active subduction zones; Gosselin *et al.*, 2020; Sibson, 2020; Rossi *et al.*, 2021) and fluid inclusion studies that demonstrate pressure cycling throughout OGD mineralisation events (Chi *et al.*, 2020; Mesquita *et al.*, 2021; Taylor *et al.*, 2021). However, regardless of the mechanism that has resulted in the movement of the mineralising fluids into the environment of deposition, it is often the case that whilst proximity to large structures (i.e. >100 km) is associated with the formation of ore deposits, mineralisation usually takes place on second and third-order structures (Sibson, 1987; Phillips and Powell, 2010). This trend may pertain to the complex nature of deformation processes; regional deviatoric stresses often result in localised variations to the mean stress (i.e. the mean of the principal stresses σ_1, σ_2, and σ_3; Ridley, 1993), with lower values being more favourable to fluid flow (Ridley, 1993). However, larger faults are likely to contain several irregularities (e.g. dilatational jogs, releasing bends); the presence of these variations, as well as small changes to fault orientation, can result in large changes in mean stress values (Hodgson, 1989). Intersections between lower order faults and large-scale structures are often associated with low mean stresses and hence, the influx of hydrothermal fluids (Hodgson, 1989; Phillips and Powell, 2010).

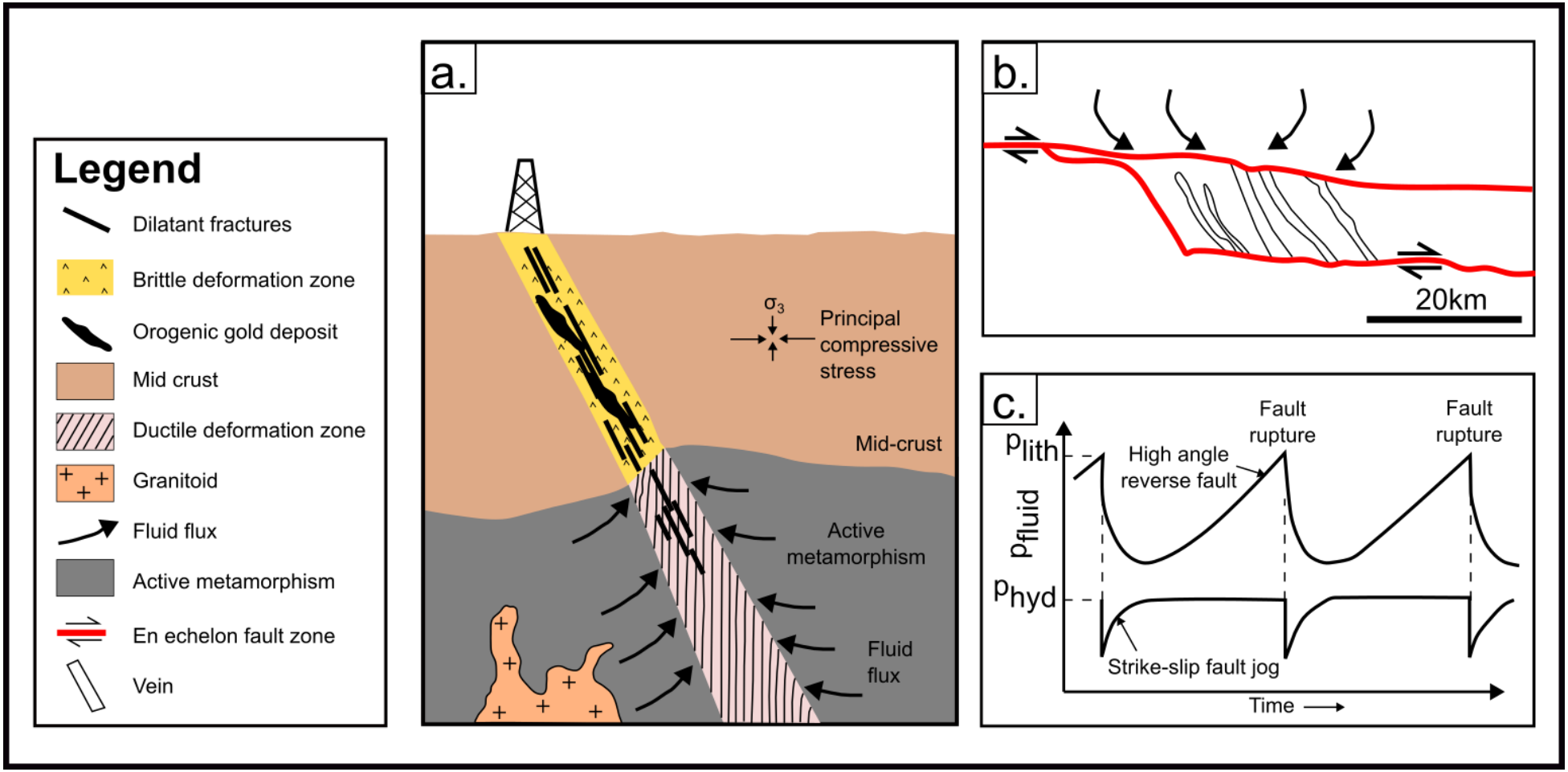

Figure 2.14. Transportation of mineralising fluids into the environment of ore deposition during faulting (adapted from Robb, 2005). **a.** Cross-section depicting processes involved in the fault valve model. **b.** Plan view of the suction pump mechanism at a regional scale (although the same principles apply at a variety of scales). **c.** Pressure fluctuations prior to and during episodes of fault rupturing in the fault valve and suction pump models. a and c were modified from Sibson *et al.* 1988, whilst b was adapted from Sibson (1987). P = pressure.

2.7. Gold precipitation mechanisms

Gold may precipitate when the metal-ligand complexes that carry them become unstable, and there are various geological processes that may cause this to happen; broadly speaking, these can be categorised as physical (pressure and temperature changes associated with the fault valve and suction pump models; Section 2.6.) or chemical (fluid mixing, or disequilibrium between the fluids and wallrocks during alteration; Section 2.2.4.). Throughout this section, differences in the precipitation mechanisms involved in the various genetic models (Section 2.2.) are highlighted where appropriate.

2.7.1. Pressure and temperature changes

Gradual pressure variations do not significantly impact the solubilities of metal-ligand complexes, although pressure itself does have an impact (albeit modest), on their solubility; pressure increases lead to volume reductions that promote the dissociation of complexes to ionic species (Seward, 1981; 1988). However, rapid pressure changes can promote gold precipitation due to their impacts on phase separation (Wilkinson and Johnston, 1996; Sahoo *et al.*, 2015; Wen *et al.*, 2015; Sun *et al.*, 2019). Assuming that hydrothermal veins form during cycles of fault rupture and increased fluid flow during earthquakes (interspersed by periods of fluid pressure buildup), Weatherley and Henley (2013) suggested that fault-hosted gold precipitation occurs via a process known as flash vaporisation. In this model, following the development of a fault jog (Fig. 2.14.b.), dilation may cause the jog volume to increase in size by very large quantities (e.g. 13,000 times during an earthquake with a magnitude of 6 on the Richter Scale; Weatherley and Henley, 2013). The fluids that migrate into the fault plane become less compressible, meaning the fluid phase expands in size by up to several orders of magnitude (increasing the likelihood of phase separation; Weatherley and Henley, 2013). Experimental evidence has shown that in low density aqueous fluids, decreases in the fluid pressure are likely to result in decreased metal-ligand stability (Migdisov *et al.*, 2014). Quartz is also less soluble at low densities and pressures (e.g. quartz solubilities at 300 and 1 MPa are 4,200 and 0.03 mg kg^{-1}, respectively; Weatherley and Henley, 2013). For this reason, each flash vaporisation event results in the coprecipitation of metals and quartz (Weatherley and Henley, 2013). However, the bulk of vein formation is thought to occur during the subsequent flow of fluids throughout the ruptured fault (Weatherley and Henley, 2013), which seals the fault for further movements and the pressure builds up beneath the fault again. Flash vaporisation is cyclical, and it must be repeated thousands of times over several kyr to generate an ore deposit (Weatherley and Henley, 2013). The flash vaporisation model is applicable to strike-slip, normal, and thrust faults and all potential sources of mineralising fluids (Weatherley and Henley, 2013). In terms of the textures associated with the flash vaporisation model, Weatherley and Henley (2013) considered the aforementioned processes to result in the creation of multigenerational quartz veins within a fracture.

Pressure is not the only change in the physical environment that can stimulate gold precipitation; temperature may play a role as well. The solubility of several metal-ligand complexes (e.g. AuCl, AuH_2S) is dependent upon temperature (Fig. 2.9.a.). Temperature changes are unlikely to be impactful in the formation of OGDs because when gold is transported in the bisulphide complex, temperature decreases are likely to increase solubility prior to 200 °C (Fig. 2.9.a.; Mikucki, 1998). However, in the greatest depths of OGD formation shown in the crustal continuum model (Fig. 2.3.), temperature decreases are considered to be the only potential mechanism for stimulating gold precipitation; this is because the more efficient precipitation mechanisms of chemical disequilibration and phase separation do not typically operate in these environments (Mikucki, 1998). However, temperature changes at these depths can only take place via adiabatic cooling and conduction, which are relatively inefficient heat loss mechanisms (Mikucki, 1998). For this reason, OGDs in which cooling is the main driver of gold precipitation typically display low-grade mineralisation scattered over large vertical distances (Mikucki, 1998).

The greater sensitivity of the solubility of AuCl complexes to temperature (Fig. 2.9.a.) means that cooling may be more effective in facilitating gold precipitation in porphyry or epithermal environments (Pokrovski *et al.*, 2014). Nonetheless, as discussed in Section 2.4., the behaviour of gold-ligand complexes is controlled by variations in the H_2S content (Pokrovski *et al.*, 2014). Provided there is more ferrous iron than sulphur in the mineralising fluid, the deposition of chalcopyrite and pyrite may extract sulphur from the solution and stimulate gold precipitation (Pokrovski *et al.*, 2014). For this reason, gold precipitation associated with magmatic-hydrothermal fluids emanating from porphyries (Section 2.2.2.) is likely to coincide with the deposition of chalcopyrite and pyrite (Sillitoe, 2010; Pokrovski *et al.*, 2014).

Collectively, the combined decrease of pressure and temperature may give rise to the phenomenon known as phase separation (Pokrovski *et al.*, 2014). In porphyry and epithermal ore-forming environments (Fig. 2.4.b.), phase separation causes hypersaline fluids to condense from vapours with low salinities (Heinrich *et al.*, 2004; Pokrovski *et al.*, 2014). Under high temperature and pressure conditions, As, S, Cu, and Au are preferentially partitioned into the vapour phase relative to Pb, Ag, Zn, and Fe (Heinrich *et al.*, 2004); this process results in the development of mineralising fluids associated with porphyry and high sulphidation epithermal deposits (after the vapour condenses; Hedenquist *et al.*, 1993; Pokrovski *et al.*, 2014). On the other hand, in the epithermal regime (<300 °C; Fig. 2.4.b.), the pressure and temperature decreases can stimulate the formation of vaporised bubbles, which causes the removal of H_2S and CO_2 from the mineralising fluid (Pokrovski *et al.*, 2014). This process may result in the deterioration of AuH_2S complexes and gold precipitation, sometimes at bonanza grades (Saunders and Schoenly, 1995; Simmons *et al.*, 2005). Textural evidence of boiling as a precipitation mechanism in epithermal deposits may include the deposition of adularia and platy calcite following replacement by quartz (Hedenquist *et al.*, 2000a, b).

2.7.2. Precipitation as a result of chemical disequilibrium

The previous section has largely considered the role of physical changes in the environment of mineralisation on the precipitation of gold and associated phases; however, it is also possible for interactions between the hydrothermal fluid and host rock to stimulate precipitation as well, mainly as a result of chemical disequilibrium.

One of the major controls on gold precipitation associated with OGDs is wallrock sulphidation (i.e. the incorporation of sulphur from the wallrock by the hydrothermal fluid, resulting in the formation of new minerals; Phillips and Powell, 2010). This process is dependent on the reactivity of Fe from the host rock with H_2S in the hydrothermal fluid; wallrock sulphidation is therefore dependent on lithology, and more likely to occur in rocks with large quantities of mafic minerals; Zoheir *et al.*, 2008; Phillips and Powell, 2010). In the field, wallrock sulphidation is commonly represented by auriferous assemblages of pyrite, pyrrhotite, and marcasite (Phillips and Powell, 2010). Wallrock sulphidation is highly effective in stimulating gold precipitation because of the fundamental controls on the stability of the metal-ligand complexes; sulphur from the percolating mineralising fluids is captured by Fe to form pyrite or arsenopyrite (Equations 4 and 5), leading to a reduction in the amount of sulphur available (Hofstra *et al.*, 1991; Zoheir *et al.*, 2008). The presence of Fe in the wallrock is crucial to the significance of this gold precipitation mechanism (Equations 4 and 5), resulting in pyrite formation (Phillips and Groves, 1983; Neall and Phillips, 1997; Phillips and Powell; 2010). Relatively neutral pH values are also favourable to the precipitation of gold via wallrock sulphidation (Fig. 2.15.).

$$FeO(silicate) + 2H_2S = FeS_2 + H_2O(aq) + H_2(g)$$

Equation 4. Pyrite formation during wall rock sulphidation with silicate (Phillips and Powell, 2010).

$$Fe_3O_4\ (oxide) + 6H_2S = 3FeS_2 + 4H_20(aq) + 2H_2(g)$$

Equation 5. Pyrite formation during wall rock sulphidation with oxide (Phillips and Powell, 2010).

Based on the diagram shown in Fig. 2.15., it can be inferred that changes in the fO_2 and pH conditions of a mineralising fluid would potentially result in gold precipitation. For example, increases in fO_2 towards the field occupied by hematite (Fig. 2.15.) may destabilise the AuH_2S complexes, particularly at higher pH values; this could feasibly be achieved by the influx of meteoric fluids (Phillips and Powell, 2010). On the hand, reduction of a mineralising fluid is particularly effective in destabilising AuH_2S complex at acidic pH values (Fig. 2.15.). In nature, the most likely mechanism for gold precipitation via fluid reduction involves the interaction between a hydrothermal fluid and carbonaceous wallrock (Connolly and Cesare, 1993; Phillips and Powell, 2010; Ward *et al.*, 2017).

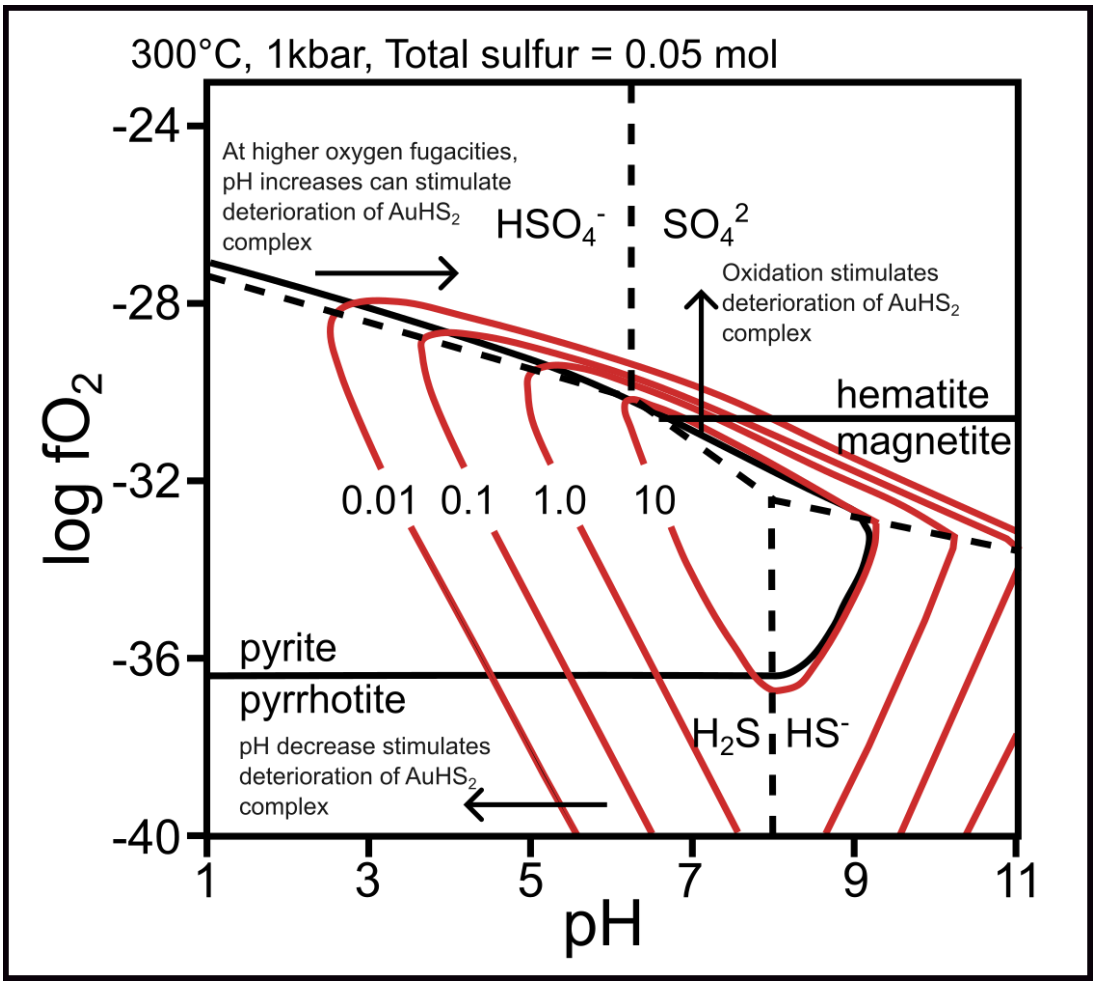

Figure 2.15. Calculated gold solubilities and mineral stability fields as a function of pH and log fO_2 at 300 °C. Adapted from Seward (1973) and Ward *et al.* 2017. The red lines display Au concentrations of 0.01, 0.1, and 10.0 ppm.

The mixing between fluids of different compositions, temperatures and acidities may facilitate gold precipitation (Mikucki, 1998; Hodkiewicz *et al.*, 2009; Neumayr *et al.*, 2007). For example, the mixing of magmatic-hydrothermal brines (with high metal concentrations as a result of the previously described phase separation processes; Section 2.7.1.) with meteoric waters results in dilution, oxidation, pH changes, and further cooling. Collectively, these processes, along with boiling (Section 2.7.1.), are important genetic processes in epithermal gold mineralisation (Fig. 2.4.b.; Simmons *et al.*, 2005; Pokrovski *et al.*, 2014). Several epithermal deposits, including Lepanto (Philippines), have δD and $\delta^{18}O$ compositions that encompass the ranges reported from meteoric and magmatic fluids, which is indicative of fluid mixing (Hedenquist *et al.*, 1998; Carman, 2003; Simmons *et al.*, 2005). Corbett and Leach (2008) described mineralogical variations associated with fluid mixing in epithermal deposits depending upon the nature of the mixing fluid; for example, deeply circulating meteoric waters (Fig. 2.4.b.) may be associated with sulphide and opal assemblages, whereas shallow oxygenated meteoric fluids (around the volcanic vent in Fig. 2.4.b.) are identifiable by the precipitation of hematite. Corbett and Leach (2008) considered acidic waters around the caps of low sulphidation deposits (Fig. 2.4.b.) to be associated with the highest gold

grades (typified by kaolinitic assemblages). As discussed previously, oxidation of bisulfide complexes to the hematite stability field (Fig. 2.15.) is an effective mechanism of stimulating gold precipitation.

Whilst fluid mixing has been suggested as an important precipitation mechanism in epithermal deposits, several researchers have suggested that it plays a minor role in the formation of OGDs (Mikucki, 1998; Pokrovski *et al.*, 2014), often on the basis that the pressure fluctuations during the mineralisation processes associated with these deposits tend to result in fluid unmixing and phase partitioning instead (Goldfarb and Groves, 2015). However, mixing between oxidising magmatic fluids and reducing mineralising fluids from the metasedimentary pile is invoked as a genetic process in the OGDs found in the St Ives Camp of Western Australia (Neumayr *et al.*, 2007). Relative to epithermal deposits, fluid mixing is considered to have less importance in the formation of Cu-Au porphyries (Pokrovski *et al.*, 2014), mainly because this environment (Fig. 2.4.b.) contains a much greater proportion of magmatic fluids and the meteoric input relative to epithermal systems is generally considered to be smaller (Hedenquist *et al.*, 1998; Watanabe and Hedenquist, 2001; Harris and Golding, 2002; Seedorff and Einaudi, 2004).

2.8. Theoretical principles underpinning the use of isotope geochemistry

As part of the present study, several isotope systems have been used to evaluate the age of mineralisation and magmatism associated with the LTVS, as well as the sources of the mineralising fluids. For this reason, it is necessary to provide an overview of the theoretical principles behind the application of these different isotope systems in geological studies. The methodologies involving isotopes that are relevant to this study can be distinguished into two categories: geochronological and stable isotope studies (Table 2.5.). Geochronology involves the application of decay rates of naturally occurring radioactive isotopes to calculate the age of the sample (Jäger, 1979). On the other hand, characterising the stable isotope geochemistry of minerals is a well-established approach for assessing the source and conditions (e.g. temperature, redox state, fluid-rock interactions) of the mineralising fluids (Ohmoto, 1972; Sheppard, 1977; Oreskes and Einaudi, 1992; Huston, 1997; Barker *et al.*, 2013). Stable isotope geochemistry mostly focuses on the relative partitioning of stable isotopes (i.e. changes in isotope ratios; Seal, 2006). In this section, the theoretical principles of different radiogenic and stable isotope systems are summarised.

The different isotope systems (Table 2.5.) have been selected based on the logistical constraints of this study and their suitability for application on the LTVS. For example, whilst $\delta^{13}C$ analyses on hydrothermal and magmatic ore deposits are common (Beinlich *et al.*, 2017; Tarasova *et al.*, 2020; Brusnitsyn *et al.*, 2022), the paragenetic interpretations produced for the LTVS in this study (Chapter 5) found that the carbonates overprint the metallic mineralisation stages at most localities; investigating the $\delta^{13}C$ signatures of the LTVS (Fig. 1.1.b.) would have limited relevance to understanding the metallogeny. Regarding ^{18}O, which is also used to study ore-forming fluids (Barker *et al.*, 2013), the most voluminous quartz phase in the localities associated with the LTVS is typically barren (Webb *et al.*, 2024a). For this reason, ^{18}O analyses would not be informative regarding the metallic mineralisation. However, the integrated application of several isotope systems can be beneficial for metallogenic studies; each isotope system is sensitive to different aspects of the ore-forming process (Campbell and Larson, 1998; Barker *et al.*, 2013; Huston *et al.*, 2023). For example, in this study, the $\delta^{34}S$ value of a sulphide mineral reflects the source of sulphur and physiochemical changes recorded by the hydrothermal fluid (Ohmoto, 1972; Seal, 2006; Hutchison *et al.*, 2020) whereas the Pb system enables the provenance of lead to be identified (Cannon *et al.*, 1961; Brevart *et al.*, 1982; Huston and Champion, 2023); collectively, this information provides a greater level of information about the LTVS than either system alone. With more financial support and time, further isotope systems would have been incorporated into the present study. For example, other researchers have noted that nitrogen and helium isotopes can be effective in fingerprinting the involvement of a mantle fluid source during OGD mineralisation (Simmons *et al.*, 1987; Jia *et al.*, 2003; Graupner *et al.*, 2006; Kerrich *et al.*, 2006; Goldfarb and Groves, 2015; Zhao *et al.*, 2022a, b). Had more time been available, it may have been possible to study the fluid inclusions within the LTVS and analyse their isotopic compositions.

System	Type of isotope system	Description of use	Sample material	References
$^{207}Pb/^{204}Pb$, $^{206}Pb/^{204}Pb$	Radiogenic (except for ^{204}Pb)	Assesses the provenance of galena, can be used to derive a model age (i.e. an estimate of the age based on ratios of the different Pb isotopes in the sample; Huston and Champion, 2023)	Galena	(Townsend *et al.*, 1998; Huston *et al.*, 2017; Huston and Champion, 2023)
Re-Os	Radiogenic	Provides ages for sulphide crystallisation	Molybdenite	(Stein *et al.*, 2001; Selby and Creaser, 2004)
$\delta^{34}S$	Stable	Fractionation in ^{34}S is linked to the temperature, fO_2 and pH of the fluid during mineralisation	Pyrite, Galena, Chalcopyrite, Molybdenite, Arsenopyrite	(Jensen, 1959; Ohmoto, 1972; Seal, 2006)
U-Pb	Radiogenic	Can be used to date various minerals (e.g. apatite and titanite)	Zircon	(Schoene *et al.*, 2013; Schoene, 2014)

Table 2.5. Summary of the different isotope systems utilised in this study.

Regarding geochronology, the mathematical formula (Equation 6) for radioactive decay is a fundamental concept. The basic principle is that a parent radionuclide becomes incorporated into the lattice of a mineral during crystallisation and over time, decays into a different daughter nucleus (Mousuf, 1952; Curran, 1953; Aldrich and Wetherill, 1958; Jaffey *et al.*, 1971; Groch, 1998; Schmitz *et al.*, 2020). Key assumptions underlying the application of Equation 6 include the following: no daughter isotopes being present when the geochronometer (i.e. a mineral phase that can be used to measure the age of a rock; Schoene *et al.*, 2013) formed, a stable decay rate over time, and no addition or removal of both parent and daughter isotopes since the formation of the mineral (Frost *et al.*, 2001; Parrish, 2003; Schoene, 2014). The names given to the various isotope systems utilised in geochronology typically begin with the parent nucleus and end with the daughter product of that specific decay path. For example, ^{238}U breaks down into ^{206}Pb, and is hence termed 'U-Pb' (Schoene, 2014).

Under closed system conditions, the measured isotopic concentrations of the parent and daughter nuclei can be used to calculate the age of the mineral (Equation 6), provided that the decay constant is known (Schmitz *et al.*, 2020). Ideal geochronometers are minerals with the following characteristics during radioactive decay: high initial parent to daughter ratios (Frost *et al.*, 2001), no uptake of daughter isotopes whilst assimilating parent isotopes during crystallisation (Harrison *et al.*, 2002; Harrison and Zeitler, 2005), phase crystallisation prior to isotope retention, and a crystallisation temperature below the closure

temperature (i.e. the temperature at which there is no longer any diffusion of the parent or daughter isotopes out of the mineral; Dodson, 1973; Braun *et al.*, 2006; Gardés and Montel, 2009). Regarding closure temperature, it is important to note that there may be slight differences in ages obtained via different geochronological methods (the closure temperature differs, depending on the mineral and isotope system used; Dodson, 1973; Braun *et al.*, 2006).

$$t = 1/\lambda \times \ln (1 + D/P)$$

Equation 6. The radioactive decay equation (Meyer and Schweidler, 1927; Faure, 1986; Shea, 2001; Huestis, 2002; Vermeesch, 2018), where t = age of the rock or mineral, λ = the decay constant, D = number of daughter atoms in the sample, P = number of parent atoms, and ln = natural log.

2.8.1. Re-Os

The Re-Os system exploits the beta decay path for ^{187}Re to ^{187}Os, a process with a half-life of 41.6×10^9 years (Smoliar *et al.*, 1996); beta decay takes place when a neutron inside the radioactive Re isotope decays into a proton, releasing an electron and an antineutrino. This changes the atomic number in the Re nucleus by 1, whilst the mass number remains constant (Konopinski, 1943; Borzov, 2006). Re-Os dating on molybdenite is widely applicable in dating sulphide mineralisation (Table 2.6) because molybdenite occurs in various types of ore deposits (Selby and Creaser, 2001; Selby *et al.*, 2009; Lawley and Selby, 2012; Li *et al.*, 2016b; Wang *et al.*, 2019; Chen *et al.*, 2020; Myint *et al.*, 2021). The Re-Os system can also be used to date organic rich rock units (Creaser *et al.*, 2002; Pietras *et al.*, 2022), making it an invaluable tool in elucidating the depositional history of sedimentary basins. Re-Os dating has also been applied to a variety of sulphides in hydrothermal ores, including pyrite (Hnatyshin *et al.*, 2015; Yue *et al.*, 2022), chalcopyrite (Lawley *et al.*, 2013; Zhimin and Yali, 2013; Deng *et al.*, 2016), and arsenopyrite (Arne *et al.*, 2001; Morelli *et al.*, 2007; Lawley *et al.*, 2015). However, these sulphides often do not contain sufficient Re concentrations to yield accurate dates (Stein *et al.*, 1998a, b; 2000; Huang *et al.*, 2015). A low Re quantity upon crystallisation also results in a low Os concentration produced by radioactive decay within the sulphide, which makes it difficult to measure the ^{187}Os content in a precise and accurate manner (Smoliar *et al.*, 1996; Selby and Creaser, 2001). Re-Os dates produced from these sulphides typically have large error ranges; for example, Re-Os dating of syngenetic pyrite at Foss (Fig. 1.1.b.) yielded dates of 604.0 ± 7.2 and 612 ± 18.6 Ma (Moles and Selby, 2023). The typical approach for calculating Re-Os dates is shown in Equation 7.

To avoid deriving Re-Os dates with large amounts of uncertainty, molybdenite was chosen for Re-Os dating in the present study (Table 2.5.), for several reasons; molybdenite occurs within the LTVS at Tomnadashan (Pattrick, 1984), meaning that it was possible to conduct Re-Os dating on this phase. Furthermore, molybdenite is robust in the face of hydrothermal alteration processes (Stein *et al.*, 1998a, b; Selby and Creaser, 2001; Bingen and Stein, 2003; Ootes *et al.*, 2007; Bingen *et al.*, 2008) and a closed system is

therefore likely to be maintained. The molybdenite crystal lattice is also impenetrable to Os following crystallisation (Stein *et al.*, 2001; Takahashi *et al.*, 2007), which simplifies the geochronological analyses because there is confidence that the ^{187}Os in the sample solely results from radioactive decay (Markey *et al.*, 2007). Regarding the closure temperature of the Re-Os decay chain within molybdenite, different estimates have been provided; some consider the closure temperature to be as low as 500°C (Suzuki *et al.*, 1996; Peng *et al.*, 2006). However, others have reported that the Re-Os molybdenite geochronometer avoids being reset during granulite facies metamorphism up to 800 °C (Stein and Bingen, 2002; Bingen and Stein, 2003), which may suggest that the closure temperature is >500 °C.

$$t = \ln(^{187}Os/^{187}Re + 1)/ \lambda$$

Equation 7. Calculating the age of a mineral utilising Re and Os isotopes, where $\lambda = {}^{187}Re$ decay constant, 1.666×10^{-11} a^{-1}. The decay constant is from Smoliar *et al.* 1996. This equation is the standard approach to Re-Os dating (Selby and Creaser, 2001; Stein *et al.*, 2001; Li *et al.*, 2017).

Whilst Re-Os dating of molybdenite is a powerful tool, there are some uncertainties associated with the interpretation of data generated using this isotope system. The main potential complication involves the intra-granular decoupling of ^{187}Re-^{187}Os (Hogmalm *et al.*, 2019). Elemental mapping of molybdenite crystals has found that the isotopes tend to cluster at specific sites within the mineral lattice; the nuggeting effect of Re and Os isotopes can lead to heterogeneous Re-Os ratios, even within a single crystal (Barra *et al.*, 2017). There are several causes of intragranular decoupling of ^{187}Re-^{187}Os in molybdenite. For example, post-mineralisation deformation of the molybdenite may lead to the development of defects within the crystal lattice where daughter ^{187}Os accumulates (Stein *et al.*, 2003; Selby and Creaser, 2004). Alternatively, variations in the Re concentration during the crystallisation event could result in some regions of the crystal being preferentially endowed in Re prior to the onset of radioactive decay (Rathkopf *et al.*, 2017; Zhai *et al.*, 2019). Furthermore, coarse-grained molybdenite crystals (i.e. >1 cm) are more susceptible to intragranular heterogeneity (Stein *et al.*, 2001; 2003; Selby and Creaser, 2004; Porter and Selby, 2010; Zhai *et al.*, 2019). Whilst the mechanisms behind this trend are not fully understood, one explanation may involve the diffusive nature of intragranular Re and Os decoupling; a large surface area to volume ratio could enable this process to occur more efficiently (Porter and Selby, 2010). Nonetheless, intragranular Re and Os decoupling means that Re-Os dating often produces a diversity of ages for the same molybdenite specimen (Zhai *et al.*, 2019), although this problem can be mitigated against by analysing a large number of samples (Porter and Selby, 2010; Zhai *et al.*, 2019).

2.8.2. U-Pb

There are four naturally occurring stable isotopes of lead; ^{204}Pb, ^{206}Pb, ^{207}Pb, and ^{208}Pb. The only non-radiogenic isotope from this list is ^{204}Pb (Holmes, 1946; Jaffey *et al.*, 1971; Woodhead and Hergt, 2000). ^{206}Pb, ^{207}Pb, and ^{208}Pb represent the ends of the ^{238}U, ^{235}U, and ^{232}Th decay chains (Huston and Champion, 2023). The decay constants for these chains are 0.155125×10^{-9} yr^{-1}, 0.98485×10^{-9} yr^{-1}, and 0.049475×10^{-9} yr^{-1}, which correspond to half-lives of 4.468, 0.704, and 14.05 Ga (Jaffey *et al.*, 1971; Huston and Champion, 2023). Unlike the Re-Os system, which only involves beta decay, the U-Pb decay chain also takes place by alpha decay (Fig. 2.16.); this process can be defined as the emission of an alpha particle (i.e. with a mass equivalent to a helium nucleus), causing the parent isotope to become an isotope of a different atomic element as a result of the change in the number of protons in the nucleus (Geiger and Nuttall, 1911; Mang, 1964; Rasmussen, 1968). The decay paths (Fig. 2.16.) result in a series of intermediate daughter isotopes and are distinctive because none of the isotopes occur in multiple series (e.g. ^{238}U does not occur in the ^{235}U or ^{232}Th decay chains). During alpha decay, the mass number changes by 4 and the atomic number changes by 2, whilst during beta decay, the mass number remains unchanged whilst the atomic number increases by 1 (Geiger and Nuttall, 1911; Mang, 1964; Schoene, 2014).

$$^{238}\text{U} \rightarrow {}^{206}\text{Pb} + 8\alpha + 6\beta + 47\text{MeV}$$
$$^{235}\text{U} \rightarrow {}^{207}\text{Pb} + 7\alpha + 4\beta + 45\text{MeV}$$
$$^{232}\text{Th} \rightarrow {}^{208}\text{Pb} + 6\alpha + 4\beta + 40\text{MeV}$$

Figure 2.16. The decay paths of ^{238}U, ^{235}U and ^{232}Th and the energy released during each decay chain (MeV = 1 million electronvolts; α and β refer to alpha and beta decay events). Adapted from Dickin (1995), Faure and Mensing (2005), and Schoene (2014).

The U-Pb decay path is the favoured method for many geochronological studies because there are several minerals with high uranium concentrations that commonly form as a result sedimentological, igneous, metamorphic, and hydrothermal processes (i.e. they are abundant and easy to analyse; Parrish, 2003; Heaman, 2009; Gehrels, 2011; Corfu, 2003; Schoene, 2014). Examples of minerals suitable for U-Pb dating include monazite, rutile, baddeleyite, and calcite (Parrish, 1990; Heaman and LeCheminant, 1993; Janots *et al.*, 2009; Zack *et al.*, 2011). However, zircon is well-suited to U-Pb geochronology for a variety of reasons; for example, zircon has a high U-Pb closure temperature (>1000 °C; Lee *et al.*, 1997; Flowers *et al.*, 2005), meaning that the Pb atoms produced during radioactive decay are not able to diffuse out of the mineral unless it is heated to these temperatures in subsequent geological events (Silver and Deutsch, 1963; Schoene, 2014). Furthermore, upon crystallisation, zircon primarily incorporates U and Th rather than

common Pb, meaning there is relative confidence that the measured daughter isotopes have resulted from radioactive decay (Villa and Hanchar, 2017). The key theoretical principle in determining a U-Pb date (e.g. Equations 8 and 9) is that the decay constants of the different decay paths (Fig. 2.16.) are known values (although as mentioned at the start of this section, having a known decay constant is an assumption underpinning all geochronological methods), meaning that by measuring the ratio of uranium to lead in a sample, it is possible to solve all aspects of Equation 6 and calculate the time passed since crystallisation began.

$$t = 1/\lambda^{238}U \ln (^{206}Pb^*/^{238}U + 1) \quad (8)$$

$$t = 1/\lambda^{235}U \ln (^{207}Pb^*/^{235}U + 1) \quad (9)$$

Equations 8 and 9. Formulae for calculating the age of a sample using uranium and lead isotope data, where t = time, λ = the decay constant, * = radiogenic Pb, and ln = natural logarithm. Adapted from Wetherill (1956) and Schoene (2014).

However, it should be noted that there are complexities with applying Equations 8 and 9 to derive U-Pb dates. The main cause of uncertainty regarding U-Pb dating is the loss of Pb from the lattice of the mineral (Schoene, 2014); for example, during alpha decay (Fig. 2.16.), zircons are often damaged by radiation, which makes them more susceptible to Pb loss during alteration at temperatures <250 °C (Ewing, 2003; Geisler *et al.*, 2003; Guitreau and Flahaut, 2019). Experimental evidence has shown that at temperatures above 250 °C, radiation damage in zircons is annealed (Ketcham *et al.*, 1999); furthermore, Pb diffusion is highly inefficient at temperatures <900 °C (Lee *et al.*, 1997; Cherniak and Watson, 2001). However, Pb loss may occur at such high temperatures in response to zircon recrystallisation (Mezger and Krogstad, 1997). Another cause of uncertainty pertains to the initial Pb content of the mineral in question; prior to the onset of the radioactive decay processes, there is likely to be some Pb present within the mineral (known as 'common Pb'), meaning the Pb measured may not reflect the results of the decay process (Schoene, 2014). There are several ways to account for this problem. For example, by directly measuring the Pb content of phases that are inferred to coprecipitate with the geochronometer (e.g. from petrographical evidence), it may be possible to assume the initial Pb content of the geochronometer and deduct it from Pb considered to arise from radioactive decay (Chamberlain and Bowring, 2001; Schoene and Bowring, 2006).

When the $^{238}U/^{206}Pb$ and $^{235}U/^{207}Pb$ yield conflicting date estimates from one another, the date is said to be 'discordant' (Wetherill, 1956; Schoene, 2014). Discordant dates can be visualised graphically. For example, the formulas in Equations 8 and 9 may be used to create diagrams with isochrons (i.e. a line joining points of equal ages or time intervals; Wendt, 1984; Zheng, 1992), or alternatively, concordia plots (Wetherill, 1956). Concordia diagrams enable the identification of Pb loss, with the 'Wetherill' curve (Fig. 2.17.a.) being

the traditional approach (Wasserburg, 1963; Pidgeon *et al.*, 1966; Schoene, 2014). These curves can be constructed by plotting $^{206}Pb^*/^{238}U$ (where * equals radiogenic) and $^{207}Pb^*/^{235}U$ ratios which yield the same ages against one another and drawing a curve through these data points (Wetherill, 1956). Mutually consistent datapoints are said to be 'concordant' and reflect the following conditions: no gain or loss of uranium or lead since the onset of decay, accurate corrections have been made for non-radiogenic (i.e. common) Pb, and the implementation of an accurate decay constant (Wetherill, 1956). Alternative approaches to the Wetherill concordia diagram include the Tera-Wasserburg concordia diagram (Fig. 2.17.b.; Tera and Wasserburg, 1972). Whilst the interpretation of the Tera-Wasserburg concordia curve is the same as the traditional Wetherill plot (Schoene, 2014; Condon *et al.*, 2023), the tighter curvature displayed by the latter throughout the Precambrian (Fig. 2.17.b.) makes it a preferable option for the visualisation of older datapoints (Schoene, 2014; Condon *et al.*, 2023).

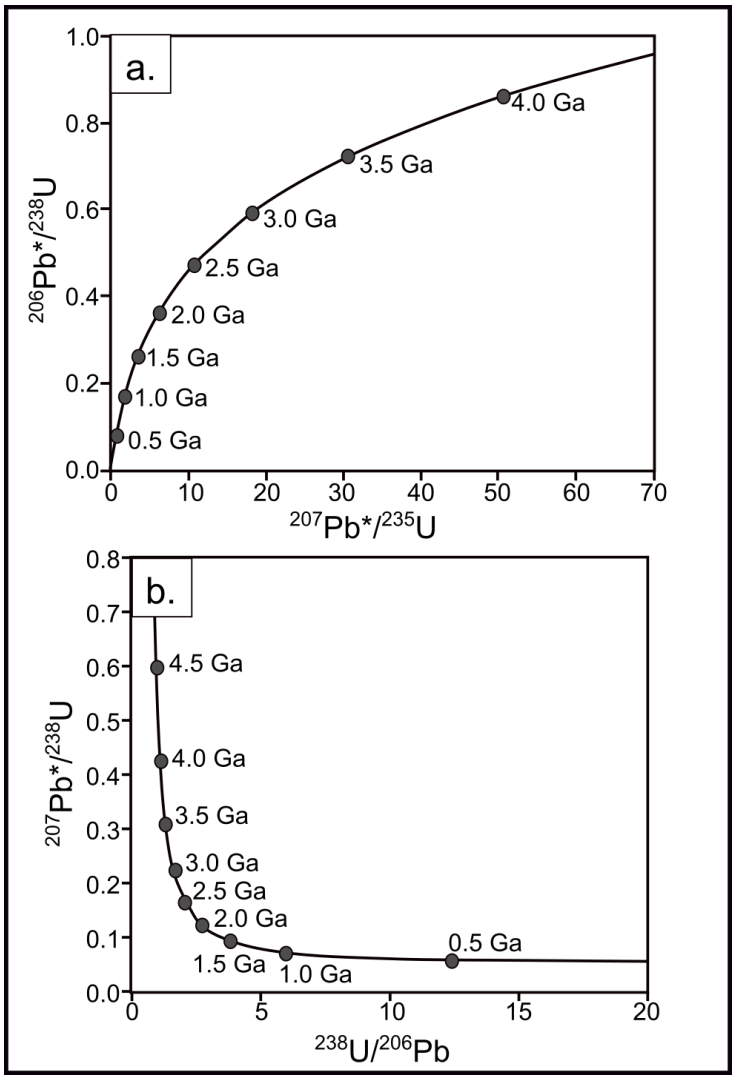

Figure 2.17. Examples of concordia curves, showing the evolution of Pb/U ratios with time in a closed system. **a.** The concordia curve (Wetherill, 1956). **b.** Tera-Wasserburg concordia curve (adapted from Tera and Wasserburg, 1972). Data points that fall along this line are 'concordant.'

Once a concordia curve has been constructed, it may be possible to highlight points at which the two decay paths yield inconsistent (i.e. discordant) ages, and thereby identify Pb loss. One such example of this is shown in Fig. 2.18. Under a scenario in which a mineral crystallises at T_0 and subsequently loses Pb at T_1 (e.g. potentially as a result of disruption to the closed system due to metamorphism), the datapoints plot below the Concordia line (Fig. 2.18.). It is possible to make an assessment on the age of disruption to the closed system, which may enable the identification of geologically important events (e.g. post-magmatic metamorphism). Aside from Pb loss and incorrect assumptions regarding initial Pb content, there are other potential causes of discordance on a Wetherill concordia plot (Schoene, 2014). For example, several minerals (including zircon) may contain older cores and younger rims and overgrowths (Bickford *et al.*, 1981; Corfu and Ayres, 1984; Wayne *et al.*, 1992; Hanchar and Rudnick, 1995). With in-situ U-Pb dating, it may be possible to avoid the mixing of different Pb domains by preferentially and consistently targeting an aspect of the grain of interest (e.g. the core; Schoene, 2014).

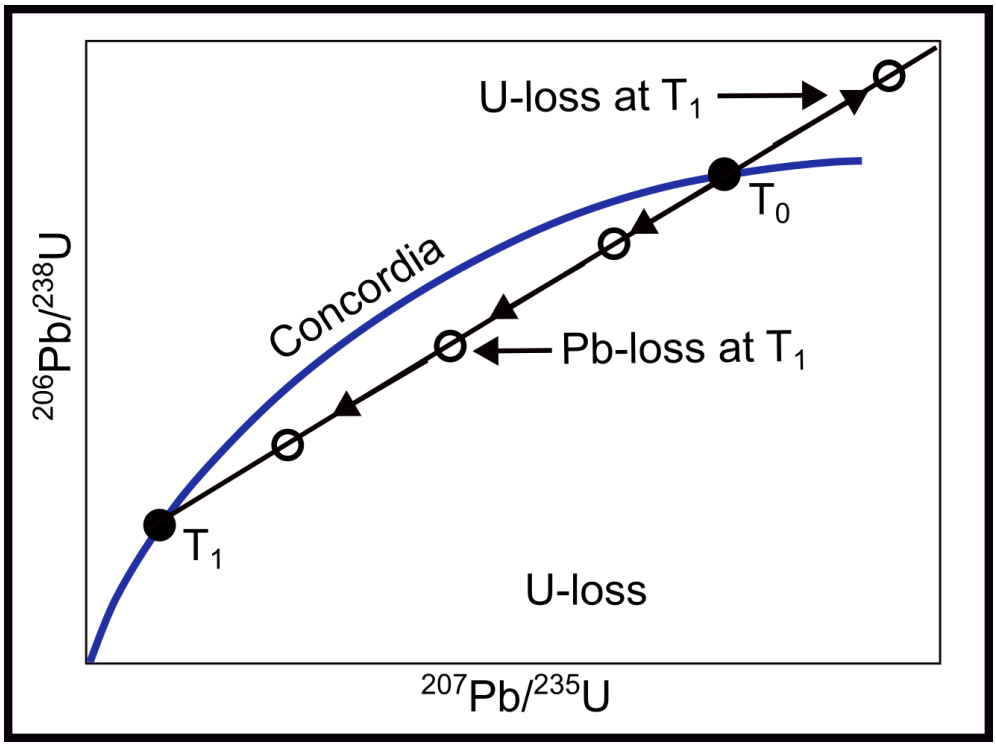

Figure 2.18. An example Wetherill concordia diagram (adapted from: Allègre, 2008; Vermeesch, 2017). Filled symbols = concordant points, empty symbols = discordant points. T = time.

SEM-BSE and SEM-CL imaging may reveal textures that are informative in contextualising and interpreting the U-Pb ages derived from zircon crystals; a comprehensive atlas of these textures was produced by Corfu (2003). Many magmatic zircon crystals display signs of 'oscillatory zonation' (i.e. the texture shown in the schematic diagram of zircon; Fig. 2.19.a.). In terms of the origins of this texture, some researchers suggest that the growth of zircon exerts a compositional effect on the magma, in which the zircon extracts elements from the melt, thereby depleting the melt (Fowler *et al.*, 2002). This process leaves behind a magma with a modified composition from which later layers of zircon precipitate, albeit with a different chemical composition from the earlier layers (Fowler *et al.*, 2002). However, the importance of processes at the crystal-melt interface in the development of zircon zonation has been debated (Hoskin, 2000; Corfu, 2003); larger-scale processes may be more important in achieving the compositional variations necessary for the formation of oscillatory zonation, such as magmatic mixing (Gagnevin *et al.*, 2010), changes in P-T conditions (Bindeman and Melnik, 2016) or the presence of impurities in the magma (Erdmann *et al.*, 2013). Further publications that provide guidance on the interpretation of zircon textures have been discussed in Chapter 6 where appropriate (Paquette *et al.*, 1995; Hoskin, 2000; Schaltegger, 2007; Olierook *et al.*, 2021). However, the Corfu (2003) publication is the main reference for identifying and describing the observed textures.

Regarding the methods that are utilised in U-Pb geochronology, the most commonly implemented approaches are shown in Fig. 2.19.; Isotope dilution-thermal ionisation mass spectrometry (ID-TIMS), Secondary ion mass spectrometry (SIMS), and laser ablation inductively coupled plasma mass spectrometry (LA-ICP-MS). Regarding ID-TIMS, this method is distinct from those involving SIMS and LA-ICP-MS because it involves the use of isotope dilution, i.e. the spiking of samples with a known quantity of one or multiple isotopic tracers (usually a mixture of ^{205}Pb, ^{202}Pb, ^{233}U and ^{236}U) for the purpose of converting ratios measured via mass spectrometry to moles of sample isotopes (Inghram, 1954; Webster, 1959; Schoene, 2014; Stracke *et al.*, 2014). Whilst methods involving SIMS or LA-ICP-MS (Fig. 2.20) may provide an in-situ context for the resulting data, they do not involve the use of isotope dilution to calculate the ratio of Pb to U (Schoene, 2014). This has implications regarding the precision and accuracy of U-Pb dates derived by these methods relative to ID-TIMS. Specifically, the use of an isotope tracer allows for the correction of mass bias (i.e. the preferential fractionation of light isotopes on the basis of mass during the measurement process) (Schoene, 2014). During ID-TIMS analyses, the U and Pb ratios of both the sample and spike isotopes are measured simultaneously (Schoene *et al.*, 2006; Stracke *et al.*, 2014; Condon *et al.*, 2015). By comparing the measured ratios of sample isotopes to their corresponding spike isotopes, it is possible to calculate a robust fractionation factor (Black *et al.*, 2004; Wotzlaw *et al.*, 2017; Schaltegger *et al.*, 2021). This factor is then used to apply a correction to the measured ratios of radiogenic uranium and lead isotopes, removing the mass bias (Schmitz and Schoene, 2007; Schoene *et al.*, 2010; Schoene, 2014). As this is not possible for U-Pb methods involving SIMS, the dates derived from this method are typically less

precise and accurate than those obtained from ID-TIMS (Schoene, 2014). The precision and accuracy of SIMS and LA-ICP-MS methods are also often reduced by the effects of ablation (Fig. 2.19.b.-c.), which liberates other elements aside from U and Pb; these may cause interference to the signal of the mass spectrometer (Horstwood *et al.*, 2003; Stern *et al.*, 2009; Sharpe and Fayek, 2016).

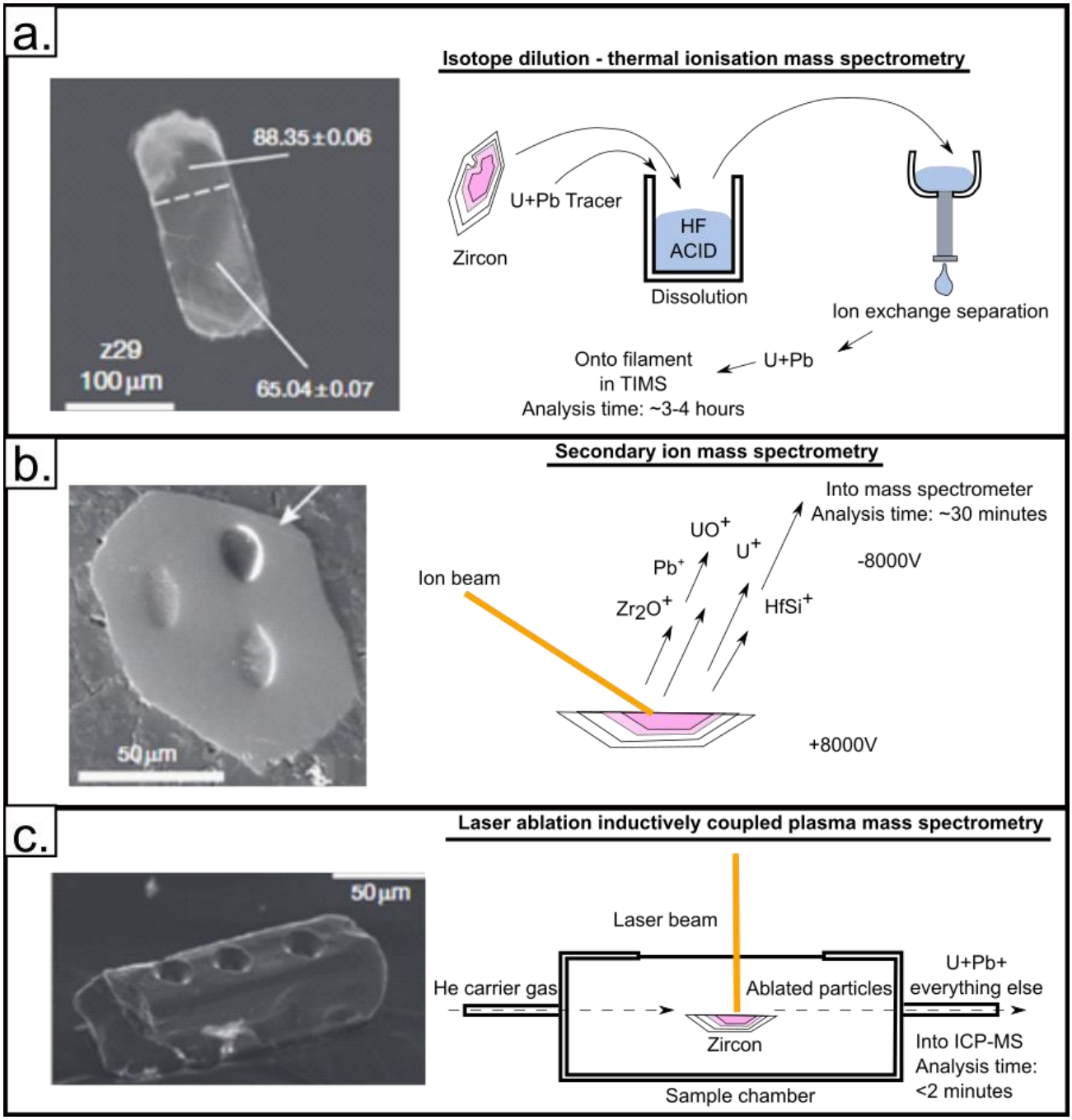

Figure 2.19. Common approaches to U-Pb geochronology (Schoene, 2014) following SEM characterisation of a zircon crystal. **a.** Isotope dilution-thermal ionisation mass spectrometry (ID-TIMS. **b**. Secondary Ion Mass Spectrometry (SIMS). **c.** Laser Ablation Inductively Coupled Plasma Mass Spectrometry (LA-ICP-MS).

However, as with other U-Pb methods, the reliability of ID-TIMS ages may be hindered by Pb loss. The traditional ID-TIMS approach attempted to ameliorate this problem by the implementation of the 'air abrasion' method (Krogh, 1982), which assumed that the outer rims of the zircons contained higher concentration of uranium (i.e. they were more prone to Pb loss) and therefore sought to remove them mechanically (Krogh, 1982). However, Mattinson (2005) developed a technique known as Chemical Abrasion Isotope-Dilution Thermal Ionization Mass Spectrometry (CA-ID-TIMS), which differs from the traditional 'air abrasion' methods because it involves partially annealing the zircons prior to chemical dissolution. The hydrofluoric acid utilised in the dissolution process is capable of seeping through microcracks and into the cores of the zircon crystals (Mattinson, 2010; 2011); for this reason, chemical abrasion may remove any portion of the crystal with high uranium concentrations (i.e. not just the rims; Mundil *et al.*, 2004; Mattinson, 2005; Davydov *et al.*, 2010; Burgess *et al.*, 2014; Huyskens *et al.*, 2016; Widmann *et al.*, 2019; McKanna *et al.*, 2022). The residue that is left behind as a result of the chemical abrasion step is therefore comprised of zircons with lower uranium concentrations (i.e. they are more likely to have remained a closed system during U-Pb decay; Mattinson, 2005; Condon *et al.*, 2023). CA-ID-TIMS was selected for the present study because this method, out of all the different U-Pb approaches that have been discussed, offers the highest degrees of precision and accuracy regarding the final age yielded for the sample in question (± 0.1 % or better; Pointon *et al.*, 2014; Manor *et al.*, 2022; Zhong *et al.*, 2022; Dufour *et al.*, 2023).

2.8.3. Sulphur isotopes

In nature, sulphur occurs as four stable isotopes: ^{32}S, ^{33}S, ^{34}S, and ^{36}S (Jensen, 1959). The application of sulphur isotopes to the study of ore deposits is well-established (Ohmoto, 1972; Ohmoto and Rye, 1979; Ohmoto, 1986; O'Neil, 1986; Ohmoto and Goldhaber, 1997; Barker *et al.*, 2013; Hutchison *et al.*, 2020) and throughout this subsection, the theoretical principles of sulphur isotopes are outlined.

2.8.3.a. The concept of $\delta^{34}S$

Out of the four stable sulphur isotopes, ^{34}S comprises ~4 % of the total amount, whereas ^{32}S represents 92 %; the abundance of ^{32}S means that deriving the ^{34}S to ^{32}S ratio is relatively straightforward (Seal, 2006). However, in stable isotope geochemistry, the abundances of different isotopes are often expressed relative to a standard reference material, denoted as a dimensionless value termed 'δ' (McKinney *et al.*, 1950). There are several reasons for expressing the stable isotope ratios as δ. For example, relative differences in stable isotope ratios can be constrained with greater precision than absolute isotopic ratios (Seal *et al.*, 2000; Brand and Coplen, 2012; Eiler *et al.*, 2014). Furthermore, for most stable isotope systems, the variation between the isotopic material of a sample and the reference standard is typically very small (and therefore difficult to distinguish); expressing the ratio via the formula shown in Equation 10 yields values that are tangibly different, making comparisons easier (Sheppard, 1981; Slater *et al.*, 2001; Criss and

Farquhar, 2008). Regarding sulphur isotopes, the Vienna Canyon Diablo Troilite (V-CDT) is used as the reference standard (Beaudoin *et al.*, 1994; Hoefs, 2009). The formula for deriving the $\delta^{34}S$ value is shown in Equation 10.

$$\delta^{34}S = \left(\frac{\left({}^{34}S/{}^{32}S \right)_{sample} - \left({}^{34}S/{}^{32}S \right)_{reference}}{\left({}^{34}S/{}^{32}S \right)_{reference}} \right) \times 1000$$

Equation 10: The formula used to calculate the $\delta 8^{34}S$ signature of a sample, where the 'reference' is the V-CDT (Seal, 2006).

2.8.3.b. Sulphur isotope fractionation in mineral formation

The $\delta^{34}S$ value of any substance is influenced by sulphur isotope fractionation (i.e. the differences in the partitioning behaviour of sulphur isotopes; Seal, 2006) relative to the parent material. However, sulphur isotope fractionation is controlled by a wide range of conditions that influence the resulting ratio of the material being studied. These controls can be categorised as either isotope exchange chemical reactions or kinetic processes (Urey, 1947; Bigeleisen and Mayer, 1947; Bigeleisen, 1952; Seal, 2006). The latter normally pertains to the role of sulphate reducing bacteria (Bacterial Sulphate Reduction; BSR), which tend to preferentially utilise ^{32}S (Southam and Sanders, 2005). This is because it is easier for bacteria to break bonds with lighter isotopes, such as the ^{32}S-O bond (Seal, 2006). Generally speaking, sulphate reducing bacteria are only active in anoxic environments; for example, the sediment-water interface (Seal *et al.*, 2000). Depending on the species present, the bacteria can survive at temperatures between 0 to 110 °C and pH conditions of 5-9.5 under varying levels of salinity below halite saturation (Canfield, 2001; Seal, 2006). By preferentially metabolising ^{32}S, the $\delta^{34}S$ values of the residual sulphate are heavier relative to any sulphides that may be present (Chambers and Trudinger, 1979; Seal, 2006). When bacterial activity is likely to have directly impacted the $\delta^{34}S$ values of sulphides during a mineralisation event or the formation of an orebody, there is likely to be a plethora of textural evidence to support this (e.g. oolitic sphalerite; Southam and Sanders, 2005).

However, another process that can impact the $\delta^{34}S$ value of a sulphide is thermomechanical sulphate reduction (TSR), which involves the reduction of aqueous sulphate at temperatures > 200 °C in environments where sulphate reducing bacteria are likely to be inactive (Seal *et al.*, 2000; Canfield, 2001). TSR may also occur when the aqueous sulphate interacts with Fe^{2+} (Shanks *et al.*, 1981; Seal, 2006). During TSR, the ^{34}S content of residual aqueous sulphate increases (Ohmoto and Lasaga, 1982). TSR may also occur as a result of sulphate interacting with organic matter and in such scenarios, the difference in $\delta^{34}S$ values between the sulphides and sulphates is <10 ‰ (Orr, 1974; Kiyosu, 1980; Seal, 2006). Whilst BSR and TSR have the same effect on sulphur isotope fractionation (i.e. an increase in the $\delta^{34}S$ values of the aqueous

sulphates), this impact is normally more extreme during BSR; with the latter, the difference in $\delta^{34}S$ values between coprecipitating sulphides and sulphates may be up to 72 ‰ (Machel *et al.*, 1995; Wortmann *et al.*, 2001; Johnston *et al.*, 2007). On the other hand, the difference in $\delta^{34}S$ values between a pair of sulphide and sulphate minerals that formed during TSR is not known to exceed 43 ‰ (Eldridge *et al.*, 2016), and is normally <10 ‰ (Sakai *et al.*, 1980; Seal, 2006).

Fundamentally, most isotopic fractionation can be explained in the context of the thermodynamic drive towards isotopic equilibrium that occurs during isotopic exchange reactions (Grootenboer and Schwarcz, 1969; Kajiwara *et al.*, 1969; Schiller and Nielsen, 1970; Kajiwara and Krouse, 1971; Kiyosu, 1973; Smith *et al.*, 1977; Hubberten, 1980; Seal, 2006). In the majority of geochemical scenarios, isotope fractionation is mass-dependent (i.e. associated with variations that occur amongst the four stable sulphur isotopes as a result of their relative differences in mass; Seal, 2006). Temperature, fO_2, and pH are all capable of exerting a control on the ^{34}S fractionation rate of minerals that precipitate from a hydrothermal solution (Ohmoto, 1972; Seal, 2006; Hutchison *et al.*, 2020). The oxidation state of the system is particularly important because the sulphur species with higher bond strengths preferentially fractionate ^{34}S; the order of ^{34}S concentration has been described as $SO_4^{2-} > SO_3^{2-} > S_x^O > S_2^-$ (Sakai, 1968; Bachinski, 1969; Seal, 2006). For this reason, sulphate minerals that coprecipitate with sulphides tend to show much higher $\delta^{34}S$ values (Seal, 2006).

Changes in fO_2 may also influence the relative concentrations of H_2S, HS^-, and S^{2-} (Parat *et al.*, 2011; Baker and Moretti, 2011; Wilke *et al.*, 2011). At higher oxygen fugacities, sulphur is more likely to speciate as sulphate molecules (Marini *et al.*, 1998; 2011); the production of SO_4^{2-} (and the relative fractionation of ^{34}S that occurs) may stimulate a decrease in the $\delta^{34}S$ of the precipitating sulphides. Furthermore, under conditions of high oxygen fugacity, sulphur disproportionation can take place, provided the temperature is below 400 °C (Equation 11; Seal, 2006). This reaction produces sulphuric acid (Equation 11); the release of H^+ ions may cause a decrease in pH of the hydrothermal fluid (Gamo *et al.*, 1997; Seal, 2006). The increase in the oxidation state resulting from the addition of HSO_4^- to the solution results in the preferential ^{34}S bonding away from the H_2S (and into HSO_4^-), explaining the low $\delta^{34}S$ values of sulphides that form in environments where SO_2 disproportionation occurs (Herzig *et al.*, 1993; Gamo *et al.*, 1997; Seal, 2006). A preferential depletion in sulphide $\delta^{34}S$ values with decreasing pH has also been demonstrated by experimental investigations. For example, Sakai (1968) describes the hypothetical scenario of how pyrite, growing in isotopic equilibrium at a temperature of 226.85 °C, would have $\delta^{34}S$ values of +5 ‰ at pH 9.5, +2.0 ‰ at pH 8, and 0 ‰ at pH 4. Such pH conditions are associated with ore-forming fluids; for example, 'orogenic' fluids have 'near neutral' pH values of 5.5 (Ridley and Diamond, 2000), whilst the mineralising fluids associated with porphyry and epithermal deposits can record pH values as low as 2 (Section 2.2.). However, Sakai (1968) noted that pH conditions frequently change during the mineralisation process, which

may involve neutralisation reactions. This may explain the broad range in $\delta^{34}S$ values that has been observed at many ore deposits globally (Ohmoto, 1972).

$$4H_2O + 4SO_2 \rightarrow H_2S + 3H^+ 3HSO_4^-$$

Equation 11. Formula for the disproportionation of SO_2 that occurs below temperatures of 400 °C (Holland, 1965; Burnham and Ohmoto, 1980).

Aside from fO_2 and pH, temperature is an important control on sulphur isotope fractionation; increasing temperatures cause the vibrational energies of the different isotope species to increase (Seal, 2006). At higher temperatures, the isotopes have higher energy levels, which makes it easier to achieve equilibrium conditions (Bigeleisen and Mayer, 1947; Seal, 2006). However, as the temperature of a system decreases, the ^{34}S fractionation rate between H_2S and a given mineral or sulphur species increases (Fig. 2.20.). For this reason, conditions of disequilibrium are likely to occur under lower temperatures (Seal, 2006). Depending on the temperature, the fractionation factors for different sulphur species may vary (Fig. 2.20.). For example, between temperatures of 300 and 100 °C (Fig. 2.20.), the fractionation factor for SO_4^{2-} increases, meaning that $\delta^{34}S$ is incorporated at a greater rate (Seal, 2006).

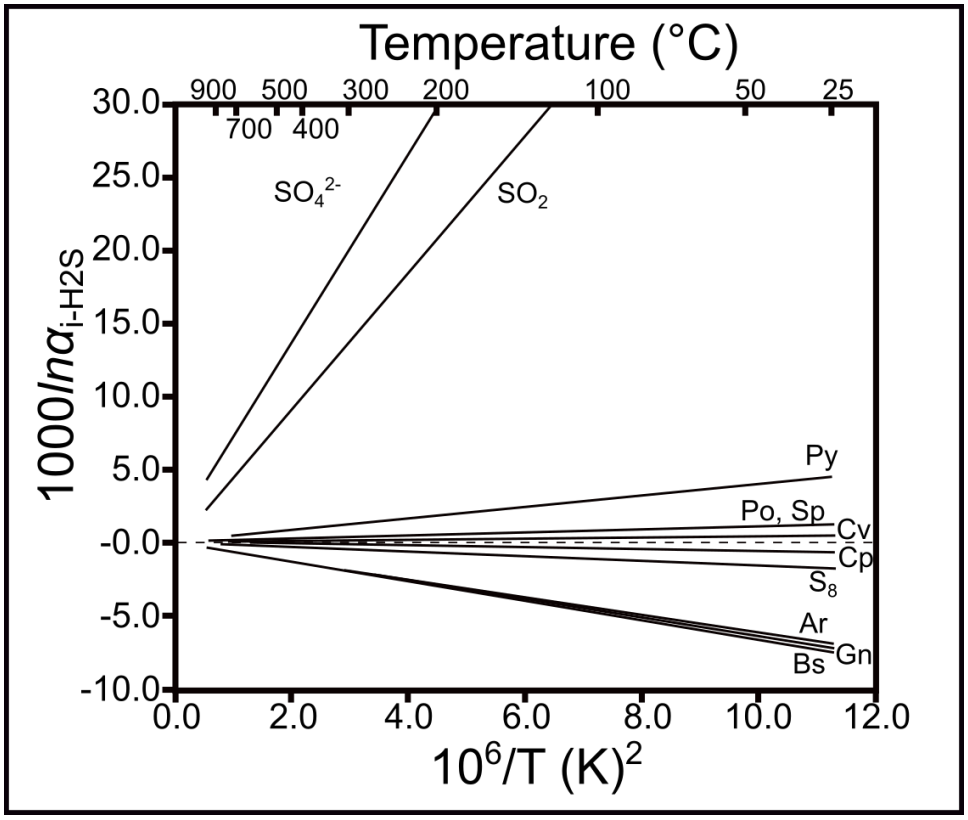

Figure 2.20. Variations in the experimentally determined equilibrium sulphur isotope fractionation factors (α) relative to H_2S for several sulphur and sulphide species over changing temperature conditions (Ohmoto and Rye, 1979; Ohmoto and Lasaga, 1982; Szaran, 1996; Hubberten, 1980; Bente and Nielsen, 1982). The dashed line represents a 0.0 ‰ 1000lnα figure. Whilst abbreviations from Warr (2021) have been used where possible (Pg. xxvii), they were not available for bismuthinite (Bi), argentite (Ar) and S (sulphur). Adapted from Seal (2006).

However, regarding the ^{34}S fractionation effect, this process is more efficient in pyrite than for other sulphides, such as galena (Smith *et al.*, 1977). This is because heavier elements, such as Pb, are able to bond more efficiently with lighter stable isotopes that have higher energy levels (e.g. ^{32}S; Seal, 2006). An example of this trend towards isotopically heavier pyrite during coprecipitation is shown in Fig. 2.21. When pyrite and galena coprecipitate, the $\delta^{34}S$ value of the pyrite is typically ~1-3 ‰ greater than the $\delta^{34}S$ value of the galena (Sakai, 1968; Bachinski, 1969; Grootenbooer and Schwarz, 1969; Kajiwara *et al.*, 1969; Kajiwara and Krouse, 1971, Salomons, 1971; Czamanske and Rye, 1974).

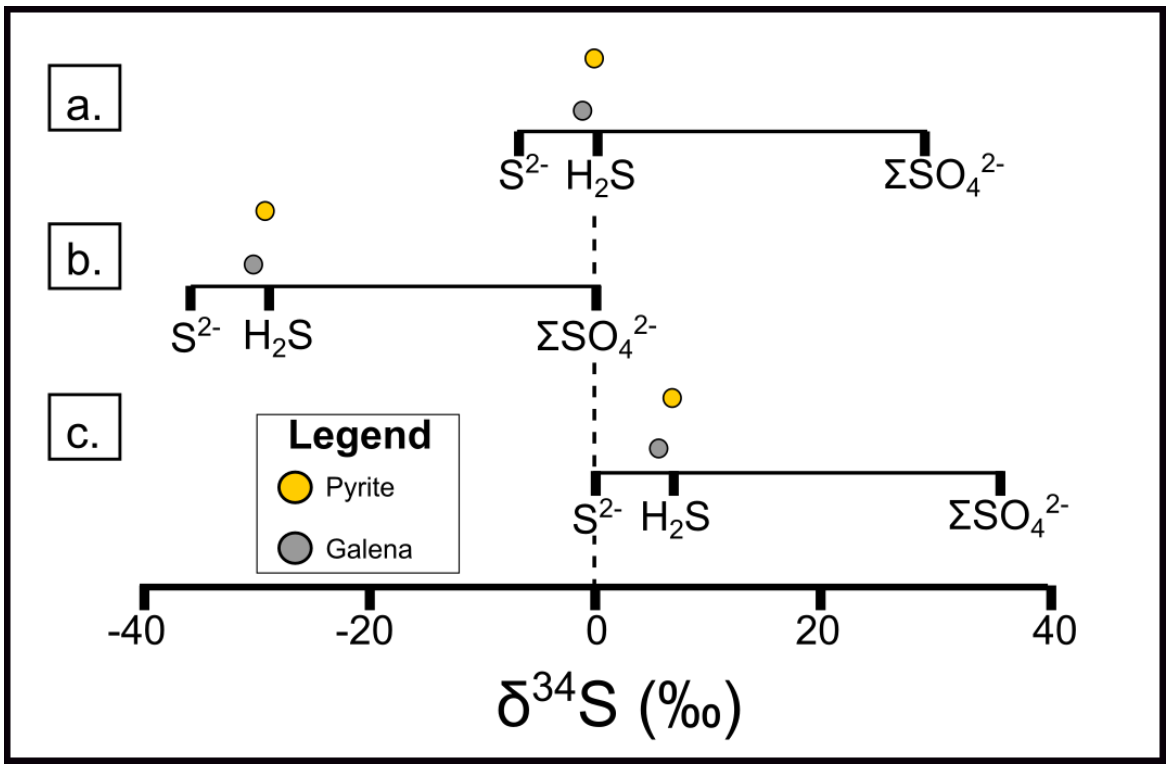

Figure 2.21. Depiction of the $\delta^{34}S$ values that can be expected to arise in pyrite and galena as a result of precipitation from a hydrothermal fluid with an initial composition of 0 ‰, assuming temperature remains constant. Each diagram demonstrates a scenario in which a different fluid species is dominant. **a.** H_2S. **b.** SO_4^{2-} and **c.** S_2^-. Adapted from Nielsen (1979) and Sharp (2017).

2.8.3.c. Controls on the $\delta^{34}S$ contents of a hydrothermal fluid

It should be noted that whilst temperature, fO_2, and pH can directly impact the $\delta^{34}S$ values of sulphides that precipitate from a hydrothermal solution (due to their impact on ^{34}S fractionation; Section 2.8.3.b.), there are also geological processes that can alter the $\delta^{34}S$ composition of a hydrothermal fluid. In this section, these processes are reviewed.

Upon generation of a hydrothermal or magmatic-hydrothermal fluid, the concentration of sulphur within the solution may have an impact on the resulting $\delta^{34}S$ values of the sulphides that precipitate. Ohmoto (1972) noted that for two solutions containing different concentrations of sulphur (0.1 and 0.001 moles/kg), more variability was reported in the $\delta^{34}S$ values from the fluid with the higher sulphur concentration (30 ‰ compared to 18 ‰). In the experiments conducted by Ohmoto (1972), it was observed that pyrite could precipitate over a wider range of pH and fO_2 conditions when the sulphur concentration was higher (i.e. the stability of pyrite was greater). In the context of an evolving fluid gradually precipitating pyrite, each precipitation event would have occurred from a fluid with a slightly different $\delta^{34}S$ value. For this reason, mineralising fluids with high sulphur concentrations may produce pyrite crystals with a wide range in $\delta^{34}S$ values (Ohmoto, 1972). The progressive fractionation of sulphides from a finite sulphur quantity is likely to result in $\delta^{34}S$ variations; Seal (2006) recommended considering this behaviour within the context of Rayleigh fractionation processes (Rayleigh, 1896; Seal and Wandless, 2003). The recommended approach is shown by Equation 12, although the fundamental theoretical consideration is that the precipitation of sulphides changes the composition (and specifically, the ^{34}S contents) of the hydrothermal fluid, meaning sulphides that subsequently precipitate from the fluid have a different composition (Seal, 2006).

$$\delta^{34}S = (\delta^{34}S_0 + 1000)f^{\alpha-1} - 1000$$

Equation 12. Rayleigh model for sulphur isotope fractionation (Seal, 2006). $\delta^{34}S_0$ = Initial $\delta^{34}S$ values, f = fraction of the original solution remaining, and α = isotopic fractionation factor.

Geological processes often cause different sulphur isotope source regions to mix with one another, which typically results in changes to the $\delta^{34}S$ values of the sulphides that precipitate (Seal, 2006). For example, the assimilation of crustal sulfur during the formation of magmatic sulphide deposits is often considered to be critical in achieving sulphur saturation of the melt, which may ultimately facilitate the formation of economic quantities of sulphides (Mavrogenes and O'Neill, 1999; Holzheid and Grove, 2002; Ripley and Li, 2003). Seal (2006) recommends considering the outcomes of mixing between components with contrasting $\delta^{34}S$ values in the context of simple mass-balance formulae (Equation 13); for example, in a scenario involving the mixing between one component ($\delta^{34}S$ = +5 ‰) comprising 0.75 molar fractions (i.e. of the mixture) and another comprising 0.25 molar fractions ($\delta^{34}S$ =+7 ‰), the resulting $\delta^{34}S$ value would be +5.25 ‰. $\delta^{34}S$ values from a single vein or locality that show minimal spread may suggest isotopic homogeneity,

implying that the sulphides precipitated from a single fluid source or well-mixed fluid (Leach *et al.*, 2006; Seal, 2006).

$$\delta_{mixture} = X_A\delta_A + X_B\delta_B$$

Equation 13. The formula for calculating the $\delta^{34}S$ value of a mixed fluid. X_A and X_B represent the molar fractions of two hypothetical fluids, A and B, whilst $\delta^{34}S_A$ and $\delta^{34}S_B$ indicate the $\delta^{34}S$ values of each fluid prior to mixing. Adapted from Seal (2006).

Wallrock sulphidation also has a notable impact on the $\delta^{34}S$ of a sulphide (Ward *et al.*, 2017; LaFlamme *et al.*, 2018; Petrella *et al.*, 2021); specifically, wallrock sulphidation in the presence of hematite (Fig. 2.15.) may lead to an increase in the oxidation state of the environment in which mineralisation takes place (Rye and Ohmoto, 1974; Ward *et al.*, 2017). Under these conditions, SO_4^{2-} is likely to speciate, which incorporates ^{34}S relative to the H_2S in the hydrothermal fluid (Ohmoto and Rye, 1979; Seal, 2006). Wallrock sulphidation in the presence of hematite (under relatively constant pH conditions) is interpreted to have resulted in the negative $\delta^{34}S$ values observed in the initial mineralisation stage at the Wallaby Gold Deposit in Western Australia (Ward *et al.*, 2017). However, the exact impact of wallrock sulphidation on the $\delta^{34}S$ of precipitating sulphides may be dependent on the mineral involved in the sulphidation; at Wallaby, later mineralisation (and wallrock sulphidation) events took place in the presence of magnetite (Ward *et al.*, 2017); this process did not oxidise the mineralising fluid to the same extent as the hematite and is suggested to be associated with the gradual increase in $\delta^{34}S$ values throughout the paragenesis of the orebody (Ward *et al.*, 2017).

2.8.3.d. $\delta^{34}S$ geothermometry

Based on the temperature dependent nature of sulphur isotope fractionation (Fig. 2.20.), it may be possible to calculate the formation temperature of a pair of minerals (e.g. galena and sphalerite); this concept is known as sulphur isotope geothermometry. For this approach to be applied robustly, there are several requirements. Firstly, the two minerals must have grown in equilibrium (Seal, 2006). In the context of hydrothermal ores, a plethora of additional textural evidence is required to demonstrate that two minerals grew in equilibrium with one another; in practice, this means two minerals that belong to the same paragenetic stage, as demonstrated by the observation of textures such as mutual intergrowths or coprecipitation (i.e., inclusions of one phase in the other). Secondly, alteration of either mineral post-precipitation must not have occurred (Seal, 2006). Thirdly, a pure separate must have been used in the isotopic analysis (i.e. the separate must not have been contaminated by other sulphides), and fourthly, the temperature dependence of the isotope fractionation factors must be known (Seal, 2006). Despite these uncertainties, sulphur isotope geothermometry is a long-established methodology employed in the study of hydrothermal ores (Lusk *et al.*, 1975; Ohmoto and Rye, 1979; Bortnikov *et al.*, 1995; Seal, 2006; Hill *et al.*, 2013).

To be able to successfully calculate the temperature recorded by a sulphide pair assumed to have grown in equilibrium, the following variables must be constrained: the $\delta^{34}S$ values of the sulphide minerals, the likely temperature range over which fractionation of the pair occurred (assumed to be 50-705°C and 50-700°C for sphalerite and galena in Equation 14), and the equilibrium isotopic fractionation factor. There are often several different options for assuming the fractionation factor; the example shown in Equation 14 pertains to an experimentally derived temperature range (Seal, 2006). However, the relevance of such experiments to natural conditions are frequently criticised, hence it may be more appropriate to derive fractionation factors using theoretical estimations involving calculated bond strengths or analysis of natural samples for which independent estimates of temperature are available (Seal, 2006).

$$T\ (°C) = \sqrt{\frac{0.73x10^6}{8.7-6.1}} - 273.15$$

Equation 14. An example of how to use $\delta^{34}S$ data to calculate the temperature recorded by a coexisting pair of sphalerite and galena, where T = temperature (adapted from Seal, 2006). It is necessary to subtract -273.15 to convert from Kelvins to °C. For this examples, $\delta^{34}S$ values of +8.7 ‰ (Gn) and +6.1 ‰ (Sp), and fractionation factors of 0.10 and -0.63 (Ohmoto and Rye, 1979), have been assumed. The assumed fractionation factors are experimentally derived temperature ranges thought to represent the isotopic fractionation of sphalerite and galena (Rye and Czamanske, 1969; Ohmoto and Rye, 1979; Ohmoto and Lasaga, 1982; Hubberten, 1980; Bente and Nielsen, 1982; Szaran, 1996).

2.8.4. Pb isotopes

As mentioned in Section 2.8.2., there are four naturally occurring isotopes of lead; ^{204}Pb, ^{206}Pb, ^{207}Pb, and ^{208}Pb. However, ^{204}Pb is not a product of radioactive decay (Jaffey, 1971; Woodhead and Hergt, 2000; Huston and Champion, 2023). Pb isotopes are particularly useful in economic geology for identifying possible sources of Pb in ore deposits (Goldhaber *et al.*, 1995; Tosdal *et al.*, 1999; Pedersen, 2000; Woodhead, 2002; Bao *et al.*, 2017; Potra and Moyers, 2017). The Pb isotope values of galena are controlled by several factors; the source of Pb (the upper crust tends to contain a greater proportion of radiogenic isotopes than the mantle; Fig. 2.22.), the mixing between Pb sources that may occur during fluid/rock interaction, and the adjustments of Pb isotope ratios during hydrothermal alteration (Cannon *et al.*, 1961; Mühe *et al.*, 1997; Carranza, 2012; Mortensen *et al.*, 2022). Large hydrothermal systems, which typically transport mineralising fluids over extensive distances, may homogenise Pb isotope ratios through mixing (Cannon *et al.*, 1961; Goldhaber *et al.*, 1995; Mortensen *et al.*, 2022), whereas systems in which Pb is derived from several distinct and local sources display more variation in their composition. Pb isotope compositions from temporally distinct mineralisation events tend to show a large amount of variation (Mortensen *et al.*, 2022), with events that are significantly younger containing a higher proportion of radiogenic Pb (Huston and Champion, 2023).

Pb isotopes, given that some of them are the products of radioactive decay, have historically had a significant role in geochronology (Stanton, 1955; Stanton and Russell, 1959; Russell and Farquhar, 1960; Romero *et al.*, 2013), in which they are often used to calculate model ages (Huston and Champion, 2023). However, it is important to draw a distinction between the concept of a 'radiometric date', derived using Re-Os and U-Pb in this study, and ages pertaining to Pb isotopes, which are 'model ages'; with the former, the date is calculated directly from the measured abundances of parent and daughter isotopes in a rock or mineral. Model ages, on the other hand, are calculated using mathematical models of Pb isotope evolution on Earth over time; these models involve various assumptions regarding the Pb contents of the sample (Stacey and Kramers, 1975; Cumming and Richards, 1975; Milot *et al.*, 2016; Huston and Champion, 2023).

The process of calculating a model Pb age involves comparing the measured isotopic ratios of the lead in the sample to a model for lead isotope evolution in the Earth over time, which can be used to construct an isochron that represents the time that has passed since the formation of the Pb source (Holmes, 1946; Huston and Champion, 2023). However, galena usually contains non-radiogenic (i.e. common) Pb, in addition to radiogenic Pb, and distinguishing between the two can be challenging (Townsend *et al.*, 1998). The typical approach to Pb isotope studies involves measuring the radiogenic isotopes and normalising these values to the non-radiogenic isotope ^{204}Pb (e.g. $^{206}Pb/^{204}Pb$, $^{207}Pb/^{204}Pb$ and $^{208}Pb/^{204}Pb$); ^{204}Pb is not produced by radioactive decay and is therefore assumed to not increase over time (Holmes, 1946; Stanton and Russell, 1959; Cannon *et al.*, 1961; Huston and Champion, 2023). The models assume that the accumulation of ^{206}Pb, ^{207}Pb, and ^{208}Pb is controlled by the amount of time that passes, the decay constants of the uranium and thorium isotopes, and the amount of this material present in the Earth at 4.54 Ga (Tatsumoto *et al.*, 1973). Models of lead evolution can be divided into two categories: 'single-stage' and 'two-stage' (Huston and Champion, 2023). Single-stage models assume that the fractionation of lead from uranium and thorium parent isotopes is continuous and do not consider the potential for later geological events to result in the fractionation of uranium and thorium into the crust relative to lead (Stanton and Russell, 1959; Tera and Carlson, 1999; Maltese and Mezger, 2020; Huston and Champion, 2023). In two-stage models, this is not the case; after the formation of Earth, geological events (e.g. crustal differentiation; Fig. 2.22.) are interpreted to have caused fractionation between uranium, lead, and thorium; these three elements are more concentrated in the crust compared to the mantle (Wedepohl and Hartmann, 1994; Palme and O'Neill, 2003). Both single and two-stage models make assumptions regarding the initial lead isotopic ratios of the Earth (based on the Canyon Diablo Meteorite) and the initial μ (Mu; $^{238}U/^{204}Pb$), κ (Kappa; $^{232}Th/^{238}U$) and ω (Omega; $^{232}Th/^{204}Pb$) values. It should also be noted that Mu values are considered to be a useful visual representation of variations in Pb isotope ratios throughout a region and in metallogenic studies, it is common for researchers to produce regional maps of the Mu value (Browning *et al.*, 1987; Blitchert-Toft *et al.*, 2016; Huston *et al.*, 2017; Huston and Champion, 2023).

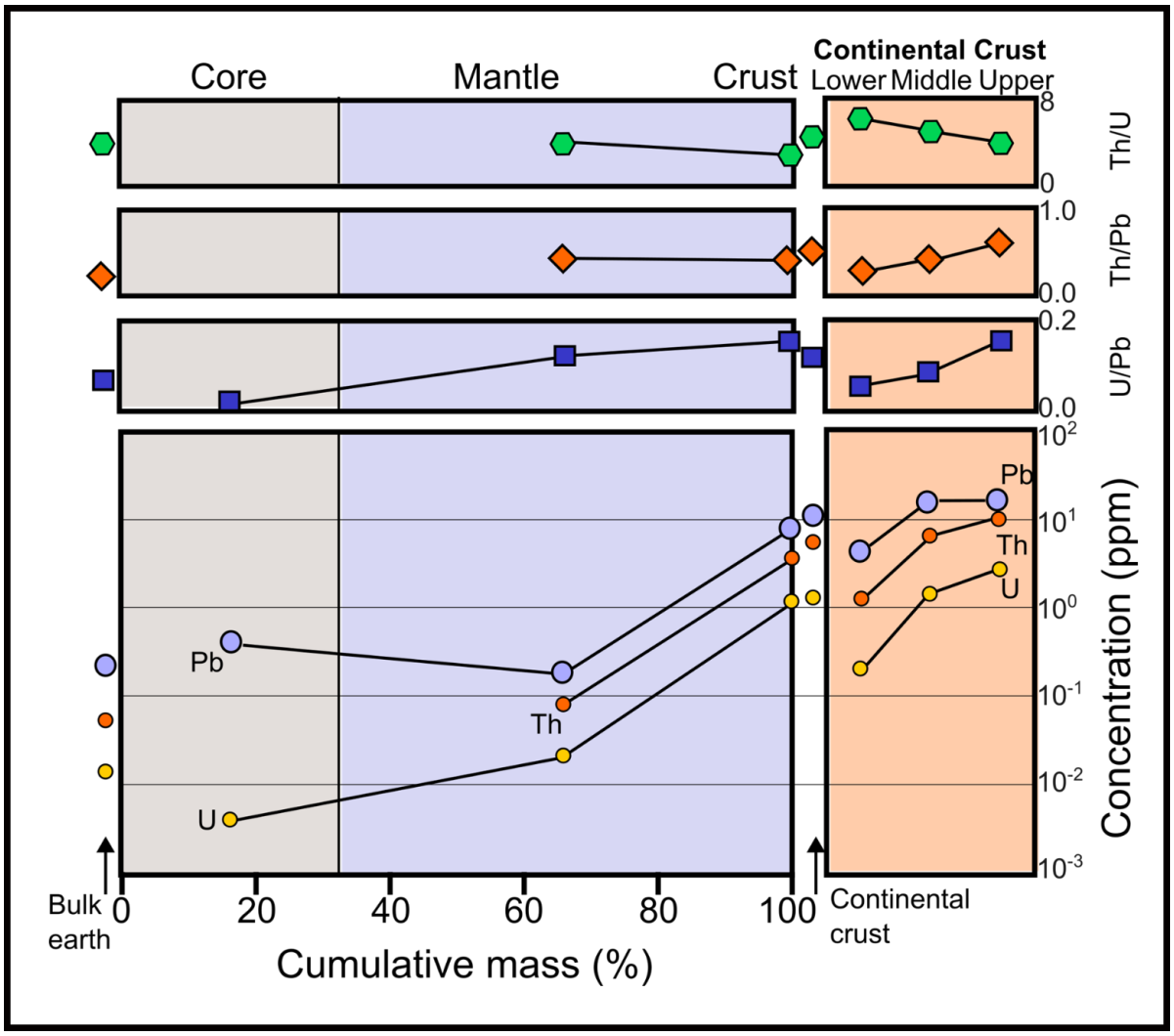

Figure 2.22. Depiction of the diversity in the concentrations of Pb, U, and Th along with variations in U/Pb, Th/U and Th/Pb ratios in the different components of Earth (adapted from Huston and Champion, 2023). Original data sources are as follows: core (McDonough, 2003), mantle (Palme and O'Neill, 2003), crust (Rudnick and Gao, 2003).

Regarding two-stage models, the differentiation of the mantle and crust resulted in the creation of regions with different Pb isotope ratios (Fig. 2.23.). There are several geological processes that caused the crust to become differentiated from the mantle; for example, density differences (silicate phases, being less dense than iron, began to cluster near the surface of Earth; Agee and Walker, 1988). Another driver of crustal differentiation was the accumulation of less dense silicate phases at shallow depths as a result of volcanism (Ogawa, 2018). Following the differentiation of the crust and mantle, uranium was partitioned more strongly into the crust; this is because uranium is a lithophile element and preferentially fractionates into less dense silicate-bearing phases, which are more common in the crust (Andersen *et al.*, 2015; Huston and Champion, 2023). As a result of radioactive decay, the crust developed higher concentrations of ^{206}Pb, ^{207}Pb, and ^{208}Pb over time; this is reflected by the lead isotope evolution curves for the continental crust and mantle, which show that the mantle has a lower amount of radiogenic Pb at any given time since the formation of the crust (Fig. 2.23.).

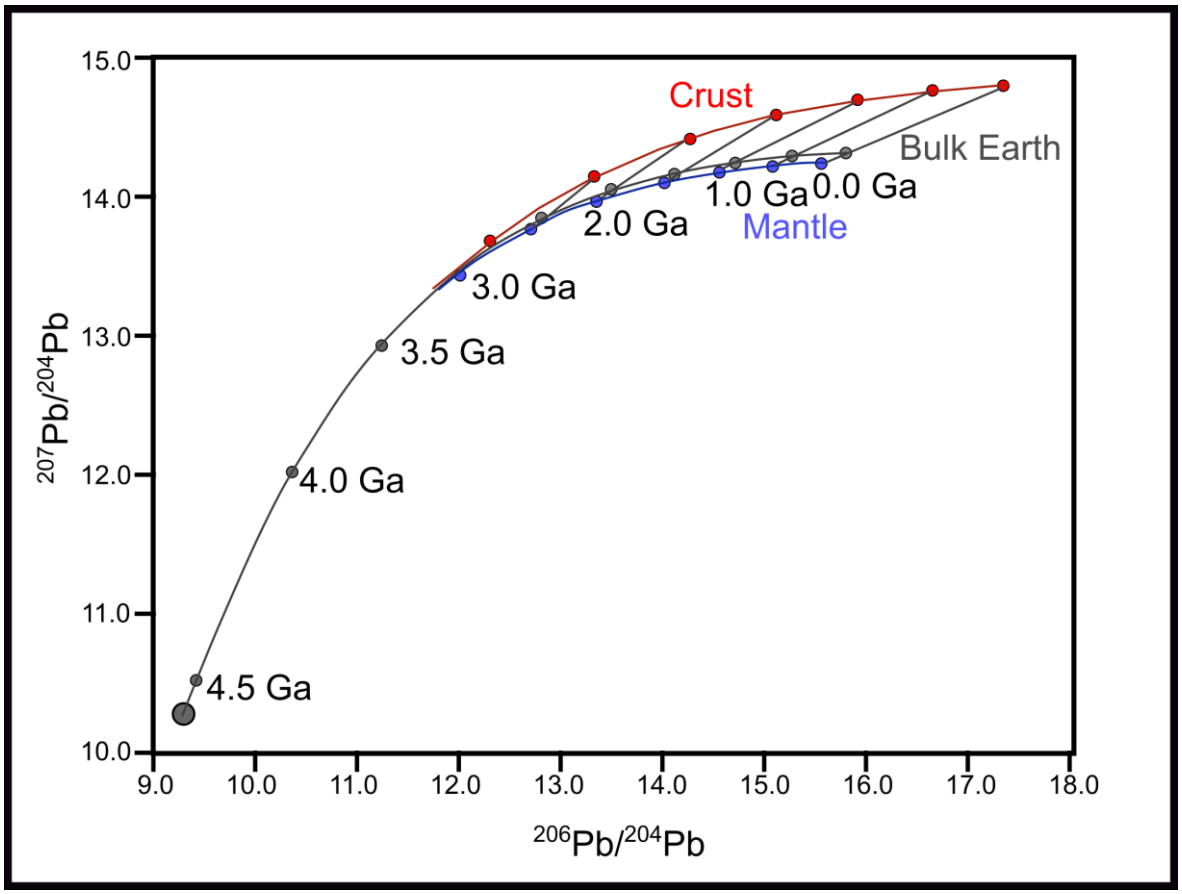

Figure 2.23. $^{206}Pb/^{204}Pb$ vs $^{207}Pb/^{204}Pb$ diagram of Pb evolution in the Earth under conditions of a two-stage model (adapted from Zartman and Doe, 1981). At 3.5 Ga, there is a divergence from 'single-stage' Pb evolution when the crust becomes differentiated from the mantle.

Ever since the two-stage model of Pb evolution was presented by Stacey and Kramers (1975; Fig. 2.24.a.-b.), several other models have since been postulated; for example, Cumming and Richards (1975) produced a model that assumes that the U/Pb and Th/U ratios in the mantle and crust change continuously over geological time. Since the 1980s, there has been an increasing focus on 'plumbotectonic' lead evolution models, in which at least four source regions with distinctive Pb values are recognised (Fig. 2.24.c., d.); mantle, lower crust, upper crust and 'orogene', the latter of which is created by recycling and extracting from the other three sources of Pb (Zartman and Haines, 1988). The term 'orogene' specifically defines the global distribution of crust formation (Zartman and Haines, 1988). Plumbotectonic models are more complex than the Stacey and Kramers (1975) scenarios because radioactive decay following crustal differentiation is not the only process that impacts the Pb isotope ratios; instead, the mixing between the different sources of Pb during orogenes also exerts a control (Zartman and Haines, 1988; Huston and Champion, 2023). The original models postulated that an 'orogene' mixing event occurred every 400 Ma, although in the later iterations this process was interpreted to occur every 100 Ma (Zartman and Haines, 1988). During the 'orogene' and subduction of oceanic crust, approximately 25 % of the quantity of incompatible elements (U, Th, and Pb) present in the subducted load are delivered back to the crust as a result of magmatism during subduction (Zartman and Haines, 1988). However, the other 75 % of the

subducted load is returned to the mantle. Between each 'orogene' event, prolonged isolation of each Pb region (the mantle or the different layers of the crust) means that radioactive decay causes further changes to the Pb isotope ratios (Doe and Zartman, 1979).

Plumbotectonic models produce estimations for Pb isotope ratios of the contemporary mantle and crust that are realistic and accurate, based on knowledge derived from direct measurements (Zartman and Haines, 1988; Huston and Champion, 2023); for this reason, the plumbotectonic curves (Fig. 2.24.c., d.) are widely used to infer the sources of Pb in ore deposits (Chiaradia *et al.*, 2006; Basori *et al.*, 2017; Potra and Moyers, 2017). However, there are difficulties in using the plumbotectonics model to calculate model ages, due to the poorly constrained parameters (e.g. the multiple stages involved in the models; Milot *et al.*, 2021). Attempts to derive Pb model ages typically utilise the Stacey and Kramers (1975) model, which has been shown to identify feasible Pb sources for a variety of geological materials (Cannon *et al.*, 1961; Townley and Godwin, 2001; Standish *et al.,* 2014; Huston and Champion, 2023). The Stacey and Kramers (1975) model has also been used to calculate model ages for several ore deposits in Ireland (Boast *et al.*, 1981; Le Huray *et al.*, 1987; Dixon *et al.*, 1990; Fallick *et al.*, 2001; Kinnaird *et al.*, 2002; Wilkinson *et al.*, 2005; Standish *et al.*, 2014). Other models that are frequently used for model age calculations include the Albarède and Juteau (1984) model, which has similar parameters to the Stacey and Kramers (1975) model, and the Cumming and Richards (1975) model, which suggests that the U/Pb ratio in the mantle changes over time; this assumption differs from the models produced by Stacey and Kramers (1975), Albarède and Juteau (1984), and Albarède *et al.* 2012 in this regard. Plumbotectonic models have ultimately been the inspiration for newer models, which are also based around the concept of isotopic and elemental exchanges between different sources of Pb; Kramers and Tolstikhin (1997) created a model involving nine regions of the Earth defined by distinct Pb isotope values, including the core.

However, when attempting to utilise any of these aforementioned models to calculate model ages of galena samples from an individual orebody or district, there are several limitations. For example, the growth curves represent global averages and there may be localised variations in some of the assumptions used in the calculations, e.g. the initial Pb compositions assumed by the model (Carr *et al.*, 1995; Sun *et al.*, 1996). Furthermore, the formation of the mantle and crust is unlikely to have been a simultaneous global event (Stacey and Kramers, 1975), meaning the initial Pb composition at 3.6 Ga (e.g. Fig. 2.23.) may not be a valid assumption for some regions. For example, some research has suggested that the crust may have formed at 3.8 Ga in the Zimbabwe Craton (Bolhar *et al.*, 2017) and South China (Zhang *et al.*, 2006). It also may be the case that samples with high uranium concentrations following crystallisation experience further Pb addition as a result of radioactive decay, meaning the model age may not represent the age of the Pb source (Holmes, 1946; Stacey and Kramers, 1975; Huston and Champion, 2023).

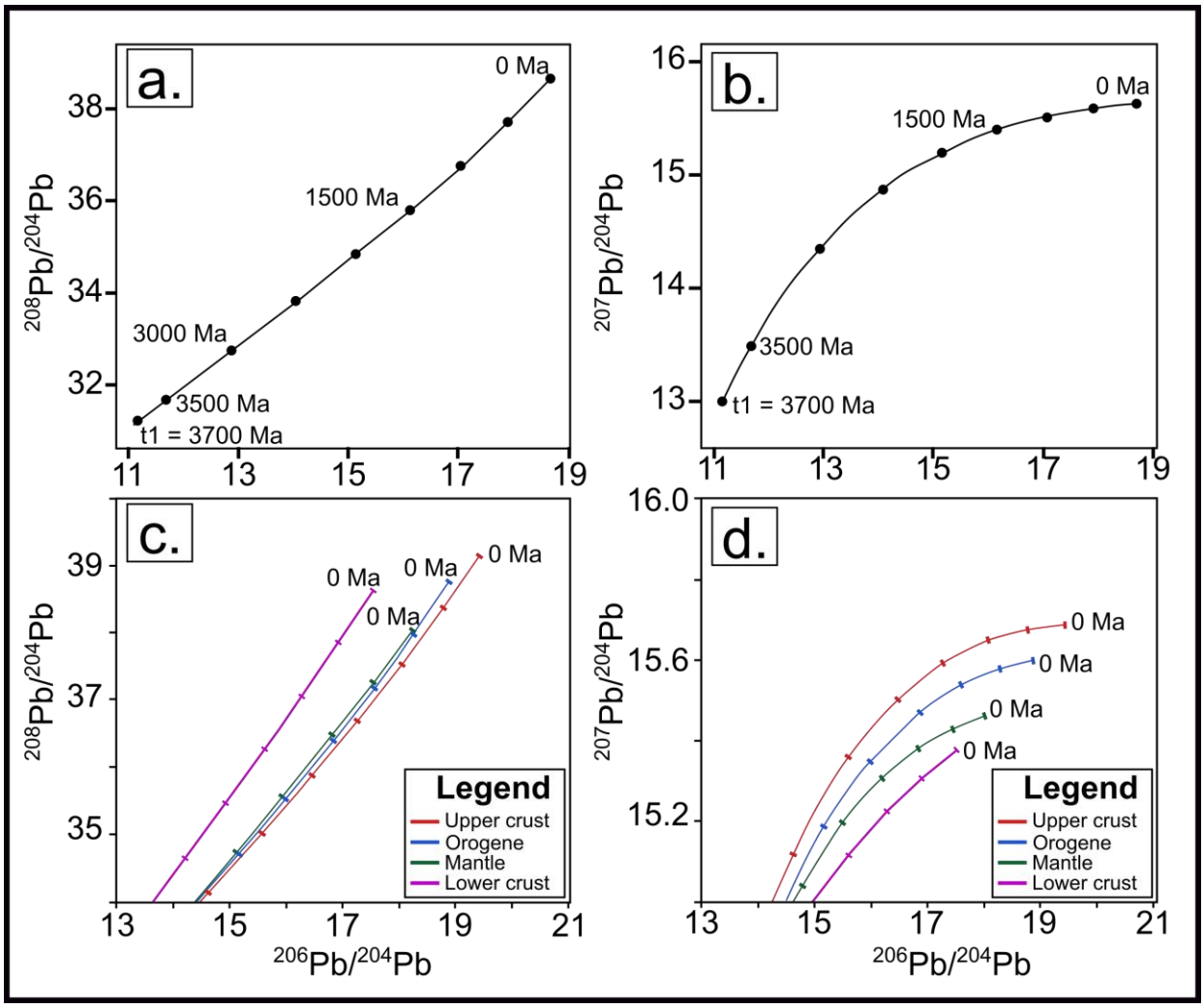

Figure 2.24. Some examples of Pb isotope evolution models for terrestrial Pb sources **a.** $^{208}Pb/^{204}Pb$ vs $^{206}Pb/^{204}Pb$. **b.** $^{207}Pb/^{204}Pb$ vs $^{206}Pb/^{204}Pb$. a and b were originally produced by Stacey and Kramers (1975), whilst **c** and **d** depict the $^{208}Pb/^{204}Pb$ vs $^{206}Pb/^{204}Pb$ and $^{207}Pb/^{204}Pb$ evolution models conceptualised by Zartman and Doe (1981). The tick marks on c and d represent intervals of 400 Ma.

2.9. Isotopic characteristics of ore deposits

Following on from the summary of the theoretical constraints underpinning the application of the different isotope systems, it is necessary to outline the results of similar, previous studies that have sought to characterise the geochemical and isotopic traits of ore deposits. The Re-Os and U-Pb isotope systems, being geochronological methods of investigation, simply reflect the ages of geological events (and therefore vary depending on the age of the deposit in question); however, there are consistent trends in the sulphur and lead isotope data that have been collected from OGDs, porphyry, and epithermal deposits, which may serve as a useful context in which to compare the results from the present study.

2.9.1. $\delta^{34}S$ studies on ore deposits

Sulphur isotopes are commonly implemented in the field of economic geology because metallic mineralisation typically involves the S^- and metal rich fluids that circulate throughout magmatic-hydrothermal systems (Gavelin *et al.*, 1960; Jowett *et al.*, 1991; Ishihara *et al.*, 2000; Liu *et al.,* 2017; Hutchison *et al.*, 2020; Li *et al.*, 2020), or alternatively, orogenic fluids carrying large quantities of H_2S (Garofalo *et al.*, 2014). Most economically important metals (e.g. Cu, Zn) are chalcophiles, meaning that reduced sulphur may be a component in their transportation or deposition (Mountain and Seward, 2003; Stefánsson and Seward, 2004; Pokrovski *et al.*, 2015). However, during transportation in aqueous hydrothermal solutions, most base metals are carried within chloride complexes (Liu *et al.*, 2014; Pokrovski *et al.*, 2015). Only at the point of mineralisation do base metals readily complex with sulphur, when the composition and prevailing conditions of the fluid have changed; for example, at lower temperatures and higher pH values (>6), zinc and lead may bond with bisulfide complexes (Seward, 1981; Pokrovski *et al.*, 2014). For this reason, the source of the sulphur as inferred by $\delta^{34}S$ studies may not reflect the source of the metals.

Regardless of this caveat pertaining to the distinction between metal and sulphur sources, the corollary of the previously outlined controls on the $\delta^{34}S$ signature of a sulphide is that distinct hydrothermal and magmatic-hydrothermal fluid systems (which generally correspond to defined ranges in temperature, oxygen fugacity and pH) often have recognisable $\delta^{34}S$ values. The most important examples of this are sulphides from magmatic and mantle-derived fluids; these consistently record $\delta^{34}S$ values of 0 to + 5 ‰ (Ohmoto, 1975). For mantle-derived melts, the $\delta^{34}S$ values are consistently 0 ± 3 ‰ (Ohmoto, 1986). However, it should be noted that other researchers have produced different estimates of the $\delta^{34}S$ value of the mantle; for example, Labidi *et al.* 2013 suggest that the range is −1.28 ± 0.33 ‰. This perhaps explains why magmatic ore deposits, which often form at high temperatures (>300 °C), typically have $\delta^{34}S$ values of ~0 ‰ (Ripley *et al.*, 1999; Seal *et al.*, 2000; Rye, 2005) and are isotopically lighter than ore deposits that form from cooler fluids. For example, the formation of Mississippi Valley Type (MVT) deposits is associated

with low temperature fluids (<200 °C) in near neutral environments (Corbella *et al.*, 2004; Anderson, 2008); MVT deposits may contain sulfides that record $\delta^{34}S$ values of >+20 ‰ (Kesler *et al.*, 1994; Peevler *et al.*, 2003; Field *et al.*, 2018). As noted previously, the interplaying factors that determine the fractionation of sulphur isotopes mean that there are exceptions to these trends and broad ranges in the $\delta^{34}S$ values associated with each deposit style (Seal, 2006). For example, the low temperatures at which MVT mineralisation occurs is conducive to BSR during sulphur isotope fractionation (Section 2.8.3.a.); some sulphides from MVT deposits have $\delta^{34}S$ values of -5 ‰ (Seal, 2006). The $\delta^{34}S$ value of a given sulphide or sulphate mineral, when considered in isolation (i.e. without other supporting lines of evidence), does not have a straightforward interpretation; in nature, values of between -72 ‰ and +147 ‰ have been recorded (Lever *et al.*, 2013; Drake *et al.*, 2021).

2.9.1.a. $\delta^{34}S$ characteristics of OGDs

OGDs display a very large range in $\delta^{34}S$ values; measurements of between -30 and +17 ‰ have been recorded globally (Quesnel *et al.*, 2023; Fig. 2.25.). In their compilation of previous studies, Quesnel *et al.* 2023 noted that most published measurements (1305) pertained to pyrite, whilst only 199 and 258 had been conducted on galena and arsenopyrite, respectively. Based on the data presented in Fig 2.25., there are no clear trends in $\delta^{34}S$ values that can be observed over geological time (i.e. OGDs of all ages record a broad range in $\delta^{34}S$ values).

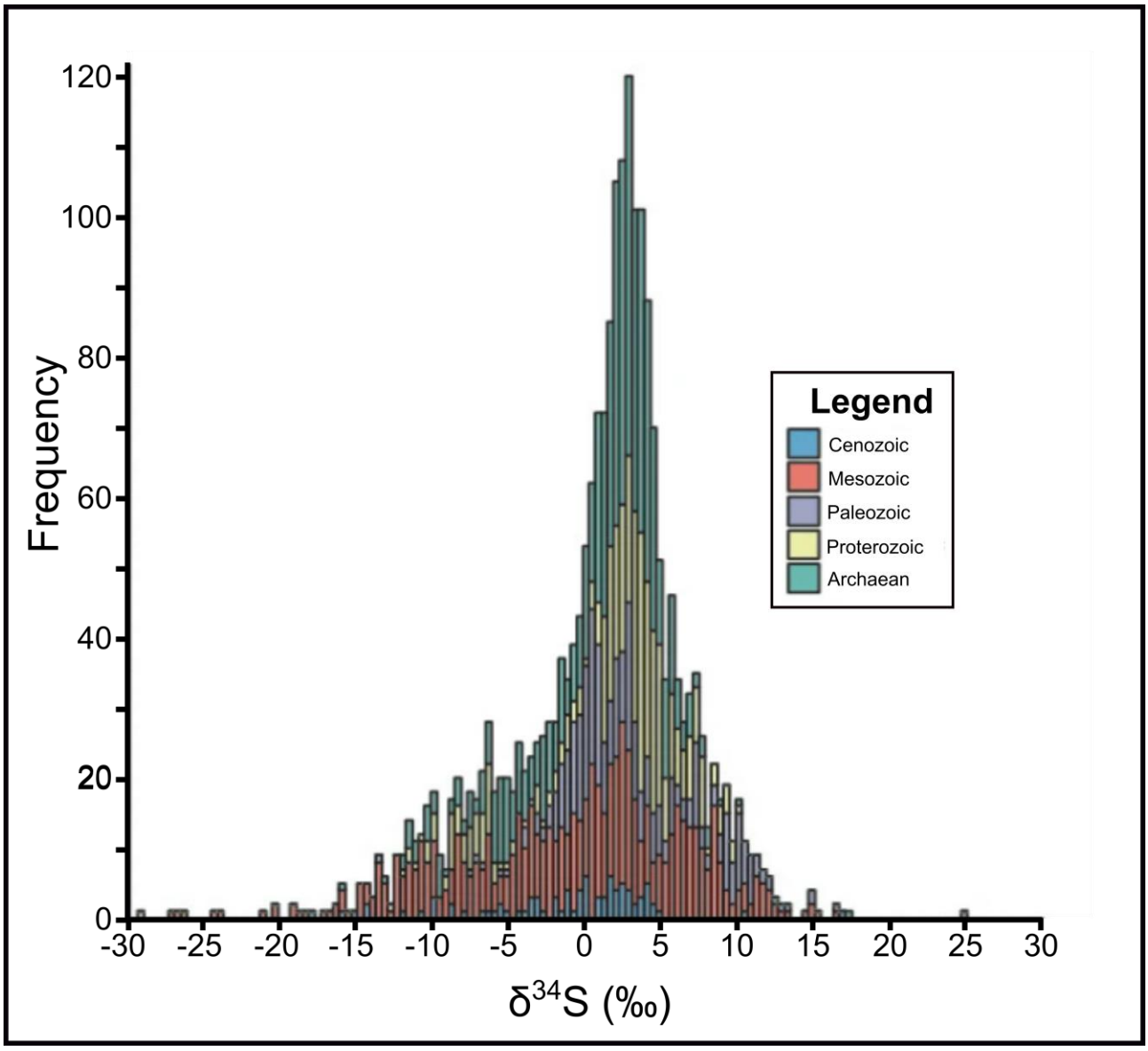

Figure 2.25. Histogram showing $\delta^{34}S$ values for OGD sulphides over geological time (adapted from Quesnel *et al.* 2023).

The broad range in $\delta^{34}S$ values from OGDs (Fig. 2.25.) is potentially linked to the sources of sulphur involved in the mineralisation processes (Quesnel *et al.*, 2023). As discussed previously in Section 2.2.1., OGDs may be the product of a fluid derived from metamorphism in the crust (Figure 2.25.). It is therefore often suggested that OGDs have a crustal source of sulphur (Goldfarb *et al.*, 2001; Chang *et al.*, 2008; Goldfarb and Groves, 2015; Quesnel *et al.*, 2023). Assuming a metamorphic origin for OGD fluids, the ^{34}S contents of the hydrothermal fluids may be influenced by the $\delta^{34}S$ value of the sulphides that are broken down during metamorphism (Quesnel *et al.*, 2023). However, Quesnel *et al.* 2023 emphasised that the synsedimentary sulphides involved in this process can have a very large range in $\delta^{34}S$ values (-50 to +16 ‰) as a result of variations in the influence of TSR and BSR (Section 2.8.3.). For example, when BSR has occurred during sulphur isotope fractionation associated with the formation of pyrite in sedimentary basins, the depletion in ^{34}S of the sulphides relative to the coprecipitating sulphates is likely to be more extreme (Section

2.8.3.b.). In these scenarios, the sulphides may be up to 72 ‰ lighter than coprecipitating sulphates (Machel *et al.*, 1995; Wortmann *et al.*, 2001; Johnston *et al.*, 2007). Depletions in $\delta^{34}S$ values of ~10 ‰ relative to sulphate during sulphur isotope fractionation associated with TSR are more common (Sakai, 1980; Seal, 2006).

It is common for researchers to consider the influence of BSR and TSR on sulphide $\delta^{34}S$ values (Section 2.8.3.) when interpreting sulphur isotope datasets associated with OGDs (Quesnel *et al.*, 2023). For example, when sulphides from OGDs record values that are > +10 ‰ (and are therefore closer to the global seawater sulfate curve; Fig. 2.26.) a TSR source of sulphur is commonly invoked (Kontak and Smith, 1989; Tornos *et al.*, 1997; Quesnel *et al.*, 2023). However, the lower $\delta^{34}S$ values (i.e. <10 ‰; Fig. 2.26.) are more likely to reflect a source of sulphur that has been influenced by BSR (Quesnel *et al.*, 2023). For example, at Sukhoi Log (approximately 600 Ma on Fig. 2.26.), the range in the $\delta^{34}S$ of the sulphides (some are as low as +5 ‰ whereas others are closer to the seawater curve; Fig. 2.26.), along with the presence of textural evidence indicative of BSR (framboidal pyrite), has been used to infer that an additional sulphur source impacted by BSR is involved in the mineralisation processes here (Chang *et al.*, 2008).

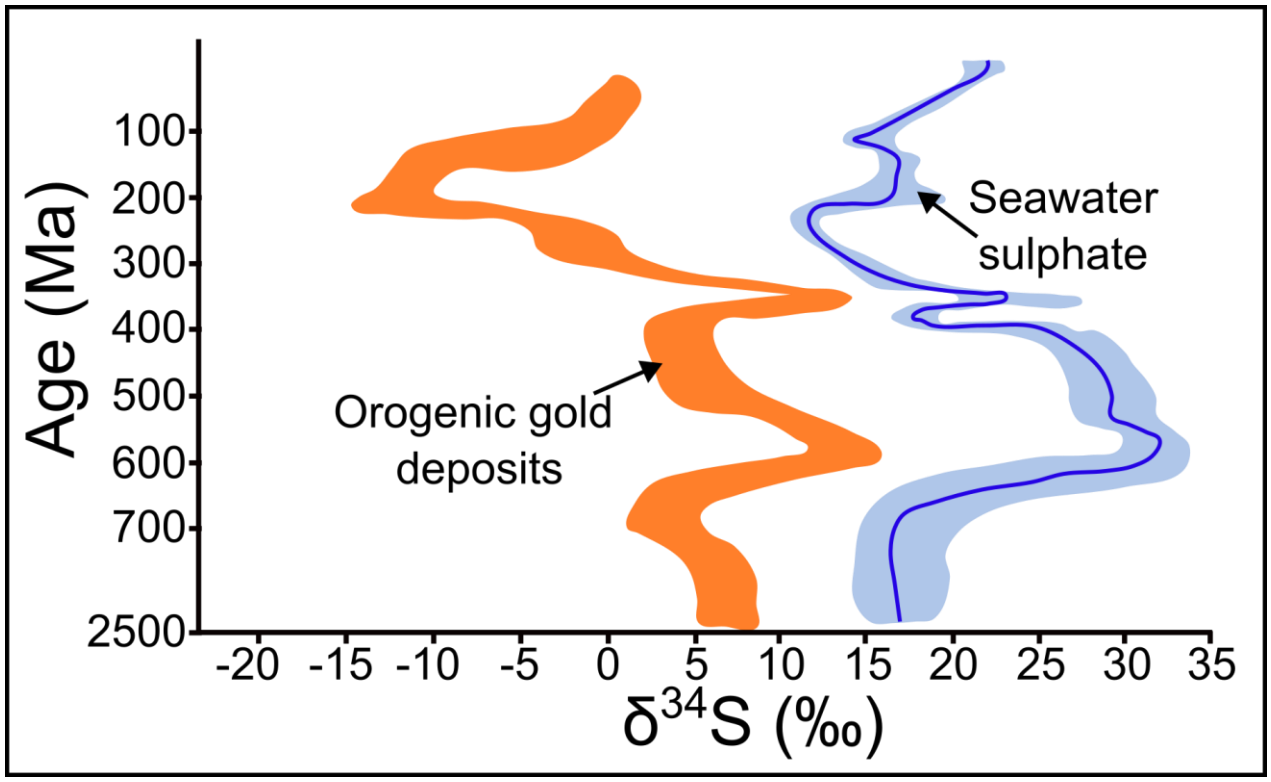

Figure 2.26. $\delta^{34}S$ values of SHOG sulphides plotted against $\delta^{34}S$ values of seawater sulphate over geological time (adapted from Chang *et al.*, 2008). The seawater curve represents data from Claypool *et al.* 1980 and Strauss (2004).

However, the $\delta^{34}S$ signature of the sulphides broken down during metamorphic devolatisation is not the only influence on the $\delta^{34}S$ values of OGD sulphides. Quesnel *et al.* 2023 emphasised that the long transportation distances associated with OGDs (Section 2.2.) were likely to result in the mixing of different sulphur sources (Section 2.8.3.c.). Furthermore, the previously outlined controls on ^{34}S at the deposit-scale (wallrock sulphidation, temperature, pH, and fO_2) may result in additional modifications to the ^{34}S contents of the hydrothermal fluid (Fedorowich *et al.*, 1991; Thode *et al.*, 1991; Couture and Pilote, 1993).

2.9.1.b. $\delta^{34}S$ characteristics of porphyry and epithermal deposits

Given that porphyry and epithermal deposits tend to share a genetic link with one another (Fig. 2.4.), the $\delta^{34}S$ characteristics of these mineralisation styles are described in tandem. Furthermore, there is a large amount of overlap in the $\delta^{34}S$ values that have been recorded from porphyry and epithermal deposits globally (Fig. 2.27.). Whilst it is typical for sulphides from porphyry deposits to cluster within the range associated with magmatic fluids (Ohmoto, 1972), a large amount of diversity is apparent on Fig. 2.27. One explanation for this diversity is that oxidised magmas (e.g. I-type granitoids) contain SO_2 and H_2S in subequal proportions (Seal, 2006); this is in contrast to S-type granitoids, in which the main sulphur compound is H_2S (Burnham and Ohmoto, 1980; Seal, 2006). As outlined in Section 2.8.3.b., sulphur disproportionation (which involves SO_2; Equation 11) causes the pH of a hydrothermal fluid to decrease and the formation of HSO_4^-, resulting in the H_2S complex becoming depleted in ^{34}S. Furthermore, the impacts of crustal sulphur assimilation during porphyry ascent are likely to vary between individual porphyry deposits (Wilkinson, 2013; Sun *et al.*, 2015; Tassara and Ague, 2022). Crustal assimilation often causes the ^{34}S of the magmatic-hydrothermal fluid to increase, given that sulphur sources higher in the crust tend to have greater $\delta^{34}S$ values (Seal, 2006; Hutchison *et al.*, 2020; 2021).

Epithermal deposits record an even greater amount of $\delta^{34}S$ variability than porphyries (Fig. 2.27.); the $\delta^{34}S$ values of sulphides from epithermal gold deposits are between -15 and 5 ‰, although there are recognised variations amongst the different subdivisions; for example, the $\delta^{34}S$ values of sulphides associated with low sulphidation deposits range between -6 and +5 ‰ (with most values being close to 0 ‰; Ohmoto and Rye, 1979; Field and Fifarek, 1985). Alkalic epithermal deposits (i.e. low sulphidation epithermal deposits that are genetically linked to intrusions containing high alkali contents; Kelley *et al.*, 2020) may record $\delta^{34}S$ ranges of between -15 and +8 ‰ (Moussa *et al.*, 2017), whilst the range in $\delta^{34}S$ values from high sulphidation epithermal mineralisation is -10 to +8 ‰ (Arribas, 1995; Moussa *et al.*, 2017). During the formation of low sulphidation epithermal deposits, the hydrothermal fluids are circulated over a much larger distance than those involved in the porphyry and high sulphidation models (Fig. 2.4.). For this reason, mineralising fluids associated with low sulphidation epithermal mineralisation may leach sulphur from a greater variety of host rocks than the other magmatic mineralisation processes described in this study (Simmons *et al.*, 2005; Wang *et al.*, 2016; 2021).

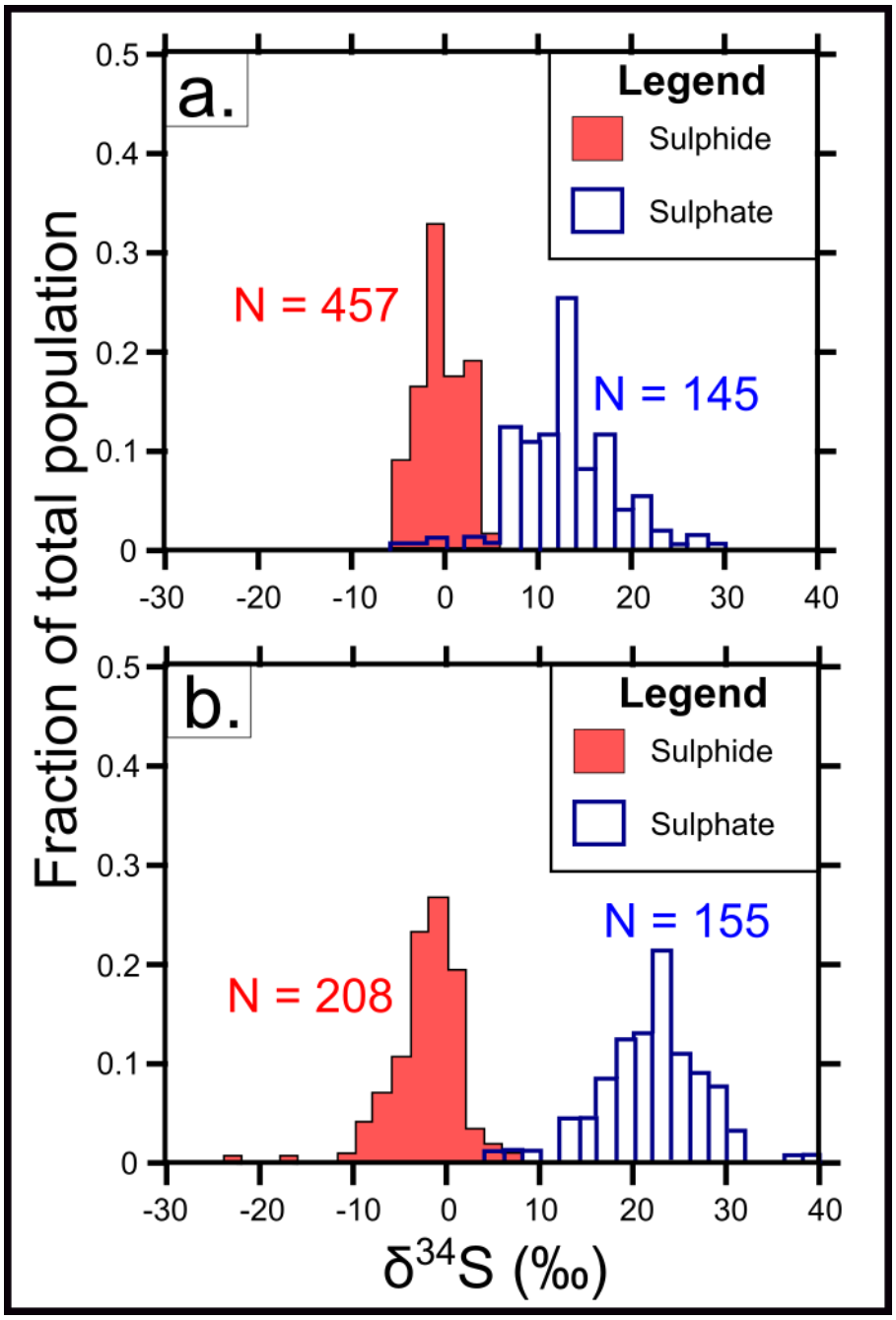

Figure 2.27. Histograms depicting $\delta^{34}S$ values recorded from **a.** Porphyry and **b.** Epithermal deposits. 'N' relates to the number of datapoints utilised to construct each histogram. Adapted from Hutchison *et al.* 2020.

Many in-situ $\delta^{34}S$ studies have been conducted on epithermal deposits (i.e. studies in which there are petrographic images to contextualise the $\delta^{34}S$ data). At times, these investigations have demonstrated that there are variations in the $\delta^{34}S$ values throughout the paragenesis of the orebody (Squire *et al.*, 2007; Voute *et al.*, 2019; Zheng *et al.*, 2021; Ma *et al.*, 2022a). This variation is often explained in the context of different $\delta^{34}S$ compositions arising in the mineralising fluid at each paragenetic stage as a result of fluid mixing (Ma *et al.*, 2022a), varying states of oxidation (Zheng *et al.*, 2021), temperature (Voute *et al.*, 2019), and pH changes (Zheng *et al.*, 2021). However, it is important to note that in some epithermal and porphyry deposits, the $\delta^{34}S$ values have remained consistent throughout the paragenesis (Tanner *et al.*, 2016; Sabeva

et al., 2017; Adam *et al.*, 2020; Zhou *et al.*, 2023); these trends are interpreted to represent an unchanging source of sulphur and when documented in epithermal deposits with $\delta^{34}S$ values <+5 ‰, are considered to represent a consistent flux of magmatic-hydrothermal fluids throughout the mineralisation processes (Sabeva *et al.*, 2017; Adam *et al.*, 2020; Zhou *et al.*, 2023). Furthermore, in-situ $\delta^{34}S$ studies have revealed that $\delta^{34}S$ zonation of pyrite is a common textural feature of pyrite associated with epithermal mineralisation (Tanner *et al.*, 2016); dynamic Eh and pH conditions within an epithermal mineralising fluid are often localised enough to the point that they can influence the $\delta^{34}S$ at the crystal-scale throughout the duration of phase precipitation (McKibben and Eldridge, 1990; Börner *et al.*, 2022).

Other research has sought to use $\delta^{34}S$ data to derive quantitative information regarding the temperature of epithermal environments. An extensive amount of sulphur isotope geothermometry has been conducted on mineral pairs from epithermal deposits; these studies tend to yield temperatures of 200 to 350 °C (Rye *et al.*, 1992; Arribas, 1995; Hedenquist *et al.*, 1998; Bethke *et al.*, 2005; Deyell *et al.*, 2005; Rye, 2005; Simmons *et al.*, 2005; Seal, 2006).

2.9.2. Pb isotope studies on ore deposits

In this subsection, the Pb isotope characteristics of galena from ore deposits with potential relevance to the LTVS are outlined. For example, Mortensen *et al.* 2022 compiled the results of several studies that investigated the Pb isotope ratios of galena from Phanerozoic OGDs. However, no such compilation of Pb isotope data exists for porphyry and epithermal deposits; instead, the broad trends derived from several studies are summarised.

2.9.2.a. Pb isotope studies on Phanerozoic OGDs

It is important to note that there are uncertainties regarding the utility of Pb isotopes in tracing the provenance of metals in OGDs (Goldfarb *et al.*, 1997; Goldfarb and Groves, 2015; Mortensen *et al.*, 2022). For example, as described in Section 2.3., the quantity of base metals in any fluid generated via metamorphic devolatisation processes is usually low (Phillips and Powell, 2010; Goldfarb and Groves, 2015). The implication of this fact is that host rocks with high Pb concentrations are likely to be a major contributor of Pb during the flow of hydrothermal fluids, meaning that the measured Pb ratios are likely to reflect the Pb isotope values of the host rocks and not the mineralising fluids (Goldfarb and Groves, 2015). However, Mortensen *et al.* 2022 argue that the common association of gold with galena (e.g. Li *et al.*, 2016b) means that Pb isotope data can still be used to evaluate the genesis of OGDs. Goldfarb and Groves (2015) also considered Pb isotope data from OGDs to be more meaningful in scenarios where the Pb concentrations of the host rocks are low.

Given the large range of overlap in Pb isotope ratios between some of the different subtypes (Fig. 2.28.; FA, SHOG and CSF), it is still uncertain as to whether Pb isotope signatures can be a useful tool in distinguishing the various Phanerozoic OGD subtypes (Torvela *et al.*, 2022). Nonetheless, the interpretations of the Pb isotope signatures (Fig. 2.28.) by Mortensen *et al.* 2022 are summarised here. Regarding the CSF subtype, a large range of variation is recorded by the compiled dataset (Fig. 2.28.); however, many datapoints plot around the curves for crustal Pb evolution. Mortensen *et al.* 2022 interpreted these trends as reflecting the derivation of Pb sources from mafic lithologies (e.g. ophiolites) at depth, with the less radiogenic Pb isotope ratios representing of a contribution from several other younger geological units within the crust. Given that the CSF subtype is spatially associated with transcrustal structures, it is perhaps likely that CSF OGDs may sit on the flow path of deeply sourced fluids, which could feasibly scavenge metals from several lithologies during transportation (Mortensen *et al.*, 2022). On the other hand, Pb isotope ratios from galena associated with the FA subtype show a relatively tight range in composition (Fig. 2.28.); Mortensen *et al.* 2022 consider this as being indicative of the extraction and transportation of Pb over a large geographical area. This process may result in the homogenisation of Pb isotope ratios (Fig. 2.28.). Regarding SLTD mineralisation (Fig. 2.28.), it is important to emphasise that in this subtype, OGD formation occurs in vein networks that are poorly interlinked; each group of veins in the entire system is likely to have a localised source of Pb (Mortensen *et al.*, 2022). For this reason, Pb isotope ratios from the SLTD subtype show a large amount of variation as a result of the contribution of Pb from several lithologies (Mortensen *et al.*, 2022). Potential Pb sources in the SLTD subtype include VMS intervals within the metasedimentary host rocks, or sedimentary rocks with elevated Au concentrations prior to metamorphism (Mortensen *et al.*, 2022). As part of their compilation, Mortensen *et al.* 2022 also presented data from the Victoria Gold Field (Australia) and Meguma (Nova Scotia, Canada) SHOG subtypes (Fig. 2.28.). However, Mortensen *et al.* 2022 only deemed the stratabound mineralisation at Meguma to be comparable to the Victoria gold deposits, with most of the other datapoints from Meguma being associated with a 'saddle-reef' style of mineralisation (i.e. hosted in anticlinal hinges) that formed 100 Ma after the stratabound veins (Chen, 2015; Mortensen *et al.*, 2022). For this reason, Mortensen *et al.* 2022 considered Pb isotope data from the SHOG subtype difficult to interpret and potentially indicative of large-scale extraction of Pb during the initial mineralisation event. Subsequent episodes of mineralisation may have exploited Pb from smaller and more localised sources (Mortensen *et al.*, 2022).

It should be noted that the aforementioned interpretations were provided by Mortensen et al. 2022, and there are alternative explanations for the trends depicted on Fig. 2.28. For example, the Otago Schist (FA subtype) appears to show some affinity with the SHOG subtype (Fig. 2.28.). Furthermore, much of the variation may pertain to the age of the deposit, with the younger mineralisation plotting in a more radiogenic portion of Fig. 2.28. This point underscores the uncertainties of using Pb isotope data to discriminate between Phanerozoic OGD subtypes

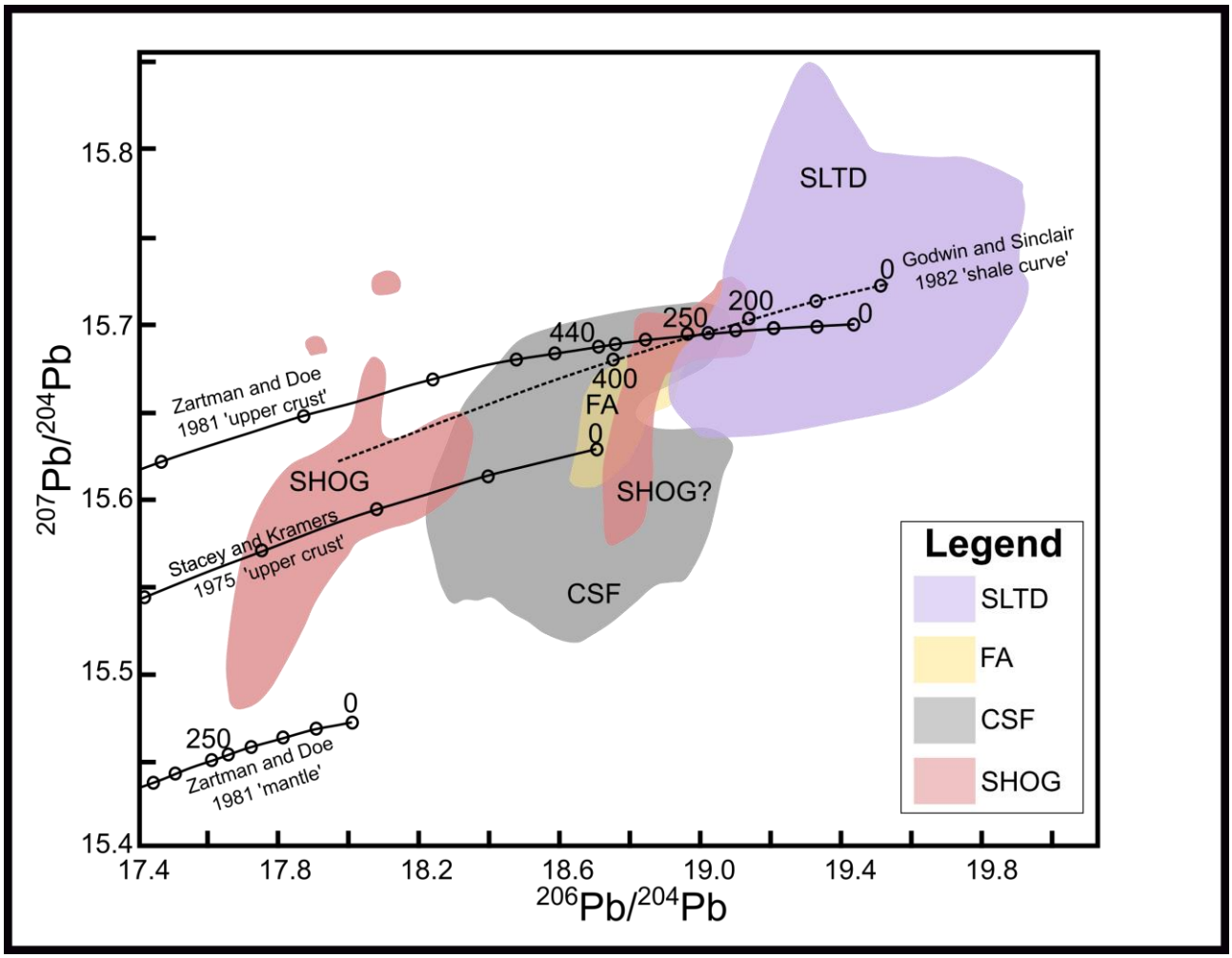

Figure 2.28. Compilation of Pb isotope analyses from the different subtypes (syn- and late tectonic dispersed, forearc, sediment-hosted orogenic gold, and crustal-scale fault; abbreviations were previously introduced in Table 2.2.) recognised by Mortensen *et al.* 2022 (adapted from Torvela *et al.*, 2022). Localities represented by the data are as follows: CSF (Sierra Nevada, California USA, and Bridge River Bralorne district, British Columbia, Canada), FA (Otago Schist Belt, New Zealand), SHOG (Victoria Gold Field, Australia; South Cariboo, British Columbia, Canada; Meguma Belt, Nova Scotia, Canada), SLTD (White Gold district, Yukon, Canada; North Cariboo district, British Columbia, Canada). The data were compiled from the studies of Farquhar and Haynes (1986), Godwin *et al.* 1988, Thorpe (2008), Mortensen *et al.* 2010, Bailey (2013), Huston *et al.* 2017. The numbers on the curves denote age (Ma).

2.9.2.b. Pb isotope studies on porphyry and epithermal deposits

Whilst there is no singular compilation for Pb isotope data from porphyry deposits, lead isotope geochemistry has been widely utilised to characterise the source of metals in this mineralisation style, particularly in South America (Tilton *et al.*, 1981; Sillitoe and Hart, 1984; Bouse *et al.*, 1999). Collectively, these studies demonstrate that porphyry deposits commonly have a mantle or lower crustal source of Pb (Bouse *et al.*, 1999). It is common for galena from porphyries to record Pb isotope ratios that plot near the mantle or 'orogene' curves (Fig. 2.24.c.-d.) of Pb evolution (Shahabpour and Kramers, 1987; Pettke *et al.*, 2010; Chugaev *et al.*, 2022). However, Pb isotope ratios that plot close to the Stacey and Kramers (1975) crustal growth curves (Fig. 2.24.a.-b.) have been reported from several porphyries (Plotinskaya *et al.*, 2017; Yang *et al.*, 2022). For this reason, several publications argue that some porphyry deposits may have a mixed source of Pb (i.e. a mixture of crustal and mantle Pb sources; Chiaradia *et al.*, 2004; Leng *et al.*, 2015; Plotinskaya *et al.*, 2017).

Regarding epithermal gold deposits, previous Pb isotope studies have suggested that the metals may typically be scavenged from several lithologies within the continental crust; as a result, epithermal mineralisation is often characterised by a more radiogenic signature than porphyry deposits (Marcoux and Milési, 1994; Sundblad *et al.*, 1991; Potra and Macfarlane, 2014; Ma *et al.*, 2022b). Where paragenetic constraint is available, it has been observed that galena in earlier paragenetic generations may be less radiogenic compared to later generations (Foley and Ayuso, 1994). For example, at Creede (Colorado, USA), the increase in radiogenic Pb observed throughout the paragenesis was interpreted to reflect a magmatic-hydrothermal fluid mixing with sources of crustal lead (Foley and Ayuso, 1994). Furthermore, Pb isotope ratios typical of mantle derived or magmatic Pb sources have also been documented in several epithermal gold deposits (Saunders *et al.*, 2016; Zhai *et al.*, 2020; Sun *et al.*, 2021).

Chapter 3: Geological Background of the Study Area

3.1. Introduction

Before considering the geological background of Loch Tay, it is first necessary to provide an overview of the wider geological setting. Scotland is comprised of the Hebridean, Northern Highland, Grampian, Midland Valley, and the Southern Uplands-Down Longford (SUDLT) terranes (Fig. 3.1.), which were accreted together during the Caledonian Orogeny. This event encompasses the Cambrian-Devonian tectonic episodes that resulted in the closure of the Iapetus Ocean (Suess, 1906; Stille, 1924; Evans and Stubblefield, 1929; Mckerrow *et al.*, 2000; Searle, 2021). Many of the sedimentological, magmatic, and structural characteristics of the Grampian Terrane are directly related to the Caledonian Orogeny (Dewey, 1969; 1971; Lambert and McKerrow, 1976; Dewey and Shackleton, 1984; McClay *et al.*, 1986; Haughton *et al.*, 1990; Trewin and Thirlwall, 2002; Oliver *et al.*, 2008; Neilson *et al.*, 2009; Chew and Strachan, 2014; Miles *et al.*, 2016, McKellar *et al.*, 2021). For this reason, a review of the Caledonian Orogeny (and the impact of this event on the Grampian Terrane) is necessary.

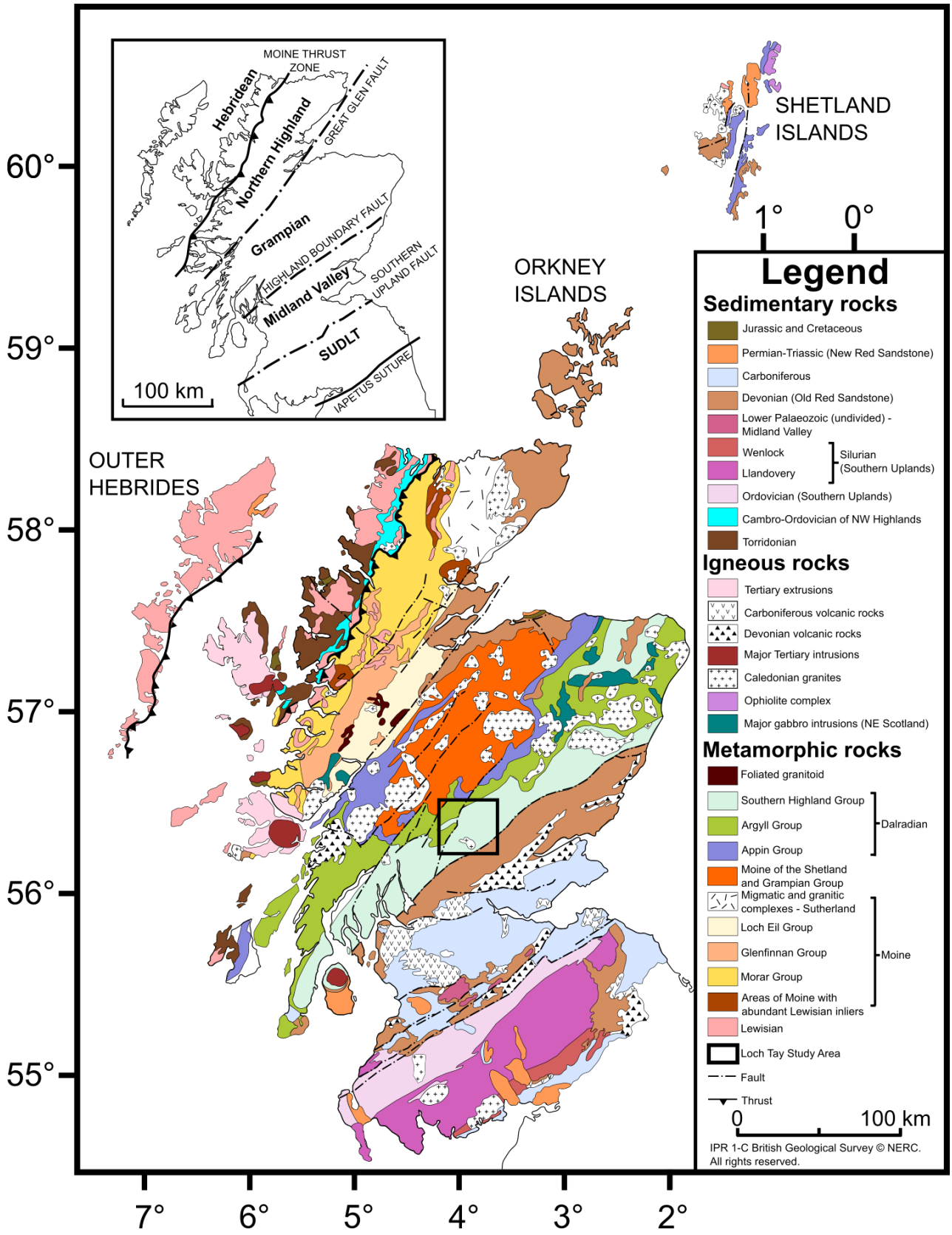

Figure 3.1. Simplified geological map of Scotland (Strachan, 2002; Searle, 2021). The inset map depicts the major terranes and their boundaries (Leslie *et al.*, 2008).

3.2. Tectonostratigraphic development of the Grampian Terrane

The Grampian Terrane is comprised of the Dalradian Supergroup, a package of volcaniclastic and sedimentary rocks that was deposited from 730 to 500 Ma (Halliday *et al.*, 1989; Tanner and Pringle, 1999; Dempster *et al.*, 2002; Cawood *et al.*, 2003; Banks *et al.*, 2007; Tanner and Sutherland, 2007; Stephenson, 2013a, b). The sedimentological development of the Dalradian Supergroup also resulted in the deposition of base metals along the Laurentian margin (Russell, 1985), which were subsequently remobilised during several episodes of ore deposit formation (Hill *et al.*, 2013; Spence-Jones *et al.*, 2018). To understand the metallogenic processes that have affected the Grampian Terrane, it is necessary to provide a brief appraisal of the history of the Dalradian Supergroup. However, it is important to note that around the Study Area (Fig. 3.1.), there are no known outcrops of the Grampian or Appin groups; for this reason, only a brief summary is provided for these two units, with the focus of this section being on the Argyll and Southern Highland groups, which host the LTVS (Fig. 3.1.).

3.2.1. Grampian Group

The Grampian Group covers large swathes of the northern portions of the Grampian Terrane (up to 4250 km^2; Stephenson *et al.*, 2013a). Stratigraphically, the Grampian Group is the oldest unit within the Dalradian Supergroup, and it is composed of psammites, semipelites, and quartzites, all of which have undergone amphibolite facies metamorphism (Stephenson *et al.*, 2013a). This unit was deposited in one of the several NE-SW trending (and relatively shallow) intracratonic basins between the Laurentia and Baltica blocks prior to 700 Ma (Anderton, 1982; Glover and Winchester, 1989; Smith *et al.*, 1999); sedimentation began after the onset of the continental rifting processes that impacted Rodinia (Anderton, 1982).

3.2.2. Appin Group

The Appin Group, which overlies the Grampian Group (Stephenson *et al.*, 2013a, b), was largely derived from sediments along the Laurentian continental shelf and is comprised of pelites, semipelites, quartzites, and metalimestones (Stephenson *et al.*, 2013a, b). Furthermore, the rapid alternation of facies and lithologies is considered to be a typical characteristic of the Appin Group (Anderton, 1985; Stephenson *et al.*, 2013a). In terms of the depositional environment of this unit, renewed rifting and subsidence ended the previous period of tectonic stability, with the initial deposition of the Appin Group alternating between nearshore tidal and offshore sediments (Glover *et al.*, 1995; Stephenson *et al.*, 2013a). Depositional conditions typically varied between a shallow marine environment and stagnant, euxinic lagoons (Stephenson *et al.*, 2013a). As the speed of rifting increased, there were higher rates of erosion in the footwall of the basin, resulting in rapid deposition. However, the high degrees of rifting eventually began to cause the basin to widen, creating large expanses that were relatively starved of sediment (Glover *et al.*, 1995); these conditions were conducive to carbonate precipitation (Stephenson *et al.*, 2013a).

3.2.3. Argyll Group

Around Loch Tay (and in particular, West of the Loch Tay Fault), much of the bedrock geology is comprised of the Argyll Group (Fig. 3.1.). This package of metasediments contains semipelites, pelites, quartzites, and metacarbonates (Stephenson *et al.*, 2013a, b). Throughout the Grampian Terrane, the Argyll Group overlies the Appin Group and underlies the Southern Highland Group (Stephenson *et al.*, 2013a, b). In Section 3.4.1., the lithological characteristics of the Argyll Group around Loch Tay are described in detail. Furthermore, SEDEX mineralisation within the Argyll Group is discussed in the context of the genetic model that has been conceptualised for Foss (Section 3.6.2.a.).

In terms of the depositional environment of the Argyll Group, sedimentation of the earliest units (i.e. the Islay Subgroup) took place in a tidal to glacial shelf under relatively shallow conditions (Stephenson *et al.*, 2013a). Regional extension between Laurentia and Baltica in the Late Neoproterozoic (Anderton, 1985) led to a deepening of the basin; however, throughout the development of the Islay Subgroup (e.g. the Schiehallion Quartzite Formation), sediment deposition kept pace with the subsidence (Stephenson *et al.*, 2013a). During the deposition of the Easdale Subgroup (which encompasses several geological units around Loch Tay, including the Killiecrankie Schist, Carn Mairg Quartzite, Ben Eagach Schist, Ben Lawers Schist, and Farragon Volcanic formations; Section 3.4.1.), the rate of subsidence increased (Stephenson *et al.*, 2013a, b). Overall, this caused the sedimentary basin to become deeper, an event manifested by the development of deep marine sediment facies; turbidite deposition was interspersed by episodes of mudstone deposition (Stephenson *et al.*, 2013a). The thinning of the lithosphere as a result of the regional extension led to the onset of magmatism (Anderton, 1985). The Farragon Volcanic and Tayvallich Volcanic formations (dated by U-Pb analyses on zircon to 601 ± 4 Ma) formed as a result of this process (Dempster *et al.*, 2002). The intensive rifting throughout the deposition of this unit represents the opening of the Iapetus Ocean (Anderton, 1985).

3.2.4. Southern Highland Group

Most of the LTVS is hosted within the Southern Highland Group (Fig. 3.1.), which is described as a 4 km thick package of metamorphosed turbidites mainly comprised of coarse-grained, poorly sorted greywackes interspersed with layers of fine-grained mudstones, volcaniclastics and limestones (Stephenson *et al.*, 2013a, b). The Southern Highland Group is distinguished from the Argyll Group by higher chlorite quantities, which may reflect reduced metamorphic grades or increased levels of volcaniclastic input (Stephenson *et al.*, 2013a).

Stephenson *et al.* 2013a noted that the Argyll and Southern Highland Groups both record sedimentary structures that are indicative of turbidite facies (graded bedding, parallel lamination, erosional bases and slump bedding being some examples; Stephenson *et al.*, 2013a, b). Furthermore, clast studies on the Argyll

and Southern Highland Groups have indicated that the sediments are likely to have been sourced from compositionally immature lithologies (Harris *et al.*, 1978; Anderton, 1980, 1985; Burt, 2002; Pickett *et al.*, 2006). The general character of the Southern Highland Group has led to the interpretation that deposition of this unit occurred during a period of rapid basin deepening; information derived from sedimentary structures demonstrates that coarse-grained sediments were deposited at various localities within submarine fans that spilled out onto the seafloor, with finer sediments being deposited as overbank deposits or outer fan facies (Stephenson *et al.*, 2013a). The flow direction of the turbiditic sequences was predominantly towards the southeast (with minor components of northeast and southeast flow; Stephenson et *al.*, 2013a). Towards the top of the Dalradian Supergroup, clasts of feldspar, high-grade metamorphic rocks, and granites become more common, which is indicative of a shift in provenance towards a less mature source region (Harris and Pitcher, 1975; Harris e*t al.*, 1978; Plant *et al.*, 1984; Anderton, 1985; Stephenson *et al.*, 2013a, b). The change in provenance may reflect the removal of younger sedimentary cover in the northwest source region and the exposure of basement rocks (Plant *et al.*, 1984; Anderton, 1985). Deposition of the Southern Highland Group ended with the accumulation of the Loch Avich lavas, which potentially represent magmatism within the Dalradian basins (e.g. around the Loch Awe region; Stephenson *et al.*, 2013a). The deposition of the Loch Avich Lavas Formation involved the accumulation of <500 km of pillow lavas with relatively minor sedimentary input (Borradaile, 1973; Stephenson *et al.*, 2013a).

3.3. Tectonic evolution of the Grampian Terrane during the Caledonian Orogeny

Following the deposition of the Dalradian Supergroup throughout the Neoproterozoic, the various terranes of Scotland (Fig. 3.1.) were assembled into their present arrangements during the Caledonian Orogeny, an event that resulted in the closure of the Iapetus Ocean and the formation of Pangaea (Mckerrow *et al.*, 2000). Specifically, the orogeny was caused by the collision of Laurentia, Avalonia, and Baltica (Dewey, 1969; Lambert and McKerrow, 1976; Dewey and Shackleton, 1984; Chew and Strachan, 2014; Dewey *et al.*, 2015; Strachan *et al.*, 2020; Searle, 2021). The Caledonian orogenic cycle began at ~500 Ma with the onset of subduction along the SE margin of Laurentia (Fig. 3.2.). It is important to emphasise that the Caledonian Orogeny occurred on a large (and sometimes diachronous) scale and in addition to the British Isles, this event is recorded in the geological history of North America (Butler, 1973; Muth *et al.*, 1979; Hall and Roberts, 1988), Greenland (Andresen *et al.*, 2007; Higgins *et al.*, 2008; Kalsbeek *et al.*, 2008), and Scandinavia (Oliver *et al.*, 1993; Andreasson *et al.*, 2003; Foulger *et al.*, 2005). The Caledonian Orogeny is also known to have impacted several regions in North and Central Europe, including what is now Germany (Giese *et al.*, 1997; Dallmeyer *et al.*, 1999; Ziegler and Dèzes, 2006) and Poland (Krawczyk *et al.*, 2008; Mazur *et al.*, 2016). This review focuses on the Grampian, Scandian, and Acadian orogenies because these are all expressed, to varying degrees, in the Grampian Terrane.

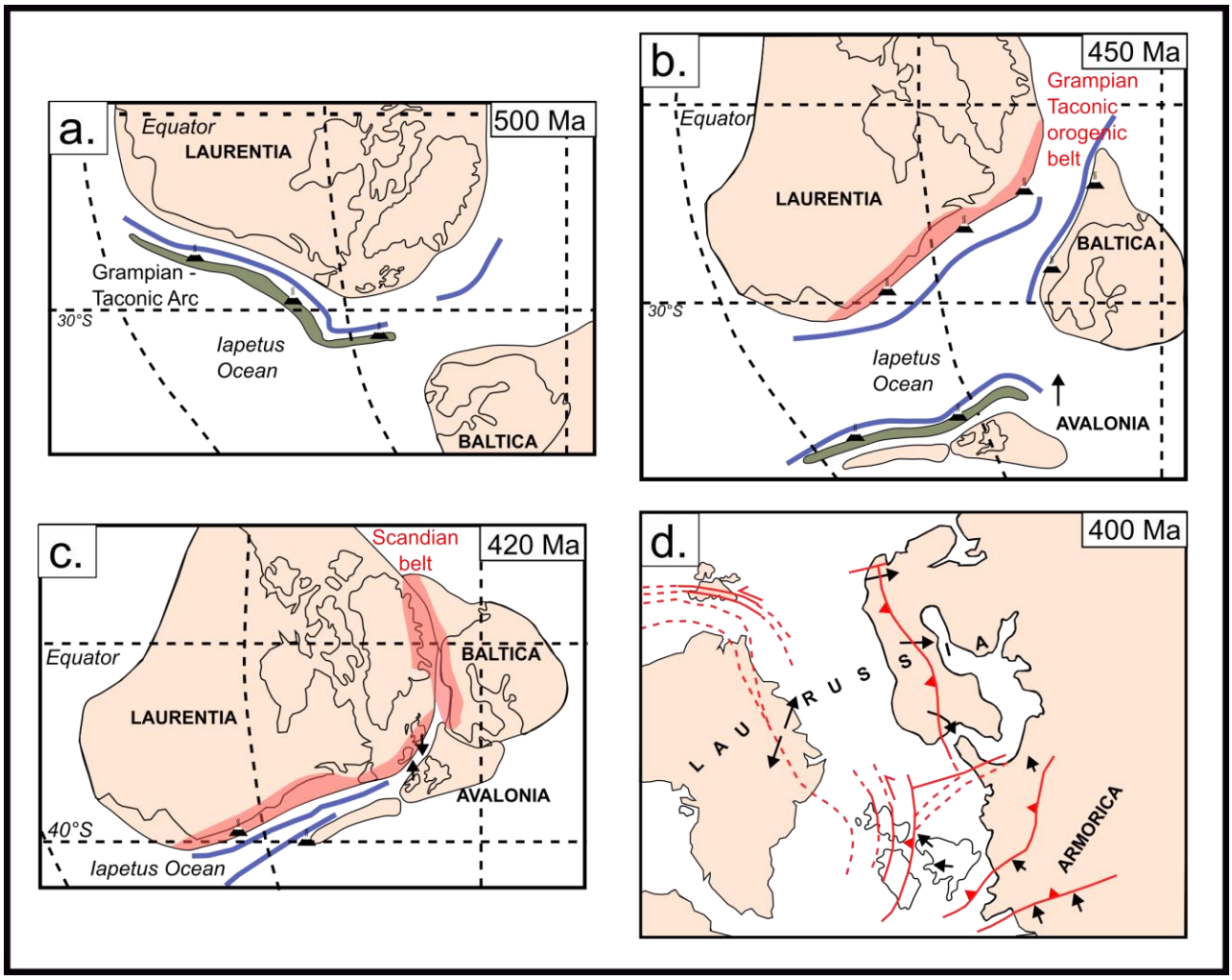

Figure 3.2. Series of figures summarising the tectonic evolution of the Caledonian orogenic cycle. **a.** 500 Ma; subduction towards the south created a volcanic arc along the Laurentian coast. **b.** 450 Ma; a subduction polarity reversal occurred prior to the subduction of oceanic lithosphere beneath Laurentia. **c.** 420 Ma; the Iapetus Ocean had nearly closed, and the Scandian Orogeny was underway. **d.** 400 Ma; deformation occurred in the British Isles during the Acadian Orogeny. These figures were adapted from Chew and Strachan (2014) and Soper *et al.* 1992 (Fig. 3.2.d.).

3.3.1. Grampian Orogeny

As mentioned previously, the Grampian Orogeny began at approximately 500 Ma when oceanic crust was subducted towards the SE (Fig. 3.2.; Chew and Strachan, 2014). Lambert and McKerrow (1976) defined the Grampian Orogeny as a series of processes culminating in the folding of the Dalradian Supergroup and the Arenig sediments on the Laurentian shelf. In Scotland, the Grampian Orogeny was caused by a collision between the Midland Valley arc-microcontinent and Laurentia (Mitchell, 1978; Oliver, 2001; Searle, 2021). Furthermore, the Grampian Orogeny was contemporaneous with the Taconic and Humberian orogenies in the Appalachians and Newfoundland (McKerrow *et al.*, 2000). During the collision between Laurentia and the Midland Valley arc-microcontinent, the Dalradian sediment package (including the Southern Highland Group) was deformed and metamorphosed (Chew and Stillman, 2009; Stephenson *et al.*, 2013a). A volcanic

arc, termed 'Grampian-Taconian', collided with Laurentia, joining the landmasses that are now Scotland, Ireland, and Newfoundland (Dewey, 1969; Dewey and Shackleton, 1984; van Staal and Dewey, 2023; Stephenson *et al.*, 2013a; Chew and Strachan, 2014). Oceanic crust was overthrust onto Laurentia; various ophiolites from this collision are preserved throughout the Grampian Terrane. Examples include the Ballantrae Complex (Church and Gayer, 1973), Clew Head, and Unst (Chew and Strachan, 2014); amphibolites from the Unst ophiolite have been dated by U-Pb methods to 484 Ma ± 4 Ma (Crowley and Strachan, 2015). This places a lower limit on the obduction event (Crowley and Strachan, 2015). The crustal thickening event during the Grampian Orogeny was relatively short-lived; it ended between 475 and 465 Ma and was accompanied by prograde metamorphism and granitoid magmatism (Baxter *et al.*, 2002; Oliver *et al.*, 2008; Mark *et al.*, 2020). Following the crustal thickening from the collision itself, there was a period of lithospheric extension before the crust began to thicken again as the orogeny continued (Viete *et al.*, 2010). The Grampian Orogeny was terminated by a polarity reversal (i.e. subduction began occurring towards the north as opposed to the southeast) that facilitated the development of an Andean-type margin along the Laurentian coast and the SUDLT (Southern Uplands Down-Longford Terrane), which was a successor to the Grampian Orogeny subduction zone (Fig. 3.2.; Mitchell, 1978; Chew and Strachan, 2014; van Staal and Dewey, 2023).

Multiple attempts have been made to constrain the timing of the metamorphic peak of the Grampian Orogeny through the calculation of mineral cooling ages; these are hypothesised to represent the post-metamorphic cooling phase of an orogeny (Cliff, 1985). Chew and Strachan (2014) summarised $^{40}Ar/^{39}Ar$ and Rb–Sr cooling dates derived from muscovite, biotite, and hornblende in previous studies (Dempster, 1985; Dempster *et al.,* 1995); the results ranged from 460 to 450 Ma. Other geochronological studies (Friedrich *et al.*, 1999a, b; Flowerdew *et al.*, 2000; Chew *et al.*, 2003; Daly and Flowerdew, 2005) are all in agreement that the post-metamorphic cooling period began at some point between 470 and 455 Ma. As such, the date for peak metamorphism in the Grampian Terrane is often quoted as 470 Ma (Chew and Strachan, 2014), with a range of 475-465 Ma sometimes being given (Friedrich *et al.*, 1999b; Dewey, 2005; Rice *et al.*, 2016). The post-Grampian period of uplift and unroofing continued until c. 430 Ma (Dempster, 1985; Soper *et al.*, 1999; Oliver, 2001). Dempster *et al.* 1995 suggested that cooling to temperatures below 300 °C took place between 460 and 430 Ma.

3.3.2. Scandian Orogeny

The Scandian phase of the Caledonian Orogeny involved the oblique docking of Avalonia against Laurentia (Fig. 3.3.). In the British Isles, the Scandian Orogeny occurred between 435 and 410 Ma (Soper *et al.*, 1992a, b; Strachan, 2002; Kinny *et al.*, 2003a, b; Kirkland *et al.*, 2013; Chew and Strachan, 2014); the event is also represented in the Northern Highland Terrane, although the precise timings are frequently debated (Jacques and Reavy*,* 1994; Dewey and Mange, 1999; Dallmeyer *et al.*, 2001; Chew and Strachan, 2014;

Corfu *et al.*, 2014). This orogenic cycle is better studied in Scandinavia, where the intensity of the collision obducted ophiolites onto the Norwegian coast and resulted in the formation of eclogite-facies rocks (Krogh *et al.*, 2011). The Scandian Orogeny did not cause significant crustal thickening in the UK (Chew and Strachan, 2014). However, sinistral-slip faults were active during the Scandian phase, with the Great Glen Fault being one example (Stewart *et al.*, 1999; 2001; Dewey and Strachan, 2003; Dewey *et al.*, 2015). Initially, the docking of Laurentia and Avalonia resulted in transpressional movements (Strachan *et al.*, 1992; Dewey and Strachan, 2003; Kinny *et al.*, 2003a, b; Fig. 3.3.), which occurred in response to a maximum principal stress that was oriented approximately north-south (Baxter *et al.*, 2002). Following initiation, a regional transition from transpression to transtension occurred throughout Scotland between 425 and 410 Ma (Fig. 3.3.b.); evidence for this transition comes from the widespread occurrence of calc-alkaline intrusions during this interval (Dewey and Strachan, 2003), which is discussed in more detail in Section 3.3.5. These intrusions were emplaced in transtensional pull-apart basins and dilatational splays (Hutton, 1982; 1988; Hutton and McErlean, 1991; Hutton and Reavy, 1992; Jacques and Reavy, 1994). The Devonian sediments (e.g. the Old Red Sandstone) were also deposited in transtensional pull-apart basins created by this event (Coward *et al.*, 1989; Friend *et al.*, 2000; Dewey and Strachan, 2003).

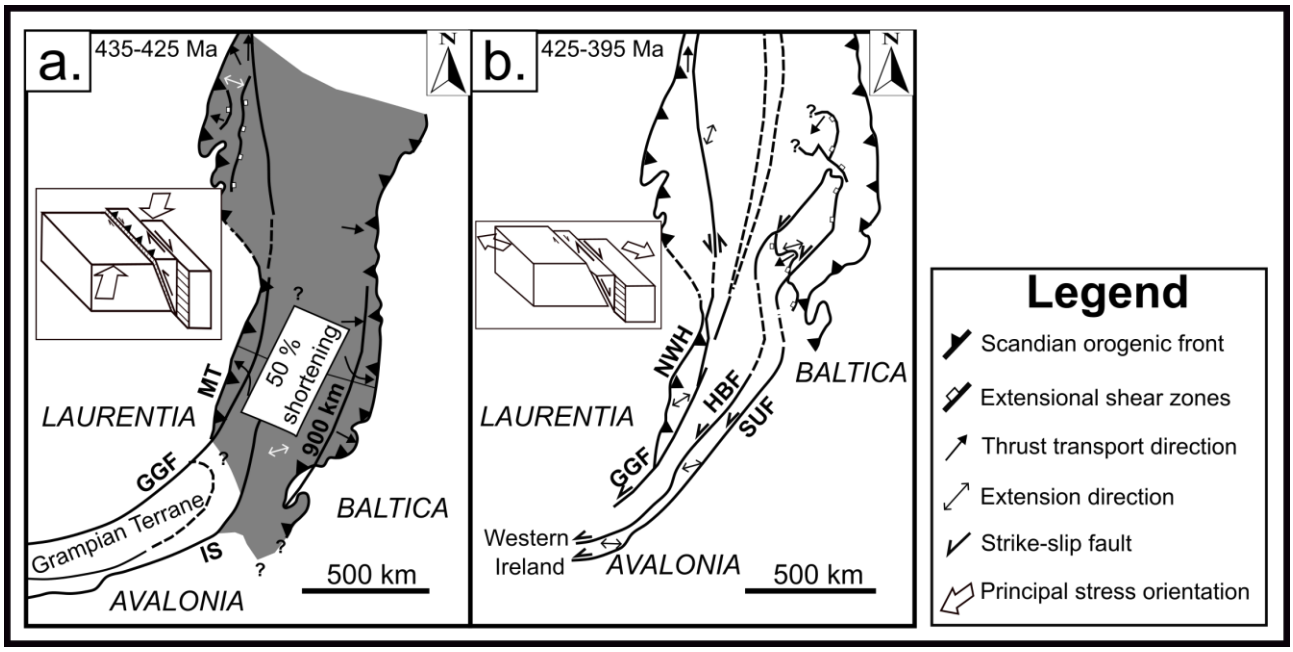

Figure 3.3. The transition from a transpressional (**a.**) to a transtensional setting (**b.**) during the Scandian Orogeny (adapted from Dewey and Strachan, 2003). Abbreviations are as follows: NWH (Northern Highlands), Great Glen Fault (GGF), IS (Iapetus Suture), Highland Boundary Fault (HBF), MT (Moine Thrust), SUF (Southern Uplands Fault). The inset diagrams depict the different deformation styles associated with each setting and were adapted from Wesnousky (2005).

3.3.3. Acadian Orogeny

In the British Isles, the Acadian Orogeny is regarded as 'proto-Variscan', i.e. it was the product of plate reconfigurations that ensued before the Variscan Orogeny (Woodcock *et al.*, 2007). The specific event identified as a root cause of the Acadian Orogeny in the UK is the N-S collision of the Midlands Microcraton with other parts of Avalonia (Woodcock *et al.*, 2007; Mendum, 2012). The Acadian Orogeny resulted in the termination of sedimentation throughout Devonian basins and involved sinistral transpression along pre-existing faults (Mendum, 2012). In the Southern British Isles, the Acadian Orogeny is constrained to 400-390 Ma (Woodcock *et al.*, 2007); however, the Acadian Orogeny is not particularly well expressed North of the Iapetus suture (Soper *et al.*, 1987; Dewey *et al.*, 2015), meaning the impact of this event on the Study Area is unclear. Throughout Scotland, some new structures were produced during the Acadian Orogeny; examples include the Strathmore Syncline and Sidlaw Anticline in the Midland Valley Terrane, which formed as a result of transpression along the Highland Boundary Fault (Jones *et al.*, 1997; Friend *et al.*, 2000; Mendum, 2012). The emplacement of leucogranites along transcurrent faults demarcates the start of Acadian transpression and strike slip faulting (Mendum and Noble, 2010), whilst the deposition of Mid-Devonian clastics at 393 Ma on the exhumed Rosemarkie Inlier (which is spatially associated with the Great Glen Fault) represents the end of the Acadian Orogeny in Northern Britain (Mendum, 2012).

3.3.4. Deformation of the Grampian Terrane

Throughout the Caledonian Orogeny, the Grampian Terrane was deformed (Fig. 3.4.), resulting in the creation of various structures (Stephenson *et al.*, 2013a, b). In this section, the deformation processes that have impacted the Grampian Terrane are summarised. This terrane can be characterised as being comprised of a NW-facing recumbent fold in the NW (the Islay Anticline) and a SW-facing recumbent fold in the SE (the Tay Nappe; Shackleton, 1958), with the Loch Awe Syncline occurring between these two structures (Fig. 3.4.) (Thomas, 1979; Stephenson *et al.*, 2013a. b). Following the Grampian Orogeny, there was a major episode of strike-slip faulting during the Scandian Orogeny (Dallmeyer *et al.*, 2001; Chew and Strachan, 2014; Corfu *et al.*, 2014). Throughout this section, the impacts of the deformation processes are discussed sequentially, beginning with the Grampian Orogeny.

Regarding the different 'complexes' that comprise the folds shown on Fig. 3.4., Thomas (1979) grouped them together depending on the nature of the folding and the lithologies contained within each complex; for example, the Southern Grampians Complex is comprised of SE-facing folds on the southeast side of the axis of the Loch Awe Syncline, as well as folds southeast of the Boundary Slide (Fig. 3.4.; Thomas, 1979). The Western Grampians Complex contains NW-facing folds NW of the Loch Awe Syncline as well as the Ossian-Geal Charn Steep Belt (Fig. 3.4.; Thomas, 1979). Finally, the Central Grampians Complex mostly represents the Grampian Group and the Central Highland Migmatite Complex (the distribution of these units is depicted on Fig. 3.1.).

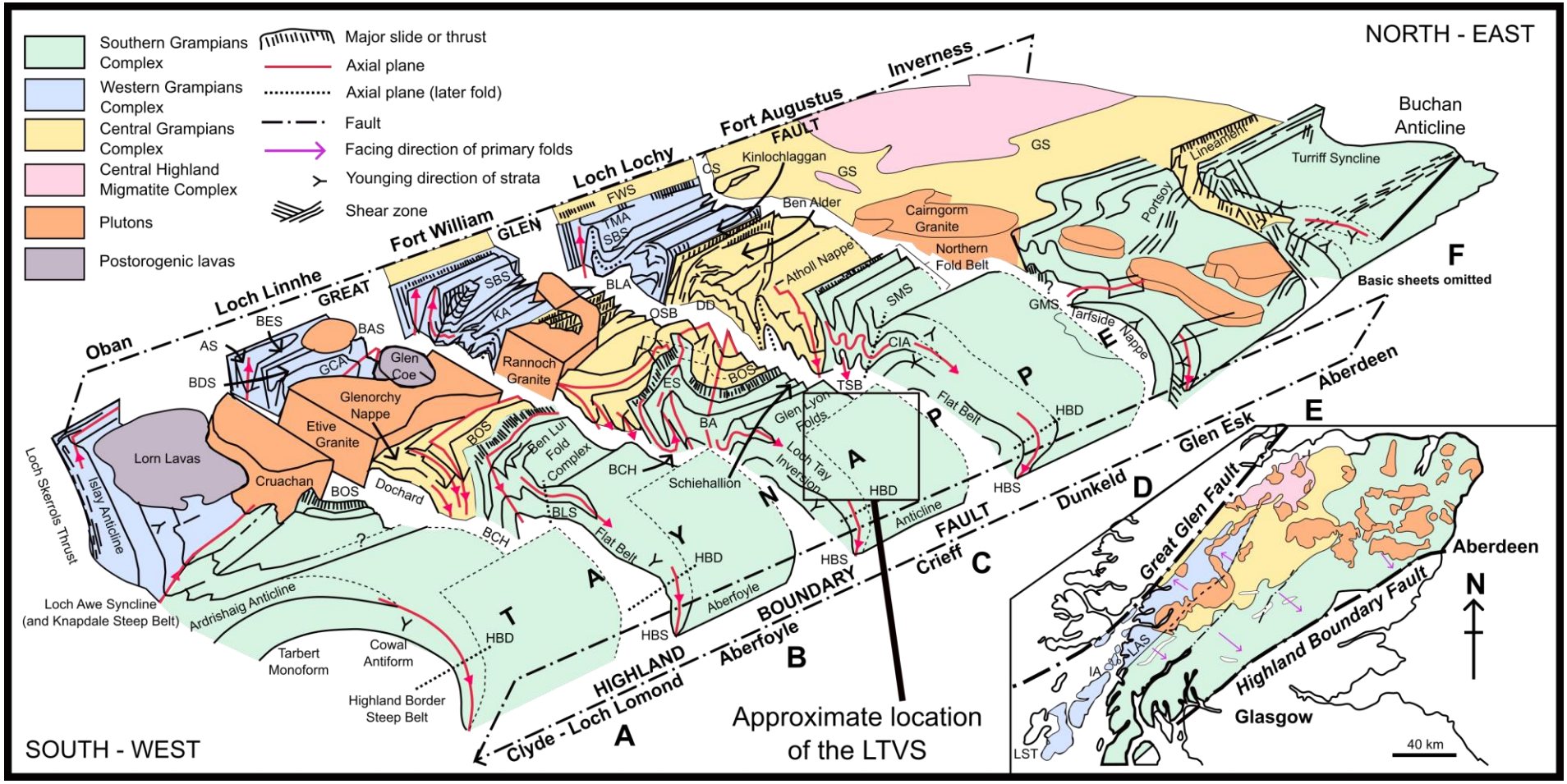

Figure 3.4. Block diagram depicting the major geological structures in the Grampian Terrane (excluding brittle faults and mafic intrusions). Adapted from Thomas (1979) and Stephenson and Gould (1995). Abbreviations are as follows: AS = Appin Syncline; BA = Bohespic Antiform, BAS = Ballachulish Slide, BCH = Beinn a'Chuallich folds, BDS = Beinn Don Syncline, BES = Benderloch Slide, BLA = Beinn na Lap Antiform, BLS = Ben Lawers Synform; BOS = Boundary Slide, CIA = Creag na h'Iolaire Anticline, CS = Corrieyairack Syncline, DD = Drumochter Dome; ES = Errochty Synform, FWS = Fort William Slide, GCA = Glen Creran Anticline, GMS = Glen Mark Slide; GS = Grampian Slide; HBD = Highland Border Downbend, HBS = Highland Border Steep Belt; KA = Kinlochleven Anticline; OSB = Geal-charn–Ossian Steep Belt, SBS = Stob Ban Synform, SMS = Sron Mhor Synform; TMA = Tom Meadhoin Anticline; TSB = Tummel Steep Belt.

In terms of the deformation processes associated with the Grampian Orogeny, these have previously been classified by their relative order of formation using a 'D-number' framework from 1 to 4 (Table 3.1.; Stephenson *et al.*, 2013a; Tanner, 2014b). However, it should be noted that the use of 'D-numbers' has been criticised, given that a heterogeneous distribution of strain during progressive deformation associated with an orogenic cycle can produce a variety of geological structures (meaning they are not temporally distinct; Coward and Potts, 1983; Holdsworth, 1990; Alsop and Holdsworth, 1993; Alsop *et al.*, 2020). Furthermore, each 'D-number' in the Grampian Terrane may not be expressed in every region and in some cases, there may be localised differences; for example, Harris *et al.* 1998 suggested that the Grampian Orogeny resulted in a fabric that predates D1 (Table 3.1.) in Callander (Perthshire). Nonetheless, the 'D-number' classifications for the Grampian Terrane serve as a useful framework (Table 3.1.) in which to consider the relative order of the formation of structures associated with the Grampian Orogeny (Stephenson *et al.*, 2013a; Tanner, 2014b). Generally speaking, the development of the entire D1-D4 fabric occurred over a period of <15 Ma (Oliver, 2001; Tanner, 2014b).

Historically, a wide range of interpretations pertaining to the development and evolution of major folds in the Grampian Terrane (including the Tay Nappe; Fig. 3.4.) have been developed; broadly speaking, these can be divided into models that emphasise obduction (Henderson and Robertson, 1982; Dewey and Mange, 1999; Dewey, 2005) or subduction (Krabbendam *et al.*, 1997; Treagus, 1999; Rose and Harris, 2000; Tanner, 2007a, b). The two categories can be distinguished by the nature of the processes involved; subduction-driven models focus on the subduction of crust beneath Laurentia, whereas in obduction-driven models, the obduction of volcanic complexes onto the Laurentian margin (e.g. the Highland Border Complex) is inferred to be the main cause of the folding (Tanner, 2014b). However, none of the previous interpretations regarding the development of Tay Nappe can account for the SE vergence recorded by this structure, which is inconsistent with models involving a northwards oceanic arc collision and overthrusting of material onto the Laurentian margin (Dewey, 2005; Dewey *et al.*, 2015). The exact processes involved in the formation of the Tay Nappe (Fig. 3.4.) therefore remain uncertain.

Name	Description of processes and structures	Age (Ma)	References
D1	• Greenschist facies deformation • NE-SW trending upright folds and ductile shears • Top-to-the-SE shear sense recorded on the upper limb of the Tay Nappe	475-473	(Tanner, 2014b)
D2	• Peak metamorphism (amphibolite facies) and maximum deformation due to continued overthrusting • Rotation and stacking of isoclinal and asymmetrical nappes • Southeast subduction became oblique	473-470	(Friedrich *et al.*, 1999a, b; Dempster *et al.*, 2002; Tanner, 2014b)
D3	• Upright to SE-steeply dipping NE-trending structures developed due to reduced deformation intensity	470-465	(Baxter *et al.*, 2002; Tanner, 2014b)
D4	• Deformation of pre-existing structures by layer-parallel shortening • NE-SW trending buckle folds • Widespread development of crenulation cleavage • Formation of Highland Border Downbend during a refolding event	465-460	(Roberts, 1974; Tanner *et al.*, 2013; Tanner, 2014b)

Table 3.1. Main deformation phases (D-phases) of the Grampian Orogeny that have been recognised within the Dalradian Supergroup.

Whilst metamorphic petrology is not the focus of this study, the broad patterns in metamorphic facies associated with the Grampian Orogeny are summarised here. The NE portion of the Grampian Terrane is the type locality for 'Buchan-type' metamorphism (Fig. 3.5.; Read, 1952; Hudson, 1980; 1985; Pattison and Goldsmith, 2022), which is characterised by relatively lower pressures and higher temperatures (e.g. the lack of garnet metamorphic zones on Fig. 3.5.). Buchan metamorphism is common in regions where the geothermal gradient is higher (England and Thompson, 1984; De Yoreo *et al.*, 1991). The occurrence of Buchan metamorphism in the eastern portions of the Grampian Terrane are linked to the isolated subduction of a hot spreading seafloor ridge that did not occur elsewhere in the wider region (Tanner, 2014b).

The Barrovian metamorphic zones in the Grampian Terrane, which in some cases host the LTVS (Fig. 3.5.), range from greenschist to amphibolite facies; generally speaking, there is a trend of increasing metamorphic grade from SE to NW, with kyanite and garnet-bearing assemblages being more typical of the central Grampians (Fig. 3.5.). Barrovian metamorphism occurred in Scotland as a result of D2 (Table 3.1.), which heated the middle crust and caused pressures to increase (Oliver *et al.*, 2000; Baxter *et al.*, 2002; Viete *et al.*, 2011). However, the isograds crosscut the Tay Nappe (Fig. 3.5.), meaning this structure was

potentially initiated prior to the onset of the peak metamorphism. Several interpretations exist regarding the cause of the heating; magmatic intrusions (Lyubetskaya and Ague, 2010a, b), hot fluids emanating from the subducting slab (Tanner, 2014b), and the production of heat during deformation (Ashcroft *et al.*, 1984; Viete *et al.*, 2010; 2011; 2013).

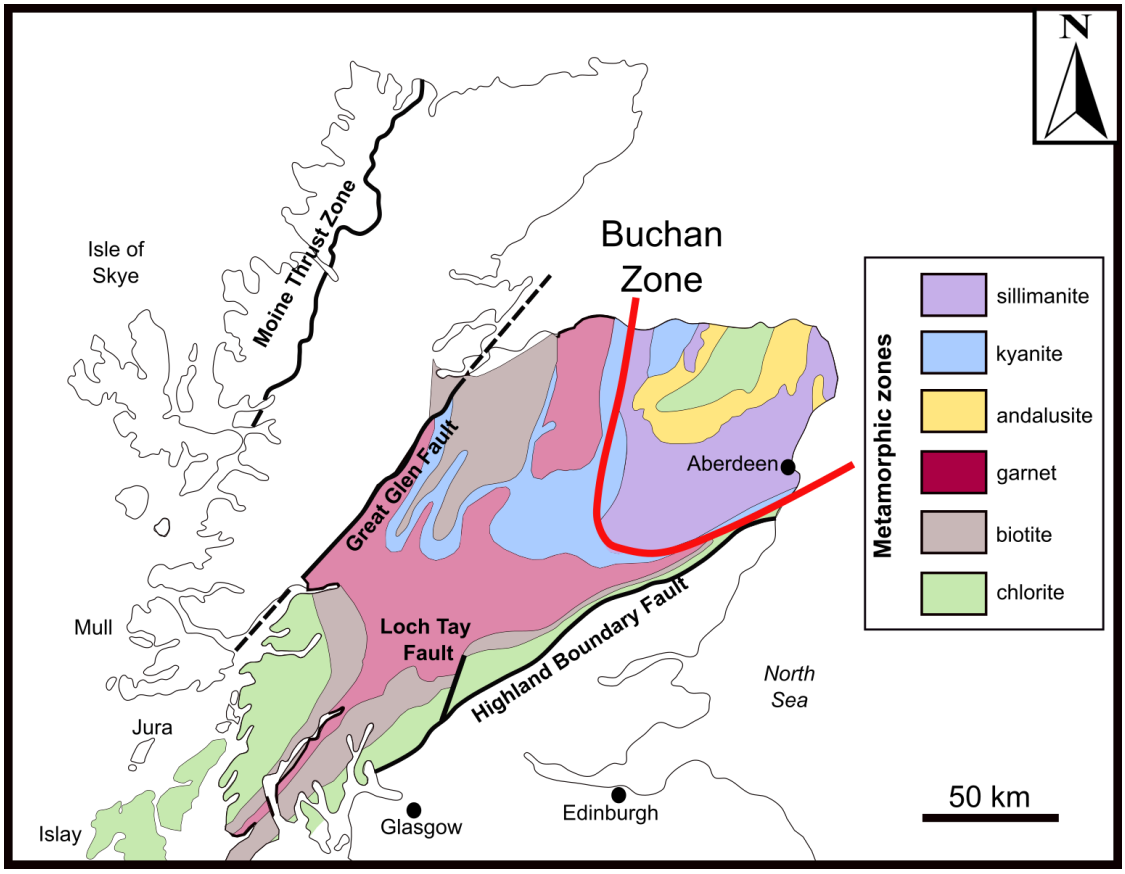

Figure 3.5. Map of the different metamorphic zones of the Grampian Terrane (Fettes, 1970, 1979; Winchester, 1974; Harte and Hudson, 1979; Gillen, 1982; Stephenson *et al.*, 2013a, b; Tanner, 2014b; Searle, 2021). The Buchan Zone is highlighted by the red line, with the rest of the terrane being represented by Barrovian facies.

Following the Grampian Orogeny, the Dalradian Supergroup was deformed by the Scandian Orogeny (Dewey and Strachan, 2003; Tanner, 2014a). In Scotland, the main impacts of this event were transpressional strike-slip movements along transcurrent faults parallel to the orogenic belt and associated subsidiary fault networks as a result of a N-S oriented maximum principal stress (Baxter *et al.*, 2002; Dewey and Strachan, 2003; Tanner, 2014a). However, at approximately 425 Ma, there was a change from left-lateral transpression to orogen-parallel left lateral transtension (Fig. 3.3.; Dewey and Strachan, 2003; Tanner, 2014a); at this time, the Grampian Terrane in Scotland was partitioned into multiple compartments by NE-trending left-lateral transcurrent faults (Tanner, 2014a; Fig. 3.6.). The initiation of these faults was essential in facilitating the emplacement of voluminous magmatism (dated to 430-390 Ma) throughout the Grampian Terrane (Hutton, 1988; Jacques and Reavy, 1994; Neilson *et al.*, 2009; Tanner, 2014b). Examples of structures that were active during this time include the Garabal, Tyndrum, Ericht-Laidon and Etive-

Laggan faults (Neilson *et al.*, 2009; Tanner, 2014a; Fig. 3.6.). However, major terrane bounding faults (e.g. the Great Glen Fault) may have developed prior to 426 Ma (Treagus, 1991). Some fault movements along major NE trending faults in the Grampian Terrane have been dated to 416-395 Ma (Treagus *et al.*, 1999; Chew and Strachan, 2014), potentially indicating the occurrence of multiple movements throughout the Scandian Orogeny.

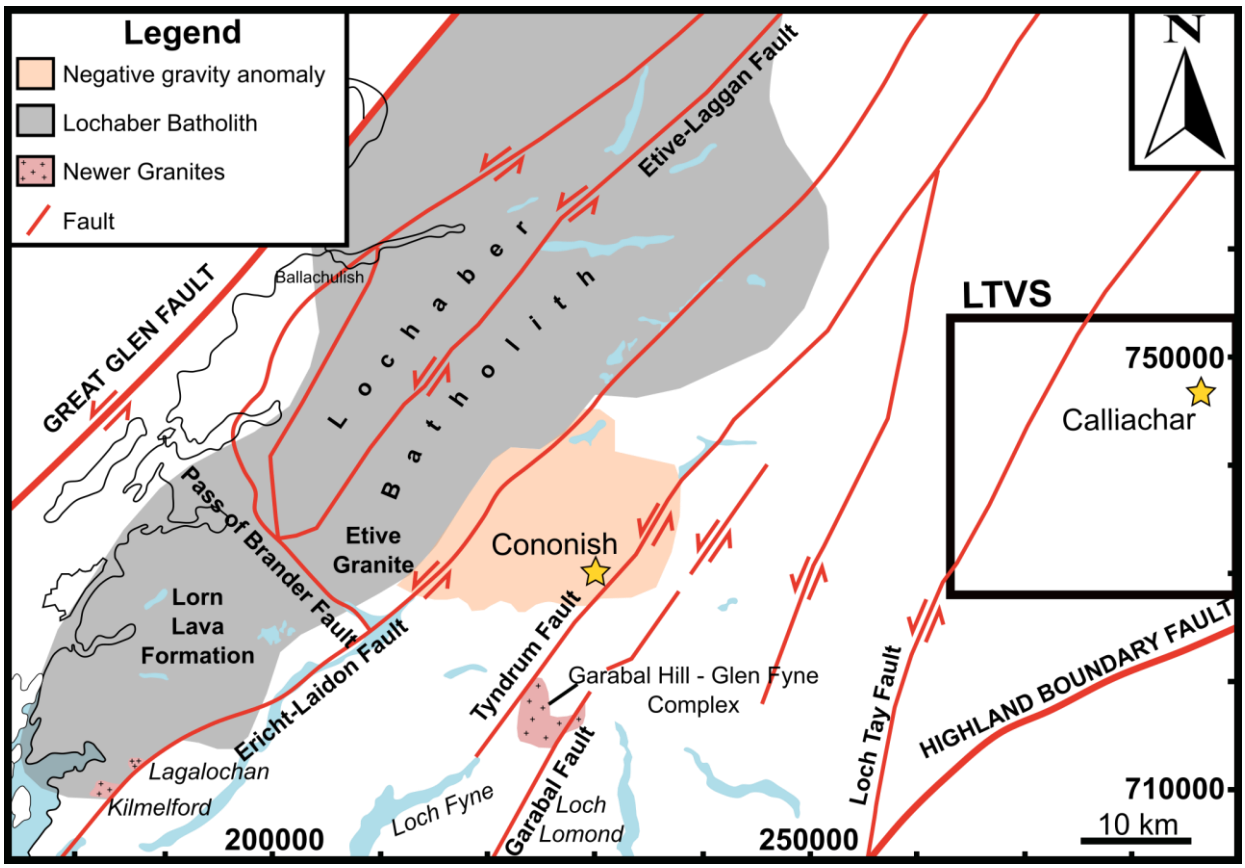

Figure 3.6. Map depicting the major orogen-parallel left-lateral faults of the Grampian Terrane that were associated with the Scandian Orogeny (adapted from Tanner, 2014a). The negative gravity anomaly was interpreted to represent the extension of the Etive Complex beneath Cononish (Tanner, 2014a).

Between the NE-trending major structures depicted in Fig. 3.6., there are many NW-SE trending fractures throughout the Grampian Terrane (Stephenson *et al.*, 2013a, b). Tanner (2014a) produced a model to explain the formation of subsidiary fractures associated with the NE major faults based on the concept of Riedel shears developing as a result of simple shearing directed along the larger structures (e.g. the Tyndrum or Garabal faults; Fig. 3.6.). In the Tanner (2014a) model (Fig. 3.7.), following the onset of shearing, a pair of Riedel shear fractures (R and R'; Fig. 3.7.) are interpreted to develop between two strike-slip faults in response to the second order maximum principal stress. In some cases, extensional fractures may have been initiated parallel to the second order maximum principal stress (Fig. 3.7.b.). Movements along the faults possibly led to the creation of some folds in the intervening rock bodies (e.g. the Orchy Dome; Tanner, 2012; 2014a).

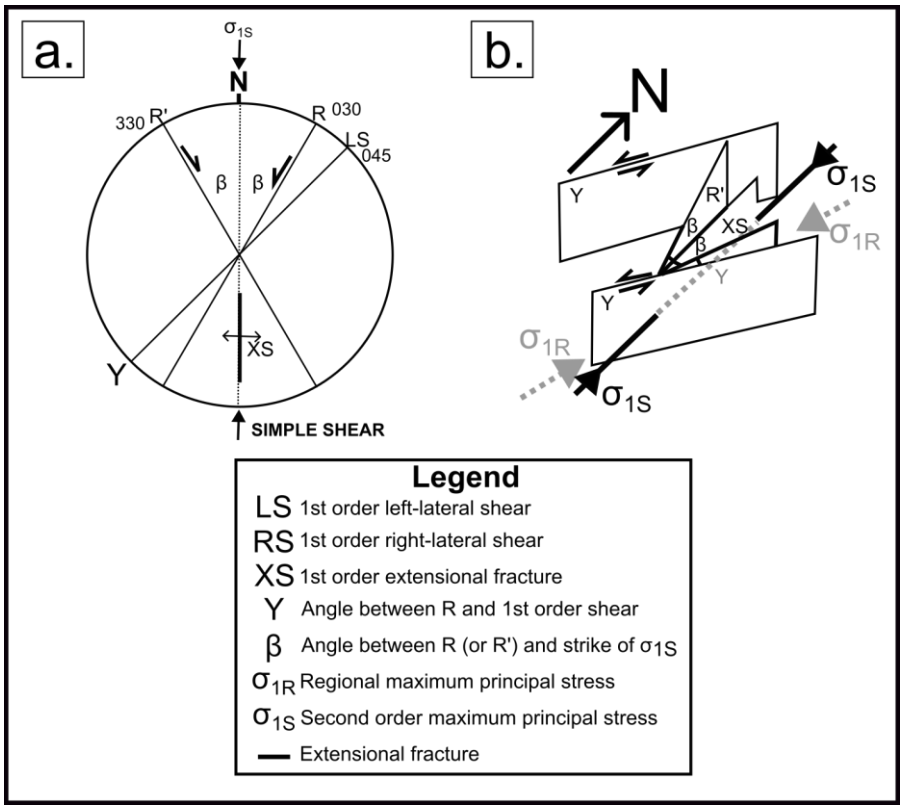

Figure 3.7. Diagrams (Tanner, 2014a) depicting the development of major fractures in rocks that are being deformed by simple shear. **a.** Strike-line diagram. **b.** 3-D representation of the simple shear when viewed from the SE.

Whilst Acadian deformation processes are not the focus of this section, they are briefly reviewed here in the context of the Highland Boundary Fault, which traverses the Study Area (Fig. 3.1.). The tectonic history of the Highland Boundary Fault has been disputed; previous researchers have suggested that the structure represents a normal fault at the edge of a graben (George, 1960), a sinistral strike-slip fault (Ryan *et al.*, 1995; Woodcock and Strachan, 2000), a reverse fault with a NW dip (Ramsay, 1964), or a boundary between different geological terranes (Bluck, 1984). Sinistral strike-slip displacement is thought to have occurred along the Highland Boundary Fault between 460 and 420 Ma (Ryan *et al.*, 1995; Dewey and Strachan, 2003; Soper and Woodcock, 2003; Cawood *et al.*, 2012), which helped to facilitate the docking of Avalonia along the Laurentian coast (Soper *et al.*, 1992b; Dewey and Strachan, 2003). The depositional gap of <40 Ma between the formation of the Highland Border Downbend during the Grampian deformation events (Table 3.1.) and the deposition of the Lower Old Red Sandstone towards the end of the Silurian may be evidence of this interpretation (Tanner, 2008). However, sinistral movements cannot explain certain features of the Highland Boundary Fault; for example, the Strathmore Syncline (which is adjacent to the Highland Boundary Fault in the Midland Valley Terrane; Mendum, 2012) has been shortened by ~20%. (Tanner, 2008). Some deformation associated with the Highland Boundary Fault is therefore likely to have occurred during the Acadian Orogeny; it has been suggested that the presently exposed Highland Boundary Fault obscures an older structure at depth (Tanner, 2008; 2014b), which potentially facilitated sinistral movements prior to being overprinted and reactivated during subsequent events (Tanner, 2008).

3.3.5. Caledonian magmatism in the Grampian Terrane

Throughout Scotland and Ireland, Caledonian magmatism occurred throughout the Grampian, Scandian, and Acadian orogenies. However, most of the intrusions were emplaced during syn- and post-Scandian times (the 'Newer Granites', which are defined as granitoids throughout the Grampian Terrane that have not been impacted by Grampian deformation events; Oliver, 2001). The focus of this summary is on occurrences of Siluro-Devonian magmatism in Scotland, as these are more likely to have been coeval with the development of the LTVS. However, references to comparable intrusions in Ireland are made where appropriate.

The first intrusions associated with the Caledonian Orogeny in the Grampian Terrane record ages ranging between 475 and 460 Ma (Fig. 3.8.) and are therefore syn-metamorphic. This interpretation is based on the U-Pb age of monazites from the Aberdeen granite, which has been dated to 470 Ma (Kneller and Aftalion, 1987), and the U-Pb ages of zircons derived from gabbros cross-cutting the Macduff Slates (468 Ma; Rogers *et al.*, 1994; Oliver, 2001). These syn-metamorphic intrusions have a relatively low $^{87}Sr/^{86}Sr$ ratio (~0.706; Pankhurst, 1970). It is possible to interpret strontium isotope data by considering the nature of the ^{87}Sr isotope, which results from the radioactive decay of ^{87}Rb via a half-life of 4.88×10^{10} years (Dickin, 2018). However, ^{87}Rb is strongly partitioned into the crust relative to the mantle, which in turn means that the crust develops higher concentrations of ^{87}Sr relative to the core during subsequent radioactive decay (Armstrong, 1968; DePaolo, 1979; Zartman and Haines, 1988); for this reason, granitoids that are associated with greater levels of crustal assimilation usually display higher $^{87}Sr/^{86}Sr$ ratios (Knesel and Davidson, 1999; Pankhurst, 1970). The low $^{87}Sr/^{86}Sr$ ratios that have been recorded from the synmetamorphic intrusions in the Grampian Terrane were interpreted by Pankhurst (1970) as being indicative of emplacement in a calc-alkaline arc. However, the Aberdeen granites, which are older, were found to have higher initial Sr and Nd values (0.7112 and -12.5, respectively; Haughton *et al.*, 1990); such trends are common outcomes of lower crustal syn-metamorphic melting (Richardson and Powell, 1976). The crustal thickening that characterised the Grampian Orogeny (Section 3.3.1.) was conducive to the generation of high temperatures that typically result in voluminous magmatic episodes (Oliver, 2001). For example, in Northern Ireland, the episode of magmatism associated with the Grampian Orogeny is represented by a series of calc-alkaline intrusions (including the Tyrone Igneous Complex) that formed between 480 Ma and 470 Ma in a volcanic island arc (Hutton *et al.*, 1985; Cooper *et al.*, 2011). Furthermore, the Tyrone Igneous Complex was crosscut by multiple continental arc intrusives that that range from 470 Ma to 464 Ma, such as the Lagt Hill tonalite and the Pomeroy granite (Cooper *et al.*, 2011). The geochemical characteristics of these units demonstrate an I-type affinity, although the assimilation of Dalradian metasediments also played a significant role in their petrogenesis (Draut *et al.*, 2009).

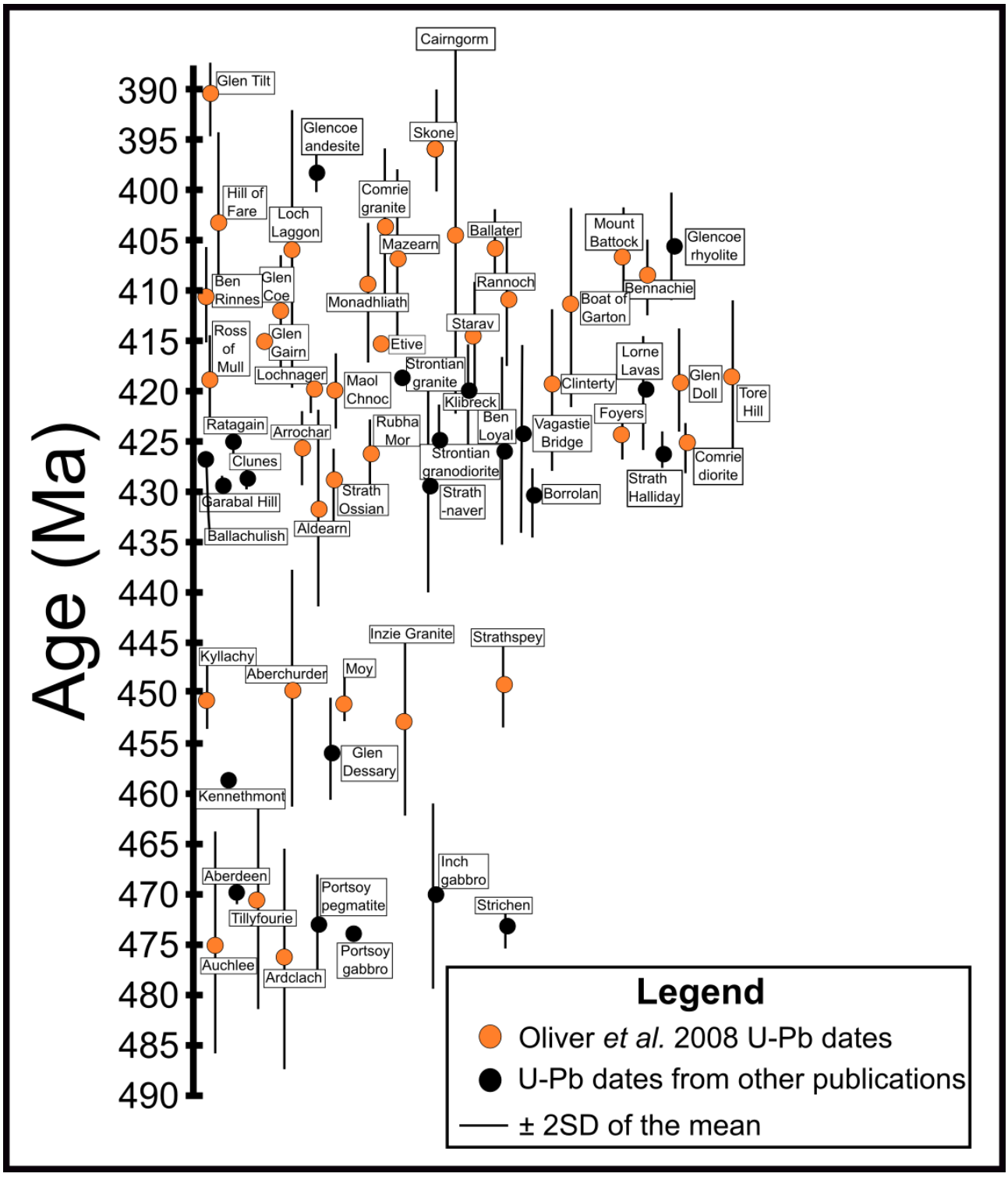

Figure 3.8. U-Pb dates from Ordovician-Devonian intrusions north of the Highland Boundary Fault (Oliver *et al.*, 2008). Dates from other publications are as follows: Borrolan (Van Breemen *et al.*, 1979), Ben Loyal (Halliday *et al.*, 1987), Aberdeen (Kneller and Aftalion, 1987), Lorne Lavas (Thirlwall, 1988), Garabal, Ratagain, Strontian granodiorite (Rogers and Dunning, 1991), Strontian (Paterson *et al.*, 1992), Kennethmont, Strichen (Oliver *et al.*, 2000), Portsoy pegmatite (Carty, 2001), Clunes (Stewart *et al.*, 2001), Inch gabbro (Dempster *et al.*, 2002), Etive (Morris and Page, 2005), Klibreck, Strathnaver, Vagastie Bridge (Kinny *et al.*, 2003a, b), Ballachulish, Glencoe rhyolite and andesite (Fraser *et al.*, 2004), Strath Halliday (Kocks and Strachan, 2006).

Oliver (2001) distinguished another group of intrusions in the Grampian Terrane that postdate the peak metamorphic event and are geochemically distinct from the 'Newer Granites.' These intrusions formed between 459 Ma and 430 Ma and are considered to pertain to decompression melting, which resulted from a long period of isostatic adjustment following the metamorphic peak (Oliver, 2001; Fig. 3.8.). Support for this hypothesis also comes from the high abundances of Barrovian metamorphic detritus within the Silurian sedimentary units of the SUDLT, implying significant uplift and erosion of the Grampian Terrane during this time (Oliver, 2001). The plutons that formed throughout this 459-430 Ma interval record high $^{87}Sr/^{86}Sr$ ratios (0.7146) and are therefore considered to have been emplaced as a result of melting of the continental crust (Oliver, 2001). As with the syn-metamorphic granites, the plutons dating to 459-430 Ma also record geochemical characteristics that are typical of S-type granitoids (Stephens, 1988).

The term 'Newer Granites' has historically been used to refer to granitoids in the Grampian Terrane that were not affected by the Grampian deformation phases (Table 3.1.) and were emplaced at the end of the Caledonian Orogeny (Atherton and Ghani, 2002; Chew and Stillman, 2009; Nielson *et al.*, 2009; Oliver *et al.*, 2008). Based on isotope studies, there is widespread consensus that the 'Newer Granites' were derived from the partial melting of material in the mantle that was enriched in Ba and Sr (Thirlwall, 1982; Halliday and Stephens, 1984; Harmon *et al.*, 1984; Halliday *et al.*, 1985; Tarney and Jones, 1994; Fowler *et al.*, 2001). Three suites ('Argyll', 'Cairngorm', and 'South of Scotland') have been recognised (Fig. 3.9.; Stephens and Halliday, 1984; Halliday *et al.*, 1985; Fowler *et al.*, 2001). The distinction between the suites is based on geochemical differences; for example, the South of Scotland Suite contains anhydrous pyroxene-mica diorites that have higher concentrations of Ni and Cr and may therefore represent derivation from a primitive melt (Stephens and Halliday, 1984). On the other hand, the Argyll Suite can be distinguished by elevated concentrations in Ba and Sr (Stephens and Halliday, 1984). The Cairngorm Suite, which occurs in the NE portion of the Grampian Terrane (Fig. 3.9.), has the most felsic composition out of the three suites (i.e. a greater proportion of silica; Stephens and Halliday, 1984). Collectively, the three suites of granitoids in the Grampian Terrane typically range from 430-405 Ma (Oliver *et al.*, 2008). Since the original publication of Fig. 3.8., the Ballachulish and Kilmelford Igneous Complexes have been dated to 433.5 ± 1.8 Ma and 425.8 ± 1.7 Ma; these are also considered to be 'Newer Granites' (Conliffe *et al.* 2010).

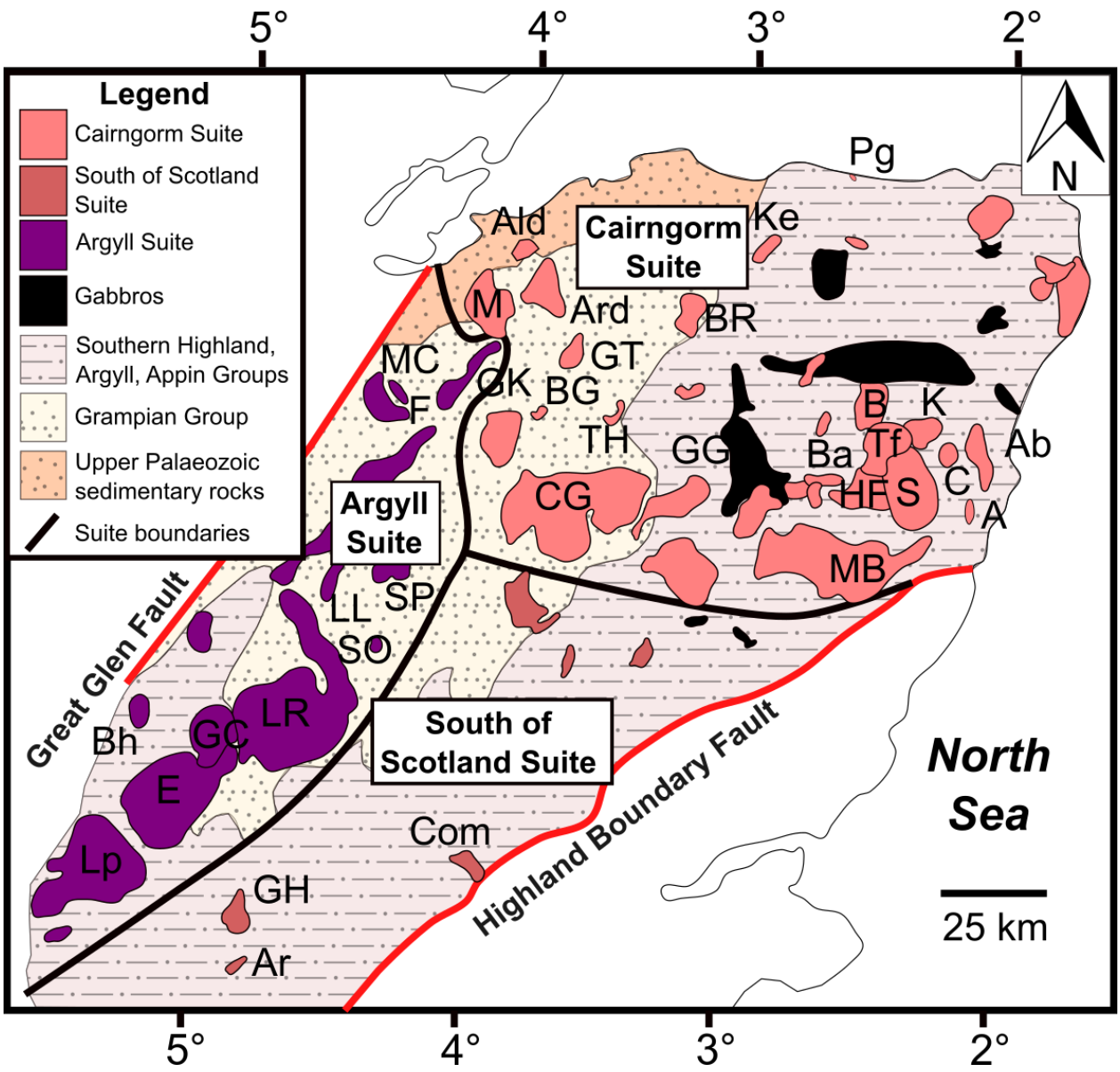

Figure 3.9. The distribution of the Cairngorm, Argyll, and South of Scotland granite suites in the Grampian Terrane (Stephenson and Gould, 1995; Trewin and Rollin, 2002; Oliver *et al.*, 2008). Abbreviations are as follows: GH (Garabal Hill appinite), Ar (Arrocher appinite), Com (Comrie Pluton), MB (Mount Battock Granite), A (Auchlee granite), S (Strichen Granite), HF (Hill of Fare granite), Ba (Ballater granite), Tf (Tillyfourie granite), C (Clinterty granite), Ab (Aberdeen Granite), Pg (Portsoy granite), Ke (Keith granite), BR (Ben Rinnes granite), TH (Tore Hill granite), CG (Cairngorm granite), BG (Boat of Garton granite), GT (Glen Tilt granite), Ard (Ardclach granite), Ald (Aldearn granite), M (Moy granite), GK (Glen Kyllachy granite), MC (Maol Chnoc granite), F (Foyers granite), SP (Strath Spey granite), LL (Loch Laggon felsite), SO (Strath Ossian granite), LR (Loch Rannoch granite), GC (Glen Coe rhyolite), Bh (Ballachulish granite), E (Etive dyke swarm), and Lp (Lorne plateau lavas).

3.3.5.a. Geodynamic setting of the 'Newer Granites'

Whilst the widespread occurrence of granitoids with an age of 430 to 390 Ma throughout Scotland and Northern England is evidence for a voluminous episode of magmatism throughout this interval of geological time (Jacques and Reavy, 1994; Oliver *et al.*, 2008; Neilson *et al.*, 2009; Cooper *et al.*, 2013), the specific geodynamic cause of the magmatism has been disputed; suggested triggers for the magmatism include volatile fluxing from a subducting slab (Thirlwall, 1981), slab breakoff, (Atherton and Ghani, 2002; Oliver *et al.*, 2008; Miles *et al.*, 2016), 'incipient delamination' (O'Reilly *et al.*, 2012), underthrusting of Avalonian crust (Miles *et al.*, 2014), and rollback of the subducted Avalonian slab (Rice *et al.*, 2018). However, it should be noted that several of these interpretations (specifically, incipient delamination and underthrusting of Avalonian crust) largely focus on explaining the geological and geochemical characteristics of the 'Trans Suture Suite', i.e. a subdivision of the Newer Granites encompassing Late Caledonian granitoids south of the Highland Boundary Fault (Brown *et al.*, 2008). The Trans Suture Suite is therefore located outside of the Grampian Terrane and furthermore, these granitoids often differ compositionally from the Newer Granites (e.g. they have an S-type signature instead of an I-type signature; Brown *et al.*, 2008). For this reason, petrogenetic models that are exclusively relevant to the Trans Suture Suite are not summarised here.

A genetic link between subduction and Late Caledonian magmatism throughout the Northern British Isles was first made by Thirlwall (1981); the high SiO_2, K_2O, Ni, V, Cr, and Mg contents of the Newer Granites were considered to be indicative of mixing between a primitive mantle source and sediments within the continental crust (Thirlwall, 1982; 1983; 1986). As such, original descriptions of the geodynamic setting of the Newer Granites invoked volatile loss from a slab that had undergone subduction, with comparisons being made to regions characterised by active volcanism, e.g. the Cascades, USA (Thirlwall, 1981). Shearing and extensional processes caused by regional transtension in the Grampian Terrane may have been conducive to magmatism during subduction (Hutton and Reavy, 1992). However, models exclusively focusing on subduction have been abandoned in light of evidence (i.e. no further sedimentation beyond 420 Ma in the accretionary prism of the SUDLT) demonstrating that the subduction of the Iapetus Ocean had ceased by c. 420 Ma (Soper *et al.*, 1992, a, b; Oliver *et al.*, 2008); subduction-driven magmatism is therefore an insufficient explanation for the continuation of the emplacement of the Newer Granites until 390 Ma (Miles *et al.*, 2016).

Regarding geodynamic models that invoke slab breakoff (Fig. 3.10.), there are several interpretations of the exact processes that may have been involved; some researchers have depicted the upwelling of the asthenosphere through a sinking slab of Avalonian crust as a unidirectional process (Fig. 3.10.a.; Atherton and Ghani, 2002; Neilson *et al.*, 2009; Graham *et al.*, 2017). Partial melting of a region in the mantle with high concentrations of Ba and Sr may have resulted in the development of appinite and lamprophyre

magmas, which ascended and melted the continental crust to generate more silicic magmas (Atherton and Ghani, 2002; Neilson *et al.*, 2009; Graham *et al.*, 2017). However, Oliver *et al.* 2008 suggested that the slab upwelling was a bidirectional process (Fig. 3.10.b.) because the granitoids in the SUDLT were, broadly speaking, emplaced contemporaneously along with those in the Grampian Terrane. The observation of coeval magmatism across both terranes was also reported by Miles *et al.* 2016, who invoked a version of bidirectional upwelling; however, this model also involves a component of lithospheric delamination (i.e. the dense lower portion of the lithosphere detaches and sinks into the underlying hotter and less dense mantle layer; Morency and Doin, 2004; Ueda *et al.*, 2012) to account for the emplacement of granitoids on the other side of the Iapetus Suture (i.e. in the Leinster-Lakeman Terrane; Freeman *et al.*, 1988; O'Reilly *et al.*, 2012) during the late stages of the Caledonian Orogeny (Fig. 3.10.c.). Approximate timings for the processes involved in slab breakoff (Fig. 3.10.) have been provided by Oliver *et al.* 2008, who suggested that the cessation of sedimentation in the SUDLT accretionary prism at c. 420 Ma and the onset of extensional volcanism at this time (Marshall *et al.*, 1994) represent the initiation of subduction and I-type magmatism. Furthermore, the preponderance of granitoids aged between 410 and 400 Ma throughout the Grampian Terrane and SUDLT (also noted by Miles *et al.* 2016) was interpreted as being indicative of the detachment of the slab during this interval (Oliver *et al.*, 2008).

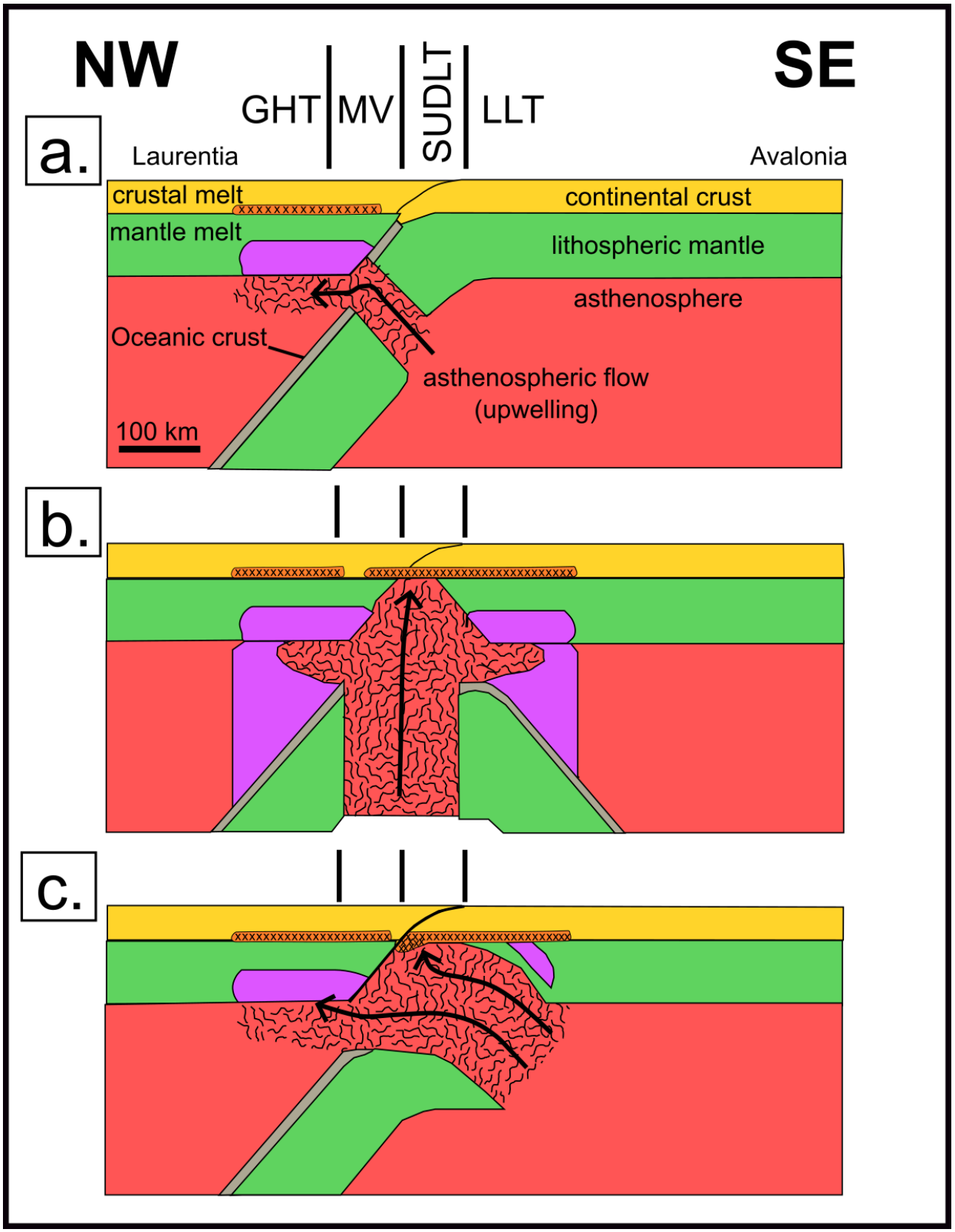

Figure 3.10. Depiction of the different interpretations regarding the processes of Avalonian slab breakoff at the end of the Caledonian Orogeny (adapted from Rice *et al.*, 2018). **a.** Unidirectional asthenospheric upwelling (Atherton and Ghani, 2002; Neilson *et al.*, 2009; Graham *et al.*, 2017). **b.** Bidirectional slab breakoff (Oliver *et al.*, 2008). **c.** Bidirectional asthenospheric upwelling (Miles *et al.*, 2016). Abbreviations are as follows: GHT = Grampian Terrane, MV = Midland Valley Terrane, SUDLT = Southern Uplands Down-Longford Terrane, LLT = Leinster-Lakeman Terrane.

In the Rice *et al.* 2018 geodynamic model for the emplacement of the Newer Granites, slab rollback is invoked (Fig. 3.11.); this process involves the subducted Avalonian slab rolling back to create space into which the asthenosphere can ascend (Fig. 3.11.). In this model, the thrusting of Avalonia under Laurentia (Fig. 3.11.a.) stimulated mantle delamination (Rice *et al.*, 2018). Given that Avalonian subduction is confirmed to have occurred towards the north (Fig. 3.2.b.), metasomatism of the lithosphere is therefore likely to have occurred in this direction as well (i.e. beneath Laurentia; Fig. 3.11.). Delamination is interpreted by Rice *et al.* 2018 to be a progressive process, eventually resulting in an influx of the asthenosphere from the northwest (Fig. 3.11.b.). The Rice *et al.* 2018 model is similar to the previously outlined slab breakoff interpretations in the sense that the upwelling of the asthenosphere is thought to have stimulated partial melting of the asthenospheric mantle and the generation of lamprophyres (Fig. 3.11.), which ascended and melted the overlying continental crust to generate more silicic intrusions and the Trans Suture Suite (a group of Devonian intrusions in the SUDLT and Lakesman-Leinster terrane; Brown *et al.*, 2008; Miles *et al.*, 2013; 2014; Barros and Menuge, 2016). Rice *et al.* 2018 suggested that the termination of subduction and the onset of transcurrent movements along the plate margin created steeply dipping faults, which acted as conduits for the ascending lamprophyres.

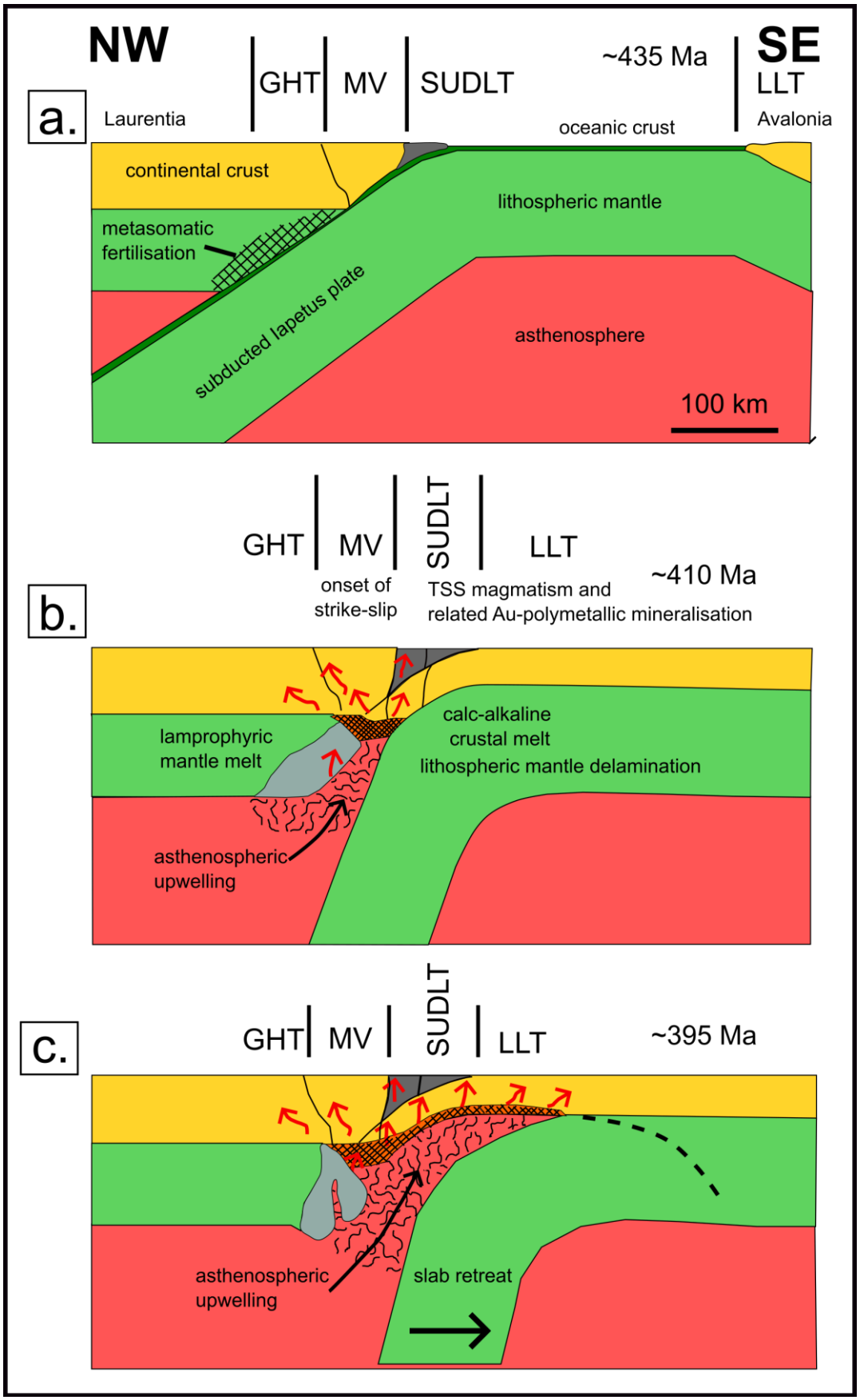

Figure 3.11. The slab rollback model (Rice *et al.* 2018). **a.** Avalonian subduction at 435 Ma. **b.** Onset of slab rollback and strike-slip faulting at 410 Ma. TSS = Trans Suture Suite. **c.** Asthenospheric upwelling begins to impact the SUDLT at 395 Ma. Abbreviations are consistent with Fig. 3.10.

The slab rollback model (Fig. 3.11.) was invoked by Rice *et al.* 2018 on the basis that elsewhere on Earth, there is geophysical evidence for post-subduction mantle delamination (van Hinsbergen *et al.*, 2010), meaning similar processes may have occurred at the end of the Caledonian Orogeny. Furthermore, Rice *et al.* 2018 suggested that granitoids in the SUDLT are slightly younger than those in the Grampian Terrane (Rice *et al.*, 2018), with granitoids in the SUDLT becoming increasingly younger with distance from the Southern Uplands Fault (Fig. 3.12.). Rice *et al.* 2018 favour slab rollback because a scenario involving the gradual upwelling of the asthenosphere can explain the difference in the relative timing between the emplacement of granitic plutons in the Grampian Terrane and SUDLT; as the Avalonian slab peeled back towards the southeast, it created space for the asthenosphere to upwell beneath the Grampian Terrane initially. Further rollback eventually created space beneath the SUDLT thereafter (Fig. 3.11.; Rice *et al.*, 2018).

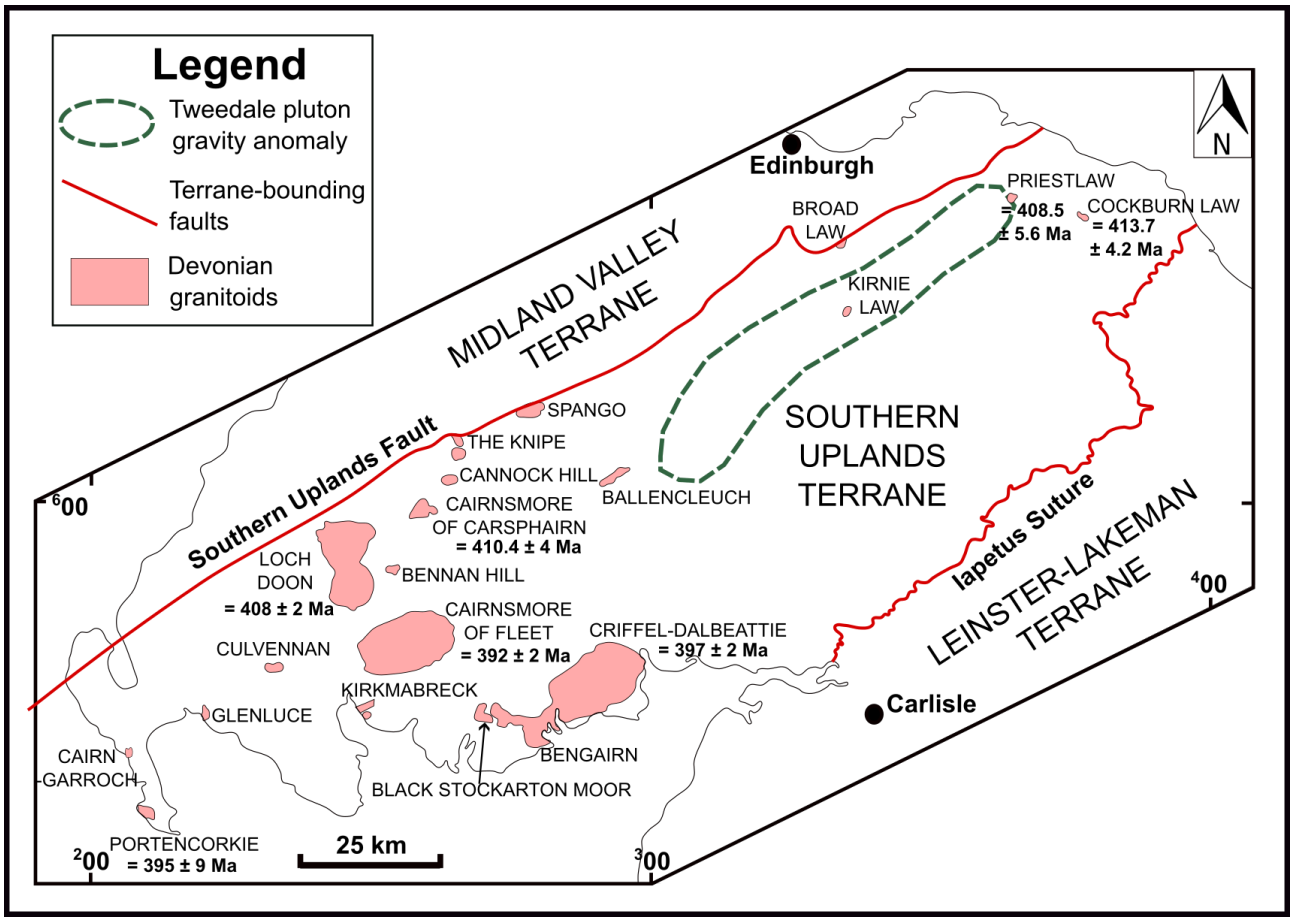

Figure 3.12. Map depicting the distribution of the granitoids in the SUDLT (adapted from Stone *et al.*, 2012). References for the radiometric dates are as follows: Cockburn Law, Priestlaw, Cairnsmore of Carsphairn (Rb-Sr; Thirlwall, 1988), Loch Doon (K-Ar), Criffel, Cairnsmore of Fleet (Rb-Sr; Stephens and Halliday, 1979), Portencorkie (U-Pb; Oliver *et al.*, 2008).

However, it should be emphasised that there is considerable uncertainty as to whether there is a gradual decrease in the ages of the granitoids from the Grampian Terrane to the SUDLT; Oliver *et al.* 2008 and Miles *et al.* 2016 considered magmatism in both terranes to be broadly coeval. For example, some granitoids in the Grampian Terrane record ages that are similar to ages reported for granitoids in the SUDLT; examples include the granite in the Comrie Pluton (404 ± 6 Ma; Oliver *et al.*, 2008) and Criffel (Fig. 3.12.; 397 ± 2 Ma). Furthermore, some of the most northerly granitoids in the Grampian Terrane, including Glen Tilt and Glen Coe (Fig. 3.9.), record ages of between 400 and 390 Ma (Oliver *et al.*, 2008). Collectively, the lack of clear evidence for a decrease in granitoid age towards the southern regions of Scotland underscores the point that previous interpretations regarding the geodynamic setting of the Newer Granites are relatively speculative, as acknowledged in Webb *et al.* 2024b.

3.4. Geological Background of the southern margin of Loch Tay

The geological history of the Study Area has been affected by the Caledonian Orogeny (Table 3.1.), which resulted in a series of Neoproterozoic metasediments (the Dalradian Supergroup) being intruded by Siluro-Devonian granitoids and crosscut by transcurrent structures that developed during the closure of the Iapetus Ocean (Section 3.3.). Around Loch Tay, the bedrock geology is diverse, with rock units ranging from the Neoproterozoic to the Devonian (Fig. 3.13.).

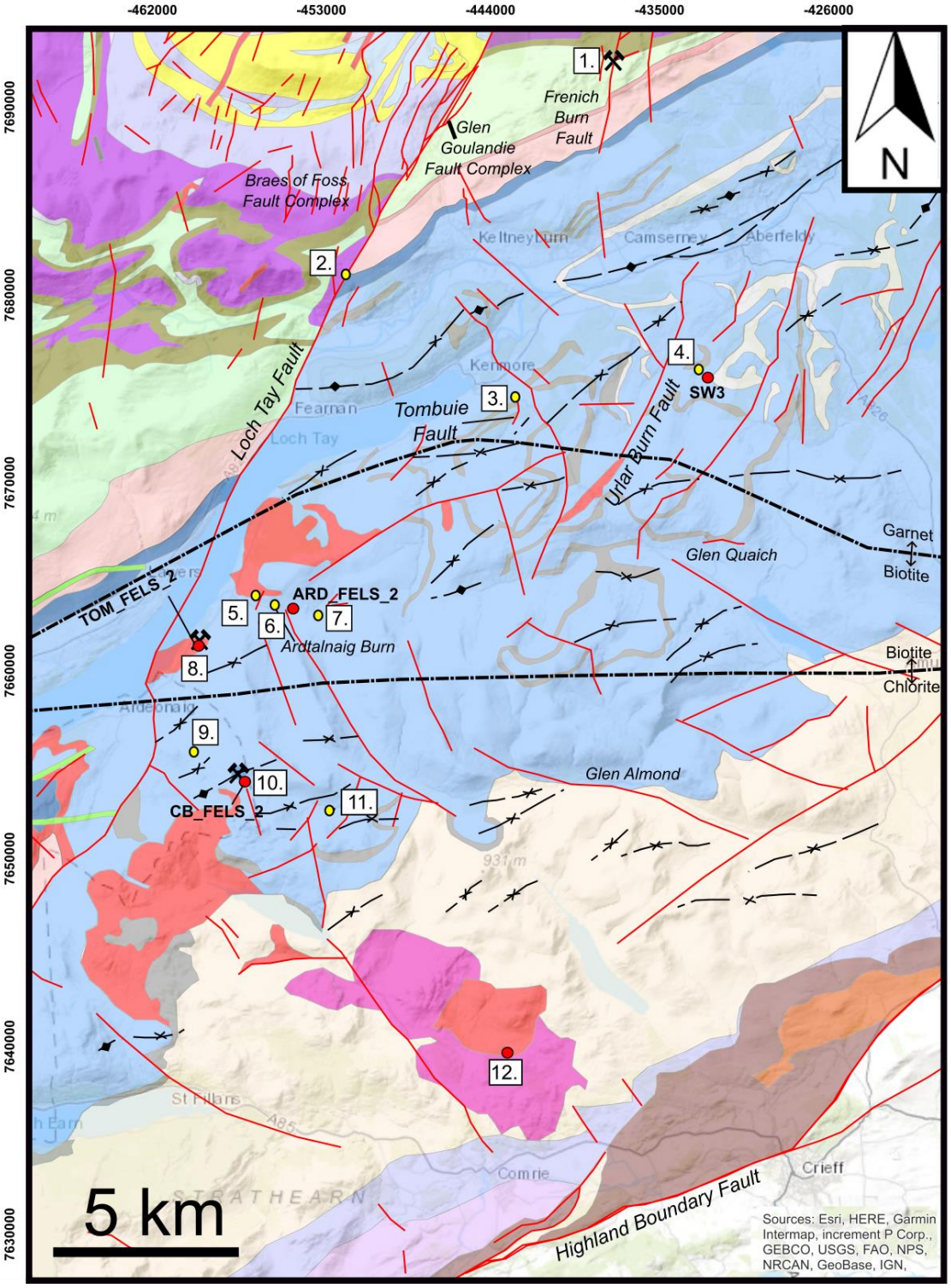

Figure 3.13. Geology of the Study Area superimposed onto a topographic basemap (Esri, 2022). The bedrock geology to the west of the LTF is from Digimap (2023) whilst to the east of this structure, the geological information was sourced from other maps (Bradbury and Smith, 1981; Torvela, 2020). Structural information represents an interpretation by Torvela (2020). Granitoids sampled for geochronology have also been labelled (at the Comrie Pluton, the mineralisation was sampled for $\delta^{34}S$ studies, not geochronology). Localities are as follows: 1 = Foss, 2 = Fortingall, 3 = Tombuie, 4 = CUB veins, 5 = Lead Trial, 6 = RX2959KA, 7 = ARD_1, 8 = Tomnadashan, 9 = Spoil Heap, 10 = Coire Buidhe, 11 = Glen Almond Vein, 12 = Comrie Pluton. The legend for the figure is shown overleaf. Stratigraphic relationships were adapted from Stephenson *et al.* 2013a.

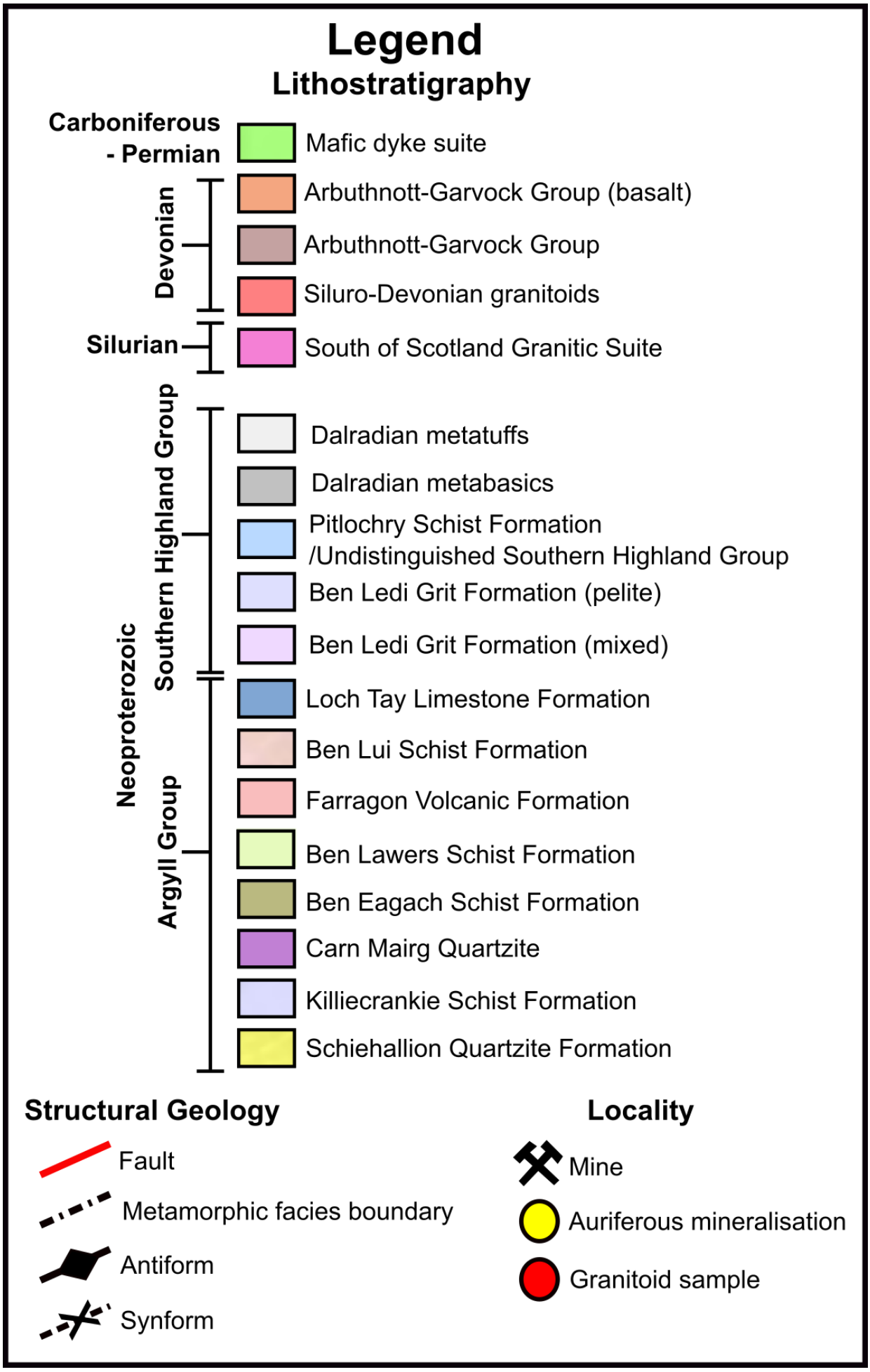
Legend
Lithostratigraphy
Carboniferous - Permian
Mafic dyke suite
Devonian
Arbuthnott-Garvock Group (basalt)
Arbuthnott-Garvock Group
Siluro-Devonian granitoids
Silurian
South of Scotland Granitic Suite
Neoproterozoic
Southern Highland Group
Dalradian metatuffs
Dalradian metabasics
Pitlochry Schist Formation /Undistinguished Southern Highland Group
Ben Ledi Grit Formation (pelite)
Ben Ledi Grit Formation (mixed)
Argyll Group
Loch Tay Limestone Formation
Ben Lui Schist Formation
Farragon Volcanic Formation
Ben Lawers Schist Formation
Ben Eagach Schist Formation
Carn Mairg Quartzite
Killiecrankie Schist Formation
Schiehallion Quartzite Formation
Structural Geology
Fault
Metamorphic facies boundary
Antiform
Synform
Locality
Mine
Auriferous mineralisation
Granitoid sample

3.4.1. Lithostratigraphy

As explained in Section 3.2., only metasediments from the Argyll and Southern Highland groups are present locally around Loch Tay. In this section, the lithological characteristics of the major geological units known to occur in the Study Area (Fig. 3.13.) are summarised.

The oldest unit around Loch Tay in the Argyll Group is the Schiehallion Quartzite Formation. This unit is described by Stephenson *et al.* 2013a as massively bedded, with crossbedding rarely being observed. Towards the base, there are beds of conglomerate, which also contain boulders of granite and metadiamictite (Treagus and King, 1978; Stephenson *et al.*, 2013a). Minor layers of limestone occur within the quartzite (Anderson, 1923; Bailey and McCallien, 1937; Stephenson *et al.*, 2013a). Around the Loch Tay Fault, the Schiehallion Quartzite has a dip value of 60 ° (Treagus, 2003) and is overlain by the Killiecrankie Schist Formation, which is described as being comprised of pelites and psammites with intercalations of coarser psammites and metamorphosed basalts (Goodman *et al.*, 1996; Stephenson *et al.*, 2013a). The Killiecrankie Schist Formation is representative of deep-water facies (Stephenson *et al.*, 2013a). Further up in the stratigraphic sequence around the LTVS, the Killiecrankie Schist Formation transitions into the Carn Mairg Quartzite Formation, a coarse-grained lithology comprised of feldspathic, pebbly quartzite and greywackes (Sturt, 1961; Roberts and Treagus, 1977; 1979; Coats *et al.*, 1984; Smith and Krabbendam, 2003); this unit also displays graded bedding (Stephenson *et al.*, 2013a).

The Carn Mairg Quartzite Formation is overlain by the Ben Eagach Schist Formation, which is comprised of graphitic pelites interbedded with metalimestones and amphibolites (Rast, 1958; Stephenson *et al.*, 2013a). This unit hosts the Foss and Duntanlich SEDEX deposits (Coats *et al.*, 1984; Hall *et al.*, 1988; Fortey *et al.*, 1993; Moles *et al.*, 2014; see Section 3.6.2.a.). The Ben Lawers Schist Formation overlies the Ben Eagach Schist Formation and is mostly comprised of calcareous pelites and semipelites interspersed with thin metalimestone and quartzite layers (Elles, 1926; Stephenson *et al.*, 2013a). Volcaniclastic green beds and metamorphosed basics are intercalated with the Ben Lawers Schist Formation; there is also another layer of stratabound sulphide mineralisation towards the top of this unit (Stephenson *et al.*, 2013a).

The next youngest unit in the Argyll Group is the Farragon Volcanic Formation, which occurs to the East of the LTF (Fig. 3.13.); despite being relatively thin (Fig. 3.13.), the Farragon Volcanic Formation is comprised of a variety of lithologies, including quartzite, psammite, metabasalts, and volcaniclastic green beds (Goodman and Winchester, 1993; Macdonald *et al.*, 2005; Fettes *et al.*, 2011; Stephenson *et al.*, 2013a). The Farragon Volcanic Formation may represent the first major episode of volcanism within the entire Dalradian Supergroup (Fettes *et al.*, 2011; Stephenson *et al.*, 2013a).

In terms of the next youngest unit, the Farragon Volcanic Formation is overlain by the Ben Lui Schist Formation (Fig. 3.13.), a fine-grained and thinly bedded semipelite (Barrow *et al.*, 1905; Bailey and

McCallien, 1937; Sturt, 1961; Crane *et al.*, 1996; Stephenson *et al.*, 2013a). The Ben Lui Schist Formation also contains both garnet and hornblende-bearing schists and thin limestone beds (Sturt, 1961; Johnstone and Smith, 1965). It should also be noted that around Tyndrum, chromium, copper and nickel-bearing minerals have been documented at the base of the Ben Lui Schist Formation (Stephenson *et al.*, 2013a); this may reflect an ophiolitic provenance for the sediments (Fortey and Smith, 1986; Power and Pirrie, 2000) and derivation of material from exposed lithospheric mantle during periods of regional extension (Chew, 2001).

Locally, the youngest unit within the Argyll Group is the Loch Tay Limestone Formation, which occurs on both sides of the Loch Tay Fault (Fig. 3.13.) and throughout the Grampian Terrane (although there are also units that are laterally equivalent, such as the Tayvallich Limestone Formation; Stephenson *et al.*, 2013a). The Loch Tay Limestone Formation is approximately 100 m thick and is comprised of crystalline metalimestone that is interspersed with graphitic mudstones and greywackes (Stephenson *et al.*, 2013a). Within the Study Area, the Loch Tay Limestone Formation hosts mineralisation; for example, at Fortingall (Fig. 3.13.), pyrite mineralisation has developed in the joints of this unit (Treagus, 2003), whereas at Coire Buidhe, an isolated outcrop of the Loch Tay Limestone Formation hosts the veins (Pattrick, 1984; see Section 3.6.1.e.).

Around Loch Tay, the Southern Highland Group is represented by the Pitlochry Schist and Ben Ledi Grit formations (Fig. 3.1.). East of the Loch Tay Fault (Fig. 3.13.), the Southern Highland Group is comprised of pelitic-metagreywacke sequences, such as the Pitlochry Schist Formation (Treagus, 2000; Stephenson *et al.*, 2013a). This unit is mostly comprised of semipelites interbedded with pelites, micaceous psammites, and pebbly psammites (Barrow, 1905; Harris *et al.*, 1994; Stephenson and Gould, 1995). Within the Pitlochry Schist Formation, there are also several fine-grained volcaniclastic layers that are green or brown (depending on their relative amount of detrital chlorite or iron oxides); these beds were derived from rhyolitic or trachytic tuff associated with a distant volcanic source (Batchelor, 2004a, b). Ixer *et al.* 1997 noted that around the CUB veins (Fig. 3.13.), the Pitlochry Schist Formation is represented by quartzites, quartz-mica schists, and metabasics (specifically, green beds and amphibolites) that dip at values <20 °. A similar description was also provided for the Pitlochry Schist Formation around Tombuie (Corkhill *et al.*, 2010; Fig. 3.13.). Whole rock element ratios (particularly regarding the aluminium contents) from both the Pitlochry Schist and Ben Lui Schist formations are very similar (Watkins, 1987).

The Pitlochry Schist Formation is overlain by the Ben Ledi Grit Formation, which occurs throughout large swathes of the Study Area and is comprised of pelites and psammites (Fig. 3.13.). Stephenson *et al.* 2013a summarised the Ben Ledi Grit Formation as being predominantly composed of turbiditic greywacke facies interspersed with several green beds and basic intrusions; a similar description was also provided by Mendum and Fettes (1985). Psammitic layers of the Ben Ledi Grit Formation are comprised of pale to dark

grey metasandstones (arenite to greywacke) with calcareous nodules (Mendum and Fettes, 1985). The pelitic portions of the Ben Ledi Grit Formation contain large quantities of detrital albite (Bowes and Convery, 1966), which may represent a redistribution of sodium during metamorphism of the Dalradian metasediment package (Bowes and Convery, 1966; Watkins, 1983; Stephenson *et al.*, 2013a).

Aside from the Dalradian metasediments, there is also Devonian cover in the Study Area, i.e. the Arbuthnott-Garvock Group (Fig. 3.13). This group comprises the previously recognised units known as the Garvock Group and the underlying Arbuthnott Group (Morton, 1979; Browne *et al.*, 2001). The Arbuthnott-Garvock Group is comprised of fluvial conglomerates, sandstones, and andesitic lavas (Phillips and Aitken, 1998; Bluck, 2000; McKellar *et al.*, 2020).

3.4.2. Igneous intrusions

The oldest igneous rocks in the Study Area are the metabasics and metatuffs (Fig. 3.13.); whilst most of the amphibolites hosted within the Argyll and Southern Highland groups (Fig. 3.13.) have an igneous origin, some of the metabasics had a sedimentary protolith (Treagus, 2000). Nonetheless, the original igneous protoliths were emplaced into the Dalradian Supergroup during the Neoproterozoic and later metamorphosed as a result of the Caledonian Orogeny (Graham, 1974; 1976). Many of these intrusions within the Dalradian Supergroup originally had tholeiitic compositions (Graham and Bradbury, 1981; Graham and Borradaile, 1984; Treagus, 2000) and were emplaced as basaltic sills during the opening of the Iapetus Ocean at approximately 600 Ma (Anderton, 1985). The igneous amphibolites are typically metres to tens of metres thick, lithologically uniform, and have sharp contact margins with their host rocks (Treagus, 2000). Locally, Treagus (2000) recognised two categories of amphibolites with an igneous protolith; schistose sills impacted by the D2 fabric (Table 3.1.) and a later, less deformed group of amphibolites with minor schistosity and randomly oriented amphibole and feldspar phenocrysts. Regarding the earlier amphibolites, these are coarse-grained (the phenocrysts are 3 cm in size); garnet and biotite are common components of their mineralogy (Treagus, 2000). The later amphibolites have a similar mineralogy, with the only difference being the presence of randomly oriented phenocrysts (Treagus, 2000). The amphibolites are most common in the Southern Highland Group (as depicted on Fig. 3.13.). However, thin amphibolite bands are also abundant in the Loch Tay Limestone Formation (Treagus, 2000). Around Tombuie (Fig. 3.13.; Locality 3), the amphibolite intrusions have fine-grained and foliated margins that are comprised of tremolite, chlorite, talc, and magnetite; however, the cores of the intrusions are unfoliated (Treagus, 2000).

The only igneous intrusions within the Study Area that have been named in the published literature are Tomnadashan (Pattrick, 1984; Smith *et al.*, 2022) and the Comrie Pluton (Stephens and Halliday, 1984; Macdonald and Fettes, 2006; Oliver *et al.*, 2008); the latter is mostly comprised of a dioritic body that has been pierced by a circular granitic plug (Fig. 3.13.; Locality 12). Different compositional subdivisions of the diorite have been recognised; hypersthene biotite diorite, two-pyroxene diorite, and a coarse-grained

amphibole diorite (Fig. 3.14.). The diorites are medium to coarse-grained and contain white plagioclase feldspars (comprised of 30-48 % anorthite), hypersthene, augite, hornblende, and biotite; the different subdivisions of the granitoid are based on the relative proportions of these phases (e.g. the hypersthene biotite diorite lacks the same quantity of augite as the 'two pyroxene' diorite; Majid, 1974). Throughout large portions of the dioritic zones of the pluton (Fig. 3.14.), the pyroxenes have been altered to chlorite, a process that may indicate the mobilisation of large quantities of aluminium. Regarding the granodiorites, Majid (1974) described these parts of the Comrie Pluton as being medium-grained (2-4 mm) and comprised of plagioclase (~75 % of the granodiorite), alkali feldspar, biotite, and hornblende. On the other hand, the granite, which comprises the core of the Comrie Pluton (Fig. 3.14.), is mostly composed of K-feldspar, quartz and oligoclase (Majid, 1974). The granite in the Comrie Pluton was described as a 'leucogranite' by Majid (1974), a type of igneous rock that typically forms as a result of the melting and assimilation of pelitic sediments (Cox *et al.*, 1979; Scaillet *et al.*, 1995; Weinberg, 2016).

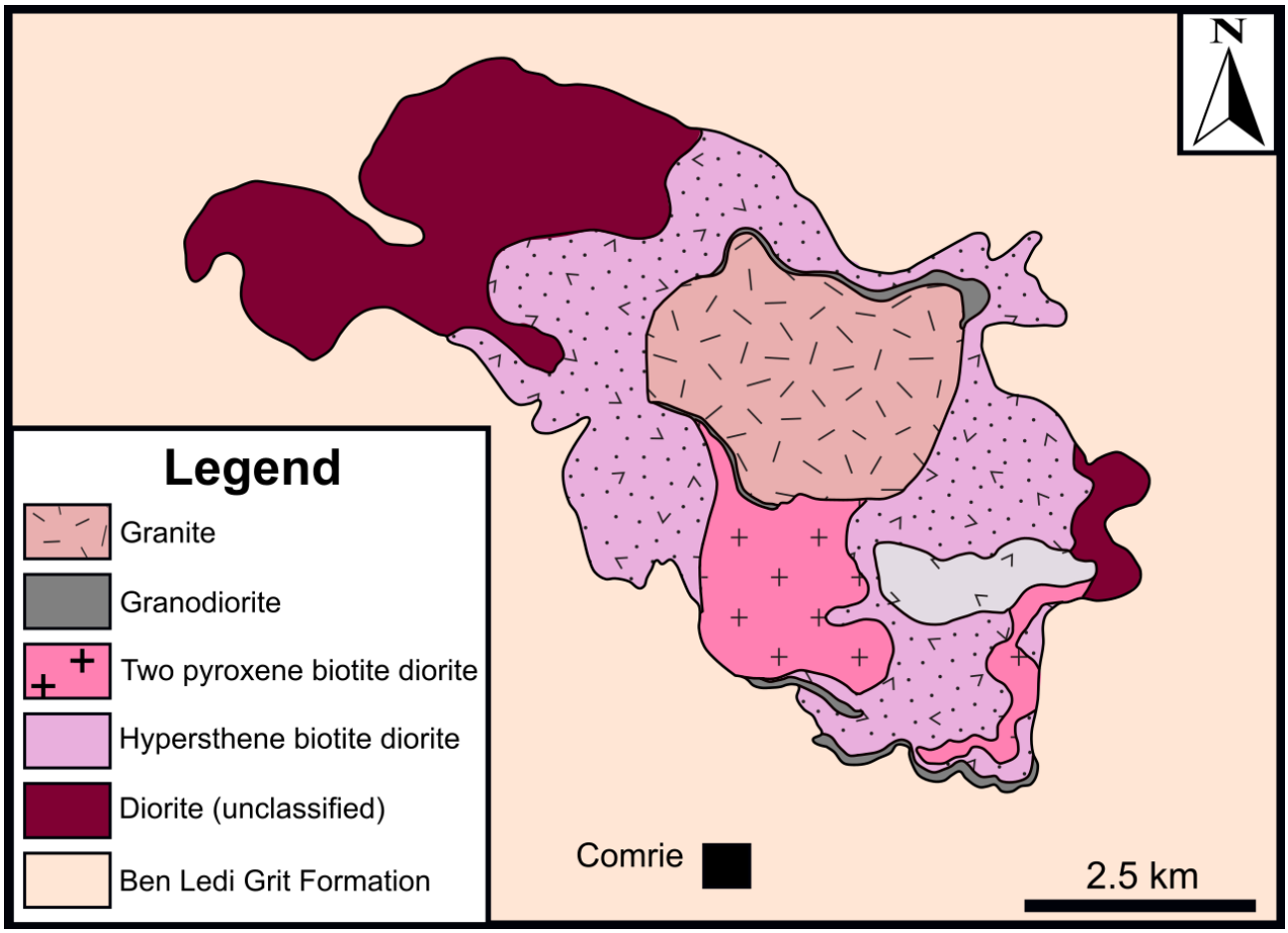

Figure 3.14. Geological map of the subdivisions of the Comrie Pluton (adapted from Majid, 1974). The location of the town of Comrie is shown by the black square.

The Comrie Pluton is the only intrusion throughout the Study Area that has been dated via radiometric methods; Turnell (1985) reported Rb-Sr results of 408 ± 5 Ma but it is not clear which portion of the intrusion (i.e. the diorite or granite) that this date pertains to. However, Oliver *et al.* 2008 dated zircons from the diorite and granite to 425 ± 3 Ma and 404 ± 6 Ma, respectively. Several different mechanisms have been suggested for the formation of the Comrie Pluton (Majid, 1974), including mixing between magmas of different compositions and magmatic differentiation. However, Majid (1974) considered partial melting of oversaturated rocks in the mantle to be the most likely scenario. This conclusion was reached on the basis of the major and trace element concentrations of the diorite, as determined by X-Ray Fluorescence (XRF), which showed that the diorite was compositionally similar to calc-alkaline magmas generated during subduction (Majid, 1974). South of the granitic core of the Comrie Pluton, the diorites are affected by a 50-150 m wide alteration halo over a distance of 2.3 km (although the style of alteration has not been described in detail; Naden *et al.,* 2010).

Previous stream sediment campaigns have also provided some information regarding the characteristics of the Comrie Pluton. Stream sediment geochemistry can yield important insights into the underlying bedrock geology of a region; by analysing the elemental composition of stream sediments, it is possible to understand the nature of the rocks and mineralisation that has contributed to the sediment load (Rollinson, 2014; Kirkwood *et al.*, 2016). Regarding the Comrie Pluton, Corkhill *et al.* 2010 compiled stream sediment geochemistry analyses from the Geochemical Baseline Survey of the Environment (G-BASE) throughout much of the Study Area (Section 3.6.), which showed that the Comrie Pluton is encompassed within a zone of Bi concentrations of 4.4-10 ppb. Furthermore, Naden *et al.* 2010 noted that As and Sb concentrations were elevated within the Comrie Pluton at a locality known as Milton Burn (Section 3.6.) but did not give specific details; the samples CMRIE4 and CMRIE7 used in this study (Appendix A; Table A.1.) were also sampled from the Milton Burn.

Aside from the other Siluro-Devonian intrusions depicted in Fig. 3.13., there are many other smaller granitoids throughout the Study Area. In the Calliachar Burn (Fig. 3.13., Locality 4), Ixer *et al.* 1997 noted that the NE trending Urlar Burn Fault (Fig. 3.13.) hosts pink and dark granitic dykes, which are interpreted to postdate the faulting. Furthermore, at Tombuie (Fig. 3.13.; Locality 3), Corkhill *et al.* 2010 described microgranite dykes that predate and postdate the local faults, although did not provide more information. References to the intrusions associated with the LTF and the subsidiary fractures that occur throughout the Study Area have also been made by Treagus (2000); for example, an intrusion at Tombuie is described as containing pyroxene and amphibole phenocrysts (Treagus, 2000). Regarding the grey porphyritic granitoids known to occur within the fault plane of the LTF, these are comprised of quartz, plagioclase, hornblende, and biotite phenocrysts set within a granular groundmass consisting of quartz and feldspar (Treagus, 2000).

3.4.3. Structural Geology

The LTVS is hosted within the Tay Nappe (Fig. 3.4.), which developed during the D1 and D2 stages of the Grampian Orogeny (Table 3.1.). In terms of the characteristics of the Tay Nappe locally, Treagus (2000) described the presence of two major folds; the Loch Tay Antiform (open, gently dipping limbs <20 °), the northern extent of which is demarcated by the Farragon Volcanic Formation (Treagus, 2000), and the Ben Lawers Synform (further north of the LTVS to Schiehallion; Fig. 3.4.). Parts of LTVS may therefore be hosted within the Flat Belt of the Tay Nappe, with the metasediments dipping gently towards the SE (Treagus, 2000). In terms of timing, the Loch Tay Antiform is considered to be a D3 structure (Table 3.1.) because it records a style of cleavage (steep-dipping, axial planar) that has been observed to postdate the peak metamorphic cleavage (D2) elsewhere in the Grampian Terrane (Treagus *et al.*, 1999; Treagus, 2000). It is important to note that for both the Loch Tay region and the wider Grampian Terrane, the stratigraphic sequence of the Tay Nappe is interpreted to be overfolded, meaning that the Argyll Group overlies the Southern Highland Group at several localities (Fig. 3.15.). However, several previous workers have suggested that in the northern portions of Loch Tay, particularly around Schiehallion, the intense folding has resulted in the Argyll Group being folded over and around the Southern Highland Group (Sturt, 1961; Treagus, 2000; Fig. 3.15.b.). For this reason, it is possible to suggest that there may be localised repetition of the Argyll Group at depth in the northern parts of the Study Area (Fig. 3.13.), a scenario that was also advocated by Tanner (2014a), who discussed it specifically within the context of mineralisation at the CUB veins and Tombuie; Tanner (2014a) advocated that the stratigraphic relationship of these localities was comparable to Cononish (Smith and Krabbendam, 2003; Tanner, 2012; Hill *et al.*, 2013) and the Easdale Subgroup (which contains SEDEX horizons; Moles *et al.* 2014) was approximately 5 km beneath the mineralisation. Regarding most of the folds depicted in Fig. 3.13., it is important to note that they represent an ongoing interpretation by Torvela (2020), and little reference to them has been made in the published literature; information on their relative timing is therefore not available. However, the folds appear to crosscut the isograds (Fig. 3.13.), potentially indicating that they formed prior to peak metamorphism in the region.

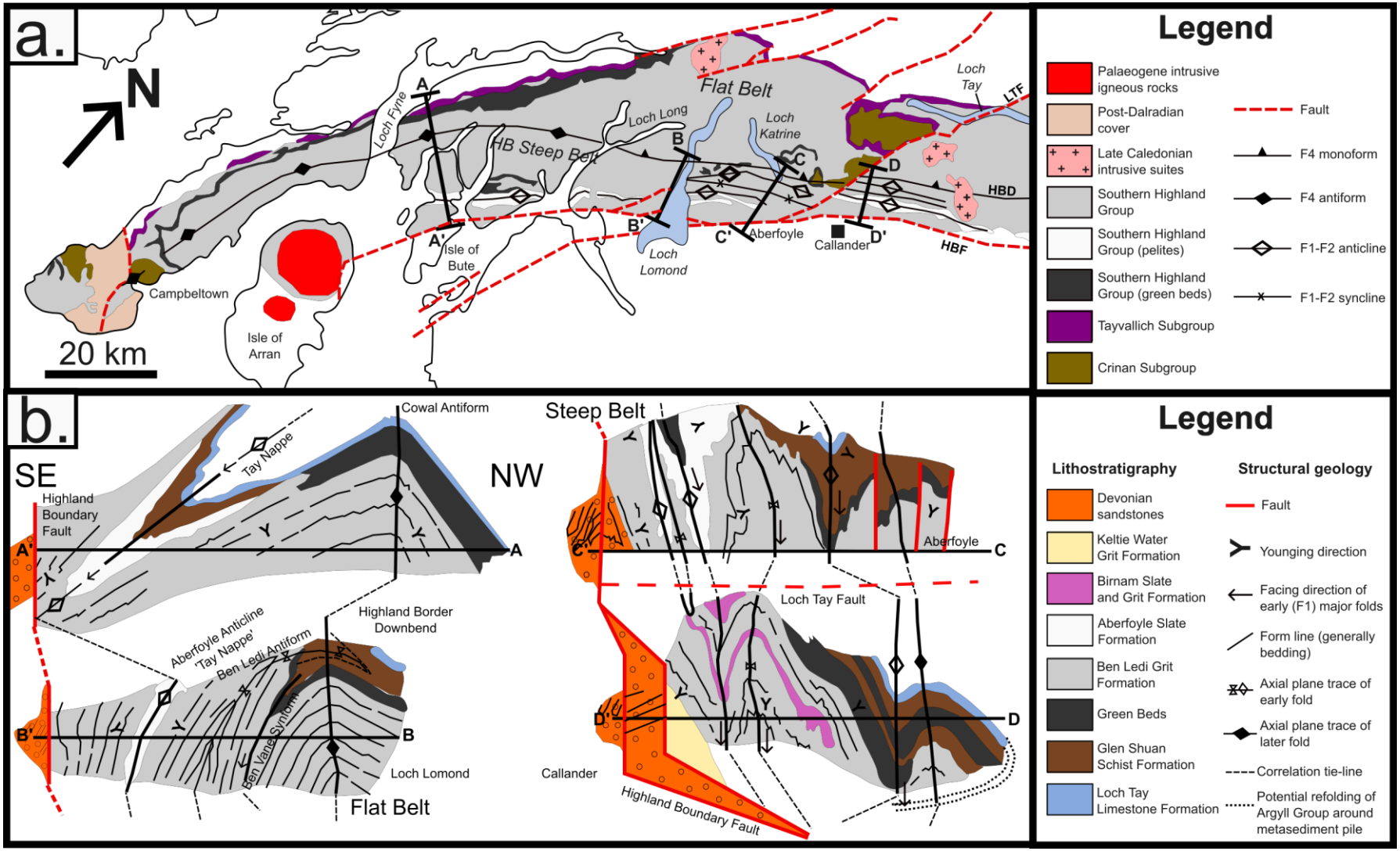

Figure 3.15. Cross-sections depicting the Tay Nappe. **a.** Location of the cross-sections within the Grampian Terrane. **b.** The cross-sections. The potential refolding of the Argyll Group around the Schiehallion region (Fig. 3.1.), which has been described by several others (Sturt, 1961; Treagus, 2000; Tanner, 2014), is also shown. Abbreviations are as follows: HBD (Highland Boundary Downbend), HBF (Highland Boundary Fault), LTF (Loch Tay Fault). Adapted from Tanner *et al.* 2013.

As depicted in Table 3.2., several faults have been described around Loch Tay, the most prominent of which is the Loch Tay Fault (Fig. 3.13.; LTF). Treagus (2000) considered the LTF to represent a splay of the Highland Boundary Fault (Fig. 3.13.), which records a similar history of strike-slip movements during the Silurian and dip-slip motions in the Carboniferous (Treagus, 2003; Tanner, 2008; McKay *et al.*, 2020). The Loch Tay Fault is known to disrupt the axial traces of the major folds regionally, e.g. the Loch Tay Antiform or Ben Lawers Synform (Bradbury, 1979; Treagus, 2003). As noted in Table 3.2., the LTF is a subregional structure that traverses the entire Study Area (Fig. 3.13.) and beyond, having been documented as far to the NE as Lecht (Nicholson and Anderton, 1989). Whilst sinistral displacements are evident from the outcrop patterns (e.g. the Loch Tay Limestone Formation east and west of the LTF; Fig. 3.13.), it is not possible to precisely match formations across the LTF and for this reason, Treagus (1991) suggested that the LTF also records dip-slip motions. Furthermore, the NE-SW trend of the subvertical Tyndrum Fault may indicate that the LTF has experienced a similar history to this structure (Treagus, 2003). The LTF is interpreted to be associated with gravity-induced collapse of the Dalradian orogenic belt at the end of the Silurian (Dempster, 1985), an event that resulted in regional transtension and normal faulting.

Fault	Trend	Description	Host rocks	Reference
Loch Tay Fault	030° NE	Subvertical; sinistral and dip-slip movements of 6.5-7.5 km; hosts microgranite and microdiorite dykes	Southern Highland and Argyll groups	Treagus (2003)
Urlar Burn Fault	016° NE	Subvertical; hosts two microdiorite dykes; 5-30 m fault zone	Southern Highland Group, Dalradian amphibolites	(Ixer *et al.*, 1997; Tanner, 2014a)
Tombuie Fault	NNE	Records sinistral and dip-slip movements; microgranites predate and postdate fault movement	Southern Highland Group, Dalradian amphibolites	(Corkhill *et al.*, 2010)
Frenich Burn Fault	010 ° N	Subvertical, records sinistral and dip-slip movements	Ben Eagach Schist and Loch Tay Limestone formations	(Treagus, 2000; 2003)
Keltney Burn Fault	160 ° NW	Dextral; 3-6 m wide fault zone hosts several pink calcite veins up to 3 m wide	Southern Highland Group, Dalradian amphibolites	(Treagus, 2000)
Glen Goulandie Fault Complex	30 ° NE	Series of 6 m quartzite breccias; fault dips 45 and 50 ° SE; strike-slip and dip-slip motions	Argyll Group; Southern Highland Group	(Treagus, 2003)
Braes of Foss Fault Complex	N-S	Single north-trending fracture (or several closely spaced fractures); only records dip-slip movements	Argyll Group	(Treagus, 2003)

Table 3.2. Compilation of faults and fault complexes that have been described around the LTVS. These faults are also labelled on Fig. 3.13.

Regarding the relative timing of the different faults shown in Fig. 3.13., several interpretations have been described in the literature. Ixer *et al.* 1997 and Tanner (2014a) suggested that the Urlar Burn Fault and the Tombuie Fault represent a conjugate pair of Riedel shears, with the angle between the Riedel fracture and the second order maximum principal stress being 15 ° (Fig. 3.16.). Furthermore, Tanner (2014a) considered both faults to represent a secondary stress field caused by sinistral movements along the LTF during the Scandian Orogeny, with the 1.5 km of sinistral displacement that has been observed along the Urlar Burn Fault (Ixer *et al.*, 1997) potentially being evidence for this interpretation (Tanner, 2014a).

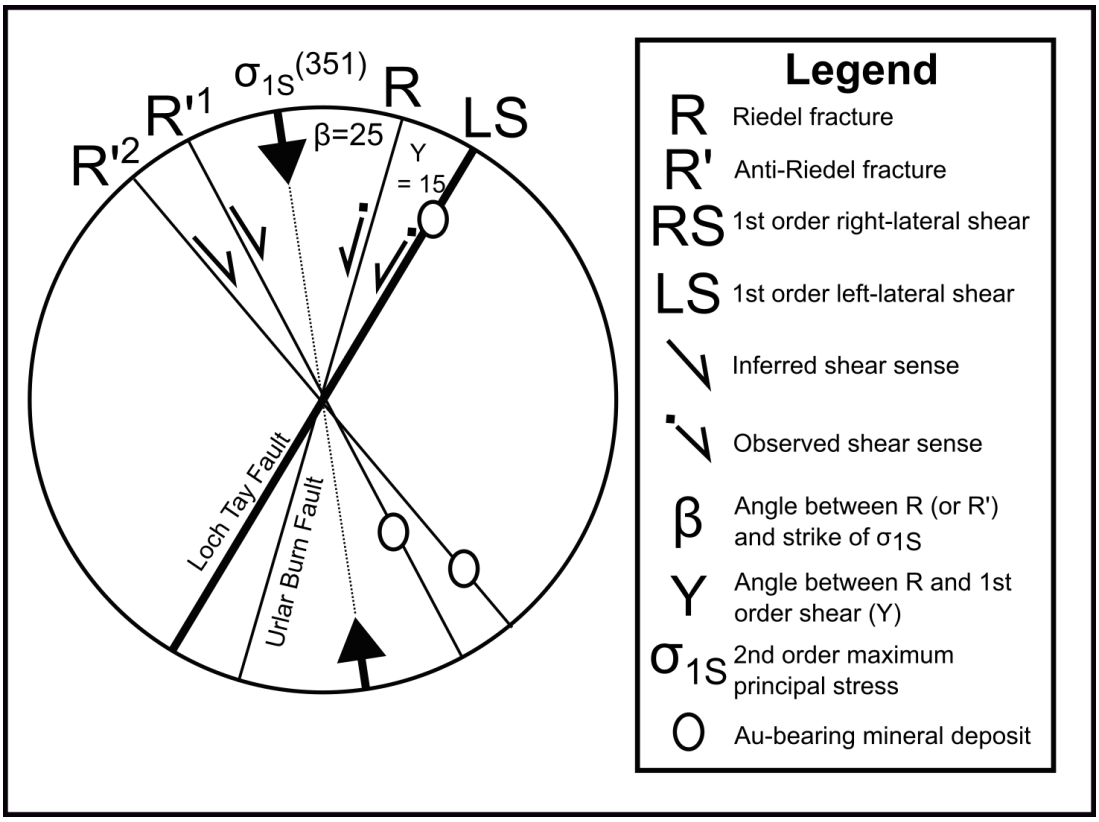

Figure 3.16. Strike-line diagram showing the relationship between the Urlar Burn Fault and the LTF. Adapted from Tanner (2014a).

However, Treagus (2000) was critical of the suggestion that the subsidiary faults associated with the LTF (Fig. 3.13.) represented Riedel shears on the basis that many of the NW-SE trending fractures throughout the Study Area do not record any evidence for sinistral movements; furthermore, the angle between many of the smaller faults and the LTF may deviate from the expected orientations of Riedel shears (Treagus, 2003). For example, the orientation of the Urlar Burn Fault (Fig. 3.13.) appears to be different from the relationships depicted in Fig. 3.16. Instead, Treagus (2000) suggested that there may have been a NW-SE tensional episode of deformation after the sinistral motions associated with the development of the LTF. However, no evidence was provided to support this interpretation (Treagus, 2000). Treagus (2003) also noted that reactivation occurred along the Glen Goulandie Fault Complex (Fig. 3.13.) during the Carboniferous because of the similarities between the structures here and the Tyndrum Fault (Fig. 3.6.), although the main stage of activity along the LTF was during the Silurian (Treagus, 2003).

3.5. Mineralisation during the Caledonian Orogeny

Whilst some of the mineralisation in the Grampian Terrane is Neoproterozoic in age (e.g. the Foss and Duntanlich SEDEX deposits), most metalliferous veins appear to have formed at some point thereafter, potentially in the Silurian or Devonian (Corkhill *et al.*, 2010; Naden *et al.*, 2010; Tanner, 2014a). The distribution of known gold and base metal deposits in the Grampian Terrane of Scotland and Ireland is shown in Fig. 3.17. This section links the current understanding of orogenic and post-orogenic processes during this event with the development of mineralisation in the Grampian Terrane.

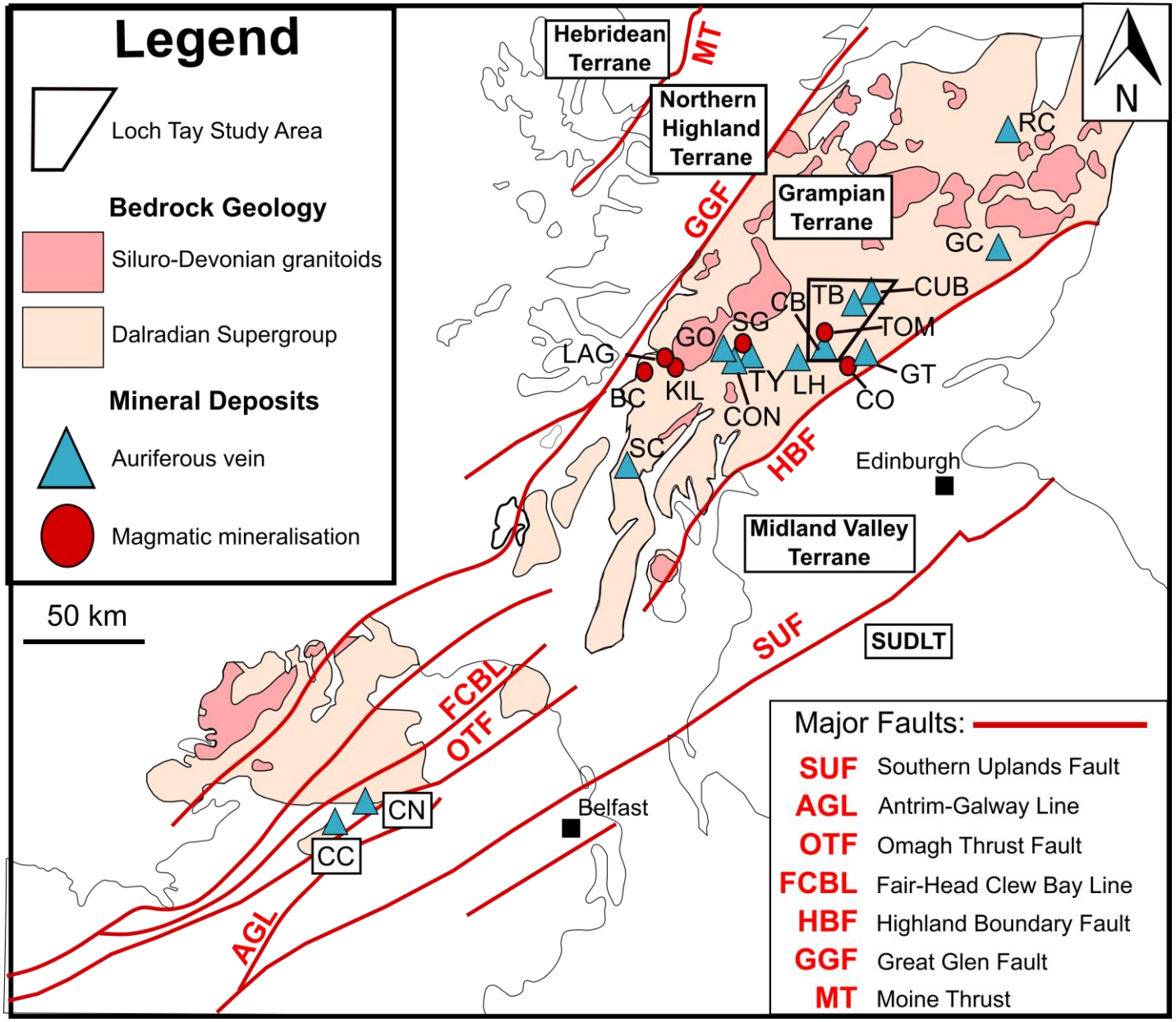

Figure 3.17. Map depicting the distribution of known auriferous veins and magmatic ore deposits in relation to the Dalradian Supergroup and Siluro-Devonian granitoids in the Grampian Terrane (adapted from Shaw *et al.*, 2022). Abbreviations are as follows: RC = Rhynie, GC = Glen Clova, CUB = Calliachar-Urlar Burns, TB = Tombuie, GT = Glen Turret, CO = Comrie Pluton, CB = Coire Buidhe, LH = Lochearnhead, TY = Tyndrum, CON = Cononish, SG = Sron Garbh, GO = Glen Orchy, LAG = Lagalochan, KIL = Kilmelford, BC = Beinn nan Chaorach, SC = Stronchullin, CN = Curraghinalt, CC = Cavanacaw. References for localities, as well as detailed descriptions, are available in Table 3.3.

3.5.1. Previous metallogenic models for the Grampian Terrane

From the 1980s, researchers began to consider the Grampian Terrane (and the various processes that created it) as part of a wider metallogenic system, involving the repeated addition of different metals to the crust with each successive tectonic event. For example, Russell (1985) used the results of previous Sm/Nd studies (Hamilton *et al.*, 1979; O'Nions *et al.*, 1983; Miller and O'Nions, 1984) to suggest that Cr, Ni, Cu, and Au were added to the Dalradian sediment pile during continental rifting, with Ba, Pb, Zn, Au, and Ag being supplied during later subduction processes. Such interpretations laid the foundations for later attempts to establish regional constraints on the formation of mineral deposits throughout the Grampian Terrane (i.e. the source of the mineralising fluids and the timing of the different mineralisation styles). In the following paragraphs, models pertaining to the development of mineralisation across the entire Grampian Terrane are summarised, which provides a context in which to consider the formation of individual mineral deposits.

There has been controversy over the origin of gold mineralisation during the Caledonian Orogeny, with previous researchers split over a metamorphic or magmatic origin. For example, Pitcairn *et al.* 2015 favoured a metamorphic origin for the fluids involved in gold mineralisation throughout the Dalradian Supergroup on the basis that bulk geochemical data show a decrease in the contents of Au, As, Sb and S with increasing metamorphic grade. This finding was replicated by the work of Parnell *et al.* 2017, who also investigated the Au concentrations in pyrite and pyrrhotite crystals from different localities in the Grampian Terrane. Both studies found that pyrite from greenschist facies rocks within the Dalradian Supergroup contains higher quantities of gold whilst pyrrhotite mineralisation within amphibolite facies rocks has relatively low gold concentrations and concluded that Au was liberated from sulphides during metamorphism. However, Pitcairn *et al.* 2015 noted that less gold may have been mobilised during peak metamorphism in the Grampian Terrane, relative to other districts in which similar studies have been conducted (e.g. the Otago Schist Belt, New Zealand; Pitcairn *et al.*, 2006). This finding may suggest that a metamorphic origin of the mineralising fluids in the Grampian Terrane would have required highly efficient fluid focusing by structural conduits (Pitcairn *et al.*, 2015).

Several researchers have suggested that gold deposits in Scotland are likely to have a magmatic or mantle-derived source. For example, the Sm/Nd isotope studies conducted by O'Nions *et al.* 1983 confirmed that some of the clastic sediments comprising the Dalradian Supergroup had a mantle-derived source and Russell (1985) speculated that this may be linked to gold mineralisation. Furthermore, relatively high Au concentrations (198 ppb) have been recorded from peridotites within the Grampian Terrane, which may indicate that the mantle beneath Scotland contained large amounts of Au during the Caledonian Orogeny (Saunders *et al.*, 2018). The first metallogenic models to directly implicate magmatic activity in the formation of auriferous veins throughout the Grampian Terrane were produced by Simpson *et al.* 1989 and

Plant *et al.* 1990. These models suggested that carbonaceous, turbidite-facies sediments associated with sedimentary basins bound by listric faults had elevated concentrations of several metals (including Au, As, and Sb) relative to other portions of the Dalradian Supergroup. The elevated concentrations of metals in these lithologies are thought to have been caused by the exhalation of hydrothermal fluids along listric faults bounding the margins of sedimentary basins (Simpson *et al.* 1989; Plant *et al.* 1990). Remobilisation of the gold from the turbidite facies sediments may have occurred in response to an increase in oxygen fugacity stimulated by the interaction between felsic magmas and meteoric fluids (Simpson *et al.* 1989; Plant *et al.* 1990; 1999).

The involvement of meteoric fluids in gold mineralisation throughout the Grampian Terrane of Scotland was advocated by Craw (1990) and Craw and Chamberlain (1996). However, unlike the Simpson *et al.* 1989 and Plant *et al.* 1990 models, Craw and Chamberlain (1996) suggested that the mixing between meteoric and metamorphic fluids derived from prograde metamorphism was the critical process in stimulating the oxidation of sulphide minerals, leading to their deterioration and the subsequent 'remobilisation' of the gold. In terms of evidence in support of this model, Craw and Chamberlain (1996) characterised fluid inclusions from sulphide-bearing veins hosted within the dilatational zones of fold hinges from the wider region around Cononish (Fig. 3.16.) and noted the presence of fluids with low salinities (1-5 wt % NaCl and KCl) and elevated CO_2 contents (3-16 wt %). The temperature recorded by these fluid inclusions was 350 ± 50 °C. Based on the similarities between these fluid inclusions and the 'orogenic' fluid that has been implicated in the formation of OGDs globally (Fig. 2.2.; Table 2.1.), Craw (1990) suggested that auriferous veins in the Grampian Terrane of Scotland have a metamorphic fluid source. However, Craw (1990) also recognised a cooler population of fluid inclusions (160-180 °C) that was characterised by CO^2 immiscibility. Craw (1990) suggested that these fluid inclusions were paragenetically later, although no petrographic evidence was provided to support this interpretation. Regardless, Craw (1990) invoked a meteoric fluid in the genetic processes associated with gold mineralisation in Scotland based on the mineralogical assemblages preserved within the veins; specifically, the occurrence of pyrite, pyrrhotite, and hematite (Craw, 1990). This is because hematite precipitates under more oxidising conditions than many sulphides (Fig. 2.15.), hence the presence of hematite was interpreted to represent the influx of a more oxidised meteoric fluid (Craw, 1990). However, regardless of their conclusions, it should be noted that the veins studied by Craw (1990) and Craw and Chamberlain (1996) did not contain economic levels of mineralisation (as noted by Naden *et al.*, 2010); it is uncertain whether these studies are representative of the processes involved in high-grade gold mineralisation throughout the Grampian Terrane.

In recent years, magmatic models for gold mineralisation throughout the Grampian Terrane have become more common (Corkhill *et al.*, 2010; Hill *et al.*, 2013; Spence-Jones *et al.*, 2018; Table 3.3.). Some of the geological characteristics of gold deposits in the Grampian Terrane, such as the abundance of sulphide minerals (Smith *et al.*, 2003) and the 465 Ma timing of peak metamorphism in the Grampian Terrane (which

predates gold mineralisation by ~50 Ma; Rice *et al.*, 2012; Spence-Jones *et al.*, 2018), may indicate that metamorphic fluids are an unlikely source of mineralising fluids throughout the wider geological setting. Furthermore, Smith *et al.* 2003 and Naden *et al.* 2010 acknowledged that some of the gold mineralisation in the Grampian Terrane must have originated from magmatic or mantle-derived fluids, although they consider this to be an additional and distinct process to the 'orogenic' models they otherwise favour for the vein-hosted occurrences of gold mineralisation.

3.5.2. Mineral deposits in the Grampian Terrane

There are multiple gold deposits that have been subjected to academic and commercial studies throughout the Grampian Terrane; it is necessary to assess the hypotheses of their genesis because similar processes may be responsible for the mineralisation around Loch Tay. In Ireland, there are several auriferous veins that have been the focus of academic research, with Bohaun (Lusty *et al.*, 2011), Cregganbaun (Halls and Zhao, 1995; Chapman *et al.*, 2000), and Croagh Patrick (Wilkinson and Johnston, 1996; Chapman *et al.*, 2000) being some examples. There are also multiple occurrences of mafic-related and SEDEX mineralisation throughout the Grampian Terrane (Smith *et al.*, 2003; Naden *et al.*, 2010; Moles *et al.*, 2014). However, most of these aforementioned localities are unlikely to be genetically similar to the LTVS (i.e. they are outside of the Grampian Terrane; Tanner, 2014a), hence they are not discussed in this section, which focuses on describing the genetic processes associated with gold mineralisation in the Grampian Terrane of Scotland.

Table 3.3. Vein-hosted gold and base metal deposits throughout the Scottish and Irish Grampians (outside of the Study Area). Where the term 'mesothermal' was used to describe the genetic model in the original publications, this has been changed to 'orogenic.' * Refers to localities where the term 'mesothermal' was originally used. The 'Abbreviation' column reflects the codes used to represent each locality in this table on Fig. 3.16. LTVS localities are shown in a different table (Table 3.4.) and have been presented on Fig. 3.13.

Name	Abbreviation	Description	Host	Geochemistry	Structure	Mineralisation	Alteration	Genetic model	References
Beinn nan Chaorach	BC	Stockwork/ disseminated sulphides in a porphyry	Ballachulish Igneous Complex	>120ppm Cu, 0.4ppm Au	Associated with NNE trending strike-slip faults	Pyrite, Chalcopyrite, Molybdenite	Potassic	Intrusion-related	(Ellis, 1977; Zhou, 1988; Smith *et al.*, 2003; Conliffe *et al.*, 2010; Naden *et al.*, 2010)
Cavanacaw	CC	16 veins trending 140 °, dipping steeply East, <6 m wide	Easdale Subgroup	Elevated Ag (274ppm)	Rotation within an ENE-WSW striking sinistral shear zone	Electrum, Pyrite, Chalcopyrite, Arsenopyrite, Galena	Sericite, silicification	Orogenic	(Wilkinson *et al.*, 1999; Naden *et al.*, 2010; Tanner, 2014a; Shaw *et al.*, 2022)
Cononish	CON	Veins hosted along a pelite-psammite contact	Appin + Argyll groups	Strong As anomaly, sporadic Sb	NE-SW Tyndrum Fault	Electrum, Pyrite, Chalcopyrite, Sphalerite, Galena, bismuth	Chlorite, Sericite, silicification, Hematite	Magmatic	(Naden *et al.*, 2010; Hill *et al.*, 2013; Spence-

Name	Abbreviation	Description	Host	Geochemistry	Structure	Mineralisation	Alteration	Genetic model	References
						tellurides, Covellite			Jones *et al.*, 2018)
Curraghinalt	CN	10 NW-SE trending subvertical veins hosted in pelites	Southern Highland Group	Regional As anomaly	Omagh Thrust	Electrum, Molybdenite, Chalcopyrite, Pyrite, Galena, Bismuth tellurides	Mica, Sericite	Orogenic	(Wilkinson *et al.*, 1999; Parnell *et al.*, 2000; Naden *et al.*, 2010; Rice *et al.*, 2016)
Glen Clova	GC	Fault-hosted Qz veins in the Glen Doll diorite	Southern Highland Group	As, Sb, Bi, Pb, Cu, and U stream sediment anomalies	Highland Boundary Fault, SE trending lineation	Auriferous Pyrite, Chalcopyrite, Molybdenite	Limonite	Magmatic	(Smith *et al.*, 2003; Naden *et al.*, 2010)
Glen Orchy	GO	Polymetallic Qz veins and Mol-bearing fractures trending 010-026°	Grampian Group	Ag, As, Sb, Te, and W	Orchy Dome, Tyndrum Fault	Pyrite, Galena, Molybdenite in different set of fractures	Sericite, Chlorite, K-feldspar	Magmatic	(Hill *et al.*, 2013; Hill, 2014)
Glen Turret	GT	Veins hosted in shear zones within the	Southern Highland Group	Au, Ag, As, Cu, Pb (220 ppm), Zn	Highland Boundary Fault	Cobalt-bearing undescribed sulphides	Specular Hematite, Hornfels	*Orogenic	(Smith *et al.*, 2003; Naden *et al.*, 2010)

Name	Abbreviation	Description	Host	Geochemistry	Structure	Mineralisation	Alteration	Genetic model	References
		diorite of the Comrie Pluton							
Tyndrum	TY	N-trending 50 cm wide Qz veins	Grampian Group	N/A	Tyndrum Fault	Chalcopyrite, Pyrite, Electrum, Hessite, Sylvanite, Pentlandite	Chlorite, K-feldspar	Magmatic	(Pattrick *et al.*, 1988; Hill, 2014)
Kilmelford	KIL	Disseminated mineralisation hosted in brecciated diorite and granodiorite	Kilmelford intrusive suite	As, Cu and Mo anomalies	Glen Domhain fault	Early Pyrite, Chalcopyrite and Molybdenite (breccia pipes) Late Galena, Sphalerite, Copper sulfosalts, and Stibnite in vugs and stringers	Sericite-Quartz-Pyrite, Propylitic, Potassic alteration haloes	Intrusion-related	(Ellis *et al.*, 1977; Zhou, 1987; Naden *et al.*, 2010; Tanner, 2014a)
Lagalochan	LAG	Base metal veins in two zones	Argyll Group	As, Cu and Mo anomalies	Glen Domhain fault	Electrum, Pyrite, Chalcopyrite, Molybdenite,	Phyllic, Potassic, argillic	Porphyry	(Polya *et al.*, 1995; Naden *et al.*, 2010;

Name	Abbreviation	Description	Host	Geochemistry	Structure	Mineralisation	Alteration	Genetic model	References
						Sphalerite, Arsenopyrite, Tennantite, Freiburgite, Tetrahedrite	alteration haloes		Tanner, 2014a)
Lochearnhead	LH	Gn-bearing veins hosted in calcareous schist	Southern Highland Group	N/A	Tay Nappe	Galena, Arsenopyrite, native gold found in the gossan	N/A	Orogenic	(Thost, 1860; Smith and Krabbendam, 2003)
Rhynie	RC	Volcaniclastic sequence with intensely altered sediments	Rhynie Group	Low tenor Ag anomaly	N/NNE half-graben; Major E-W shear zones	Au + Ag + Cu + Pb + Zn + Mn bearing phases	Two facies; K-feldspar + Quartz + Ilmenite and Smectite + Quartz + K-feldspar + Chlorite + Calcite	Low sulphidation epithermal	(Smith *et al.*, 2003; Baron *et al.*, 2004; Naden *et al.*, 2010; Mark *et al.*, 2011)
Stronchullin	SC	40 cm wide vein dipping 70 °W west; pelite and psammite	Argyll Group	As, Sb and Bi anomalies	Tay Nappe axis; N-S vein	Galena, Sphalerite, Chalcopyrite, Pyrite, Covellite,	Argillic alteration haloes	Orogenic	(Smith *et al.*, 2003; Naden *et al.*, 2010)

Name	Abbreviation	Description	Host	Geochemistry	Structure	Mineralisation	Alteration	Genetic model	References
		contact favoured				various sulfosalts			
Sron Garbh	SG	Appinite-diorite intrusion	Late Caledonian pluton	Enriched in Au, PGEs, Pt/Pd ratio = 0.8	Orchy Dome; Tyndrum Fault	Chalcopyrite-Pyrite, Millerite, Ni-Co-As sulphides	N/A	Mafic	(Graham *et al.*, 2017)

In Table 3.3., the 'suggested genetic model' column simply quotes the terminology that other researchers have used to characterise these ore deposits, often relying only upon their geological characteristics to do so; in most cases, compelling evidence for an 'orogenic' genetic model is therefore lacking. Furthermore, the precise location of some occurrences may be called into question, given the limited amounts of published information available (e.g. Lochearnhead). There are also many other localities throughout Scotland where only detrital gold has been retrieved (Fig. 3.18.). The information regarding in-situ occurrences of mineralisation (Table 3.3.) is therefore by no means exhaustive and there are likely to be many undiscovered auriferous veins throughout the Scottish Grampians (Fig. 3.18.).

Most of the 'orogenic' veins (Table 3.3.) are known only from artisanal 19th century mine workings, or the actions of junior exploration companies and the Mineral Reconnaissance Programme operated by the British Geological Survey (BGS) in the 20th century, which mainly sought to document their occurrence and economic potential. However, Cavanacaw has been mined since 2005 (Parker and Pearson, 2012), and Cononish was mined between 2020 and 2023 (Scotgold, 2023); furthermore, Curraghinalt is awaiting the outcome of a planning permission application (Dalradian Resources, 2018). Preliminary genetic models for these deposits have been developed in response to commercial interest (Fig. 3.19.); in some cases, detailed parageneses have been produced (Fig. 3.20.). Several studies were also conducted on the magmatic deposits throughout the Grampian Terrane (e.g. Kilmelford and Lagalochan; Table 3.3.), which in some cases display high gold concentrations (Table 3.3.). Throughout the rest of this section, the known genetic characteristics of mineral deposits in the Grampian Terrane are summarised (i.e. similar processes may have impacted the LTVS).

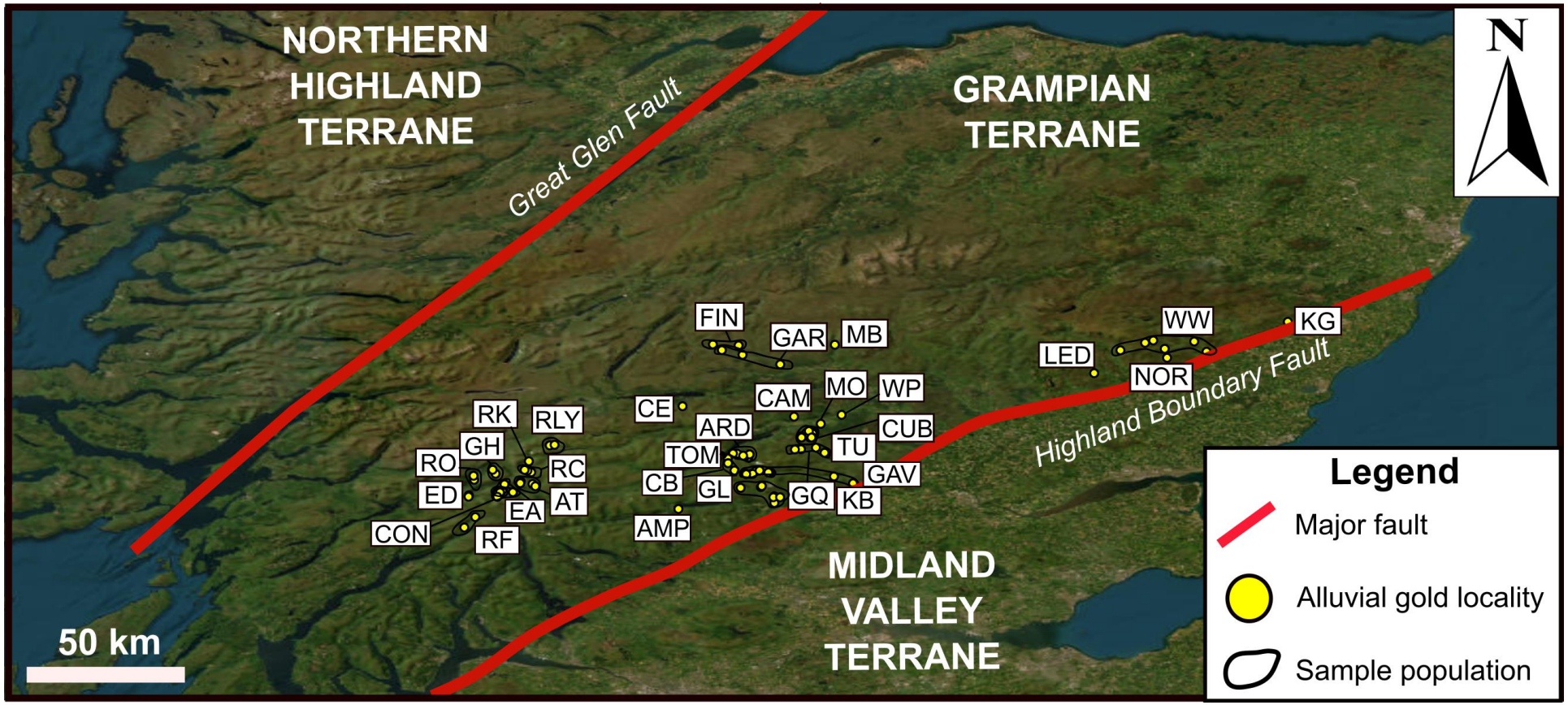

Figure 3.18. Map of known alluvial gold localities in the Grampian Terrane of Scotland (Google Maps, 2024). Abbreviations are as follows: AMP = Ample, ARD = Ardtalnaig, AT = Auchtertrye, CAM = Camsernay, CB = Coire Buidhe, CE = Carrie, CON = Cononish, CUB = Calliachar-Urlar Burns, EA = East Anie Burn, ED = Eas Daimh, FIN = Finglen, GAR = Garry, GH = Ghaimhain, GL = Glen Lednock, GQ = Glen Quaich, GAV = Glen Almond, KB = Keltie Burn, KG = Knowlegreen, LED = Lednathie, MB = Monzie, MO = Moness, NOR = Noran, RC = River Corallan, RF = River Fyne, RO = River Orchy, RK = River Kinglass, RLY = River Lyon, TOM = Tomnadashan, TU = Tuerrich, WP = Westpark, and WW = Westwater. Locality references were compiled from several sources (Gunn *et al.*, 1996; Chapman *et al.*, 2002; Savastano, 2024).

3.5.2.a. Curraghinalt

At Curraghinalt (Fig. 3.17.), molybdenite mineralisation has been dated via Re-Os methods to 457 Ma (Rice *et al.*, 2016); this is relatively close to the lowest possible date for the Grampian metamorphic peak at 465 Ma (Rice *et al.*, 2016). Previous paragenetic interpretations of Curraghinalt have shown that the gold may be associated with bismuth tellurides (Parnell *et al.*, 2000; Rice *et al.*, 2016). Furthermore, the Curraghinalt fluid inclusion data are indicative of magmatic input; homogenisation temperatures >400 °C, salinities slightly above those envisioned for OGDs (10 wt % NaCl + KCl), and CO_2 concentrations of 15 wt % (Parnell *et al.*, 2000). Rice *et al.* 2016 argue that these characteristics are by-products of the specific nature of the orogenic setting, where the subduction of continental shelf sediments resulted in elevated salinities and rapid uplift caused meteoric mixing and CO_2 dilution. There are several intrusive suites around Curraghinalt, with none of these being <464 Ma (Cooper *et al.*, 2011); however, Rice *et al.* 2016 suggest that the Pomeroy granite (an intrusion ~5 km SE of Curraghinalt) has a similar age (460 Ma) to mineralisation at Curraghinalt. Regardless, there is still much uncertainty regarding the role of magmatism in the formation of this deposit. It should also be noted that $^{40}Ar/^{39}Ar$ dating of a sericite sample in the wallrock from one of the Curraghinalt veins yielded an age of 424.4 ± 2.8/3.6 Ma (Rice *et al.*, 2016). This was interpreted to reflect fault reactivation at the end of the Caledonian Orogeny (Rice *et al.*, 2016).

3.5.2.b. Cavanacaw

It was previously believed that Curraghinalt and Cavanacaw were genetically related (Wilkinson *et al.*, 1999; Parnell *et al.*, 2000). However, a recent study by Shaw *et al.* 2022 found that this is unlikely to be the case. The strike of the veins at each deposit is significantly different (Shaw *et al.*, 2022), as is the paragenesis; the main sulphide mineralisation stage at Cavanacaw is dominated by arsenopyrite (Parnell *et al.*, 2000; Fig. 3.20.). Furthermore, at Cavanacaw, the electrum is not associated with the same paragenetic stage as the tellurides, and instead coincides with the formation of galena, sphalerite, and chalcopyrite (Parnell *et al.*, 2000; Fig. 3.20.). The gold alloy compositions (which are a proxy for the pressure, temperature, and composition of the mineralising fluids; Chapman *et al.*, 2002), also differ between the two (Chapman *et al.*, 2000; Parnell *et al.*, 2000). This information, in addition to a new structural model explaining the origin of Cavanacaw, was used by Shaw *et al.* 2022 to conclude that this deposit is younger than Curraghinalt. Cavanacaw formed as the result of progressive sinistral transpression during the Scandian Orogeny (Shaw *et al.*, 2022). The evidence for this interpretation stems from the age of the 'Sperrin Mountain Suite', which was dated by U-Pb methods to 426.69 ± 0.85 Ma (Cooper *et al.*, 2013) and is crosscut by some of the auriferous veins at Cavanacaw (Shaw *et al.*, 2022). This group of calc-alkaline intrusions was emplaced under stress conditions compatible with the development of the West Sperrin Knee Bend, a transpressive structure regarded as contemporaneous with the Creevan Swing, which facilitated the development of mineralisation at Cavanacaw (Shaw *et al.*, 2022). Altogether, the collective evidence indicates that

mineralisation at Cavanacaw is <425 Ma and occurred under transpressional stress conditions (Shaw *et al.*, 2022). It is important to emphasise that aside from a broad constraint on the timing of mineralisation at Cavanacaw, considerably little is known about the genetic model, particularly regarding the source of the mineralising fluids.

3.5.2.c. Cononish

With regards to gold mineralisation at Cononish, some of the nearby molybdenite fractures in Glen Orchy were dated by Re-Os methods to 470 Ma by Hill (2014). Tanner (2012) considered the other veins around Tyndrum to be temporally coincident with the emplacement of the Lochaber Batholith (430-425 Ma), which may have contributed fluids towards the mineralisation. However, auriferous veins within the mine at Cononish were radiometrically dated to 408 ± 2 Ma and 407 ± 1 Ma using Ar/Ar methods on K-feldspar (Rice *et al.*, 2012; Table 3.4.), although it should be noted that the paragenetic context of the feldspar is unknown (this phase is not depicted in the paragenetic interpretation produced by Spence-Jones *et al.* 2018; Fig. 3.20.c.).

In terms of the genetic model that has been postulated for Cononish, the description of the events (Fig. 3.18.) represents the interpretation of Hill (2014). The first stage involved synsedimentary faulting and deposition, leading to the creation of half-grabens throughout the Dalradian Supergroup and SEDEX mineralisation at ~635 Ma (Fig. 3.19.a.; Section 3.6.2.a.). At c. 475 Ma, the Grampian Orogeny (Table 3.1.) resulted in the folding and overturning of the sedimentary packages in the Dalradian Supergroup (Hill, 2014; Section 3.3.4.). Immediately after the orogeny, metamorphic fluids carrying Mo and Ti ascended through fractures to form the veinlets around Glen Orchy (Hill, 2014). In the genetic model for Cononish (Fig. 3.19.), an age of 428 Ma for Platinum Group Metal mineralisation in the Sron Garbh lamprophyres and appinites has been suggested (Hill, 2014), although no geochronological analyses have ever been presented to confirm this interpretation (Graham *et al.*, 2017). Mafic intrusions such as Sron Garbh have typically been attributed to the episode of post-collisional magmatism that occurred throughout Scotland between 430 and 408 Ma (Section 3.3.5.a.; Tarney and Jones, 1994; Neilson *et al.*, 2009). Previous sulphur isotope studies have been conducted on Sron Garbh; $\delta^{34}S$ values as heavy as +5 ‰ were recorded (Graham *et al.*, 2017). These trends were interpreted to reflect the assimilation of crustal sulphur (Graham *et al.*, 2017). At 407 Ma, Hill (2014) suggested that an intrusion was emplaced locally, leading to the development of the short-lived magmatic-hydrothermal system associated with the formation of auriferous veins at Cononish (Fig. 3.19.f.).

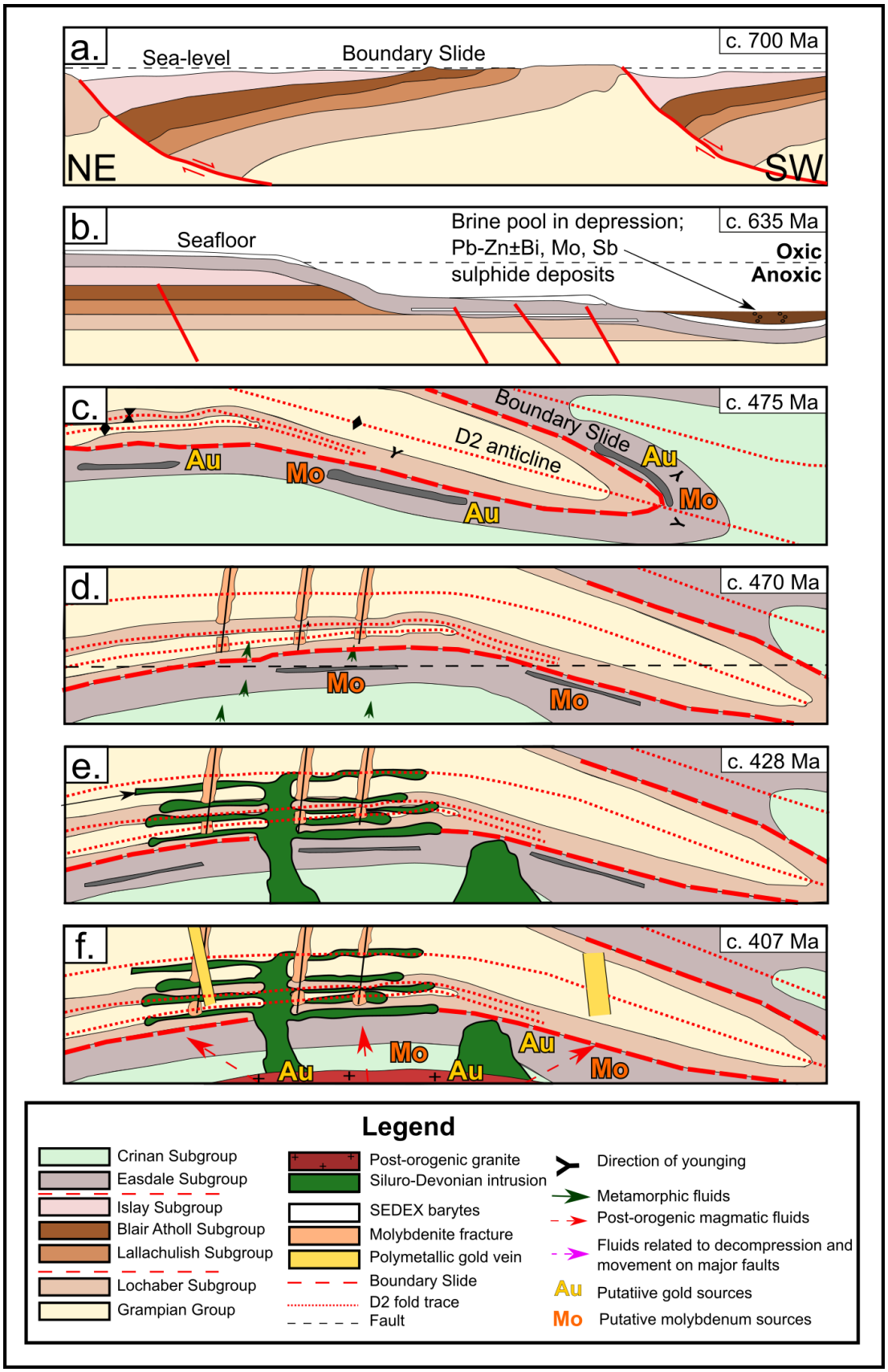

Figure 3.19. Genetic model for the formation of Cononish (adapted from Hill, 2014). The sequence of events is as follows: **a.** Formation of the Boundary slide. **b.** SEDEX mineralisation. **c.** Grampian Orogeny. **d.** Synmetamorphic molybdenite mineralisation. **e.** Lamprophyre emplacement. **f.** Gold mineralisation. The interpreted timing of each event by Hill (2014) is shown on the figure.

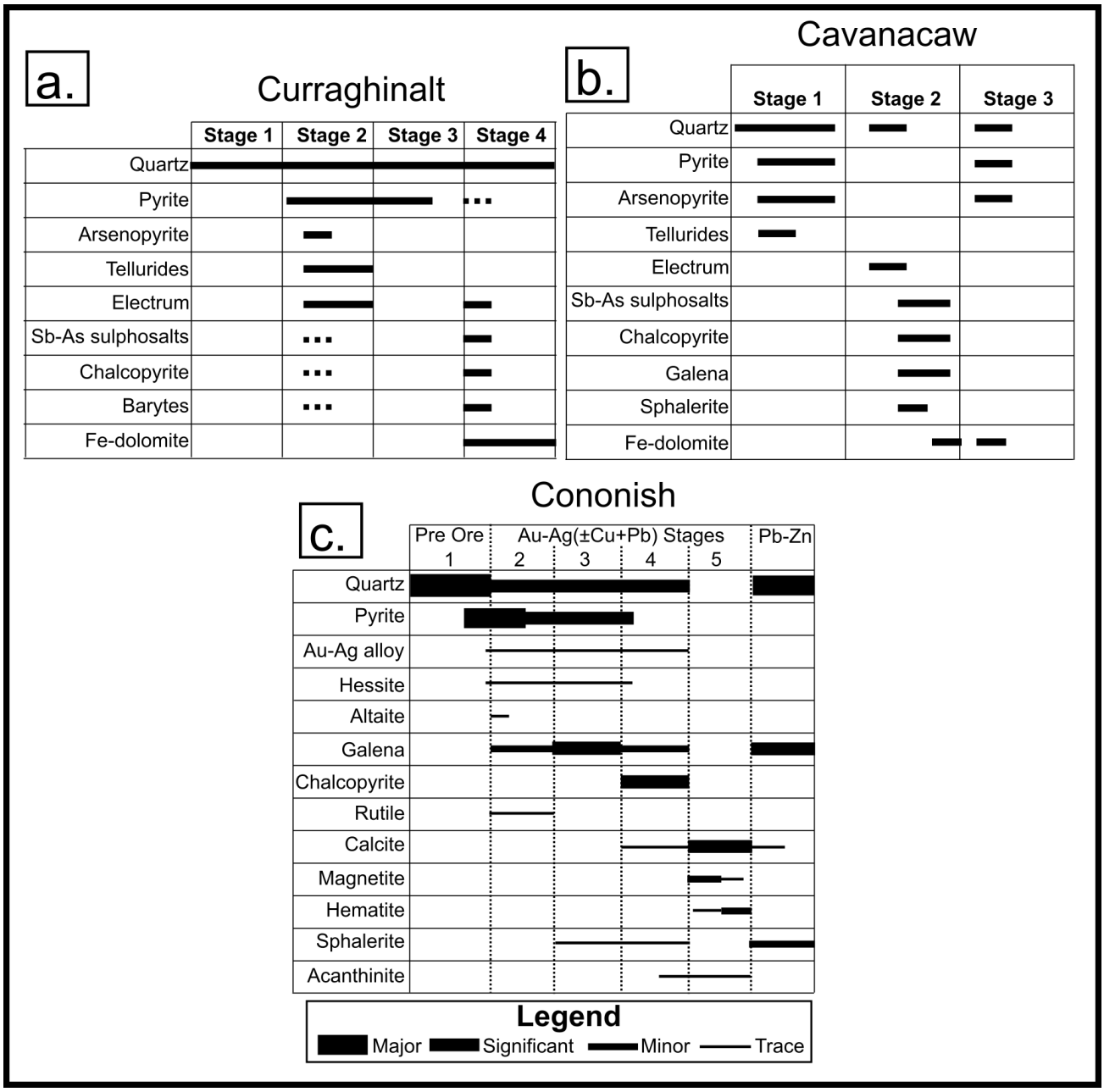

Figure 3.20. Paragenetic interpretations that have been produced for Curraghinalt (**a.**), Cavanacaw (**b.**), and Cononish (**c.**). The dashed lines represent minor phases. The interpretations for Curraghinalt and Cavanacaw were produced by Parnell *et al.* 2000, whilst the paragenesis for Cononish has been adapted from Spence-Jones *et al.* 2018.

3.5.2.d. Rhynie

Epithermal gold mineralisation occurs in the Rhynie Chert, a hot spring sinter Lagerstätte renowned for containing exceptionally preserved arthropods and plants (Rice *et al.*, 2002; Mark *et al.*, 2011). Here, auriferous veins occur in fault-bounded slivers of andesite and sedimentary rocks that show high degrees of hydrothermal alteration (Baron *et al.*, 2004); this mineralisation has been dated to 407 Ma (Mark *et al.*, 2011). Out of the two alteration facies recognised by Baron *et al.* 2004, the K-feldspar + quartz + illite assemblage within the andesite contains the most gold, with 100 ppb Au being recorded from arsenic-bearing pyrite (Mark *et al.*, 2011). These portions of the Rhynie Chert may represent the subsurface feeder zone of the epithermal deposit (Rice *et al.*, 2002). Anomalous concentrations of W and Mo in hydrothermally altered rocks, in conjunction with the mineralisation age (407 Ma) being similar to the age of the Inner Starav granite, were used by Mark *et al.* 2011 to link the mineralisation to a subsurface granitic heat engine. However, the specific intrusion or group of intrusions associated with the mineralisation is unknown (Mark *et al.*, 2011). Palaeontological and palaeogeographical evidence also implicate meteoric water in the mineralisation processes (Mark *et al.*, 2011), as is typical of the genetic model for low sulphidation epithermal mineralisation (Fig. 2.4.b.). However, Mark *et al.* 2011 emphasised the role of magmatism in the formation of the auriferous veins in the Rhynie Chert and compared the genetic processes with the post-subduction porphyry and epithermal classes of deposits recognised by Richards (2009), in which Au is derived from alkaline magmas.

3.5.2.e. Other gold and base metal deposits in Scotland

For most of the mineral deposits in Table 3.3, published information is scant. However, known aspects of their genetic models are described here. Porter and Selby (2010) undertook Re-Os dating of molybdenite from the Etive Complex (Fig. 3.6.). The reported absolute ages (414.6 ± 2.1 and 414.7 ± 2.1 Ma) were coeval with the U-Pb ages of the emplacement of the host pluton; a genetic link between base metal mineralisation and magmatism is therefore confirmed at this locality (Porter and Selby, 2010). Whilst individual porphyries in the Grampian Terrane (Table 3.3.) may not have their own specific genetic models, such occurrences of magmatic mineralisation were categorised and described in the Grampian Terrane by Lowry *et al.* 1995, who undertook a regional fluid inclusion study on Grampian porphyries and distinguished them on the basis of geothermometry. Deposits that formed at ~560 °C were interpreted to reflect orthomagmatic cooling and meteoric mixing (Lowry *et al.*, 1995). The second category of porphyries were emplaced at shallower depths and temperatures of ~460 °C (Lowry *et al.*, 1995).

3.5.3. Previous $\delta^{34}S$ studies in Scotland and Ireland

Several $\delta^{34}S$ studies have been conducted on Scottish and Irish occurrences of gold mineralisation, igneous intrusions, and synsedimentary sulphides (Fig. 3.21.). It is possible to make regional inferences based on the data in Fig. 3.21.; many gold deposits in Scotland and Ireland record relatively low $\delta^{34}S$ values, which may indicate a contribution from magmatic or mantle derived fluids (Fig. 3.21.). In terms of data from the region around Loch Tay, two datapoints for Tomnadashan (Lowry *et al.,* 2005) were used to construct the range for 'LC porphyries' (Fig. 3.21.). Aside from this, there are a limited amount of peer-reviewed $\delta^{34}S$ data from the LTVS. However, Smith (1996) conducted measurements on sulphides collected from several localities within the LTVS (as part of an unpublished PhD thesis); the results from Fortingall, Tomnadashan, Coire Buidhe, Tombuie, and the CUB veins are depicted on Fig. 3.21. The $\delta^{34}S$ values from Tomnadashan are similar to mantle-derived $\delta^{34}S$ values, whilst the Comrie Pluton has a slightly heavier signature (Lowry *et al.*, 2005) that falls outside of this range (Fig. 3.21.). Fortingall had the most depleted $\delta^{34}S$ values throughout the entire Loch Tay region; on the other hand, Tombuie and the CUB veins recorded the heaviest values (i.e. >+10 ‰; Fig. 3.21.). Furthermore, the $\delta^{34}S$ values from Coire Buidhe were between +2.7 and +4.8 ‰ (Smith, 1996; Fig. 3.21.).

Regarding the $\delta^{34}S$ data from Curraghinalt and Cavanacaw, the 'Dalradian metasediments' datapoints pertain to two occurrences of pyrite that were described as being distant from the veins and therefore classified as synsedimentary; however, no further information on the provenance of these samples was provided (Parnell *et al.*, 2000). The Curraghinalt and Cavanacaw $\delta^{34}S$ values are similar (+5 to +11 ‰; Fig. 3.21.); furthermore, the $\delta^{34}S$ values recorded from both deposits are heavier than the $\delta^{34}S$ values reported from the synsedimentary sulphides (-20 ‰; Fig. 3.21.). For this reason, Parnell *et al.* 2000 ruled out a contribution of metasedimentary sulphur in the mineralisation processes at Curraghinalt and Cavanacaw and concluded that the Tyrone Igneous Complex ($\delta^{34}S$ values of +9 to +13 ‰; Fig. 3.21.) was a more feasible source of sulphur in the auriferous veins at both localities (Parnell *et al.*, 2000).

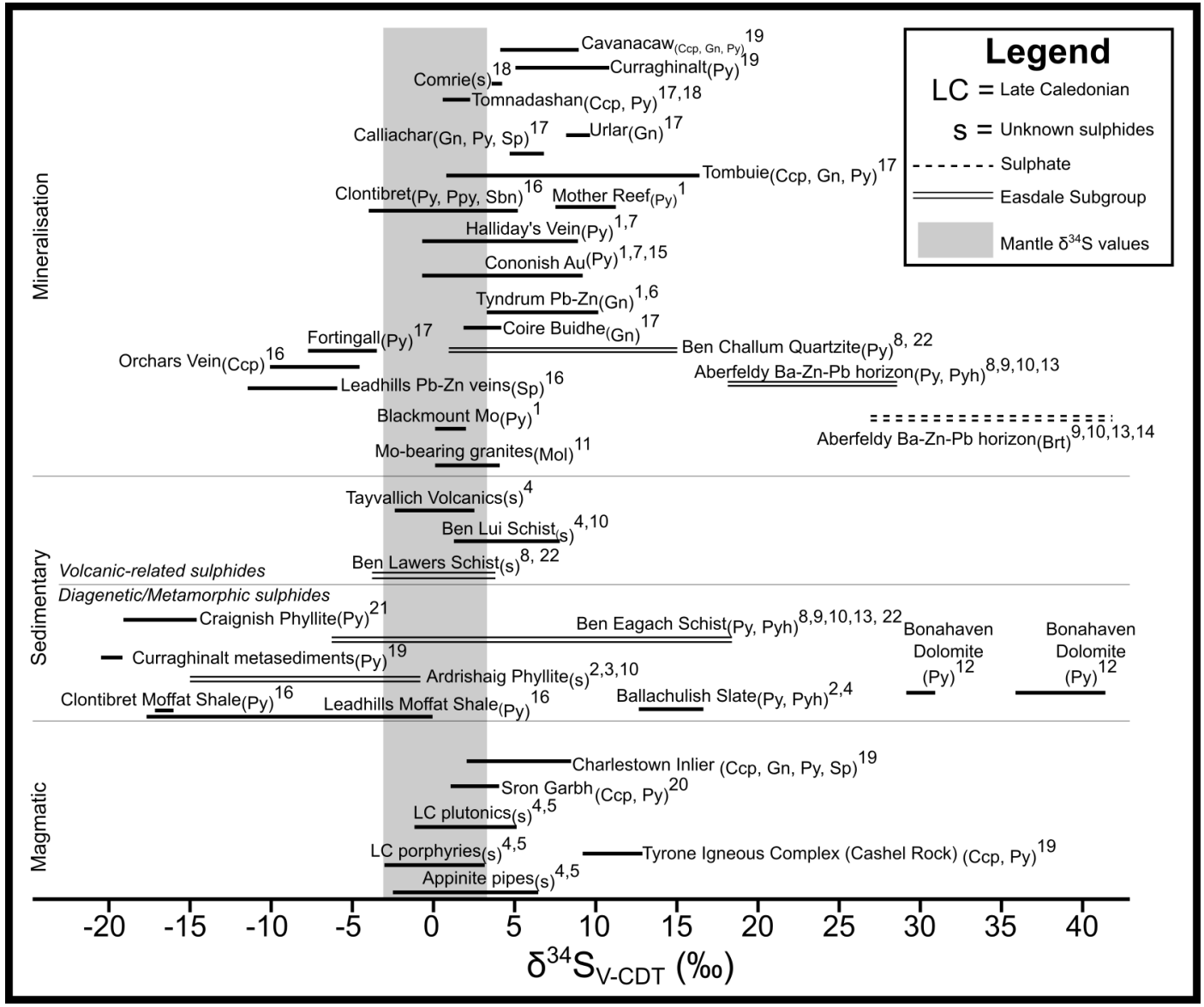

Figure 3.21. $\delta^{34}S$ data from gold/base metal mineralisation throughout Scotland and Ireland (adapted from Hill *et al.*, 2013). Mantle-derived magmatic melts typically have $\delta^{34}S$ values of 0 ± 3 ‰ (Ohmoto, 1986). References for the localities where the data were derived are as follows: 1 = Curtis *et al.* 1993, 2 = Hall *et al.* 1988, 3 = Hall *et al.* 1994a, 4 = Lowry (1991), 5 = Lowry *et al.* 1995, 6 = Pattrick *et al.* 1983, 7 = Pattrick *et al.* 1988, 8 = Scott *et al.* 1987, 9 = Scott *et al.* 1991, 10 = Willan and Coleman (1983), 11 = Conliffe *et al.* 2009, 12 = Hall *et al.* 1994b, 13 = Moles *et al.* 2014, 14 = Hall *et al.* 1987, 15 = Spence-Jones *et al.* 2018, 16 = Rice *et al.* 2018, 17 = Smith (1996), 18 = Lowry *et al.*, 2005, 19 = Parnell *et al.*, 2000, 20 = Graham *et al.* 2017., 21 = Parnell *et al.*, 2017, 22 = Hill *et al.*, 2013. The 'Magmatic' (values derived from igneous rocks) and 'Sedimentary' categories represent ranges for different units collected throughout the Grampian Terrane and SUDLT. The 'Mineralisation' category reflects $\delta^{34}S$ data from metallic mineralisation (often veins).

To constrain the sources of sulphur involved in the mineralisation processes at Cononish, Hill *et al.* 2013 constructed a $\delta^{34}S$ dataset comprising ~130 measurements (with a small number representing in-situ analyses) from the orebodies and host lithologies (diagenetic sulphides) throughout the region around Cononish (Fig. 3.17.). The $\delta^{34}S$ values for the Au-rich paragenetic stage (i.e. Stage 4 pyrite; Fig. 3.20.c.) of the Cononish orebody were then plotted graphically, alongside the ranges for the different lithologies present around Cononish (Fig. 3.22.). This graph enabled different contributions of magmatic sulphur to be modelled against the observed $\delta^{34}S$ values (+12 ‰) that were recorded from the latest paragenetic stage of pyrite at Cononish (Stage 4; Fig. 3.20.c.). Excluding a metasediment-only source for the mineralising fluids (a scenario that Hill *et al.* 2013 deemed to be unrealistic, given the frequency of magmatic pulses throughout the 430-390 Ma interval; Neilson *et al.*, 2009; Miles *et al.*, 2016), only a fluid with 68 % magmatic sulphur mixing with fluids from the Easdale Subgroup (e.g. the Aberfeldy Ba-Zn-Pb horizon; Fig. 3.21.) could explain the $\delta^{34}S$ signature recorded from the Stage 4 pyrite (i.e. +12 ‰) of Cononish.

However, Hill *et al.* 2013 also recognised that other lithologies within the Dalradian Supergroup may have contributed sulphur to the mineralising fluids at Cononish; many of the $\delta^{34}S$ values recorded from this locality were between +5 and +8 ‰ (Pattrick *et al.*, 1983; Hill *et al.*, 2013), meaning it is not necessary to invoke a SEDEX source of sulphur. For example, the synvolcanic sulphides within the Ben Eagach Schist Formation are <+8 ‰ (Fig. 3.21.); Hill *et al.* 2013 considered these volcanogenic horizons to be a feasible source of some of the sulphur in the auriferous veins at Cononish, and potentially even a source of the gold, given the occurrence of gold inclusions within the chalcocite assemblages that have been described in some horizons from the Ben Lawers Schist Formation (Moles, 1985). However, it must be stressed that the source of the gold at Cononish is uncertain. Gold mineralisation is known to occur in SEDEX deposits (Emsbo, 2000); it is therefore possible to suggest that the gold at Cononish may have been derived from the same source as some of the isotopically heavier galena and pyrite. Alternatively, the synsedimentary sulphides within the Ben Eagach Schist Formation have $\delta^{34}S$ values of <16 ‰ (Fig. 3.21.), meaning this unit could also have contributed sulphur to the mineralising fluids associated with the isotopically lighter values at Cononish (e.g. the $\delta^{34}S$ range depicted for molybdenite; Fig. 3.22.).

An additional $\delta^{34}S$ study was conducted on Cononish by Spence-Jones *et al.* 2018, who derived data from the three pyrite generations of the orebody. Each paragenetic stage at Cononish yielded a distinct $\delta^{34}S$ signature; furthermore, an overall increase in $\delta^{34}S$ values was observed throughout the paragenesis (from +1 to +10 ‰; Spence-Jones *et al.*, 2018). The $\delta^{34}S$ values of pyrite in the first paragenetic stage were <+2 ‰ (Spence-Jones *et al.*, 2018) and within the $\delta^{34}S$ range of 'LC porphyries' and mantle-derived magmatic melts (Fig. 3.21); for this reason, pyrite in the initial paragenetic stage at Cononish was interpreted to reflect a pulse of magmatic-hydrothermal fluids. However, the heavier $\delta^{34}S$ values in the second and third pyrite generations are outside of the range for LC porphyries and mantle-derived fluids (Fig. 3.21.). To explain this

trend, Spence-Jones *et al.* 2018 invoked the metasedimentary mixing process described by Hill *et al.* 2013 (specifically, mixing between I-type magmatic sulphur and synsedimentary sulphides within the Ben Eagach Schist Formation; Fig. 3.22.) and suggested that metasedimentary sulphur may have been released from the host rocks in response to contact metamorphism stimulated by the magmatic fluids. Alternatively, there may have been an increasing amount of fluid/rock interaction throughout the formation of the vein, which ultimately stimulated the release of sulphur (Spence-Jones *et al.*, 2018).

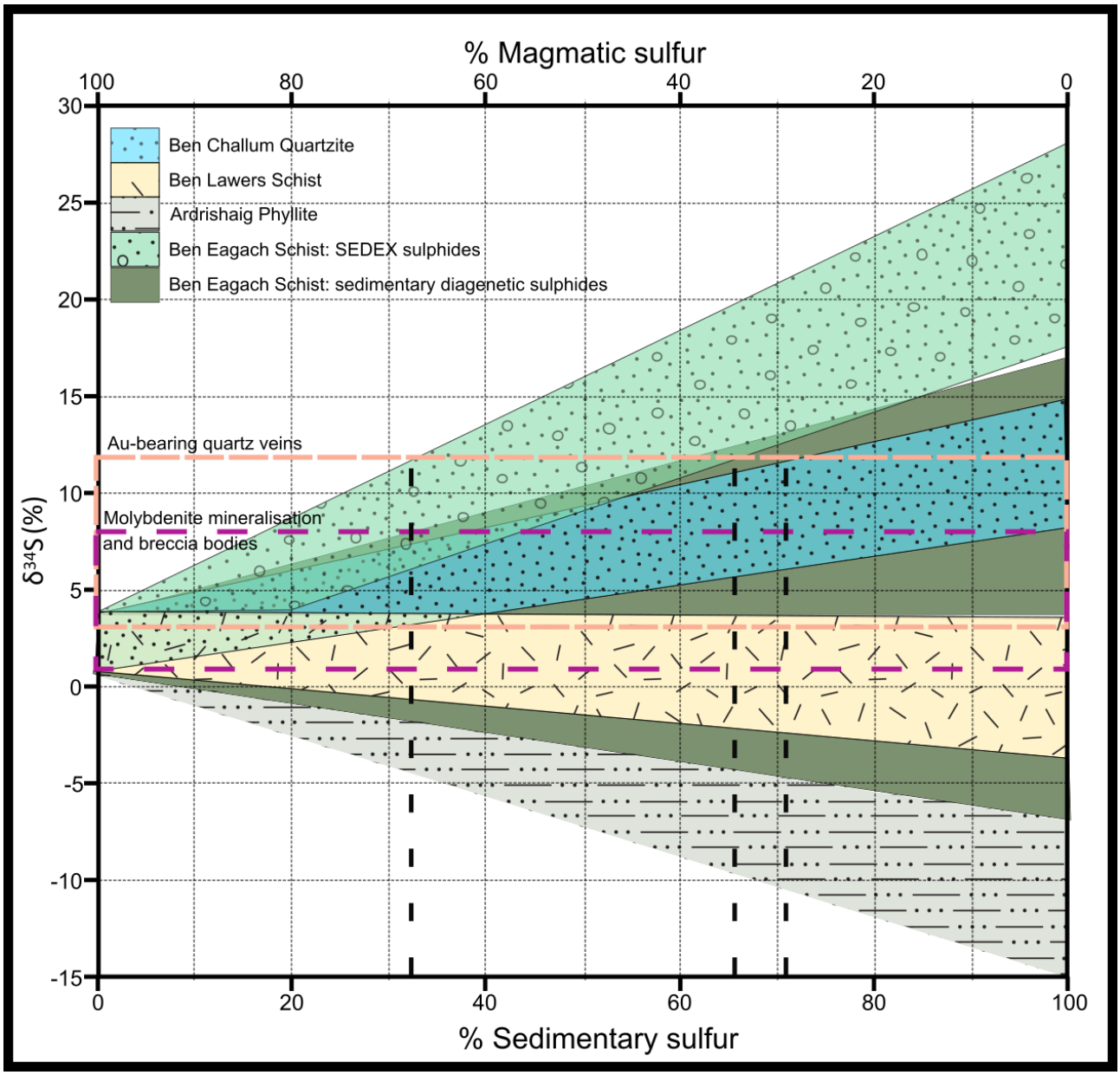

Figure 3.22. The mixing diagram originally produced by Hill *et al.* 2013, which sought to evaluate scenarios for explaining the $\delta^{34}S$ profile recorded at Cononish. The dashed vertical lines illustrate mixtures that could give rise to $\delta^{34}S$ values of +12 ‰ (reported from Stage 4 at Cononish; Fig. 3.19.c). For example, a mixture comprising 33 and 66 % magmatic sulphur (assuming an average of +2 ‰ for granitoids in the Grampian Terrane; Lowry *et al.,* 1995) and sulphur from the SEDEX horizons within the Ben Eagach Schist Formation could feasibly result in $\delta^{34}S$ values of +12 ‰.

3.5.4. Previous Pb isotope studies in Scotland and Ireland

Other researchers have collected Pb isotope data from a variety of geological features in Scotland and Ireland, including ore deposits, sediments, and granitoids; the results of these studies are compiled in Fig. 3.23. However, the majority of datapoints were derived by Standish *et al.* 2014, who presented Pb isotope data from 34 occurrences of gold mineralisation in Ireland. Geographically, the Standish *et al.* 2014 data (Fig. 3.23.) represents two regions; the northwest terrane and the southeast terrane, which are situated on each side of the Iapetus Suture in Ireland. Pb measurements from the southeast terrane have higher $^{208}Pb/^{204}Pb$ values and more consistent $^{207}Pb/^{204}Pb$ values relative to the northwest terrane (Fig. 3.23.). Given the similarities between the Pb data from the granites in the southeastern terrane and the mineralisation (Fig. 3.23.), Standish *et al.* 2014 invoked a magmatic-hydrothermal fluid source in this region. However, the northwestern terrane consistently recorded less radiogenic values than the southeastern terrane; this was interpreted as being evidence for a much older Pb source in this region, e.g. Neoproterozoic basement (Standish *et al.*, 2014). Given that some of the Pb datapoints lie outside of the range encompassed by the southeastern terrane granites (but are still not as depleted in radiogenic Pb samples in the northwestern terrane; Fig. 3.23.), Standish *et al.* 2014 also suggested that Lower Palaeozoic sediments were a Pb source for some of the gold mineralisation in Ireland (Standish *et al.*, 2014). Collectively, the broad range in Pb isotope values from Irish occurrences of mineralisation and the occurrence of several Pb sources were used by Standish *et al.* 2014 to conclude that the principal controls on gold mineralisation in Ireland are structural and unrelated to differential Au endowment throughout the Irish sediment pile.

Until relatively recently, published Pb analyses were unavailable for the LTVS. However, some data have been collected as part of an ongoing PhD by Savastano (2024); the results of these analyses (Fig. 3.23.) are included within Appendix F (Table F.2.). Datapoints are only available for four localities; Lead Trial, Calliachar Burn, Coire Buidhe, and Urlar Burn (Table F.2.). The Savastano (2024) data from the LTVS shows a close overlap with the SEDEX values and represents some of the least radiogenic mineralisation in Ireland and Scotland, sitting below most of the Standish *et al.* 2014 data from Ireland (Fig. 3.23.). With the exception of Lead Trial, most of the Savastano (2024) data displays similarities with Cononish and Cavanacaw (Fig. 3.23.).

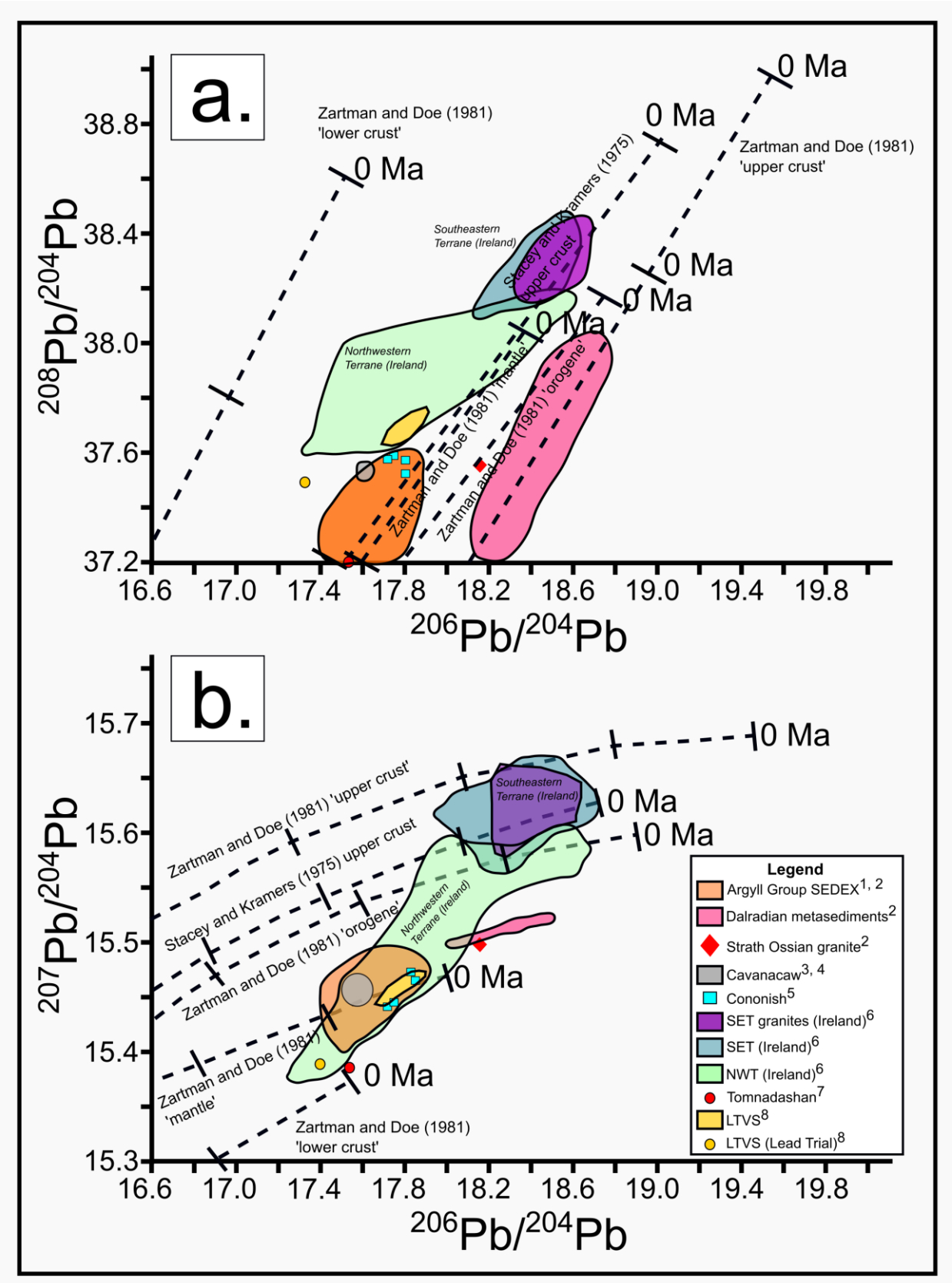

Figure 3.23. Pb isotope data from Ireland and Scotland. **a.** $^{208}Pb/^{204}Pb$ **b.** $^{206}Pb/^{204}Pb$. The abbreviations are as follows: SET (southeastern terrane), NWT (northwestern terrane). All datapoints represent galena, with the exception of the granites (feldspar) and Dalradian metasediments (whole rock data). References are as follows: 1 = Clayburn *et al.* 1983, 2 = Clayburn (1988), 3 = Parnell *et al.* 2000, 4 = O'Keefe, 1987, 5 = Swainbank *et al.* 1981, 6 = Standish *et al.* 2014, 7 = Moorbath (1962), 8 = Savastano (2024).

3.6. Mineralisation in the Study Area

As noted in Section 3.5., there are a wide variety of mineralisation styles around Loch Tay (Fig. 3.13.). It is appropriate to make a distinction between Neoproterozoic SEDEX mineralisation (e.g. Foss), and the NW-SE trending veins associated with the end of the Caledonian Orogeny. Understanding the genesis of the latter is the principle aim of this study. However, the SEDEX genetic model for Foss is summarised later in this section because it may have been a source of metals in the later vein-hosted mineralisation (Hill *et al.*, 2013; Spence-Jones *et al.*, 2018).

Previous studies have sought to characterise the metallogeny of the LTVS on a larger scale (i.e. across several localities). For example, Corkhill *et al.* 2010 investigated variations in stream sediment geochemistry throughout the Study Area and noted how the veins clustered in a region marked by elevated Bi concentrations (Fig. 3.24.). They termed this a 'bismuth anomaly', and drew comparisons with other magmatic-hydrothermal deposits, e.g. Creede (Colorado, USA; Hayba, 1997). However, no attempt to quantify the regional background concentrations of bismuth was made, meaning it is impossible to assess whether the elevated concentrations are true statistical anomalies. Only a small number of the LTVS localities occur within regions demarcated by elevated Bi concentrations, e.g. Coire Buidhe (Corkhill *et al.*, 2010). However, it may be possible to validate the conclusions of Corkhill *et al.* 2010 regarding the distribution of Bi around Loch Tay by considering the mineralogy of the LTVS (which is discussed in more detail in Section 3.6.1.). For example, at Coire Buidhe, the elevated Bi concentrations (Fig. 3.24.) correspond to the documented occurrence of bismuth phases at this locality (e.g. lillianite; Pattrick, 1984). The same applies to Tombuie (Fig. 3.24.); phases that contain bismuth (e.g. hessite) are common here (Corkhill *et al.*, 2010).

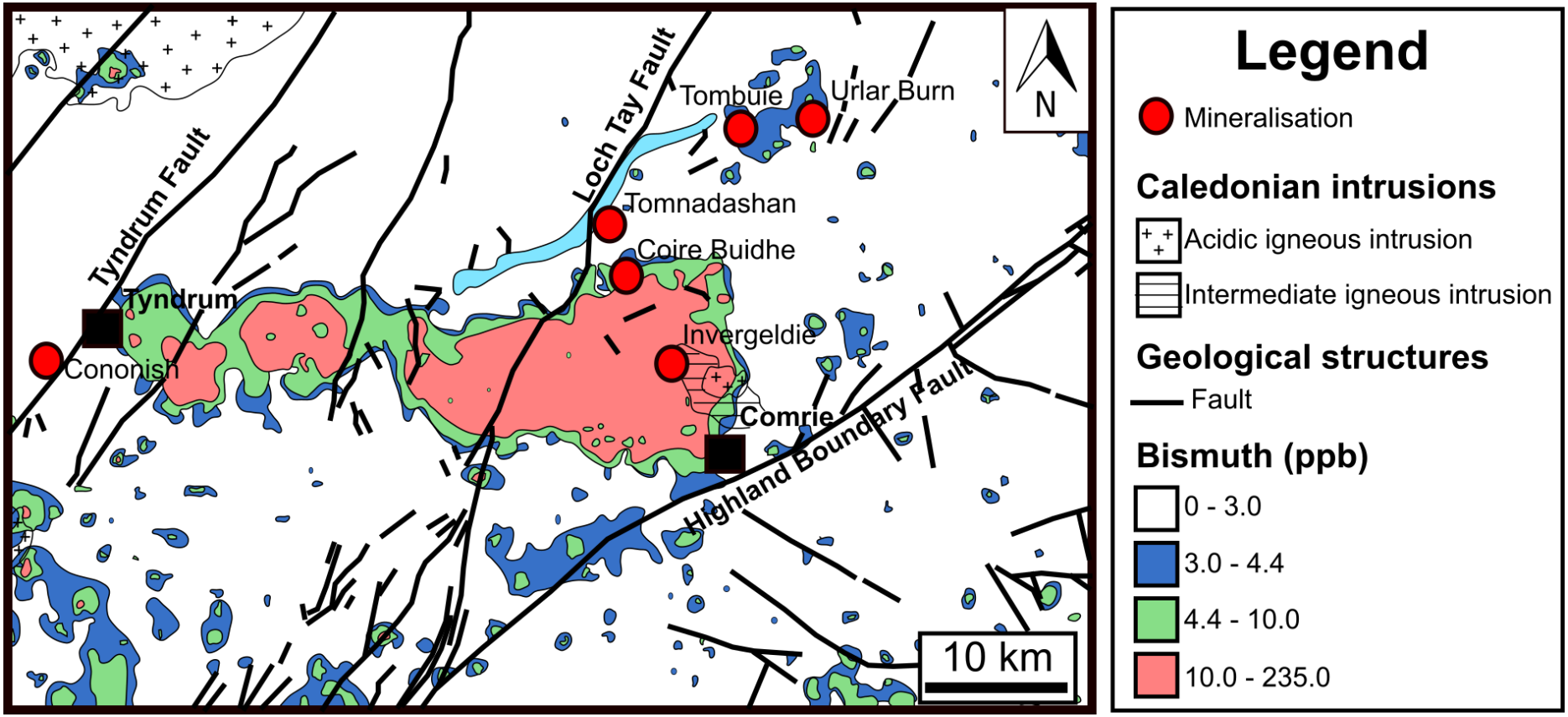

Figure 3.24. Map displaying bismuth concentrations across the Grampian Highlands (adapted from Corkhill *et al.*, 2010). The data were originally derived from stream sediment sampling (G-BASE data originally published by Johnson and Breward, 2004).

Regarding alluvial gold around Loch Tay, Chapman *et al.* 2023 conducted a study on gold geochemistry using 1887 gold particles (including several of the sampling sites depicted on Fig. 3.25.). However, it is important to emphasise that the Chapman *et al.* 2023 publication involved several localities (Sma Glen, Keltie Burn, and Glen Lednock) that are not within the LTVS (although they come from the same broader region; Fig. 3.25.). Nonetheless, Chapman *et al.* 2023 were able to distinguish populations of gold particles by alloy composition and inclusion assemblages. Two categories were interpreted; 'orogenic' and 'magmatic/epithermal.' The former pertains to Glen Almond, Calliachar Burn, and Glen Quaich whilst the latter represents Sma Glen, Keltie Burn and Glen Lednock (Chapman *et al.*, 2023; Fig. 3.25.)

It should also be noted that there are several ongoing studies on gold particles that have been retrieved from Tomnadashan and Lead Trial (Fig. 3.13.); this work, whilst preliminary, has confirmed that gold particles from the Lead Trial and the Ardtalnaig Burn contain inclusions of molybdenite and bismuth tellurides (Savastano, 2023; Webb *et al.*, 2023; Savastano, 2024). More research is needed to characterise the assemblage of mineral inclusions within the gold that has been retrieved from Tomnadashan.

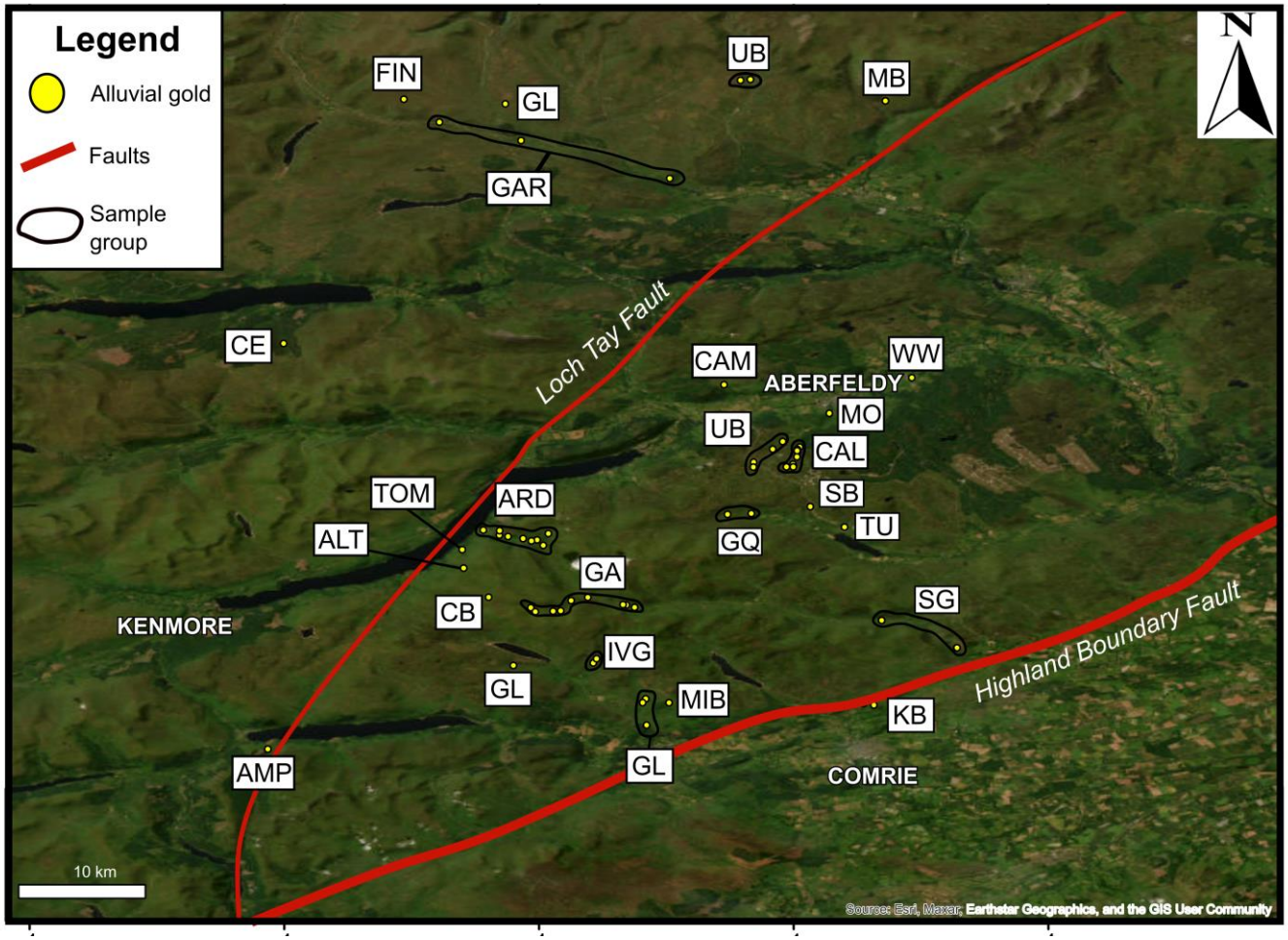

Figure 3.25. Map of localities where alluvial gold has been characterised as part of the studies by Chapman *et al.* 2023 and Savastano (2024). Abbreviations are as follows: ALT = Allt A Mheinn, AMP = Ample, ARD = Ardtalnaig Burn, CAL = Calliachar Burn, CAM = Camsernay, CB = Coire Buidhe, CE = Carrie, FIN = Finglen, GAR = Garry, GA = Glen Almond, GQ = Glen Quaich, IVG = Invergeldie, KB = Keltie Burn, MB = Monzie, MIB = Milton Burn, MO = Moness, TOM = Tomnadashan, SB = Shian Burn, SG = Sma Glen, TU= Tuerrich, UB = Urlar Burn, WW = Westwater. Each 'sample group' represents the same tributary or stream. The locations have been compiled from a variety of original source materials (Chapman *et al.*, 2000; 2002; 2023; Savastano, 2024).

Regarding the in-situ occurrences of mineralisation, these were previously depicted in Fig. 3.13.; there are several deposit-scale studies that have been conducted on the different localities within the LTVS, the results of which are described, where appropriate, in the following paragraphs. The characteristics of the different veins and occurrences of mineralisation around Loch Tay are compiled in Table 3.4. It is also important to note that two of the localities investigated in this study (ARD_1 and RX2959KA; Table 3.4.) represent pieces of boulder float (>1 m in size) that were sampled by Green Glen Minerals (Lavalle, 2020b; Green Glen Minerals, 2021). These boulders do not represent in-situ mineralisation, although they potentially provide an opportunity to characterise the $\delta^{34}S$ and Pb isotope values from the wider Ardtalnaig Estate. The sample from Tombuie (Fig. 3.13., Locality 3) used in this study (Appendix A; 2003.1G.M.637) was also derived from boulder float.

In terms of the order of presentation, metalliferous veins or mineral deposits that were characterised using vein petrography and/or isotope geochemistry in this study are presented first. However, Foss and Fortingall (Table 3.4.), even though no such data were derived from these localities, are important to summarise for the wider context of this study; the results of previous investigations into Foss and Fortingall are described in a separate subsection.

Table 3.4. Compilation of the known mineral deposits around Loch Tay. The locality numbers shown in this table can be cross-referenced with the locality numbers shown on Fig. 3.13. The * indicates localities that were not characterised using petrography or isotope geochemistry in this study.

Name	Locality Number	Description	Host	Geochemistry	Structure	Mineralisation	Alteration	Genetic model	References
Foss and Duntanlich*	1	Neoproterozoic SEDEX Barytes deposits	Argyll Group; Ben Eagach and Ben Lawers Schist formations	Ba, Pb, Zn enrichments	Creag nah Iolaire Anticline	Several Barytes horizons <20 m thick, sulphides well-developed at the bas2e	Post-depositional diagenetic and metamorphic processes	SEDEX	(Ruffell *et al*, 1998; Naden *et al.*, 2010; Moles *et al*, 2014)
Fortingall*	2	Quartz ± Carbonate veins trending 180 °; adjacent to an outcrop of the LTF	Pelite, meta-limestone	As enriched (>1000 ppm), 42 ppm Au	Loch Tay Fault	Pyrite and Arsenopyrite	Carbonate	N/A	(Treagus, 2003; Naden *et al.*, 2010)
Tombuie	3	Au-rich Quartz ± Carbonate veins trending 130-160 °	Southern Highland Group	30-44 ppb Bi	Tombuie Fault	Au, Bi, Ag and Te bearing phases, late stage Galena	Lack of intensive hydrothermal alteration	Epithermal	(Corkhill *et al.*, 2010; *Naden et al.*, 2010)
Calliachar-Urlar Burns	4	14 vuggy Quartz veins <2 m wide, 140-160° trend	Southern Highland Group	As anomalies, Sb enrichment	NE fault (Urlar Burn Fault)	Electrum, Pyrite, Galena, Sphalerite, Chalcopyrite, Arsenopyrite, Tennantite,	Chlorite, Sericite, Carbonate up to 20 m from the veins	Orogenic	(Ixer *et al*, 1997; Naden *et al.*, 2010)

						Tetrahedrite, Pyrite + Galena form veinlets			
Lead Trial	5	NW-SE trending Quartz veins with high gold grades, up to 1m thick	Rhyolites, Southern Highland Group	Enriched in Pb, Zn, Ba, Au, Hg	LTF, NW-SE trending faults (Fig. 3.13.)	Galena, Sphalerite, Electrum, Barytes, Pyrite, Chalcopyrite, Carbonate	Chlorite, Sericite, silicification	N/A	(Lavelle, 2020b)
RX2959KA	6	Schist boulder containing a Quartz vein with Galena and Chalcopyrite mineralisation	Southern Highland Group	Au grades of 11.5 g/t		Coarse Galena, Vuggy Quart2z, trace Chalcopyrite	Silicification	N/A	(Lavalle, 2020b)
ARD_1	7	Schist boulder containing a Quartz vein with Galena fragments	Southern Highland Group	Au grades of 17.5 g/t		Barytes, Galena, Quartz, Carbonate	Silicification	N/A	(Lavalle, 2020b)
Tomnadashan	8	Porphyry Cu-Mo; disseminated and vein-hosted mineralisation	Diorite and granite	As anomalies	LTF, crosscut by a NW-SE trending	Disseminated and veinlet Pyrite, Chalcopyrite, Tetrahedrite, Molybdenite,	Sericite, Chlorite, Talc, Carbonate, Rutile, Tennantite,	Porphyry	(Pattrick, 1984; Naden *et al.*, 2010)

					splay (Fig. 3.13.)	Bismuth tellurides, Gold	Tetrahedrite, Albite		
Spoil Heap	9	Auriferous trending NW-SE Quartz vein at the base of Meall nan Oighreag	Southern Highland Group	Au grades of 7 g/t	N/A	Arsenopyrite, Chalcopyrite, Galena, Pyrite, Sphalerite, nickeliferous phases,	N/A	N/A	(Green Glen Minerals, 2021)
Coire Buidhe	10	18 parallel NE-SW Quartz veins, historic silver mine	Loch Tay Limestone Formation	As anomalies	NW-SE trending faults (Fig. 3.13.)	Electrum, Pyrite, Chalcopyrite, Sphalerite, Galena, Tetrahedrite, Covellite	Chlorite, Sericite, silicification, Hematite	N/A	(Pattrick, 1984; Naden *et al.*, 2010)
Glen Almond Vein (GAV)	11	NNW-SSE striking <20 cm vein crosscutting metasedimentary schists	Southern Highland Group; metapelite	Elevated Au concentrations	WNW-ESW and SW-NE trending faults (Fig. 3.13.)	Vein-hosted Galena, Sphalerite, Pyrite, Chalcopyrite Massive, euhedral, and vuggy Quartz	Sericite	N/A	(Webb *et al.*, 2024a)
Comrie Pluton	12	Disseminated sulphides within	Granite and diorite	As anomalies, Sb enrichment	Highland Boundary	Pyrite, Chalcopyrite,	K-feldspar, Carbonate	Porphyry	(Naden *et al.*, 2010)

		the potassic core of a porphyry			Fault	Galena, Molybdenite, Bismuth Tellurides			

3.6.1. Siluro-Devonian mineralisation around Loch Tay

Throughout the course of this study, the following localities were investigated using isotope geochemistry or petrography (or a combination of both); the CUB veins, Tombuie, Lead Trial, RX2959KA, ARD_1, Tomnadashan, Coire Buidhe, Spoil Heap, the GAV, and the Comrie Pluton (Table 3.4.). In this subsection, the results and observations from previous studies on the aforementioned localities are described.

3.6.1.a. Calliachar and Urlar Burns

The CUB veins are a series of polymetallic NW-SE trending auriferous veins that crosscut metasediments and sporadically outcrop within the Calliachar Burn and the Urlar Burn (Fig. 3.26.). In terms of the characteristics of the host rocks, rapidly alternating (potentially every few metres) quartzites, mica schists, and metabasics (e.g. amphibolites; Fig. 3.26.) contain outcrops of the CUB veins and typically dip at low angles (<20 °) (Ixer *et al.*, 1997). Locally, the host rocks contain garnet-bearing metamorphic assemblages (Ixer *et al.*, 1997). It was also noted by Ixer *et al.* 1997 that the CUB veins attain greater thicknesses when they crosscut competent, well-jointed rocks (e.g. quartzites), whilst in the pelitic lithologies (which have lower competencies and fewer joints), the veins are narrower. Regarding their discovery, the CUB veins were identified by Colby Gold plc in 1988 after a 7 ppm Au anomaly was recorded from stream sediment measurements in the Calliachar Burn (Ixer *et al.*, 1997). Subsequent drilling and trenching resulted in the identification of 14 veins (each assigned a ‘V’ number; Fig. 3.26.).

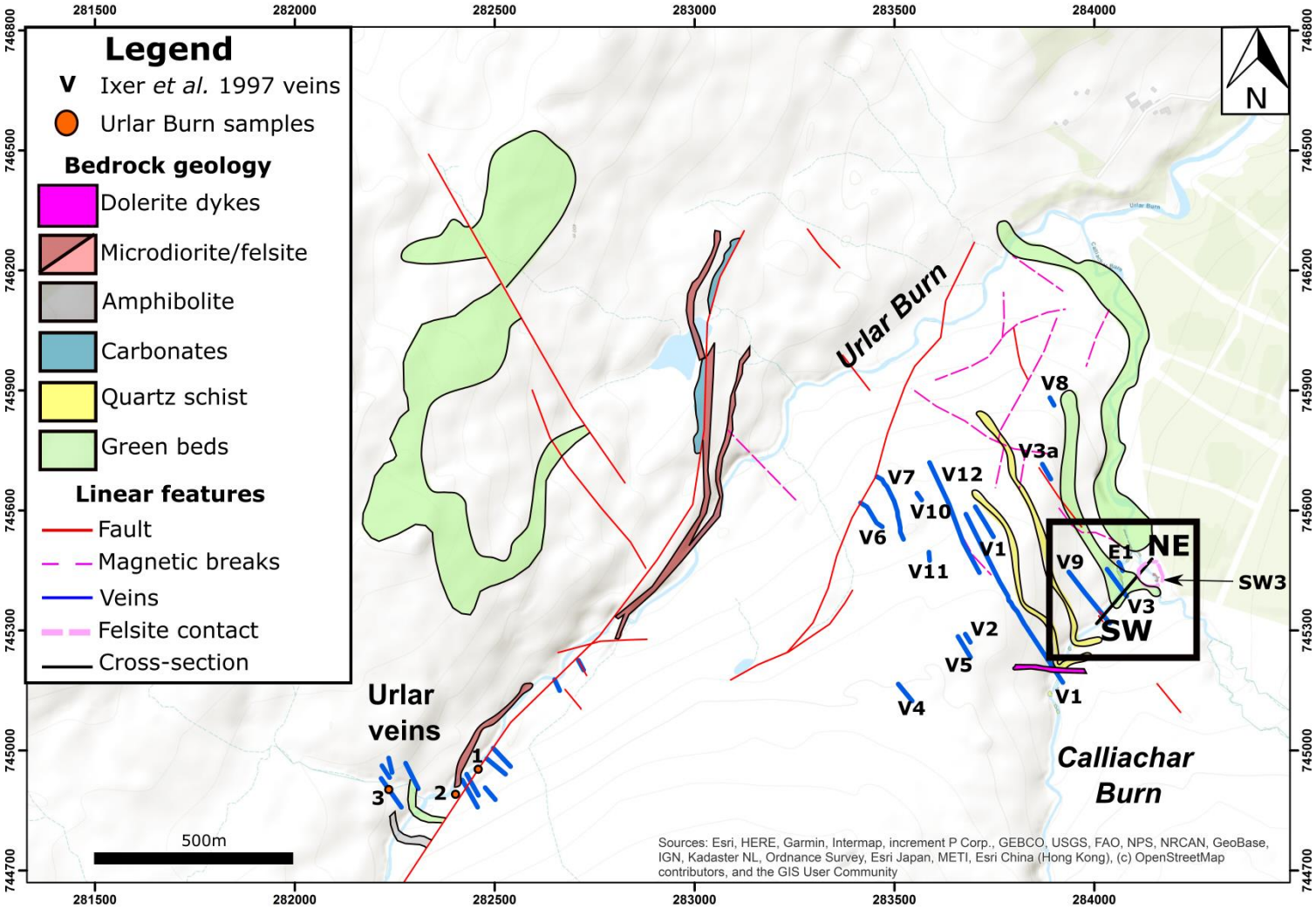

Figure 3.26. Geological map of the veins in the Calliachar Burn and the Urlar Burn (Ixer *et al.*, 1997; Lavelle, 2020b; Fig. 3.13., Locality 4) overlain on Esri (2022) topography. Around the Urlar Burn, the numbers correlate with the following samples (Appendix A): 1 = UB_VEINa, 2 = UB_VEINb, 3 = UV_SHa. E1 refers to a 2.5 cm wide sulphide-bearing vein discovered by Green Glen Minerals (Lavelle, 2020b). The black box represents the location of Fig. 3.27.

Vein 1 (Fig. 3.26.; herein referred to as the 'Discovery Vein') was the main target for the exploration campaign spearheaded by Colby Gold plc (Ixer *et al*., 1997). The average grade for auriferous veins around the Calliachar Burn was 8.81 g/t over a strike length of 87.5 m (Ixer *et al.*, 1997). More veins were identified as a result of digging trenches in the Urlar Burn, although these were not subjected to extensive investigation (Ixer *et al.*, 1997). The different CUB veins have been classified according to their gold and base metal contents (Table 3.5.).

Vein type	Description
High grade gold	Veins 1 (Discovery), 3, 6 and 7; cataclastic galena and pyrite (i.e. the galena and pyrite are fractured); minor sphalerite, chalcopyrite, arsenopyrite, electrum; 5-20 m wallrock bleaching; 77-150 g/t Au in V6, <480 g/t in the gossan
Base metal	Veins 2, 4, 5, 8 and 12; galena, chalcopyrite, sphalerite, pyrite and arsenopyrite; minimal cataclasis or wallrock alteration; Low gold grades (0.5 g/t and <2 g/t for V5 and V12)
Barren	No significant quantities of gold or base metals

Table 3.5. Vein types recognised by Ixer *et al.* 1997 in the Calliachar Burn.

Whilst paragenetic descriptions of the CUB veins have been made previously (Ixer *et al.*, 1997), the lack of supporting petrographic evidence means that these interpretations should be treated with caution. Here, the paragenetic relations within the CUB veins that were described by Ixer *et al.* 1997 are summarised. In the veins around the Calliachar Burn, pyrite, pyrrhotite, and arsenopyrite crystals occur in the initial paragenetic stage. It is important to emphasise that Ixer *et al.* 1997 described the parageneses of the veins collectively, without specific references to any of the 'V' numbers shown in Fig. 3.26. Nonetheless, the aforementioned phases were brecciated and cemented by a second paragenetic stage comprised of chalcopyrite, galena, sphalerite, and sulfosalts (Ixer *et al.,* 1997). The pyrite and arsenopyrite contains electrum, although gold was also introduced into the system along with base metal sulphides and silver tellurides in the second paragenetic stage (Ixer *et al.*, 1997). Regarding the veins in the Urlar Burn, Ixer *et al.* 1997 suggested that they were mineralogically comparable to the 'high-grade' veins (albeit with lower gold grades); galena is more common than pyrite, which has been engulfed by cobaltite and gersdorffite (Ixer *et al.*, 1997). The pyrite has also been brecciated by a similar assemblage to the second paragenetic stage at Calliachar (Ixer *et al.*, 1997). The veins in the Urlar Burn may also contain a greater proportion of Sb, Te, and Hg (Ixer *et al.*, 1997). In addition to the study by Ixer *et al.* 1997, some petrographic descriptions of the CUB veins were provided by Naden *et al.* 2010, who noted that the veins are comprised of at least four quartz generations; base metal mineralisation also typically favours vugs within the quartz.

Based on the geochemical and fluid inclusion data, Ixer *et al.* 1997 sought to characterise the genetic processes associated with the CUB veins. The geochemical and paragenetic similarities and differences between the two localities led Ixer *et al.* 1997 to suggest that the CUB veins represent different parts of the

same system. Furthermore, the observation of similarities between the 'high-grade' veins and the veins in the Urlar Burn was interpreted as evidence that the variation does not pertain to temporally separated mineralisation events; instead, the variations may reflect spatial changes within the same hydrothermal system during a single mineralisation episode (Ixer *et al.*, 1997). Regarding the genetic model, Ixer *et al.* 1997 tentatively suggested that mantle or magmatic-derived fluids may have ascended along the Urlar Burn Fault (Fig. 3.26.) and mixed with fluids at higher levels in the crust. This interpretation was based on the fluid inclusion populations that there were described from the CUB veins (see Section 3.6.3.).

In terms of igneous intrusions, geological mapping campaigns by Green Glen Minerals discovered a dyke in the Spring of 2021 (Appendix A; SW3). This intrusion had a felsic composition (Fig. 3.27.). The white phenocrysts of plagioclase feldspar show signs of flow banding (Fig. 3.27.), with grey quartz and mica forming a fine-grained (<2 mm) groundmass of anhedral crystals. This sample (SW3) was selected for CA-ID-TIMS dating (Chapter 5).

Figure 3.27. The granitic dyke in the Calliachar Burn (SW3) that was sampled by Green Glen Minerals (Lavelle, 2020a).

Based on the position of SW3 and the dip direction of the contact with the metasediments (Fig. 3.27.), it is possible that the dyke may intersect with V3 at depth (Fig. 3.28.). The cross-section also indicates that V3 is mostly hosted within the Green Beds, whilst V9 traverses the Quartz Schist (Fig. 3.28.). However, without more structural data, these interpreted subsurface relationships (Fig. 3.28.) remain speculative.

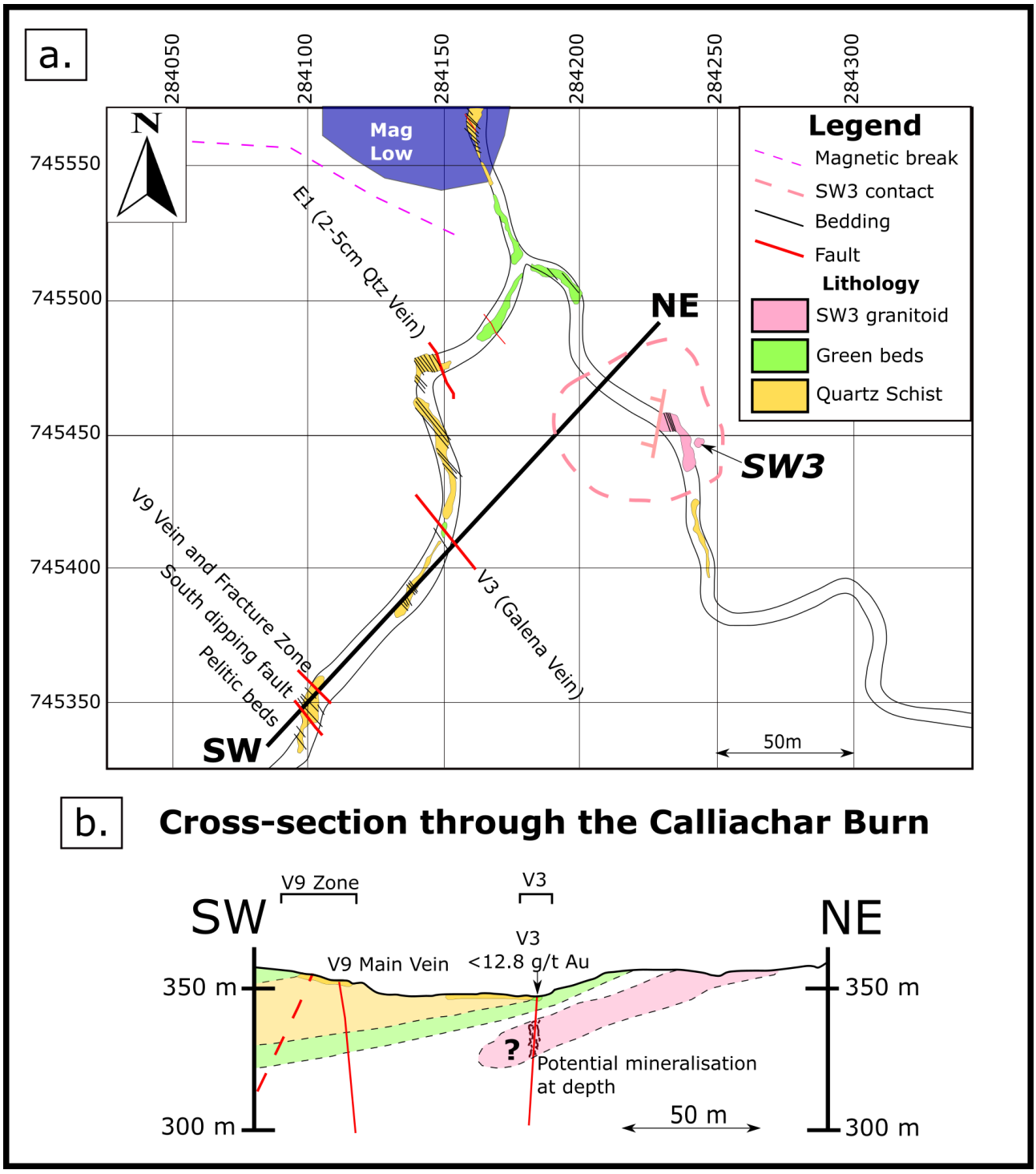

Figure 3.28. Subsurface relationships within a portion of the Calliachar Burn as interpreted by Lavelle (2020a). **a.** The location of the cross-section in the Calliachar Burn and **b.** The geological cross-section. The legend for a and b is the same. The location encapsulated by this figure is depicted on Fig. 3.25.

3.6.1.b. Tombuie

The veins around Tombuie (Fig. 3.29.) were originally explored by Colby Gold plc (Corkhill *et al.*, 2010), who exposed them by digging trenches. Regarding the host rocks of the mineralisation, this information is uncertain; Corkhill *et al.* 2010 described the host rocks as belonging to the Pitlochry Schist Formation (Fig. 3.29.). However, Naden *et al.* 2010 stated that the veins at Tombuie are hosted within a hornblende-bearing portion of the Ben Ledi Grit Formation (Section 3.4.1.), close to an amphibolite contact. This discrepancy in the literature underscores the fact that much of the area covered by the Pitlochry Schist Formation in the regional geological map (Fig. 3.13.) is largely undifferentiated and the nature of the host rocks at some localities within the LTVS may therefore be uncertain (especially given the lack of outcrop; see Section 4.5.). Regardless, Corkhill *et al.* 2010 and Naden *et al.* 2010 both noted the occurrence of a felsic intrusion situated within 1 km of the veins (Fig. 3.29.).

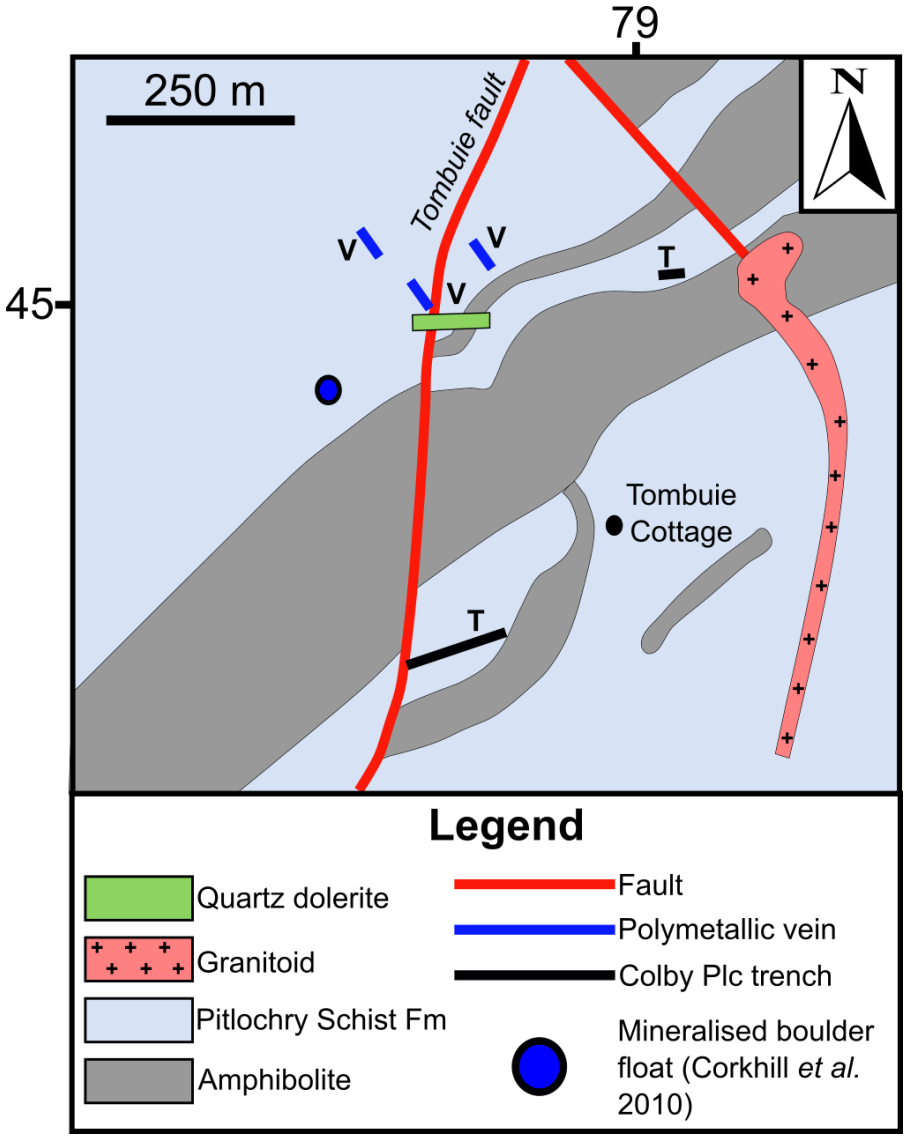

Figure 3.29. Geological map of the mineralisation at Tombuie annotated with the locations of veins, trenches dug by Colby Gold plc, and mineralised boulder float. Adapted from Corkhill *et al.* 2010 and Treagus (2000).

The average grade recorded from the veins at Tombuie (Fig. 3.29.) was 2 g/t, although some grab samples returned values of 29 g/t (Ixer *et al.*, 1997). Tombuie has been compared to the Creede deposit (Colorado, USA; Corkhill *et al.*, 2010), which is of the low sulphidation epithermal variety (Hayba, 1997; Table 2.1.). Corkhill *et al.* 2010 also noted many similarities between the Tombuie and CUB veins, in terms of paragenesis, mineralogy, strike and the occurrence of mercurian electrum (Ixer *et al.*, 1997). Corkhill *et al.* 2010 also described the occurrence of a 2 mm wide molybdenite veinlet, which carried rutile.

3.6.1.c. Lead Trial and Ardtalnaig

As mentioned in Chapter 1, the prospect known as Lead Trial (Fig. 3.13., Locality 6) refers to a 19th century artisanal lead mining operation situated on the SE margin of Loch Tay, close to Tomnadashan (Fig. 3.13., Locality 5). However, it is important to highlight the distinction between the localities around Lead Trial and the 'Lead Trial' itself, which refers to a NW-SE trending polymetallic vein that crosscuts the Southern Highland Group and Siluro-Devonian granitoids (Fig. 3.13.), as well as the disused tips immediately adjacent to this vein. On the other hand, several pieces of mineralised boulder float (ARD_1 and RX2959KA; Fig. 3.13., Localities 6 and 7) closer to the Ardtalnaig Burn have also been sampled as part of this study and by Green Glen Minerals (e.g. the RX2959KA sample shown in Fig. 3.30.). Finally, detrital gold has been retrieved via panning material from both Lead Trial and the Ardtalnaig Burn (Fig. 3.25.); these samples were analysed by several researchers (Chapman *et al.*, 2023; Webb *et al.*, 2023; Savastano, 2024). Gold particles in this region contain inclusions of sphalerite, galena, pyrite, chalcopyrite, molybdenite, and bismuth tellurides (Webb *et al.*, 2023).

Figure 3.30. The RX2959KA sample collected and photographed by Green Glen Minerals (Fig. 3.13., Locality 6). The sample is comprised of coarse-grained galena infilling vuggy quartz.

In recent years, Lead Trial has been the main target for gold exploration by Green Glen Minerals in the Study Area (Green Glen Minerals, 2021); several boreholes were drilled in 2021 (EGR-001, EGR-002, EGR-003, EGR-004, EGR-005, and EGR-006). The best result from this exploration campaign came from EGR-002, in which 4.44 g/t Au was recorded over an interval of drill core measuring 1.65 m (Green Glen Minerals, 2021). At the time of writing, Green Glen Minerals are waiting for a new long-term agreement to be forged with the landowners before further exploration can proceed.

3.6.1.d. Tomnadashan

This abandoned copper mine, which is adjacent to the LTF (Fig. 3.31.), was developed by the 5th Earl of Breadalbane in the 19th century. Extraction began in 1840 and continued for twenty years, with pyritic and cupriferous ores being targeted (Devéria, 2001). Historical records clearly show that the ore minerals were taken by artisanal miners to a smelter 400 m to the NW (NN 687 377) of the mine (Devéria, 2001; Smith *et al.*, 2022). The locations of the smelter and disused tips are depicted on Fig. 3.31.

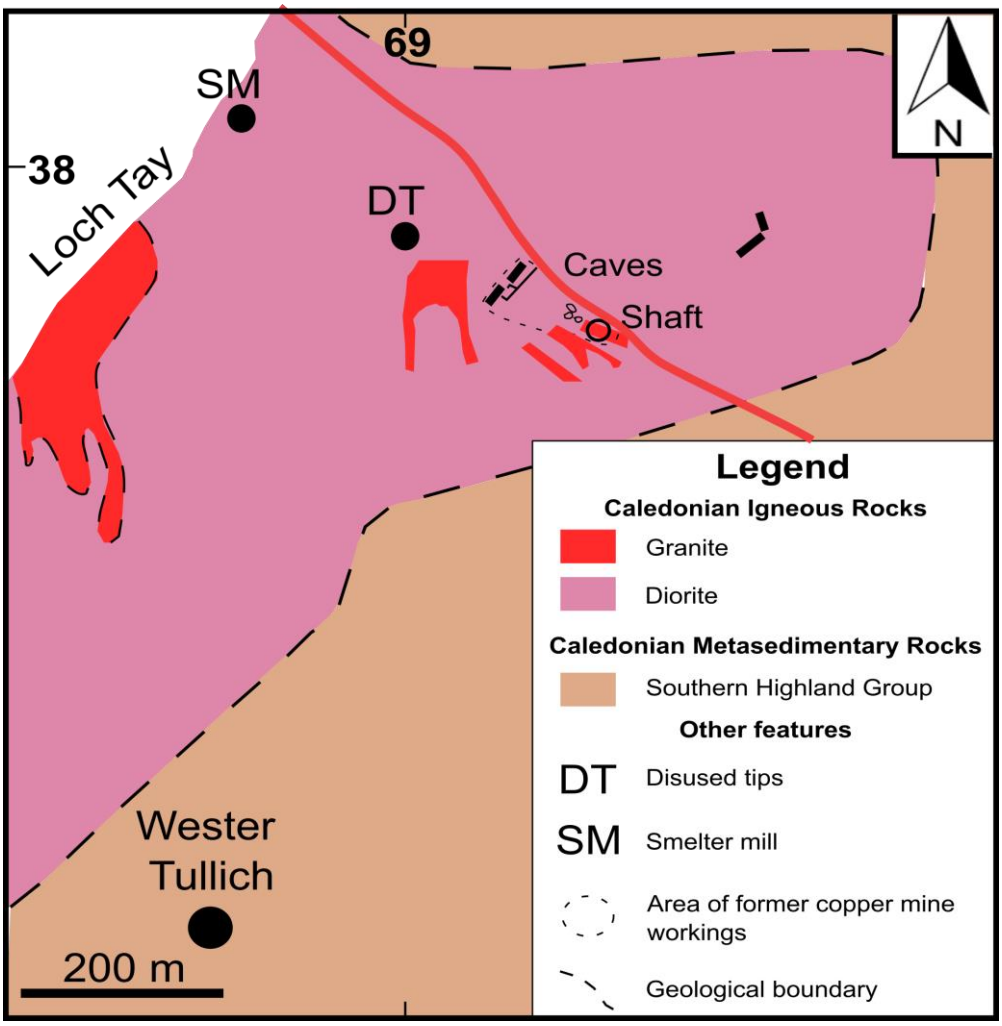

Figure 3.31. Geological map of Tomnadashan, demonstrating that the porphyry is comprised of diorite and granite. The locations of the disused tips and artisanal smelter mill (i.e. the sampling locality for TOM_MOLY_SM; Appendix A) are clearly marked. Adapted from Pattrick (1984), Smith *et al.* 2022, and Webb *et al.* 2024b.

Many of the pre-existing publications on Tomnadashan describe the mineralisation as belonging to the 'Cu-Mo porphyry' category of mineral deposits (Pattrick, 1984; Smith *et al.,* 2022). This classification is invoked on the basis of the mineralogy (Table 3.6.), which is typical of Cu-Mo porphyries globally (Berger *et al.*, 2008; Sillitoe, 2010). Some of the mineralisation is disseminated within the host pluton (Fig. 3.30); however, most of the mineralisation is concentrated along a NW-SE trending fault between diorite and granodiorite within the mine (Smith, 1996). Henwood (1871) described how two lodes 15-100 cm wide trending E-W and NW-SE were targeted during mining; the E-W trending lode is offset by the NW-SE trending lode. Furthermore, the intersection between the lodes is heavily mineralised (Henwood, 1871).

Stage	Description
1	Pyrite + molybdenite + bismuthinite inclusions, tennantite, aikinite and hodrushite
2	Chalcopyrite + galena + native bismuth + tetrahedrite

Table 3.6. The two paragenetic stages of mineralisation recognised at Tomnadashan by Pattrick (1984) and Smith *et al.* 2022.

Geologically, the mine is situated within a composite igneous intrusion comprised of diorite, granodiorite, and granite (Pattrick, 1984). Regarding the petrological characteristics of the host rocks, Naden *et al.* 2010 described the diorite as being fine-grained with large quantities of amphibole crystals, whilst the granite was noted to have a porphyritic texture; feldspars form coarse phenocrysts in a finer groundmass comprised of quartz and biotite.

Tomnadashan has been the focus of several exploration campaigns since the 1960s (Naden *et al.*, 2010; Smith *et al.*, 2022). Gold and silver grades of 1.58 g/t and 200 g/t have been recorded (Smith *et al.*, 2022). There are 19 different mineral species at Tomnadashan (Smith *et al.*, 2022); the paragenetic relations of these phases (Table 3.6.) were previously inferred by using the law of cross-cutting relationships. Pyrite crystals are cross-cut by veinlets containing chalcopyrite, bismuth minerals, galena, and Cu-Bi sulfosalts (Naden *et al.*, 2010). A transition from a tennantite to a tetrahedrite-bearing assemblage (Table 3.6.) is interpreted to reflect a fall in temperature from 500 °C to 390 °C, which favoured the substitution of Sb over As (Smith *et al.*, 2022).

Regarding the alteration assemblages at Tomnadashan, descriptions in the published literature are limited (Pattrick, 1984; Smith and Highton, 2022). Smith (1996) noted that potassic alteration zones demarcate the granitic lenses, whilst patches of propylitic alteration can be found throughout the entire intrusion (Smith, 1996). Pattrick (1984) suggested that hydrothermal alteration at Tomnadashan was limited to the immediate vicinity of the porphyry. For this reason, Pattrick (1984) considered Tomnadashan to represent a localised hydrothermal system that was unrelated to the mineralisation processes at Coire Buidhe (Fig. 3.13., Locality 10).

Moorbath (1962) calculated a model age for the galena from Tomnadashan of 530 ± 60 Ma using Pb isotope values. However, the Holmes (1946) model for Pb evolution that was used by Moorbath (1962) has since been demonstrated to yield inaccurate ages (Stacey and Kramers, 1975; Zartman and Doe, 1981; Huston and Champion, 2023). Regardless, the data in Moorbath (1962) were used to calculate the $^{206}Pb/^{204}Pb$ and $^{207}Pb/^{204}Pb$ ratios of galena from Tomnadashan (17.6 and 15.3, respectively; Moorbath, 1962; Webb *et al.*, 2024b); these values are displayed alongside the Pb analyses from the present study (Chapter 5). Some limited $\delta^{34}S$ work has also been done on pyrite samples from Tomnadashan; mean $\delta^{34}S$ values of +0.5 and +2.0 ‰ were described from the porphyry and plutonics, respectively (Lowry *et al.*, 2005). These results were considered to be within the expected range of 'Lower Caledonian porphyries' (Lowry *et al.*, 2005; Fig. 3.21.).

3.6.1.e. Coire Buidhe

Silver grades of 600 oz Ag/ton of lead ore have been reported from this 19th century mine (Fig. 3.13., Locality 9; Pattrick, 1984), which is situated at the peak of Meall nan Oighreag (Fig. 3.32.a.). To the south of Coire Buidhe (Fig. 3.13.), there is a large granitoid. Naden *et al.* 2010 also referred to the presence of felsite and quartz-dolerite dykes in the vicinity of the mine at Coire Buidhe but did not give specific information regarding their location. The veins are hosted within flat-lying metalimestones and calcareous schists that belong to the dolomitised portions of the Loch Tay Limestone Formation (Section 3.4.1.; Pattrick, 1984), which is brown in colour (Naden *et al.*, 2010). The Loch Tay Limestone Formation was brecciated and silicified during the veining event; pyrrhotite mineralisation is concentrated within the host rocks, with limited quantities of this phase occurring within the veins (Naden *et al.*, 2010). Furthermore, the sulphide mineralisation is absent in the non-calcareous schists (Naden *et al.*, 2010).

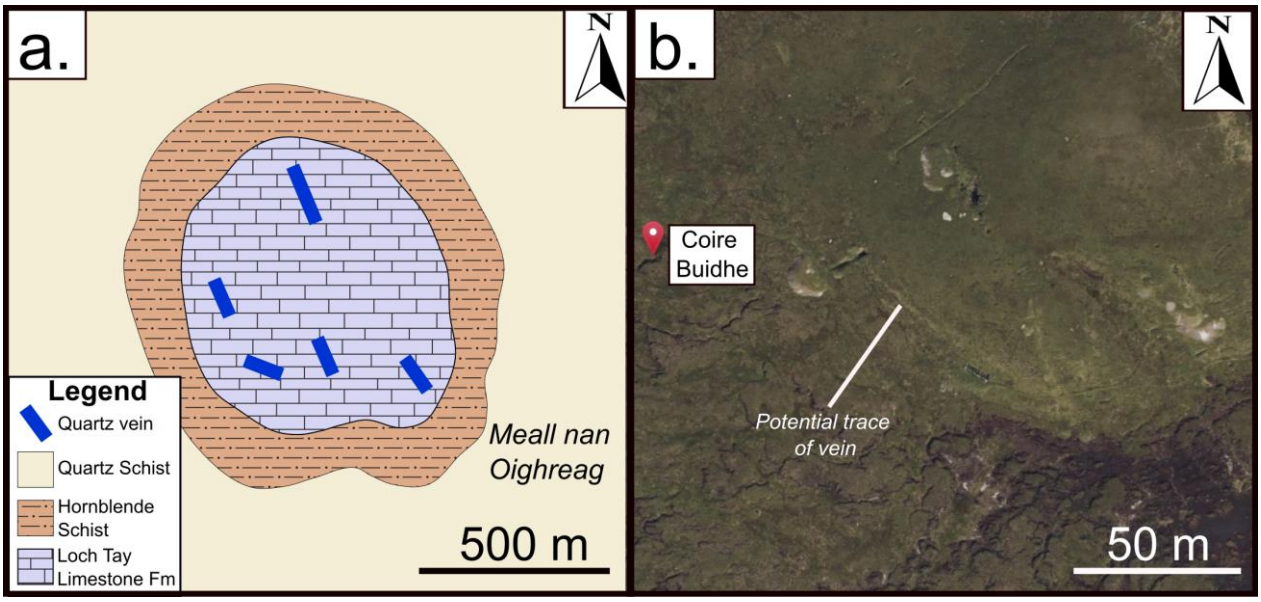

Figure 3.32. Maps of Coire Buidhe (Fig. 3.13., Locality 10). **a.** Geological map of the mine at Coire Buidhe (adapted from Pattrick, 1984). **b.** Satellite image of the mine and disused tips (Google Maps, 2024).

In terms of the mineralogy, Naden *et al.* 2010 summarised the ore minerals at Coire Buidhe as galena, electrum, pyrrhotite, pyrite, chalcopyrite, sulfosalts, and bismuth minerals (Table 3.4.). There is scant information regarding the gold at this locality in the published literature, although Wilson and Cadell (1884) referred to two small 'nuggets' found within the disused tips (Fig. 3.32.b.). Electrum is also hosted in fractured galena crystals (Pattrick, 1984). The galena occurs in mineral assemblages with pyrrhotite and Pb-Bi-Ag sulfosalts (Pattrick, 1984). Regarding other phases at Coire Buidhe, Naden *et al.* 2010 noted the presence of quartz, carbonate, and siderite.

At the base of Meall nan Oighreag, there is an additional working (i.e. distinct from Coire Buidhe, which occurs at the peak of Meall nan Oighreag) that has not been named in the literature, termed 'Spoil Heap' in this study (Fig. 3.13., Locality 8). Green Glen Minerals collected a grab sample of mineralised quartz from this locality (Fig. 3.33.), which yielded Au grades of 7 g/t (Green Glen Minerals, 2021). From the satellite image (Fig. 3.33.), it is also possible to discern a NW-SE trend of the vein that may have been worked by the artisanal miners.

Figure 3.33. Satellite imagery (Google Maps, 2024) of Spoil Heap (Fig. 3.13.; Locality 9) annotated with the orientation of the vein (demarcated by the trench). See Appendix A for the Grid Reference.

3.6.1.f. Glen Almond

The Glen Almond Vein (GAV; Fig. 3.13., Locality 10) was discovered by researchers from the University of Leeds and Green Glen Minerals (Webb *et al.*, 2024a). This vein, which also trends NW-SE (Table 3.4.; Fig. 3.13.), has been characterised as part of the present study and was the focus of a recent publication (Webb *et al.*, 2024a); the GAV is therefore described in more detail in Chapter 5. Mineralogically, the GAV is mostly comprised of quartz, siderite, pyrite, chalcopyrite, and galena, with sphalerite and electrum being minor phases (Webb *et al.*, 2024a).

3.6.1.g. Comrie Pluton

The Comrie Pluton has been explored by multiple companies since the 1960s (Naden *et al.*, 2010). One grab sample recorded 90 ppm Au, and a panned concentrate contained 100 ppm Au; furthermore, three 1 m channel samples had a maximum grade of 1.43 ppm Au (Naden *et al.*, 2010). Separate drilling and blasting campaigns produced rock samples containing multiple pyrite generations and chalcopyrite; sulphide mineralisation frequently occurs in miarolitic cavities (Naden *et al.*, 2010). Colby Gold plc found pathfinder elements similar to Lead Trial at this locality (e.g. Ba, Zn, Sb, Hg) throughout the alteration zone that extends to the south of the granite. Naden *et al.* 2010 described the mineralisation at Milton Burn (which occurs within the Comrie Pluton; Naden *et al*., 2010; Fig. 3.14.) as brecciated quartz and carbonate veins situated within a shear zone trending N-S. Fluid flow appears to have been extensive, with some veins being <3 m in length. Veinlets, disseminated mineralisation, and potassic alteration were also recognised (Naden *et al.*, 2010).

Previous $\delta^{34}S$ isotope studies have been conducted on the mineralisation within the Comrie Pluton; for example, Lowry *et al.* 2005 derived a mean $\delta^{34}S$ value of +4.5 ‰ (based on five measurements) from pyrite crystals at this locality. However, it is unknown which portion of the Comrie Pluton (e.g. the igneous subdivisions in Fig. 3.14.) these measurements originally came from. Nonetheless, Lowry *et al.* 2005 considered the sulphur isotope profile of the Comrie Pluton to be typical of 'Lower Caledonian plutonics' (Fig. 3.21.).

3.6.2. Other occurrences of mineralisation in the Study Area

As mentioned in the introduction to Section 3.6., Foss and Fortingall were not characterised by vein petrography or isotope geochemistry in this study, although it is important to summarise their previously known characteristics for the wider context of the interpretation and discussion that are presented in Chapters 6 and 7.

3.6.2.a. Foss and Duntanlich mines

The Foss and Duntanlich barytes deposits represent SEDEX mineralisation (Table 3.4), a category of mineral deposit that is frequently described in the published literature on ore deposits (Emsbo, 2000; Leach *et al.*, 2005; Sangster, 2018); however, it is important to emphasise that the SEDEX deposits around Loch Tay formed during the Neoproterozoic (Moles and Selby, 2022) and are therefore much older than the LTVS (Fig. 3.13.). SEDEX mineralisation is associated with the venting of hydrothermal fluids onto the seafloor (Fig. 3.34.). A key aspect of this genetic model involves stratified seawater overlying a sedimentary basin with varying topography, which resulted in the simultaneous deposition of barytes in shallow and deep-water portions of the sedimentary basin (Fig. 3.34.). The variable topography (Fig. 3.34.) was caused by normal faulting, which occurred in response to extensional tectonics during the deposition of the Argyll and

Southern Highland groups (Moles *et al.*, 2014). Finally, variations in the Pb-Zn content of the barytes horizons are associated with the occurrence of a brine pool that was situated away from the main vent; experimental evidence indicates that SEDEX brines are denser than seawater and upon being discharged at the vent, they flow along the seafloor and accumulate in topographic depressions (Fig. 3.34.; Sangster, 2001). At Cononish, Neoproterozoic SEDEX horizons have been implicated as a source of base metals, although only in the later paragenetic stages (i.e. pyrite from Stage 4 of the paragenesis; Fig. 3.20.; Spence-Jones *et al.*, 2018).

These barytes deposits, which continue along strike for >25 km, have estimated reserves of >20 million tonnes (Moles *et al.*, 2014). Only 1 million tonnes have been extracted since Foss opened in 1984 and further operations are planned at Duntanlich (Moles *et al.*, 2014). Pyrite from the Foss and Duntanlich barytes horizons, which are <100 m apart within the wider stratigraphic sequence, yielded Re-Os ages of 604.0 ± 7.2 Ma and 612.1 ± 18.6 Ma (Moles and Selby, 2023). The barytes horizons have been stratigraphically correlated with similar occurrences of mineralisation in Scotland and NW Ireland (Moles *et al.*, 2014).

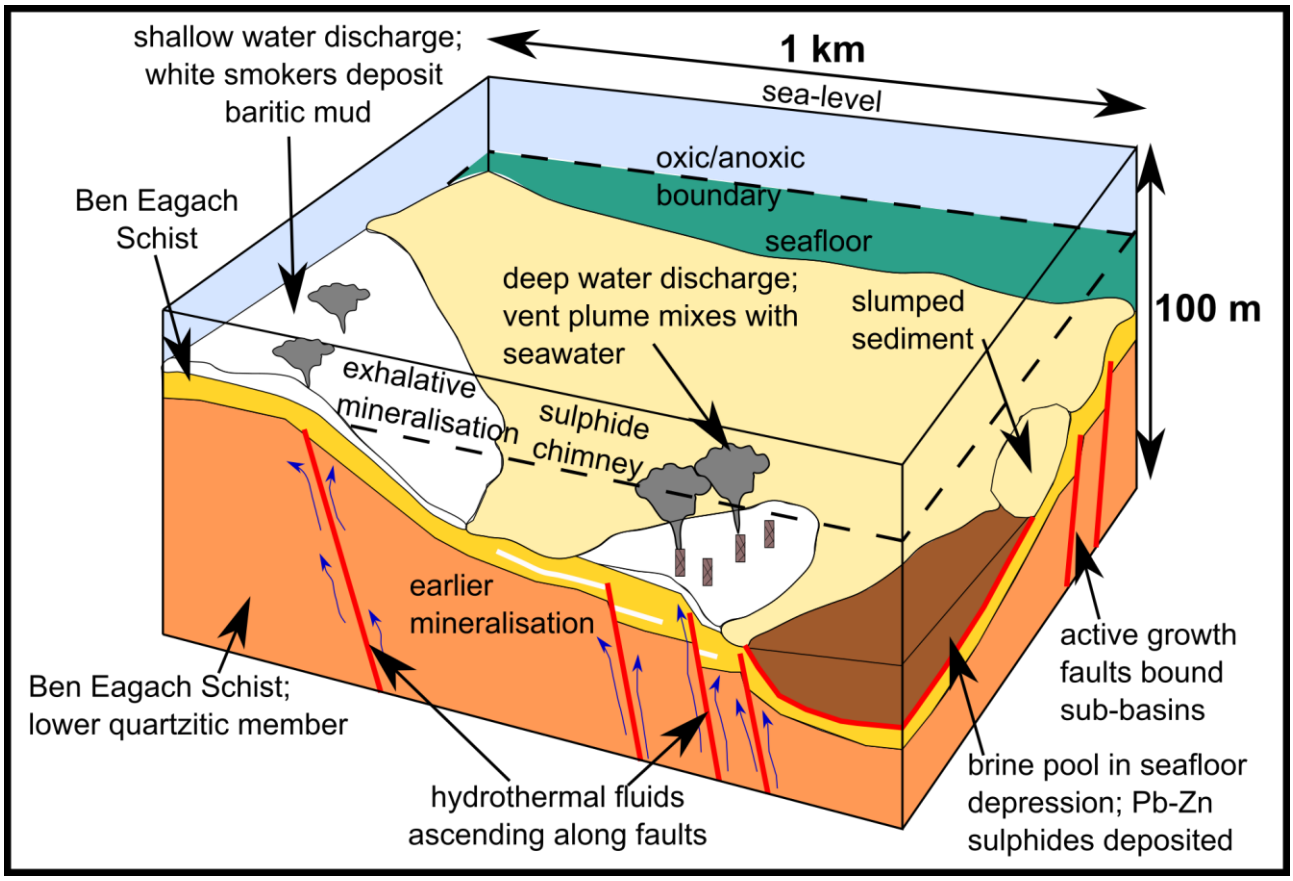

Figure 3.34. The genetic model for the Foss and Duntanlich barytes deposits (adapted from Moles *et al.*, 2014).

3.6.2.b. Fortingall

This locality (Fig. 3.13.; Locality 2) is notable for hosting an outcrop of the LTF (Treagus, 2003); however, some previous publications have referred to metallic mineralisation at Fortingall. For example, Treagus (2000) described how NW-SE trending veins are hosted within the Pitlochry Schist Formation; mineralisation has infilled joints and faults (with strike values of 180 °) in the Loch Tay Limestone Formation and the Dalradian metabasics (Treagus, 2003; Naden *et al.*, 2010). Regarding the metallic phases present, the mineralogical assemblages are predominantly comprised of pyrite, pyrrhotite, and arsenopyrite (Treagus, 2000). The fracture-hosted mineralisation also contains galena veinlets (1-5 mm thick) that may represent a later paragenetic stage (Treagus, 2000). However, it is important to emphasise that the descriptions of paragenetic relationships at Fortingall are not supported by high-quality petrographic imagery (Treagus, 2000); nonetheless, the main stage of mineralisation reportedly involved the precipitation of sphalerite with chalcopyrite inclusions, prior to the injection of the quartz ± carbonate veinlets that contain galena (Treagus, 2000). Whilst granitoids around Fortingall are not visible on the geological map, Treagus (2000) noted the presence of felsites in the vicinity of the veins. These felsites hosted pods of pyrite (0.1 to 0.3 cm wide) and contained minor quantities of disseminated chalcopyrite (Treagus, 2000).

3.6.3. Fluid inclusion studies on the LTVS

Several fluid inclusion studies have been conducted on the LTVS by Smith (1996), Ixer *et al.* 1997, and Naden *et al.* 2010. As part of a wider study on the sources of metalliferous fluids in the Grampian Terrane of Scotland, Naden *et al.* 2010 compiled the previous fluid inclusion studies from the LTVS localities using the PhD thesis of Smith (1996) and the limited amount of data produced by Ixer *et al.* 1997. However, a major caveat hindering the utility of this fluid inclusion data is the lack of paragenetic context. Nonetheless, the conclusions and metallogenic implications of previous fluid inclusion studies are explored in this subsection. Naden *et al.* 2010 considered the fluid inclusion populations from the Calliachar Burn and Tombuie to be similar, given their comparable temperature ranges, and classified both occurrences of mineralisation as ‘Au-quartz’ veins with a similar genetic link. Although the fluid inclusion temperatures from Coire Buidhe are comparable to those recorded from the Calliachar Burn and Tombuie (Table 3.7.), Naden *et al.* 2010 considered Coire Buidhe to represent a different style of mineralisation termed ‘Pb-Zn ± Au’; the reasons behind this decision are unclear.

Calliachar-Urlar Burn veins		
Type	**Description**	**Reference**
1	Aqueocarbonic, homogenisation temperatures of 300 °C, salinities 4-8 wt % NaCl; more common in the Urlar Burn; trace CH_4C00_3 and N_2	(Smith, 1996; Ixer *et al.*, 1997; Naden *et al.*, 2010)
2	Primary/secondary, aqueocarbonic tri-phase inclusions (L_{aq} + LCO_2 + VCO_2); homogenisation temperatures of 225-245 °C; 1.4-4.3 wt % NaCl; Sodic brine	
3	Two phase (L_{aq} + V) 120-270 °C homogenisation temperatures; the salinity is 2-13 wt % NaCl with an average of 8 wt % NaCl	
4	Pseudosecondary/secondary L_{aq} + V inclusions; homogenisation temperatures of 91-175°C; salinities of 10.2-13.7 wt % NaCl; Ca/Mg cation in the brine	
Tombuie		
Type	**Description**	**Reference**
1	CO_2 rich inclusions with other volatiles are present; these inclusions are also saline (3.3-15 wt % NaCl) and described as sodi-potassic brines	(Smith 1996; Naden *et al.*, 2010)
2	Aqueocarbonic inclusions with minimal CO_2	
3	Aqueous, CO_2 free brines with homogenisation temperatures between 120 and 425 °C and salinities of 3-14 wt % NaCl	
Tomnadashan		
Type	**Description**	**Reference**
1	Aqueocarbonic inclusions with homogenisation temperatures >350°C	(Smith, 1996; Naden *et al.*, 2010)
2	Liquid vapour inclusions (>300 °C) containing multisolids (halite and sylvite)	
3	Biphase aqueous inclusions; 110-250 °C, 5-10 wt % NaCl	
Coire Buidhe		
Type	**Description**	**Reference**
1	Aqueocarbonic inclusions with homogenisation temperatures >350 °C	(Naden *et al.*, 2010)
2	Liquid vapour inclusions (>300 °C) containing multisolids (halite and sylvite)	
3	Biphase aqueous inclusions; 110-250 °C, 5-10 wt % NaCl	
Comrie Pluton		
Type	**Description**	**Reference**
1	Myrmekitic microgranite with quartz veinlets; contains high salinity (35 wt % NaCl), high temperature (>300 °C) secondary inclusions	(Naden *et al.*, 2010)

Table 3.7. Summary of previous fluid inclusion studies on different localities within the LTVS and the Comrie Pluton. Different types of fluid inclusion populations have been discovered at each locality, although they all pertain to vein quartz.

It is important to note that Naden *et al.* 2010 also provided interpretations for the different populations in fluid inclusions throughout the Grampian Terrane; the LTVS was also discussed within the context of these interpretations (Table 3.8.). For example, Naden *et al.* 2010 noted that Tomnadashan and the Comrie Pluton have very similar fluid inclusion populations (Table 3.7.; Table 3.8.). The high salinities and temperatures were used to support a magmatic origin (Naden *et al.*, 2010). Furthermore, it is notable that a variety of fluid inclusion types occur at several localities in the LTVS (Table 3.7.); it is uncertain as to whether these contrasts in fluid inclusion data relate to fluid evolution or the mixing of other fluid sources throughout the parageneses. For example, Ixer *et al.* 1997 suggested that the range in fluid inclusion populations recorded from the CUB veins was the result of much hotter mineralising fluids mixing with meteoric fluids during the mineralisation processes. However, there is no further evidence to support this interpretation.

Type	Description	Fluid source	Examples
1	High salinity (> 35 wt % NaCl), high temperature (> 300 °C); interpreted to have introduced gold and base metals into the Grampian Terrane	Magmatic or prograde metamorphism	Lagalochan, **Tomnadashan**, **Comrie Pluton**
2	High temperature (250-400 °C), moderate salinity (7-10 wt %), volatile-rich (CO_2+CH_4+N_2, 15–25 wt % NaCl); may or may not occur within auriferous veins		Arrochar Complex
3	Moderate to high temperature (200-350 °C), moderate salinity (7-10 wt %), contains volatiles (minor CO_2+CH_4+N_2, 10-15 wt %)	Unknown; cooler equivalent of Types 1 and 2	**Calliachar Burn**
4	Low to moderate temperatures (150-250 °C), low salinity brines (<10 wt % NaCl) with negligible volatile component; occurs in sphalerite	Magmatic-hydrothermal fluids emanating from intrusions	Stronchullin
5	Low temperature (<150 °C), high salinity (20 wt % NaCl) brines	MVT basinal brines	Stronchullin, Curraghinalt, **Coire Buidhe**,
6	Aqueous monophase fluid inclusions	Unknown; low temperature equivalent of Types 4 or 5	N/A

Table 3.8. Summary of the different categories of fluid inclusion populations recognised by Naden *et al.* 2010 throughout the Grampian Terrane. Bold text pertains to examples where Naden *et al.* 2010 have classified the LTVS fluid inclusion populations (Table 3.7.).

3.7. Research questions, hypotheses and aims

Based on the studies that have previously been described, it is clear that whilst some of the auriferous veins in the Grampian Terrane have been well characterised in terms of their metallogeny, this is not the case for the LTVS. There is considerable uncertainty regarding the ages of mineralisation and magmatism, as well as the source and conditions of the mineralising fluids locally; the existence of a detailed understanding regarding the parageneses of several veins in the LTVS is similarly lacking.

However, the results of previous metallogenic studies on auriferous veins throughout the Grampian Terrane may have potential implications for the metallogeny of the LTVS. For example, in Scotland, gold mineralisation at Cononish (Section 3.5.2.c.) and the Rhynie Chert (Section 3.5.2.d.) is genetically linked to magmatism (Mark *et al.*, 2011; Rice *et al.*, 2012; Hill *et al.*, 2013; Spence-Jones *et al.*, 2018). Furthermore, the genetic model postulated by Ixer *et al.* 1997 for the CUB veins involved deeply sourced magmatic or mantle-derived mineralising fluids. The results from investigations into the mineralisation at Tomnadashan (Pattrick, 1984) and Tombuie (Corkhill *et al.*, 2010), which also invoked magmatic processes, may indicate that the LTVS is a magmatic-hydrothermal mineralising system. However, the discovery of 'orogenic' gold particles by Chapman *et al.* 2023 from the LTVS could be evidence that a variety of fluid and metal sources have been involved in the mineralisation. It is also important to emphasise that several studies on gold metallogeny throughout the Grampian Terrane have invoked fluid mixing in the genetic model; for example, the mixing of magmatic and crustal sources of sulphur at Cononish (Hill *et al.*, 2013; Spence-Jones *et al.*, 2018), or the mixing between a magmatic fluid and meteoric waters at the CUB veins (Ixer *et al.*, 1997). Collectively, it has been possible to consider the results from previous investigations into Grampian metallogeny (including those that are relevant locally to the LTVS) and formulate a series of research questions (Table 3.9.) and hypotheses (Table 3.10.) for the present study.

No.	Research question	Objective
1	*How old is the mineralisation in the LTVS?*	Produce radiometric dates for some of the mineralisation in the LTVS using geochronology (e.g. Re-Os dating on molybdenite from Tomnadashan; Section 2.8.1.)
2	*How old is the magmatism associated with LTVS?*	Produce radiometric dates for the granitoids around Loch Tay using geochronology (e.g. U-Pb dating of zircons via CA-ID-TIMS; Section 2.8.2.)
3	*How did the veins in the LTVS (particularly regarding the mineralisation) evolve over time?*	Create paragenetic interpretations for several veins within the LTVS using reflected light microscopy (RLM) and SEM; Webb *et al.* 2024a).
4	*What is the source of the ore-forming fluids in the LTVS?*	Use sulphur (Section 2.8.3.) and lead (Section 2.8.4.) isotopes to evaluate the potential sources of sulphur and lead in the LTVS

Table 3.9. A list of research questions that were investigated throughout the duration of this study.

No.	Hypothesis	Rationale
1	*'Mineralisation in the LTVS is genetically related to Late-Caledonian magmatism'*	The literature review demonstrated that Scottish gold deposits are often associated with magmatism (i.e. dated intrusions in the Grampian Terrane are coeval with existing mineralisation dates at Rhynie and Cononish); this is also likely to be the case in the LTVS.
2	*'Veins throughout the LTVS have a variety of metal and fluid sources'*	Published data from elsewhere have often revealed that auriferous veins have a diverse range of fluid and metal sources (Standish *et al.*, 2014; Mortensen *et al.*, 2022; Quesnel *et al.*, 2023)
3	*'Several mineralisation events have occurred in the LTVS'*	The interpretation of different mineralising fluids in the LTVS (Chapman *et al.*, 2023) may suggest that multiple mineralisation events have infilled the same structures.

Table 3.10. Hypotheses that were formulated at the outset of this study.

Chapter 4: Methodologies

4.1. Introduction

In this chapter, the methodologies utilised in answering the research questions of this study (Table 3.9.) are summarised. Given the importance of paragenetic context in the evaluation of the geochronological and stable isotope datasets (Table 4.1.), a detailed description of the methodology for establishing the paragenesis of a hydrothermal vein (adapted from Webb *et al.* 2024a) is provided here. Furthermore, details regarding the approach to fieldwork and sample collection are explained in this chapter.

4.2. Understanding and interpreting the 'paragenesis' of a hydrothermal vein

To answer Research Question 3 (Table 3.9.) and provide a context in which to interpret the isotope datasets from this study, it was necessary to develop paragenetic interpretations for several of the LTVS localities. The term 'paragenesis' is defined as the 'association of minerals in rocks and rock suites in relation to their origin' (Bowes, 1989). In economic geology, paragenetic studies typically involve constraining the relative order in which the phases comprising a hydrothermal vein formed (Kamilli, 1998). There are several processes by which phases can form in a vein or rock; for example, during a singular and gradual crystallisation episode (e.g. fractional crystallisation), or as a result of repeated fluid injections interspersed by periods in which no crystallisation occurs. Phases may also form as a result of the continuous evolution of a rock during metamorphism. Alternatively, a combination of these processes over time may be responsible for phase precipitation (Webb *et al.*, 2024a).

The objective of conducting paragenetic studies on hydrothermal veins is to constrain the context of phases within the overall evolution or development of the vein, which may ultimately direct further analyses and data interpretation. During the formation of a hydrothermal vein, precipitation occurs at different times (during repeated fluid flow episodes, or gradually over time) because of changes in the pore fluid pressure, composition, and temperature of a hydrothermal fluid; furthermore, these processes are not necessarily exclusive and a combination of them may result in temporally separated precipitation events. Developing an understanding of the paragenesis of a given hydrothermal vein has several applications; for example, paragenetic studies may lead to an understanding of the typical phases associated with metals (e.g. gold). Furthermore, paragenetic investigations can enable specific episodes of hydrothermal fluid flow to be correlated with distinct mineralogical assemblages of commercial interest. Both of these outcomes from paragenetic studies may be used to create strategies for subsequent mineral exploration programmes (Webb *et al.*, 2024a).

When deciding on the number of samples required for a paragenetic study, this depends on the study aims and the nature of the overall investigation; however, care should be taken to select samples that are representative (Webb *et al.*, 2024a). Fundamentally, most paragenetic investigations are limited by the small number of observations that can be made relative to the overall size of the system being investigated; hydrothermal veins can be several kilometres long, whereas paragenetic studies only capture information from approximately 100 cm^2 (at most) of the mineralisation (i.e. the total amount of the vein that is observed during petrography; Webb *et al.*, 2024a). Should structural interpretations be necessary (for example, the interpretation of fabrics using transmitted light, or crystallographic studies involving Electron Backscatter Diffraction), it is recommended that the samples chosen for analysis are as representative as possible (Webb *et al.*, 2024a). Provided that a systematic and reproducible procedure is implemented when characterising the sample prior to analysis (i.e. to constrain aspects of the system deemed to be representative), then the resulting paragenetic interpretations are likely to be robust (Webb *et al.*, 2024a). For this reason, it is essential to make detailed observations regarding the mineralogy of the veins, rock textures, and relevant geological structures; it is also important to properly document any localised anisotropic variations (for example, crystal zonation; Webb *et al.*, 2024a).

A more detailed description of the recommended approach for textural mapping is provided in Webb *et al.* 2024a, although here, the broad principles are described. Focusing on the law of cross-cutting relationships (Steno, 1669) is always preferable because this is the most powerful indicator of relative age (Fig. 4.1.a.; Webb *et al.*, 2024a). The law of included fragments can also be informative in this regard; for example, in Fig. 4.1.b., the garnet has grown around and enclosed the younger feldspar crystals. However, in hydrothermal systems, inclusions typically arise as a result of coprecipitation (Imai, 1999; Webb *et al.*, 2024a). Another potentially important indicator of paragenetic relations is alteration, defined here as a phase in a rock being completely or partially replaced by another phase due to chemical reactions between the original phase and an ambient hydrous or carbonitic fluid phase (Schwartz, 1959; Mathieu, 2018; Webb *et al.*, 2024a). Alteration textures are particularly common in rocks proximal to magmatic intrusions that contain a significant vapour phase, and within and around hydrothermal vein systems (Hu *et al.*, 2014; Fougerouse *et al.*, 2016; Zhu *et al.*, 2021; Webb *et al.*, 2024a).

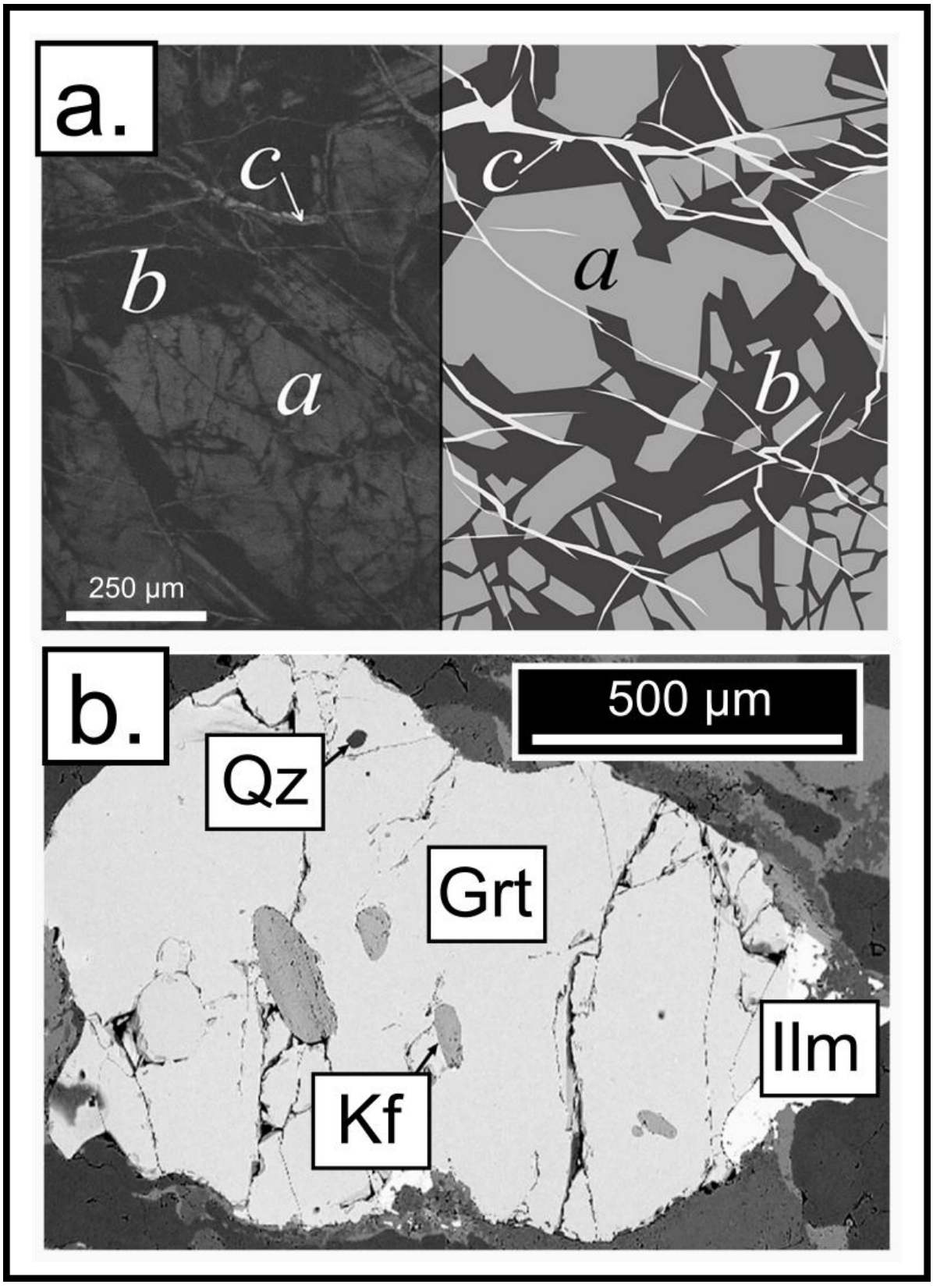

Figure 4.1. Examples of textures typically used to interpret paragenesis (adapted from Webb *et al.*, 2024a). **a.** The law of crosscutting relationships is illustrated by an SEM-CL image (left) and a line drawing (right) of three different quartz generations (the alphabetical order of each generation corresponds to relative timing, e.g. *b* formed before *c*). **b.** K-feldspar and quartz inclusion within a garnet crystal from a metamorphic rock, with the garnet representing the younger, enclosing phase.

There are often challenges regarding the interpretation of textural relationships during paragenetic studies; for example, applying the law of cross-cutting relationships or the law of included fragments is not always straightforward. In dynamically crystallising systems and in systems where the fluid composition is in a constant state of flux, phases may coprecipitate sequentially. This can result in the misleading impression that mineral inclusions represent a prior mineralisation event (Webb *et al.*, 2024a). Exsolution textures can further complicate the interpretation of mineral inclusions; in the case of the so-called 'chalcopyrite disease', in which chalcopyrite manifests itself as intergrowths within sphalerite (Eldridge *et al.*, 1988; Bortnikov *et al.*, 1991), the inclusions may be coeval (i.e. they do not represent a prior mineralisation event; Webb *et al.*, 2024a). The law of crosscutting relationships, which is the most powerful paragenetic criterion (Webb *et al.*, 2024a), is also subject to problems associated with evolving fluid compositions and the physiochemical conditions of precipitation. Pyrite typically precipitates from hydrothermal solutions faster than other phases; however, pyrite can also experience both brittle and ductile deformation over a range of P-T conditions. For example, pyrite often fractures due to thermal expansion associated with depressurisation (Cox *et al.*, 1981; Liu *et al.*, 2010), which is a typical process during the formation of hydrothermal veins. However, it is important to note that depressurisation is often a much later process, even if it occurs as part of the same continuous event. These fractures may be infilled with other phases (gold, other sulphides) throughout the same ongoing event; this can result in the incorrect interpretation that the cross-cutting relationship has developed as a result of a later fluid injection.

Another texture frequently used to support paragenetic interpretations is euhedral crystal morphology, which is hypothesised to develop during the early paragenetic stages of an orebody (i.e. when there is more space for crystal growth; Wilson, 1994; Ahmed *et al.*, 2009). The growth of later paragenetic stages is constrained by the presence of the early euhedral crystals; subsequent phases must grow around them, leading to anhedral morphologies (Webb *et al.*, 2024a). However, during the development of a hydrothermal vein, the injection of later fluids can result in dissolution and vug formation, creating the cavities necessary to promote euhedral crystal growth in the later paragenetic stages (Webb *et al.*, 2024a). Furthermore, phases with very high surface energies (e.g. garnet, pyrite) usually form euhedral crystals. This means that the growth of coprecipitating phases is constrained, and the crystals develop anhedral morphologies (Carstens, 1986; Arrouvel and Eon, 2019). In such circumstances, euhedral growth may not be informative of paragenetic relationships (Webb *et al.*, 2024a).

4.3. Sample collection

A detailed list of the localities and their geographical coordinates can be found in Appendix A. However, the localities (and their corresponding number on Fig. 3.13.) that were sampled in this study can be summarised as follows; Tombuie (Locality 3), Calliachar-Urlar Burns (Locality 4), Lead Trial (Locality 5), RX2959KA (Locality 6), ARD_1 (Locality 7), Tomnadashan (Locality 8), Spoil Heap (Locality 9), Coire Buidhe (Locality 10), Glen Almond Vein (Locality 11), and the Comrie Pluton (Locality 12). The only samples not listed here are the granitoids that were used for radiometric U-Pb dating; the locations of these samples have been added to Fig. 3.13. Regarding the protocol for sample naming, the locality name was logically abbreviated (e.g. Lead Trial was known as 'LDT') before prescribing a number to the sample depending on the order that it was collected in during fieldwork. Permission was granted by Nature Scotland to sample the intrusions at Tomnadashan (which is a SSSI; Smith *et al.*, 2022).

Whilst the primary focus of fieldwork was to collect samples for subsequent analytical work, observations were made during fieldwork that have, where appropriate, been used to inform and contextualise the results of this study. During sampling, a Chartwell notebook was always carried for the purposes of making observations and interpretations in the field, as well as for the primary recording of GPS coordinates and structural data. A SUUNTO-MC2 Mirror Compass Clinometer was used to measure the strike and dip values of bedding, foliation, cleavage, and faults. Photographs were taken on a Samsung A10 smartphone. Core-logging of the boreholes around Lead Trial was undertaken in the summer of 2021, utilising logging sheets provided by Green Glen Minerals. However, it is important to emphasise that sampling of the core was not undertaken in the present study; Green Glen Minerals collected the samples of the core that were analysed (Appendix C, Fig. C.2.; K30118KA) during an exploration drilling campaign in 2021.

Throughout the course of geological fieldwork, it was not possible to collect all of the samples that were required for the analytical work in this study. To circumvent this limitation, several specimens were sourced from external organisations and partners. Due to the cost of the Re-Os analyses, only three samples from Tomnadashan could be dated; TOM_MOLY_SM, PA_MOLY and G.002.26.2417.2 (Appendix A). These were provided by Dr Stephen Moreton, Peder Aspen, and National Museums Scotland (NMS), respectively. Issues with sample collection at Tomnadashan meant that galena could also not be found here during fieldwork in 2021 and 2022; NMS donated a sample (Appendix A; G.2019.101.7), which was also utilised to create polished block B0018 (Appendix A). Regarding SW3 (i.e. the granitic dyke sourced from the Calliachar Burn for radiometric dating; Fig. 3.26.), this sample was collected by Green Glen Minerals. The poor outcrop exposure in the Calliachar Burn and Tombuie meant that it was not always possible to sample the mineralisation here for $\delta^{34}S$ and Pb isotope analyses; for this reason, the National Museum of Wales (NMW) donated several samples to this study (Appendix A; 2003.1G.M.637, 2003.1G.M.604 a-p, 2003.1G.M.626 a-v, 2003.1G.M.627, and 2003.1G.M.630).

4.4. Sample Analysis

Beyond the broad descriptions of the methodologies implemented in this study (Table 4.1.), more detailed information regarding the preparation and the analytical procedures that were followed is provided in Appendix B. Regarding the $\delta^{34}S$ and Pb isotope studies, the samples that were analysed are described in Appendix A. Furthermore, images deemed to be representative of the mineralogical associations at each locality have also been provided (Fig. 4.2.; Fig. 4.3.). However, SEM petrography (Table 4.1) was utilised to contextualise and interpret the data derived from each method (i.e. within the context of a paragenetic interpretation) where appropriate. Generally speaking, SEM was the main method used for petrography, although a separate RLM study was conducted on polished blocks from Tomnadashan that were loaned by the University of Edinburgh. For this reason, it was possible to include an RLM image in the paragenetic interpretation that was produced for Tomnadashan (Webb *et al.*, 2024b).

As part of National Environment Isotope Facility (NEIF) grant 2649.0423, a large amount of petrographic characterisation was conducted to support the application (i.e. to provide a justification for the analyses that were requested). For example, petrographic mapping of the polished blocks made from the mineralisation samples (Fig. 4.2.; Fig. 4.3.) was carried out in order to select targets for in-situ $\delta^{34}S$ analyses at the Scottish Universities Environmental Research Centre (SUERC). Furthermore, zircons in thin sections from the granitoids around Loch Tay were characterised and imaged in SEM, to provide context for the requested CA-ID-TIMS analyses (i.e. to provide evidence that the zircons originated as a result of magmatic crystallisation).

In the following subsections, important information regarding the analytical procedures is presented (type of analysis, instrument used, standards, blanks and error margins), although as mentioned previously, the full descriptions of the methods are provided in Appendix B.

4.4.1. CA-ID-TIMS

Regarding the CA-ID-TIMS analyses, these measurements were conducted on mineral separates (zircons) that were extracted from crushed granitoid samples (Appendix A) and dissolved by the process described in Appendix B. To measure the various isotopic ratios (e.g. U/Pb), the Thermo-Electron Triton Thermal Ionization Mass Spectrometer at the British Geological Survey was used. Regarding blanks, the in-house National Isotope Geoscience Laboratory blank comprised of $^{206}Pb/^{204}Pb = 18.099 \pm 3.02$ %, $^{207}Pb/^{204}Pb = 15.545 \pm 1.758$ %, and $^{208}Pb/^{204}Pb = 37.824 \pm 2.814$ % was included within these analyses. In terms of analytical standards, the NBS 982, NBS 981, and U 500 standards were implemented.

4.4.2. Re-Os

The Re-Os analyses (which involve mineral extraction, in this case molybdenite) were conducted at Durham University Material using a Thermo Scientific TRITON mass spectrometer, with the principles of negative thermal ionisation mass spectrometry being used to measure the isotope abundances (in accordance with the method outlined by Li *et al.* 2017; Appendix B). To evaluate the accuracy and reproducibility of the molybdenite Re-Os analytical approach, the Henderson molybdenite reference material (RM8599) was used as a standard. Nine analyses of RM8599 yielded a weighted mean of 27.695 ± 0.038 (2SD, MSWD = 0.53), which is consistent with the recommended value 27.66 ± 0.10 Ma (Markey *et al.*, 2007) and previous analyses at Durham University (Lawley and Selby, 2012). During this study, the Re and Os blanks were 2 and 0.5 pg, with an $^{187}Os/^{188}Os$ value of 0.24 ± 0.01 (n = 6, 2SD; Li *et al.*, 2017).

4.4.3. $\delta^{34}S$

In this study, two types of $\delta^{34}S$ analyses have been conducted; in-situ (SUERC) and measurements without any in-situ imagery to contextualise them (University of Leeds). The latter, which comprises the majority of the dataset, is summarised first. These analyses were conducted on mineral extracts (a Dremel was used to drill powders out of hand specimens collected during fieldwork prior to analysis) in the Cohen Geochemistry Laboratory at the University of Leeds and involved the use of Elementar PYRO cube attached to an IsoPrime continuous flow mass spectrometer. To prepare the samples, the following quantities of material were weighed into tin cups measuring 8 x 5 mm; 0.028 to 0.047 mg of pyrite, 0.112 to 0.187 mg of galena, 0.043 to 0.072 mg of chalcopyrite, and 0.037 to 0.062 mg of molybdenite. Analytical blanks were generated by taking measurements of empty tin cups. The following internationally accepted standards were used in the analyses; NBS-127 (+20.3 ‰), NBS-123 (+17.01 ‰), IAEA S-1 (−0.30 ‰), and IAEA S-3 (−32.06 ‰) and given a $\delta^{34}S$ value of +20.3 ‰ (He et al., 2020). The raw values were also compared against the chalcopyrite standard CP-1, which had been given a value of −4.56 ‰ (He *et al.*, 2020). In terms of precision, repeat analyses of a laboratory standard comprised of $BaSO_4$ were within ± 0.3 ‰ (within 1 SD) of each other.

Regarding the in-situ analyses (laser spots) conducted at SUERC, the laser sulphur system was developed in-house and consists of three key systems; the laser system (i.e. the laser, microscope, motorised X-Y-Z stage, imaging system and the vacuum chamber), a vacuum line to purify the gas, and a mass spectrometer to perform the measurement. In terms of standards, repeat measurements on an internal CP1 chalcopyrite standard and international lab standards (NBS 123 sphalerite and IAEA-S-3 barium sulphate) yielded values that were consistently better than ± 0.3 ‰ (Kelley and Fallick, 1990).

4.4.4. Pb

Whilst more information regarding the analytical procedure can be found in Appendix B, here, the overarching principles of the Pb isotope analyses are summarised here. Mineral extracts were created by using a Dremel to drill galena powders out of hand specimens; the analyses were conducted using a Thermo Fisher Scientific Neptune Plus MC-ICP-MS. The precision of the method was evaluated using repeat analyses of NBS 981 Pb reference solution (which had been spiked with Tl). Average values derived for each of the NBS 981 (the standard) ratios (previously corrected for mass bias) were then compared to the known values for this reference (double spike: $^{206}Pb/^{204}Pc = 16.9417$, $^{207}Pb/^{204}Pb = 15.4996$, $^{208}Pb/^{204}Pb = 36.724$, $^{207}Pb/^{206}Pb = 0.91488$, $^{208}Pb/^{206}Pb = 2.1677$; Thirlwall, 2002). Following this, the sample data was normalised in accordance with the average relative deviation of measured reference values from the true value. Internal uncertainties (i.e. the reproducibility of the ratios that were measured) were propagated relative to uncertainties of external origin (i.e. the excess amounts of variance affiliated with the reproducibility of NBS 981 reference material; between 0.004 and 0.008).

Method	References	Rationale	Research question (Table 3.9.)
Petrographic characterisation (using Scanning Electron Microscopy and Reflected Light Microscopy)	(Niedrig, 1978; Marshall, 1988; Götze *et al.*, 2001; Götze, 2009; Götze and Kempe, 2009; Stevens-Kalceff, 2009; Götze and Möckel, 2012; Rusk, 2012; Frelinger *et al.*, 2015)	Establish the relationship between phases at different localities, enabling the construction of paragenetic interpretations	*How did the veins in the LTVS (particularly regarding the mineralisation) evolve over time?*
U-Pb	(Mattinson, 1973; 2005; Schmitz and Schoene, 2007; Hiess *et al.*, 2012; Vermeesch, 2018)	Provide radiometric dates for the age of magmatism around Loch Tay	*How old is the magmatism associated with LTVS?*
Re-Os	(Nier, 1950; Gramlich *et al.*, 1973; Creaser *et al.*, 1991; Morgan *et al.*, 1991; Völkening *et al.*, 1991; Roy-Barman, 1993; Shirey and Walker, 1995; Cohen and Waters, 1996; Shen *et al.*, 1996; Birck *et al.*, 1997; Selby and Creaser, 2001; Lawley and Selby, 2012; 2013; Li *et al.*, 2017)	Provide radiometric dates for the age of mineralisation at Tomnadashan	*How old is the mineralisation in the LTVS?*
$\delta^{34}S$	(Sakai, 1968; Ohmoto, 1972; Kelley and Fallick, 1990; Wagner *et al.*, 2002; Seal, 2006; He *et al.*, 2020)	Constrain the sources of sulphur and assess the conditions of mineralisation within the LTVS	*What is the source of the ore-forming fluids in the LTVS?*
Pb isotopes	(Cannon, 1961; Hirata, 1996; Thirlwall, 2002; Woodhead, 2002; Westner *et al.*, 2021, 2021; Klein *et al.*, 2022; Huston and Champion, 2023)	Constrain the sources of Pb involved in the formation of the LTVS	

Table 4.1. Summary of the methodologies implemented in this study. The rationale is clearly explained and the link to each research question (Table 3.9.) is indicated. Publications from which the methodologies have been derived are listed in a separate column and incorporated into the description of each analytical procedure in Appendix B.

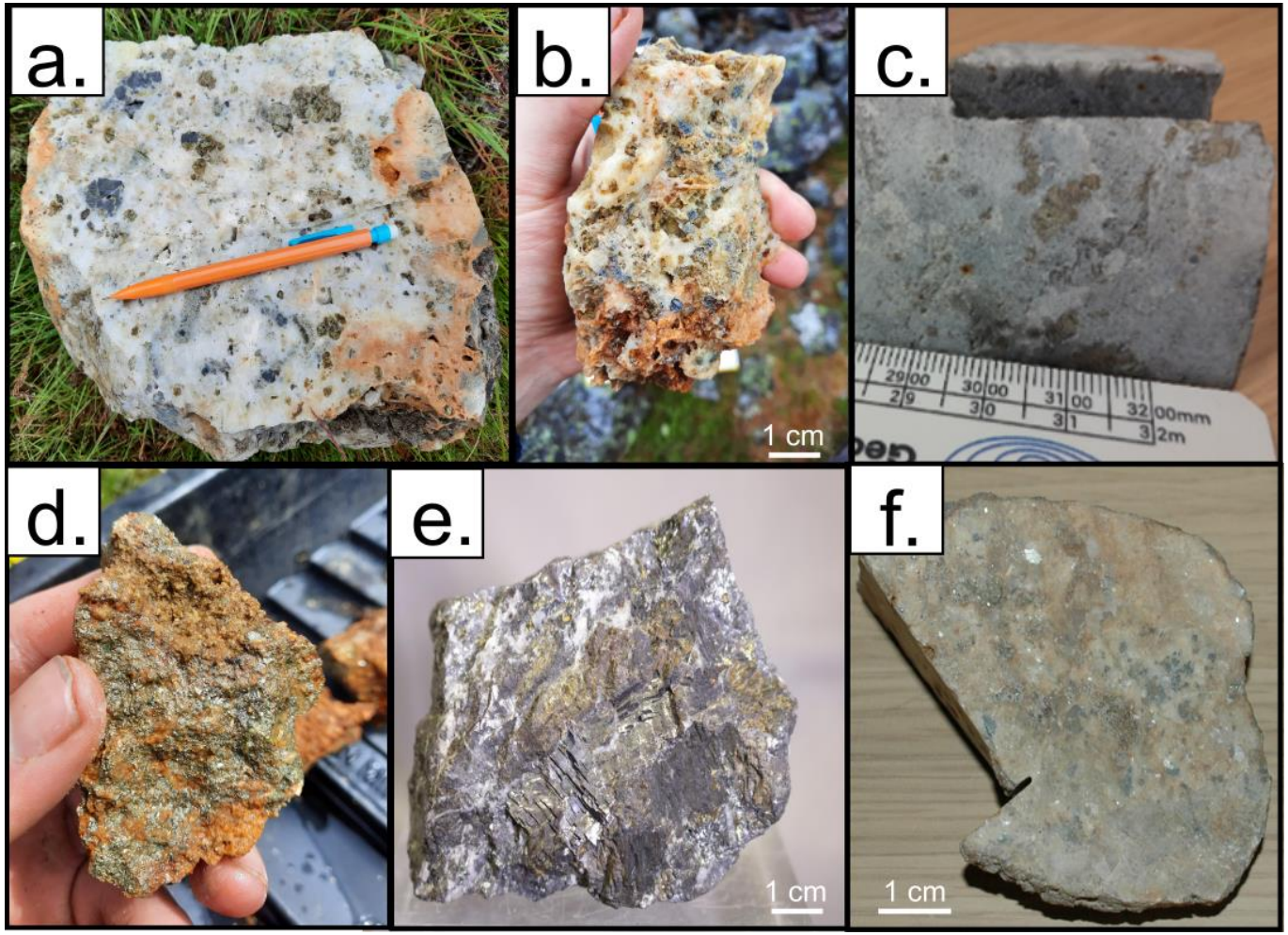

Figure 4.2. Hand specimens of the mineralisation at Lead Trial (a-c) and Tomnadashan (d-f; Webb *et al.*, 2024b) that were used in the $\delta^{34}S$ and Pb isotope analyses of this study. Samples names are indicated in brackets and are described further in Appendix A. **a + b.** Brecciated galena and sphalerite hosted in vuggy quartz. Several of the Lead Trial samples (LDT_LSa-d) were created using this material. **c.** Core sample (K30118KA) collected by Green Glen Minerals, showing sphalerite mineralisation in schist. **d.** Pyrite disseminated in the granitoids at Tomnadashan (SW_TOM_PYa). **e.** Galena sample (B0018) from Tomnadashan; (©) National Museum of Scotland. **f.** Sample of the quartz ± carbonate vein at Tomnadashan (Appendix A; TOM_QTZ).

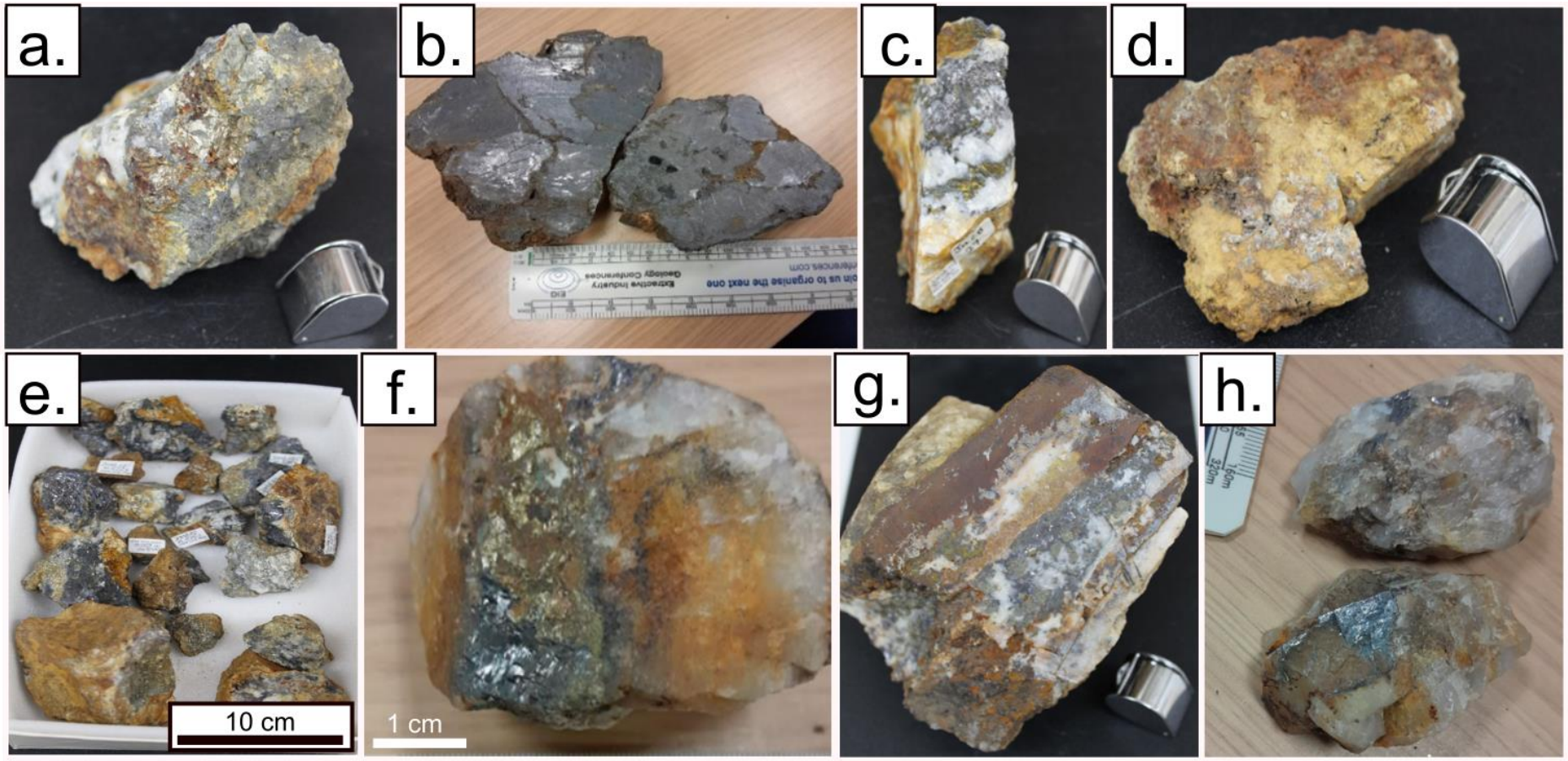

Figure 4.3. Hand specimens of the mineralisation at the metasediment-hosted veins within the LTVS that were used for the $\delta^{34}S$ and Pb isotope analyses in this study. Samples names are indicated in brackets and are described further in Appendix A. a-e represent the veins in the Calliachar Burn (Fig. 3.25.). **a.** Discovery Vein (2003.1G.M.627). **b.** V3 (CAL_GN, LSCV1). **c.** V5 (2003.1G.M.630). **d.** V6 (2003.1G.M.604 a-p; 65004). **e.** V7 (2003.1G.M.626 a-v). **f.** Urlar Burn (UB_SH). **g.** Tombuie (2003.1G.M.637). **h.** Coire Buidhe (CB_GAL).

4.5. Limitations and uncertainties of the methodologies

The various approaches used throughout this study have several limitations and uncertainties, which are explored in this section. A generic limitation is a lack of data, or rather, further data collection may be necessary to better elucidate several of the trends uncovered as a result of this study. Research in economic geology is often impacted by the field-based and laboratory-intensive nature of the work, two factors that make it difficult to collect large numbers of representative samples. Should other researchers conduct further studies into the metallogeny of the LTVS, they may discover mineralogical associations or trends in the stable isotope data that were judged not to occur throughout the course of the present study. The LTVS is impacted by these generic limitations regarding data collection; the terrain is often challenging, and outcrop exposure is obscured by vegetation cover. This meant that sampling was time-consuming and only a limited amount of material could be collected from rock outcrops. Furthermore, many of the abandoned mine workings are inaccessible (e.g. Coire Buidhe; Fig. 3.13., Locality 10), meaning that in-situ samples were not available and disused tips frequently needed to be sampled instead. Whilst historical records clearly show that assumptions regarding the relationships between the disused tips and in-situ mineralisation occurrences are correct (e.g. Tomnadashan; Devéria, 2001), there may be a degree of uncertainty regarding the provenance of some samples; in addition, the wider geological context may be unknown.

4.5.1. Paragenetic studies on hydrothermal veins

A fundamental limitation was the issue of scale; individual veins and vein systems can be several kilometres long, whereas polished blocks and thin sections only permit scrutiny at a much smaller scale, even when large numbers of samples are studied. This means that the resulting paragenetic interpretations may not be truly representative of relations between phases in an orebody (Webb *et al.*, 2024a). A common ramification of this issue of scale is that many paragenetically informative criteria simply may not be observed when attempting to establish the paragenesis. In this study, for example, there were no obvious occurrences of alteration and dissolution textures (Webb *et al.*, 2024a), which are powerful indicators of paragenetic relationships. This does not mean that such textures are absent within the LTVS; they may just not have been captured in any of the thin sections or polished blocks that were characterised. However, the issue of scale has been mitigated against by studying as many samples (including those deemed to be representative of textures observed in the field) as possible (Webb *et al.*, 2024a).

4.5.2. Geochronology

In this study, it was originally intended to use an SEM to map out the positions of dateable minerals (e.g. apatite, monazite, and xenotime; Table 2.5.) in thin sections from the LTVS and use LA-ICP-MS to produce in-situ dates that could be linked to paragenetic stages. However, this approach was abandoned because following SEM characterisation, it became apparent that primary dateable minerals (i.e. those of hydrothermal origin) are very rare in the LTVS. Even where they do occur in quantities sufficient for statistically significant results (>10), they are too small (<20 µm) to be targeted via LA-ICP-MS (e.g. the monazite in the quartz vein at Tomnadashan; Section 5.3.2.). Furthermore, in the mineralised samples from Lead Trial (Fig. 3.13.; Locality 5), there was considerable uncertainty over whether the dateable minerals (e.g. zircon, apatite) hosted in the quartz were the result of primary growth or inheritance from the granitoid wallrock during brecciation associated with the veining event, given the anhedral morphologies and small sizes (<20 µm) of the crystals. For these reasons, Re-Os analyses on molybdenite from Tomnadashan were the only option for directly establishing the age of mineralisation in the LTVS.

With regards to the Re-Os analyses, the biggest limitation with of this dataset is that the ages refer to material that was not collected in in-situ. Given the multistage paragenesis of Tomnadashan (see Section 5.3.2.), having such data would have been invaluable. However, it is important to emphasise that a single analytical protocol for in-situ Re-Os dating of molybdenite is still under development, and there are several problems with such approaches, most notably the intra-granular decoupling of ^{187}Re-^{187}Os (Hogmalm *et al.*, 2019). Elemental mapping of molybdenite crystals has found that the isotopes tend to cluster at specific sites within the mineral lattice; this nuggeting effect of Re and Os isotopes can lead to heterogeneous Re-Os ratios, even within a single crystal (Barra *et al.*, 2017). Theoretically, this means that different parts of the same molybdenite crystal can record different ages. The focus in this study was on generating a robust and defensible age for a single mineralisation event. For this reason, Re-Os analyses via wet chemistry (within the context of a robust paragenetic interpretation) were judged to be the best approach. However, it must be emphasised that the molybdenite depicted in the paragenetic interpretation does not represent the same specimens as those utilised in the Re-Os analyses. Finally, another limitation with the Re-Os dataset is a lack of data; ages could only be derived from three samples, partly because of the cost of the analyses and the failure to find suitable molybdenite specimens during the field campaigns of 2021 and 2022. To circumvent these constraints, care was taken in choosing samples. Different forms of molybdenite (vein-hosted and disseminated) were dated, as well as a fine-grained sample (Appendix A; G.1878.49.10.1); regarding the latter, fine grains of molybdenite are known to yield more robust Re-Os dates because of their smaller grain size and greater surface area, which makes them more resistant to the diffusion of Re and Os (Lawley and Selby, 2012).

The same limitation (i.e. a lack of paragenetic context) exists with the U-Pb dataset; the raw data are supported by SEM images of the zircon but these datapoints cannot be linked to specific SEM images. Unlike the Re-Os dating, where there was no option but to date the molybdenite via the previously described method, it was decided that the CA-ID-TIMS approach of dating zircons was more appropriate than in-situ methods involving LA-ICP-MS. This decision was made based on the probable ages of the granitoids. Previous studies have found that the granitoids in this part of Scotland were emplaced from approximately 430 to 390 Ma (Oliver *et al.*, 2008; Neilson *et al.*, 2009; Miles *et al.*, 2016). For ages within two standard deviations (SD) of the mean, the age resolution on U-Pb dates derived via SIMS or LA-ICP-MS is typically ±2 %. For a rock sample that is 400 Ma, these methods would result in 8 Ma margins of error. This would make distinguishing between several granitoids of a similar age highly challenging. Even though the petrographic context is lost with the CA-ID-TIMS approach used in this study, the uncertainty of dates derived from this method is at the ± 0.1 % 2SD level. For samples that are ~400 Ma, this level of uncertainty can highlight any potential differences in the age of the granitoids around Loch Tay. However, the loss of the capability to date zircons in-situ was still a hindrance; even though zircon was observed during SEM characterisation of the thin section from ARD_FELS_2 (the granitic dyke collected in close proximity to the Ardtalnaig Burn; Fig. 3.13.), when the separation for CA-ID-TIMS was conducted on the rock sample, no zircons could be recovered. The decision to use wet chemistry for geochronology in this study therefore meant that some potential opportunities for geochronology (ARD_FELS_2) were lost. Ultimately, the loss of paragenetic context from the granitoids is less of an issue (relative to the hydrothermal veins in the LTVS) because there is only one stage in which the zircon could have formed (magmatic crystallisation).

4.5.3. $\delta^{34}S$ datasets

The biggest limitation with the $\delta^{34}S$ data that were not collected in-situ is that the measurements lack paragenetic context; this data was constructed using the mass spectrometer at the University of Leeds (Appendix B). However, detailed photographs are available for most of the hand specimens that were used in the analyses (Fig. 4.2.; Fig. 4.3.). To derive usable datapoints, the following quantities of material needed to be weighed for each measurement; 0.028 to 0.047 mg of pyrite, 0.112 to 0.187 mg of galena, 0.043 to 0.072 mg of chalcopyrite, and 0.037 to 0.062 mg of molybdenite. Weighing such small quantities was prone to error and several analyses failed because either too much or too little sulphide had been placed into the tin cups (Appendix B). The lack of paragenetic context has been mitigated against by the inclusion of the in-situ $\delta^{34}S$ dataset, a term used to indicate $\delta^{34}S$ measurements that were collected using the in-situ laser at SUERC. Regardless, both datasets (in-situ and data that is not in-situ) complement one another and mitigate against their respective weaknesses. For example, whilst paragenetically constrained $\delta^{34}S$ data are preferable, the data collection process was time consuming and dependent upon access to external facilities (i.e. the in-situ laser at SUERC), which made generating large quantities of data difficult. When it comes to establishing the broad regional trends, the $\delta^{34}S$ analyses without paragenetic context are superior

in this regard; large quantities of data can be collected at a faster rate. The process for preparing the samples for $\delta^{34}S$ analyses via the mass spectrometer at the University of Leeds is also more straightforward; with the in-situ measurements, a single mistake in the analytical procedure can result in failure to generate a datapoint. These caveats aside, some of the $\delta^{34}S$ analyses at the University of Leeds failed due to sample contamination during the weighing procedure (Appendix B; Section B.5.1.).

There were several limitations with the in-situ $\delta^{34}S$ laser analyses. To generate enough SO_2 gas for the mass spectrometer, an area equivalent to the scorched portion of the pyrite (Fig. 4.4.) needed to be ablated with the laser; these analyses are destructive and cannot be revisited for further SEM imagery. However, the spot size of the laser was 80 µm, meaning it was necessary to move the laser across the sample during each measurement. Galena was ablated to a greater extent when struck by the laser, resulting in clouds of dust that obscured the view of the camera, making it harder to navigate the laser during the ablation process. This ultimately introduces an element of uncertainty regarding exactly what was ablated. Further issues with the in-situ laser analyses stemmed from the process of working the sulphur isotope line, or rather, condensing the gas. The valve sequence (Appendix B; Section B.5.2.) is prone to error; specifically, turning the incorrect valve during the course of each analysis can result in the loss of gas that had been isolated during the ablation (and therefore, the loss of a usable datapoint). The fundamental difficulties involved with running the line restricted the number of datapoints that could be collected in a single day to <6. The problems associated with the reflected light microscope attached to the laser and the accompanying digital camera pertained to sample navigation; with such a restricted field of view (Fig. 4.4.), it was challenging to locate the targets that had previously been selected for analysis. This slowed down the process of taking measurements throughout the course of each day of measurements.

During in-situ $\delta^{34}S$ analyses, several factors can impede the development of precise and accurate sulphur isotope measurements; for example, there may be spectrometer interferences due to the presence of species such as S_2, HSO_2, and H_2SO_2 that form in the source of the mass spectrometer throughout the course of these analyses (Kelley and Fallick, 1990). However, experimental work by Kelley and Fallick (1990) using the laser at SUERC found that repeat measurements on internal (CP1 chalcopyrite) and international lab standards (NBS 123 sphalerite and IAEA-S-3 barium sulphate) yielded values that were consistently better than ± 0.3 ‰ (Kelley and Fallick, 1990). In terms of the precision of the sulphur isotope measurements from the dataset without in-situ context, these values varied between 0.16 and 0.26 ‰ and represent the reproducibility of the check standards (within 1 SD) used throughout the course of the analyses (Appendix B; Section B.5.2.).

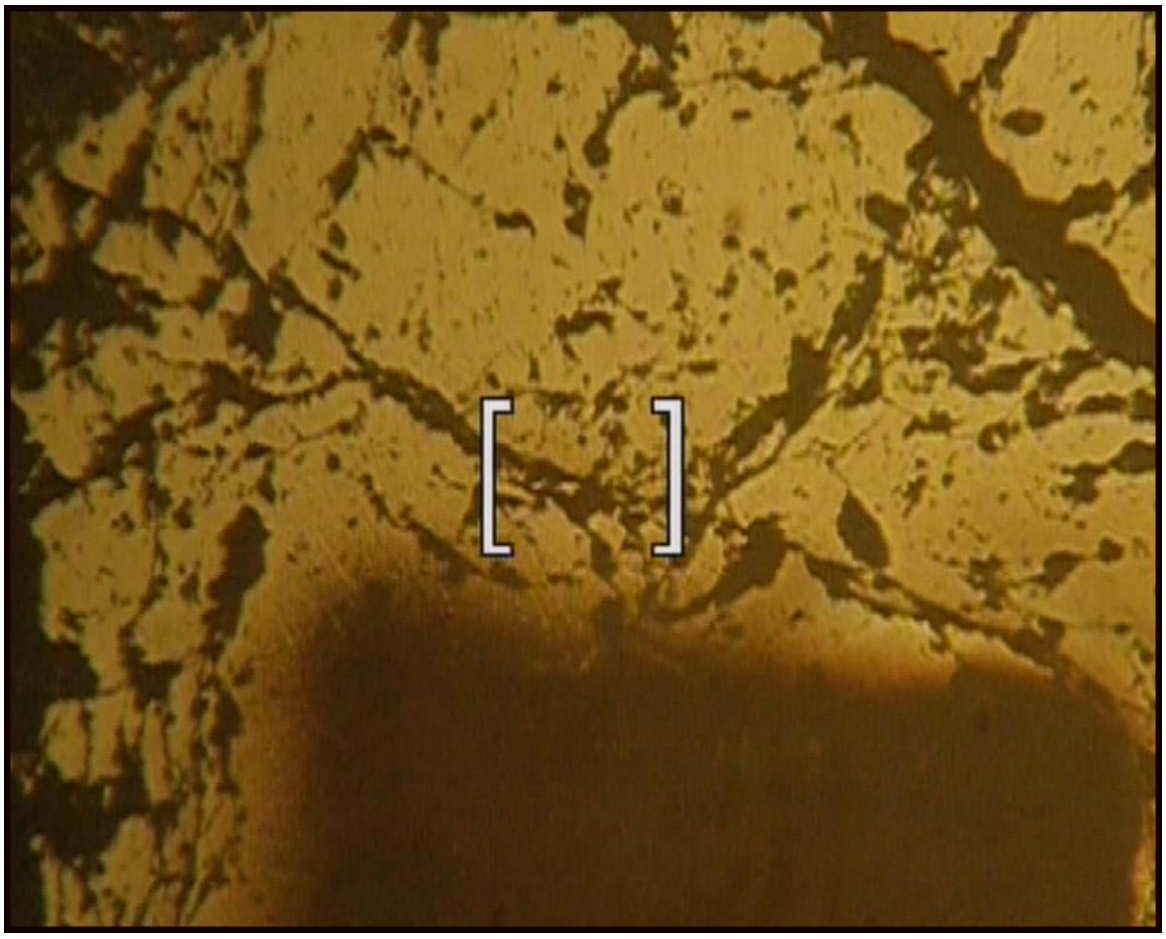

Figure 4.4. An example of a reflected light microscope image of the pyrite from V6 in the Calliachar Burn (DISC_004; Appendix A) that was generated during in-situ laser ablation $\delta^{34}S$ analyses at SUERC. Note that the equipment lacks the capability to be zoomed out from the current field of view (spot size, represented by the white box, = 80 µm). The blurry area represents the region that had just been ablated by the laser following an analysis.

4.5.4. Pb isotopes

Wet chemistry methodologies were selected for this study because the margins of error for the datapoints are much smaller than in-situ measurements involving SIMS (Yesares *et al.*, 2019). However, measurements via wet chemistry cannot preferentially target certain parts of a galena crystal or an individual paragenetic stage (i.e. they dissolve entire samples); this may be problematic because some of the LTVS localities contain multiple generations of galena. The galena samples that were prepared for these analyses came from coarse-grained (>1 cm) occurrences that were easy to sample (i.e. pure galena could be removed without contamination from other sulphides).

Another uncertainty with the Pb isotope dataset is the potential for Pb isotope abundances to change after the galena crystallises (Huston and Champion, 2023). Subsequent mineralisation events or post-mineralisation internal decay may add radiogenic lead to the galena lattice, meaning that the source or age of Pb are not the only factors controlling the final Pb isotope ratios (Huston and Champion, 2023). Alternatively, later hydrothermal fluids or supergene enrichment may remove radiogenic Pb from the galena (Huston and Champion, 2023). Sometimes, there may be textural evidence for post-crystallisation changes in Pb isotope ratios; for example, different zones within a galena crystal that record contrasting Pb isotope values (Hart *et al.*, 1981; Deloule *et al.*, 1986; Crocetti *et al.*, 1988; Li *et al.*, 2016a).

Chapter 5: Observations and results

5.1. Introduction

In this chapter, the results of the various methods utilised to investigate the research questions (Table 3.9.) are described. However, observations derived from the field campaigns in 2021 and 2022 are also summarised. Aside from fieldwork, the results of this study can be split into two categories; textural observations compiled during petrographic characterisation (i.e. using SEM, RLM, and optical microscopy) and quantitative data derived from the isotope analyses.

5.2. Observations from geological fieldwork

As part of this study, approximately three weeks of geological fieldwork were conducted around Loch Tay in July 2021 and May 2022. Observations from several LTVS localities with potential relevance to the interpretation of the petrographic and isotope datasets are outlined in this section.

5.2.1. Calliachar Burn

Throughout the course of this study, the Calliachar Burn (Fig. 3.13., Locality 4) was visited repeatedly, both in 2021 and 2022. Whilst a large number of fractures were observed, most were unmineralised. Regarding the host rocks associated with the Discovery Vein (Fig. 5.1.a.), these were characterised as dark brown, medium-grained psammites with a relatively low amount of jointing (compared to the well-jointed pelitic schist observed elsewhere in the Calliachar Burn throughout the field campaigns). Brecciation of the wallrock during the veining event has resulted in the entrainment of psammite fragments within the quartz matrix (Fig. 5.1.b.). During fieldwork, a strike and dip measurement (142/88 ° NE) was taken from the Discovery Vein. There are also several quartz veinlets splaying away from the Discovery Vein (e.g. the vein next to the compass in Fig. 5.1.a.); the quartz groundmass in these veinlets was noted to display a syntaxial growth habit. Furthermore, the quartz crystals are relatively coarse (>0.5 cm) and have an anhedral morphology. In both the Discovery Vein and the veinlets, no sulphide mineralisation could be observed.

It was possible to identify and characterise V3 (Fig. 3.26.) during the fieldwork associated with this study. Unlike the Discovery Vein, V3 was observed to crosscut both pelites and psammites (Fig. 5.1.c.). At outcrop, V3 was described as a 10 cm wide subvertical quartz vein (Fig. 5.1.c.) with a trend of 142 °. Regarding the mineralogy, no sulphide mineralisation could be observed, although the quartz groundmass was noted to display a sheeted appearance; individual crystals are subhedral and <5 mm in size (Fig. 5.1.d.).

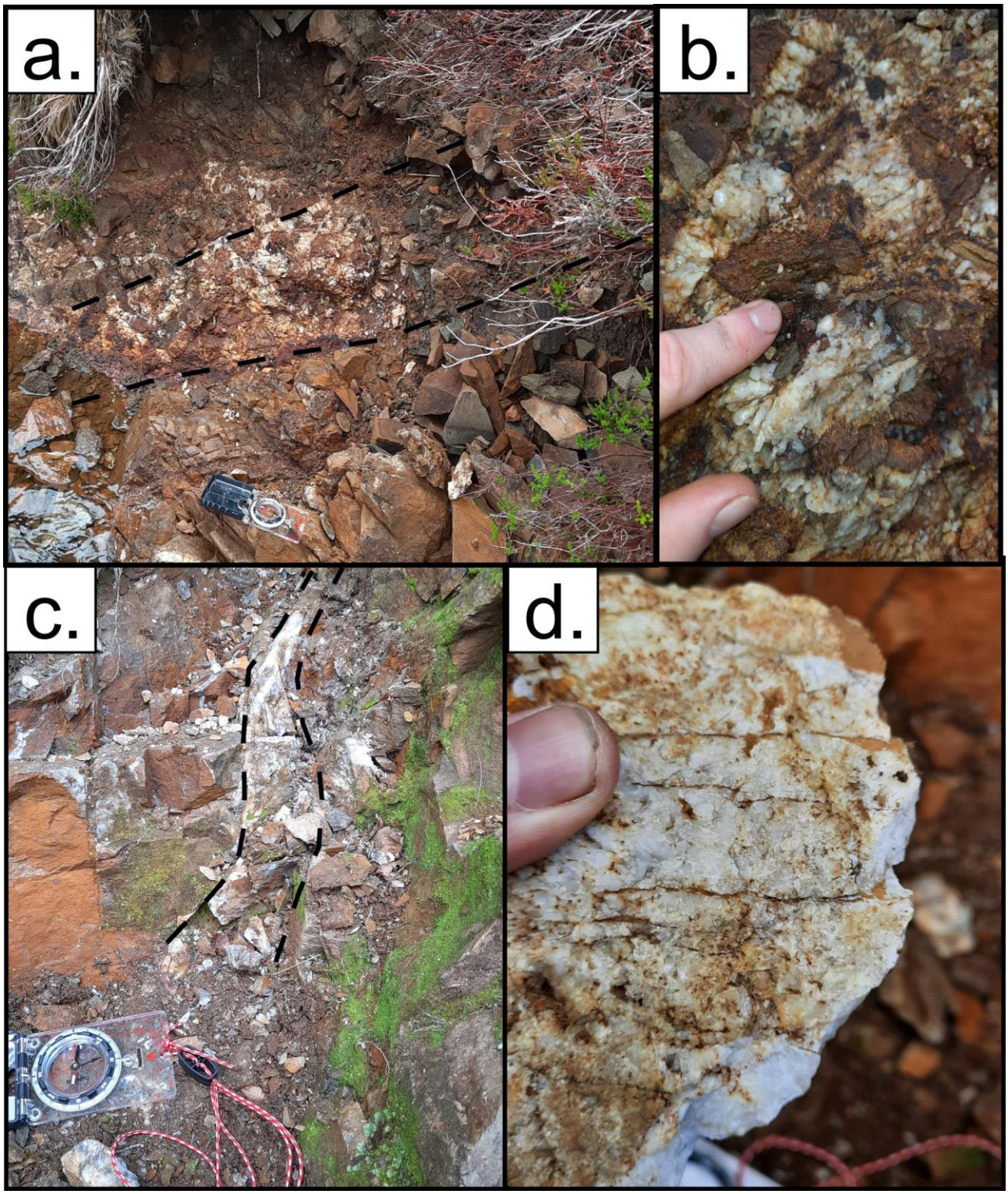

Figure 5.1. Images of different veins in the Calliachar Burn. **a-b.** The Discovery Vein, including an example of brecciated psammite wallrock entrained within the quartz. **c-d.** An outcrop and hand specimen from V3 demonstrating the sheeted nature of the quartz generations. The veins are indicated by dashed lines.

5.2.2. Ardtalnaig

During the 2022 field campaign, an attempt to locate the boulder float sampled by Green Glen Minerals (ARD_1 and RX2959KA; Table 3.4.) was made; whilst RX2959KA (Fig. 3.13.; Locality 6) could not be found, Green Glen Minerals were able to provide a sample for Pb isotope analyses (Appendix A). However, it was possible to locate ARD_1 (Fig. 3.13.; Locality 7); this boulder contains a schistose host rock that has been crosscut by a mineralised quartz vein. Notes made at this locality describe a fine-grained, brown-grey schist host rock with prominent bedding planes (Figure 5.2.a.). The schist was very hard as a result of intense silicification. Mineralogically, ARD_1 contains large galena crystals (<1 cm) hosted in vuggy quartz (Fig. 5.2.b.), which was also noted to host barytes mineralisation.

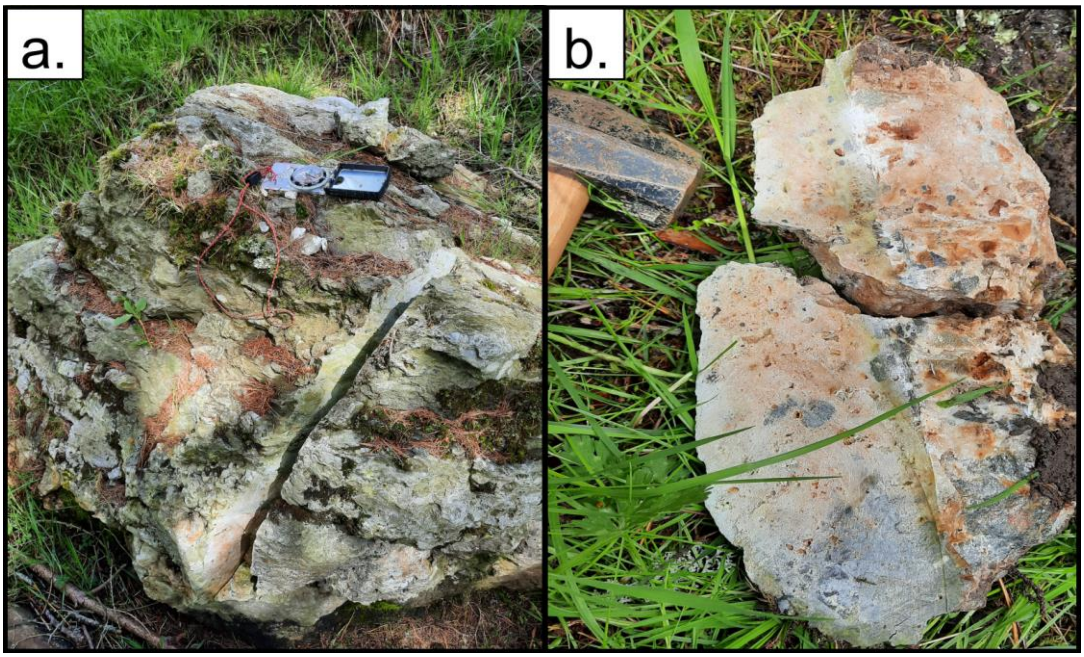

Figure 5.2. 'ARD_1' boulder float. **a.** The boulder at outcrop and **b.** The mineralised sample (galena and vuggy quartz) used for $\delta^{34}S$ and Pb analyses.

As part of the wider attempt to collect granitoid samples for U-Pb geochro2nology, different parts of the region around Ardtalnaig (Fig. 3.13; Localities 6 and 7) were visited in 2022. Most of the fractures observed within the Ardtalnaig Burn were unmineralised (i.e. similar to the Calliachar Burn). Furthermore, a pink granitoid displaying sharp contact margins with the schist host rock was discovered during the excursion to the Ardtalnaig Burn (Fig. 5.3.a.; ARD_FELS_1). The ARD_FELS_1 granitoid is <2 m wide and does not display any obvious signs of mineralisation (Fig. 5.3.a.). Mineralogically, ARD_FELS_1 is mostly comprised of quartz, although flecks of biotite mica and black amphibole crystals also occur in the groundmass. Another granitoid (ARD_FELS_2) was found near the Ardtalnaig Burn (Fig. 5.3.b) in relatively close proximity to RX2959KA (Fig. 3.13., Locality 6). Unlike ARD_FELS_1, the outcrop of this light grey granitoid was > 10 m wide (Fig. 5.3.b.); furthermore, the ARD_FELS_2 granitoid has been crosscut by many thin (<0.5 cm) quartz veinlets, although no sulphide mineralisation was observed during fieldwork.

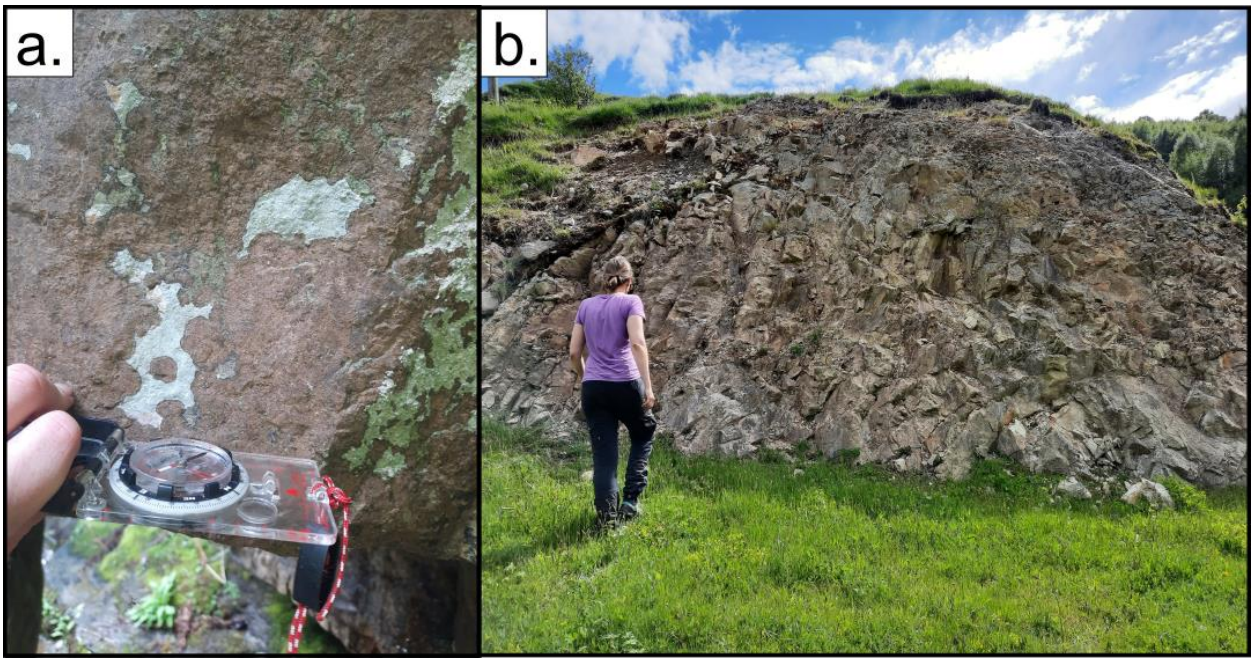

Figure 5.3. Granitoid outcrops around the Ardtalnaig Burn (Fig. 3.13.). **a.** The ARD_FELS_1 dyke, which crosscuts schists of the Southern Highland Group. **b.** ARD_FELS_2, which represents a much larger intrusion that has been impacted by extensive hydrothermal alteration.

5.2.3. Lead Trial

During fieldwork, two outcrops of the vein at Lead Trial were identified; both the pelitic schists and granitoids are crosscut by this vein, which is demarcated by sharp contact margins (Fig. 5.4.). In the pelitic host rocks, brecciation of the wallrock has been intense and cockade quartz growth was observed around the brecciated clasts (Fig. 5.4.a.). Further up the hill, the vein crosscuts the granitoids; intense sericitisation has resulted in a white colouration of the outcrop (Fig. 5.4.b.). The vein here has a sheeted appearance, which potentially represents the occurrence of several quartz generations (Fig. 5.4.b.). The veinlets splaying from the main outcrop (Fig. 5.4.) contain quartz crystals that display a syntaxial growth habit.

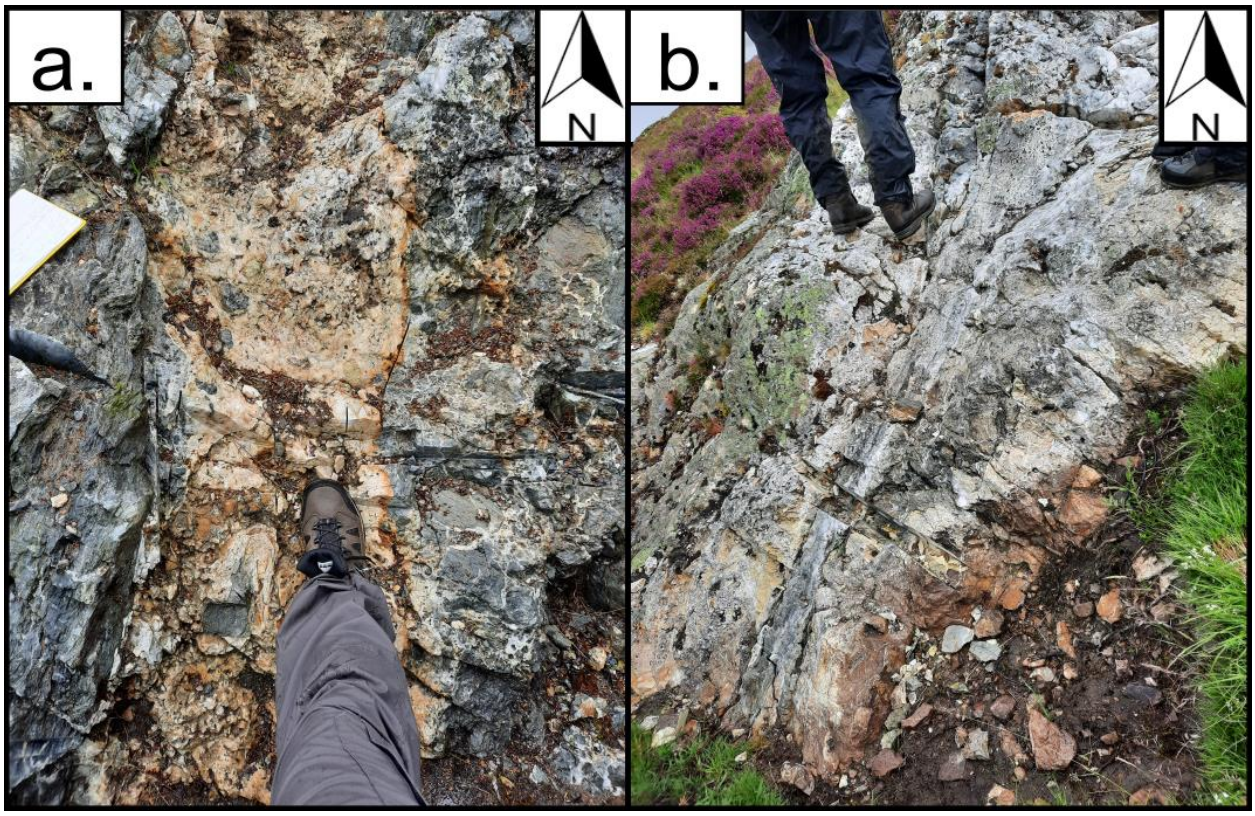

Figure 5.4. Outcrops of the vein known as 'Lead Trial' (Fig. 3.13.; Locality 5). **a.** The vein crosscutting pelites. Samples LDT1 and LDT2 came from this outcrop. **b.** The vein crosscutting the granitoid. The LDT4 sample was collected from the centre of the vein outcrop here. More sample information can be found in Appendix A.

Core-logging and sampling was carried out at Lead Trial in July 2021, for the purposes of characterising the mineralisation and obtaining sulphide samples for $\delta^{34}S$ and Pb isotope analyses. Unfortunately, photography during core-logging in 2021 was not possible due to a lack of suitable equipment; instead, photographs were taken by Torvela (2021). Regarding the lithologies that are associated with Lead Trial, these include rhyolites, psammites, amphibolites and mica schists (Fig. 5.5.). The rhyolite (Fig. 5.5.a-b) that outcrops on the surface (Fig. 3.13.) is creamy white to tan grey and fine-grained (crystal size < 1 mm); over 90 % of this lithology is comprised of quartz. Whilst vugs and vesicles do occur, they were noted to be relatively uncommon. Below the rhyolite, there is a package of Dalradian metasediments that is comprised of finely laminated and fine-grained (<1 mm) pelites that grade into psammites (Fig. 5.5.b-c.). Mineralisation was frequently recorded in the metasediments; the largest mineralised interval encompassed 30 cm of the core from EGR-001 at 30 m. Sphalerite and galena are the most common metallic minerals in the metasediments; there is also an isolated occurrence of visible gold hosted within a quartz vug approximately 1 cm away from the galena and sphalerite crystals (Fig. 5.5.c.). Trace amounts of chalcopyrite were also described in the galena and sphalerite assemblage within the metasediments at depths of 25 to 26 m in EGR-001 (Appendix C; Fig. C.1.). During core-logging, the psammite was characterised as a sandy mica schist with subrounded grey quartz grains of a medium grain size (i.e. 1-5 mm). Both the pelites and psammites display intense hydrothermal veining (Appendix C; Fig. C.1.; Fig. C.2.).

However, whilst a greater quantity of metallic mineralisation may occur in the metasediments at Lead Trial, the more competent granitoid has been fractured to a greater extent and hosts more veins (Fig. 5.5.b.). In some parts of the core, mineralisation was noted to correspond to transitions between psammite and pelite (e.g. Appendix C; Fig. C.2., 25-32 m).

Regarding the lithologies that underlie the metasediments, EGR-001 and EGR-002 (the boreholes that were logged in this study; Appendix C) intersected a porphyritic granitoid (Fig. 5.5.d-e.) at depths of 63 and 55 m, respectively (Appendix C; Fig. C.1.; Fig. C.2.). This lithology was classified as dacite during core-logging, and it continues until depths of 79 m (Appendix C; Fig. C.1.). Mineralogically, the dacite is mostly comprised of amphibole and plagioclase phenocrysts (Fig. 5.5.e.). However, throughout the entire dacite interval, the plagioclase has been sericitised (Fig. 5.5.d.). This style of alteration is distinct from the bleached haloes around the quartz veinlets that were frequently observed in the dacite (Fig. 5.5.e.). The 'bleaching' has also impacted unmineralised veins (Fig. C.2.; 64-69 m). It is uncertain what the bleaching represents, aside from the colour change and decrease in grain size (Fig. 5.5.e.). Mineralogically, the veinlets in the dacite contain galena and sphalerite (Fig. C.1.; 69-70 m), although small amounts of pyrite also occur (Fig. C.1.; 63.6 m).

Below the dacite, mineralisation becomes less common throughout the rest of the metasediments (Fig. C.1.; 79-106 m), although a quartz ± carbonate veinlet array containing sphalerite and galena was documented at 91 m (Fig. C.1.). The deepest lithology recorded during core-logging was an intensely fractured and veined rhyolite that has been altered to a greenish colour (potentially chlorite; Fig. 5.5.f.); however, the amount of sulphide mineralisation in this lithology is relatively minor (Appendix C; Fig. C.1.-C.2.). In terms of alteration, silicification and sericitisation were noted to have occurred in the green rhyolite (Fig. 5.5.f.), with carbonate precipitation occurring in the vugs throughout this unit.

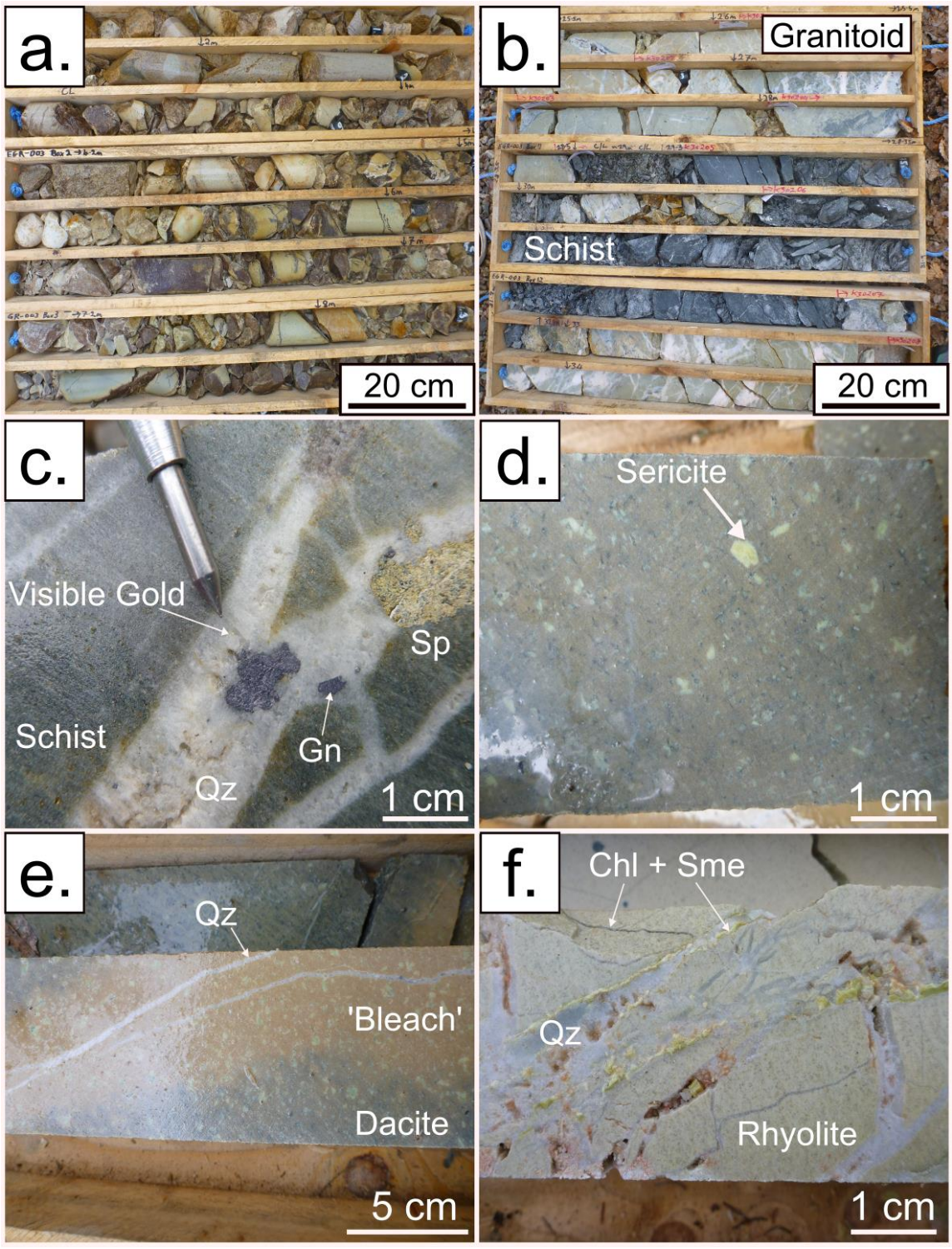

Figure 5.5. Examples of the different lithologies that occur around Lead Trial, as documented during core-logging (photographed by Torvela, 2021). The lithologies are presented as they were encountered in the core (i.e. from top to bottom). **a.** Rhyolite; light brown, fine-grained (EGR-003). **b.** Interval depicting the difference between the schist and rhyolite, which is more competent and hosts more veins (EGR-003). **c.** Occurrence of visible gold, along with sphalerite and galena, in a quartz vein traversing the schist (EGR-001). **d.** Dacite, which is relatively unaltered (EGR-002). **e.** An example of the 'bleach' alteration that impacts the dacite around sulphide-bearing quartz veinlets (EGR-002). **f.** Rhyolite at the bottom of EGR-001, which has turned green, potentially as a result of chloritisation. The location of each borehole is shown on Fig. 5.6., whilst summary logs for EGR-001 and EGR-002 are presented in Appendix C.

As part of this study, a variety of geological and geochemical maps produced by Green Glen Minerals (Lavelle, 2020b) were overlain in ArcGIS and digitised to create a composite geological map (Fig. 5.6.). This map demonstrates that the vein at Lead Trial (shown in dark yellow on Fig. 5.6.) has a similar orientation to the NW-SE trending fractures throughout the wider region (Fig. 5.6.). Furthermore, these fractures, which traverse both the schist and the granite, are typically characterised by high Au concentrations (>5 ppm; Fig. 5.6.). The host rocks for the mineralisation at Lead Trial are also depicted on Fig. 5.6.; the veins occur within a gently dipping and folded package of Dalradian metasediments (mostly schists) alternating with granitoids, which host most of the mineralisation (i.e. fewer veins occur within the metasediments; Fig. 5.6.).

Collectively, it was possible to use the core-logs (Appendix C) and the geological map (Fig. 5.6.) to produce a cross-section of the hypothesised subsurface relationships at Lead Trial (Fig. 5.7.). The vein at Lead Trial continues to a depth of at least 50 m from the topographic surface (Fig. 5.7.b.), where it traverses the rhyolite and dacite before potentially intersecting the 90 m interval in EGR_001 (Fig. 5.7.b.; Appendix C, Fig. C.1.). Here, several mineralised quartz veinlets were noted to occur over a 1 m interval.

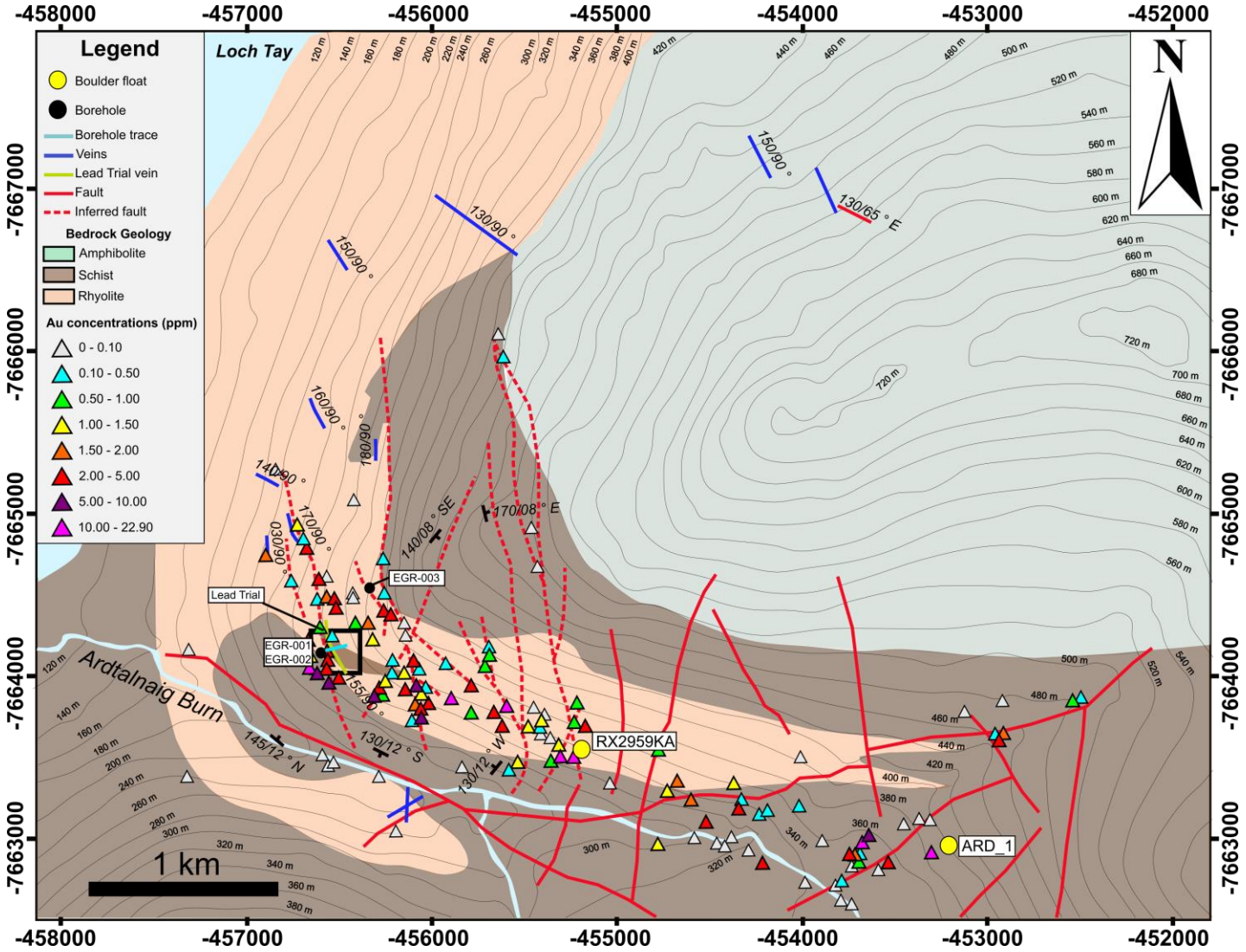

Figure 5.6. Geological map of the region around Lead Trial. This figure was made by georeferencing several maps produced by Green Glen Minerals (Lavalle, 2020b) and then digitising them to produce a composite map (Esri, 2022), with the vein at Lead Trial (shown in Fig. 5.4.) highlighted. Whilst the other veins were mapped by Green Glen Minerals, there is limited information regarding their characteristics (e.g. sulphide content). The black box shows the location of Fig. 5.7.

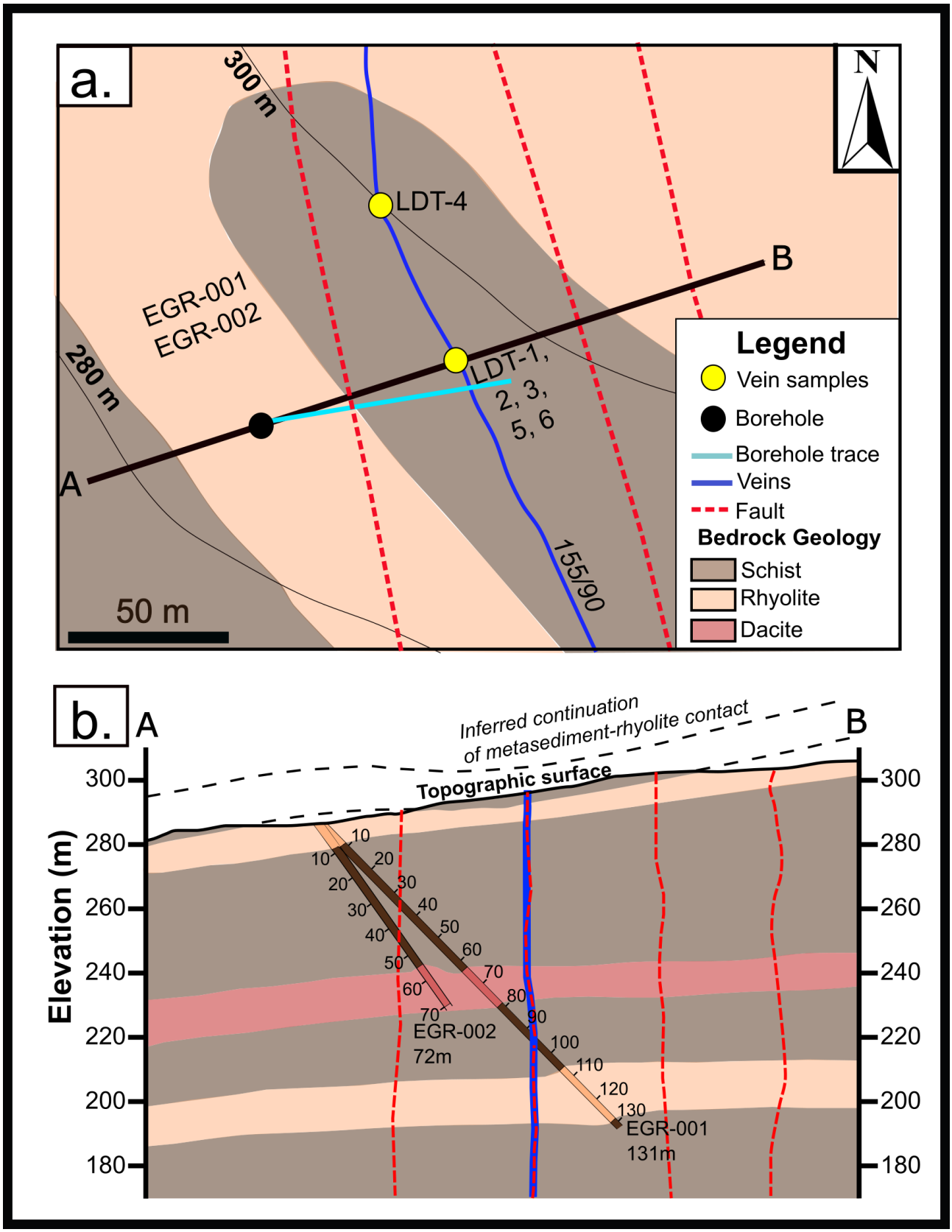

Figure 5.7. Geological map of the region traversed by the cross-section through Lead Trial, which was constructed using the core-logs in Appendix C. **a.** The region targeted by EGR-001 and EGR-002 (the black box in Figure 7). LDT-4 is a rock sample (Appendix A) collected from the outcrop shown in Fig. 5.4.b., whilst LDT-1, LDT-2, LDT-3, LDT-5, and LDT-6 (Appendix A) were sampled from the outcrop depicted in Fig. 5.4.a. **b.** Cross-section through the boreholes.

5.2.4. Tomnadashan

Tomnadashan was visited in both 2021 and 2022 as part of an attempt to sample molybdenite for Re-Os dating (Section 5.4.2.); some representative photographs from this locality are depicted in Fig. 5.8. The molybdenite observed in the field was unsuitable for Re-Os dating (i.e. it was too fine-grained and disseminated amongst other phases; deriving an uncontaminated sample was not possible); for this reason, specimens of molybdenite from Tomnadashan were obtained from NMS and private mineral collections (Section 4.3.). During fieldwork, it was also noted that specimens of granite, particularly those within the potassic alteration halo, contained a greater quantity of sulphide minerals (Fig. 5.8.d.) relative to the diorite that comprises most of the pluton (Fig. 3.31). Furthermore, the diorite zones within the intrusion have been impacted by chloritisation, which is manifested by a light green colour overprinting the otherwise dark grey colour of the diorite (Fig. 5.8.a.).

Inside the mine, it was possible to identify the NW-SE trending contact between the granite and diorite that hosts most of the mineralisation at Tomnadashan (Fig. 5.8.b.; Naden *et al.*, 2010); a strike and dip measurement of this fault (150/60 ° W) was taken here. Remnants of the vein-hosted mineralisation (which has largely been extracted) are also visible in Fig. 5.8.b. Where the granite outcrops inside the mine, it occurs as linear masses demarcated by a pinkish red colour (Fig. 5.8.c.), which is an indicator of potassic alteration. Pyrite and chalcopyrite were the most commonly observed phases (Fig. 5.8.d). Following the fieldwork campaigns, it was possible to create a modified version of the geological map originally produced by Smith (1996), which has now been annotated with the structural measurement taken in this study from the faulted contact between the diorite and granite (Fig. 5.9.).

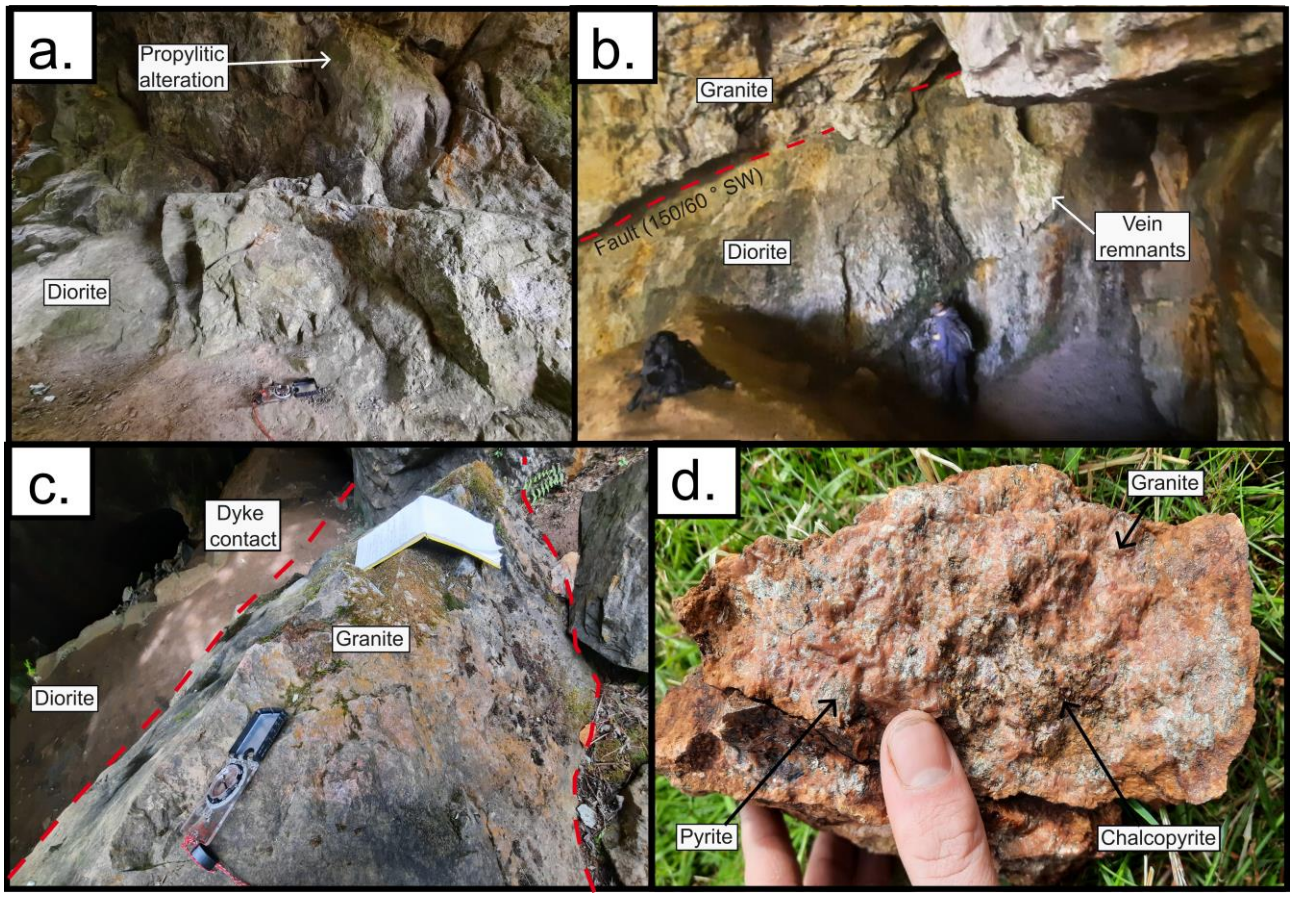

Figure 5.8. Structural and petrological features of interest at Tomnadashan. **a.** Diorite (Fig. 3.30.) that has been impacted by chloritisation. **b.** NW-SE trending fault juxtaposing the granite and diorite (Fig. 3.30.). **c.** Granitic dyke within the mine that was sampled for U-Pb geochronology (Appendix A; TOM_FELS_2). **d.** Granite displaying potassic alteration and sulphide mineralisation, which was sampled for $\delta^{34}S$ analyses (Appendix A; TOM_FELS).

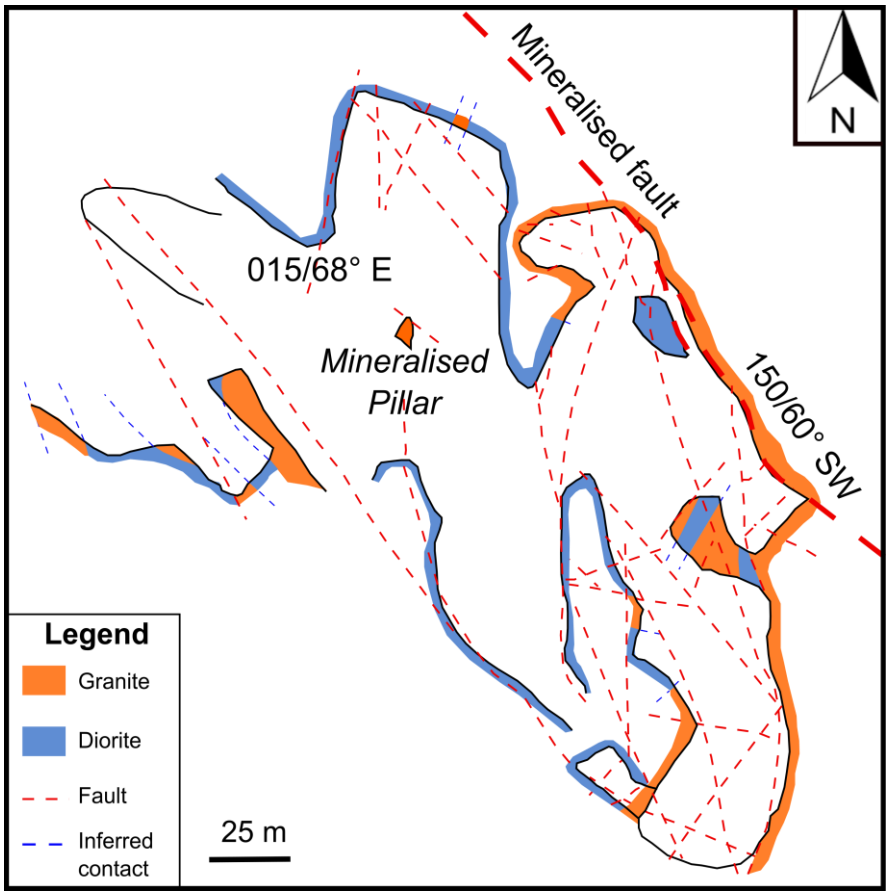

Figure 5.9. Geological map of the mine at Tomnadashan (adapted from Smith, 1996). The structural measurement is novel (i.e. derived from this study), whilst the geological boundaries and fault positions were adapted from Smith (1996). This figure was presented in Webb *et al.* 2024b.

5.2.5. Coire Buidhe and Spoil Heap

In July of 2021, a single day was spent at Coire Buidhe and Spoil Heap (Fig. 3.13.; Localities 9 and 10). A granitoid, termed CB_FELS_2, was discovered close to the peak of Meall nan Oighreag (Fig. 3.13.). It is important to emphasise that CB_FELS_2 is not depicted on any geological maps (i.e. it does not represent the large granitoid to the southwest of Coire Buidhe in Fig. 3.13.). Nonetheless, the CB_FELS_2 granitoid is a greenish grey colour, although some portions of it are a pinker hue (Fig. 5.10.c.). Mineralogically, the granitoid is fine-grained (with most crystals being <1 mm); no sulphide mineralisation could be observed in the field, although thin carbonate veinlets traverse the quartz groundmass (Fig. 5.10.c.). As part of the same excursion, Spoil Heap was also visited; however, due to the lack of outcrop, it was not possible to characterise the host rocks here. Based on the geological map of the Study Area (Fig. 3.13.), this locality is likely to be hosted within the Pitlochry Schist Formation. Samples of the mineralisation (Fig. 5.10.a.-b.) were collected for $\delta^{34}S$ and Pb isotope analyses. The quartz groundmass in the vein at Spoil Heap is coarse-grained (e.g. >1 cm; Fig. 5.10.a.); mineralogically, Spoil Heap can be distinguished from Coire Buidhe by the presence of arsenopyrite and the lack of large quantities of galena (at Coire Buidhe, galena is the most common phase; Section 3.6.1.e.).

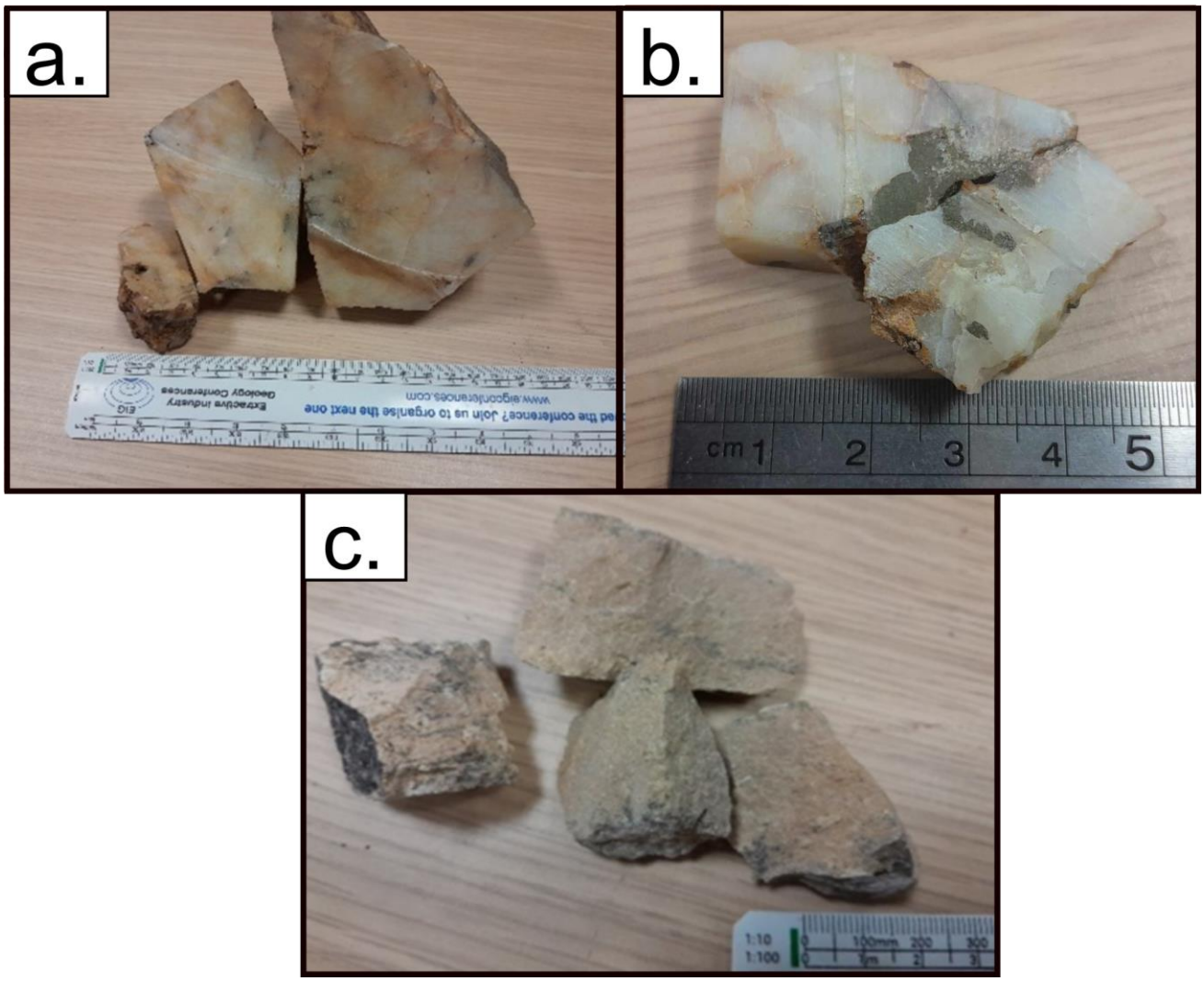

Figure 5.10. Images of the pyrite mineralisation (**a-b**) and the CB_FELS_2 granitoid (**c**) collected during the 2021 field campaign. The samples of the mineralisation were retrieved from Spoil Heap (Fig. 3.13., Locality 9), whilst the CB_FELS_2 granitoid occurs ~500 m to the SW of Coire Buidhe (Fig. 3.13., Locality 10).

5.2.6. Glen Almond Vein

The Glen Almond Vein (GAV), which was visited in July of 2021, has a mineralogy that is mostly comprised of pyrite (Fig. 5.11.). During fieldwork, a measurement of the strike and dip of the GAV was also taken (124/72 ° NE). Furthermore, sericite alteration and black sphalerite were described in the fieldwork notebook (although alteration was also noted to be minimal). The GAV displays a sharp contact with the schist host rock, which is fine-grained and finely laminated with a light brown colouration (Fig. 5.11.).

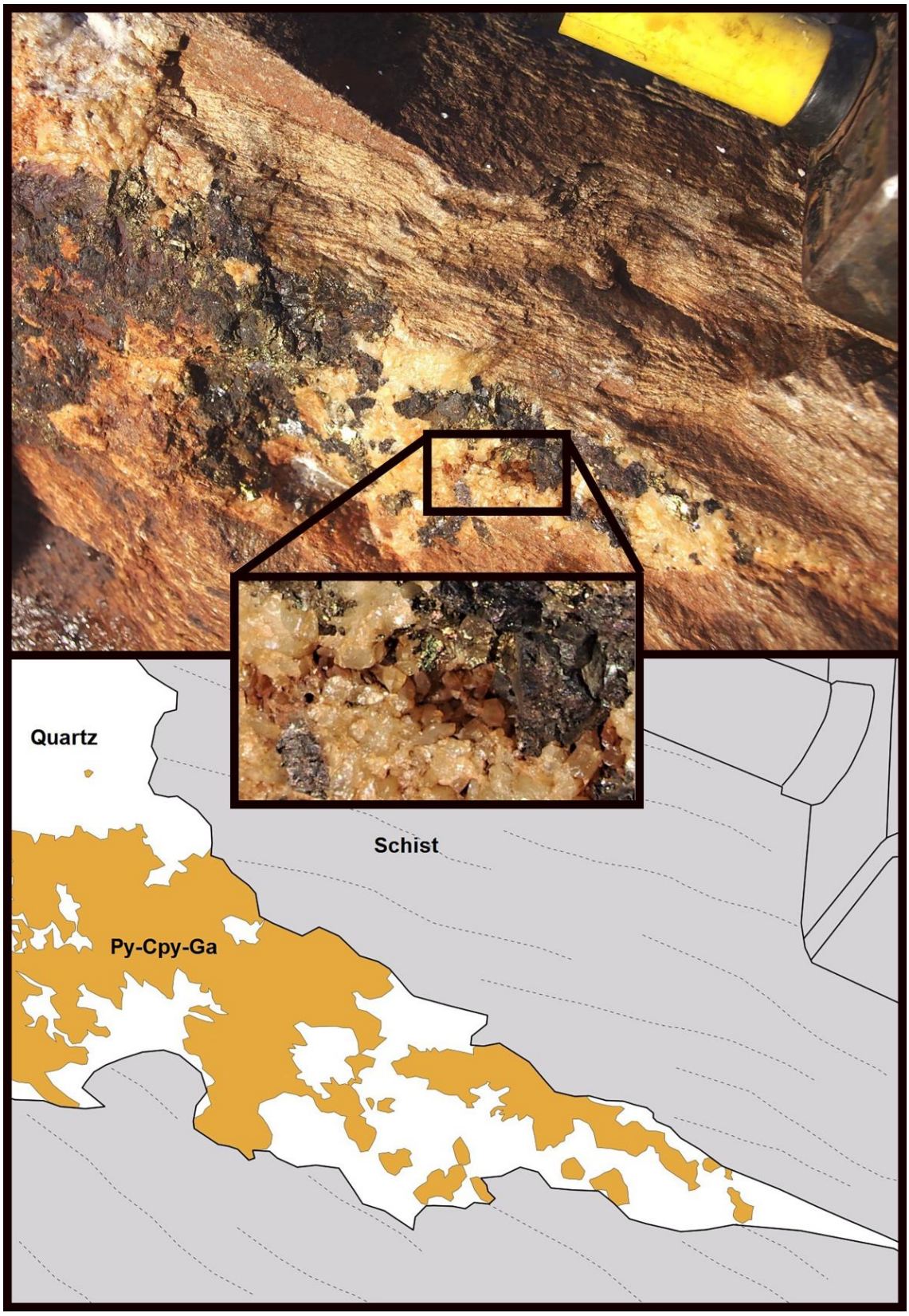

Figure 5.11. Photograph and line drawing of a sulphide-rich portion of the Glen Almond Vein at outcrop (containing chalcopyrite, galena, and pyrite). The vein texture is massive, although there are sporadic vugs that contain sub- to euhedral quartz and sulphide crystals (inset). The outcrop surface is oblique to the strike of the vein, meaning that the vein margins may appear to be irregular; in reality, the contact between the vein and host rocks is sharp. Reproduced from Webb *et al.* 2024a.

5.2.7. Comrie Pluton

The Comrie Pluton was visited as part of an excursion to the Milton Burn (Fig. 3.13.; Locality 12) to collect alluvial gold during the 2021 Field Campaign. This locality is situated within the granitic portion of the Comrie Pluton (Fig. 3.13.; Naden *et al.*, 2010). Chalcopyrite, pyrite and flaky biotite crystals were observed (Fig. 5.12.). The potassic alteration halo also contains arsenopyrite; however, mineralised boulders of diorite were observed to record an assemblage that is comparable to the granite. However, potassic alteration is not pervasive in the granite; some silicified portions unaffected by the potassic alteration halo were also described.

Figure 5.12. An example of chalcopyrite and pyrite mineralisation hosted within the granitic core of the Comrie Pluton (Fig. 3.13., Locality 12). The granite has been impacted by potassic alteration (Appendix A; CMRIE7).

5.3. Textural observations from the granitoids and veins around Loch Tay

In this section, results from the textural mapping that was conducted throughout this study (using SEM, RLM, and optical microscopy) are outlined. A full description of the samples from which the following images were derived, as well as the specific sampling locality, is provided in Appendix A. Regarding the reporting of petrographic characteristics from hydrothermal veins, the format recommended by Webb *et al.* 2024a has been used; a series of representative petrographic images from the vein are presented and observations of the textural relationships from these images are compiled in tables. Where more than one generation of a phase is present at a given locality, the stage in question has been added to the abbreviation shown in the image. For example, at Lead Trial, there are six stages of mineralisation (A to F), and three stages of galena. 'GnA' refers to galena from Stage A, whereas 'GnC' refers to galena from Stage 3. In the final paragenetic interpretations (Fig. 6.1.), these stage letters have been converted into stage numbers, meaning that the term 'GnA' pertains to Stage 1 (i.e. the first stage) of the mineralisation at Lead Trial. On the other hand, the term 'GnC' denotes the galena that comprises Stage 3 of the paragenesis (Fig. 6.1.).

5.3.1. Textural observations from the granitoids

Whilst some of the granitoids in the Study Area are evidently mineralised (e.g. the Comrie Pluton; Fig. 5.12.), it is unknown whether the other granitoids throughout the region host any mineralisation. Understanding the relationship between mineralisation and magmatism is important for answering Research Questions 1 and 2 (Table 3.9.), and for this reason, SEM petrography and age determinations in this study have been used to characterise the mineralisation within the different granitoids around Loch Tay. Prior to SEM analysis, the thin sections from the granitoids were scanned with a Leica UC7 Ultramicrotome, which was used to create images of the entirety of each thin section; in addition to the previously outlined field observations from the granitoids (as well as the descriptions provided for CB_FELS_2 and SW3 in Appendix A), the thin section images demonstrate the existence of textural and compositional variations throughout the granitoids associated with the LTVS (Fig. 5.13.). ARD_FELS_1 is mostly comprised of a fine-grained (<1 mm) groundmass of vuggy quartz; unlike the pinkish tint that can be observed in outcrop (Fig. 5.3.a.), the rock is light brown in thin section. Phenocrysts of biotite and feldspar are visible, although the latter has been extensively sericitised (i.e. the white rectangular morphologies within the groundmass; Fig. 5.13.a.). On the other hand, ARD_FELS_2 is overwhelmingly (i.e. >90 %) comprised of rounded, coarse-grained quartz crystals (< 5 mm), although coarse-grained plagioclase feldspar phenocrysts also occur (Fig. 5.13.b.). ARD_FELS_2 has a much lighter colouration than ARD_FELS_1, potentially reflecting a higher silica content.

Regarding TOM_FELS_2, which represents the granitic dyke within the mine at Tomnadashan (Fig. 5.8.c.), there are some very large phenocrysts of plagioclase feldspar and biotite mica (< 1cm) set in a medium grained quartz matrix (1-5 mm; Fig. 5.13.c.). In the thin section, chloritisation of the biotite (represented by the green colour) is visible, as is the pink tint of potassic alteration impacting the feldspar crystals (Fig. 5.13.c.). The granitoids from Coire Buidhe (CB_FELS_2) and SW3 (Calliachar Burn) are a similar colour (Fig. 5.13.d.-e) and may have a similar composition; however, the crystals in SW3 are larger. Furthermore, the plagioclase in SW3 shows signs of flow banding (i.e. the phenocrysts are arranged into bands; Fig. 5.13.e.).

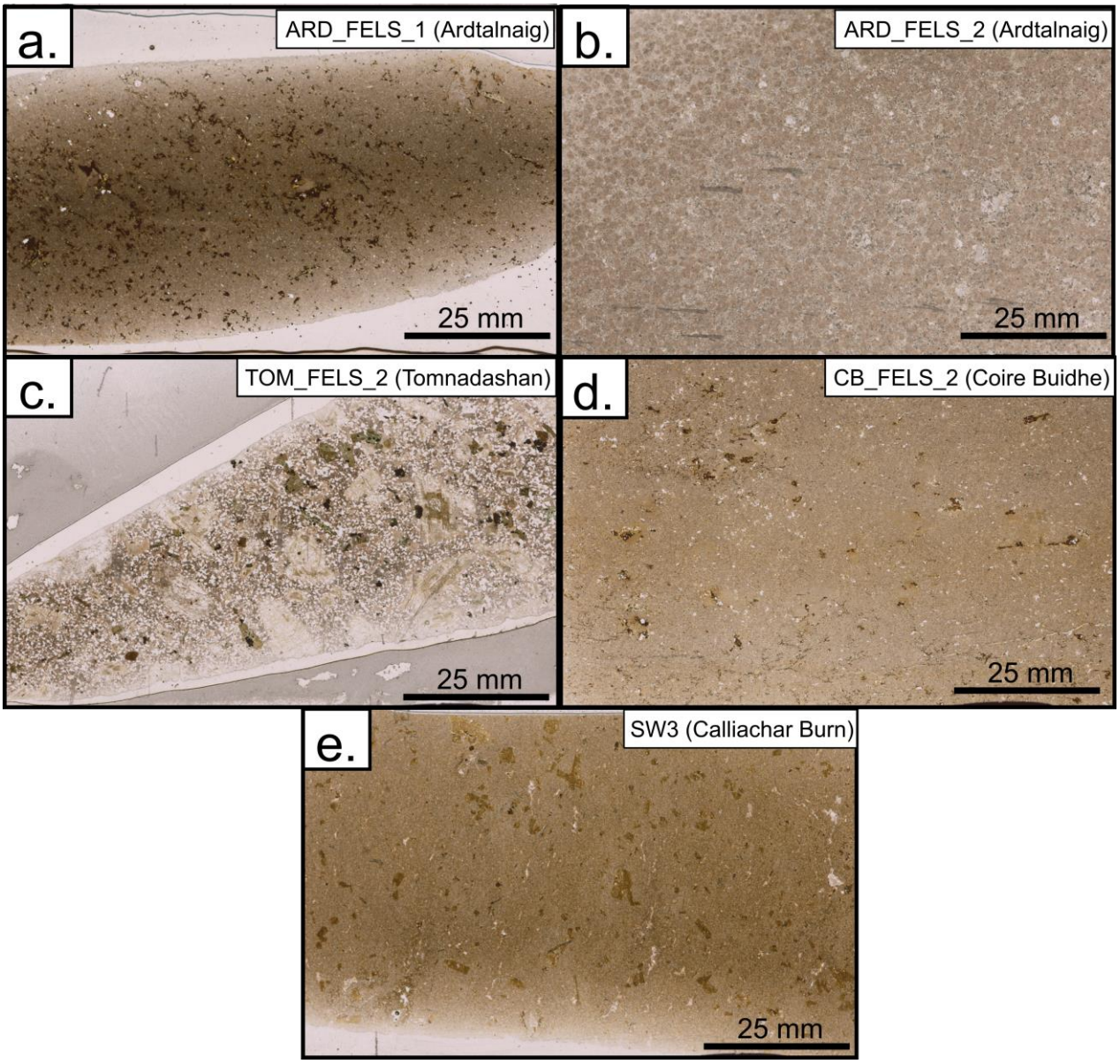

Figure 5.13. Thin sections of the different granitoids that were characterised via SEM in this study. **a.** ARD_FELS_1 (Ardtalnaig). **b.** ARD_FELS_2 (Ardtalnaig). **c.** TOM_FELS_2 (Tomnadashan). **d.** CB_FELS_2 (Coire Buidhe). **e.** SW3 (Calliachar Burn). All images were captured in Plane Polarised Light (PPL).

In the following pages, SEM images of zircons from the different thin sections are presented (Fig. 5.14.); these images have been used in Chapters 6 and 7 to provide a context in which to consider the U-Pb radiometric dates (Section 5.4.). Despite evident petrographic differences (grain size, mineral proportions, and textures) in the granitoids around Loch Tay (Fig. 5.13.), there are some commonalties; for example, the coprecipitation of zircon with apatite was consistently observed (Fig. 5.14.). This textural relationship is manifested by occurrences in which the zircon is adhered onto an apatite crystal (i.e. the two are mutually intergrowing with one another; Fig. 5.14.a., c., and d.). However, it was not always possible to observe direct points of contact between the zircon and apatite (Fig. 5.14.b.) and there were some instances of isolated zircon crystals within the quartz groundmass (Fig. 5.14.b.). In terms of morphology, the larger zircons (> 30 μm) have a rectangular habit (Fig. 5.14.b.); however, the smaller zircon crystals have irregular edges and are in some cases fragmented (Fig. 5.14.c.).

When the zircons were characterised in SEM-CL, internal textures were commonly observed. For example, zircons from the ARD_FELS_1 granitoid show distinctive dark and light banded zones that are parallel to the crystal margins (Fig. 5.15.a). However, the nature of the internal differences that were observed varied depending on the granitoid; the cores of the zircons from CB_FELS_2 (Coire Buidhe) are much darker than the rims (Fig. 5.15.c). On the other hand, in TOM_FELS_2 (Tomnadashan), the cores of the zircons were much lighter than some portions of the rims (Fig. 5.15.b.). The zircon crystals observed in SW3 (Calliachar Burn; Fig. 5.15.d.) are smaller than those in the other granitoids (typically <30 μm); however, the zircons within SW3 were texturally similar to the zircons from CB_FELS_2 (i.e. lighter rims, darker cores).

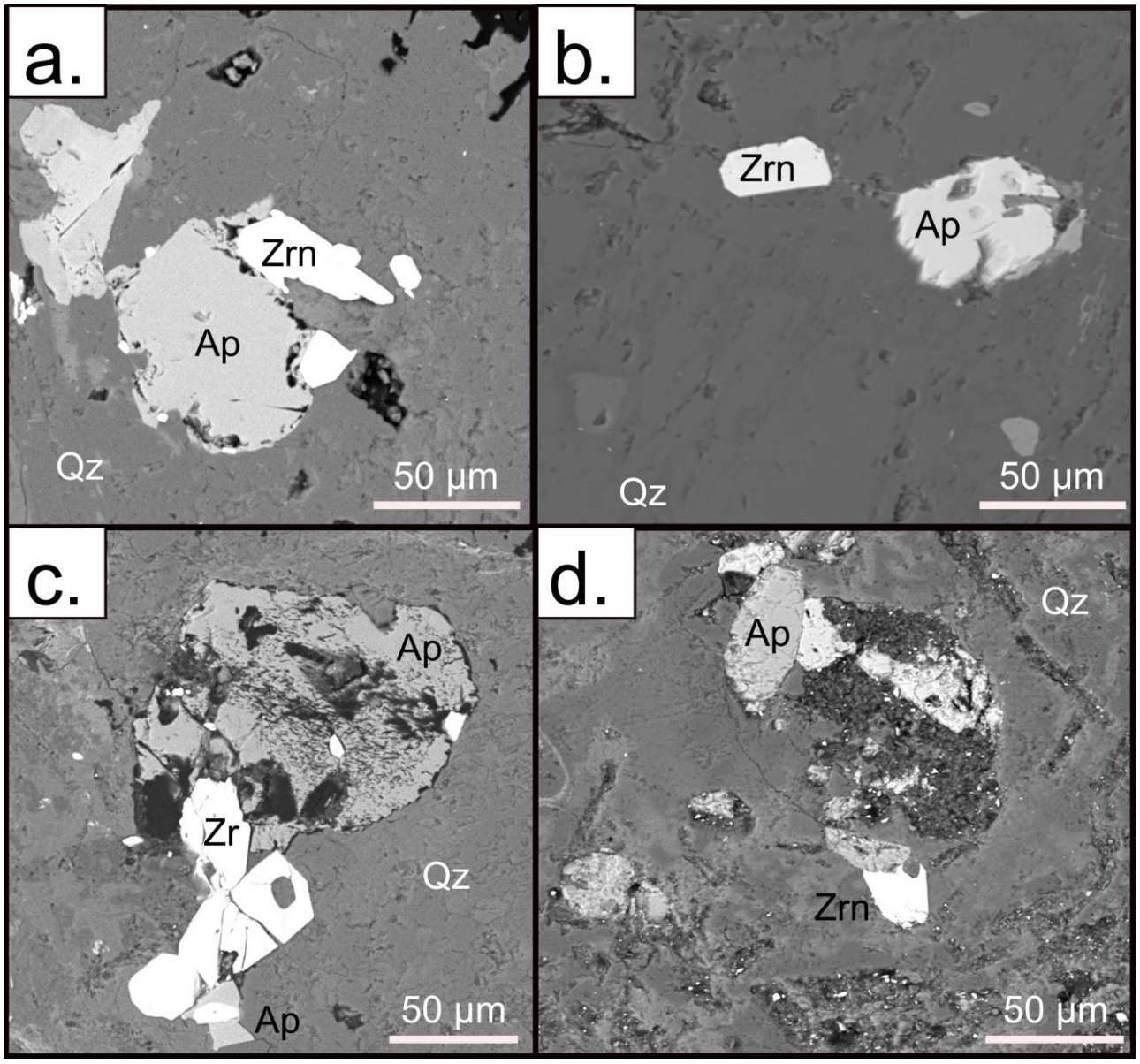

Figure 5.14. SEM-BSE images depicting the textural relationships of zircon, which was frequently observed to display a close spatial relationship with apatite. **a.** Ardtalnaig (ARD_FELS_1). Note the potential inclusion of quartz within the zircon crystal. **b.** Tomnadashan (TOM_FELS_2) **c.** Coire Buidhe (CB_FELS_2) and **d.** Calliachar Burn (SW3). Some of the quartz may display signs of zoning.

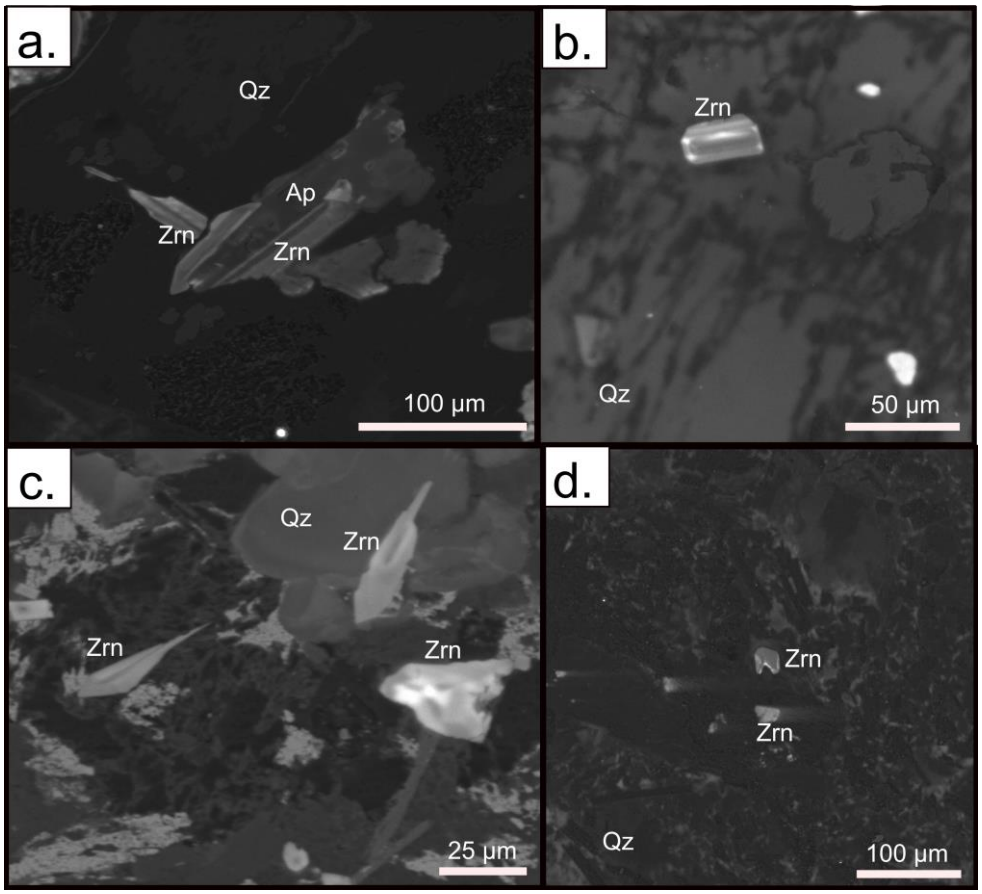

Figure 5.15. SEM-CL images of zircons and coprecipitating phases. **a.** Ardtalnaig (ARD_FELS_1). **b.** Tomnadashan (TOM_FELS_2). **c.** Coire Buidhe (CB_FELS_2). **d.** Calliachar Burn (SW3).

Throughout the petrographic work undertaken in this study, no metallic mineralisation could be identified in CB_FELS_2 (Coire Buidhe) or SW3 (Calliachar Burn). However, the granitoids from Ardtalnaig (ARD_FELS_1) contain disseminated mineralisation; whilst some sphalerite was documented in the vugs (Fig. 5.16.a.), the disseminated mineral assemblage here was typically comprised of euhedral pyrite crystals (which contain coeval galena blebs; Fig. 5.16.b.). In ARD_FELS_2, galena crystals were observed to be larger than the pyrite (> 50 µm; Fig. 5.16.c.); furthermore, zircons were observed alongside the metallic mineralisation in this intrusion (Fig. 5.16.c.), although their morphology (acicular) and appearance (grungy, darker in SEM-BSE) was considerably different from the previously described occurrences in ARD_FELS_1, TOM_FELS_2, CB_FELS_2, and SW3 (Fig. 5.15.). In TOM_FELS_2, which represents one of the granitic dykes at Tomnadashan (Fig. 5.8.c.), metallic mineralisation was a common component of the assemblage (Fig. 5.16.d.-f.).

Based on the SEM petrographic work that has been undertaken in this study, it is possible to recognise two types of granitoids: 1) unmineralised granitoids that have been impacted by no or very limited amounts of hydrothermal alteration, such as the granitoids around Coire Buidhe (CB_FELS_2) and the Calliachar Burn (SW3), and 2) granites that are mineralised and intensely altered (e.g. ARD_FELS_2 and TOM_FELS_2).

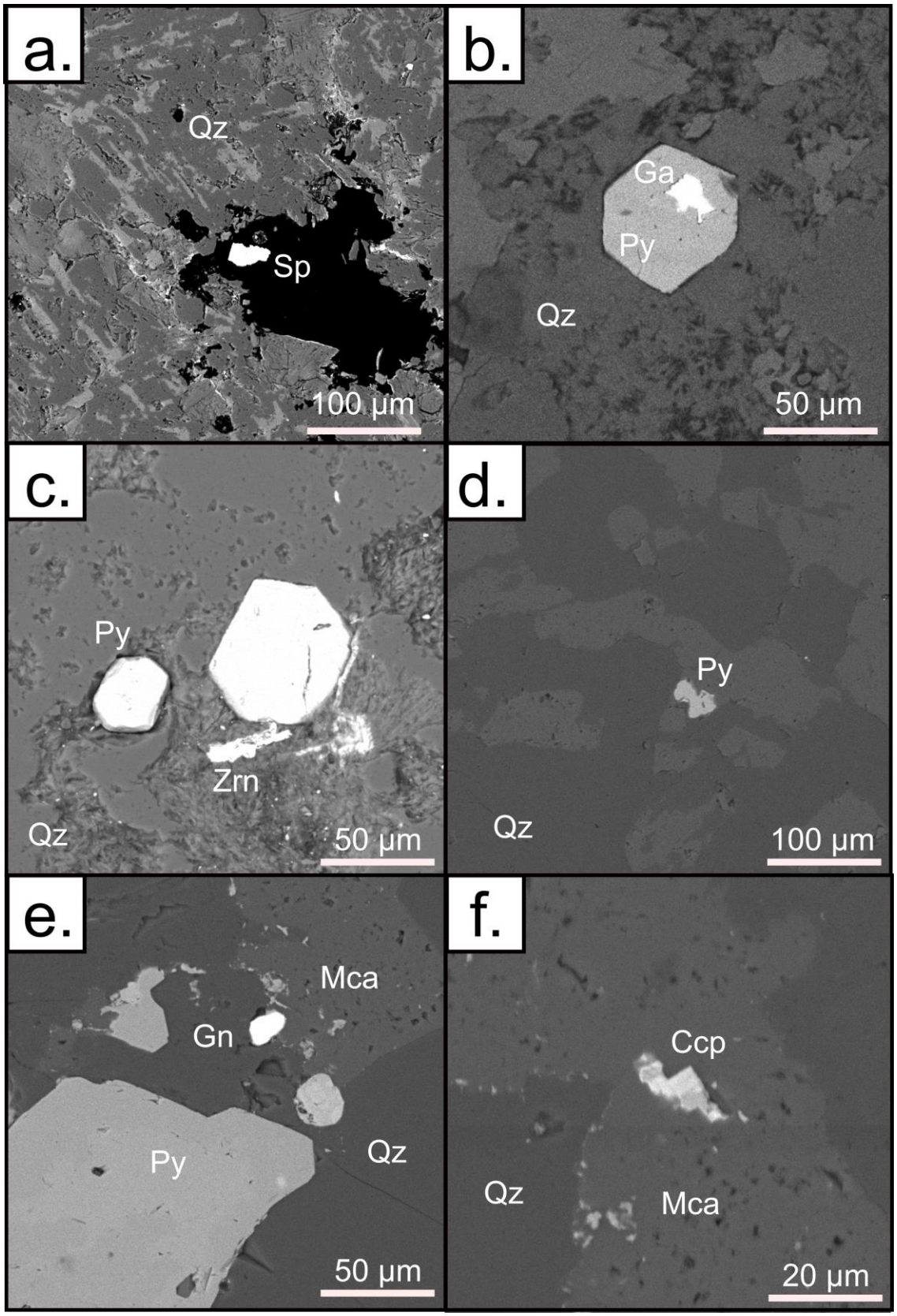

Figure 5.16. SEM-BSE images showing various types of mineralisation in the granitoids around Loch Tay. **a.** ARD_FELS_1; sphalerite crystal in a quartz vug. **b.** ARD_FELS_2; pyrite and galena coprecipitating in the quartz groundmass. **c.** ARD_FELS_2; pyrite crystals growing alongside zircon that is potentially hydrothermal in origin. **d.** TOM_FELS_2; disseminated pyrite. **e.** TOM_FELS_2; alteration assemblage including galena and pyrite. **f.** TOM_FELS_2; hydrothermal mica and chalcopyrite.

5.3.2. Textural observations from Tomnadashan

In this section, the characteristics of the different phases recorded from Tomnadashan during petrography (Table 5.1.) are summarised. The quartz that accompanies the metallic phases (e.g. pyrite; Fig. 5.17.a.) showed a homogenous response in SEM-CL and was observed to contain pyrite crystals (Fig. 5.17.a.); pyrite is a common phase in both the granitoid (Fig. 5.17.b., d., e.) and the quartz vein (Fig. 5.17.f.-h.). However, the pyrite can be distinguished on the basis of the coeval inclusions that it contains; PyA hosts coeval inclusions of BiTe (Fig. 5.17.d.) and chalcopyrite (Fig. 5.17.e.), whilst inclusions of galena and copper sulfosalts were recorded in PyC (Fig. 5.17.f.-h.). Fractures within PyA also contain molybdenite crystals (Fig. 5.17.b.), whereas PyC does not display any association with this phase. Regarding the relationship between sphalerite and galena at Tomnadashan, these two phases mutually intergrow with one another, which is evident in the G.2019.101.7 hand specimen (Appendix A) and the coeval inclusions of galena within the sphalerite (Fig. 5.17.i.). However, the galena has brecciated and entrained the earlier chalcopyrite (CcpA; Fig. 5.17.e.) that is coeval with PyA. There is also a veinlet dominated episode of mineralisation at Tomnadashan, which has introduced quartz, tetrahedrite, and chalcopyrite into the system (Fig. 5.17.f., j.).

The sample of the quartz vein at Tomnadashan (Appendix A; TOM_QTZ) records a voluminous episode of siderite precipitation that has brecciated and entrained the previously formed phases, including chalcopyrite (Fig. 5.17.a.); the striped pattern of the siderite makes it readily distinguishable from the quartz in SEM-BSE (Fig. 5.17.a.). However, some monazite crystals were observed within the siderite matrix; the monazites are euhedral and display internal zonation (Fig. 5.17.k.). In some instances, barytes veinlets were observed to crosscut the monazite (Fig. 5.17.k.). The siderite has also been crosscut by dolomite (Fig. 5.17.l.).

During petrographic characterisation of the thin sections and polished blocks, gold was not observed at Tomnadashan; however, a separate study on gold particles that were panned from the stream flowing out of the entrance to the mine revealed the presence of BiTe inclusions (wittichenite) within the gold (Fig. 5.17.c).

Mineral	Thin section(s) ID	A	B	C	D	E	F
Quartz	TOM_QTZ; TD-0 (vein)	QzA-C; indistinguishable SEM-CL response; featureless subhedral Qz crystals in the quartz vein, sometimes growing alongside Py (Fig. 5.17.a.)			Hairline fractures crosscuting sulphides/sulfosalts (Fig. 5.17.j.)		
Pyrite	SW_TOM_PYa + b (disseminated), TOM_QTZ (vein)	PyA; <1 cm crystals with inclusions of Mol and Bi tellurides (Fig. 5.17.b., d.); spatially coincides with CcpA (Fig. 5.17.e.); crosscut by TtrD (Fig. 5.17.f.)		PyC; contains inclusions of Gn, Tnt and Ttr (Fig. 5.17.g., h.)			
Bi tellurides	SW_TOM_PYa (disseminated)	Inclusions within PyA (Fig. 5.17.d.)					
Chalcopyrite	SW_TOM_PYa + b (disseminated), TOM_QTZ, B0018 (vein)	CcpA; intergrows with PyA (Fig. 5.17.e.)			CcpD; late-stage veinlets crosscutting Ttr (Fig. 5.17.j.)		
Molybdenite	B003 (disseminated)		Inclusions occurring in the fractures				

Mineral	Thin section(s) ID	A	B	C	D	E	F
			within PyA (Fig. 5.17.b.)				
Galena	TOM_QTZ, B0018 (vein)			GnC; voluminous stage, brecciates CcpA (Fig. 5.17.i.); GnC also occurs as coeval inclusions in PyC (Fig. 5.17.g.)			
Sphalerite	B0018 (vein)			SpC coprecipitates with GnC (Fig. 5.17.i.)			
Tetrahedrite	TOM_QTZ (vein)			TtrC occurs as inclusions within PyC (Fig. 5.17.h.)	TtrD crosscuts PyA and TntC (Fig. 5.17.f.)		
Tennantite	TOM_QTZ (vein)			TntC occurs as inclusions within PyC (Fig. 5.17.g.); envelopes PyA (Fig. 5.17.f.); may form a solid solution series with TtrC (Fig. 5.17.h.)			

Mineral	Thin section(s) ID	A	B	C	D	E	F
Monazite	TOM_QTZ (vein)					Intergrows with voluminous Sd (Fig. 5.17.k.)	
Siderite	TOM_QTZ (vein)					Fe-bearing, zoned (Fig. 5.17.a.); coprecipitates with Mnz (Fig. 5.17.k.)	
Dolomite	TOM_QTZ (vein)						Veinlets crosscutting or replacing Sd (Fig. 5.17.l.)
Barytes	TOM_QTZ (vein)						Veinlets crosscutting all phases (Figure. 5.17.b., k.)

Table 5.1. Observations made during petrographic characterisation of samples from Tomnadashan (Fig. 3.13.; Locality 8), with references to representative SEM images. The terms 'disseminated' and 'vein' are used to demonstrate the origin of the samples. In the 'Thin section ID' column, the brackets after each sample indicate whether the mineralisation is disseminated in the granitoid or hosted in the vein. A version of this table has appeared in Webb *et al.* 2024b. The stage letters A-F pertain to distinct paragenetic stages.

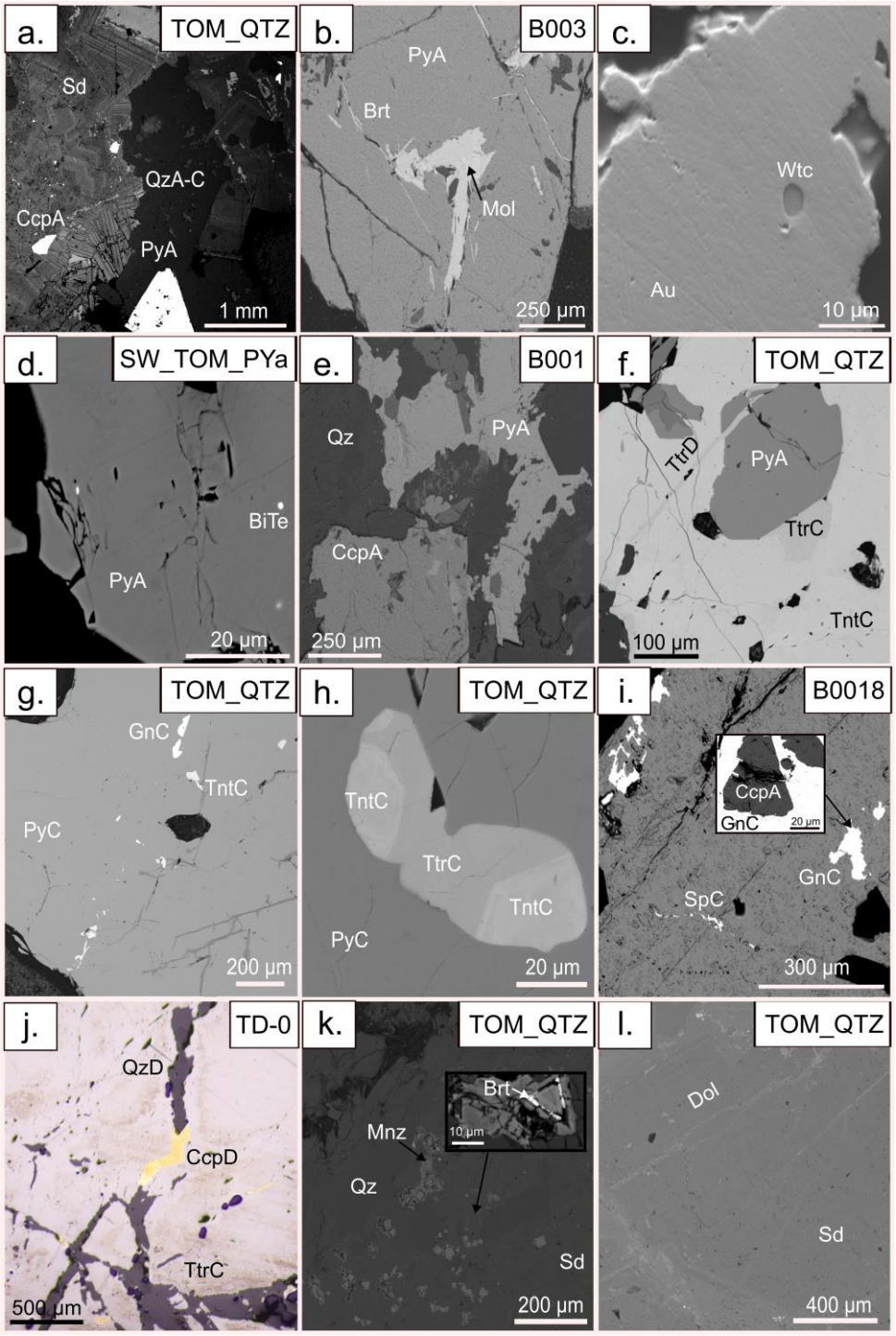

Figure 5.17. Scanning electron and reflected light microscope images of representative textures illustrating the relationships described from Tomnadashan (Table 5.1.). **a.** Siderite crosscutting quartz. **b.** Molybdenite precipitating in PyA fractures. **c.** Gold particle that was recovered from the stream flowing out of the entrance to the mine. **d.** Coeval BiTe inclusions within pyrite (PyA). **e.** Chalcopyrite (CcpA) growing alongside PyA. **f.** Copper sulfosalt veinlets crosscutting PyA. **g-h.** Galena, and copper sulfosalts demonstrating a solid solution series, occurring as coeval inclusions within PyC. **i.** Galena inclusions precipitating within sphalerite. **j.** RLM image showing veinlets containing quartz (QzD) and chalcopyrite (CcpD) crosscutting Tetrahedrite (TtrC). **k.** Barytes infilling monazite that is coeval with the siderite. **l.** Late-stage dolomite veinlets crosscutting or replacing the siderite. b, e and i ©National Museums Scotland. This figure has been adapted from Webb *et al.* 2024b.

5.3.3. Textural observations from Lead Trial

The paragenetic observations at this locality are summarised in Table 5.2. At Lead Trial, the disseminated mineralisation in the granitoid is comprised of a pyritic assemblage with minor amounts of galena and sphalerite (Fig. 5.16.b.; Fig. C.2., 60 m). However, the vein-hosted mineralisation at this locality is different; galena and sphalerite are the primary constituents of the assemblage (Fig. 5.18.d.), with pyrite only occurring amongst entrained clasts of the granitoid breccia (Fig. 5.18.a.). Regarding the quartz at Lead Trial, at least four generations were recognised during petrographic characterisation (Table 5.2.); QzB (coarse, euhedral crystals > 100 μm), QzC (fine-grained, anhedral, most voluminous), QzD (lamellar and euhedral crystals that grow in the vugs of QzB and QzC), and QzE (veinlets that crosscut pre-existing phases). These different quartz generations (Fig. 5.18.c., g.) are described in Table 5.2.

The finer grained QzC coincides with the precipitation of large quantities of galena and sphalerite (Fig. 5.18.g.). Whilst it was not observed in the thin sections at Lead Trial, core-logging of the prospect found that small amounts of chalcopyrite coincide with the voluminous galena and sphalerite (Fig. C.2., 25-32 m). Furthermore, the thin section from RX2959KA (Fig. 3.13.; Locality 6) demonstrated the occurrence of chalcopyrite blebs within the large galena crystals (Fig. 5.18.e.). SEM images of the gold particles retrieved from crushed rock samples collected at Lead Trial (Fig. 5.18.f.) also indicate that some of the gold at this locality (AuC) contains sphalerite and galena inclusions.

Mineral	Thin section(s) ID	A	B	C	D	E	F
Pyrite	K30182KA, ARD_FELS_2	Pyrite crystals <200 µm are disseminated throughout the granitoid wallrock (Fig. 5.18.b.)					
Galena	K30182KA, ARD_FELS_2	GnA; coprecipitates with euhedral PyA in the groundmass of the granitoid (Fig. 5.18.a.)		GnC; voluminous galena stage, some crystals >1 cm (Fig. 5.18.d., e.)	GnD; microscopic galena veinlets that rim vugs in QzB and QzC (Fig. 5.18.g., h.)		
Quartz	LDT3, LDT4, K30118KA		QzB; coarsest Qz crystals observed (>100 µm), display patchy zoning in SEM-CL (Fig. 5.18.c.); brecciated by later Qz generations	QzC; very fine-grained and anhedral, most voluminous quartz stage (Fig. 5.18.c.)	QzD; lamellar, euhedral, and coarse crystals in QzB and QzC vugs (Fig. 5.18.g.)	QzE; late-stage veinlets that brecciate previous Qz generations (Fig. 5.18.c.)	
Sphalerite	LDT1			SpC; intergrows with the voluminous galena stage (Fig. 5.18.d.)			
Chalcopyrite	RX2929KA			Occurs as inclusions within the			

Mineral	Thin section(s) ID	A	B	C	D	E	F
				voluminous galena stage (Fig. 5.18.e.)			
Gold	RX2967KA, LDT1			AuC; coprecipitates with Sp and GnC (Fig. 5.18.f.); finer grained than AuC	AuD; coarse particles hosted within QzB and QzD vugs (Fig. 5.18.i., j.)		
Barytes	K30118KA						Late-stage veinlets that infill previous Qz generations (Fig. 5.18.k.)
Carbonate	K30118KA						Late-stage veinlets that infill previous Qz generations (Fig. 5.18.l.)

Table 5.2. Observations made during petrographic characterisation of samples from Lead Trial (Fig. 3.13.; Locality 5), with references to representative SEM images (Fig. 5.18.).

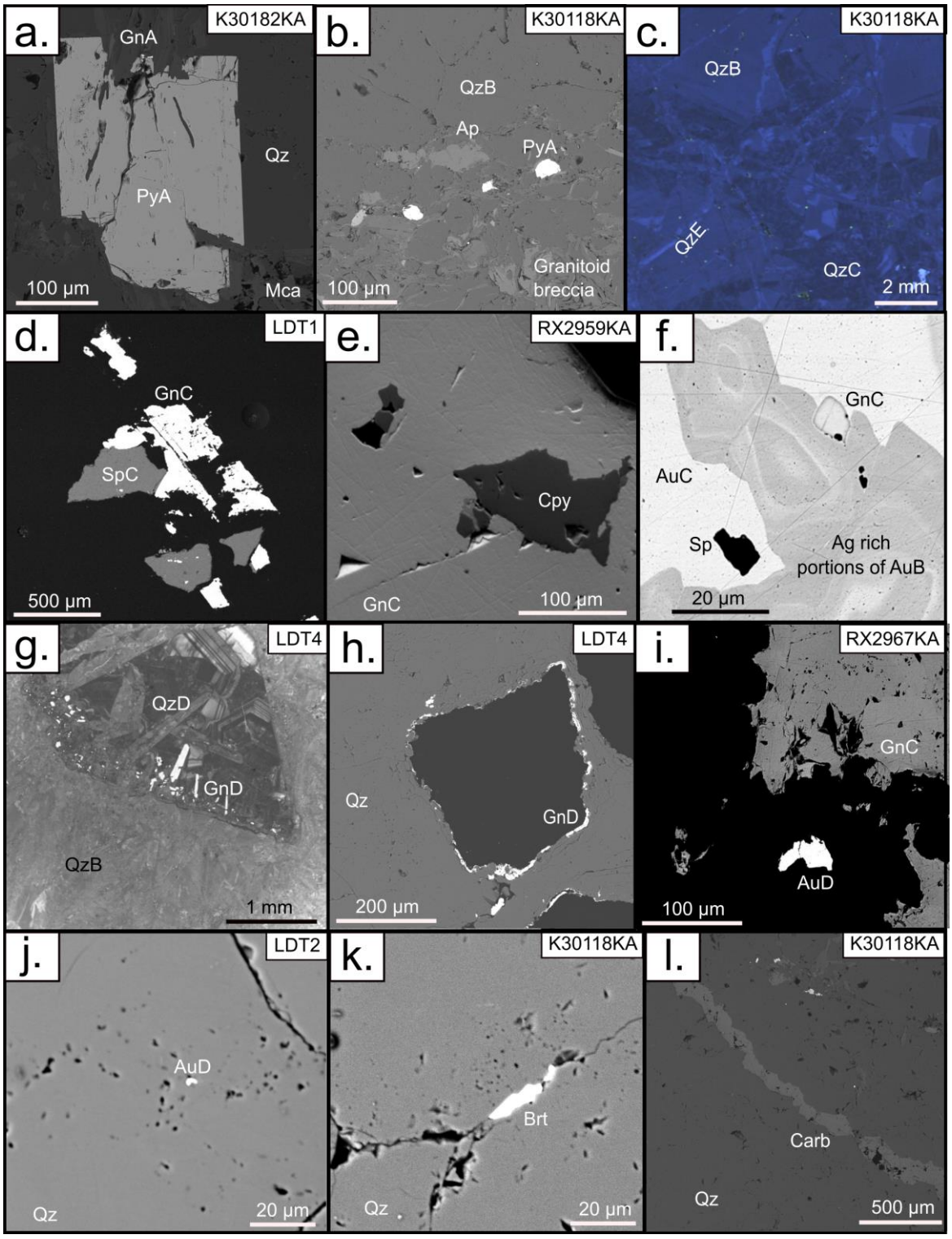

Figure 5.18. SEM-BSE and SEM-CL images of representative vein textures illustrating the relationships described in Table 5.2. **a.** Euhedral pyrite crystal (rimmed by galena) occurring within brecciated granitoid wallrock. **b.** Pyrite and granitoid breccia that has been entrained by QzA. **c.** SEM-CL images demonstrating the morphological differences between QzA (euhedral), QzB (brecciated), and QzD (veinlets). **d.** Voluminous galena and sphalerite mineralisation event. **e.** Coeval chalcopyrite inclusion within galena. **f.** Gold particle from crushed rock samples collected at Lead Trial, which contains inclusions of galena and sphalerite. **g-j.** QzD, GnD and AuD within quartz vugs (QzB and QzC). **k + l.** Late stage barytes and carbonate veinlets crosscutting the Qz groundmass. With the exception of c. and g. (SEM-CL), all images are SEM-BSE.

5.3.4. Textural observations from the GAV

The petrographic observations from the GAV were outlined in Webb *et al.* 2024a and are paraphrased in this section (Table 5.3.). In SEM-CL, it was possible to identify a euhedral quartz generation that displayed internal zonation (QzA; Fig. 5.19.a., b.); QzA was brecciated by the injection of later quartz generations, which yielded homogenous SEM-CL responses (Fig. 5.19.b., c.). However, the differences in the associated sulphide assemblages indicate that there are at least two generations of quartz with similar characteristics in SEM-CL; for this reason, the quartz yielding homogenous SEM-CL responses has been termed QzB and QzC (Table 5.3.). However, another quartz generation (Fig. 5.19.c.; thin hairline fractures) has brecciated the earlier Qz generations; this material has been termed QzE (Fig. 5.19.c.). The final generation of quartz (QzE) has also coincided with the brecciation of carbonates (DolD) in the GAV. DolD occurs as sub to euhedral crystals that occupy fractures crosscutting the phases that precipitated in Stages A-C (Fig. 5.19.j.). Regarding the pyrite, this phase shows an association with QzB and QzC (Fig. 5.19.b.). It was possible to distinguish two categories of pyrite; some crystals were darker when observed in SEM-BSE (PyB; Fig. 5.19.d.), whilst others (PyC) were lighter in colour and precipitated in the fractures of PyB (Fig. 5.19.d.-g.). There were also variations in the inclusion assemblages recorded by PyB and PyC; rounded blebs of gold (AuB), chalcopyrite (CcpB), galena (GnB), and sphalerite (SpB) occur in PyB (Fig. 5.19.e., f.). On the other hand, Energy-Dispersive X-Ray (EDX) analyses demonstrated that PyC contained detectable amounts of As (unlike PyB). Furthermore, transitional zones between PyB and PyC may contain small crystals of galena (GnC) and chalcopyrite (Fig. 5.19.f.).

Other sulphides have also been recorded in the GAV; for example, there are two generations of chalcopyrite and three generations of sphalerite (Table 5.3.), which form coeval inclusions within PyB (Fig. 5.19.e.); chalcopyrite typically occupies the interfaces between PyB and PyC. The second generations of chalcopyrite (CcpC) and sphalerite (SpC) occur as mm-scale grains that coprecipitate with one another, PyC, and both generations of gold (Fig. 5.19.g.-i.). It was also possible to observe chalcopyrite inclusions within SpC and a final type of sphalerite (SpE) that coprecipitates with the coarse galena generation (GnE) and QzE (Fig. 5.19.j.). DolD has been fractured during the injection of GnE, SpE, and QzE (Fig. 5.19.j.). With regards to galena, there are two types of this phase within the GAV: bleb-like inclusions within PyB and crystals along the PyB and PyC boundary (Fig. 5.19.d.-f.). The later galena generation (GnE) is associated with hairline fractures in the quartz and the late sphalerite generation (SpE) that crosscuts all previous phases (Table 5.3.).

Two categories of gold were recognised at the GAV during petrographic characterisation: micron-scale inclusions within PyB (Fig. 5.19.e.) and Stage C AuC precipitating in fractures within the earlier sulphides (Fig. 5.19.f., g.; Table 5.3.). In addition to being able to distinguish AuB and AuC by their textural differences, the Ag contents in the alloys of each generation differed (c. 25-26 wt % Ag in AuB, 35-37 wt % Ag in AuC; Webb *et al.*, 2024a).

Mineral	Thin section(s) ID	A	B	C	D	E
Quartz	AVRE	QzA; early Qz stage, often zoned; brecciated by all later phases (Fig. 5.19.a., b.)	QzB and QzC infilled fractures brecciating the zoned QzA, brecciated by DolD; QzB and QzC are indistinguishable in SEM-CL (Fig. 5.19.b.)			QzE; hairline fractures crosscutting all previous generations and sulphides (Fig. 5.19.c., j.)
Pyrite	RC2, RC5		PyB: darker in SEM-BSE, no As (contrary to PyC); some Sp, Gn, Ccp and Au inclusions (<5 µm; Fig. 5.19.d.–f.)	PyC: lighter than PyB in SEM-BSE, c. 1.5 wt % As; As rims around/in fractures within PyB, or as individual crystals; small Gn, Ccp along interfaces between PyB and PyC; coprecipitates with Au, Sp and Ccp (Au often in fractures in the py) (Fig. 5.19.b., d.–g.)		
Chalcopyrite	RC5		Small blebs of Ccp within PyB (Fig. 5.19.e.)			
	RC1, RC2, RC3, RC4			CcpC: fractured, co-precipitates with late PyC, AuC, SpC; crosscut by fractures infilled by		

Mineral	Thin section(s) ID	A	B	C	D	E
				QzE and GnE; also occurs as small inclusions within SpC (Fig. 5.19.i.)		
Galena	RC2, RC5		GnB: <5µm, co-precipitating with Au in the PyB, which is darker in SEM-BSE and lacks As (Fig. 5.19.f.)	GnC: small (<10 µm) blebby grains along interfaces between PyB and PyC (Fig. 5.19.f.)		
	RC1					GnE: large >100 µm crystals in hairline fractures; intergrown with SpE; crosscuts all earlier phases (Fig. 5.19.j.)
Sphalerite	RC1, RC2, RC5		SpB; coeval bleb-like inclusions within PyB (Fig. 5.19.f.)	SpC; large crystals (>300 µm) mutually intergrowing with PyC (Fig. 5.19.h.)		SpE: very large (>100 µm) crystals intergrown with GnE; crosscuts all earlier phases (Fig. 5.19.j.)
Gold	RC2, RC4		AuB: Blebby Au inclusions within PyB (<5 µm), co-precipitates with Gn;	AuC: co-precipitates with Ccp and Qz in cracks; Higher Ag content~35%		

Mineral	Thin section(s) ID	A	B	C	D	E
			lower Ag content~25% than AuC (Fig. 5.19.e.)	than AuB and coarser (<100 µm) (Fig. 5.19.f.-h.)		
	AVRE		AuC or AuB: circular gold grains, <5 µm in QzB+C (Fig. 5.19.f., g.)			
Dolomite	AVRE, RC1			Crosscuts earlier phases; crosscut by sulphides and hairline fractures; crystals <100 µm (Fig. 5.19.j.)		

Table 5.3. Observations made during petrographic characterisation of samples from the Glen Almond Vein, with references to representative SEM images (Fig. 5.19.). This table is a revised iteration of a similar table that appeared in Webb *et al.* 2024a.

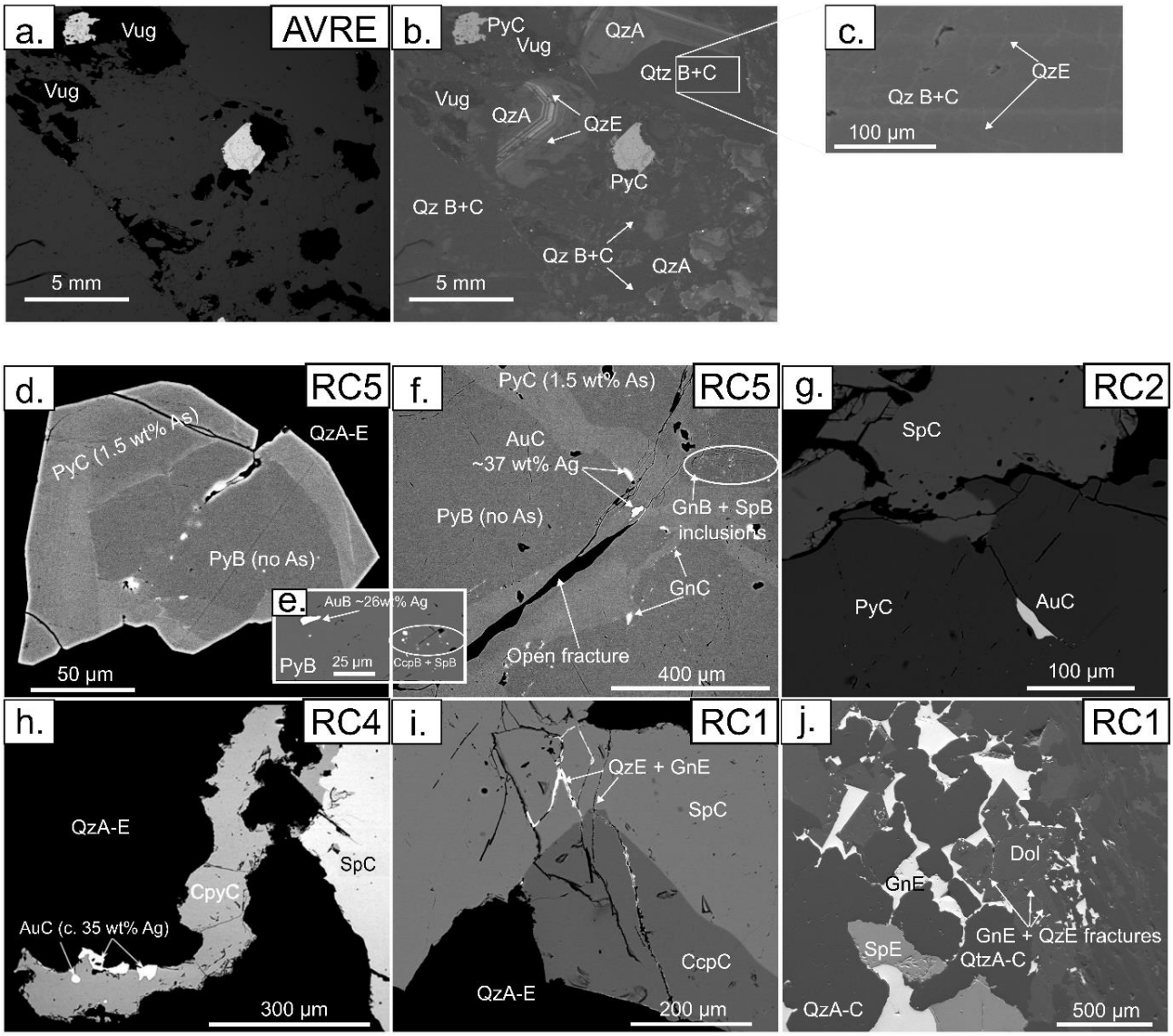

Figure 5.19. SEM-CL and SEM-BSE photographs of representative vein textures illustrating the relationships described in Table 5.3. **a.** SEM-BSE image: the vugs and the pyrite grains (light grey) are clearly imaged. **b + c.** SEM-CL imaging enables the observation of three different types of quartz in the sample. High-contrast SEM-CL detail of the homogeneous QzB + C is depicted in c. **d–g.** High-contrast SEM-BSE images of various pyrite stages. **h + i.** SEM-BSE images showing the relationships between Stage C sphalerite, chalcopyrite, and gold, and a later, Stage E galena and quartz. **j.** SEM-BSE image showing an Mg-rich carbonate brecciating the early phases that is in turn brecciated by the late sphalerite, galena, and quartz. This figure has been modified from Webb *et al.* 2024a.

5.4. Results of radiometric dating

In this section, the results derived from the U-Pb and Re-Os analyses that were conducted on the granitoids around Loch Tay and molybdenite from Tomnadashan are summarised, respectively. Regarding the description of the Re-Os ages, this has been paraphrased from Webb *et al.* 2024b.

5.4.1. U-Pb geochronology of the Siluro-Devonian granitoids

Full analytical results for the CA-ID-TIMS dating that was conducted in this study are presented in Appendix D (Table D.1.) and plotted on the U-Pb concordia diagrams in Fig. 5.20. The ages are reported as $^{206}Pb/^{238}U$ ages (Table D.1.). When assessing the age of a given intrusion on the basis of U-Pb ages recorded by zircons, the recommended approach is to take a weighted mean of the $^{206}Pb/^{238}U$ dates (Condon *et al.*, 2023); this mean, along with the mean square of weighted distributions (MSWD), reflects the average crystallisation time of zircons from the sample. Therefore, the ages of the granitoids around Loch Tay can be summarised as follows; 418.53 ± 0.13 Ma (ARD_FELS_1), 418.87 ± 0.15 Ma (TOM_FELS_2), 419.42 ± 0.28 Ma (CB_FELS_2), and 419.10 ± 0.20 Ma (SW3). As depicted on the rank-order plots (Fig. 5.20.), these intrusions record variability in the U-Pb dates (from the mean age) that is smaller than the analytical uncertainty. However, there is slightly more spread in the data from CB_FELS_2; the zircon fractions from this sample record ages between 420.42 and 418.64 Ma (Table D.1.).

In terms of the Wetherill-Concordia diagrams that were produced from the U-Pb data (Table D.1.) in IsoplotR (Fig. 5.20.), most of the radiometric dates have uncertainty ellipses that intersect with their concordia curves. However, this is not always the case; for example, in ARD_FELS_1, z3 and z2 record ^{207}Pb values that are above the concordia curve (Fig. 5.20.a.). Furthermore, in TOM_FELS_2 (z1) and CB_FELS_2 (z2), some fractions also have ^{207}Pb values that do not intersect with the concordia curves (Fig. 5.20.b., c.). ^{207}Pb loss has occurred in SW3, with the uncertainty ellipse of z4 plotting to the left of the concordia curve (Fig. 5.20.d.).

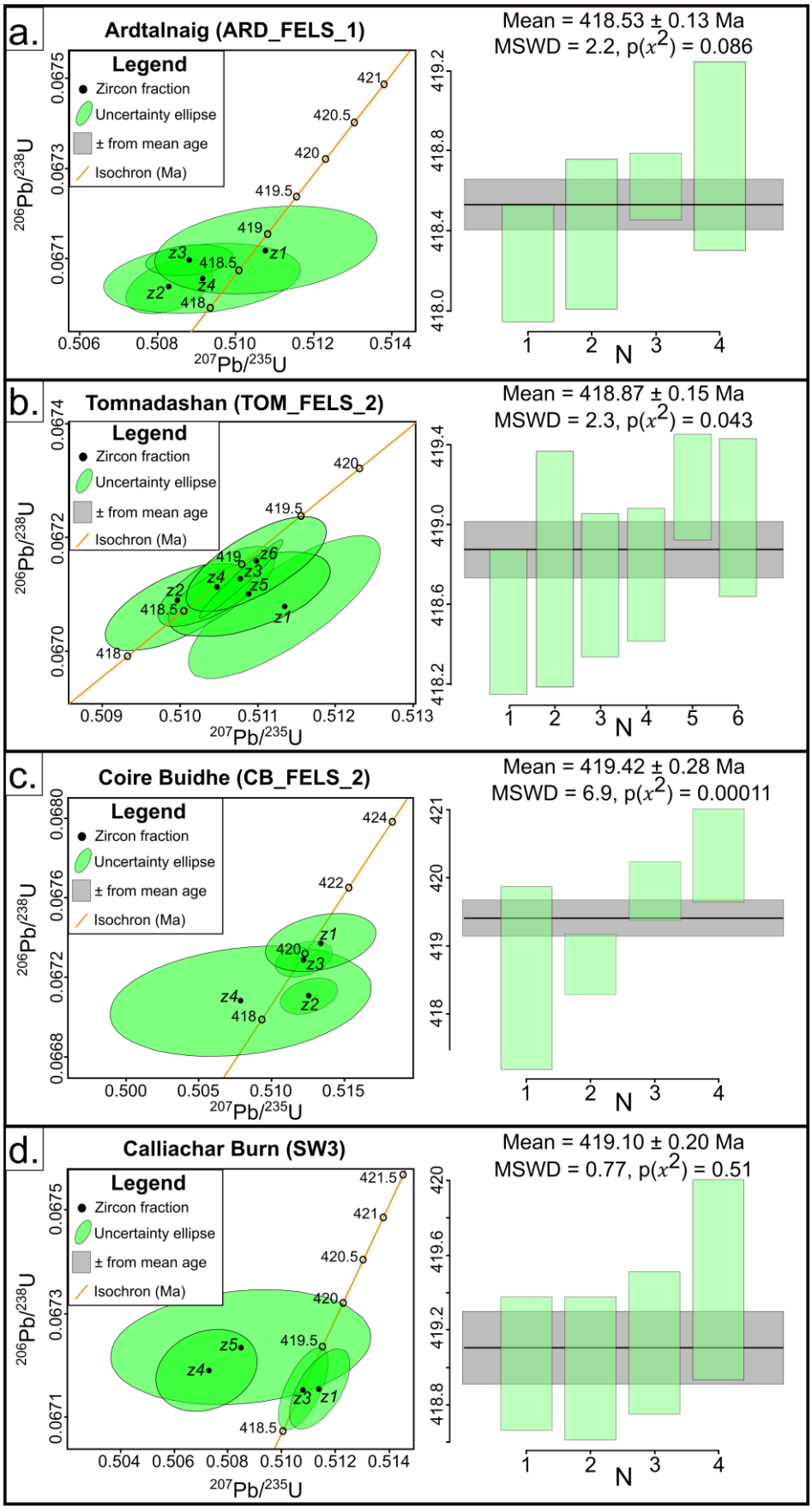

Figure 5.20. Concordia and rank-order plots for the zircon fractions (Table D.1.) from the granitoids around Loch Tay. **a.** Ardtalnaig (ARD_FELS_1). **b.** Tomnadashan (TOM_FELS_2). **c.** Coire Buidhe (CB_FELS_2). **d.** Calliachar Burn (SW3). The plots were created using IsoplotR (Vermeesch, 2018).

5.4.2. Re-Os ages of the molybdenite from Tomnadashan

Regarding the Re-Os age determinations, TOM_MOLY_SM and PA_MOLY were collected from the smelter mill described by Devéria (2001). However, a third sample from the mine was provided by NMS (G.1878.49.10.1). Images of these samples are depicted in Fig. 5.21., with the finer grain size in G.1878.49.10.1 being visible. TOM_MOLY_SM and PA_MOLY, which represent quartz veinlets crosscutting the igneous host rocks (Fig. 5.21.a.-b.), contain molybdenite flakes that are larger (2-4 mm in size).

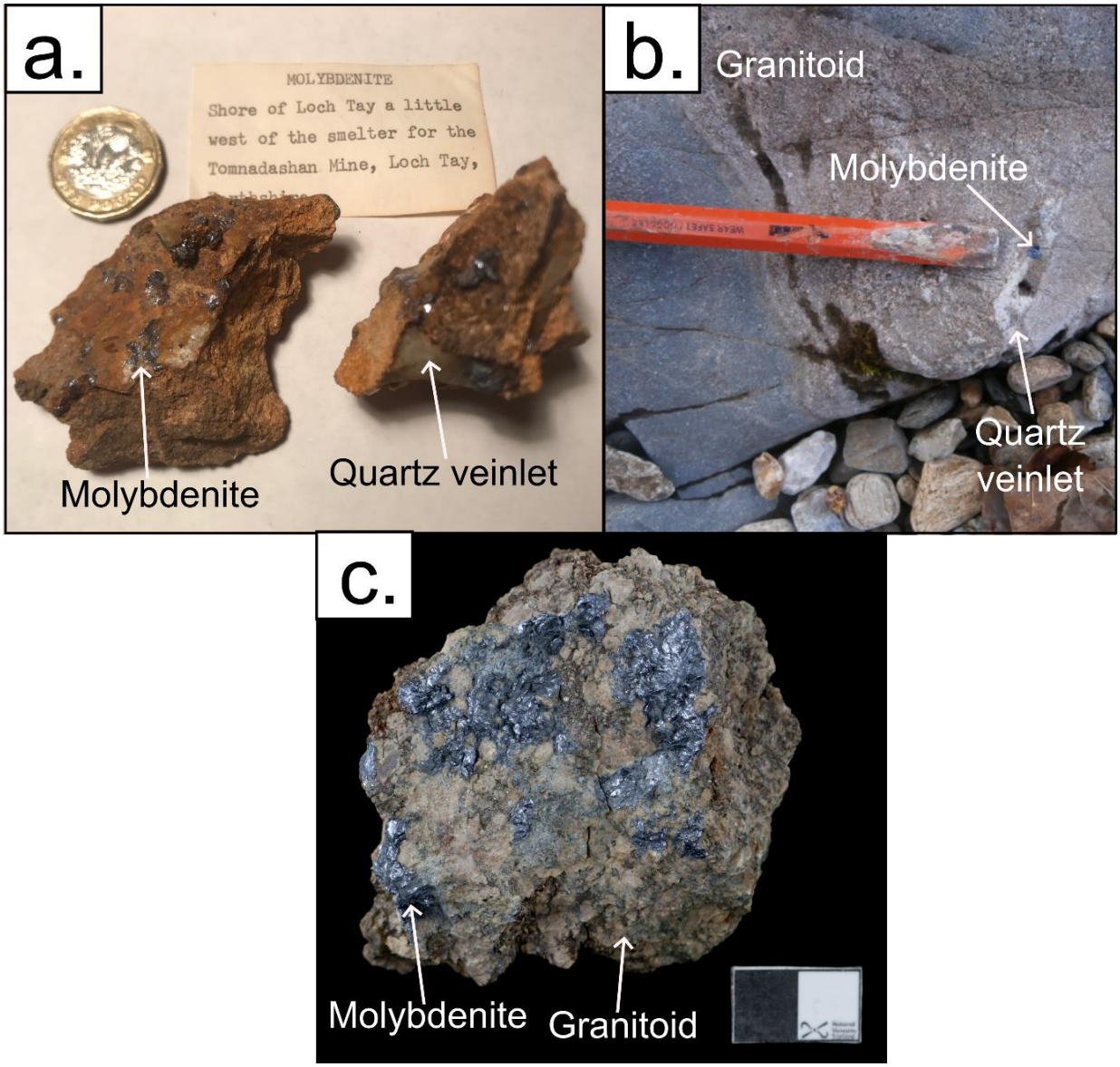

Figure 5.21. Samples of molybdenite from Tomnadashan that were dated via the Re-Os chronometer (reproduced from Webb *et al.*, 2024b). **a.** TOM_MOLY_SM (vein-hosted molybdenite). **b.** PA_MOLY (vein-hosted molybdenite). **c.** G.1878.49.10.1 (molybdenite disseminated in the granitoid host rock with pyrite). (© National Museums Scotland).

The results of the Re-Os dating are presented in Table 5.4. The Re concentrations in all samples were high; 123.48 ppm (TOM_MOLY_SM), 209.9 ppm (G.1878.49.10.1), and 106.11 ppm (PA_MOLY) (Table 5.4.). The ^{187}Os concentrations recorded by these samples were also high; 548.3 ppb (TOM_MOLY_SM), 924.0 ppb (G.1878.49.10.1), and 471.6 ppb (PA_MOLY). The ages obtained throughout the course of these analyses can be described as 419 ± 2.1 Ma to 423 ± 2.2 Ma. The error margins for the results were mutually consistent (c. 0.5 % error), which is indicative of a negligible amount of uncertainty and error associated with the procedure.

Sample	Description	Re (ppm)	±	^{187}Re (ppm)	±	^{187}Os (ppb)	±	Age (Ma)	±
TOM_MOLY_SM	Vein-hosted molybdenite	123.48	0.4	77.61	0.2	548.3	1.4	422.6	2.1
G.1878.49.10.1	Disseminated molybdenite	209.9	0.8	131.9	0.5	924.0	2.9	419.0	2.1
PA_MOLY	Vein-hosted molybdenite	106.11	0.4	66.69	0.2	471.6	1.2	423.0	2.2

Table 5.4. Results of Re-Os dating of molybdenite from Tomnadashan. Osc is the common Osmium within the sample, calculated using the double spike method. Sample information can be found in Appendix A.

5.5. $\delta^{34}S$ results from the LTVS

Throughout the Study Area, the $\delta^{34}S$ signature of the sulphides ranges from -1 to +13 ‰ (Fig. 5.22.). However, several datapoints fall somewhere in the middle of this range (Fig. 5.22.). Whilst the $\delta^{34}S$ results yielded by the in-situ analyses on pyrite were similar to those without petrographic constraint (Fig. 5.23.a.), for galena, they were consistently different; specifically, the $\delta^{34}S$ values reported from the mass spectrometer at the University of Leeds are often significantly lower than those derived via methods lacking paragenetic context (Fig. 5.23.b.; Lead Trial, Coire Buidhe, Tomnadashan, and the GAV).

In terms of linking these trends to the regional geology, the $\delta^{34}S$ values around Lead Trial and Tomnadashan (herein recognised as a distinct system and referred to as 'Lead Trial-Tomnadashan') are consistently lower than those recorded from elsewhere (Fig. 5.22.; Fig. 5.23.). Whilst only one measurement is available, the $\delta^{34}S$ value of galena from ARD_1 was indistinguishable from the Lead Trial datapoints (Fig. 5.23.b.). Many of the veins in the eastern portions of the Study Area, which are hosted by metasediments (e.g. the CUB veins, Tombuie, Coire Buidhe, and Spoil Heap), are usually characterised by $\delta^{34}S$ values of >+3 ‰ (Fig. 5.22.). Herein, these localities are considered to represent a population termed the 'metasediment-hosted veins.' Furthermore, it was common for individual localities to record a broad range in $\delta^{34}S$ values, regardless of whether the population belongs to the 'Lead Trial-Tomnadashan' or 'metasediment-hosted veins' categories. For example, at Lead Trial, $\delta^{34}S$ values ranged between -1 and +5 ‰ (Fig. 5.23.b.), whilst at the GAV, the pyrite displays $\delta^{34}S$ values of between +9 to +13 ‰. However, V7 (Calliachar Burn) is an exception to the overall trend of broad $\delta^{34}S$ ranges at each locality; here, $\delta^{34}S$ values from pyrite were consistently between +8 and +9 ‰ (Fig. 5.23.a.). Furthermore, whilst only two datapoints are available from the Comrie Pluton, measurements on distinct hand specimens (Appendix A; CMRIE4 and CMRIE7) yielded values (+4.9 and +5.3 ‰; Table E.1., No. 102-103) that were very similar (Fig. 5.23.a.).

Regarding the metasediment-hosted veins, despite consistently recording $\delta^{34}S$ values > +3 ‰ (Fig. 5.23.), localities within this population display a large amount of variation. Pyrite crystals from Spoil Heap and the CUB veins yielded similar values (e.g. +8 ‰; Fig. 5.23.a.), whereas the $\delta^{34}S$ values from pyrite in the GAV and Tombuie were typically heavier (between +9 and +13 ‰). The same trend was not observed in the galena $\delta^{34}S$ dataset; Tombuie recorded values > +12 ‰ (in comparison to the $\delta^{34}S$ measurements on galena from the GAV, which were between +5.5 and +8.5 ‰; Fig. 5.23.b.). In terms of the 'base metal' and 'high-grade' vein classifications recognised by Ixer *et al.* 1997 (Table 3.5.), V3, V6, and V7 ('high-grade' veins) recorded similar $\delta^{34}S$ values (Fig. 5.23.b.), whilst V5 (the only 'base metal vein' included in this study) was isotopically heavier, as were galena crystals from the Urlar Burn (between +7 and +9.5 ‰; Fig. 5.23.b.). $\delta^{34}S$ values from the galena samples collected at Coire Buidhe and Spoil Heap were also similar to the datapoints for the 'high-grade' veins in the Calliachar Burn (Table 3.5.; Fig. 5.23.b.).

There is no clear relationship between the $\delta^{34}S$ values and the metamorphic grade of the metasediments; whilst some of the highest $\delta^{34}S$ measurements were recorded from amphibolite facies host rocks (the CUB veins and Tombuie; Fig. 5.22.), Spoil Heap and the GAV occur within the greenschist facies zone (Fig. 5.22.) and display $\delta^{34}S$ values between +7 and +13 ‰. In terms of the relationship between $\delta^{34}S$ and structural geology, localities adjacent to the LTF (e.g. Tomnadashan, Lead Trial, and Fortingall) record the lowest $\delta^{34}S$ values (Fig. 5.22.). On the other hand, the heaviest $\delta^{34}S$ values are associated with subsidiary faults that trend NE-SW, including the Urlar Burn Fault and the Tombuie Fault (Fig. 5.22.). Measurements from the GAV, which is one of the isotopically heaviest localities (Fig. 5.22.), also cluster within a number of smaller-scale faults. Given that most of the LTVS is hosted within the Southern Highland Group (Fig. 5.22.), it is difficult to discern any relationship between host rocks and $\delta^{34}S$ values. However, the most depleted $\delta^{34}S$ values occur at Fortingall (Smith, 1996), which as described previously, represents the trace of the LTF (Fig. 5.22.). Furthermore, the $\delta^{34}S$ values at Coire Buidhe represent measurements from mineralisation that is hosted in the Argyll Group; again, an association with isotopically lighter $\delta^{34}S$ measurements (relative to the rest of the metasediment-hosted veins in the East) is observed. However, at Coire Buidhe, isotopically heavier $\delta^{34}S$ measurements (>+5 ‰; Fig. 5.22.b.) were also recorded. The occurrence of Dalradian metabasics and amphibolites corresponds with $\delta^{34}S$ values >+5 ‰ (e.g. at Tombuie and the CUB veins; Fig. 5.22.). Regionally, some of the lowest $\delta^{34}S$ values (<+2 ‰) occur within the granitoids at Lead Trial and Tomnadashan (Fig. 5.22.). However, the $\delta^{34}S$ values within the granitic portions of the Comrie Pluton (Fig. 5.23.a.; +4.8 and +5.3 ‰) were isotopically heavier than the sulphides associated with the granitoids at Tomnadashan.

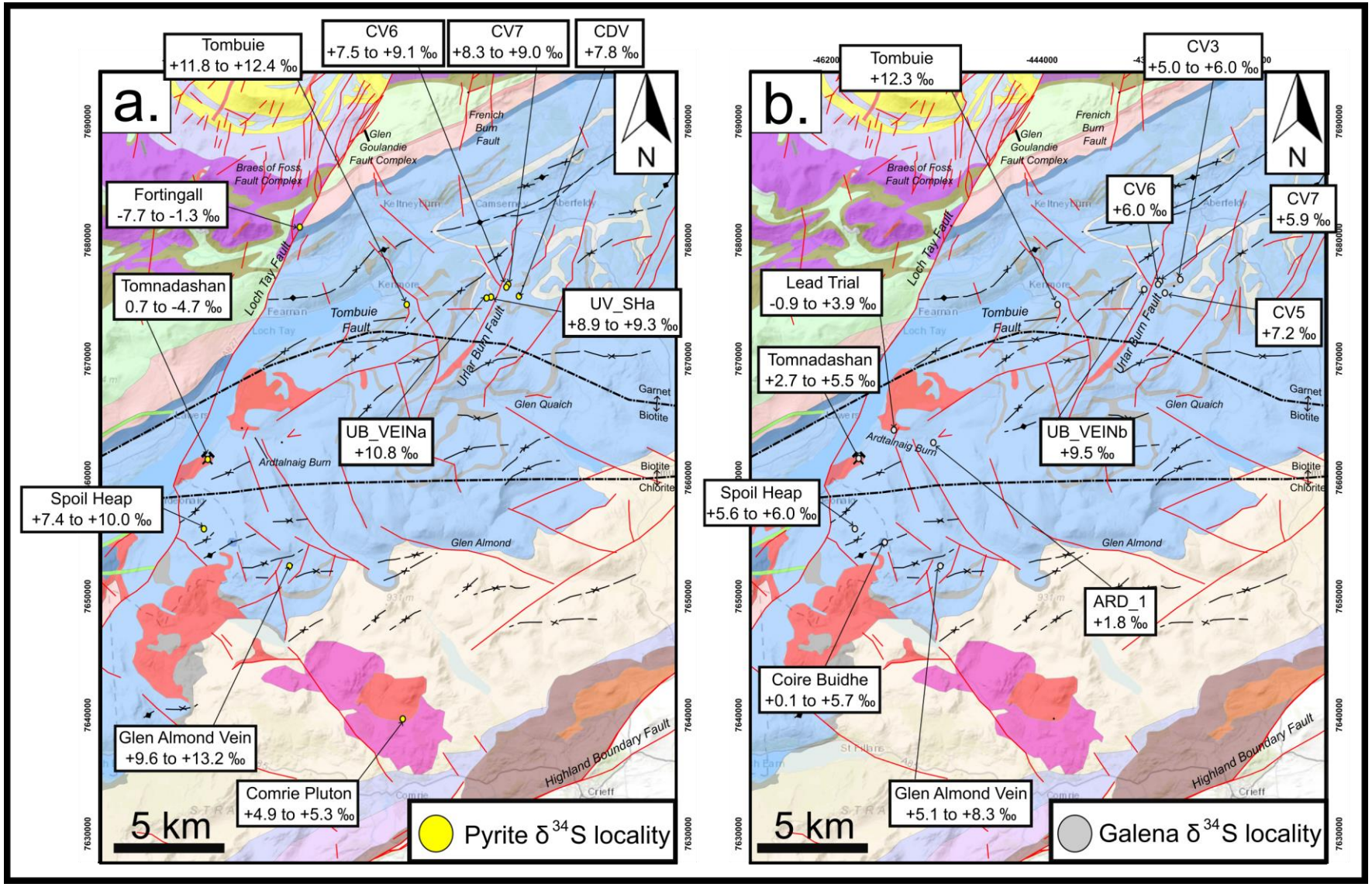

Figure 5.22. Modified versions of the geological map (Fig. 3.13.) annotated with the $\delta^{34}S$ results for **a.** Pyrite and **b.** Galena samples from the LTVS. The legend for the geological information on this figure is consistent with the legend shown in Fig. 3.13. The Fortingall measurements were reproduced from Smith (1996).

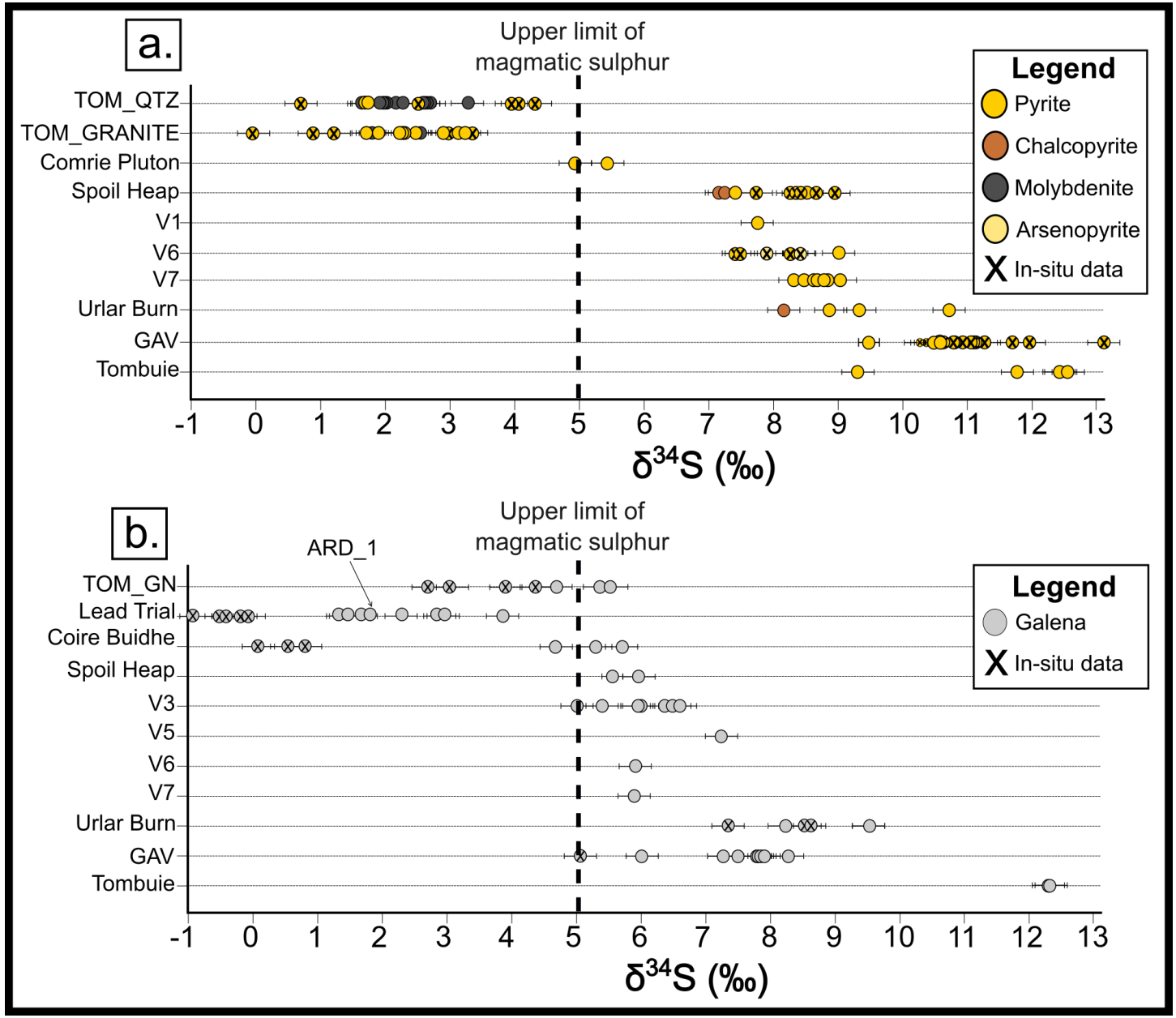

Figure 5.23. Results of the $\delta^{34}S$ analyses displayed in a graphical format (see Appendix E for the full dataset). The 'V' number refers to the 'V' series in the Calliachar Burn (e.g. Fig. 3.25.; V1 = Discovery Vein). 'TOM_QTZ' has been used as an abbreviation for the quartz vein at Tomnadashan (Appendix A; TOM_QTZ), whilst 'TOM_GRANITE' is used to denote mineralisation disseminated in the granitoid at this locality. 'TOM_GN' refers to G.2019.101.7 (Appendix A). **a.** Pyrite and associated phases. **b.** Galena (the single 'ARD_1' measurement has been included with the rest of the Lead Trial samples and annotated for clarity).

The histogram (Fig. 5.24.) is a useful tool for visualising the distribution of $\delta^{34}S$ measurements derived throughout the course of this study. For example, it is possible to identify measurements from pyrite crystals throughout the LTVS that consistently cluster around +2 and +11 ‰ (termed 'Population 1' and 'Population 2' on Fig. 5.24.). The greater range in spread around the peak associated with pyrite from Population 2 may be indicative of a larger amount of heterogeneity associated with this population, which encompasses the metasediment-hosted veins of the LTVS. However, this trend is not replicated in the galena $\delta^{34}S$ data; instead, the galena $\delta^{34}S$ values are scattered across the spectrum recorded by the entire LTVS (Fig. 5.24.b.). This trend is likely to reflect the nature of the galena dataset; specifically, with the exception of Lead Trial/Ardtalnaig, repeat measurements have not been conducted on most of the localities for which galena data was derived.

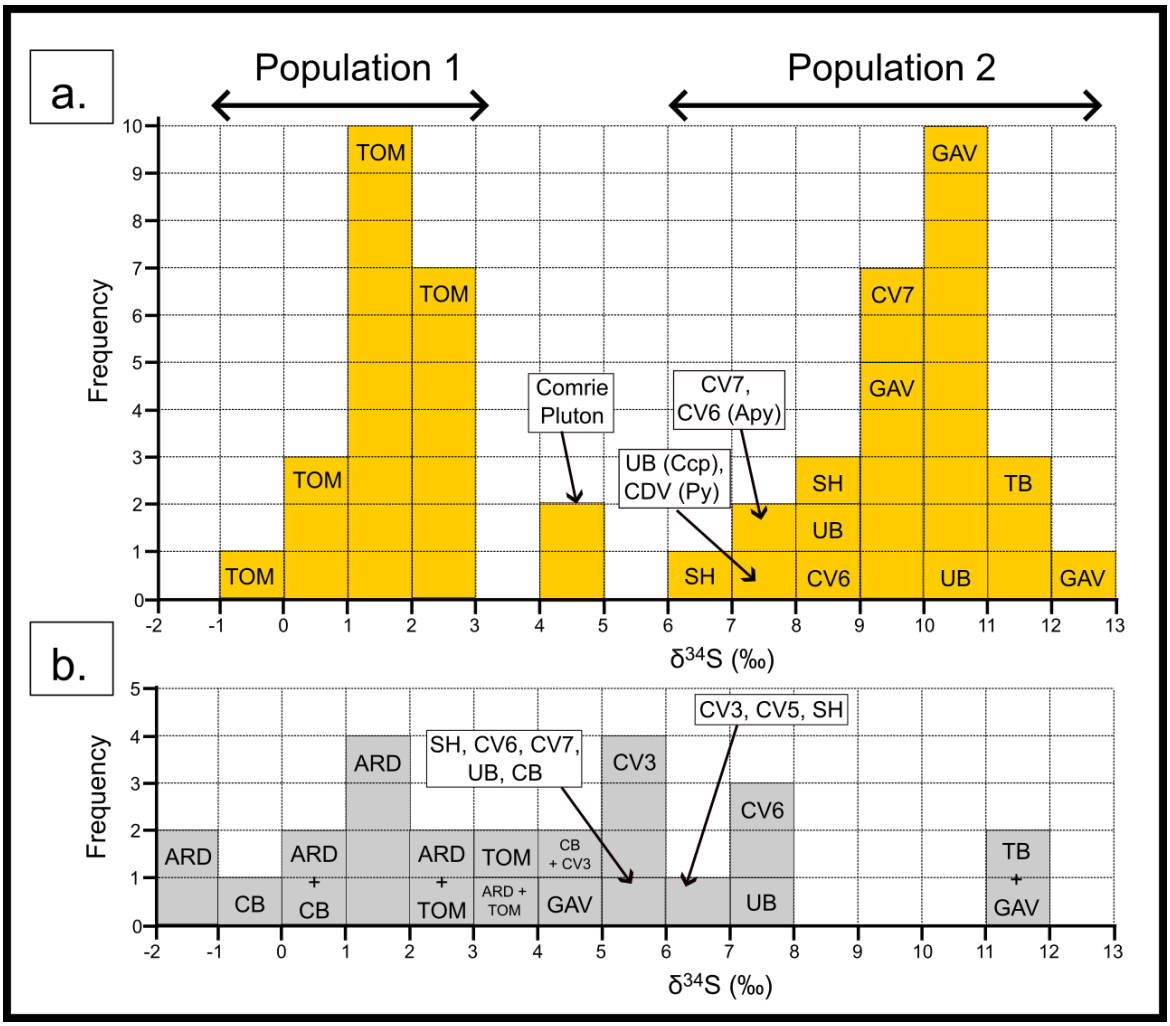

Figure 5.24. Histograms showing the frequency of the $\delta^{34}S$ datapoints recorded in the LTVS (rounded to whole numbers). **a.** Pyrite. **b.** Galena. Abbreviations are as follows: ARD = Ardtalnaig (including Lead Trial), TOM = Tomnadashan, CB = Coire Buidhe, SH = Spoil Heap, GAV = Glen Almond, CO = Comrie Pluton, TB = Tombuie, UB = Urlar Burn (UV_SHa/UV_SHb/UB_GAL), UVi = UB_VEINa. The 'C' stands for Calliachar, with the following number or abbreviation referring to a specific vein, e.g. CV3 = Calliachar V3, and CDV = Discovery Vein. The top of each bar represents the frequency of a $\delta^{34}S$ measurement at a specific locality, e.g. +2 ‰ was recorded from pyrite at Tomnadashan ten times, whilst -1 ‰ was recorded from galena at Coire Buidhe on a singular occasion.

Regarding the $\delta^{34}S$ data that were collected in-situ, the petrographic context of every measurement taken is depicted in the pages overleaf (Fig. 5.25.; Fig. 5.26.). Furthermore, a series of SEM images providing further context for the in-situ measurements are depicted in Fig. 5.27. In the following paragraphs, the broad trends observed from the in-situ $\delta^{34}S$ dataset are summarised. In-situ analyses on galena from Lead Trial consistently targeted the Stage 3 Gn generation (Table E.1.; No. 52-56) that was observed to mutually intergrow with sphalerite (Fig. 5.18.d.). In localities with a robust and published paragenetic interpretation (Tomnadashan and GAV), it is not possible to differentiate paragenetic stages by $\delta^{34}S$ signature, with each paragenetic stage recording a broad range of $\delta^{34}S$ values. For example, PyA from Tomnadashan is characterised by a $\delta^{34}S$ range of -0.1 to +3.3 ‰ (Table E.1.; No. 17-21), whilst PyC records a $\delta^{34}S$ range of +0.7 to +4.4 ‰ (Table E.1.; No. 3-7). However, the mean $\delta^{34}S$ value of PyA (Table E.2.; +1.7 ‰) is lighter than the mean $\delta^{34}S$ value of PyC (Table E.2.; +3.1 ‰). Regarding the $\delta^{34}S$ values of the molybdenite samples at Tomnadashan, these datapoints fell within a range of +1.8 and +3.4 ‰ (Table E.1.; No. 30-42).

At the GAV, the $\delta^{34}S$ values from PyB and PyC are also similar; PyB has $\delta^{34}S$ values of between +10.4 and +13.2 ‰, whilst PyC recorded values of between +10.56 and +11.95 ‰ (Table E.1.; No. 77-92). The mean $\delta^{34}S$ values from PyB and PyC are nearly identical (Table E.2.; +11.0 and +11.2 ‰). The inability to distinguish pyrite generations on the basis of $\delta^{34}S$ values at Tomnadashan and the GAV is emphasised by Fig. 5.27.; for example, PyA at Tomnadashan may record values of + 0.9 ‰ (Fig. 5.27.b.), whereas some PyC values are +0.7 ‰ (Fig. 5.27.c.). In the GAV, there are also instances where PyB and PyC record near-identical values (e.g. +11.0 and +11.1 ‰; Fig. 5.27.e., f.).

Where crystals large enough to measure repeatedly with the laser were encountered, intracrystal variation (i.e. dissimilar $\delta^{34}S$ measurements within a single crystal) was commonly observed (e.g. Fig. 5.25.e.; Fig. 5.26.c., d., f.). Occasionally, $\delta^{34}S$ values increased towards the crystal margins; an example of this trend is shown in the polished block from the Urlar Burn (Fig. 5.26.f.). Intracrystal $\delta^{34}S$ zonation was also observed at Tomnadashan; $\delta^{34}S$ values of between +2.7 and +4.3 ‰ were recorded within a single galena crystal (Fig. 5.26.c.).

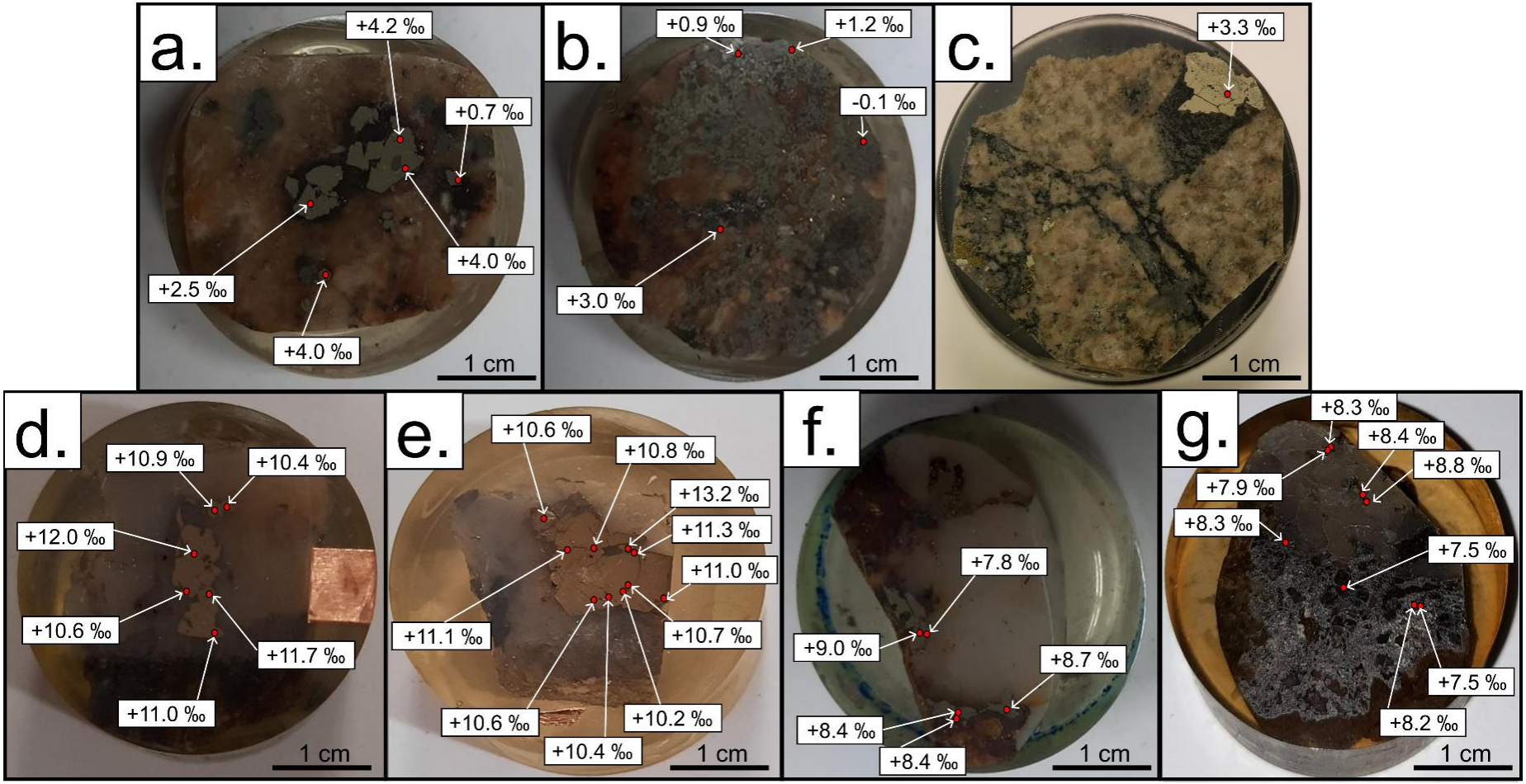

Figure 5.25. Images of the polished blocks containing pyrite crystals that were targeted with the laser during in-situ $\delta^{34}S$ analyses. The red dots represent individual measurements, which have been annotated with the relevant $\delta^{34}S$ values. **a.** Tomnadashan, TOM_QTZ (Table E.1.; No. 3-7); disseminated pyrite and sulfosalts within the quartz vein. **b.** Tomnadashan, SW_TOM_PYa (Table E.1.; No. 17-20); disseminated pyrite and chalcopyrite within the granitoids. **c.** Tomnadashan, B001 (Table E.1.; No. 21); disseminated chalcopyrite, molybdenite, and pyrite within the granitoid. **d.** GAV, RC3 (Table E.1.; No. 77-82); PyB and PyC occurring close to the contact with the schist wallrock. **e.** GAV, RC5 (Table E.1.; No. 83-92); coarse-grained pyrite, which contains coeval inclusions of gold. **f.** Spoil Heap, CB1 (Table E.1.; No. 65-69); pyrite and chalcopyrite crystals. **g.** V6 (Calliachar Burn), 65004 (Table E.1.; No. 119-122, 124-125); a crushed mixture of pyrite, arsenopyrite, and sphalerite. Sample information is provided in Appendix A.

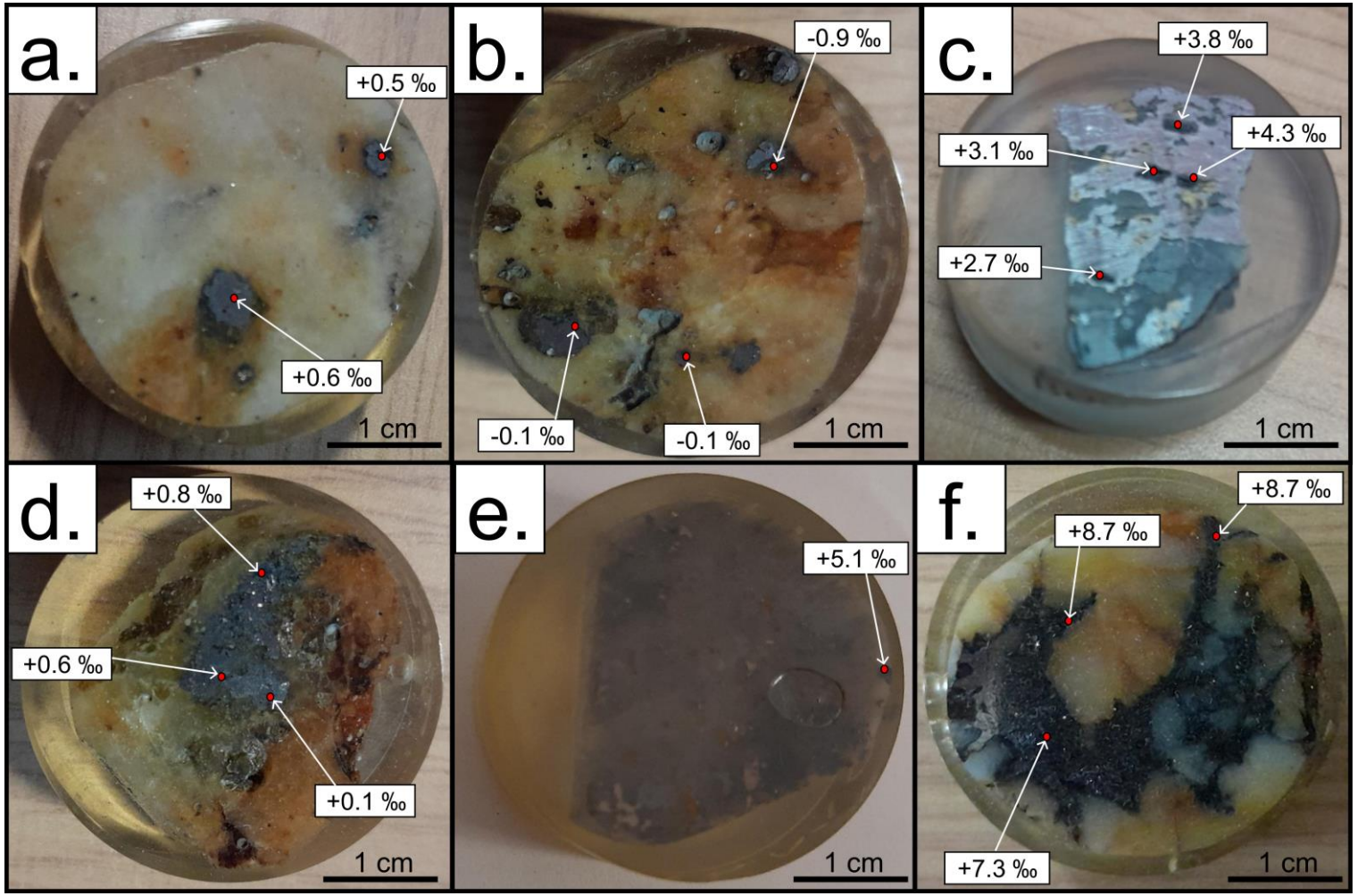

Figure 5.26. Images of the polished blocks containing galena crystals that were targeted with the laser during in-situ $\delta^{34}S$ analyses. The red circles represent analyses (annotated with $\delta^{34}S$ values). **a.** LDT_LSa, Lead Trial (Table E.1.; No. 55-56); coarse-grained galena, mutually intergrowing with sphalerite. **b.** LDT_LSe, Lead Trial (Table E.1.; No. 52-54); mutually intergrowing galena and sphalerite. **c.** B0018, Tomnadashan (Table E.1.; No. 26-29); voluminous galena with inclusions of chalcopyrite and sphalerite. **d.** CB_GAL, Coire Buidhe (Table E.1.; No. 60-62); galena crystal intergrowing with sphalerite. **e.** RC1, GAV (Table E.1.; No. 101); late-stage galena crystal infilling fractures in the quartz. **f.** UB_GAL, Urlar Burn; stage of voluminous galena mineralisation, infilling fractures within quartz crystals (Table E.1.; No. 141-143). Sample information is provided in Appendix A.

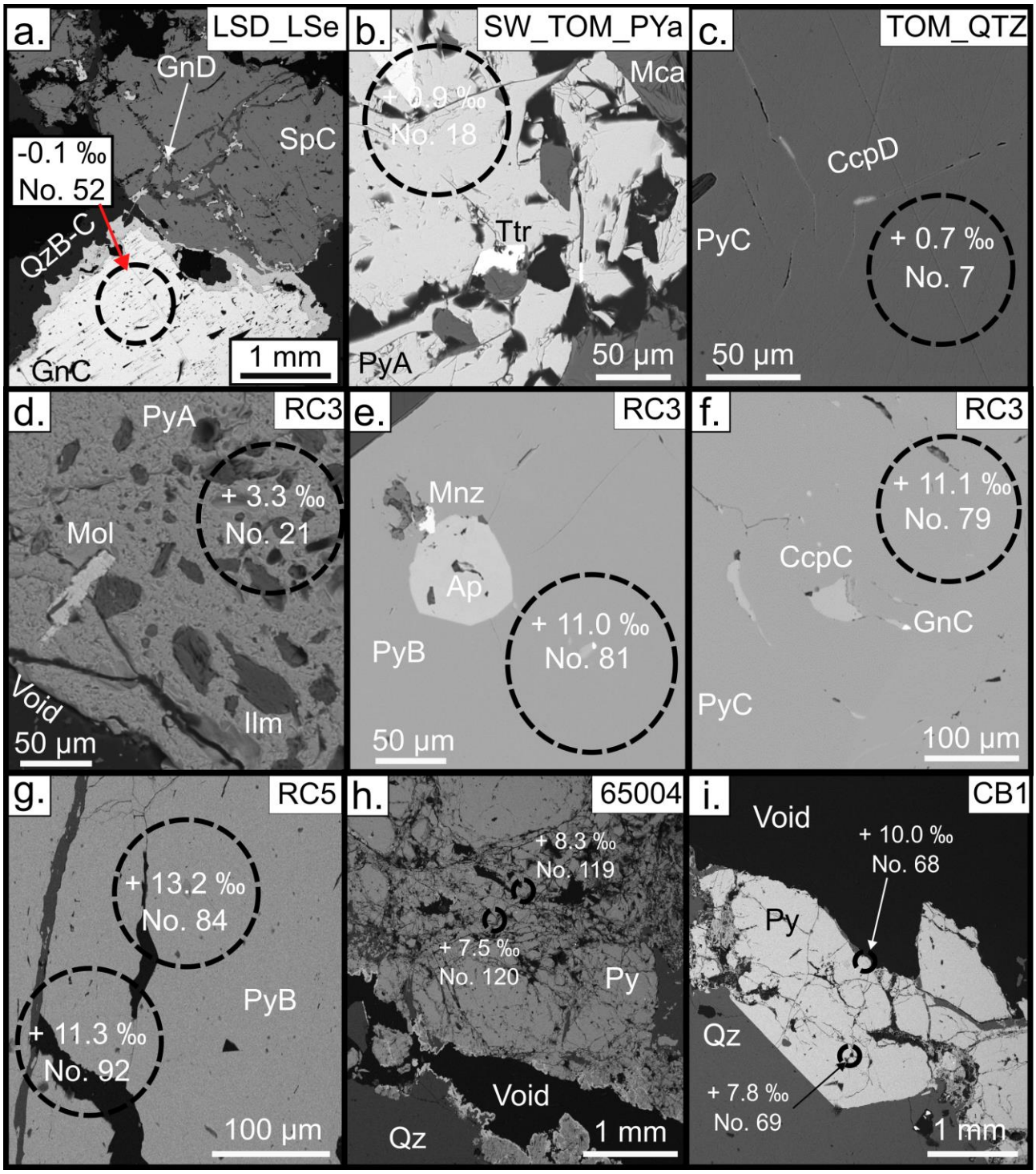

Figure 5.27. Images depicting in-situ $\delta^{34}S$ datapoints (black circles) that are important with regards to the interpretation of the sulphur isotope dataset. **a.** Lead Trial; Stage 3 mutually intergrowing galena and sphalerite. **b.** Tomnadashan; disseminated PyA in the granitoid that has been crosscut by Stage 3 sulphosalts. **c.** Tomnadashan; Stage 3 PyC, which has been traversed by CcpD. **d.** Tomnadashan; PyA and molybdenite disseminated in the granitoid. **e.** GAV; Stage 2 PyB coprecipitating with monazite and apatite. **f.** GAV; Stage 3 PyC (i.e. the As-bearing generation). **g-i.** Examples of intracrystal $\delta^{34}S$ zonation at the GAV, V6 (Calliachar Burn), and CB1. The 'No.' corresponds to Appendix E (Table E.1.), which contains a compilation of $\delta^{34}S$ datapoints derived in this study.

5.6. Results of Pb isotope studies on the LTVS

Whilst the Pb isotope data derived throughout this study are depicted in Fig. 5.28., the values are also presented in Appendix F (Table F.1.). Throughout the LTVS, a range in the Pb isotope ratios of galena is observed; there is a simple pattern of variation, with the ^{208}Pb and ^{207}Pb isotope ratios being lowest around Lead Trial and the Ardtalnaig Estate (Fig. 5.28.). Elsewhere, these ratios are higher (i.e. around the previously described 'metasediment-hosted veins' population that was discerned from the $\delta^{34}S$ studies); the most radiogenic datapoints represent samples from the Calliachar Burn (Fig. 5.28.). Samples from the GAV and Spoil Heap form intermediate populations between Lead Trial and the CUB veins (Fig. 5.28.). The Pb isotope ratios from Tombuie, the CUB veins, and Coire Buidhe are similar (Fig. 5.28.). Furthermore, the measurements on Tomnadashan from this study yielded values that were more radiogenic than the analyses conducted by Moorbath (1962) on galena from this locality; the reasons behind this difference are explored further in Chapter 6.

Regarding the individual populations that have been coloured on Fig. 5.28., there is some variation in the ranges. The values from Lead Trial and Ardtalnaig were consistently similar and despite several measurements being taken, the area encompassed by this population is relatively small (Fig. 5.28.). However, this is not the case for many of the metasediment-hosted veins; the areas covered by Spoil Heap and the CUB veins are much larger (Fig. 5.28.). The one potential exception to this trend is Coire Buidhe, which despite recording a relatively large amount of variation in the $^{208}Pb/^{204}Pb$ ratios (Fig. 5.28.a.), shows a limited range in $^{207}Pb/^{204}Pb$ ratios (Fig. 5.28.b.). The entire $^{206}Pb/^{204}Pb$ vs $^{207}Pb/^{204}Pb$ dataset from the LTVS that was derived in this study plots beneath the Zartman and Doe (1981) curve for the mantle between 400 and 0 Ma (Fig. 5.28.). On the other hand, the $^{206}Pb/^{204}Pb$ vs $^{208}Pb/^{204}Pb$ dataset from the LTVS curve plots above the curve for the upper crust produced by Stacey and Kramers (1975) (Figure 5.28.a.).

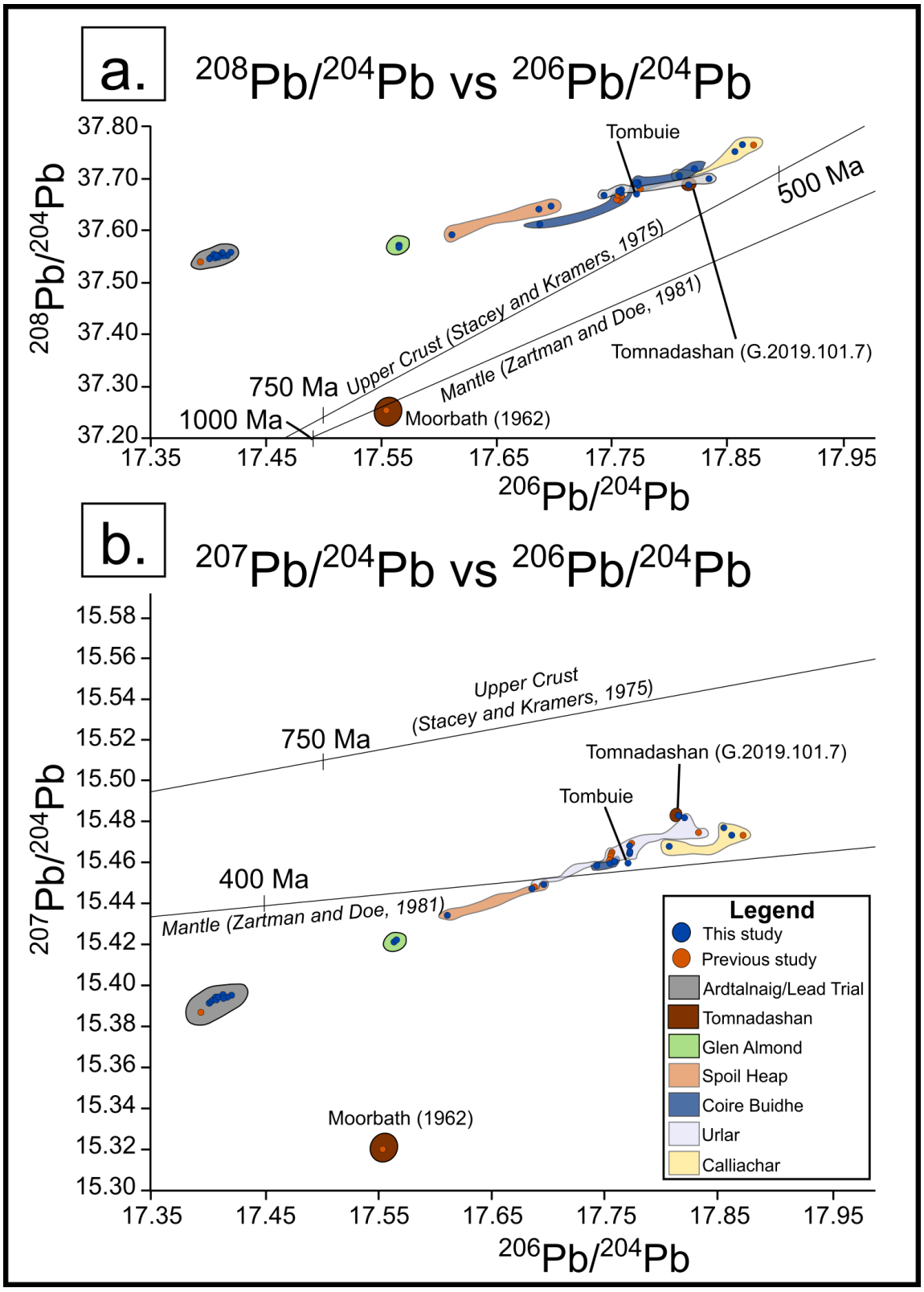

Figure 5.28. Pb isotope results presented alongside the relevant global lead evolution curves produced by Stacey and Kramers (1975) and Zartman and Doe (1981). With the exception of the Moorbath (1962) datapoint, the 'Previous study' category represents data collected by Savastano (2024). Results are presented as datapoints (blue and orange circles) enclosed within populations (coloured regions) that represent different localities. The measurement from Tombuie is annotated, given that only a single datapoint is available. **a.** $^{206}Pb/^{204}Pb$ vs $^{208}Pb/^{204}Pb$. **b.** $^{206}Pb/^{204}Pb$ vs $^{207}Pb/^{204}Pb$.

The model Pb ages derived from the Global Lead Isotope Database are presented in Appendix F (Table F.3.), although the results from the different models are shown in Fig. 5.29. A consistent trend observed in every model is the relative order of the different localities; model ages from Lead Trial and Ardtalnaig are consistently older than those recorded from the metasediment-hosted veins in the east, with some of the GAV and Spoil Heap localities forming an intermediate population between these two extremes (Fig. 5.29.). Model ages derived using the Stacey and Kramers (1975) model were between 510 and 220 Ma, whereas the Cumming and Richards (1975) model yielded ages of 830-560 Ma. In terms of the ages derived from the Albarède and Juteau (1984) and Albarède *et al.* 2012 models, these were 580-310 and 680-440 Ma, respectively (Fig. 5.29.). All models considered indicate that the model age distribution from the CUB veins, Tombuie, and Coire Buidhe is consistently similar (Fig. 5.29.).

The Tomnadashan Pb model ages show a relatively large amount of variation (Fig. 5.29.); for example, the Cumming and Richards (1975) model indicates that the galena from Tomnadashan is similar to the samples from Spoil Heap and the GAV, whereas the youngest age reported by the Albarède and Juteau (1984) model (Fig. 5.29.c.; 310 Ma) came from Tomnadashan. When considering this variation, it is important to consider the nature of the samples; the galena from this study (G.2019.101.7; Appendix A) plotted alongside the other metasediment-hosted veins (e.g. Coire Buidhe, Tombuie, and the CUB veins), whereas the datapoint representing a calculation using the ratios provided by Moorbath (1962) did not (Fig. 5.29.a.-c.). However, in the Albarède *et al.* 2012 model, both the galena sample from Tomnadashan analysed in this study and the Moorbath (1962) sample yielded a similar model age of 480 Ma (Fig. 5.29.d.).

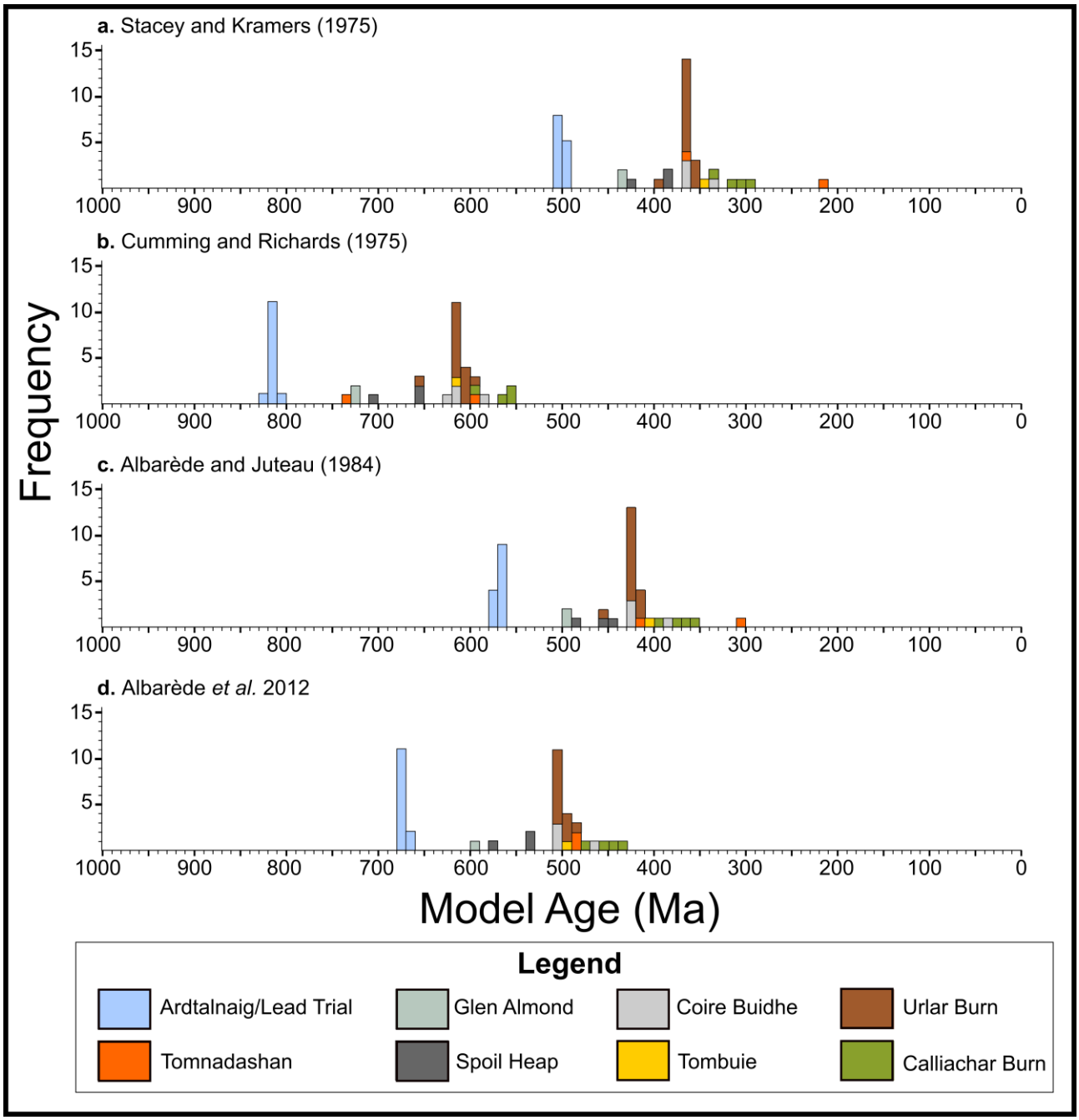

Figure 5.29. A histogram of Pb model ages derived by inputting the Pb isotope ratios from LTVS galena samples (Appendix F) into the 'LI_model_age()' function in the GlobaLID database, which calculates model ages using several models (Cumming and Richard, 1975; Stacey and Kramers, 1975; Albarède and Juteau, 1984; Albarède *et al.*, 2012) for galena samples from the LTVS.

Chapter 6: Interpretation

6.1. Introduction

The focus of this chapter is on explaining the meaning of the various datasets that were presented in Chapter 5, thereby enabling for a comprehensive synthesis and discussion of the wider ramifications of the data in Chapter 7. To make sure that the distinction between Chapters 6 and 7 is clear, the former is limited to an overall interpretation of the trends recorded by each dataset. The meaning of these interpretations regarding the genetic model for mineralisation in the LTVS is addressed in Chapter 7.

6.2. Petrography of the Loch Tay granitoids

In the granitoids around Loch Tay that were characterised as part of this study, zircon was consistently observed to coprecipitate with apatite (Fig. 5.14.). Zircons from the igneous groundmass of each intrusion showed internal variations (Fig. 5.15.) that may be similar to some of the primary growth textures described by Corfu (2003). For example, in ARD_FELS_1 (Fig. 5.15.a.), the striped bands within the zircon crystals on each side of the darker apatite may be typical of the texture that Corfu (2003) recognised as 'oscillatory zonation.' This texture commonly arises as a result of zircon growth during magmatic crystallisation (Fowler *et al.*, 2002; Corfu, 2003). The genesis of these textures is described in Chapter 2 (Section 2.8.2.) and their occurrence is consistent with a magmatic origin of the zircon crystals that were observed in the granitoids around Loch Tay throughout this study (Hoskin, 2000; Fowler *et al*., 2002; Corfu, 2003; Gagnevin *et al.*, 2010; Erdmann *et al.*, 2013).

Regarding the CB_FELS_2 granitoid, zircons from this intrusion have cores that are slightly lighter than the rims (Fig. 5.15.c.). This may be typical of the 'core and rim' textures described by Corfu (2003), of which there are several varieties (Olierook *et al.*, 2021); furthermore, core and rim textures can be challenging to interpret. For example, recrystallisation of zircons may lead to the development of this texture (Corfu, 2003), or alternatively, resorption by a later magma can result in the formation of sharp boundaries between different growth zones (Gagnevin *et al.*, 2010). The CB_FELS_2 thin section (Fig. 5.15.c.; the first zircon from the right-hand side) also demonstrates the occurrence of 'patchy zoning' (Paquette *et al.,* 1995), which may have arisen as a result of strain experienced by the zircon during the final emplacement event (Corfu, 2003). Assigning specific textures to the zircons observed in TOM_FELS_2 and SW3 is more challenging. For example, the zircon from TOM_FELS_2 (Fig. 5.15.b.) may display signs of banding, although the rim is much lighter than the core; there is no straightforward way of classifying this texture, which resembles several textures (e.g. oscillatory zonation, core and rim). The same interpretation can be applied to the zircon crystal observed in SW3 (Fig. 5.15.d.). Nonetheless, many of the granitoids around Loch Tay display textures that are typical of primary growth during magmatic crystallisation (Corfu, 2003).

However, the zircon crystals observed in ARD_FELS_2 (which could not be dated via CA-ID-TIMS; Section B.3.) displayed similarities with zircons considered by Corfu (2003) to have a hydrothermal origin, such as the spongy texture and needle-like morphology (Fig. 5.16.c.). The zircons in ARD_FELS_2 were also observed to be spatially coincident with sulphide mineralisation (Fig. 5.16.c.) and during fieldwork, the ARD_FELS_2 outcrop was described as being heavily altered and mineralised by small sulphide-bearing quartz veinlets (Section 5.2.2.). Corfu (2003) noted that needle-shaped acicular zircon crystals were common in rapidly crystallising granites that are emplaced at subvolcanic depths; furthermore, zircon morphology is known to be an unreliable criterion for establishing a magmatic or hydrothermal origin (Schaltegger, 2007). For the aforementioned reasons, it is not certain whether ARD_FELS_2 contains zircon crystals that precipitated from hydrothermal fluids. Nonetheless, the ARD_FELS_2 granitoid was ultimately not dated via CA-ID-TIMS.

The most important ramification of the petrographic studies on the granitoids around Loch Tay is that the U-Pb dates (Fig. 5.20.) likely pertain to the ages of the intrusions. Another key observation from the petrography conducted on the granitoids is that some of them (ARD_FELS_1, ARD_FELS_2, and TOM_FELS_2) host sulphide minerals (Fig. 5.16.) whilst others (CB_FELS_2 and SW3) do not (or rather, were not observed to host mineralisation throughout the petrographic characterisation that was undertaken in this study). In the case of the ARD_FELS_1 and ARD_FELS_2 granitoids (Fig. 5.16.a., b.), the mineralisation occurs in vugs; furthermore, the core-logs from Lead Trial (Appendix C) and other field observations presented in Chapter 5 (Fig. 5.4.; Fig. 5.5; Fig. 5.7.) demonstrate that the veins around Lead Trial crosscut the granitoids at this locality. However, at Tomnadashan, the sulphide mineralisation coincides with the potassic alteration halo (Fig. 5.16.d.); for this reason, some of the mineralisation at this locality may be contemporaneous with the emplacement of the granitoids that altered the diorite (Fig. 5.8.).

6.3. Paragenetic interpretations of Tomnadashan, Lead Trial, and the GAV

In Fig. 6.1., a summary chart of the paragenetic interpretations produced for the different LTVS localities that were characterised as part of this study (Section 5.3.) is provided. The paragenetic interpretations (Fig. 6.1.; Webb *et al.*, 2024a, b) illustrate how the mineralogy of the different localities within the LTVS has evolved over time. Furthermore, the parageneses provide a useful framework in which to consider the results of the Re-Os, $\delta^{34}S$, and Pb isotope datasets. Each paragenesis has been constructed using the observations from Chapter 5 (Section 5.3.) and in this section, the reasoning behind the different paragenetic interpretations (Fig. 6.1.) is explored.

The paragenetic interpretation for Tomnadashan is shown in Fig. 6.1.a., which also includes the phases that Pattrick (1984) identified within the initial paragenetic stage at this locality (i.e. the phases that were not observed in this study, such as aikinite and hodrushite; Table 3.6.). At Tomnadashan, the distinction between PyA (Stage 1) and PyC (Stage 3) is supported by the tendency for sulphosalt veinlets to crosscut PyA (but not PyC; Fig. 5.17.f). Furthermore, the inclusion assemblage differs between the pyrite generations; PyA contains bismuth tellurides, whereas PyC hosts galena and sulfosalt inclusions (Table 5.1.). The gold retrieved from the stream flowing out of the mine at Tomnadashan (Fig. 3.31.) contained a wittichenite inclusion (Fig. 5.17.c.), which may indicate that gold is coeval with BiTe and therefore part of Stage 1 (Fig. 6.1.a.). Molybdenite was observed within the fractures of PyA (Fig. 5.17.b.); the law of crosscutting relationships (Section 4.2.) indicates that this phase must postdate Stage 1 (Fig. 6.1.a.). However, assessing the relationship between molybdenite and the Stage 3 assemblage (Fig. 6.1.a.) was more challenging because it was not possible to directly observe the interaction between these phases during petrographic characterisation; as outlined in Chapter 4 (Section 4.5.), obtaining representative samples in any paragenetic study is a common limitation. Nonetheless, molybdenite was not observed to be associated with PyC in this study and many Cu-Mo porphyries display a paragenesis in which molybdenite occurs in the initial paragenetic stages before being overprinted by assemblages dominated by galena and copper sulphosalts, potentially as a result of the mineralising fluids cooling down (Berger *et al.*, 2008). Furthermore, Pattrick (1984) described molybdenite as preceding the galena and copper sulphosalts at Tomnadashan (Table 3.6.), which is also the line of reasoning taken here (Fig. 6.1.a.).

In terms of the later stages of mineralisation at Tomnadashan, the Stage 3 sulphosalts (e.g. TtrC and TntC; Fig. 5.17.h.) are crosscut by veinlets containing quartz, tetrahedrite, and chalcopyrite (Fig. 5.17.j.). This veinlet dominated stage is considered to represent Stage 4 of the Tomnadashan paragenesis (Fig. 6.1.). However, during petrographic characterisation, it was not possible to observe the interactions between Stages 5 and 6 (the relative order of which is confirmed by the occurrence of barytes crosscutting monazite; Fig. 6.1.) and the earlier paragenetic stages associated with the sulphide mineralisation. However, it is

generally the case that fluids in magmatic-hydrothermal porphyry systems evolve towards a cooler and more carbonatitic composition over time (Sillitoe, 2000; Sun *et al.*, 2017; Park *et al.*, 2021); for this reason, the siderite, monazite, dolomite, and barytes are considered to postdate the metallic mineralisation from Stages 1-4 (Fig. 6.1.a.).

Regarding the paragenesis of Lead Trial, it was possible to distinguish six paragenetic stages via petrographic characterisation (Fig. 6.1.b.). The initial paragenetic stage is disseminated within the granitoids at Lead Trial (Fig. 5.16.b); this Stage 1 mineralisation has been brecciated and entrained during the precipitation of QzA (Fig. 5.18.a.), justifying the decision to place the disseminated pyrite, galena, and sphalerite in the initial stage of the paragenetic interpretation (Fig. 6.1.a.). Whilst sphalerite was not observed during SEM characterisation, the core-logs from Lead Trial (Appendix C) show that this phase occurs with galena and pyrite in the dacite host rock (Fig. C.2.; 62.5-65.8 m). A minor component of sphalerite mineralisation is therefore inferred to have occurred during Stage 1 (Fig. 6.1.a.). However, the Stage 1 assemblage experienced brecciation and entrainment during the precipitation of QzB (Fig. 5.18.a.). The euhedral morphology of QzB is potentially indicative of unimpeded growth into an open space; it is therefore likely that the precipitation of QzB occurred prior to the injection of QzC. Regarding the voluminous stage of galena and sphalerite (Fig. 6.1.b.; Stage 3), these phases mutually intergrow with one another (Fig. 5.18.d.) and are therefore coeval (Fig. 6.1.b.). Whilst chalcopyrite was not observed in any of the thin sections or polished blocks from Lead Trial during petrographic characterisation, coeval inclusions of this phase were documented in the RX2959KA (Fig. 3.13., Locality 6) thin section (Fig. 5.18.e.); furthermore, minor quantities of chalcopyrite were observed in the galena and sphalerite assemblage within the schist during core-logging (Fig. C.1.; 23-25 m). Collectively, the available evidence suggests that chalcopyrite is a minor yet coeval component of the Stage 3 mineralisation at Lead Trial (Fig. 6.1.b.).

As described in Chapter 5, there are two categories of gold at Lead Trial; AuC (contains coeval inclusions of GnC and SpC; Fig. 5.18.f.) and AuD (gold hosted in quartz vugs; Fig. 5.18.i.-j.), which are associated with Stages 3 and 4, respectively (Fig. 6.1.b.). The paragenetic relationship between the two is based on the observation that AuD infills vugs within the QzB and QzC groundmass of the vein, whereas AuC is coeval with QzC and the voluminous sulphide mineralisation associated with Stage 3 (Fig. 6.1.). In addition to AuD, these vugs have been infilled by volumetrically minor galena veinlets (GnD; Fig. 5.18.h.) and a generation of quartz (QzD) that yields a contrasting SEM-CL response to QzB and QzC (Fig. 5.18.g.), potentially at the same time as the precipitation of the gold (Fig. 5.18.b.). The final paragenetic stages at Lead Trial are characterised by quartz veinlets (QzE) that have crosscut the previous quartz and sulphide generations (Fig. 5.18.b.), followed by the influx of a fluid containing barium and carbonates (Fig. 5.18.k., l.); however, it was not possible to directly observe the relationships between these phases during petrographic characterisation. For this reason, the relative order between Stages 5 and 6 (Fig. 6.1.b.) may differ.

Unlike the rest of the LTVS (i.e. localities other than Lead Trial), the quartz generations at Lead Trial yielded drastically different SEM-CL responses from one another; several crystal sizes and contrasting morphologies were observed during petrographic characterisation (Table 5.2). As discussed in Chapter 4, different SEM-CL responses in quartz are typically caused by crystal lattice defects associated with trace element substitution (Götze, 2009; Götze and Kempe, 2009; Götze and Möckel, 2012). The variation in SEM-CL response throughout the paragenesis at Lead Trial may reflect the substitution of different trace elements at each paragenetic stage, potentially as a result of either an evolving fluid or the reactivation of the vein and subsequent injection of a new fluid. Given the thickness of the veins at Lead Trial relative to others in the LTVS (e.g. <1 m wide at outcrop; Fig. 5.4.), as well as observable textural differences in the quartz across the breadth of the veins at outcrop (Fig. 5.4.), the scenario of repeated fracturing and fluid injection is more likely.

Regarding the paragenesis of the GAV (Fig. 6.1.c.), multiple generations of quartz (which comprises large quantities of the vein) were also distinguishable in SEM-CL (Fig. 5.19.b.). The euhedral and zoned textures of QzA are indicative of open-space growth, meaning that these crystals are interpreted as comprising the first paragenetic stage; furthermore, QzA has been fractured by the injection of the homogeneous QzB and QzC generations (Fig. 5.19.b., c.). The second and third stages of the GAV paragenesis comprise a continuum of precipitation; the gold and sulphides may vary in terms of their composition and textures (Fig. 5.19.d.-f.) but the lack of a contrasting SEM-CL response between QzB and QzC may suggest that the composition of the mineralising fluid did not change. However, the decision to differentiate Stage 2 and Stage 3 stems from the observation of mineralogical variations between the two. The first gold generation (Fig. 5.19.e.; AuB) occurs as inclusions within PyB (alongside other sulphides; Fig. 5.19.e.), whilst the Stage 3 gold (AuC) occupies fractures within PyB and PyC (Fig. 5.19.g.). The AuB alloy has a lower Ag content (~25 wt %) than the AuC (~35 wt %) (Webb *et al.*, 2024a). However, the difference in the Ag values of the AuB and AuC gold alloys may not be large enough to indicate a genetic difference between the two gold generations; some evidence has demonstrated that the Ag wt % values of gold particles can vary throughout the duration of a single episode of hydrothermal flow (Gammons and Williams-Jones, 1997). Furthermore, a continuum of Ag contents in gold particles is frequently recognised from studies involving large gold grain datasets (Chapman *et al.*, 2021). Nonetheless, the textural and compositional characteristics that have been identified in this study (e.g. the occurrence of SEM-CL variations throughout the quartz paragenesis), including the observed differences in the associated sulphides (Table 5.3.), would indicate that AuB and AuC precipitated at different times (i.e. during separate fluid events). This interpretation may suggest that the GAV formed during repeated cycles of fracturing, fluid injection, and sealing induced by mineral precipitation.

Although a large in-situ $\delta^{34}S$ dataset (Appendix E; Table E.1.) was compiled as part of this study, most of the $\delta^{34}S$ and Pb data lacks paragenetic context, a limitation that was discussed in Section 4.5. However, it may

be possible to use the paragenetic interpretations (Fig. 6.1.) to make inferences about the likely paragenetic stage that much of the isotope data comes from. For example, at the GAV, the Stage 5 galena is voluminous and even visible in the polished blocks (Fig. 5.26.e.), whilst the Stage 2 galena occurs as microscopic blebs (Fig. 5.19.f.). Therefore, in terms of probability (i.e. the more voluminous stage is more likely to be sampled during drilling or panning), it is more likely that the $\delta^{34}S$ and Pb analyses on galena from the GAV pertain to Stage 5 of the paragenesis (Fig. 6.1.c.). Similarly, at Lead Trial, the Stage 3 galena is more voluminous than galena from Stages 1 and 4 (i.e. at Lead Trial, most of the galena belongs to Stage 3). Any $\delta^{34}S$ and Pb analyses from the Ardtalnaig region are therefore more likely to come from the galena that occurs in Stage 3 of the paragenesis (Fig. 6.1.b.). For Tomnadashan, relating the paragenetic interpretation (Fig. 6.1.a.) to specific isotope measurements is more challenging because both stages of pyrite (PyA and PyC) are common phases and although they typically occur in different parts of the mineralisation (i.e. PyA is typically disseminated in the granitoid whereas PyC comprises most of the pyrite in the vein; Table 5.1.), they are not spatially exclusive, as previously discussed. However, in terms of the $\delta^{34}S$ and Pb analyses on galena from Tomnadashan, this data only pertains to the G.2019.101.7 sample (Fig. 5.26.c.), the entirety of which belongs to Stage 3 of the paragenesis at this locality (Fig. 6.1.a.).

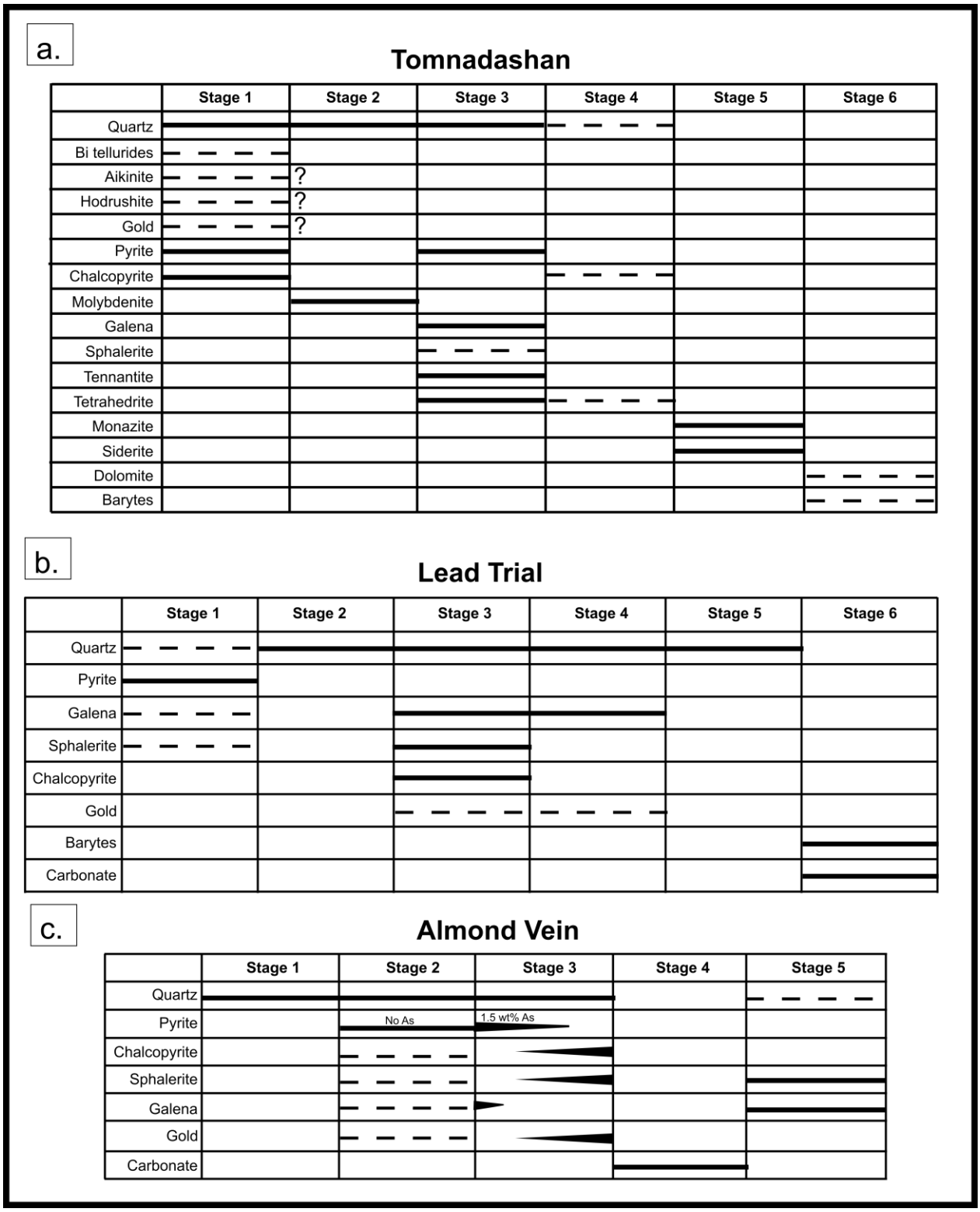

Figure 6.1. Paragenetic interpretations of the mineralisation at **a.** Tomnadashan, **b.** Lead Trial, and **c.** The Glen Almond Vein (GAV). The parageneses of Tomnadashan and the GAV have been adapted from Webb *et al.* 2024a and b. Question marks represent phases identified by Pattrick (1984) that were not observed in this study.

6.4. U-Pb and Re-Os geochronological datasets

As outlined in Section 5.4.1., the dates from the granitoids around Loch Tay can be summarised as follows; 418.62 ± 0.13 Ma (ARD_FELS_1), 418.80 ± 0.16 Ma (TOM_FELS_2), 419.42 ± 0.28 Ma (CB_FELS_2), and 419.10 ± 0.20 Ma (SW3). These dates are very similar and potentially indicate the occurrence of widespread magmatism throughout the Loch Tay region between 420 and 418 Ma, in addition to the emplacement of the diorite and granite intrusions within the Comrie Pluton at 425 ± 3 Ma and 404 ± 6 Ma, respectively (Oliver *et al.*, 2008). There does not appear to be any detectable spatial variation in the ages of the granitoids around Loch Tay (e.g. from North to South, which has been described in the Grampian Terrane by Rice *et al.*, 2018).

The MSWD values (Fig. 5.20.) are a measurement of the goodness of fit, i.e. a measurement of the precision of the single datapoints relative to their scatter (Reiners *et al.*, 2017; Keller *et al.*, 2018; Condon *et al.*, 2023). When zircon fractions record indistinguishable ages, the MSWD values are typically close to 1 (Castorina and Petrini, 1989; Wendt and Carl, 1991; Condon *et al.*, 2023); this situation may be applicable to the SW3 granitoid, which has an MSWD value of 0.77 (Fig. 5.20.d.). However, the higher MSWD values of 2.2 and 2.3 from ARD_FELS_1 and TOM_FELS_2 (Fig. 5.20.a.-b.) are indicative of a slightly higher amount of discordance (relative to that observed in SW3) (Wendt and Carl, 1991; Li *et al.*, 2019; Condon *et al.*, 2023). The MSWD value from CB_FELS_2 is much higher (6.9; Fig. 5.20.c.), which is potentially indicative of a relatively large amount of discordance within this dataset. For this reason, the calculated mean age of CB_FELS_2 (419.42 ± 0.28 Ma) may not be representative. However, given the similarity in the dates recorded by all zircon fractions that were analysed in this study (i.e. a range of 420-418 Ma; Appendix D), the higher degree of discordance does not have any ramifications for the overall interpretation of the U-Pb data; instead, it may be more appropriate to describe the age of CB_FELS_2 as a range (Appendix D, Table D.1.; 420.4-418.6 Ma).

As discussed in Chapter 2, there are several causes of discordance in U-Pb systems; the mixing of different age domains, Pb loss, disequilibrium between intermediate and daughter products, and incorrect assumptions regarding the initial (common) Pb contents of the sample, or a combination thereof (Corfu and Ayres, 1984; Schoene *et al.*, 2006; Schoene, 2014). In the following paragraphs, the potential causes of discordance in the CA-ID-TIMS dataset (Table D.1.) are explored.

One of the advantages of in-situ U-Pb dating is that it may be possible to preferentially target a similar part of the zircon crystal with each analysis (e.g. the core; Schoene, 2014). However, given the nature of the CA-ID-TIMS methodology (i.e. the complete dissolution of individual zircon crystals, as opposed to manual target selection with a laser during petrography), it is not possible to choose specific analysis sites with such a high level of resolution. For this reason, there is a risk that the CA-ID-TIMS analyses may have been conducted on crystals with older cores and younger rims, or overgrowths with contrasting ages to the rest

of the crystal. However, throughout the petrographic work undertaken in the present study, no such textures were observed (Section 6.2.); furthermore, the spread in the dataset from each intrusion is very small, which is additional evidence against the mixing of different age domains as a potential cause of discordance.

Whilst the chemical abrasion process involved in the methodology utilised in this study (Appendix B; Section B.3.) is specifically designed to minimise Pb loss, there are several examples in the literature of zircon crystals recording Pb loss following chemical abrasion (Ramezani *et al.*, 2007; Davydov *et al.*, 2010; Mackinder *et al.*, 2019; Gaynor *et al.*, 2022). The technique is therefore imperfect and unable to mitigate against Pb loss completely. For this reason, a minor amount of Pb loss may be responsible for the discordance observed in Fig. 5.20. However, it is difficult to speculate about the causes of Pb loss in the granitoids around Loch Tay; a variety of geological processes are responsible for this phenomenon, including high temperature metamorphism, metamictisation, and recrystallisation (Pidgeon *et al.*, 1966; Geisler *et al.*, 2003; Schoene *et al.*, 2013; Schoene, 2014). However, it must be stressed that the very narrow range in U-Pb dates (420-418 Ma) recorded in this study means that the aforementioned discordant fractions do not have major ramifications for the interpretation (and importantly, the synthesis) of the CA-ID-TIMS dataset.

Regarding the Re-Os ages of molybdenite from Tomnadashan, all samples yielded similar ages that are within error of one another (Table 5.4.), meaning the likely mineralisation interval is c. 425-417 Ma. The results are mutually consistent with low uncertainty margins (~0.5 % uncertainty). Such trends may be indicative of isotopic homogeneity within the molybdenite crystals that were analysed at Tomnadashan (i.e. limited Re-Os decoupling) (Stein *et al.*, 2003; Selby and Creaser, 2004; Porter and Selby, 2010). Furthermore, the similarity between the ages of the disseminated and vein-hosted molybdenite (Fig. 5.21.) provides additional evidence that all of the molybdenite at Tomnadashan occurs within the same paragenetic stage (Stage 2; Fig. 6.1.a.), although more analyses would be needed to confirm this. Given the occurrence of molybdenite within one of the earlier paragenetic stages (Stage 2 out of 6; Fig. 6.1.a.), it is likely that the Re-Os ages in this study pertain to the initial mineralisation processes at this locality (and potentially the wider LTVS, given the contemporaneous nature of the veining in the Study Area).

In summary, the U-Pb and Re-Os datasets both demonstrate that the emplacement of several granitoids around Loch Tay occurred at ~420-418 Ma (Fig. 5.20.); furthermore, the age of mineralisation at Tomnadashan has been constrained to c. 425-417 Ma (Table 5.4.). Collectively, the available evidence indicates that magmatism and mineralisation are temporally coeval in some parts of the LTVS.

6.6. $\delta^{34}S$ datasets

As described in Chapter 5, the $\delta^{34}S$ values of the sulphides from the LTVS range from -1 to +13 ‰. Whilst the $\delta^{34}S$ results from the in-situ analyses on pyrite were similar to those lacking paragenetic context (Fig. 5.23.a.), measurements from both methods consistently yielded different calculated $\delta^{34}S$ values for the galena; specifically, the in-situ $\delta^{34}S$ measurements are typically lower than those without a paragenetic constraint (Fig. 5.23.b.; Lead Trial, Coire Buidhe, Tomnadashan, and the GAV). The reasons behind this trend are unclear; one possible interpretation is that the samples analysed without the paragenetic context offered by the in-situ measurements are more likely to contain impurities, given the sample preparation process and the difficulty of obtaining a pure mineral separate using the Dremel (Appendix B; Section B.5.). Many of the galena samples that recorded the largest discrepancies between the in-situ and analyses without paragenetic context came from localities where the galena contains a variety of inclusions; for example, at Tomnadashan and Lead Trial, the galena hosts inclusions of chalcopyrite and sphalerite (Fig. 6.1.a.-b.). During sample preparation with the Dremel, this material may have become mixed in with the galena that was analysed, resulting in a slight drift towards isotopically heavier values. On the other hand, using the laser at SUERC meant that it was possible to ablate relatively pure portions of the galena crystal (i.e. the laser could selectively target parts of the crystal without inclusions), meaning these values may be more representative of the $\delta^{34}S$ signature at each of the different localities within the LTVS. However, the in-situ measurements, given that they target a much smaller region of the crystal, are perhaps more likely to represent extreme values in the overall range; the measurements without in-situ context may instead represent a homogenised value for the entire crystal. It is also possible that the differences between the two analyses is coincidental and simply indicative of a broad range in $\delta^{34}S$ values at specific localities. For example, whilst the in-situ and analyses without paragenetic context on the CB_GAL samples from Coire Buidhe in this study yielded values of +0.1 and +5.7 ‰ (Fig. 5.23.), Smith (1996) reported a result of +2.68 ‰, which provides evidence that there may simply be a diverse range of $\delta^{34}S$ values here (as opposed to any discrepancy caused by the analytical procedures).

In Chapter 5 (Section 5.5.), the concept of the $\delta^{34}S$ values from 'Lead Trial-Tomnadashan' and the 'metasediment-hosted veins' being considerably different was introduced; it may be possible to discriminate between these populations on the basis of $\delta^{34}S$ values <+3 ‰ (i.e. typical of mantle-derived magmatic melts; Ohmoto, 1986). The approximate distribution of these populations is shown on Fig. 6.2. However, such a division is not straightforward; Coire Buidhe records a broad range in $\delta^{34}S$ values, which are in some cases >+5 ‰ (Fig. 5.23.b.) and similar to the metasediment-hosted veins (e.g. Spoil Heap and V3; Fig. 5.23.b.). Furthermore, it is difficult to classify mineralisation associated with the Comrie Pluton (which records $\delta^{34}S$ values of >+5 ‰, despite being classified as a magmatic occurrence of mineralisation; Naden *et al.*, 2010) and Fortingall, where the $\delta^{34}S$ values are as low as -7.73 ‰ (Smith, 1996). Taking these

aforementioned exceptions aside, most of the $\delta^{34}S$ data for pyrite from the LTVS clusters around two peaks in the histogram; +2 and +11 ‰ (Fig. 5.24.). Each peak on the histogram (Fig. 5.24.) may be associated with a distinct mineralising fluid. The sulphides from Lead Trial, Tomnadashan, and potentially Coire Buidhe fall within the different ranges of $\delta^{34}S$ values recognised for mantle or magmatic-hydrothermal fluids by previous researchers; <+5 ‰ (Ohmoto, 1972; Hutchison *et al.*, 2020), <+3 ‰ (Ohmoto, 1986), and -1.28 ‰ ± 0.33 (Labidi *et al.*, 2013). However, regarding the isotopically heavier metasediment-hosted veins (e.g. GAV, Tombuie, and Urlar Burn), identifying potential sources of sulphur is more challenging. The only commonalities within this population are metasedimentary host rocks and $\delta^{34}S$ values of >+5 ‰, although the range of recorded $\delta^{34}S$ values from these veins is wide; V3 (Calliachar Burn) is characterised by $\delta^{34}S$ values of +5 ‰, whilst some of the sulphides sampled from Tombuie had $\delta^{34}S$ values of +12.5 ‰ (Fig. 5.23.b.). As described in Chapter 2 (Section 2.8.3.), synsedimentary sulphides can have $\delta^{34}S$ values of >+16 ‰ (Seal, 2006; Quesnel *et al.*, 2023), meaning the fluids involved in the formation of the metasediment-hosted veins could have a crustal source of sulphur, as is envisioned in several genetic models for OGDs (Section 2.3.1.).

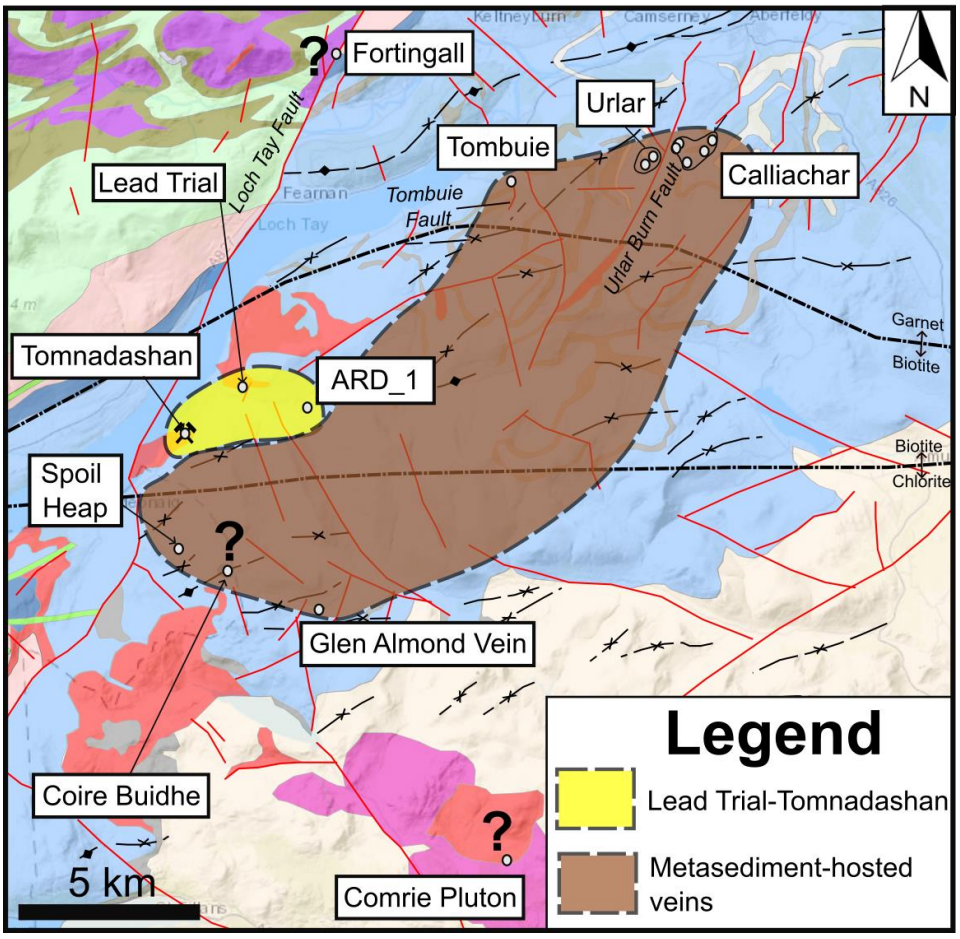

Figure 6.2. Geological map depicting the distribution of 'Lead Trial-Tomnadashan' ($\delta^{34}S$ values <+3 ‰) and the 'metasediment-hosted veins' ($\delta^{34}S$ values >+3 ‰). The distinction between the two is based on the upper limit for mantle-derived magmatic sulphur (+3 ‰) described by Ohmoto (1986). Localities with uncertain affinities to either population are shown by a question mark. The legend is the same as the one in Fig. 3.13.

In Chapter 5 (Section 5.5.), the link between structural geology and the $\delta^{34}S$ values was also summarised; isotopically heavier $\delta^{34}S$ values occur along lower order faults (in contrast to the lighter values from Lead Trial and Tomnadashan, which are associated with the LTF; Fig. 6.2.). Assuming a scenario in which the mineralising fluids originally migrated along larger-scale structures (e.g. the LTF), further migration of the fluid into the lower order structures may have been accompanied by a greater level of crustal sulphur assimilation. It is also possible that the smaller structures (e.g. the Urlar Burn Fault or the Tombuie Fault) were connected to sources of sulphur that were not intersected by the LTF.

The in-situ $\delta^{34}S$ dataset is most informative when interpreted within the context of the previously constrained parageneses of the different veins. At the GAV, there is no detectable difference in the $\delta^{34}S$ values between PyB and PyC; however, at Tomnadashan, the mean $\delta^{34}S$ value of PyA is +1.7 ‰, whilst the mean $\delta^{34}S$ value of PyC is +3.1 ‰ (Appendix E; Table E.2.). Regarding the GAV, the lack of any temporal increase or decrease in $\delta^{34}S$ values throughout the paragenesis is tentative evidence that the source of sulphur did not change between Stages 2 and 3 (Fig. 6.1.c.), although this is an interpretation based on data from two sulphide generations and therefore cannot be stated with certainty; further isotope studies on phases throughout the paragenesis would be required to confirm this hypothesis. Nonetheless, this observation is consistent with the interpretations derived from the paragenetic studies (Fig. 6.1.), which demonstrate that the different localities in the LTVS likely formed during repeated fracturing events and the influx of multiple fluid pulses. In terms of the evolution of the $\delta^{34}S$ values at Tomnadashan (from +1.7 ‰ to +3.1 ‰ between PyA and PyC; Fig. 6.1.), this may reflect some assimilation of isotopically heavier sulphur from the Dalradian Supergroup.

In addition to the source of sulphur (i.e. magmatic or derived from the Dalradian metasediment pile), the physiochemical parameters of the mineralisation environment (e.g. temperature, pH, and fO_2) may also exert a control on the $\delta^{34}S$ values of the sulphides within each paragenetic stage (Ohmoto, 1972; Seal, 2006; Hutchison *et al.*, 2020). This is because the fractionation of sulphur isotopes, particularly for pyrite, is controlled to a large extent by these variables (Chapter 2; Section 2.8.3.b.). In terms of evaluating the relative importance of each variable at Tomnadashan and the GAV, it is important to emphasise that wallrock sulphidation was not observed in the field at the latter (Section 5.2.), meaning pH changes may be of relatively less importance here. However, at Tomnadashan, sulphide mineralisation was observed to occur within the potassic alteration zone (Fig. 5.8.d.). The dynamic pH conditions (i.e. the change from acidic to alkaline pH values; Sillitoe, 2010; Watanabe *et al.*, 2018) associated with this process may have caused fluctuations in the $\delta^{34}S$ values of PyA and PyC (Fig. 6.1.a.). Furthermore, given the evidence of brecciation and repeated fluid injection events throughout the LTVS, it may be possible that the different localities have experienced large amounts of pressure changes and high temperature gradients with their

surrounding wallrocks (Section 2.7.). This process could also have influenced the $\delta^{34}S$ values within individual paragenetic stages.

Regardless of the exact cause of the range in $\delta^{34}S$ values at individual paragenetic stages within the LTVS, the in-situ $\delta^{34}S$ analyses confirm that the $\delta^{34}S$ values of pyrite from Tomnadashan and the GAV differ by a relatively large amount (i.e. ~9 ‰; Fig. 5.26.); this may suggest that both localities (and the respective 'Lead Trial-Tomnadashan' and 'metasediment-hosted vein' populations that they represent) did not form from the same mineralising fluid. However, it is unknown whether the range in $\delta^{34}S$ values recorded by galena at Coire Buidhe represent a paragenetic evolution, i.e. an increase from -0.1 ‰ in the initial stages to +6 ‰ later on (or vice versa). It is also important to note that the mineralisation at Coire Buidhe is hosted within limestone (Fig. 3.13., Locality 10), meaning that neutralisation reactions during the mineralisation processes may have been conducive to dynamic pH conditions; this could also have been a contributing factor in the broad range of $\delta^{34}S$ values recorded from this locality.

As described in Chapter 2 (Section 2.8.3.b.), pyrite and galena exhibit different $\delta^{34}S$ isotope fractionation factors, with pyrite preferentially incorporating ^{34}S; this trend occurs because heavier elements, such as Pb, are able to bond more efficiently with lighter isotopes that have higher energy levels (e.g. ^{32}S; Seal, 2006). This relationship is evident at most localities where $\delta^{34}S$ data was derived from both pyrite and galena, with the $\delta^{34}S$ values of pyrite typically being slightly heavier (Fig. 5.23.). However, galena from Stage 3 at Tomnadashan (Fig. 6.1.a) records slightly heavier $\delta^{34}S$ values than the pyrite that also occurs within this paragenetic stage (+0.7 to +4.0 ‰ for PyC and +2.7 to +5.5 ‰ for GnC; Table E.1.). There are several interpretations for this trend, which contradicts the principles of isotope fractionation (galena should theoretically develop lighter $\delta^{34}S$ values than pyrite during coprecipitation; Fig. 2.21.). For example, the paragenetic interpretation (Fig. 6.1.a.) may be incomplete, or the G.2019.101.7 sample of galena could pertain to a different paragenetic stage (and potentially a distinct hydrothermal fluid) than PyC. However, there is no textural evidence that the interpreted paragenesis for Tomnadashan (Fig. 6.1.a.) is incorrect. Alternatively, the provenance of this galena sample may be uncertain, although the NMS records clearly indicate that it was collected from Tomnadashan. Another explanation may involve the complex interactions that occur between precipitating phases and their original hydrothermal fluid. During a prolonged episode of fluid influx, pyrite and galena may have precipitated at several times, resulting in gradual variations to the ^{34}S contents of the fluid; whilst some coprecipitation of the two may have occurred (Fig. 5.17.g.), it is possible that the PyC analysed in-situ precipitated towards the end of the fluid flow event, when the fluid was depleted in $\delta^{34}S$. Such trends may occur as a result of Rayleigh crystallisation processes (Section 2.8.3.c.; Seal, 2006). However, it is uncertain as to whether closed system conditions could arise in an environment where textural evidence indicates a dynamic system (e.g. repeated brecciation, multiple fluid injections). An alternative interpretation involves fluid mixing; during the

formation of Stage 3 at Tomnadashan (Fig. 6.1.a.), there may have been an influx of a new fluid during the formation of this paragenetic stage, which caused the ^{34}S contents of the entire fluid to change. However, whilst there are several hypotheses for the comparable $\delta^{34}S$ values recorded from PyC and GnC, it is not possible to provide a firm conclusion regarding these trends.

The in-situ $\delta^{34}S$ analyses revealed evidence of intracrystal $\delta^{34}S$ zonation in several sulphide crystals from the LTVS; for example, the rims of galena in UB_GAL are isotopically heavier than the core of the crystal (Fig. 5.27.f.) and large variations in $\delta^{34}S$ values were recorded over relatively short distances in the PyB crystals within RC5 (Fig. 5.27.g.). There are several interpretations for the occurrence of $\delta^{34}S$ zonation within sulphide crystals. For example, during the crystallisation of pyrite, mixing with an isotopically heavier fluid could drive the $\delta^{34}S$ signature slightly higher (Wagner *et al.*, 2016; Börner *et al.*, 2022), resulting in a rim with a higher $\delta^{34}S$ value than the core. Alternatively, $\delta^{34}S$ zonation of pyrite is a common feature in environments with dynamic Eh and pH conditions (as well as dynamic temperatures) throughout the precipitation or evolution of a single crystal, meaning each generation or zone inherits a distinct $\delta^{34}S$ signature from the crystal/fluid interface (Crowe *et al.*, 1990; McKibben and Eldridge, 1990; Tanner *et al.*, 2016; Börner *et al.*, 2022). Dynamic mineralising conditions are also supported by the textural evidence from the LTVS (e.g. repeated brecciation and fluid influx, vuggy quartz). For example, Corkhill *et al.* 2010 described the star-like morphology of sphalerite inclusions within pyrite at Tombuie, which were interpreted as high temperature exsolution textures (akin to those described by Marignac, 1989). Similar replacement textures (e.g. chalcopyrite disease) were described at the CUB veins by Ixer *et al.* 1997.

Regarding the CUB veins, it is important to note that the categories recognised by Ixer *et al.* 1997 (Table 3.5.) may be distinguishable in terms of their $\delta^{34}S$ values; specifically, galena from the 'high-grade' veins (V3, V6, and V7; Table 3.5.) is isotopically lighter than the galena derived from the singular 'base-metal' vein (Table 3.5.; V5) and the veins in the Urlar Burn (between +5 and +6.5 ‰ for the 'high-grade' veins and between +7 to +9.5 ‰ for V5 and the veins in the Urlar Burn; Fig. 5.23.b.). For this reason, it may be possible to suggest that the Urlar Burn represents a distinct population from the veins in the Calliachar Burn. The differences in $\delta^{34}S$ values observed throughout the CUB veins is less prominent in the dataset from the pyrite crystals, which Ixer *et al.* 1997 considered to be paragenetically earlier than the galena; this may suggest that the two populations increasingly diverged from one another over time.

Throughout the course of this study, most of the $\delta^{34}S$ datapoints were derived from pyrite and galena; however, several measurements were taken from other sulphides (molybdenite, chalcopyrite, and arsenopyrite), and an interpretation of these data is provided here. Regarding the molybdenite from Tomnadashan, the $\delta^{34}S$ values ranged between +1.8 and +3.4 ‰ (Fig. 5.23.a; Table E.1., No. 30-42), which is mostly within the range of mantle-derived sulphur (Fig. 3.20.; Ohmoto, 1986). However, the singular

molybdenite crystal that was retrieved during panning from Tomnadashan (Appendix A; MOLY_CONC) recorded $\delta^{34}S$ values of +1.9 and +3.4 ‰, which is potentially indicative of $\delta^{34}S$ zonation. Regarding the chalcopyrite, the $\delta^{34}S$ values of these samples were lighter than the results reported from pyrite at Spoil Heap and the Urlar Burn (Fig. 5.23.a.); this is consistent with the principles of isotope fractionation (Fig. 2.20.), potentially indicating that pyrite and chalcopyrite coprecipitated at these localities.

6.5.1. Sulphur isotope geothermometry

Locality	Species	Sample	$\delta^{34}S$ (‰)	$\delta^{34}S$ (‰)	Range (°C)	Calculated T (°C)	±
Spoil Heap	Py	CB3	+7.43	1.63	250-600	548.3	55
	Gn		+5.80				
Tombuie	Py	2003.1G.M.637	12.16	0.10	250-600	3043.5	305
	Gn		12.26				
Urlar	Py	UB_SH	+9.25	1.07	250-600	375.3	37.5
	Ccp		+8.18				

Table 6.1. Sulphur isotope fractionation data and calculated apparent equilibrium temperatures for mineral pairs in the LTVS. The reference for the pyrite-galena and pyrite-chalcopyrite temperature ranges is Kajiwara and Krouse (1971), who suggest using 10 % uncertainty margins for the calculated temperatures. These calculations are justifiable because they were performed using mineral pairs derived from the same hand specimen, meaning it is possible to assume that coprecipitation might have occurred. Although paragenetic interpretations are not available for these samples, Ixer *et al.* 1997 described chalcopyrite and pyrite as being coeval in the CUB veins. Furthermore, coeval galena inclusions within pyrite are described at Tombuie by Corkhill *et al.* 2010.

As discussed in Section 2.8.3.d., there are several problems associated with the application of sulphur isotope geothermometry; the calculated temperatures (Table 6.1.) reflect $\delta^{34}S$ datapoints that were collected from the same rock sample (e.g. Fig. 4.2.; Fig. 4.3.), meaning that it is reasonable to assume that coprecipitation (and equilibrium growth) may have occurred (Seal, 2006). However, the calculation from Tombuie is unrealistic (the hottest fluid inclusions from this locality were 425 °C; Table 3.7.). This may indicate that at Tombuie, pyrite and galena occur in distinct paragenetic stages and precipitated from different hydrothermal fluids (and therefore did not grow under equilibrium conditions with one another). The same interpretation can be applied to Spoil Heap (Fig. 3.13., Locality 9), where the calculated temperature is also unrealistic; the hottest fluid inclusions reported from Coire Buidhe were 275-375 °C (Table 3.7.). The only realistic calculated temperature pertains to the sample from the Urlar Burn (375.3 °C; Table 6.1.), although given the error margins, the lower estimate of this temperature is ~337 °C. This calculated temperature is comparable to the hottest fluid inclusions (337 °C) reported from the CUB veins (Table 3.7.; Type 1, Ixer *et al.*, 1997). Naden *et al.* 2010 also noted that fluid inclusions with temperatures of >300 °C were more common in the Urlar Burn, which is similar to the value calculated in this study.

6.6. Pb isotope studies

As with the $\delta^{34}S$ data, a range in the Pb isotope ratios of galena from the LTVS is observed; Pb isotope data from Lead Trial and Ardtalnaig represent the least radiogenic values, whilst the metasediment-hosted veins (e.g. the CUB veins and Tombuie) recorded more radiogenic Pb isotope ratios. These trends are also evident from the regional distribution of Mu values (Fig. 6.3.). However, galena samples from the GAV and Spoil Heap form an intermediate population between the two extremes (Fig. 6.3.). Only two datapoints are available from Tomnadashan and they are significantly different from one another; Moorbath (1962) provided $^{206}Pb/^{204}Pb$ and $^{207}Pb/^{204}Pb$ values of 17.6 and 15.3 (respectively), whilst in this study, the $^{206}Pb/^{204}Pb$ and $^{207}Pb/^{204}Pb$ values were found to be 17.8 and 15.5 (Appendix F; Table F.3.). More analyses are needed to accurately characterise the signature here. However, it should be noted that the TIMS methodology utilised by Moorbath (1962) is known to be far less accurate than the ICP-MS analyses that were implemented in the present study (Hirata, 1996; Woodhead, 2002; Huston and Champion, 2023). Whilst the results of the Moorbath (1962) analysis are presented for context (Fig. 5.28.), the focus of the following interpretation is on the datapoint derived from G.2019.101.7 (Appendix A; Table A.1.). Nonetheless, the similar distribution of the CUB veins, Coire Buidhe, and Tombuie (Fig. 5.28.b.) may suggest that they share the same Pb source. However, the relationship between these localities and Spoil Heap, as well as the GAV, is uncertain; both Spoil Heap and the GAV are less radiogenic than the other metasediment-hosted veins (Fig. 5.28).

In terms of selecting a model of Pb evolution to focus on when interpreting the model ages and Mu values, it is important to emphasise that the Stacey and Kramers (1975) model has regularly been used to derive this information from gold and base metal mineralisation in the wider geological setting (as discussed in Section 2.8.4.). Furthermore, the Stacey and Kramers (1975) model was favoured by Milot *et al.* 2021 on the basis that it often yielded ages for geological materials that were feasible and accurate, in contrast to the Cumming and Richards (1975) model. However, the applicability of the Stacey and Kramers (1975) model to the LTVS is uncertain, given the close alignment between the datapoints collected in this study (Fig. 5.28.) and the curve produced by Zartman and Doe (1981). For this reason, several models have been used to calculate data from the LTVS, with each model demonstrating that the samples from Lead Trial are less radiogenic than the measurements taken elsewhere (Fig. 6.3.). Collectively, the approach of implementing several models may assist in mitigating against the limitations of transposing individual models for Pb evolution at the global scale to individual districts (Section 2.8.4.), such as the LTVS.

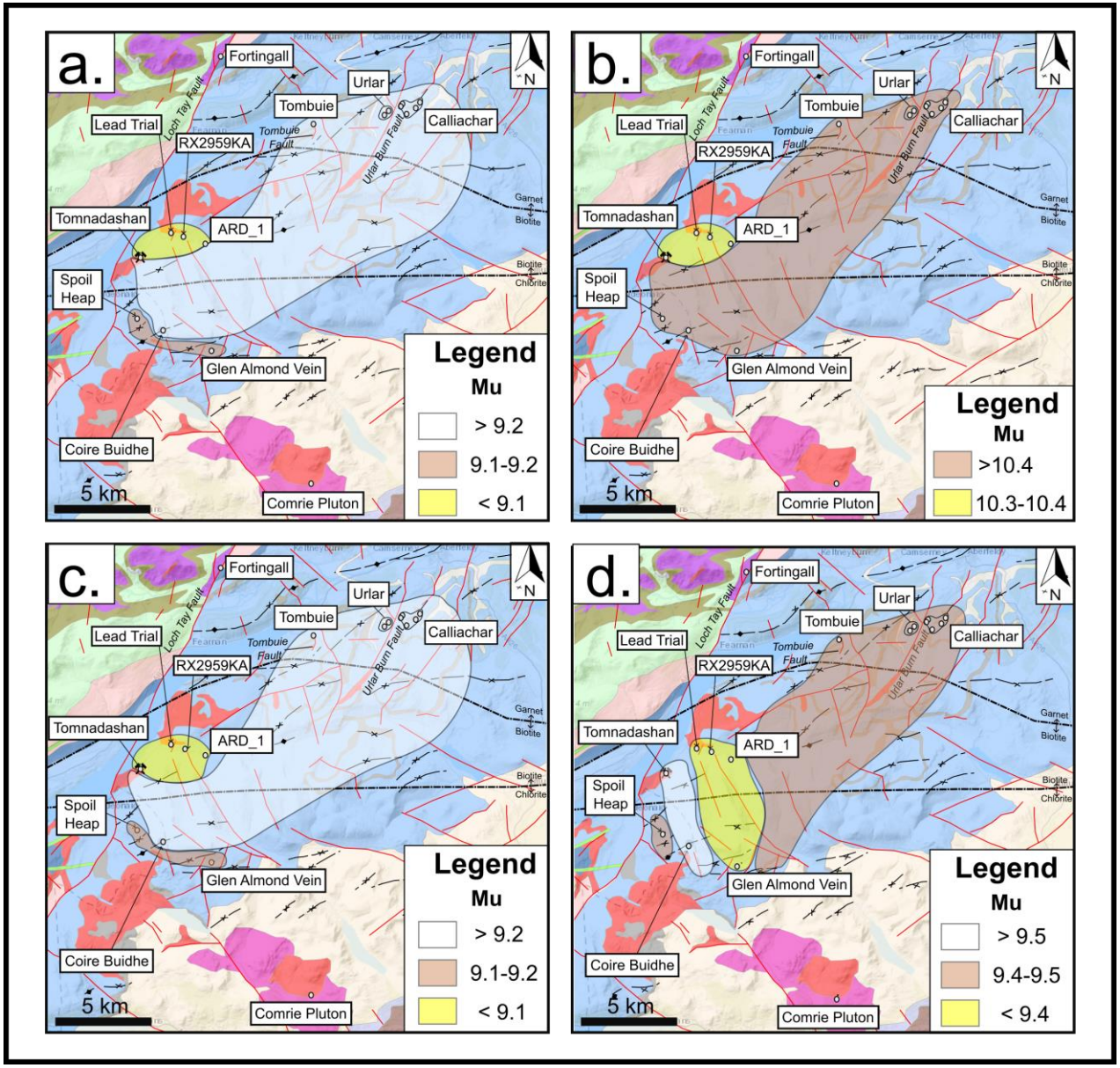

Figure 6.3. Simplified geological map depicting the variation in Mu ($^{238}U/^{204}Pb$) values calculated by the different models (Appendix F). The Mu values have been rounded to one decimal place prior to depiction on these maps. **a.** Stacey and Kramers (1975). **b.** Cumming and Richards (1975). **c.** Albarède and Juteau (1984). **d.** Albarède *et al.* 2012. The geological legend is the same as the one presented in Fig. 3.13. In some cases, the mapped ranges overlap as a result of the contrasting Pb values derived from Tomnadashan in this study (G.2019.101.7) and by Moorbath (1962). Value fields have been defined on the basis that all localities record a variation in Mu on the order of approximately 0.3 (Appendix F; Table F.3.), with three populations being discernible within this range.

Typically, when different Pb isotope populations are derived from the same prospect or region, this is interpreted as being evidence of multiple mineralisation events (Mortensen *et al.*, 2022; Huston and Champion, 2023). Regarding the potential number of mineralisation events in the LTVS, whilst it may be possible to recognise Lead Trial and Ardtalnaig as a distinct population (Fig. 5.28.), the large range in Pb isotope ratios throughout the metasediment-hosted veins is more challenging to explain. For example, in the different models that were used to calculate Pb model ages (Appendix F; Table F.3.), the Mu values for the GAV and Spoil Heap were sometimes lower than the rest of the metasediment-hosted veins (Fig. 6.3.). Furthermore, the Pb isotope ratios of galena from these localities were less radiogenic than the rest of the metasediment-hosted veins (Fig. 5.28.b.). Until further geochronological analyses are available, it is unknown whether the GAV and Spoil pertain to a distinct mineralisation event from the rest of the metasediment-hosted veins. Another possible explanation is that the mineralisation event involved in the formation of the metasediment-hosted veins exploited a variety of localised Pb sources of different ages, resulting in a large range in the Pb ratios recorded from these localities.

However, it is also important to note that in some instances, regional variations in Pb isotope ratios are interpreted as reflecting a prolonged mineralisation event, potentially involving the mixing between several sources of Pb along crustal fluid transport pathways (Stanton and Russell, 1959; Cannon *et al.*, 1961; Zoe and Dartman, 1981; Mortensen *et al.*, 2022). Given that the LTVS galena samples appear to form a trendline, with the quantity of radiogenic Pb increasing towards the east, it may also be possible to suggest that the entire LTVS has been impacted by a prolonged mineralisation event, initially involving mantle derived Pb that became increasingly mixed with crustal sources as the fluids moved throughout the package of Dalradian metasediments. However, it is not possible to evaluate both scenarios (distinct mineralisation events or a single prolonged mineralisation event involving mixing) without a detailed consideration of several other studies; further commentary on this topic is provided in Chapter 7.

Regarding the model ages (Fig. 5.29.), this dataset is capable of providing valuable insights into the age of the source that provided Pb to the mineralising fluid (Albarède *et al.*, 2012; Milot *et al.*, 2021; Huston and Champion, 2023). In essence, the model ages are indicative of how long ago the lead separated from a specific source region (Stacey and Kramers, 1975; Albarède *et al.*, 2012; Huston and Champion, 2023). Most of the model ages calculated in this study (Fig. 5.29.) do not exceed the age of the Dalradian Supergroup (i.e. the host rocks for much of the LTVS), which was deposited between 800 and 600 Ma (Stephenson *et al.*, 2013a, b). This finding does not preclude a metasedimentary source of Pb in the LTVS. However, the tendency for galena samples from the LTVS to plot beneath the curve for mantle Pb evolution produced by the Zartman and Doe (1981) plumbotectonics model (of which it is not possible to calculate reliable model Pb ages from; Section 2.8.4.) may be further evidence of a mantle source of Pb in the LTVS (potentially in the least radiogenic samples within the dataset, i.e. the datapoints from Lead Trial and Ardtalnaig).

Despite a large number of analyses being conducted on galena samples from Lead Trial and Ardtalnaig, the spread of the model ages recorded from this region are very narrow (<30 Ma; Fig. 5.29.), a trend that is also reflected by the tight distribution of the Pb isotope ratios from the galena samples (Fig. 5.29.). This may indicate that the source of Pb involved in the formation of these localities was relatively homogeneous, in terms of Pb isotope characteristics. For this reason, it may be possible to rule out a Pb contribution from the Dalradian metasediments in the mineralising fluids associated with Lead Trial and Ardtalnaig. As described by Mortensen *et al.* 2022, packages of metasediments tend to show large amounts of lateral variation with regards to the lithologies that are present; Pb may have been scavenged from multiple horizons, each with a contrasting Pb isotope signature. The result of a crustal Pb contribution tends to be a heterogeneous distribution of Pb isotope signatures and model ages (Mortensen *et al.*, 2019; 2022). However, when Pb is transported and homogenised over large distances, the range of Pb isotope compositions tends to be much narrower; this trend has been described from the FA subtype of Phanerozoic OGDs (Mortensen *et al.*, 2022). Regarding the metasediment-hosted veins in the east, the spread in recorded model ages is much larger (Fig. 5.29.), which would be consistent with mineralising fluids exploiting different crustal Pb sources over a geographically widespread region.

To summarise, Pb isotope ratios from the LTVS are diverse and varied, a trend that is also reflected in the model Pb ages (Fig. 5.29.). Both datasets are consistent with multiple sources of Pb throughout the LTVS; it is possible to recognise a less radiogenic and isotopically homogeneous mantle-derived source of Pb, and a likely contribution from varied and more radiogenic Pb sources within the Dalradian metasediment package. However, when the Pb datasets are evaluated in isolation, it is not possible to conclude whether the trends are indicative of multiple mineralisation events or a prolonged mineralisation event resulting in the mixing between different Pb sources. This topic is explored further in Chapter 7.

Chapter 7: Discussion

7.1. Introduction

The purpose of this chapter is to discuss the results from this study in the context of the body of previous research pertaining to the geology of the Study Area, the metallogenic processes operating in the Grampian Terrane, and the application of various isotope systems in the study of ore deposits. Where applicable, novel contributions to this pre-existing knowledge are outlined. This chapter differs from the one prior in the sense that the interpretations of the data are used to synthesise the outcomes of this study against the background literature reviewed in Chapters 2 and 3. Furthermore, answers to the aims outlined in Section 1.1., as well as the research questions and hypotheses (Section 3.7.), are provided in this chapter.

7.2. Wider implications of the LTVS paragenetic interpretations

In addition to providing a context for the isotope datasets, the paragenetic interpretations (Fig. 6.1.) have several ramifications for the development of the LTVS and the nature of the mineral system locally. Throughout this section, the wider implications of the paragenetic interpretations of Tomnadashan, Lead Trial, and the GAV are explored in detail.

7.2.1. Tomnadashan

As described in Section 6.3.1., the mineralogy and paragenesis of Tomnadashan is comparable to many other Cu-Mo porphyries (Gustafson and Hunt, 1975; Berger *et al.*, 2008; Sillitoe, 2010); molybdenite occurs in an earlier paragenetic stage (Stage 2; Fig. 6.1.a.), with the later stages (Stages 3-6; Fig. 6.1.a.) containing chalcopyrite, pyrite, sphalerite, galena, and tetrahedrite in variable proportions. However, the vein-hosted nature of the mineralisation at Tomnadashan (i.e. concentrated along a faulted contact within the mine; Pattrick, 1984; Naden *et al.*, 2010) indicates that the diorite porphyry outcropping on the shore of Loch Tay (Fig. 3.31.) is unlikely to have been the source of the mineralising fluids. Whilst the paragenetic sequence of Tomnadashan is supportive of a magmatic-hydrothermal fluid source at this locality, the exact source of these fluids is unknown; they may have been derived from a concealed pluton throughout the wider region (e.g. buried at depth along the LTF) or associated with the emplacement of the granitoids (e.g. TOM_FELS_2) into the diorite. This interpretation may be supported by the distribution of the alteration haloes at Tomnadashan; the granites have been impacted by potassic alteration and are more heavily mineralised than the surrounding diorite, which has experienced sericitisation (Fig. 5.8.). Such trends are consistent with the typical porphyry genetic model (Fig. 2.4.), in which fluids migrating away from a granitic core cause potassic alteration in the granites initially, prior to the formation of cooler alteration assemblages (e.g. phyllic and propylitic haloes; Fig. 2.5.) at further distances from the granite (Sillitoe, 2010; Pacey *et al.*, 2016; Watanabe *et al.*, 2018; Duan *et al.*, 2021). However, it should be noted that not all

porphyries are granitic in composition (Sillitoe, 2010), hence the aforementioned scenario may not be readily transposable to other porphyry deposits. Nonetheless, the intrusive relationships at Tomnadashan are typical of those documented from the wider geological setting; Siluro-Devonian granitoids throughout Scotland (Fig. 3.1.) are often comprised of older dioritic portions with younger granitic masses piercing into the core (Thirlwall, 1982; 1983; Miles *et al.*, 2014; 2016). The relationships between the diorite and granite in the Comrie Pluton are another example of this trend locally (Majid, 1974; Fig. 3.14.).

Given the mineralogy of Stage 3 at Tomnadashan (specifically, the switch from a molybdenite-bearing assemblage to one that contains copper sulphosalts; Fig. 6.1.a.), as well as the range of fluid inclusion populations reported from this locality (Table 3.7.; Type 3), it is likely that the fluids involved in the post-Stage 2 mineralisation (Fig. 6.1.a.) were cooler, a conclusion that was also reached by Smith *et al.* 2022. Many porphyry systems contain vein-hosted mineralisation that postdates the disseminated mineralisation within the porphyry host rock; the formation of these later veins is often linked to the remobilisation of metals from the potassic alteration halo (Gammons and William-Jones, 1997; Sillitoe, 2010). The presence of a mineralogical assemblage containing tennantite and tetrahedrite at Tomnadashan is typical of 'intermediate sulphidation' deposits, in which boiling, as well as meteoric fluid mixing, are important precipitation mechanisms (Simmons *et al.*, 2005; Sabeva *et al.*, 2017).

Regarding the gold at Tomnadashan, it was established in Chapter 6 that the gold mineralisation is likely to have occurred during the formation of Stage 1 of the paragenesis, and may therefore be coeval with pyrite, chalcopyrite and bismuth tellurides (Fig. 6.1.a.). Further evidence for this interpretation may come from the trends that have been observed at other porphyry deposits; for example, Pokrovski *et al.* 2014 suggested that the coprecipitation of gold with pyrite and chalcopyrite was typical of porphyry mineralisation, given that the precipitation of these minerals often extracts sulphur from the hydrothermal solution (therefore triggering gold precipitation; Pokrovski *et al.*, 2014; Section 2.7.2.).

7.2.2. Lead Trial

The paragenesis of Lead Trial (Fig. 6.1.b.) is similar to the paragenetic sequence commonly reported from epithermal gold deposits globally; many epithermal veins record a minor component of pyrite prior to a major episode of sulphide and gold mineralisation (e.g. Stages 3 and 4; Fig. 6.1.b.), which is subsequently overprinted by barren calcite and dolomite veinlets (Arribas *et al.*, 1995; Cooke and Simmons, 2000; Hedenquist, 2000a, b; Albinson *et al.*, 2001). The decision to classify Lead Trial as an epithermal deposit is also supported by the plethora of textural evidence that was described from this locality during fieldwork (Section 5.2.3.); many epithermal deposits display textures such as vuggy quartz, extensive brecciation, and sheeted quartz generations indicative of several episodes of fracturing and fluid injection (Sibson, 1981; Simmons *et al.*, 2005; Taylor, 2007; Sporli and Cargill, 2011; Zhai *et al.*, 2020) and are therefore similar to the LTVS in this regard. These textural characteristics are also common in OGDs (Section 2.2.1.; Groves *et al.*, 1998; Goldfarb *et al.*, 2001), although the mineralogy of Lead Trial (i.e. a lack of pyrrhotite and arsenopyrite, minor quantities of pyrite; Fig. 6.1.b.) is more similar to epithermal styles of mineralisation (Table 2.1.). It may also be possible to rule out the presence of high sulphidation epithermal processes locally, given the absence of the argillic alteration assemblages (Section 2.2.4.; Meyer and Hemley, 1967; Reed, 1997; Parry *et al.*, 2002; Hedenquist and Arribas, 2022) and the lack of any association between gold and enargite (Arribas, 1995; Hedenquist *et al.*, 2000a, b; 2004). These characteristics are typical of high sulphidation epithermal deposits (Section 2.2.3.) but they were not identified within the LTVS. Furthermore, the preponderance of galena and sphalerite at Lead Trial is typical of low sulphidation epithermal deposits (Table 2.1.; Simmons *et al.*, 2005).

Despite petrographically characterising several thin sections from Lead Trial (Appendix A) throughout the course of this study, gold was only observed within the vugs that are scattered throughout the QzB and QzC groundmass (Fig. 5.18.i., j.); direct spatial associations between gold and sulphide minerals were observed within detrital gold particles (Fig. 5.18.f.) that were retrieved from the disused tips next to the vein (i.e. adjacent to the vein shown in Fig. 5.4.). Whilst the coprecipitation of gold and pyrite in hydrothermal systems is better known globally, thermodynamic modelling (Li *et al.*, 2022b) has demonstrated that gold and galena can precipitate at the same time during the rapid decrease in H_2S associated with phase separation (which frequently occurs at shallow depths and low pressures, or during the processes associated with the fault valve model; Table 2.4.; Fig. 2.15). This finding provides support for the interpretation in the present study; specifically, that gold coprecipitated as a minor phase alongside the voluminous Stage 3 galena mineralisation (Fig. 5.18.f.). However, the origin of the coarser gold, which is observed to mantle the voluminous galena and sphalerite from Stage 3 (Fig. 5.18.i.), is more uncertain. Gold has also been observed within galena cracks at Tombuie (Corkhill *et al.*, 2010) and Coire Buidhe (Pattrick, 1984). Furthermore, coeval inclusions of gold occur within the galena crystals that comprise the

'high-grade' veins recognised by Ixer *et al.* 1997 in the Calliachar Burn (i.e. V3, V6, and V7; Table 3.5.); throughout the LTVS, there is commonly a spatial association between gold and galena, which justifies the decision to use $\delta^{34}S$ and Pb isotope data to interpret the processes associated with gold mineralisation throughout the Study Area. Several explanations have been postulated to explain the occurrence of gold within the cracks of sulphides (although they tend to focus on pyrite as opposed to galena). For example, sulphides may shrink soon after precipitation, forming cracks in which gold from the same hydrothermal fluid can precipitate (Sahoo *et al.*, 2015; Rogowitz *et al.*, 2018; Li *et al.*, 2020; Fougerouse *et al.*, 2021; Li *et al.*, 2022b). Alternatively, gold may migrate into the cracks following remobilisation from the sulphide lattice during CDR processes (Section 2.5.; Hastie *et al.*, 2020; 2021).

Many magmatic systems exhibit a coarsening of gold particles throughout the evolution of the system (Chapman *et al.*, 2017); the interpretation that the coarser gold (AuD) occurs within a later paragenetic stage is therefore plausible. However, it is unknown whether AuD was brought in by another episode of hydrothermal fluid flow or remobilised from sulphides that formed earlier in the paragenesis (Fig. 6.1.b.). Given the field and petrographic observations from Lead Trial, which demonstrate the occurrence of multiple fluid flow events (Fig. 5.4.; Fig. 6.1.b.), as well as the fact that previous research has described how gold grains in the later paragenetic stages of several auriferous veins in the Grampian Terrane have been 'remobilised' (e.g. Curraghinalt; Parnell *et al.*, 2000), it may be feasible to speculate that the coarser gold mineralisation at Lead Trial (Stage 4, AuD; Fig. 6.1.b.) originated from the remobilisation of gold from sulphides within the earlier paragenetic stages (e.g. Stage 1 or Stage 3; Fig. 6.1.a.). However, during petrographic characterisation (Section 5.3.3.), no textural evidence for gold remobilisation was observed (e.g. CDR textures; Section 2.5.). The corollary of this finding is that the introduction of coarser gold (AuD) at Lead Trial may not necessarily have been from a proximal source; for this reason, it may be possible to invoke a genetic model in which the mineralising fluids are transported over extensive distances (or have been derived from several fluid sources). However, it is therefore not possible to make a judgement on whether the gold has been transported by metal-ligand complexes (Pearson, 1963; Barnes, 1979; Stefánsson and Seward, 2003; Fig. 2.8.) or colloidal processes (Saunders, 1990; Gartman *et al.*, 2018; Petrella *et al.,* 2020; Section 2.4.2.), meaning the deposit-scale triggers for gold precipitation at individual localities within the LTVS remain uncertain.

Lead Trial and Tomnadashan have textures and mineralogies that differ substantially; for example, at Lead Trial, the quartz is massive and vuggy, and there are evident contrasts in the SEM-CL response of each generation (Table 5.2.). On the other hand, the hydrothermal quartz generations at Tomnadashan are largely homogeneous in SEM-CL (Table 5.1.) and brecciation has been less intense. The cockade textures at Lead Trial (Fig. 5.4.a.) were also not observed at Tomnadashan. In terms of mineralogical differences, pyrite, chalcopyrite, and molybdenite are the major phases present at Tomnadashan (Fig. 6.1.a.), whilst

these phases are only present in minor quantities around Lead Trial (e.g. molybdenite inclusions occur in detrital gold panned from Ardtalnaig Burn; Webb *et al.*, 2023). However, gold particles retrieved from the region around Lead Trial contained inclusions of bismuth tellurides and molybdenite, which may provide evidence for a genetic link to the mineralising fluids associated with Stages 1 and 2 at Tomnadashan (Fig. 6.1.a.). It is likely that Tomnadashan and Lead Trial comprise a porphyry-epithermal tract (e.g. Fig. 2.4.b.), with Tomnadashan forming closer to the core of the porphyry and Lead Trial representing the distal expression of the same fluids. However, whilst both localities are within close proximity to one another (Fig. 3.13.), the structural relationship between the two is unclear; some of the faults around Lead Trial (Fig. 5.6.) may link up with the LTF at depth, which could have provided a common pathway for mineralising fluids to migrate towards both Tomnadashan and Lead Trial.

7.2.3. Glen Almond Vein

The GAV lacks several phases that were described at Tomnadashan (e.g. molybdenite and bismuth tellurides; Fig. 6.1.). However, the GAV is mineralogically similar to Lead Trial in some respects (e.g. the presence of a barren euhedral quartz generation, and two episodes of gold precipitation; Fig. 6.1.). The vuggy quartz and euhedral crystal growth (Fig. 5.11.) may indicate that the GAV has also formed as a result of several episodes of fracturing and fluid flow during dilation (Webb *et al.*, 2024a). However, the GAV contains a much larger quantity of pyrite than Lead Trial (Fig. 6.1.). It is unknown whether these subtle variations in vein mineralogy relate to distinct fluid sources or specific fluid-rock interactions along different pathways of a common fluid (Webb *et al.*, 2024a).

Unlike Tomnadashan and Lead Trial, assigning a genetic model to the GAV is more challenging; the mineralogy of this locality is similar to both OGDs and epithermal gold deposits (Table 2.1.), even though the GAV also has some textures (vuggy quartz) that are perhaps indicative of a shallow mineralisation depth (<5 km; Fig. 2.3.). Furthermore, the GAV is entirely hosted in metasediments belonging to the Southern Highland Group, and unlike Lead Trial, extensive brecciation could not be observed (Fig. 5.11.). The narrower width (<20 cm; Fig. 5.11.) of the GAV may also indicate that the amount of fracturing and fluid influx at this locality was relatively lower (compared to Lead Trial). Unlike many of the other localities in the LTVS (Fig. 3.13.), the GAV is not spatially associated with any of the granitoids that are known throughout the Study Area. The GAV also lacks the native Bi and Pb-Bi-Ag sulphosalts that have been described at Coire Buidhe (Pattrick, 1984). As acknowledged in Webb *et al.* 2024a., it is not possible to assign a magmatic or orogenic classification to the GAV on the basis of mineralogy or paragenesis alone.

7.2.4. Implications of the paragenetic interpretations for mineral exploration

The paragenetic interpretation for the GAV has several ramifications for exploration and metallogenic processes associated with the LTVS (Webb *et al.*, 2024a). At the GAV, a direct observation between galena and gold precipitation (Fig. 6.1.c.; Stage 3 AuC) could not be observed (unlike Lead Trial, where AuC contains coeval inclusions of galena; Fig. 5.18.f.), although both gold and galena comprise the coeval inclusions that were observed within the Stage 2 PyB (Fig. 6.1.c.). It is not clear whether this textural relationship is representative of the wider LTVS; further investigation is required, but nonetheless, should this prove to be a generic feature, it may have ramifications for interpreting geochemical data derived from regional soil sampling surveys (Webb *et al.*, 2024a). Around the GAV, the lead concentrations of the soil samples may not be the best proxy for the occurrence of gold mineralisation; instead, zinc or copper are more likely to be associated with the development of gold mineralisation locally. Furthermore, arsenopyrite does not occur within the GAV, although minor quantities of As have been documented in Stage 3 PyC (Fig. 5.19.d.). Similarly, As may also be an unreliable proxy for the occurrence of gold mineralisation around the GAV (Webb *et al.*, 2024a).

Unlike the GAV, gold precipitation at Lead Trial is associated with galena (Stages 3 and 4; Fig. 6.1.), meaning that elevated Pb concentrations in soil samples may be indicative of further occurrences of gold mineralisation. However, at Tomnadashan, gold is associated with bismuth tellurides (Fig. 5.17.c.) and is potentially coeval with PyA (Fig. 6.1.a.) (Webb *et al.*, 2024b). It may therefore be possible to suggest that soil sampling campaigns focusing on bismuth concentrations could assist in the identification of regions around Tomnadashan with the potential to contain gold mineralisation, although given the low gold grades that have been reported from this locality (<1.58 g/t; Smith *et al.*, 2022), it is uncertain as to whether further exploration would be worthwhile.

7.3. The relationship between magmatism and mineralisation around Loch Tay

It is important to emphasise that only four igneous intrusions throughout the entire Study Area were dated, and it is unlikely that they encapsulate the range in magmatic activity around Loch Tay completely; the ages of the diorite and granite portions within the Comrie Pluton (404 ± 6 and 425 ± 3 Ma; Oliver *et al*., 2008) are evidence for this interpretation. Nonetheless, it is clear from both geochronological datasets presented in this study (U-Pb and Re-Os; Table 5.4.; Fig. 5.20.) that the granitoid ages (which encompass a range of 420 to 418 Ma; Section 5.4.1.) are similar to the ages of molybdenite mineralisation at Tomnadashan (c. 425-417 Ma; Table 5.4.). Furthermore, the 418.87 ± 0.15 Ma age of the granitic dyke within the mine (TOM_FELS_2; Appendix A) is very similar to the age of mineralisation at Tomnadashan. This may be further evidence that the emplacement of granitoids in and around Tomnadashan (Figure 5.9.c.) was responsible for the introduction of mineralising fluids at this locality (Webb *et al.*, 2024b).

The temporal overlap between a regional 420-418 Ma interval of magmatism (encompassing an area of approximately 100 km^2; Fig. 3.13.) and the age of molybdenite at Tomnadashan (425-417 Ma; Table 5.4.) is consistent with a magmatic or mantle-derived origin of some of the mineralising fluids associated with the LTVS (and that Hypothesis 1 is accurate; Table 3.10.). This argument is further supported by the widespread emplacement of granitoids throughout the Grampian Terrane at this time (Atherton and Ghani, 2002; Oliver *et al.*, 2008; Nielsen *et al.*, 2009; Miles *et al.*, 2016). Other intrusions throughout the wider geological setting with a comparable age to the mineralisation at Tomnadashan and the granitoids dated in this study (ARD_FELS_1, TOM_FELS_2, CB_FELS_2, and SW3) include Ratagain, the Lorne Lavas, Clinterly and Lochnagar (Fig. 3.8.). The transition from transpression to transtension at approximately 425 Ma (Dewey and Strachan, 2003; Fig. 3.3.) may have been favourable to the emplacement of granitoids along strike-slip structures created by the Scandian Orogeny (e.g. the LTF; Fig. 3.6; Tanner, 2014a). It should be noted that other major fault lines could have acted as conduits for the ascending plutons throughout this interval of time, such as the Highland Boundary Fault (Ryan *et al.*, 1995; Soper and Woodcock, 2003; Tanner, 2008; Cawood *et al.*, 2012). Rice *et al.* 2018 also advocated for this scenario (Fig. 3.11.).

Based on the evidence available, it is possible to conclude that the development of magmatic-hydrothermal systems, such as Lead Trial-Tomnadashan, was simply a by-product of regional magmatism. Given that the Loch Tay granitoids (as well as the other 'Newer Granites' throughout the Grampian Terrane) are typically considered to be I-type granites derived from the melting of subducted oceanic crust in the Laurentian asthenosphere (Thirlwall, 1986; Oliver *et al.*, 2008; Neilson *et al.*, 2009; Miles *et al.*, 2016), the mineralising fluids released by these intrusions are herein described as having a 'mantle-derived magmatic' source. It is important to use this terminology because models of post-subduction magmatism in the Grampian Terrane

and SUDLT (Atherton and Ghani, 2002; Neilson *et al.*, 2009; Miles *et al.*, 2016; Rice *et al.*, 2018) show that the upwelling of the asthenosphere never ascends into the shallow depths of the continental crust; instead, the asthenosphere is interpreted to stall at the base of the crust and trigger magmatic underplating, which ultimately results in the I-type plutons that rise throughout the crust (Fig. 3.10; Fig. 3.11.). These plutons eventually led to the development of magmatic-hydrothermal mineral systems (e.g. Lead Trial-Tomnadashan). As such, the aforementioned processes of plutonic ascent and I-type granitoid emplacement are judged to be the only viable mechanisms by which mineralisation in the LTVS can have any genetic link to the mantle, in terms of a potential source of mineralising fluids. The term 'mantle-derived magmatic' removes ambiguity regarding the ultimate source of the metals but it also avoids any connotations of auriferous fluids in the mantle directly ascending along structures such as the Highland Boundary Fault or LTF. Instead, I-type granites generated at the mantle-crust interface may have ascended these structures and injected mineralising fluids into the LTVS. Rice *et al.* 2018 considered the asthenosphere beneath Scotland at the end of the Caledonian Orogeny (Fig. 3.10.; Fig. 3.11.) to have elevated contents of gold as a result of metasomatism during subduction associated with the closure of the Iapetus Ocean; it may therefore be possible to suggest that the I-type granites developed high metal contents during partial melting. Furthermore, measurements of Au concentrations in peridotites from the Grampian Terrane indicate that the mantle beneath Scotland may have had elevated gold concentrations (Section 3.3.5.; Saunders *et al.*, 2018), which provides further support for the aforementioned scenario.

However, it is uncertain as to why some of the 'Newer Granites' throughout the Grampian Terrane are mineralised (e.g. Kilmelford, Lagalochan; Table 3.3.), whilst others are not (Fig. 3.8.). The difference in metal content may ultimately pertain to a heterogeneous distribution of gold and other metals in the mantle beneath Scotland (i.e. some I-type granites were generated from a source region with high Au concentrations that was not typical of the entire mantle beneath Scotland). Alternatively, perhaps different portions of the Dalradian Supergroup had higher concentrations of metals and crustal assimilation of metasediments in these regions of the Grampian Terrane was conducive to the development of mineralisation. Nonetheless, it must be emphasised that the controls on fertility throughout the Grampian Terrane remain poorly constrained.

It should be noted that Goldfarb and Pitcairn (2023) were critical of the suggestion that temporal similarities between the age of a granitoid and the age of mineralisation was firm evidence of a genetic link between the two events, as such occurrences do not preclude the possibility of a different fluid source facilitating the development of mineralisation. For this reason, the present study involved the use of isotope geochemistry to further examine the source of the mineralising fluids. As explained in Chapter 6, the $\delta^{34}S$ values of Lead Trial and Tomnadashan are consistent with a magmatic-hydrothermal fluid source, as are the mineralogies present within the paragenesis (Fig. 6.1.) and the textures observed in the field (e.g.

the similarities between Lead Trial and epithermal deposits; Section 7.2.2.). Furthermore, there are several granitoids (e.g. TOM_FELS_2) that are coeval with the mineralisation at Tomnadashan. All lines of evidence are consistent with the interpretation that Lead Trial-Tomnadashan is a magmatic-hydrothermal system, a suggestion that is realistic and compatible with the present geological knowledge of the Study Area. However, there are several auriferous veins in the Grampian Terrane (Fig. 3.17.) that are not known to be spatially associated with coeval granitoids (e.g. Lochearnhead or Stronchullin; Table 3.4.), meaning there may have been other sources of mineralising fluids (e.g. metamorphic fluids) in different parts of the Grampian Terrane.

7.4. Source and conditions of mineralising fluids in the LTVS

As described in Chapters 5 and 6, it is possible to recognise broad differences in the geochemical characteristics of the mineralising fluids associated with 'Lead Trial-Tomnadashan' and the 'metasediment-hosted veins.' Specifically, the Lead Trial-Tomnadashan system is mostly associated with $\delta^{34}S$ values of <+3 ‰ (i.e. the upper limit of magmatic sulphur recognised by Ohmoto, 1986; Fig. 3.21.), whilst the metasediment-hosted veins are typically (but not exclusively) characterised by $\delta^{34}S$ values >+3 ‰ (Fig. 5.23.; Table E.1.). For the rest of this chapter, the mineralising fluids associated with the LTVS are divided into two categories; 'Fluid Type 1' (FT1), which represents the range of magmatic sulphur (i.e. -3 to +3 ‰; Ohmoto, 1986, Fig. 3.21.), and 'Fluid Type 2' (FT2), a term that refers to localities with $\delta^{34}S$ values outside of this range. The origin of both fluids (the respective $\delta^{34}S$ range of each type is depicted on Fig. 7.1.), as well as the relationship between them, is explored throughout the rest of this section. However, it must be emphasised that the terms of FT1 and FT2 are not intended to indicate a relative timing (i.e. they do not necessarily indicate distinct mineralisation events), and simply serve as a descriptive classification (i.e. recognising the two categories of fluid that are evident from the sulphur isotope datasets; mantle-derived magmatic and non-magmatic). There are several reasons as to why the types of mineralising fluids in the LTVS have been classified by $\delta^{34}S$ values as opposed to the Pb isotope ratios. For example, in Section 7.3., it was established that the spatial relationships, field observations, mineralogy and limited gold microchemistry collectively indicate that Tomnadashan and Lead Trial comprise a porphyry-epithermal system (e.g. Fig. 2.4.). The similarity between these two localities is evidenced by the $\delta^{34}S$ profile from this region (i.e. 'Lead Trial-Tomnadashan'), which is distinct from the isotopically heavier $\delta^{34}S$ values that were recorded from the rest of the LTVS (i.e. the metasediment-hosted veins). Making such divisions on the basis of the Pb isotope dataset is more challenging; for example, the Pb isotope ratios of galena from Tomnadashan (G.2019.101.7) plot alongside the metasediment-hosted veins (Fig. 5.28.b.). However, generally speaking, samples that yielded $\delta^{34}S$ values typical of the FT1 classification also recorded the least radiogenic Pb isotope ratios in the LTVS (i.e. Lead Trial and Ardtalnaig; Fig. 5.28.b.).

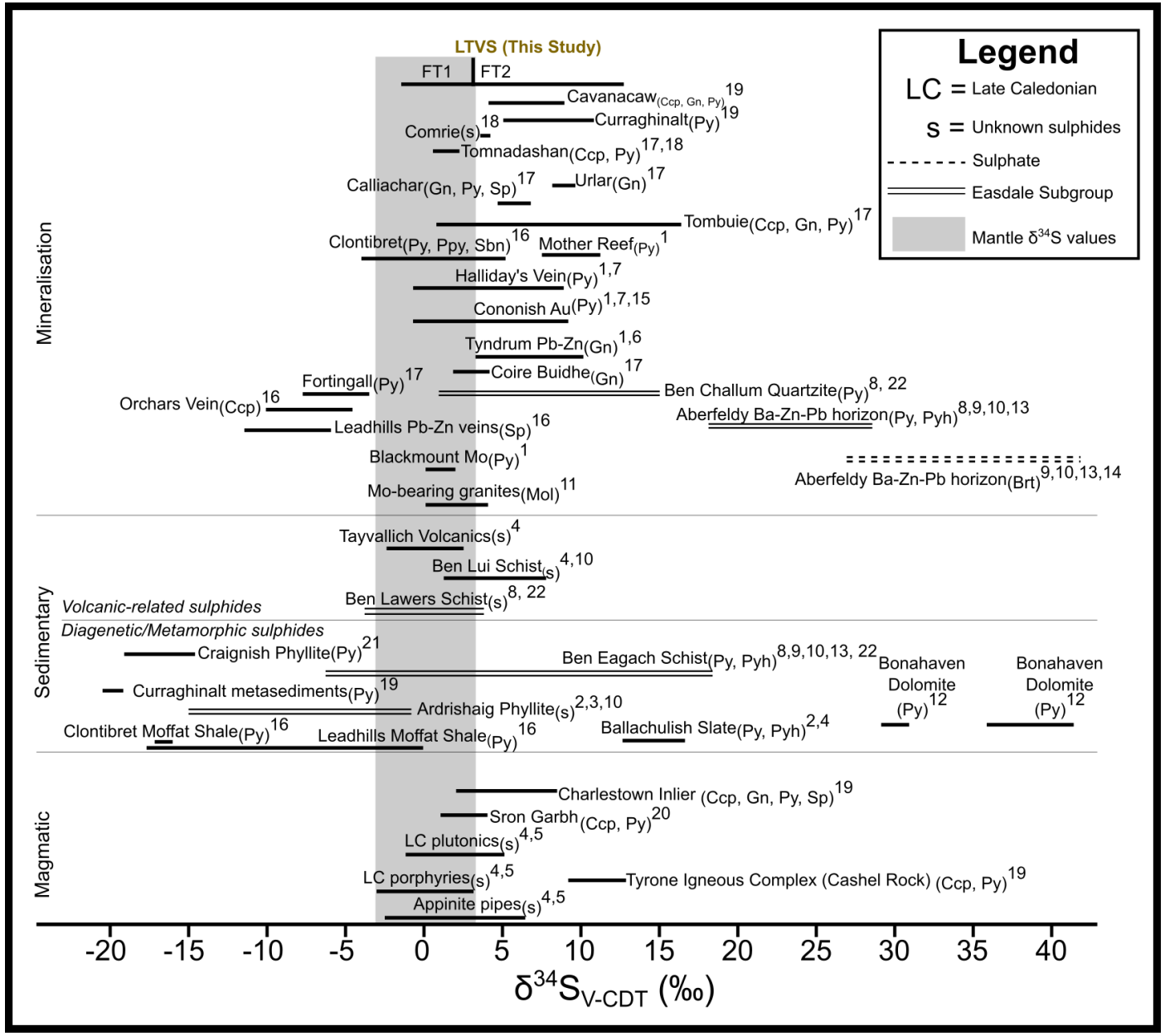

Figure 7.1. $\delta^{34}S$ data from gold/base metal mineralisation throughout Scotland and Ireland, now annotated with data from this study. Mantle-derived magmatic melts typically have $\delta^{34}S$ values of 0 ± 3 ‰ (Ohmoto, 1986). References for the localities where the data were derived are as follows: 1 = Curtis *et al.* 1993, 2 = Hall *et al.* 1988, 3 = Hall *et al.* 1994, 4 = Lowry (1991), 5 = Lowry *et al.* 1995, 6 = Pattrick *et al.* 1983, 7 = Pattrick *et al.* 1988, 8 = Scott *et al.* 1987, 9 = Scott *et al.* 1991, 10 = Willian and Coleman (1983), 11 = Conliffe *et al.* 2009, 12 = Hall *et al.* 1994b, 13 = Moles *et al.* 2014, 14 = Hall *et al.* 1987, 15 = Spence-Jones *et al.* 2018, 16 = Rice *et al.* 2018, 17 = Smith (1996), 18 = Lowry *et al.* 2005, 19 = Parnell *et al.* 2000, 2017 = Graham *et al.* 2017. The 'Magmatic' and 'Sedimentary' categories represent ranges for different units collected throughout the Grampian Terrane and SUDLT.

7.4.1. FT1

This fluid, which is recognisable around Tomnadashan and Lead Trial (e.g. the preponderance of $\delta^{34}S$ values within the -3 to +3 ‰ range; Fig. 5.23.), represents the only mineralising fluid in the LTVS for which there is a geochronological constraint. The molybdenite from Tomnadashan, which has a mean $\delta^{34}S$ value of +2.5 ‰ (Appendix E; Table E.2.) and can therefore be classified as FT1, was dated in this study to c. 425-417 Ma (Table 5.4.); this age is coeval with some of the granitoids around Loch Tay (ARD_FELS_1, TOM_FELS_2, CB_FELS_2, SW3; Fig. 5.20.). Assigning a magmatic-hydrothermal origin to FT1 is therefore relatively straightforward. However, in the following subsections, the characteristics of the sources of lead and sulphur are explored in detail, as these may vary to some extent (depending upon the locality or paragenetic stage in question). FT1 is also recognisable at Coire Buidhe (Table E.1.; No. 60-62) and Fortingall, where Smith (1996) recorded two $\delta^{34}S$ values of -1.3 and -2.0 ‰ from pyrite.

7.4.1.a. Sources of lead in FT1

As discussed in Chapter 6, the galena from Lead Trial and Ardtalnaig displays the least radiogenic Pb values in the LTVS (Fig. 5.28.b.). Furthermore, there is a very limited spread in the Pb isotope ratios and model ages from these localities (Fig. 5.28.; Fig. 5.29.), which is consistent with a source of Pb that is relatively isotopically homogenous (Section 6.6.). Given the close alignment between the Lead Trial and Ardtalnaig galena samples and the Zartman and Doe (1981) model of Pb evolution in the mantle (Fig. 5.28.b.), as well as the lack of any lower crustal basement to the Dalradian Supergroup locally in this portion of the Grampian Terrane (Fig. 3.4.), the only feasible source of Pb for these localities is the mantle. Magmatic-hydrothermal fluids emanating from I-type granitoids generated by the partial melting of subducted oceanic crust in the asthenosphere beneath Laurentia (Thirlwall, 1982; 1983; Neilson *et al.*, 2009) may have delivered mantle-derived Pb into the region now encompassed by the LTVS.

However, whilst it has previously been established that Lead Trial and Tomnadashan comprise part of the same mineral system (based on sulphur isotope signatures, the similarity between Stages 1 and 2 of the Tomnadashan paragenesis, and the inclusion assemblage within gold from the region around Ardtalnaig) and are related to FT1, there are uncertainties regarding the nature of the fluids in the later stages of the paragenesis at Tomnadashan (Stage 3 onwards; Fig. 6.1.a.). Specifically, the Pb isotope data from the galena sample that was collected at Tomnadashan (G.2019.101.7) plots alongside the measurements from the metasediment-hosted veins (e.g. the CUB veins, Tombuie, and Coire Buidhe; Fig. 5.28.b.). The Pb isotope ratios observed at Stage 3 of the paragenesis (Fig. 6.1.a.) also correspond to the appearance of copper sulphosalts, which as discussed in Section 7.2.1., are likely to represent a cooler mineralising fluid (Smith *et al.*, 2022). It may be possible to speculate that the initial fluids associated with Lead Trial-Tomnadashan were magmatic-hydrothermal; however, eventually these fluids may have mixed with crustal

lithologies over time, explaining the radiogenic signature observed in the later paragenetic stages (i.e. G.2019.101.7.; Fig. 5.28.). Crustal assimilation of Pb from the Dalradian metasediment package may have occurred from Stage 3 of the paragenesis onwards (Fig. 6.1.a.). The example from Tomnadashan demonstrates the potential for FT1 fluids to evolve over time, a concept that is explored further in the context of FT2 (Section 7.4.2.) and the genetic model for the LTVS (Section 7.6.). Finally, it should be noted that elevated Pb isotope ratios of have been observed in the later paragenetic stages of other porphyry and epithermal deposits; these trends are similarly interpreted as being the result of magmatic-hydrothermal fluids mixing with crustal sources of Pb over time (Foley and Ayuso, 1994).

7.4.1.b. Sources of sulphur in FT1

The previously discussed interpretation, that Lead Trial-Tomnadashan represents a magmatic-hydrothermal system, is also supported by the $\delta^{34}S$ values of the mineralisation from this region, which are encompassed by the various ranges of magmatic sulphur that have been described by previous researchers (e.g. 0 ± 3 ‰; Ohmoto, 1986) and the range of $\delta^{34}S$ values recorded from 'Lower Caledonian' porphyries throughout Scotland (Fig. 7.2.). Furthermore, the mean $\delta^{34}S$ value of molybdenite from Tomnadashan was +2.5 ‰ (Table E.2.), which is considerably lighter than the values Hill *et al.* 2013 reported from Cononish (specifically, Glen Orchy; +6.0 to +6.6 ‰); this is an important comparison because the 470 Ma molybdenite from Glen Orchy was interpreted as having a crustal source of sulphur (Hill *et al.*, 2013), which is evidently not the case at Tomnadashan (given the relatively depleted $\delta^{34}S$ values; Fig. 5.23.a.).

One interpretation of the depleted $\delta^{34}S$ isotope profile associated with Lead Trial-Tomnadashan is that the mineralising fluids involved in FT1 did not mix extensively with other sulphur sources (resulting in a relatively primitive isotopic signature). Previous research has described how the $\delta^{34}S$ values of Tomnadashan are consistent with a mineralising fluid that has undergone minimal modification from the original sulphur source due to rapid ascent and transportation (Lowry *et al.*, 1995; 2005). Tomnadashan, being located directly adjacent to the LTF (Fig. 3.13.), may have been in a position that was favourable to the rapid movement of plutons generated during the onset of regional transtension after 425 Ma (Dewey and Strachan, 2003). As discussed in Section 3.4.2., the fault plane of the LTF is known to host several granitoids, both locally and throughout the wider Schiehallion region (Treagus, 2000). It is also important to note that the trace of the LTF displays a kink immediately to the south of Tomnadashan (Fig. 3.13.), which may be indicative of a transtensional releasing bend locally (Wesnousky, 2005). In Section 2.6., it was noted that large structures such as the LTF may frequently deviate from their overall trend, which can give rise to low mean stress values; these conditions are favourable to the flow of hydrothermal fluids (Hodgson, 1989; Ridley, 1993; Phillips and Powell, 2010).

The LTF may have acted as a conduit for channelling the I-type plutons associated with voluminous magmatism at the end of the Caledonian Orogeny and their associated magmatic-hydrothermal fluids into the shallower depths of the LTVS. In such a scenario, the mineralising fluids would not have had an opportunity to mix with crustal sources of sulphur. However, this process does not explain the range in $\delta^{34}S$ values that have been recorded from PyA at Tomnadashan (-0.1 to +3.3 ‰; Table E.1.; No. 17-20). Further evidence for the concept that the FT1 fluids began to evolve around Lead Trial-Tomnadashan may occur in the form of the $\delta^{34}S$ values of the galena at Tomnadashan, which consistently cluster above the +3 ‰ boundary of mantle-derived magmatic sulphur (Ohmoto, 1986; Fig. 5.23.b.; Fig. 5.26.c.). The relatively radiogenic Pb composition of galena from Stage 3 in the paragenesis of Tomnadashan (Fig. 5.28.b.; Fig. 6.1.a.) indicates that some assimilation of crustal material at Tomnadashan occurred over time. It should also be noted that a single measurement from Lead Trial yielded a $\delta^{34}S$ value of +3.9 ‰ (Table E.1.; No. 48), which could also be evidence for crustal sulphur assimilation. Collectively, the evidence suggests that the initial fluids associated with Lead Trial-Tomnadashan were of the FT1 variety, although over time and throughout the paragenesis, they may have started to assimilate material from the Dalradian metasediment package.

However, it is also possible that the small variations in the $\delta^{34}S$ values (i.e. some values >+3 ‰; Fig. 5.23.) of Lead Trial-Tomnadashan may pertain to the nature of porphyry and epithermal environments of mineralisation; such trends are often indicative of dynamic changes in fO_2, pH and temperature (McKibben and Eldridge, 1992; Tanner *et al.*, 2016; Börner *et al.*, 2022). Furthermore, in the context of porphyries, those associated with more oxidised magmas (i.e. I-type granitoids) tend to show more variability in their $\delta^{34}S$ values because SO_2 and H_2S (the former of which contains a greater quantity of ^{34}S) are present in subequal proportions (Section 2.9.1.b.), meaning there are commonly internal variations in the ^{34}S contents of mineralising fluids associated with I-type porphyries (Seal, 2006). On the other hand, porphyries associated with S-type granites show much narrower ranges in $\delta^{34}S$ because H_2S is the dominant sulphur species (Burnham and Ohmoto, 1980; Seal, 2006). Altogether, the sulphur isotope profile of Tomnadashan is consistent with an I-type granitoid fluid source.

7.4.2. FT2

The sources and conditions of the mineralising fluids associated with the metasediment-hosted veins are more difficult to explain and there is no straightforward resolution to this problem, given the isotopically heavier $\delta^{34}S$ values that were typically recorded from most of these localities (>+3 ‰; Fig. 5.23.). In terms of assessing the origins of FT2, candidate fluid sources can be broadly split into two end members; magmatic-hydrothermal (e.g. porphyry or epithermal deposits; Fig. 2.4.b.) or 'orogenic' (Ridley and Diamond, 2000; Phillips and Powell, 2010; Pitcairn *et al.*, 2015).

7.4.2.a. Evaluating the potential of an 'orogenic' source of FT2

Given the microchemical characteristics of the detrital gold that has been retrieved throughout the region around Loch Tay (i.e. the presence of a sulphoarsenide-dominated suite in the metasediment-hosted veins), a magmatic-hydrothermal fluid source cannot be invoked to explain all of the observed geochemical characteristics of the LTVS (Chapman *et al.*, 2023). The $\delta^{34}S$ values of sulphides from the metasediment-hosted veins are also typical of OGDs interpreted to have a metamorphic fluid source (Kontak and Smith, 1989; Tornos *et al.*, 1997; Goldfarb and Groves, 2015; Huston *et al.*, 2023). Furthermore, several previous publications have referred to the potential role that 'orogenic' fluids may have had in facilitating gold mineralisation throughout the Grampian Terrane (Craw and Chamberlain, 1996; Pitcairn *et al.*, 2015; Rice *et al.*, 2016). For the aforementioned reasons, it is necessary to give consideration to the hypothesis that the metasediment-hosted veins are genetically linked to metamorphic fluids.

However, there are several fundamental problems with classifying any of the localities within the LTVS as 'orogenic'; for example, the age of mineralisation in the LTVS (as constrained by the Re-Os analyses in this study; Table 5.4.) postdates the peak metamorphic event in the Grampian Terrane (465 Ma; Friedrich *et al.*, 1999a, b; Baxter *et al.*, 2002; Rice *et al.*, 2016) by >40 Ma, meaning that any 'orogenic' fluids would need to have been retained in the Dalradian Supergroup for tens of millions of years. As outlined in Section 2.3.1., metamorphic rocks lack the necessary geological characteristics (e.g. high porosities and storativities; Yardley and Cleverley, 2013) to support such a scenario. Furthermore, invoking the 'deeper-later' models of metamorphism (Stüwe *et al.*, 1993; Stüwe, 1998) is not possible because the metamorphic history of the Grampian Terrane is well-constrained and there is no evidence of prograde metamorphism occurring after 465 Ma (Friedrich *et al.*, 1999a, b; Dewey, 2005; Rice *et al.*, 2016). However, it may be possible that evidence for 'deep-late' metamorphism is simply not detectable at the present exposure level, although this interpretation is speculative.

In this study, radiometric dating of molybdenite at Tomnadashan has revealed that some of the mineralisation around Loch Tay is c. 425-417 Ma (Table 5.4.). Crucially, mineralisation in the LTVS occurred

after the switch from transpression to transtension that occurred at 425 Ma (Dewey and Strachan, 2003; Fig. 3.3.) and during the voluminous episode of magmatism throughout the Grampian Terrane at the end of the Caledonian Orogeny (430-390 Ma; Miles *et al.*, 2014; 2016). However, Mortensen *et al.* 2022 suggested that the CSF, FA, and SLTD subtypes form under conditions of transpression during active orogenic events (Table 2.2.). The SHOG subtype may occur in a range of tectonic settings, including some that are comparable to the LTVS; however, the features of this style of mineralisation (i.e. mostly disseminated or stratabound; Table 2.2.) are significantly different from the auriferous veins around Loch Tay. Collectively, the results from the present study indicate that the geological characteristics of the LTVS are dissimilar from any of the Phanerozoic OGD subtypes recognised by Mortensen *et al.* 2022.

The strongest evidence against a metamorphic fluid source for the LTVS is the Pb isotope dataset that was collected as part of this study. Galena samples from the LTVS (and importantly, the metasediment-hosted veins associated with FT2) yielded Pb isotope ratios that were far less radiogenic than any of the Phanerozoic OGD subtypes recognised by Mortensen *et al.* 2022, which broadly align with the Stacey and Kramers (1975) model for Pb evolution in the upper crust (Fig. 2.28.; Farquhar and Haynes, 1986; Godwin *et al.*, 1988; Thorpe, 2008; Mortensen *et al.*, 2010; Bailey, 2013; Huston *et al.*, 2017). Instead, the Loch Tay dataset clusters very close to the Zartman and Doe (1981) model for Pb evolution in the mantle (Fig. 5.28.b.), potentially indicating that the Pb was transported from this source region into the LTVS by magmatic processes at the end of the Caledonian Orogeny (i.e. during voluminous magmatism).

Further evidence against an 'orogenic' origin for the LTVS comes from the previous fluid inclusion studies (Table 3.7.). Whilst the fluid inclusion data from the LTVS largely lacks paragenetic constraint, the measurements consistently implicate the involvement of a fluid >300 °C in the formation of the metasediment-hosted veins (Table 3.7.). However, in these previous studies, lower temperature populations were also recognised (<150 °C; Table 3.7.). In the CUB veins, salinities are typically <5 wt % NaCl, with maximum values of 13.7 wt % NaCl being recorded (Table 3.7.); such characteristics are more similar to porphyry and epithermal deposits as opposed to OGDS (Table 2.1.; Fig. 2.2.).

7.4.2.b. Sources of lead in FT2

As discussed in the previous section, the close alignment between the datapoints representing galena samples from the LTVS and the mantle curve for Pb evolution produced by Zartman and Doe (1981) (Fig. 5.28.b.) is perhaps strong evidence for a mantle source of Pb in the entire system. Furthermore, many porphyry and epithermal deposits plot near the Zartman and Doe (1981) curve of Pb evolution in the mantle (Shahabpour and Kramers, 1987; Bouse *et al.*, 1999; Pettke *et al.*, 2010; Saunders *et al.*, 2016; Zhai *et al.*, 2020; Sun *et al.*, 2021 Chugaev *et al.*, 2022), as discussed in Section 2.9.2.b. When compared against

Pb measurements that have been made from Scotland and Ireland (Fig. 7.2.), galena from the LTVS is less radiogenic than all other localities considered, with the only exception being some measurements taken in the Northwestern Terrane of Ireland (Fig. 7.2.), which Standish *et al.* 2014 interpreted as representing the derivation of Pb from a pre-Dalradian (i.e. Lewisian or Grenvillian) lithology. Whilst pre-Dalradian units are known to occur in the northern regions of the Grampian Terrane and the Isle of Islay (Fig. 3.1.; Stephenson *et al.*, 2013a, b), they are not present locally (Fig. 3.4.); the mantle may therefore be the only potential source of less radiogenic Pb for the LTVS.

However, as discussed in Chapter 2, there are limitations with transposing global models (e.g. Stacey and Kramers, 1975; Cumming and Richards, 1975; Zartman and Doe, 1981) to individual districts (Huston and Champion, 2023), such as the LTVS. Crustal sources of Pb should therefore not be completely discounted on this basis. Furthermore, whilst most researchers consider the ^{208}Pb vs ^{204}Pb ratio to be relatively insensitive to changes in Pb sources (Huston and Champion, 2023), and hence many publications tend to emphasise the trends shown in the ^{207}Pb vs ^{204}Pb dataset (Mortensen *et al.*, 2022; Torvela *et al.*, 2022), it is important to note that the former dataset from the LTVS displays more affinities with the Stacey and Kramers (1975) curve (Fig. 5.28.a.). The presence of both 'mantle' and 'crustal' Pb affinities in the LTVS may therefore be evidence that both sources have contributed Pb to the mineralisation. In addition, several researchers have suggested that some of the sediments in the Dalradian Supergroup were derived from a mantle source (O'Nions *et al.*, 1983; Russell, 1985) or alternatively, Lewisian basement northwest of the Grampian Terrane (Hamilton *et al.*, 1979; O'Nions *et al.*, 1983; Miller and O'Nions, 1984); it may therefore be anticipated that sources of Pb in the Dalradian Supergroup are less radiogenic than sedimentary or metasedimentary sources of Pb in other geological terranes, where the lithologies hosting the mineralisation may be younger and more radiogenic (e.g. the SET of Ireland; Fig. 7.2.). Some of the characteristics of the Pb isotope dataset for the metasediment-hosted veins are consistent with the involvement of crustal Pb sources. For example, the distribution of Pb in the metasediment-hosted veins is very scattered; specifically, the GAV and Spoil Heap are considerably less radiogenic than Coire Buidhe, the CUB veins, or Tombuie, despite similar $\delta^{34}S$ values being recorded from these localities in some cases (e.g. the similarity between Tombuie and the GAV; Fig. 5.28.b.). As discussed in Chapter 6, one possible explanation for this disparity may be that the GAV and Spoil Heap did not form during the same mineralisation event as the rest of the metasediment-hosted veins, although at present there is limited evidence for such an interpretation. However, it may be possible to consider the variation in Pb isotope ratios of galena from the metasediment-hosted veins within the context of FT2; given the consistent occurrence of FT2 $\delta^{34}S$ values (i.e. $\delta^{34}S$ values outside of the -3 to +3 ‰ range) and the Type 1 gold population dominated by sulphides and sulphoarsenides (i.e. the population of detrital gold that Chapman *et al.* 2023 considered to be inconsistent with a purely magmatic-hydrothermal origin) throughout the metasediment-hosted veins (Chapman *et al.,* 2023), it may be possible to suggest that FT2 has operated over a more geographically widespread region than FT1. Mortensen *et al.*

2022 described how mineralising systems that act over large regions may exploit a variety of Pb sources, particularly when there is a lack of connectivity between fault systems; around Loch Tay, the metasediment-hosted veins are spatially associated with subsidiary fractures of the LTF (e.g. the Urlar Burn or Tombuie faults, or the interlinked fractures around the GAV) which in many cases, do not appear to be connected to one another (based on the map patterns; Fig. 3.13.). However, it should be noted that the current understanding regarding subsurface relationships in the LTVS (Fig. 3.13.) is limited and there may be some instances where the different structures around the metasediment-hosted veins link up at depth. Regardless, it is possible to suggest that FT2 involved the exploitation of a variety of Pb sources, a characteristic that may reflect different lithologies (i.e. a crustal source of Pb) contributing towards the overall mineralisation processes or influencing the overall composition of the mineralising fluid.

In terms of assessing potential sources of Pb that were involved in FT2 (beyond the mantle), it is important to highlight the close overlap in Pb isotope compositions from the metasediment-hosted veins and SEDEX horizons from the Argyll Group (Fig. 7.2.). Crucially, the Lead Trial and Ardtalnaig galena samples record Pb isotope values that are dissimilar from the range encompassed by SEDEX sulphides (Fig. 7.2.), potentially indicating that this source of Pb was not involved in FT1. Others have also suggested that SEDEX horizons throughout the Grampian Terrane may have contributed metals to the mineralising fluids associated with the gold mineralisation (Hill *et al.*, 2013; Spence-Jones *et al.*, 2018) and as explained in Chapter 3, SEDEX horizons from the Easdale Subgroup are suggested to underlie the CUB veins and Tombuie (Tanner, 2014a). The interpretation that SEDEX horizons may have acted as a source of Pb for FT2 at some localities is therefore feasible, given the geological characteristics of the Study Area.

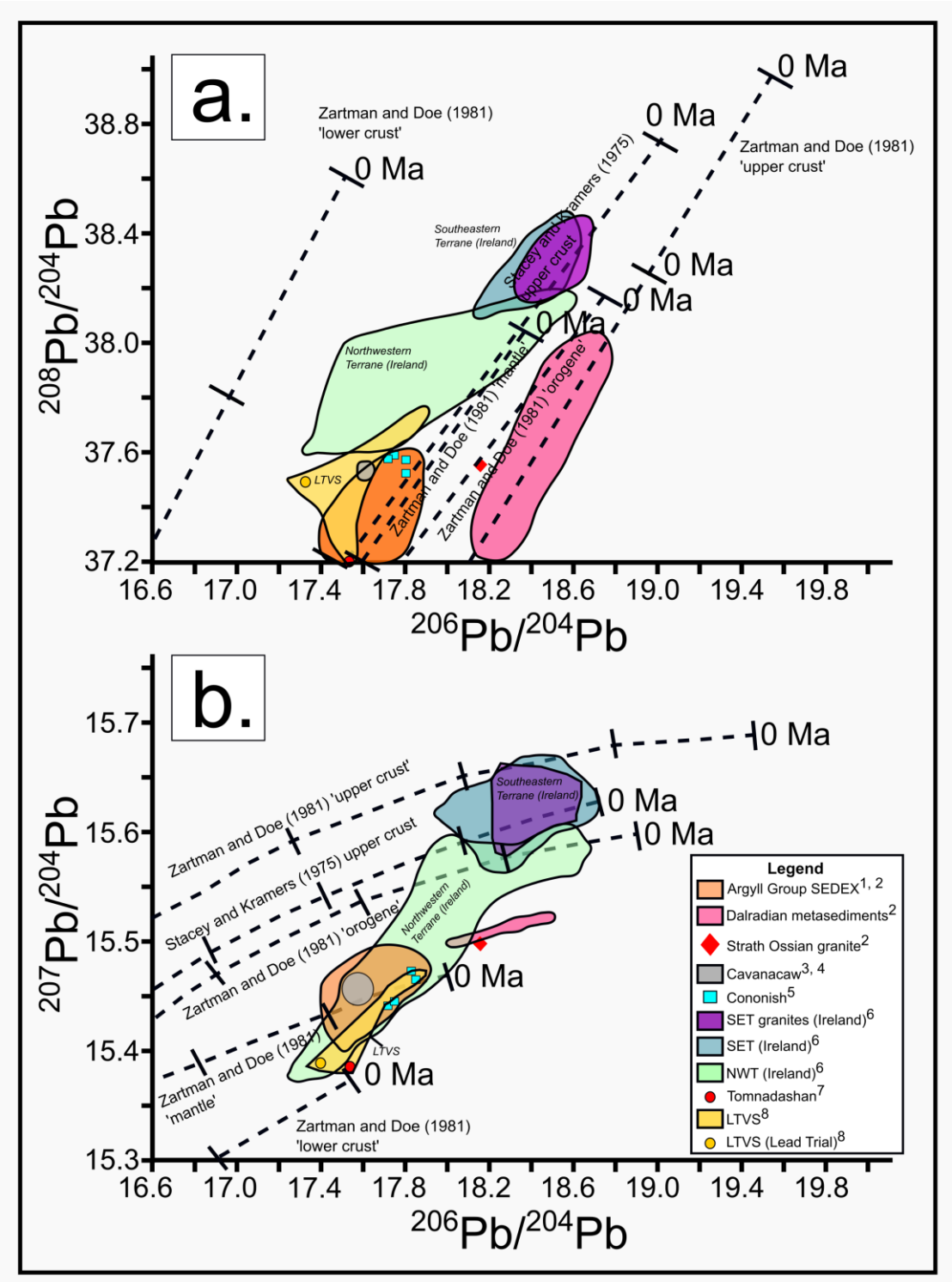

Figure 7.2. Pb isotope data from Ireland and Scotland, overlain with the Pb data from this study (a version of this figure was presented in Chapter 3). **a.** $^{208}Pb/^{204}Pb$ vs $^{206}Pb/^{204}Pb$. **b.** $^{207}Pb/^{204}Pb$ vs ^{206}Pb vs ^{204}Pb. The abbreviations are as follows: SET (southeastern terrane), NWT (northwestern terrane), LTVS (Loch Tay Vein System). All datapoints represent galena, with the exception of the granites (feldspar) and Dalradian metasediments (whole rock data). References are as follows: 1 = Clayburn *et al.* 1983, 2 = Clayburn (1988), 3 = Parnell *et al.* (2000), 4 = O'Keefe, 1987, 5 = Swainbank *et al.* 1981, 6 = Standish *et al.* 2014, 7 = Moorbath (1962), 8 = Savastano (2024). The tick marks represent intervals of 400 Ma.

7.4.2.c. Sources of sulphur in FT2

As discussed at the beginning of Section 7.4., the FT2 fluid is defined by $\delta^{34}S$ values that fall outside of the range of mantle-derived magmatic sulphur (-3 to +3 ‰; Ohmoto, 1986; Fig. 7.1.). All metasediment-hosted veins that are encompassed by the LTVS can be linked to FT2, which has characteristics of crustal sources of sulphur. Further evidence for this interpretation is summarised throughout the rest of this subsection.

Regarding the Smith (1996) data from Fortingall (Fig. 3.13., Locality 2), it may not be possible to explain this dataset without invoking a contribution of a crustal source of sulphur in FT2. The $\delta^{34}S$ values (-7.7 to -1.3 ‰; Smith, 1996) from Fortingall are very low and plot beneath the $\delta^{34}S$ range for the mantle (Fig. 3.21.). These values may represent the involvement of a metasedimentary horizon that contains synsedimentary sulphides with depleted $\delta^{34}S$ values in the mineralisation processes locally; as discussed in Chapter 2, the impacts of BSR on sulphur isotope fractionation during the formation of synsedimentary pyrite can result in a difference of up to 72 ‰ between coprecipitating sulphides and sulphides (Machel *et al.*, 1995; Wortmann *et al.*, 2001; Johnston *et al.*, 2007). For this reason, synsedimentary sulphides may show very isotopically depleted $\delta^{34}S$ values, with some being as low as -50 ‰ (Quesnel *et al.*, 2023); in the Grampian Terrane, synsedimentary sulphides with $\delta^{34}S$ values of -20 ‰ have been recorded (e.g. the metasediments around Curraghinalt; Fig. 3.21.). As described in Chapter 2, when isotopically depleted synsedimentary sulphides contribute sulphur to a mineralising fluid (e.g. during breakdown as a result of metamorphic devolatisation), it is possible for the resulting ^{34}S contents of the fluid to be depleted as a result. Occurrences of synsedimentary pyrite from the Grampian Terrane in Scotland with $\delta^{34}S$ values comparable to Fortingall include some portions of the Ben Eagach Schist Formation and the Ardrishaig phyllites (Fig. 3.21.), although only the former is present in the vicinity of Fortingall (Fig. 3.13.). However, in a scenario involving the mixing between a magmatic-hydrothermal FT1 fluid similar to those involved in mineralisation at Lead Trial and the most isotopically depleted horizons within the Ben Eagach Schist Formation, a fluid with $\delta^{34}S$ values similar to Fortingall would arise (Equation 15).

$$\delta_{mixture} = X_A\delta_A + X_B\delta_B$$

$$\delta_{mixture} = 0.9 \times -6 + 0.1 \times 1.4$$

$$\delta_{mixture} = -5.3\ ‰$$

Equation 15. Simple mass balance calculation (using the approach recommended in Equation 13; Seal, 2006) demonstrating how the most isotopically depleted $\delta^{34}S$ values from the Ben Eagach Schist Formation (Fig. 3.21.; -6 ‰) could give rise to $\delta^{34}S$ values similar to Fortingall after a magmatic-hydrothermal mineralising fluid assumed to have a composition similar to Lead Trial (mean $\delta^{34}S$ of +1.4 ‰; Table E.2.) undergoes extensive mixing with sediments from this unit. X = Molar fraction, $\delta = \delta^{34}S$.

Whilst the $\delta^{34}S$ data from the metasediment-hosted veins is typically heavier than Lead Trial-Tomnadashan (i.e. >+5 ‰; Fig. 5.23.), it is important to note that isotopically lighter values within the range of magmatic sulphur were recorded from Coire Buidhe (Fig. 5.23.b.; +0.1 to +0.6 ‰). When these $\delta^{34}S$ values are considered with those reported from the rest of the metasediment-hosted veins, a range of +0.1 to +13.0 ‰ becomes apparent (Fig. 5.23.); this range is comparable to the dataset from Cononish, where a process involving the mixing between an I-type granitoid and sulphur derived from the Dalradian metasediment pile (which has $\delta^{34}S$ values of between -20 and +40 ‰; Fig. 3.21) has been invoked (Fig. 3.22.; Hill *et al.*, 2013; Spence-Jones *et al.*, 2018). Given the similarities between the sulphur isotope profile of Cononish and the LTVS, it may be feasible to suggest that a version of this mixing process has happened locally in the Study Area.

7.4.2.d. Examining the mixing processes involved in FT2

Whilst the in-situ $\delta^{34}S$ dataset is of a limited scale (Appendix E; Table E.1.), it is important to note that some tentative textural evidence for mixing was observed in measurements that were made from the metasediment-hosted veins; for example, in UB_GAL (Fig. 5.26.f.), the rims of the galena crystals are isotopically heavier than the cores, a trend that was also observed in the CB1 sample from Spoil Heap (Fig. 5.25.f.; Fig. 5.27.i). This is evidence that the composition of FT2 was capable of changing throughout the duration of the precipitation of metalliferous phases at individual mineralised structures, which may be anticipated as a result of the influx of an isotopically heavier fluid throughout the crystallisation process. However, the very small amount of spread in the $\delta^{34}S$ data that was observed in the pyrite from V7 (Calliachar Burn; Fig. 5.23.) is consistent with isotopic homogeneity (Seal, 2006), meaning that the $\delta^{34}S$ ratios at some localities may not have changed extensively in the environment of mineralisation.

In addition to the contextual evidence derived from the genetic model for Cononish, in which magmatic sulphur is interpreted to have mixed with synsedimentary sulphides from the Dalradian Supergroup (Fig. 3.20.; Hill *et al.*, 2013; Spence-Jones *et al.*, 2018), further support for the occurrence of similar mixing processes locally may come the $\delta^{34}S$ dataset that was collected as part of the present study. For example, the heaviest $\delta^{34}S$ values (+13 ‰) in the LTVS come from Tombuie and the GAV (Fig. 5.23.) and they are similar to the $\delta^{34}S$ values recorded from Stage 4 Pyrite (Fig. 3.20.c) at Cononish (+12 ‰; Hill *et al.*, 2013); based on the potential sources of sulphur around Cononish (I-type granitoids, synsedimentary sulphides within the Dalradian Supergroup; Fig. 3.21.), Hill *et al.* 2013 suggested that it was not possible for such isotopically heavy values to develop without a sulphur contribution from the Ben Eagach Schist SEDEX horizons (Fig. 3.22.; 66 % magmatic and 34 % metasedimentary sulphur). Invoking a mixing process between these lithologies and I-type granitoids around the LTVS is feasible because SEDEX horizons with similar $\delta^{34}S$ values to those around Cononish are known to occur locally at Foss (Fig. 3.13., Locality 1; Moles *et al.*, 2014). Furthermore, based on the structural geology of the NE portion of the Study Area (i.e. around the CUB veins; Fig. 3.13.), Tanner (2014a) suggested that the Easdale Subgroup (which contains SEDEX horizons; Moles *et al.*, 2014) underlies the CUB veins and Tombuie. The isotopically heaviest $\delta^{34}S$ values in the LTVS from Tombuie may therefore be associated with the mixing between sulphur from an I-type granitoid and SEDEX horizons at depth (Equation 16). However, given the overturned nature of the Tay Nappe south of Loch Tay (Fig. 3.4.), it is uncertain whether SEDEX horizons underlie the GAV and can therefore be implicated in the isotopically heavy $\delta^{34}S$ values that have been recorded at this locality (Fig. 5.23.a.).

$$\delta_{mixture} = X_A\delta_A + X_B\delta_B$$

$$\delta_{mixture} = 0.33 \times 2 + 0.67 \times 18$$

$$\delta_{mixture} = +12.7\ ‰$$

Equation 16. Simple mass balance formulae (using the approach recommended in Equation 13; Seal, 2006) demonstrating how the mixing between an I-type granitoid (assumed to have an average $\delta^{34}S$ value of +2 ‰; Lowry *et al.*, 1995) and sulphur from some SEDEX horizons within the Ben Eagach Schist Formation; values of +18 ‰ are known to occur locally at Foss (Locality 1, Fig. 3.13.; Moles *et al.*, 2014). The scenario described at Cononish (i.e. a mixture with between 33 and 66 % magmatic sulphur) can give rise to $\delta^{34}S$ values that are similar to Tombuie (e.g. +12 to +13 ‰; Table E.1.). X = Molar fraction, $\delta = \delta^{34}S$.

The mixing process identified by Hill *et al.* 2013 may also be capable of explaining the range in $\delta^{34}S$ values associated with the metasediment-hosted veins (+1 to +13 ‰; Fig. 5.23.), as the components involved in the mixing are dependent upon the geological characteristics of different parts of the LTVS. Various metasedimentary units throughout the Grampian Terrane contain synsedimentary sulphides with $\delta^{34}S$ values of between +1 and +15 ‰ and are therefore isotopically lighter than the SEDEX horizons within the Ben Eagach Schist Formation (Fig. 3.21.). Examples that may be relevant to the LTVS include synvolcanic horizons within the Ben Lui Schist (+3 to +8 ‰; Fig. 3.21.) and Ben Lawers Schist (-4 to +4 ‰; Fig. 3.21.) formations, or the non-SEDEX horizons within the Ben Eagach Schist Formation (-6 to +18 ‰; Fig. 3.21.); all of the aforementioned lithologies occur within the Study Area (Fig. 3.13.). Based on the mixing diagram created by Hill *et al.* 2013 (Fig. 3.22.), or the formula produced by Seal (2006) for evaluating the mixing of two sulphur sources (Equation 13), it can be inferred that mixing between an I-type granitoid and any of the aforementioned units (in variable proportions) may be capable of producing sulphides with $\delta^{34}S$ values of between +5 and +10 ‰ (e.g. Equation 17), a range that is encompassed by the $\delta^{34}S$ data from the metasediment-hosted veins in the LTVS (Fig. 5.23.). The exact $\delta^{34}S$ signature of FT2 at any given locality within the LTVS is therefore potentially dependent on the host rocks that surround the different I-type granitoids throughout the Study Area (Fig. 3.13.). For example, a granitoid emplaced in the vicinity of Spoil Heap or Coire Buidhe would have mixed with different host rocks (e.g. the Southern Highland Group) from a granitoid emplaced in the vicinity of Tombuie (e.g. SEDEX horizons; Tanner, 2014a), explaining the contrast in the $\delta^{34}S$ values between these localities. Given the presence of FT1 at Fortingall (i.e. $\delta^{34}S$ values of -1.3 and -2.0 ‰; Smith, 1996), it may also be possible to suggest that a magmatic-hydrothermal fluid has mixed with isotopically depleted horizons within the Dalradian Supergroup, giving rise to $\delta^{34}S$ values as low as -7.7 ‰ (Smith, 1996).

$$\delta_{mixture} = X_A\delta_A + X_B\delta_B$$

$$\delta_{mixture} = 0.33 \times 2 + 0.67 \times 8$$

$$\delta_{mixture} = +6\ ‰$$

Equation 17. Simple mass balance formulae (using the approach recommended in Equation 13; Seal, 2006) demonstrating how the mixing between sulphur from an I-type granitoid (+2 ‰; Lowry *et al.*, 1995) and metasedimentary sulphur from the Ben Lui Schist Formation (+8 ‰; Fig. 3.21.) would result in an isotopically lighter $\delta^{34}S$. This scenario may be applicable to the veins in the Calliachar and Urlar Burns, which given their lighter $\delta^{34}S$ profile, may not have undergone mixing with sulphur from SEDEX horizons. This example is important in demonstrating the control that localised lithological variations exert on the mixing process associated with the metasediment-hosted veins, explaining the diversity in $\delta^{34}S$ values within this population. X = Molar fraction, $\delta = \delta^{34}S$.

Whilst a limited amount of $\delta^{34}S$ data is available from the Comrie Pluton, and it is therefore challenging to make an assessment regarding the relationship between this locality and FT1 or FT2, the dataset may provide some evidence for crustal assimilation of Dalradian metasediments (i.e. the aforementioned mixing process) during the emplacement of I-type granitoids in the Study Area. The $\delta^{34}S$ values of pyrite from the Comrie Pluton consistently sit outside of the range for 'Lower Caledonian' porphyries (-3 to +3 ‰) in the Grampian Terrane (Fig. 3.20.); in this study, values of +4.9 and +5.3 ‰ were reported from pyrite within the granitic core of the Comrie Pluton (Fig. 3.13., Locality 12), whilst Lowry *et al.* 2005 described the mean $\delta^{34}S$ value of sulphides from this locality as being +4.5 ‰. The relatively heavy $\delta^{34}S$ values of sulphides from the Comrie Pluton may reflect a mixing process between an I-type granitoid and the Dalradian metasediment package, which provides further justification for the decision to invoke similar genetic processes for the origin of FT2. However, it must be stressed that the nature of the $\delta^{34}S$ values from the Comrie Pluton are poorly understood; for example, the elevated values may pertain to a mantle source of sulphur that became enriched in $\delta^{34}S$ during subduction (Labidi *et al.*, 2013), as opposed to any processes related to crustal contamination.

The greatest limitation with transposing the mixing process described by Hill *et al.* 2013 at Cononish to the LTVS is the lack of any $\delta^{34}S$ data from several of the geological units that are present locally; whilst the $\delta^{34}S$ signature of some of the lithologies (e.g. the Ben Lui Schist, Ben Lawers, and Ben Eagach Schist formations) within the Study Area has been well characterised by regional studies throughout the wider Grampian Terrane (Fig. 3.21.), no data is available for the Pitlochry Schist or Ben Ledi Grit formations, which cover large swathes of the region around Loch Tay and in some cases host the LTVS (Fig. 3.13.). For example, the Pitlochry Schist Formation is comprised of both turbiditic sediments (e.g. pelites and psammites; Barrow, 1905; Harris *et al.*, 1994; Stephenson and Gould, 1995) and volcaniclastic horizons (Batchelor, 2004a, b), which may contain synsedimentary sulphides with different $\delta^{34}S$ values. This lack of data means that it is

difficult to identify lithologies that may have contributed sulphur to the mineralising fluids, beyond the probable contribution of SEDEX horizons (the $\delta^{34}S$ values of which are relatively well-constrained locally; Fig. 3.20; Moles *et al.*, 2014). It should also be noted that during fieldwork (Chapter 5, Section 5.2.), synsedimentary sulphides were not observed at any of the localities within the LTVS; the limitations regarding sampling in the Study Area (specifically, the lack of outcrop; Section 4.5.) may hinder further attempts to obtain this data.

Given the lack of certainty regarding the $\delta^{34}S$ values of synsedimentary and synvolcanic sulphides within the lithologies associated with the LTVS, it may be possible to consider the potential involvement of basinal or meteoric fluids in the mixing process. Meteoric fluid influx is known to be an important stimulant of mineralisation in several genetic models, including epithermal (Hedenquist and Lowenstern, 1991; Hedenquist *et al.*, 1993; Albinson *et al.*, 2001), porphyry (Heinrich *et al.*, 2004; Seedorff *et al.*, 2005; Sillitoe, 2015), and OGD-related processes (Craw *et al.*, 2009), mainly as a result of the impact meteoric fluids can have in terms of causing the hydrothermal solutions to cool or become diluted (which reduces the availability of ligands for metal-ligand complexing; Section 2.7.; Pokrovski *et al.*, 2014). Furthermore, meteoric fluids have been implicated in gold and base metal mineralisation throughout the Grampian Terrane (Craw, 1990; Curtis *et al.*, 1993; Lowry *et al.*, 1995; Chamberlain and Craw, 1996). Ixer *et al.* 1997 also hypothesised that the fluid inclusion population at the CUB veins may reflect the mixing between mantle-derived and meteoric fluids (given the range in temperatures recorded from the fluid inclusion populations here; Table 3.7.), although there is limited evidence to support this assertion. Meteoric and basinal fluids can in some cases contain large quantities of sulphur and record isotopically heavy $\delta^{34}S$ values (e.g. > +10 ‰; Kesler *et al.*, 1994; Seal, 2006; Peevler *et al.*, 2013; Field *et al.*, 2018). It may therefore be possible to suggest that meteoric fluids have also been involved in the mixing process associated with FT2.

7.4.2.e. Siluro-Devonian magmatism and FT2

In terms of interpreting the origin of FT2, the isotopic characteristics of the metasediment-hosted veins would suggest that this fluid developed as a result of fluids with a similar composition and $\delta^{34}S$ signature to FT1 mixing and assimilating crustal sources of sulphur as they migrated away from a pluton. Whilst it is possible to firmly link the development of FT1 to an age of mineralisation (c. 425-417 Ma; Table 5.4.) and the emplacement of granitoids throughout the LTVS (420-418 Ma; Fig. 5.20.), the lack of radiometric dates from any of the metasediment-hosted veins means that it is more challenging to iden8tify potential magmatic fluid sources for FT2 throughout the Study Area. For example, some FT2 fluids may have developed towards the end of the same mineralisation event as FT1, perhaps as a result of mixing between magmatic-hydrothermal fluids associated with the emplacement of SW3 or CB_FELS_2 and crustal sources of sulphur around the CUB veins, Coire Buidhe and Spoil Heap. However, it is also possible that FT2 may have originated from intrusions that were emplaced at a different time (i.e. potentially younger or older than the intrusions dated to 420-418 Ma in the present study). For example, the cross-section produced by Lavelle (2020a) indicated that the SW3 granitoid in the Calliachar Burn (Fig. 3.27.) is crosscut by V3 (Fig. 3.28.b.), which may suggest that the formation of the CUB veins occurred after the emplacement of the 420-418 Ma granitoids dated in this study (Fig. 5.20.). However, it must be stressed that the subsurface relationships in the Calliachar Burn are poorly constrained, and the age of the CUB veins is unknown. As discussed in Section 3.4.2., several undated Siluro-Devonian granitoids are spatially associated with the LTVS; examples include the granite at Tombuie (Fig. 3.29.) or the microdiorite that has been emplaced along the Urlar Burn Fault (Fig. 3.26.). The granitic pluton to the SW of Coire Buidhe has also not been dated (Fig. 3.13.), nor have the mineralised felsites around Fortingall (Treagus, 2000). Furthermore, none of the granitoids within the fault plane of the LTF have been dated (Treagus, 2000). Given the lack of knowledge regarding the subsurface geology around Loch Tay, it is also possible that there are other granitoids at depth (i.e. their existence is unknown). However, Giggenbach (1992) and Goldfarb and Pitcairn (2023) are critical of genetic models for mineral deposits involving a fluid contribution from intrusions that are not confirmed to exist, hence no attempt to link the LTVS to intrusions in the subsurface has been made in the present study. Finally, whilst the diorite and granite within the Comrie Pluton has been dated to 425 ± 3 and 404 ± 6 Ma (Oliver *et al.*, 2008), the gold particles from the metasediment-hosted veins recorded an assemblage of mineral inclusions (sulphides and sulphoarsenides) that was distinct from the inclusions reported in gold particles (molybdenite, bornite, and BiTe minerals) collected from Keltie Burn, Sma Glen, and Glen Lednock (Fig. 3.25.) (Chapman *et al.*, 2023). This may indicate that the development of FT2 and the metasediment-hosted veins of the LTVS was not genetically related to the emplacement of the Comrie Pluton.

Even though it is not possible to link the emplacement of specific intrusions to mineralisation processes associated with the metasediment-hosted veins, the characteristics of FT2 (i.e. a magmatic-hydrothermal

fluid that has developed a heavier $\delta^{34}S$ profile as a result of mixing with crustal sulphur sources, as evidenced by the sulphur isotope dataset, the lack of evidence for OGD related processes and the various aforementioned lines of evidence, from mineralogy to fluid inclusions, that are consistent with a magmatic-hydrothermal system) is perhaps more typical of epithermal gold deposits; OGDs are not characterised by fluid sources that have a large magmatic component (Section 2.3.; Goldfarb and Groves, 2015; Goldfarb and Pitcairn, 2023). Furthermore, the textural characteristics of the metasediment-hosted veins (vuggy quartz, extensive brecciation) are consistent with an epithermal origin. Other researchers have also classified the metasediment-hosted veins as epithermal; Corkhill *et al.* 2010 compared the mineralogy and textures at Tombuie with those recorded from the low sulphidation epithermal deposit at Creede (Colorado, USA; Hayba, 1997), whilst Ixer *et al.* 1997 suggested that the CUB veins potentially had an epithermal origin on the basis of the fluid inclusion data (specifically, the temperature and salinities of th8e entire population of fluid inclusions that were characterised here; Table 3.7.), which show similarities with fluid inclusions from epithermal gold deposits globally (Table 2.1.; Hedenquist and Lowenstern, 1994). Furthermore, calculated sulphate-sulphide pairs from epithermal deposits globally have yielded temperatures between 200 and 350 °C (Rye *et al.*, 1992; Arribas, 1995; Hedenquist *et al.*, 1998; Bethke *et al.*, 2005; Deyell *et al.*, 2005; Rye, 2005; Simmons *et al.*, 2005; Seal, 2006), which is similar to the lower estimate of 338 °C derived from the galena-chalcopyrite pair in this study. However, this calculated temperature is not incompatible with the temperatures of fluids involved in OGDs (Table 2.1.) and is only indicative of an epithermal origin for the metasediment-hosted veins when considered along with the other aforementioned lines of evidence.

As discussed in Chapter 2 (Section 2.9.1.b.), various estimates for the $\delta^{34}S$ values of different categories of epithermal gold deposits have been published; sulphides from low sulphidation epithermal deposits are typically between -6 and +5 ‰ (Ohmoto and Rye, 1989; Field and Fifarek, 1985), whereas the alkalic and high sulphidation varieties of epithermal deposit record ranges of -15 to +8 and -10 to +8 ‰, respectively (Arribas, 1995; Moussa *et al.*, 2017). However, the range in $\delta^{34}S$ values for high sulphidation epithermal deposits is also unlikely to be relevant given the lack of evidence (i.e. argillic alteration; Meyer and Hemley, 1967; Simmons *et al.*, 2005) for such processes locally. Regardless, a similar range (-23 to +9 ‰; Fig. 2.27.) for all varieties of epithermal deposits was reported by Hutchison *et al.* 2020. Given that most values from the metasediment-hosted vein lie within these aforementioned ranges (Fig. 5.23.), the discrepancy may be of minor importance and simply reflect the fact that epithermal gold deposits in Scotland are likely to involve the assimilation of sulphur from isotopically heavier SEDEX horizons throughout the Dalradian Supergroup (or another isotopically heavier source of sulphur, such as meteoric or basinal brines). Epithermal deposits are known to scavenge components from the crust during fluid migration, meaning their isotopic signatures are likely to be influenced by their host rocks to some extent (Marcoux and Milési, 1994; Sundblad *et al.*, 1991; Potra and Macfarlane, 2014; Ma *et al.*, 2022b).

7.5. Evaluating the number of mineralisation events in the LTVS

Based on the paragenetic interpretation of Tomnadashan, in which molybdenite comprises the second stage out of six (Fig. 6.1.a.), it is likely that the Re-Os ages of molybdenite (Table 5.4.) pertain to the initial mineralisation event around Loch Tay, given the contemporaneous initiation of the LTVS (Webb *et al.*, 2024b). Lead Trial is likely to represent the distal expression of the mineralising fluids (FT1) associated with Stages 1 and 2 at Tomnadashan, given the spatial relationship between these two localities (Fig. 3.13.) and their similar $\delta^{34}S$ profiles (i.e. consistently <+3 ‰; Fig. 5.23.). Furthermore, the similarity between the inclusions within detrital gold particles from Lead Trial and Ardtalnaig (i.e. the presence of molybdenite and BiTe inclusions; Webb *et al.*, 2023; Savastano, 2024) is further evidence for a genetic to link to Stages 1 and 2 at Tomnadashan (which are also comprised of molybdenite and bismuth tellurides; Fig. 6.1.a.). However, it is unknown whether the metasediment-hosted veins (and FT2) are genetically related to the same mineralising fluids as Lead Trial and Tomnadashan (especially given the lack of geochronological constraint). As discussed in Section 6.6., the trends in the Pb isotope dataset (Fig. 5.28.) may be indicative of distinct mineralisation events (given the spread in Pb isotope ratios; Stanton and Russell, 1959; Cannon *et al.*, 1961; Mortensen *et al.*, 2022; Huston and Champion, 2023) or a single prolonged mixing event throughout the LTVS. In this subsection, a detailed discussion on the most likely scenario is provided.

As mentioned previously, Pb isotope ratios from the LTVS display a gradual increase from West (Lead Trial) to East (the metasediment-hosted veins; Fig. 5.28.b.). It may therefore be possible to suggest that the metasediment-hosted veins formed as a result of the magmatic-hydrothermal fluid (FT1) around Lead Trial-Tomnadashan mixing with crustal Pb sources (and thereby evolving into FT2) during fluid migration towards the east. The change between individual localities from West to East is relatively moderate (e.g. the increase in Pb isotope ratios from Tombuie to the CUB veins; Fig. 5.28.b.), which is perhaps consistent with a gradually evolving mineralising fluid migrating throughout the LTVS. Furthermore, whilst the distinct populations of $\delta^{34}S$ recorded on the histogram (Fig. 5.24.) may be consistent with the concept of temporally separated mineralising fluids, evidence from Cononish has demonstrated that such variation can arise as a result of a magmatic-hydrothermal fluid mixing with sulphur sources in the Dalradian metasediments throughout the same mineralisation event (Hill *et al.*, 2013). The observation that heavier $\delta^{34}S$ values and more radiogenic galena samples are associated with lower order (relative to the LTF) NW-SE trending structures (i.e. Riedel shears or an episode of transtension postdating the main movements on the LTF; Treagus, 2000; Tanner, 2014a) is also consistent with a single mixing event; assuming that the initial mineralising fluids were generated at depth as a result of magmatic-hydrothermal processes, it may anticipated that they would gradually migrate into the later, lower order structures over time (Sibson *et al.*, 1988; Hodgson, 1989; Cox, 2005; Phillips and Powell, 2010), with an increasing transportation distance corresponding to a greater degree of mixing. However, whilst the LTF may be a relatively continuous

structure (Bradbury *et al.*, 1979; Nicholson and Lecht, 1989), most of the lower order structures throughout the Study Area are relatively disconnected and there is no evidence that they are linked to the LTF (Fig. 3.13.). There is no evidence that a percolation threshold (Section 2.6.) has been exceeded throughout the region. It is therefore uncertain whether the structural characteristics of the LTVS could facilitate the movements of hydrothermal fluids over such a large scale (i.e. from Tomnadashan to the CUB veins; Fig. 3.13.). Furthermore, most of the structures observed in the Calliachar Burn and around Lead Trial were noted to be unmineralised during fieldwork (Chapter 5), which potentially indicates that many of the mapped faults (Fig. 3.13.) formed after the mineralisation processes (and therefore could not facilitate large-scale fluid migration during the c. 425-417 Ma mineralisation interval identified by the present study).

Although it may be possible to postulate a genetic model involving a singular mineralisation event throughout the entire LTVS (and the gradual evolution of FT1 into FT2 over time), there is currently a lack of data to support this interpretation (e.g. the subsurface characteristics of the different fault networks are poorly constrained; Fig. 3.13.). Furthermore, scrutiny of the isotope datasets presented in this study are indicative of at least two mineralisation events; in the following paragraphs, evidence in support of this conclusion is discussed.

Whilst the Pb isotope data derived in this study is presented in Section 6.6., further insight can be attained by contextualising these results against the studies that have been conducted throughout the UK and Ireland as a whole (Fig. 7.2.). The range encompassed by the LTVS is very broad, especially when compared to individual deposits such as Cavanacaw or Cononish (Fig. 7.2.). In the case of the latter, which has a mineralisation interval that has been well-defined by prior geochronological analyses (c. 408 Ma; Rice *et al.*, 2012), the Pb isotope ratios for Cononish (Fig. 7.2.) may represent the variation in Pb isotope composition that could reasonably be expected to arise during a single mineralisation episode in the Grampian Terrane. Furthermore, Mortensen *et al.* 2022 noted that when the transportation of hydrothermal fluids occurs over large distances throughout a single mineralising episode (a scenario that might be applicable to a mineralising fluid migrating throughout the 100 km^2 encompassed by the LTVS), Pb isotope compositions tend to be homogenised and therefore similar. For the collective LTVS, this is not the case (i.e. the Lead Trial and Ardtalnaig samples are considerably different from the metasediment-hosted veins in the East; Fig. 5.28.b.). It is also possible that the mineralising fluids associated with the metasediment-hosted veins could have assimilated Pb sources from the host rocks during mineralisation, which may explain the large range in Pb isotope ratios that is recorded by the entire dataset from these localities (e.g. the GAV and Spoil Heap; Fig. 5.28.b.).

Further evidence for temporally separated mineralisation events may come from the $\delta^{34}S$ data that was derived from the CUB veins. As noted in Chapters 5 and 6, the 'high-grade' veins in the Calliachar Burn are

isotopically lighter than the 'base metal' veins (Table 3.5.) and those in the Urlar Burn (Fig. 5.23.b.). Given that the Calliachar and Urlar Burns are geographically proximal localities (Fig. 3.13.), this large amount of variation that occurs over a relatively small distance (e.g. the area encompassed by Fig. 3.26.) may be the result of temporally separated mineralisation events. However, it is important to note that Ixer *et al.* 1997 considered the CUB veins to represent the same hydrothermal system. To resolve the genetic relationships between the different veins in the Calliachar Burn and the Urlar Burn, further geochronological analyses are required.

The last line of evidence to consider when evaluating the potential of distinct mineralisation events in the LTVS is the microchemical data from detrital gold particles that was presented by Chapman *et al.* 2023. This study recognised two distinct categories of gold populations; orogenic and magmatic-hydrothermal/epithermal (Chapman *et al.*, 2023). The different affinities (sulphoarsenides in the 'orogenic' population, BiTe minerals in those associated with magmatic-hydrothermal activity; Chapman *et al.*, 2023) of each population may be difficult to explain in the context of a single fluid evolving throughout the entirety of the LTVS during a prolonged mineralisation event.

Regarding the timing of the other mineralisation events in the LTVS (i.e. aside from the c. 425-417 Ma age of molybdenite; Table 5.4.), there are several possibilities. Mineralisation may have occurred at the same time as the formation of auriferous veins at Cononish (408 Ma; Rice *et al.*, 2012) and Rhynie (407 Ma; Mark *et al.*, 2011). The age of the mineralised granite in the Comrie Pluton (404 ± 6 Ma; Oliver *et al.*, 2008) may provide further evidence for the suggestion that a mineralisation event occurred in the region around Loch Tay at this time. Further evidence for the occurrence of mineralisation events after the formation of Tomnadashan and Lead Trial may come from the cross-section for the Calliachar Burn, which demonstrates that V3 crosscuts the SW3 granitoid (Fig. 3.28.); as described in Section 7.3., SW3 has an age (419.1 ± 0.2 Ma; Fig. 5.20.) that is coeval with the Re-Os dates derived in this study (Table 5.4.). However, the mineralisation processes associated with the metasediment-hosted veins may have begun shortly after the formation of Lead Trial-Tomnadashan; Porter and Selby (2010) dated molybdenite in the Etive Complex (Fig. 3.6.) to 414.6 ± and 414.7 ± 2.1 Ma (Section 3.5.2.e.), meaning that mineralisation processes at this time were also occurring elsewhere in the Grampian Terrane. Given the onset of voluminous magmatism at 430 Ma (Neilson *et al.*, 2009; Miles *et al.*, 2014) and the switch to regional transtensional at 425 Ma (Dewey and Strachan 2003; Fig. 3.3.), it is also feasible to speculate that the FT2 fluids originated as a result of the fluid release from a pluton slightly older than 420-418 Ma; such intrusions occur locally (e.g. the diorite within the Comrie Pluton; 425 ± 3 Ma; Oliver *et al.*, 2008). However, the contemporaneous nature of the veining in the LTVS (as indicated by their consistent NW-SE orientation; Table 3.4.) and the position of molybdenite in the paragenetic interpretation at Tomnadashan (Stage 2 out of six paragenetic stages; Fig.

6.1.) may suggest that the formation of Tomnadashan at c. 425-417 Ma represents the earliest mineralisation event associated with the Caledonian Orogeny throughout the Study Area.

In this paragraph, a specific explanation regarding the concept of multiple mineralisation events in the context of the LTVS is provided. The evidence from the present study demonstrates that Lead Trial-Tomnadashan formed during the same mineralisation event, in response to an FT1 fluid (which potentially began to evolve into FT2 over time) and the emplacement of granitoids between ~420 and 418 Ma throughout this portion of the LTVS. However, there is no evidence to suggest that the metasediment-hosted veins have a direct genetic link to the mineralising fluids involved in the formation of Lead Trial-Tomnadashan. Instead, these localities may have formed during the emplacement of granitoids at a later point in time and within other regions of the LTVS, resulting in the exploitation of different sources of sulphur and lead (relative to the sources involved in the formation of Lead Trial-Tomnadashan). It must be stressed that this conclusion is tentative and further geochronological analyses on the metasediment-hosted veins are needed to identify intrusions that may have provided the mineralising fluids associated with their development.

7.6. Genetic model for gold mineralisation around the southern margin of Loch Tay

Based on previous research and the datasets presented in this study, it is possible to describe a preliminary genetic model for the auriferous mineralisation processes around Loch Tay (Fig. 7.3.). Following the onset of regional transtension at 425 Ma (Dewey and Strachan, 2003), voluminous magmatism began in the Grampian Terrane, resulting in the emplacement of granitoids at Tomnadashan (TOM_FELS_2), Ardtalnaig (ARD_FELS_1), Coire Buidhe (CB_FELS_2), Calliachar Burn (SW3) and potentially others that have yet to be identified. Major fault lines in the Grampian Terrane, such as the Highland Boundary Fault and the LTF (Fig. 7.3.), were structurally favourable to large-scale fluid flow (as evidenced by the extensive silicification and carbonatisation preserved on the fault plane within the LTF; Treagus, 2000; 2003). Some of the I-type plutons were able to exploit these structures and ascend through the crust rapidly, resulting in the formation of Lead Trial-Tomnadashan. The fluids (FT1) associated with the mineralisation in this tract are magmatic-hydrothermal in origin and have a genetic link to the emplacement of the granitoids dated in this study, an interpretation that is also supported by the $\delta^{34}S$ profile of Lead Trial-Tomnadashan (Fig. 5.26.) and the Pb isotope ratios of galena at Lead Trial (Fig. 5.28.b.).

The mixing between magmatic-hydrothermal fluids and the Dalradian metasediment package is likely to have given rise to FT2 (i.e. $\delta^{34}S$ values >+3 ‰) in some regions of the LTVS, although without geochronology, it is not possible to assign an age to the development of FT2 in the metasediment-hosted veins. Crustal sources of sulphur in the Study Area contain synsedimentary or synvolcanic sulphides with $\delta^{34}S$ values heavier than sulphur derived from I-type granitoids (e.g. SEDEX horizons; Fig. 7.1.), meaning that the mixing between the different sources may have increased the ^{34}S contents of FT1 fluids, resulting in a transition to FT2. Similar processes have been described at Cononish (Hill *et al.*, 2013; Parnell *et al.*, 2017; Spence-Jones *et al.*, 2018), which occurs within the same geological setting as the LTVS. However, it must be emphasised that the influx of FT1 and FT2 fluids are not necessarily temporally exclusive events throughout the Study Area; for example, it is possible that some of the metasediment-hosted veins (e.g. Coire Buidhe or the CUB veins) formed shortly after the emplacement of the granitoids dated in this study (e.g. CB_FELS_2 and SW3). In this scenario, FT1 and FT2 may have been active within different parts of the LTVS at the same time; for example, there could have been an FT1 fluid at Lead Trial-Tomnadashan and an FT2 fluid facilitating mineralisation in the CUB veins. Alternatively, the FT2 fluids may have developed as a result of a later mineralisation event associated with intrusions younger than those dated in this study, perhaps around the time when similar mixing processes were occurring at Cononish (e.g. 408 Ma; Rice *et al.*, 2012). Ultimately, further geochronological analyses are needed to resolve this issue.

Given the unlikelihood of a mineralising fluid migrating throughout the entire LTVS during a single event, it is possible that FT2 fluids developed in association with different plutons (i.e. relative to the FT1 fluids that are firmly linked to the emplacement of the intrusions around Lead Trial-Tomnadashan) scattered throughout the LTVS (Fig. 3.13.). Depending upon the host rocks associated with each intrusion, the sources involved in the mixing process are likely to differ, explaining the broad range in $\delta^{34}S$ values associated with the metasediment-hosted veins. For example, around Tombuie, assimilation of SEDEX horizons (which are known to underlie this locality; Tanner, 2014a) is likely to have resulted in $\delta^{34}S$ values of +13 ‰ (Fig. 5.23.), whereas at Spoil Heap, SEDEX horizons are likely to have been absent in this region (due to the overfolding; Fig. 3.4.), explaining the isotopically lighter values that are recorded from this locality. Furthermore, it is possible that deposit-scale processes (e.g. greater amounts of hydrothermal wallrock interaction and mixing with the host rocks in the environment of mineralisation) could have led to further modifications to the $\delta^{34}S$ values of the metasediment-hosted veins (e.g. the 'high-grade' veins at Calliachar; Table 3.5.).

Another key observation regarding the metasediment-hosted veins and the occurrence of FT2 is that both tend to be associated with lower order structures (although there are some exceptions, such as Fortingall; Fig. 5.22.a.). One explanation for this trend is that the lower order faults may have been less favourable to fluid flow (relative to the LTF), which corresponded to a slower rate of plutonic ascent. A reduced speed of plutonic emplacement could have stimulated a greater amount of crustal assimilation (and thereby the mixing of different sulphur sources). However, prolonged fluid pulses at individual localities (e.g. Tomnadashan or Fortingall) may have eventually resulted in crustal assimilation; Spence-Jones *et al*. 2018 suggested that changes induced by the introduction of magmatic-hydrothermal fluids into a system (e.g. contact metamorphism or varying fluid/rock ratios) can eventually stimulate mixing between different sources of sulphur. For this reason, it may be possible to state that the development of FT2 is a natural product of the evolution of FT1, although it is also likely that the genesis of an FT2 fluid is associated with the location of plutonic emplacement within the overall LTVS; plutons emplaced along the LTF are more likely to preserve their FT1 signature throughout the duration of mineralisation at a single deposit or structure.

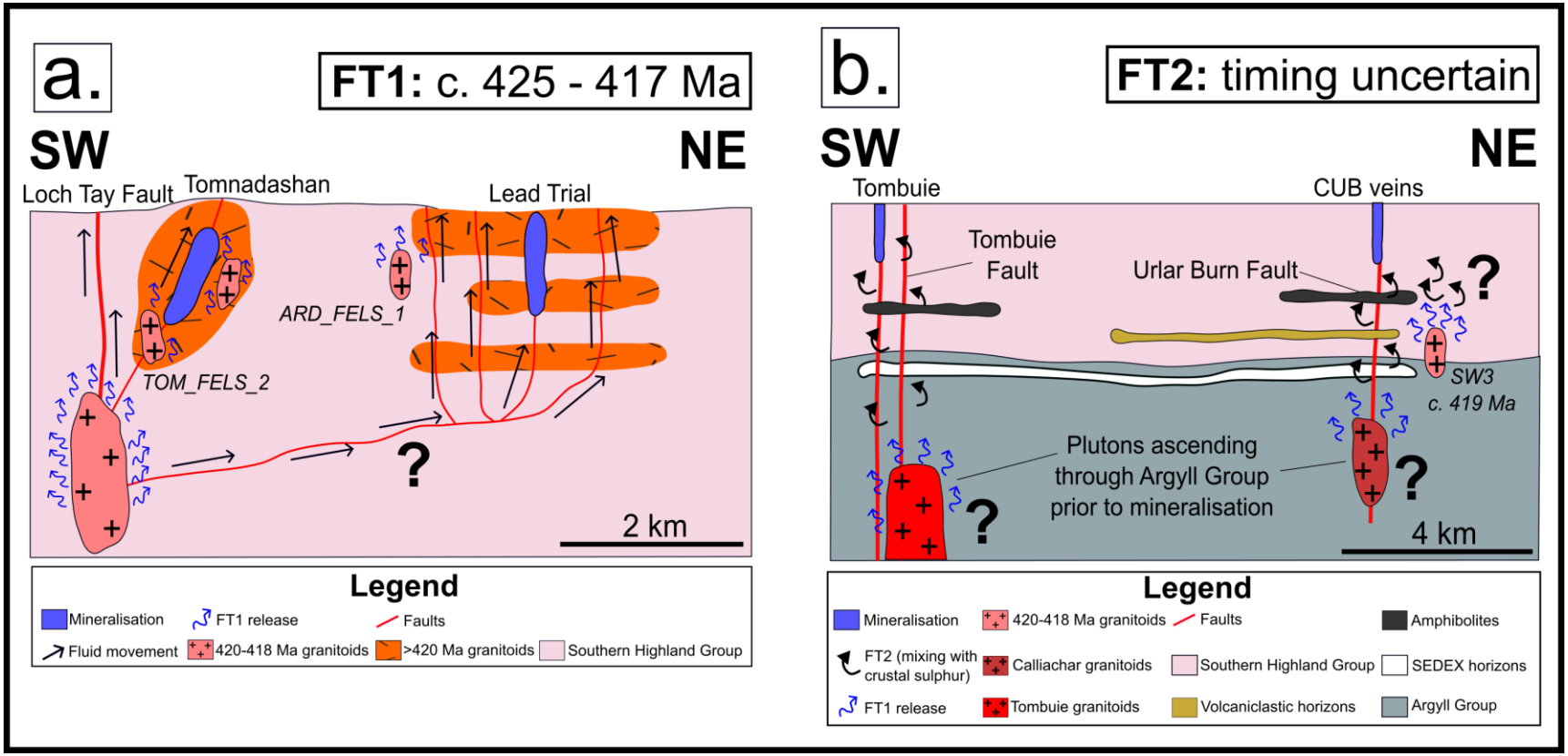

Figure 7.3. Preliminary genetic model for the LTVS, presented using approximated SW-NE cross-sections through different localities (Fig. 3.13.). **a.** The development of Lead Trial-Tomnadashan at c. 425-417 Ma. **b.** The hypothesised development of FT2 and the metasediment-hosted veins, using Tombuie and the CUB veins as an example. The Calliachar Burn and Tombuie granitoids are known to exist locally (Fig. 3.25.; Fig. 3.28.), although they remain undated. The emplacement of SW3 may also represent a potential source of the FT2 fluids (i.e. the original FT1 fluids prior to mixing). Radiometric dating on the metasediment-hosted veins is needed to establish the most likely scenario. Different lithologies have been added beneath each locality to emphasise that the mineralising fluids associated with the different metasediment-hosted veins may have had different flow paths (i.e. they mixed with different lithologies). For example, whilst SEDEX horizons and amphibolites are described in the vicinity of the CUB veins (Treagus, 2000; Tanner, 2014a), it is possible that the mineralising fluids associated with the latter mixed with another lithology that was absent at Tombuie, explaining the difference in $\delta^{34}S$ values between the two localities. For example, volcaniclastic layers within the Pitlochry Schist Formation (Batchelor, 2004a, b) may pinch out. Ultimately, more research is needed to establish the structural and subsurface geology of the LTVS before an assessment on the feasibility of the example scenarios depicted in this figure can be made.

Collectively, it has been possible to use the results of the present study to consider the genesis of the LTVS within the MSA (e.g. the source of the mineralising fluids, transport pathways and geodynamic triggers; Table 7.1.). However, as noted in Section 7.3., the controls on fertility within the Grampian Terrane of Scotland (in the context of gold mineralisation) remain poorly understood. The switch to transtension is judged to be the critical event in stimulating the development of the LTVS, given the voluminous magmatism that ensued (Oliver *et al.*, 2008; Neilson *et al.*, 2009). The magmatic-hydrothermal activity, in addition to distributing gold and other metals from the mantle, was able to exploit a variety of metal and fluid sources higher in the crust. The LTF is judged to be the critical transport pathway (Table 7.1.) in the formation of Lead Trial-Tomnadashan, although the formation of the metasediment-hosted veins is likely to have involved the transportation of mineralising fluids along lower order structures, such as the Urlar Burn Fault or Tombuie Fault (Fig. 3.13.). Furthermore, given the occurrence of some localities (e.g. the Glen Almond Vein or Coire Buidhe) within the core of the Highland Border Downbend (Fig. 3.15.), it may be possible to suggest that this structure has played a role in focusing and transporting the mineralising fluids.

As discussed in Chapter 7, there is considerable uncertainty regarding the mechanisms involved in the transportation of gold in hydrothermal fluids associated with the LTVS (e.g. Lead Trial; Section 7.2.2.), meaning it is difficult to interpret the 'traps' (i.e. mechanisms inducing gold precipitation) for the entire LTVS. However, during fieldwork, a variety of textures were observed; for example, mineralisation at the GAV has involved minimal hydrothermal alteration, whereas wallrock sulphidation has occurred at Tomnadashan. Neutralisation reactions between the Loch Tay Limestone Formation and the mineralising fluids at Coire Buidhe (Naden *et al.*, 2010) could have triggered mineralisation at this locality. It may be possible to suggest that the LTVS does not have a universal 'Deposit-scale trap', or rather, no singular process is responsible for the development of mineralisation at every single locality (Table 7.1.). Instead, a variety of processes (e.g. mixing, cooling, temperature and pressure changes, chemical disequilibrium; Section 2.7.) are likely to have operated throughout the Study Area.

Genetic component	**Description**
Geodynamic setting	Transition from transpression to transtension at ~425 Ma; onset of voluminous magmatism
Source of metals and ligands	Mantle, lithologies within the Dalradian Supergroup (e.g. SEDEX horizons), potentially meteoric/basinal brines
Transport pathways	Loch Tay Fault and lower order strike-slip structures
Deposit-scale trap	Variable; the difference in mineralisation styles throughout the LTVS indicates that there is not a single process responsible for the development of gold mineralisation

Table 7.1. Genetic aspects of the LTVS, considered within the components of the MSA (McCuaig *et al.*, 2010; McCuaig and Hronsky, 2014; Joly *et al.*, 2015).

7.7. Comparing the LTVS to other polymetallic vein systems in the Grampian Terrane

The Re-Os and U-Pb datasets presented in this study indicate the occurrence of a mineralisation event at c. 425-417 Ma (Table 5.4.) that was coeval with the emplacement of several granitoids around Loch Tay between 420 and 418 Ma (Fig. 5.20.). This event may have occurred at the same time as mineralisation at Cavanacaw, which has been constrained, using structural evidence, to an age of <425 Ma (Shaw *et al.*, 2022; Fig. 7.4.). The Cavanacaw deposit does not display any relations with known magmatic intrusions, although some of the nearby occurrences of auriferous veins are spatially associated with a c. 425 Ma calc-alkaline suite (Cooper *et al.*, 2013). Furthermore, the age of mineralisation in the LTVS is coeval with the c. 424 Ma age of fault reactivation at Curraghinalt (Rice *et al.*, 2016). Collectively, the data derived in this study indicate that there may have been coeval mid-Silurian gold-base metal mineralisation events of probable magmatic-hydrothermal origin across the Grampian Terrane, from Scotland to Northern Ireland (Fig. 7.4.). However, it should be noted that the genetic model for the LTVS (Fig. 7.3.) may not be readily transposable to other parts of the Grampian Terrane (particularly at localities where auriferous veins are not spatially associated with Siluro-Devonian granitoids, e.g. Glen Cova or Lochearnhead; Fig. 3.17); other fluid sources and genetic processes may be linked to mineralisation throughout the wider geological setting.

As mentioned in Section 7.4., galena from the LTVS has some of the least radiogenic compositions throughout Scotland and Ireland (Fig. 7.2.), with values plotting below the Zartman and Doe (1981) curve for mantle Pb evolution. However, it is important to note that the metasediment-hosted veins plot near the data from Cavanacaw and Cononish (Fig. 7.2.). This may indicate that, regionally speaking, Lead Trial-Tomnadashan represents a distinct system, which perhaps has a closer connection with the mantle than several of the other localities within the Grampian Terrane. The Pb isotope data from Cavanacaw, which was originally presented in Parnell *et al.* 2000 (and references therein), shows close overlap with the Pb isotope ratios of galena from SEDEX horizons within the Argyll Group and is similar to the metasediment-hosted veins in this regard (Fig. 7.2.). However, SEDEX horizons have not been described in the vicinity of Cavanacaw (Parnell *et al.*, 2000; Rice *et al.*, 2016; Shaw *et al.*, 2022); instead, the source of Pb in this deposit is suggested to be the Tyrone Igneous Complex, which records similar Pb isotope ratios to the auriferous mineralisation (Parnell *et al.*, 2000). The example of Cavanacaw, which evidently does not have a SEDEX source of Pb, may suggest that some of the other lithologies in the Dalradian Supergroup around the LTVS (i.e. aside from the SEDEX horizons) have contributed Pb to the mineralising fluids locally. Further studies to establish the Pb isotope ratios typical of the different lithologies (i.e. potential crustal sources of Pb) could be useful in assessing this hypothesis further, especially given that the range encompassed by the

SEDEX horizons within the Argyll Group (Fig. 7.2.) is based on a limited number of measurements (Clayburn *et al.*, 1983; Claypool, 1988).

The occurrences of synsedimentary pyrite within the Dalradian metasediments around Curraghinalt are extremely depleted in $\delta^{34}S$, displaying values of -22 ‰ in some cases (Fig. 3.21.); although the dataset is limited, Parnell *et al.* 2000 considered this to be evidence against a sulphur contribution from metasediments within the Dalradian Supergroup at Cavanacaw and Curraghinalt, given the sulphur isotope profile here is comparable to the LTVS (i.e. comprised of values between +4 and +11 ‰; Parnell *et al.*, 2000). However, the mean $\delta^{34}S$ values for synvolcanic sulphides from the Tyrone Igneous Complex and the Charlestown Inlier were +6.7 ± 2 ‰ (Parnell *et al.*, 2000; Fig. 3.21) and are therefore comparable to the $\delta^{34}S$ data recorded from the veins. For this reason, Parnell *et al.* 2000 suggested that sulphur in Cavanacaw and Curraghinalt has been scavenged from the synvolcanic sulphides underlying the deposit. This interpretation may have ramifications for the LTVS; the $\delta^{34}S$ values of synvolcanic sulphides have been characterised throughout Scotland (Fig. 3.21.). For example, the Ben Lui Schist Formation records $\delta^{34}S$ values that are, in some cases, as high as +8 ‰ (Fig. 3.20.; Lowry, 1991). However, unlike Cavanacaw and Curraghinalt, the occurrences of $\delta^{34}S$ values in the LTVS of >+12 ‰ (Fig. 5.23.) mean that the variety in $\delta^{34}S$ values recorded by this study cannot be explained solely by invoking a synvolcanic source of sulphur, although synvolcanic sulphides may well have contributed to the mixing process locally.

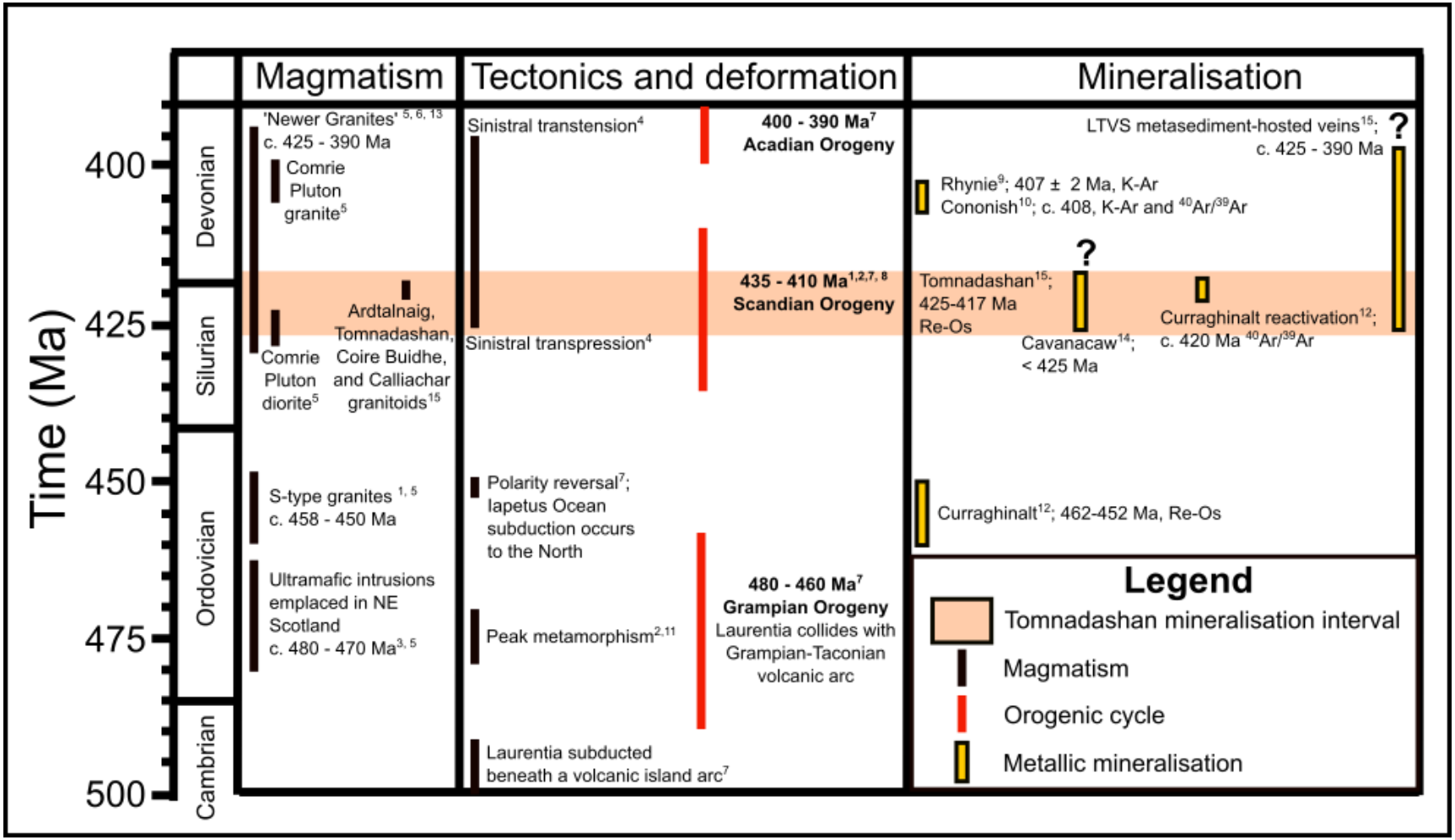

Figure 7.4. Timeline of tectonic, magmatic, deformation, and mineralisation events throughout the Grampian Terrane from the Ordovician to the Silurian. The references for the events (superscript numbers) are as follows: 1 = (Jacques and Reavy, 1994), 2 = (Dallmeyer *et al.*, 2001), 3 = (Oliver, 2001), 4 = (Dewey and Strachan, 2003), 5 = (Oliver *et al.*, 2008), 6 = (Neilson *et al.*, 2009), 7 = (Chew and Strachan, 2014), 8 = (Corfu *et al.*, 2014), 9 = (Mark *et al.*, 2011), 10 = (Rice *et al.*, 2012), 11 = (Tanner, 2014a) 12 = (Rice *et al.*, 2016), 13 = (Rice *et al.*, 2018), 14 = (Shaw *et al.*, 2022; Shaw, 2023) 15 = this study. Events that are poorly constrained (e.g. the age of Cavanacaw or the metasediment-hosted veins in the LTVS) have been annotated with a question mark. This figure has been adapted from Webb *et al.* 2024b.

Chapter 8: Conclusions

8.1. Introduction

This chapter summarises the main findings of the present study (providing answers to the research questions outlined in Table 3.9.) and also provides potential avenues for further research. Overall, this study has resolved several unknown aspects of the metallogeny around Loch Tay (the ages of mineralisation and magmatism, the sources of the mineralising fluids, and the evolution of the different veins over time).

8.2. The age of magmatism around Loch Tay

Despite sporadically outcropping throughout the breadth of the Study Area (Fig. 3.13.), the four granitoids that were dated in this study consistently yielded ages between 420 and 418 Ma. It is clear that this episode of regional magmatism is similar to the age of mineralisation at Tomnadashan (c. 425-417 Ma). Furthermore, the granitoids record similar ages to other 'Newer Granites' throughout Scotland, which were emplaced between 430 and 390 Ma (Oliver *et al.*, 2008; Miles *et al.*, 2014; 2016). The onset of regional transtension at c. 425 Ma (Dewey and Strachan, 2003) is judged to be the critical process for stimulating magmatism and mineralisation around Loch Tay.

8.3. The age of mineralisation in the LTVS

In this study, the first geochronological ages of mineralisation within the LTVS have been derived; three samples of molybdenite from Tomnadashan (Table 5.4.) yielded similar ages of 423 ± 2.1 Ma, 422.6 ± 2.1 Ma, and 419 ± 2.1 Ma (Webb *et al.*, 2024b). These ages are comparable to the ages of the granitoids dated in this study, which is evidence for Hypothesis 1 (Table 3.10.). The paragenetic study on Tomnadashan found that molybdenite occurs in Stage 2 out of the six paragenetic stages that were recognised (Fig. 6.1.a.). Given the contemporaneous nature of mineralisation in the LTVS, this date may pertain to one of the earlier mineralisation events within the entire mineral system. However, the large spread in Pb isotope measurements of galena from the LTVS (Fig. 5.28.) and the U-Pb age of the mineralised granite within the Comrie Pluton (404 ± 6 Ma; Oliver *et al.*, 2008) may indicate that there have been multiple mineralisation events in the LTVS (potentially confirming Hypothesis 3; Table 3.10.). It should be noted that further geochronological analyses are required on the metasediment-hosted veins to assess the ages of the other localities, such as the GAV or CUB veins, before firm conclusions regarding the number of mineralisation events can be made.

8.4. Source of the mineralising fluids in FT1

Based on the sulphur isotope datasets, it is possible to recognise a mineralising fluid with clear affinities to mantle-derived magmatic fluids (defined in this study as $\delta^{34}S$ values between -3 and +3 ‰; Fig. 7.3.). This fluid (FT1) is mostly represented around the Lead Trial-Tomnadashan porphyry-epithermal tract (Fig. 6.3.; Fig. 7.3.), although some of the $\delta^{34}S$ data from galena sampled at Coire Buidhe also falls within the FT1 classification (Table E.1.; No. 60-62). It is therefore possible that the composition of FT1 may have evolved over time. The Re-Os age of molybdenite at Tomnadashan (c. 425-417 Ma; Webb *et al.*, 2024b) represents a mineralisation event involving FT1.

8.5. Source of the mineralising fluids in FT2

As discussed in Chapter 5, the $\delta^{34}S$ profile of sulphides from the metasediment-hosted veins is difficult to reconcile with a purely magmatic source. Instead, a genetic model involving ascending plutons that melted the package of Dalradian metasediments and assimilated crustal sulphur is suggested to have facilitated the development of FT2. The mineralisation processes associated with FT2 are therefore comparable to those that have been described at Cononish (Hill *et al.* 2013). However, it is difficult to assess the relative timing of FT2 without radiometric dates for mineralisation in the metasediment-hosted veins and several of the other granitoids throughout the Study Area. There may be some instances in which an FT2 fluid has developed as a result of the continuous evolution and modification of FT1 fluids over time; potential indications of this have been observed at Tomnadashan, where the $\delta^{34}S$ values of the pyrite increase slightly throughout the paragenesis; furthermore, the Pb in galena from Stage 3 of the paragenesis (Fig. 6.1.a.) is likely to have a crustal source. Isotopically heavier $\delta^{34}S$ values have also been documented at Lead Trial (+3.9 ‰; Table E.1.; No. 48). However, it is uncertain as to whether the CUB veins formed as a result of the mixing between magmatic sulphur and metasedimentary sulphur during the emplacement of the SW3 granitoid; for example, there are several other intrusions throughout this region (e.g. the granitoids emplaced along the Urlar Burn Fault; Fig. 3.25.) that are undated and may therefore have been emplaced during a later or earlier magmatic event. The 404 ± 6 Ma age of the Comrie Pluton (which demonstrates the potential for plutons with ages of <418 Ma to occur locally throughout the Study Area), as well as the occurrence of gold mineralisation at Cononish and Rhynie (408 and 407 Ma; Fig. 7.4.), may indicate that FT1 and FT2 fluids developed after the formation of Tomnadashan (i.e. during another mineralisation event). However, it must be stressed that geochronological evidence is needed to provide a constraint on the timing of the genesis of FT2 in the LTVS. Nonetheless, it is possible to suggest that a variety of fluid and metal sources have been involved in the formation of FT2 (providing evidence for Hypothesis 2; Table 3.10.).

8.6. Relationships between the LTVS and other OGD genetic models

Whilst previous research (Craw and Chamberlain, 1996; Ixer *et al.*, 1997; Pitcairn *et al.*, 2015) has suggested that OGD genetic models are relevant to both the Grampian Terrane and the LTVS, the present study has found no evidence for such processes locally; the LTVS has $\delta^{34}S$ values that are typical of magmatic-hydrothermal tracts and the Pb isotope compositions from galena samples throughout this region are significantly less radiogenic than those described from the Phanerozoic OGD subtypes recognised by Mortensen *et al.* 2022. Furthermore, the age of mineralisation in the LTVS corresponds with Late Caledonian magmatism and has therefore occurred towards the end of the orogenic cycle. This is in contrast to the tectonic setting of most Phanerozoic OGD categories that were identified by Mortensen *et al.* 2022, which tend to form during the collisional and transpressional stages of the orogen (Table 2.2.). The SHOG subtype may form in a wider range of tectonic settings (Table 2.2.); however, the characteristics of this subtype are not replicated locally in the LTVS (i.e. most of the mineralisation in the LTVS is not disseminated or stratabound).

8.7. Implications of research

The outcomes of this research provide several implications with relevance to mineral exploration around Loch Tay and the ongoing debate regarding the genesis of gold deposits during orogenic cycles in the Grampian Terrane:

- **New vein parageneses:** novel paragenetic interpretations have been produced for Tomnadashan, the GAV, and Lead Trial, which have provided an important context in which to consider the isotope data derived in the present study. Furthermore, the approach taken towards characterising parageneses in this study may serve as a useful template for other researchers who seek to produce paragenetic interpretations of hydrothermal veins, as advocated in Webb *et al.* 2024a.
- **Regional mineralisation in the Grampian Terrane:** the geochronological analyses have demonstrated the occurrence of a mineralisation event around Loch Tay at c.425-417 Ma, which is approximately the same age as mineralisation at Cavanacaw (<425 Ma; Shaw *et al.*, 2022). This gives rise to the possibility that the onset of transtension at c. 425 Ma (Dewey and Strachan, 2003) resulted in a regional mineralisation event throughout the Grampian Terrane (Webb *et al.*, 2024b).
- **Magmatism and mineralisation around Loch Tay:** this study demonstrates that OGD genetic models are unlikely to be relevant to mineralisation in the Study Area; the LTVS is comprised of polymetallic veins that are genetically linked to magmatism, although the metasediment-hosted veins have formed from magmatic fluids that were modified by varying degrees of interactions with local lithologies. However, the mineralisation around Lead Trial and Tomnadashan represents the

actions of mantle-derived magmatic fluids (i.e. the release of mineralising fluids from I-type granitoids).

- **Ramifications for mineral exploration:** the enhanced understanding of the metallogeny of the LTVS could inform approaches to future mineral exploration. Around the GAV, gold is associated with Fe-bearing phases; future soil sampling campaigns focusing on zinc and copper may be useful in highlighting regions with further gold mineralisation (Webb *et al.*, 2024a). At Lead Trial, elevated concentrations of Pb may correspond to zones of gold mineralisation.

8.8. Opportunities for future research

The results from this study have identified the following opportunities for further research:

- **Paragenetic studies:** developing paragenetic interpretations for the other veins in the LTVS (e.g. Coire Buidhe or the CUB veins) would provide a further context for the evaluation of the $\delta^{34}S$ and Pb datasets that have been produced in the present study.
- **Geochronological analyses:** U-Pb dating on carbonate veins at Fortingall or K-Ar dating on sericite associated with the metasediment-hosted veins may yield information that could be incorporated into the metallogenic model for the LTVS. Further CA-ID-TIMS analyses on the undated intrusions around Loch Tay would assist in the identification of potential sources of FT2.
- **Geophysical surveys:** attempting to find plutons around several of the metasediment-hosted veins, such as the CUB veins or Coire Buidhe could help to identify intrusions that may have contributed magmatic-hydrothermal fluids to the LTVS. Furthermore, geophysical investigations may provide a better constraint on the structural geology of the Study Area.
- **Stable isotope studies:** further $\delta^{34}S$ analyses on specific localities (e.g. the 'base-metal' veins in the Calliachar Burn; Table 3.5.) would enable for a more robust interpretation of the trends observed in this study. For example, collecting $\delta^{34}S$ data from synsedimentary sulphides and sulphates around Loch Tay could assist in the identification of specific lithologies that contributed sulphur to the mineralising fluids associated with the LTVS. It may also be possible to exploit other isotope systems (e.g. N, B) to investigate the potential influence of mantle-derived magmatic fluids.
- **Fluid inclusion studies:** Now that robust paragenetic interpretations have been constructed for several localities within the LTVS, it may be possible to conduct new fluid inclusion studies and observe how the mineralising fluids have changed throughout the development of each vein.
- **Gold microchemistry:** More research is needed to characterise the suite of mineral inclusions within the gold particles that have been collected from Tomnadashan and assess how populations of detrital gold from both Tomnadashan and Lead Trial compare with the two populations of gold particles (orogenic and magmatic-hydrothermal/epithermal) recognised by Chapman *et al.* 2023.

Bibliography

Abzalov, M. 2007. Zarmitan Granitoid-hosted Gold Deposit, Tian Shan Belt, Uzbekistan. *Economic Geology*, **102**(3), pp.519-532.

Adam, M.M.A., Lv, X., Abdel Rahman, A.A., Stern, R.J., Abdalrhman, A.A.A. and Ullah, Z. 2020. In-situ sulfur isotope and trace element compositions of pyrite from the Neoproterozoic Haweit gold deposit, NE Sudan: Implications for the origin and source of the sulfur. *Ore Geology Reviews*, **120**, article no: 103405 [no pagination]

Agee, C.B. and Walker, D. 1988. Mass balance and phase density constraints on early differentiation of chondritic mantle. *Earth and Planetary Science Letters*, **90**(2), pp.144-156.

Ahmed, A., Arai, S. and Ikenne, M. 2009. Mineralogy and Paragenesis of the Co-Ni Arsenide Ores of Bou Azzer, Anti-Atlas, Morocco. *Economic Geology*, **104**, pp.249-266.

Albarède, F. and Juteau, M. 1984. Unscrambling the lead model ages. *Geochimica et Cosmochimica Acta*, **48**(1), pp.207-212.

Albarède, F., Desaulty, A.M. and Blichert-Toft, J. 2012. A geological perspective on the use of Pb isotopes in Archaeometry, **54**(5), pp.853-867.

Albinson, T., Norman, D.I., Cole, D., and Chomiak, B. 2001, Controls on formation of low-sulphidation epithermal deposits in Mexico: Constraints from fluid inclusion and stable isotope data. *Society of Economic Geologists Special Publication*, **8**, pp.1-32.

Aldrich, L.T. and Wetherill, G.W., 1958. Geochronology by radioactive decay. *Annual Review of Nuclear Science*, **8**(1), pp.257-298.

Allan, M.M., Mortensen, J.K., Hart, C.J., Bailey, L.A., Sánchez, M.G., Ciolkiewicz, W., McKenzie, G.G. and Creaser, R.A. 2013. Magmatic and Metallogenic Framework of West-Central Yukon and Eastern Alaska. In: *Tectonics, Metallogeny, and Discovery*. Denver: Society of Economic Geologists, pp.111-168.

Allègre, C.J. *Isotope geology*. Cambridge University Press, 2008.

Alsop, G.I. and Holdsworth, R.E. 1993. The distribution, geometry and kinematic significance of Caledonian buckle folds in the western Moine Nappe, northwestern Scotland. *Geological Magazine*, **130**(3), pp.353-362.

Alsop, G.I., Weinberger, R., Marco, S. and Levi, T. 2020. Folding during soft-sediment deformation. *Geological Society, London, Special Publications*, **487**(1), pp.81-104.

Andersen, M.B., Elliott, T., Freymuth, H., Sims, K.W. W., Niu, Y. and Kelley, K.A. 2015. The terrestrial uranium isotope cycle. *Nature*, **517**(7534), pp.356-359.

Anderson, E.M. 1923. The geology of the schists of the Schiehallion district (Perthshire). *Quarterly Journal of the Geological Society*, **79**(1-4), pp.423-445.

Anderson, G.M. 2008. The mixing hypothesis and the origin of Mississippi Valley-Type ore deposits. *Economic Geology*, **103**(8), pp.1683-1690.

Anderton, R. 1980. Distinctive pebbles as indicators of Dalradian provenance. *Scottish Journal of Geology*, **16**(2-3), pp.143-152.

Anderton, R. 1982. Dalradian deposition and the late Precambrian–Cambrian history of the N Atlantic region: a review of the early evolution of the Iapetus Ocean. *Journal of the Geological Society*, **139**(4), pp.421-431.

Anderton, R. 1985. Sedimentation and tectonics in the Scottish Dalradian. *Scottish Journal of Geology*, **21**(4), pp.407-436.

Andreasson, P., Gee, D., Whitehouse, M. and Schoberg, H. 2003. Subduction-flip during Iapetus Ocean closure and Baltica-Laurentia collision, Scandinavian Caledonides. *Terra Nova*, **15**(6), pp.362-369.

Andresen, A., Rehnstrom, E.F. and Holte, M. 2007. Evidence for simultaneous contraction and extension at different crustal levels during the Caledonian orogeny in NE Greenland. *Journal of the Geological Society*, **164**(4), pp.869-880.

Armstrong, R.L. 1968. A model for the evolution of strontium and lead isotopes in a dynamic Earth. *Reviews of Geophysic*s, **6**(2), pp.175-199.

Arne, D.C., Bierlin, F.P., Morgan, J.W. and Stein, H.J. 2001. Re-Os dating of sulfides associated with gold mineralization in Central Victoria, Australia. *Economic Geology*, **96**(6), pp.1455-1459.

Arribas Jr, A. 1995. Characteristics of high-sulphidation epithermal deposits, and their relation to magmatic fluid. *Mineralogical Association of Canada.*

Arribas, A., Jr., Hedenquist, J.W., Itaya, T., Okada, T., Concepción, R.A. and Garcia, J.S. 1995. Contemporaneous formation of adjacent porphyry and epithermal Cu-Au deposits over 300 ka in northern Luzon, Philippines. *Geology*, **23**, pp.337-340.

Arrouvel, C. and Eon, J.-G. 2019. Understanding the surfaces and crystal growth of pyrite FeS2. *Materials Research*, **22**(1).

Ashcroft, W.A., Kneller, B.C., Leslie, A.G. and Munro, M. 1984. Major shear zones and autochthonous Dalradian in the north-east Scottish Caledonides. *Nature*, **310**, pp.760-762.

Atherton, M.P. and Ghani, A. 2002. Slab breakoff: a model for Caledonian, Late Granite syn-collisional magmatism in the orthotectonic (metamorphic) zone of Scotland and Donegal, Ireland. *Lithos*, **62**(3-4), pp.65-85.

Audétat, A. and Simon, A.C. 2012. Magmatic Controls on Porphyry Copper Genesis. In: Jeffrey Hedenquist, J.W., Harris, M., Camus, F. ed(s). *Geology and Genesis of Major Copper Deposits and Districts of the World: A Tribute to Richard H. Sillitoe*. Littleton, Colorado: Society of Economic Geologists.

Bachinski, D.J. 1969. Bond strength and sulfur isotopic fractionation in coexisting sulfides. *Economic Geology*, **64**(1), pp.56-65.

Bailey, E.B. and McCallien, W.J. 1937. III.—Perthshire Tectonics: Schiehallion to Glen Lyon. *Earth and Environmental Science Transactions of The Royal Society of Edinburgh*, **59**(1), pp.79-117.

Bailey, L.A. 2013. Late Jurassic fault-hosted gold mineralization of the Golden Saddle deposit, White Gold district, Yukon Territory. MSc thesis, University of British Columbia.

Baker, T., Achterberg, E. van, Ryan, C.G. and Lang, J.R. 2004. Composition and evolution of ore fluids in a magmatic-hydrothermal skarn deposit. *Geology*, **32**(2), pp.117-120.

Baker, D. and Moretti, R. 2011. Modeling the solubility of sulphur in magmas: a 50-year old geochemical challenge. *Reviews in Mineral Geochemistry*, **73**, pp.167-213.

Balashov, V.N. and Yardley, B.W.D. 1998. Modelling metamorphic fluid flow with reaction–compaction–permeability feedbacks. *American Journal of Science*, **298**, pp.441-470.

Banks, C.J., Smith, M., Winchester, J.A., Horstwood, M.S.A., Noble, S.R. and Ottley, C.J. 2007. Provenance of intra-Rodinian basin-fills:the lower Dalradian Supergroup, Scotland. *Precambrian Research*, **153**, pp.46-64.

Bao, Z., Li, Q. and Wang, C.Y. 2017. Metal source of giant Huize Zn-Pb deposit in SW China: New constraints from in situ Pb isotopic compositions of galena. *Ore geology reviews*, **91**, pp.824-836.

Barker, S.L.L., Dipple, G.M., Hickey, K.A., Lepore, W.A. and Vaughan, J.R. 2013. Applying stable isotopes to mineral exploration: teaching an old dog new tricks. *Economic Geology*, **108**(1), pp.1-9.

Barnes, H.L. 1979. Solubilities of ore minerals. In: Barnes, H.L. ed. *Geochemistry of hydrothermal ore deposits.* Second edition. New York: John Wiley & Sons, pp.404-460.

Baron, M., Hillier, S., Rice, C., Czapnik, K. and Parnell, J. 2004. Fluids and hydrothermal alteration assemblages in a Devonian gold-bearing hot-spring system, Rhynie, Scotland. *Transactions of the Royal Society of Edinburgh: Earth Sciences*, **94**(4), pp.309-324.

Barra, F., Deditius, A., Reich, M., Kilburn, M.R., Guagliardo, P. and Roberts, M.P. 2017. Dissecting the Re-Os molybdenite geochronometer. *Scientific Reports*, **7**(1), article no: 16054 [no pagination]

Barros, R. and Menuge, J.F. 2016. The origin of spodumene pegmatites associated with the Leinster Granite in southeast Ireland. *The Canadian Mineralogist*, **54**(4), pp.847-862.

Barrow, G., Grant Wilson, J.S. and Craig, E.H. 1905. The geology of the country around Blair Atholl, Pitlochry and Aberfeldy. Memoir of the British Geological Survey, Scotland (Sheet 55).

Basori, M.B.I., Zaw, K., Meffre, S., Large, R.R. and Wan Hassan, W.F. 2017. Pb-isotope compositions of the Tasik Chini volcanic-hosted massive sulfide deposit, Central Belt of Peninsular Malaysia: Implication for source region and tectonic setting. *Island Arc*, **26**(2), article no: 12177 [no pagination]

Batchelor, R.A. 2004a. Air-fall tuffs in the Southern Highland Group, Dalradian Supergroup, at Birnam, Perthshire. *Scottish Journal of Geology*, **40**(1), pp.67-72.

Batchelor, R.A. 2004b. More air-fall tuffs from the Southern Highland Group, Dalradian Supergroup, Scotland. *Scottish Journal of Geology*, **40**(2), pp.181-184.

Baxter, F.B., Ague, J.J. and Depaolo, D.J. 2002. Prograde temperature–time evolution in the Barrovian type-locality constrained by Sm/Nd garnet ages from Glen Clova, Scotland. *Journal of the Geological Society, London*, **159**, pp.71-82.

Beaudoin, G., Taylor, B.E., Rumble, D. and Thiemens, M. 1994. Variations in the sulfur isotope composition of troilite from the Cañon Diablo iron meteorite. *Geochimica et Cosmochimica Acta*, **58**(19), pp.4253-4255.

Beaudoin, G. and Chiaradia, M., 2016. Fluid mixing in orogenic gold deposits: Evidence from the HO-Sr isotope composition of the Val-d'Or vein field (Abitibi, Canada). *Chemical Geology*, **437**, pp.7-18.

Beinlich, A., Barker, S., Dipple, G., Gupta, M. and Baer, D. 2017. Stable isotope (δ13C, δ18O) analysis of sulfide-bearing carbonate samples using laser absorption spectrometry. *Economic Geology*, **112**(3), pp.693-700.

Benning, L.G. and Seward, T.M. 1996. Hydrosulphide complexing of Au (I) in hydrothermal solutions from 150–400 °C and 500–1500 bar. *Geochimica et Cosmochimica Acta*, **60**(11), pp.1849-1871.

Bente, K. and Nielsen, H. 1982. Experimental S isotope fractionation studies between coexisting bismuthinite (Bi 2 S 3) and sulfur (S°). *Earth and Planetary Science Letters*, **59**(1), pp.18-20.

Berger, B., Ayuso, R., Wynn, J. and Seal, R. 2008. *Preliminary model of porphyry copper deposits*. United States Geological Survey: Reston.

Bethke, P.M., Rye, R.O., Stoffregen, R.E. and Vikre, P.G. 2005. Evolution of the magmatic-hydrothermal acid-sulfate system at Summitville, Colorado: Integration of geological, stable-isotope, and fluid inclusion evidence. *Chemical Geology*, **215**, pp.281-315.

Bickford, M.E., Chase, R.B., Nelson, B.K., Shuster, R.D. and Arruda, E.C. 1981. U-Pb studies of zircon cores and overgrowths, and monazite: Implications for age and petrogenesis of the northeastern Idaho batholith. *The Journal of Geology*, **89**(4), pp.433-457.

Bierlein, F.P., Cartwright, I. and McKnight, S. 2001. The role of carbonaceous 'indicator' slates in the genesis of lode gold mineralization in the Western Lachlan Orogen, Victoria, southeastern Australia. *Economic Geology*, **96**, pp.431-451.

Bigeleisen, J. and Mayer, M. 1947. Calculation of Equilibrium Constants for Isotopic Exchange Reactions. *The Journal of Chemical Physics*, **15**(5), pp.261-267.

Bigeleisen, J. 1952. The Effects of Isotopic Substitution on the rates of Chemical Reactions. *The Journal of Physical Chemistry*, **56**(7), pp.823-828.

Bindeman, I.N. and Melnik, O.E. 2016. Zircon survival, rebirth and recycling during crustal melting, magma crystallization, and mixing based on numerical modelling. *Journal of Petrology*, **57**(3), pp.437-460.

Bingen, B. and Stein, H. 2003. Molybdenite Re–Os dating of biotite dehydration melting in the Rogaland high-temperature granulites, S Norway. *Earth and Planetary Science Letters*, **208**(3-4), pp.181-195.

Bingen, B., Davis, W.J., Hamilton, M.A., Engvik, A.K., Stein, H.J., Skar, O. and Nordgulen, O. 2008. Geochronology of high-grade metamorphism in the Sveconorwegian nelt, S. Norway; U-Pb, Th-Pb, and Re-Os data. *Norwegian Journal of Geology*, **88**, pp.12-42.

Birck, J.L., Barman, M.R. and Capmas, F. 1997. Re-Os isotopic measurements at the femtomole level in natural samples. *Geostandards newsletter*, **21**(1), pp.19-27.

Black, L.P., Kamo, S.L., Allen, C.M., Davis, D.W., Aleinikoff, J.N., Valley, J.W., Mundil, R., Campbell, I.H., Korsch, R.J., Williams, I.S. and Foudoulis, C. 2004. Improved 206Pb/238U microprobe geochronology by the monitoring of a trace-element-related matrix effect; SHRIMP, ID–TIMS, ELA–ICP–MS and oxygen isotope documentation for a series of zircon standards. *Chemical Geology*, **205**(1-2), pp.115-140.

Blitchert-Toft, J., Delile, H., Lee, C.T., Stos-Gale, Z., Billström, K., Andersen, T., Hannu, H. and Albarède, F. 2016. Large-scale tectonic cycles in Europe revealed by distinct P b isotope provinces. *Geochemistry, Geophysics, Geosystems*, **17**(10), pp.3854-3864.

Bluck, B.J. 1984. Pre-Carboniferous history of the Midland Valley of Scotland. *Transactions of the Royal Society of Edinburgh: Earth Sciences*, **75**, pp.275-295.

Bluck, B.J. 2000. Old Red Sandstone basins and alluvial systems of Midland Scotland. *Geological Society, London, Special Publications*, **180**(1), pp.417-437.

Boast, A.M., Coleman, M.L. and Halls, C. 1981. Textural and stable isotopic evidence for the genesis of the Tynagh base metal deposit, Ireland. *Economic Geology*, **76**(1), pp.27-55.

Boehlke, J. K. and Kistler, R. W. 1986. Rb-Sr, K-Ar, and stable isotope evidence for the ages and sources of fluid components of gold-bearing quartz veins in the northern Sierra Nevada foothills metamorphic belt, California. *Economic Geology*, **81**(2), pp.296-322.

Bolhar, R., Hofmann, A., Kemp, A. I. S., Whitehouse, M. J., Wind, S. and Kamber, B.S. 2017. Juvenile crust formation in the Zimbabwe Craton deduced from the O-Hf isotopic record of 3.8–3.1 Ga detrital zircons. *Geochimica et Cosmochimica Acta*, **215**, pp.432-446.

Börner, F., Keith, M., Bücker, J. L., Voudouris, P., Klemd, R., Haase, K., Kutzschbach, M. and Schiperski, F. 2022. In-situ trace element and S isotope systematics in pyrite from three porphyry-epithermal prospects, Limnos Island, Greece. *Frontiers in Earth Science*, **10,** article no: 916107 [no pagination]

Borradaile, G.J., 1973. 1. Dalradian Structure and Stratigraphy of the Northern Loch Awe District, Argyllshire. *Earth and Environmental Science, Transactions of The Royal Society of Edinburgh*, **69**(1), pp.1-21.

Bortnikov, N., Genkin, A., Dobrovol'skaya, M., Muravitskaya, G. and Filimonova, A. 1991. The nature of chalcopyrite inclusions in sphalerite; exsolution, coprecipitation, or 'disease'?. *Economic Geology*, **86**, pp.1070-1082.

Bortnikov, N.S., Dobrovol'skaya, M.G., Genkin, A.D., Naumov, V.B. and Shapenko, V.V. 1995. Sphalerite-galena geothermometers; distribution of cadmium, manganese, and the fractionation of sulfur isotopes. *Economic Geology*, **90**(1), pp.155-180.

Borzov, I.N. 2006. Beta-decay rates. *Nuclear Physics A*, **777**, pp.645-675.

Bottrell, S. H., and Miller, M.F. 1989. Analysis of reduced sulfur species in inclusion fluids. *Economic Geology*, **84**(4), pp.940-945.

Bouse, R.M., Ruiz, J., Titley, S.R., Tosdal, R.M. and Wooden, J.L. 1999. Lead isotope compositions of Late Cretaceous and early Tertiary igneous rocks and sulfide minerals in Arizona; implications for the sources of plutons and metals in porphyry copper deposits. *Economic Geology*, **94**(2), pp.211-244.

Bowes, D.R. and Convery, H.J.E. 1966. The composition of some Ben Ledi grits and its bearing on the origin of albite schists in the south-west Highlands. *Scottish Journal of Geology*, **2**(1), pp.67-75.

Bowes, D.R. 1989. *The Encylopedia of Igneous and Metamorphic Petrology*. New York: Van Nostrand Reinhold.

Brace, W.F. 1961. Mohr construction in the analysis of large geologic strain. *Geological Society of America Bulletin*, **72**(7), pp.1059-1079.

Bradbury, H.J. 1979. Migmatisation, deformation and porphyroblast growth in the Dalradian of Tayside, Scotland. *Geological Society, London, Special Publications*, **8**(1), pp.351-356.

Bradbury, H.J. and Smith, R.A. 1981. *Pitlochry*. 1:50,000. Keyworth: British Geological Survey.

Brand, W.A. and Coplen, T.B. 2012. Stable isotope deltas: tiny, yet robust signatures in nature. *Isotopes in Environmental and Health Studies*, **48**(3), pp.393-409.

Braun, J., Van der Beek, P. and Batt, G. 2006. *Quantitative thermochronology: numerical methods for the interpretation of thermochronological data*. Cambridge: Cambridge University Press.

Breeding, C.M. and Ague, J.J. 2002. Slab-derived fluids and quartz-vein formation in an accretionary prism, Otago Schist, New Zealand. *Geology*, **30**(6), pp.499-502.

Brevart, O., Dupré, B. and Allegre, C.J. 1982. Metallogenic provinces and the remobilization process studied by lead isotopes; lead-zinc ore deposits from the southern Massif Central, France. *Economic Geology*, **77**(3), pp.564-575.

Brimhall, G.H. and Crerar, D.A. 1987. Ore fluids: magmatic to supergene. *Reviews in Mineralogy and Geochemistry*, **17**, pp.235-321.

Brown, P., Ryan, P., Soper, N. and Woodcock, N. 2008. The Newer Granite problem revisited: a transtensional origin for the Early Devonian Trans-Suture Suite. *Geological Magazine*, **145**(2), pp.235-256.

Browne, M.A.E., Smith, R.A. and Aitken, A.M. 2001. A lithostratigraphical framework for the Devonian (Old Red Sandstone) rocks of Scotland south of a line from Fort William to Aberdeen. Keyworth: British Geological Survey.

Browning, P., Groves, D.I., Blockley, J.G. and Rosman, K.J.R. 1987. Lead isotope constraints on the age and source of gold mineralization in the Archean Yilgarn Block, Western Australia. *Economic Geology*, **82**(4), pp.971-986.

Brusnitsyn, A., Sadykov, S., Perova, E. and Vereshchagin, O. 2022. Genesis of Barite–Galena Ores at the Ushkatyn-III Deposit, Central Kazakhstan: Analysis of Geological, Mineralogical, and Isotopic (δ34S, δ13C, δ18O) Data. *Geology of Ore Deposits*, **64**(3), pp.78-103.

Burgess, S.D., Bowring, S. and Shen, S.Z. 2014. High-precision timeline for Earth's most severe extinction. *Proceedings of the National Academy of Sciences*, **111**(9), pp.3316-3321.

Burnham, C.W. 1962. Facies and types of hydrothermal alteration. *Economic Geology*, **57**(5), pp.768-784.

Burnham, C.W. and Ohmoto, H. 1980. Late-stage process of felsic magmatism. *Society of Mining Geology Japan Special Issue*, **8**, pp.1-11

Burnham, C. 1985. Energy release in subvolcanic environments; implications for breccia formation. *Economic Geology*, **80**(6), pp.1515-1522.

Burt, C.E. 2002. Sedimentary environments and basin evolution of the upper Dalradian: Tayvallich Subgroup and Southern Highland Group. Ph.D. thesis, University of Leeds.

Butler, J.R. 1973. Paleozoic deformation and metamorphism in part of the Blue Ridge thrust sheet, North Carolina. *American Journal of Science*, **273-A**, pp.72-88.

Butterworth, N., Steinberg, D., Müller, R., Williams, S., Merdith, A. and Hardy, S. 2016. Tectonic environments of South American porphyry copper magmatism through time revealed by spatiotemporal data mining. *Tectonics*, **35**(12), pp.2847-2862.

Campbell, I.H. and Hill, R.I. 1988. A two-stage model for the formation of the granite-greenstone terrains of the Kalgoorlie-Norseman area, Western Australia. *Earth and Planetary Science Letters*, **90**(1), pp.11-25.

Campbell, A.R. and Larson, P.B. 1998. Introduction to Stable Isotope Applications in Hydrothermal Systems. In: Richards, J. and Larson, P. ed(s). *Techniques in Hydrothermal Ore Deposits Geology*. Society of Economic Geologists.

Candela, P. 1991. Physics of aqueous phase evolution in plutonic environments. *American Mineralogist*, **76**, pp.1081-1091.

Canfield, D.E. 2001. Biogeochemistry of sulfur isotopes. *Reviews in mineralogy and geochemistry*, **43**(1), pp.607-636.

Cannon, R.S., Pierce, A.P., Antweiler, J.C. and Buck, K.L. 1961. The data of lead isotope geology related to problems of ore genesis. *Economic Geology*, **56**(1), pp.1-38.

Carlson, W.D., Denison, C. and Ketcham, R.A. 1995. Controls on the nucleation and growth of porphyroblasts: kinetics from natural textures and numerical models. *Geological Journal*, **30**, pp.207-225.

Carman, G.D. 2003. Geology, mineralization, and hydrothermal evolution of the Ladolam gold deposit, Lihir Island, Papua New Guinea. *Society of Economic Geologists Special Publication*, **10**, pp.247-284.

Carr, G.R., Dean, J.A., Suppel, D.W. and Heithersay, P.S. 1995. Precise lead isotope fingerprinting of hydrothermal activity associated with Ordovician to Carboniferous metallogenic events in the Lachlan fold belt of New South Wales. *Economic Geology*, **90**(6), pp.1467-1505.

Carranza, E. Geochemical characteristics of mineral deposits: implications for ore genesis. 2012. *Geochemistry: Exploration, Environment, Analysis*, **12**(2), pp.89-92.

Carstens, H. 1986. Displacive Growth of Authigenic Pyrite. *Journal of Sedimentary Research*, **56**, pp.252-257.

Carty, J.P. 2001. Deformation magmatism and metamorphism in the Portsoy Shear Zone, north-east Scotland. Ph.D. thesis, University of Derby.

Castorina, F. and Petrini, R. 1989. Radiometric geochronology: some constraints to the isochron method by an iterative least-squares approach. *Geochemical journal*, **23**(3), pp.101-109.

Cawood, P.A., Nemchin, A.A., Smith, M. and Loewy, S. 2003. Source of the Dalradian Supergroup constrained by U–Pb dating of detrital zircon and implications for the East Laurentian margin. *Journal of the Geological Society*, **160**(2), pp.231-246.

Cawood, P.A., Merle, R.E., Strachan, R.A. and Tanner, P.W.G. 2012. Provenance of the Highland Border Complex: constraints on Laurentian margin accretion in the Scottish Caledonides. *Journal of the Geological Society*, **169**(5), pp.575-586.

Célérier, B. 1995. Tectonic regime and slip orientation of reactivated faults. *Geophysical Journal International*, **122**(2), pp.141-161.

Chamberlain, K.R. and Bowring, S.A. 2001. Apatite–feldspar U–Pb thermochronometer: a reliable, mid-range (~ 450° C), diffusion-controlled system. *Chemical Geology*, **172**(1-2), pp.173-200.

Chambers, L.A. and Trudinger, P.A. 1979. Microbiological fractionation of stable sulfur isotopes: a review and critique. *Geomicrobiology Journal*, **1**(3), pp.249-293.

Chang, Z., Large, R. and Maslennikov, V. 2008. Sulphur isotopes in sediment-hosted orogenic gold deposits: Evidence for an early timing and a seawater sulphur source. *Geology*, **36**(12), pp.971-974.

Channer, D.M.D. and Spooner, E.T.C. 1994. Combined gas and ion chromatographic analysis of fluid inclusions: Applications to Archean granite pegmatite and gold-quartz vein fluids. *Geochimica et Cosmochimica Acta*, **58**(3), pp.1101-1118.

Chapman, R.J., Leake, R.C. and Moles, N.R. 2000. The use of microchemical analysis of alluvial gold grains in mineral exploration: experiences in Britain and Ireland. *Journal of Geochemical Exploration*, **71**(3), pp.241-268.

Chapman, R., Leake, B. and Styles, M. 2002. Microchemical Characterization of Alluvial Gold Grains as an Exploration Tool. *Gold Bulletin*, **35**(2), pp.53-65.

Chapman, R., Mileham, T., Allan, M. and Mortensen, J. 2017. A distinctive Pd-Hg signature in detrital gold derived from alkalic Cu-Au porphyry systems. *Ore Geology Reviews*, **83**, pp.84-102.

Chapman, R., Banks, D., Styles, M., Walshaw, R., Piazolo, S., Morgan, D., Grimshaw, M., Spence-Jones, C., Matthews, T. and Borovinskaya, O. 2021. Chemical and physical heterogeneity within native gold: implications for the design of gold particle studies. *Mineralium Deposita*, **56**(8), pp.1563-1588.

Chapman, R., Torvela, T. and Savastano, L. 2023. Insights into regional metallogeny from detailed compositional studies of alluvial gold: An example from the Loch Tay Area, Central Scotland. Minerals, **13**(2), article no: 140 [no pagination]

Chen, Q. and Nur, A. 1992. Pore fluid pressure effects in anisotropic rocks: Mechanisms of induced seismicity and weak faults. *Pure and Applied Geophysics PAGEOPH*, **139**(3-4), pp.463 -479.

Chen, L. 2015. Further Re–Os Arsenopyrite geochronology from selected Meguma Au deposits, Meguma Terrane, Nova Scotia: Possible evidence for a protracted gold-forming system. MSc thesis, University of Alberta.

Chen, J., Fu, L., Selby, D., Wei, J., Zhao, X. and Zhou, H. 2020. Multiple episodes of gold mineralization in the East Kunlun Orogen, western Central Orogenic Belt, China: Constraints from Re-Os sulfide geochronology. *Ore Geology Reviews*, **123,** article no: 103587 [no pagination]

Cherniak, D. J. and Watson, E. B. 2001. Pb diffusion in zircon. *Chemical Geology*, **172**(1-2), pp.5-24.

Chew, D.M., 2001. Basement protrusion origin of serpentinite in the Dalradian. *Irish Journal of Earth Sciences*, **19**, pp.23-35.

Chew, D., Daly, J., Page, L. and Kennedy, M. 2003. Grampian orogenesis and the development of blueschist-facies metamorphism in western Ireland. *Journal of the Geological Society*, **160**(6), pp.911-924.

Chew, D. and Stillman, C. 2009. Late Caledonian Orogeny and magmatism. In: C. Holland and I. Sanders. ed(s). *Geology of Ireland.* 2nd edition. Dunedin Academic, pp.143-173.

Chew, D. and Strachan, R. 2014. The laurentian caledonides of Scotland and Ireland. *Geological Society, London, Special Publications*, **390**(1), pp.45-91.

Chi, G., Diamond, L. W., Lu, H., Lai, J. and Chu, H. 2020. Common Problems and Pitfalls in Fluid Inclusion Study: A Review and Discussion. *Minerals*, **11**, article no: 1 [no pagination]

Chiaradia, M., Fontboté, L. and Paladines, A. 2004. Metal Sources in Mineral Deposits and Crustal Rocks of Ecuador (1° N–4° S): A Lead Isotope Synthesis. *Economic Geology*, **99**(6), pp.1085-1106.

Chiaradia, M., Konopelko, D., Seltmann, R. and Cliff, R.A. 2006. Lead isotope variations across terrane boundaries of the Tien Shan and Chinese Altay. *Mineralium Deposita*, **41**(5), pp.411-428.

Chugaev, A.V., Plotinskaya, O.Y., Dubinina, E.O., Stepanov, S.Y., Gareev, B.I., Batalin, G.A., Rassokhina, I.V., Chizhova, J.N., Bondar, D. and Abramova, V.D. 2022. Mixed crustal-mantle source of porphyry Cu-Mo deposits of the Urals: Pyrite trace element geochemistry and Pb–S isotope data. *Journal of Geochemical Exploration*, **242**, article no: 107075 [no pagination]

Church, W. and Gayer, R. 1973. The Ballantrae ophiolite. *Geological Magazine*, **110**(6), pp.497-510.

Clayburn, J.A.P., Harmon, R.S., Pankhurst, R.J. and Brown, J.F. 1983. Sr, O, and Pb isotope evidence for origin and evolution of Etive Igneous Complex, Scotland. *Nature*, **303**, pp.492-497.

Clayburn, J.A.P. 1988. The crustal evolution of Central Scotland and the nature of the lower crust: Pb, Nd and Sr isotope evidence from Caledonian granites. *Earth and Planetary Science Letters*, **90**(1), pp.41-51.

Claypool, G.E., Holser, W.T., Kaplan, I.R., Sakai, H. and Zak, I. 1980. The age curves of sulfur and oxygen isotopes in marine sulfate and their mutual interpretation. *Chemical geology*, **28**, pp.199-260.

Cliff, R. 1985. Isotopic dating in metamorphic belts. *Journal of the Geological Society*, **142**(1), pp.97-110.

Coats, J.S., Fortey, N.J., Gallagher, M.J. and Grout, A. 1984. Stratiform barium enrichment in the Dalradian of Scotland. *Economic Geology*, **79**(7), pp.1585-1595.

Cohen, A.S. and Waters, F.G. 1996. Separation of osmium from geological materials by solvent extraction for analysis by thermal ionisation mass spectrometry. *Analytica Chimica Acta*, **332**(2-3), pp.269-275.

Condon, D. J., Schoene, B., McLean, N. M., Bowring, S. A. and Parrish, R. R. 2015. Metrology and traceability of U–Pb isotope dilution geochronology (EARTHTIME Tracer Calibration Part I). *Geochimica et Cosmochimica Acta*, **164**, pp.464-480.

Condon, D., Schoene, B., Schmitz, M., Schaltegger, U., Ickert, R., Amelin, Y., Augland, L., Chamberlain, K., Coleman, D., Connelly, J., Corfu, F., Crowley, J., Davies, J., Denyszyn, S., Eddy, M., Heaman, L., Huyskens, M., Gaynor, S., Kamo, S., Kasbohm, J., Keller, C., MacLennan, S., McLean, S., Noble, S., Ovtcharaova, M., Paul, A., Ramezani, J., Rioux, M., Sahy, D., Scoates, J., Szymanowski, D., Tapster, S., Tichomirowa, M., Wall, C., Wotzlaw, J., Yang, C. and Yin, Q. Recommendations for the Reporting and Interpretation of Isotope Dilution U-Pb Geochronological Information. Bulletin of the Geological Society of America [submitted].

Conliffe, J., Wilton, D.H., Feely, M., Lynch, E.P. and Selby, D. 2009. S-isotope analyses of molybdenite in the Appalachian–Caledonian Orogen. *Abstracts with Programs, Geological Society of America Northeastern section–44th annual meeting, 22-24 March 2009, Portland (ME)*. Boulder, CO: Geological Society of America, p.81.

Conliffe, J., Selby, D., Porter, S. and Feely, M. 2010. Re–Os molybdenite dates from the Ballachulish and Kilmelford Igneous Complexes (Scottish Highlands): age constraints for late Caledonian magmatism. *Journal of the Geological Society*, **167**(2), pp.297-302.

Connolly, J.A.D. and Cesare, B. 1993. C-O-H-S fluid composition and oxygen fugacity in graphitic metapelites. *Journal of Metamorphic Geology*, **11**, pp.379-388.

Cooke, D.R. and Simmons, S.F. 2000. Characteristics and genesis of epithermal gold deposits. *Reviews in Economic Geology*, **13**, pp.221-244.

Cooper, M., Crowley, Q., Hollis, S., Noble, S., Roberts, S., Chew, D., Earls, G., Herrington, R. and Merriman, R. 2011. Age constraints and geochemistry of the Ordovician Tyrone Igneous Complex, Northern Ireland: implications for the Grampian orogeny. *Journal of the Geological Society*, **168**(4), pp.837-850.

Cooper, M., Crowley, Q., Hollis, S., Noble, S. and Henney, P. 2013. A U–Pb age for the Late Caledonian Sperrin Mountains minor intrusions suite in the north of Ireland: timing of slab breakoff in the Grampian terrane and the significance of deep-seated, crustal lineaments. *Journal of the Geological Society*, **170**(4), pp.603-614.

Corbella, M., Ayora, C. and Cardellach, E. 2004. Hydrothermal mixing, carbonate dissolution and sulfide precipitation in Mississippi Valley-type deposits. *Mineralium Deposita*, **39**(3), pp.344-357.

Corbett, G. and Leach, R. 2008. Fluid Mixing as a mechanism for bonanza grade epithermal gold formation. *Terry Leach Symposium 2008, 17 October 2008, Sydney*. Australian Institute of Geoscientists, pp.83-92.

Corfu, F. and Ayres, L.D. 1984. U-Pb age and genetic significance of heterogeneous zircon populations in rocks from the Favourable Lake area, Northwestern Ontario. *Contributions to Mineralogy and Petrology*, **88**, pp.86-101.

Corfu, F. 2003. Atlas of Zircon Textures. *Reviews in Mineralogy and Geochemistry*, **53**(1), pp.469-500.

Corfu, F., Gasser, D. and Chew, D.M. 2014. New perspectives on the Caledonides of Scandinavia and related areas: introduction. *Geological Society, London, Special Publications*, **390**(1), pp.1-8.

Corkhill, C., Ixer, R., Mason, J., Irving, D. and Pattrick, R. 2010. Polymetallic auriferous vein mineralization near Loch Tay, Perthshire, Scotland. *Scottish Journal of Geology*, **46**(1), pp.23-30.

Couture, J.F. and Pilote, P. 1993. The geology and alteration patterns of a disseminated, shear zone-hosted mesothermal gold deposit; the Francoeur 3 Deposit, Rouyn-Noranda, Quebec. *Economic Geology*, **88**(6), pp.1664-1684.

Coward M.P. and Potts G.J. 1983. Complex strain patterns developed at the frontal and lateral tips to shear zones and thrust zones. *Journal of Structural Geology*, **5**, pp.383-399.

Coward, M.P., Enfield, M.A. and Fischer, M.W. 1989. Devonian basins of Northern Scotland: extension and inversion related to Late Caledonian—Variscan tectonics. *Geological Society, London, Special Publications*, **44**(1), pp.275-308.

Cox, K.G., Bell, J.D. and Pankhurst, R.J. 1979. *The Interpretation of Igneous Rocks*. London: George Allen and Unwin.

Cox, S., Etheridge, M. and Hobbs, B. 1981. The experimental ductile deformation of polycrystalline and single crystal pyrite. *Economic Geology*, **76**, pp.2105-2117.

Cox, D.P. and Singer, D.A. 1986. Mineral deposit models, US Government. Printing Office.

Cox, S., Sun, S., Etheridge, M., Wall, V. and Potter, T. 1995. Structural and geochemical controls on the development of turbidite-hosted gold quartz vein deposits, Wattle Gully Mine, central Victoria, Australia. *Economic Geology*, **90**, pp.1722-1746.

Cox, S.F. 1999. Deformational controls on the dynamics of fluid flow in mesothermal gold systems. *Geological Society, London, Special Publications*, **155**(1), pp.123-140.

Cox, S.F. 2005. Coupling between Deformation, Fluid Pressures, and Fluid Flow in Ore-Producing Hydrothermal Systems at Depth in the Crust. In: Hedenquist, J., Thompson, J., Goldfarb, R. and Richards, J. ed(s). *One Hundredth Anniversary Volume*. Society of Economic Geologists.

Crane, A., Goodman, S., Krabbendam, M.K., Leslie, A.G., Paterson, I.B., Robertson, S. and Rollin, K. 1996. *Geology of the Glen Shee district: Memoir of the British Geological Survey, Sheet 56W and adjacent areas (Scotland)*. Keyworth: British Geological Survey.

Craw, D. 1990. Regional fluid and metal mobility in the Dalradian metamorphic belt, Southern Grampian Highlands, Scotland. *Mineralium Deposita*, **25**, pp.281-288.

Craw, D. and Chamberlain, C. 1996. Meteoric incursion and oxygen fronts in the Dalradian metamorphic belt, southwest Scotland: a new hypothesis for regional gold mobility. *Mineralium Deposita*, **31**(5), pp.365-373.

Craw, D., Windle, S.J. and Angus, P.V. 1999. Gold mineralization without quartz veins in a ductile-brittle shear zone, Macraes Mine, Otago Schist, New Zealand. *Minerallium Deposita*, **34**, pp.382-394.

Craw, D., Upton, P., and Mackenzie, D.J. 2009. Hydrothermal alteration styles in ancient and modern orogenic gold deposits, New Zealand. *New Zealand Journal of Geology and Geophysics*, **52**(1), pp.11-26.

Craw, D., Upton, P., Yu, B., Horton, T. and Chen, Y. 2010. Young orogenic gold mineralisation in active collisional mountains, Taiwan. *Mineralium Deposita*, **45**(7), pp.631-646.

Creaser, R.A., Papanastassiou, D.A. and Wasserburg, G.J. 1991. Negative thermal ion mass-spectrometry of osmium, rhenium, and iridium. *Geochimica et Cosmochimica Acta*, **55**, pp.397-401.

Creaser, R., Sannigrahi, P., Chacko, T. and Selby, D. 2002. Further evaluation of the Re-Os geochronometer in organic-rich sedimentary rocks: a test of hydrocarbon maturation effects in the Exshaw Formation, Western Canada Sedimentary Basin. *Geochimica et Cosmochimica Acta*, **66**(19), pp.3441-3452.

Criss, R.E. and Farquhar, J. 2008. Abundance, Notation, and Fractionation of Light Stable Isotopes. *Reviews in Mineralogy and Geochemistry*, **68**(1), pp.15-30.

Crocetti, C. A., Holland, H. D. and McKenna, L. W. 1988. Isotopic composition of lead in galenas from the Viburnum Trend, Missouri. *Economic Geology*, **83**(2), pp.355-376.

Crowe, D.E., Valley, J.W. and Baker, K.L. 1990. Micro-analysis of sulfur-isotope ratios and zonation by laser microprobe. *Geochimica et Cosmochimica Acta*, **54**(7), pp.2075-2092.

Crowley, Q.G. and Strachan, R.A. 2015. U-Pb zircon constraints on obduction initiation of the Unst Ophiolite: an oceanic core complex in the Scottish Caledonides?. *Journal of the Geological Society*, **172**(3), pp.279-282.

Cumming, G. L. and Richards, J. R. 1975. Ore lead isotope ratios in a continuously changing earth. *Earth and Planetary Science Letters*, **28**(2), pp.155-171.

Curran, S.C. 1953. The determination of geological age by means of radioactivity. *Quarterly Reviews, Chemical Society*, **7**(1), pp.1-18.

Curtis, S.F., Pattrick, R.A.D., Jenkin, G.R.T., Fallick, A.E., Boyce, A.J. and Treagus, J.E. 1993. Fluid Inclusion and stable isotope study of fault related mineralisation in Tyndrum area, Scotland. *Transactions of the Institute of Mining and Metallurgy (Section B: Applied Earth Science),* **102**, pp.39-47.

Curzi, M., Cipriani, A., Aldega, L., Billi, A., Carminati, E., van der Lelij, R., Vignaroli, G. and Viola, G. 2023. Architecture and permeability structure of the Sibillini Mts. Thrust and influence upon recent, extension-related seismicity in the central Apennines (Italy) through fault-valve behavior. *GSA Bulletin,* **136** (1-2), pp.3-26.

Czamanske, G.K. and Rye, R.O. 1974. Experimentally Determined Sulphur Isotope Fractionations between Sphalerite and Galena in the Temperature Range 600 degrees to 275 degrees °C. *Economic Geology*, **69**(1), pp.17-25.

Dallmeyer, R.D., Giese, U., Glasmacher, U. and Pickel, W. 1999. First 40Ar/39Ar age constraints for the Caledonian evolution of the Trans–European Suture Zone in NE Germany. *Journal of the Geological Society*, **156**(2), pp.279-290.

Dallmeyer, R.D., Strachan, R.A., Rogers, G., Watt, G.R. and Friend, C.R.L. 2001. Dating deformation and cooling in the Caledonian thrust nappes of north Sutherland, Scotland: insights from 40Ar/39Ar and Rb–Sr chronology. *Journal of the Geological Society, London*, **158**, pp.501-512.

Dalradian Resources. 2018. Technical Report for the Curraghinalt Gold Project. Filed on SEDAR. Northern Ireland.

Daly, J. and Flowerdew, M. 2005. Grampian and late Grenville events recorded by mineral geochronology near a basement–cover contact in north Mayo, Ireland. *Journal of the Geological Society*, **162**(1), pp.163-174.

Damdinov, B.B., Huang, X.W., Goryachev, N.A., Zhmodik, S.M., Mironov, A.G., Damdinova, L.B., Khubanov, V.B., Reutsky, V.N., Yudin, D.S., Travin, A.V. and Posokhov, V.F. 2021. Intrusion-hosted gold deposits of the southeastern East Sayan (northern Central Asian Orogenic Belt, Russia). *Ore Geology Reviews*, **139**, article no: 104541 [no pagination]

Davydov, V.I., Crowley, J.L., Schmitz, M.D. and Poletaev, V.I. 2010. High-precision U-Pb zircon age calibration of the global Carboniferous time scale and Milankovitch band cyclicity in the Donets Basin, eastern Ukraine. *Geochemistry, Geophysics, Geosystems*, **11**(2), article no: Q0AA04 [no pagination]

De Yoreo, J.J., Lux, D.R. and Guidotti, C.V. 1991. Thermal modelling in low-pressure/high-temperature metamorphic belts. *Tectonophysics*, **188**(3-4), pp.209-238.

Deloule, E., Allegre, C.J. and Doe, B.R. 1986. Lead and sulfur isotope microstratigraphy in galena crystals from mississippi valley-type deposits. *Economic Geology*, **81**(6), pp.1307-1321.

del Ventisette, C., Montanari, D., Sani, F. and Bonini, M. 2006. Basin inversion and fault reactivation in laboratory experiments. *Journal of Structural Geology*, **28**(11), pp.2067-2083.

Dempster, T. 1985. Uplift patterns and orogenic evolution in the Scottish Dalradian. *Journal of the Geological Society*, **142**(1), pp.111-128.

Dempster, T., Hudson, N. and Rogers, G. 1995. Metamorphism and cooling of the NE Dalradian. *Journal of the Geological Society*, **152**(2), pp.383-390.

Dempster, T., Rogers, G., Tanner, P., Bluck, B., Muir2, R., Redwood, S., Ireland, T. and Paterson, B. 2002. Timing of deposition, orogenesis and glaciation within the Dalradian rocks of Scotland: constraints from U–Pb zircon ages. *Journal of the Geological Society*, **159**(1), pp.83-94.

Deng, X.-H., Wang, J.-B., Pirajno, F., Wang, Y.-W., Li, Y.-C., Li, C., Zhou, L.-M. and Chen, Y.-J. 2016. Re–Os dating of chalcopyrite from selected mineral deposits in the Kalatag district in the eastern Tianshan Orogen, China. *Ore Geology Reviews*, **77**, pp.72-81.

DePaolo, D.J. 1979. Implications of correlated Nd and Sr isotopic variations for the chemical evolution of the crust and mantle. Earth and Planetary Science Letters, **43**(2), pp.201-211.

Devéria, R. 2001. Tomnadashan: a re-examination of a 19th century copper mining and smelting operation in Perthshire, Scotland. *Historical metallurgy*, **35**, pp.87-98.

Dewey, J.F. 1969. Evolution of the Appalachian/Caledonian Orogen. *Nature*, **222**(5189), pp.124 -129.

Dewey, J. 1971. A model for the Lower Palaeozoic evolution of the southern margin of the early Caledonides of Scotland and Ireland. *Scottish Journal of Geology*, **7**(3), pp.219-240.

Dewey, J. and Shackleton, R.M. 1984. A model for the evolution of the Grampian tract in the early Caledonides and Appalachians. *Nature*, **312**(5990), pp.115-121.

Dewey, J. and Mange, M. 1999. Petrography of Ordovician and Silurian sediments in the western Irish Caledonides: tracers of a short-lived Ordovician continent-arc collision orogeny and the evolution of the Laurentian Appalachian-Caledonian margin. *Geological Society, London, Special Publications*, **164**(1), pp.55-107.

Dewey, J. and Strachan, R.A. 2003. Changing Silurian–Devonian relative plate motion in the Caledonides; sinistral transpression to sinistral transtension. *Journal of the Geological Society, London,* **160**, pp.219-229.

Dewey, J. 2005. Orogeny can be very short. *Proceedings of the National Academy of Sciences*, **102**(43), pp.15286-15293.

Dewey, J., Dalziel, I.W., Reavy, R.J. and Strachan, R.A. 2015. The Neoproterozoic to Mid-Devonian evolution of Scotland: a review and unresolved issues. *Scottish Journal of Geology*, **51**(1), pp.5-30.

Deyell, C.L., Bissig, T. and Rye, R.O. 2005. Isotopic evidence for magmatic-dominated epithermal processes in the El Indio-Pascua Au-Cu-Ag Belt and relationship to geomorphologic setting. *Society of Economic Geologists Special Publication*, **11**, pp.55-73.

Dickin, A.P. 1995. *Radiogenic Isotope Geology*. Cambridge: Cambridge University Press.

Dickin, A.P. 2018. *Radiogenic Isotope Geology*. Third edition. Cambridge: Cambridge University Press.

Digimap.edina.ac.uk. 2023. Digimap. [online] Available at: <https://digimap.edina.ac.uk/os> [Accessed 20 April 2022].

Dixon, P.R., Le Huray, A.P. and Rye, D.M., 1990. Basement geology and tectonic evolution of Ireland as deduced from Pb isotopes. *Journal of the Geological Society*, **147**(1), pp.121-132.

Dodson, M. H. 1973. Closure temperature in cooling geochronological and petrological systems. *Contributions to Mineralogy and Petrology*, **40**(3), pp.259-274.

Doe, B.R. and Zartman, R.E. 1979. Plumbotectonics: the phanerozoic. *Geochemistry of hydrothermal ore deposits,* pp.22-70.

Dong, G. and Morrison, G.W. 1995. Adularia in epithermal veins, Queensland: Morphology, structural state and origin. *Mineralium Deposita*, **30**, pp.11-19.

Doublier, M.P., Thébaud, N., Wingate, M.T.D., Romano, S.S., Kirkland, C.L., Gessner, K., Mole, D.R. and Evans, N. 2014. Structure and timing of Neoarchean gold mineralization in the Southern Cross district (Yilgarn Craton, Western Australia) suggest leading role of late Low-Ca I-type granite intrusions. *Journal of Structural Geology*, **67**, pp.205-221.

Drake, H., Roberts, N. M. W., Reinhardt, M., Whitehouse, M., Ivarsson, M., Karlsson, A., Kooijman, E. and Kielman-Schmitt, M. 2021. Biosignatures of ancient microbial life are present across the igneous crust of the Fennoscandian shield. *Communications Earth & Environment*, **2**(1), article no: 102 (2021) [no pagination]

Draut, A., Clift, P., Amato, J., Blusztajn, J. and Schouten, H. 2009. Arc–continent collision and the formation of continental crust: a new geochemical and isotopic record from the Ordovician Tyrone Igneous Complex, Ireland. *Journal of the Geological Society*, **166**(3), pp.485-500.

Duan, G., Ram, R., Xing, Y., Etschmann, B. and Brugger, J. 2021. Kinetically driven successive sodic and potassic alteration of feldspar. *Nature Communications*, **12**(1).

Dufour, F., Davies, J. H. F. L., Greenman, J. W., Skulski, T., Halverson, G. P. and Stevenson, R. 2023. New U-Pb CA-ID TIMS zircon ages implicate the Franklin LIP as the proximal trigger for the Sturtian Snowball Earth event. *Earth and Planetary Science Letters*, **618**, article no: 118259 [no pagination]

Eiler, J.M., Bergquist, B., Bourg, I., Cartigny, P., Farquhar, J., Gagnon, A., Guo, W., Halevy, I., Hofmann, A., Larson, T. E., Levin, N., Schauble, E. A. and Stolper, D. 2014. *Frontiers of stable isotope geoscience*. *Chemical Geology*, **372**, pp.119-143.

Eilu, P. and Groves, D.I. 2001. Primary alteration and geochemical dispersion haloes of Archaean orogenic gold deposits in the Yilgarn Craton: the pre-weathering scenario. *Geochemistry: Exploration, Environment, Analysis*, **1**(3), pp.183-200.

Einaudi, M.T., Hedenquist, J.W., and Inan, E. 2003. Sulphidation state of fluids in active and extinct hydrothermal systems: Transitions from porphyry to epithermal environments. *Society of Economic Geologists Special Publication,* **10**, pp.285-314

Einaudi, M., Hedenquist, J. and Esra Inan, E. 2005. Sulphidation State of Fluids in Active and Extinct Hydrothermal Systems: Transitions from Porphyry to Epithermal Environments. *Volcanic, Geothermal, and Ore-Forming Fluids*, pp.285-313.

Eldridge, C., Bourcier, W., Ohmoto, H. and Barnes, H. 1988. Hydrothermal inoculation and incubation of the chalcopyrite disease in sphalerite. *Economic Geology*, **83**, pp.978-989.

Eldridge, D. L., Guo, W. and Farquhar, J. 2016. Theoretical estimates of equilibrium sulfur isotope effects in aqueous sulfur systems: Highlighting the role of isomers in the sulfite and sulfoxylate systems. *Geochimica et Cosmochimica Acta*, **195**, pp.171-200.

Elles, G.L. 1926. The Geological Structure of Ben Lawers and Meall Corranaich,(Perthshire). *Quarterly Journal of the Geological Society*, **82**(1-4), pp.304-331.

Ellis, R.A., Coats, J.S., Haslam, H.W., Michie, U.M., Fortey, N.J., Johnson, C.E. and Parker, M.E. 1977. *Investigation of disseminated copper mineralisation near Kilmelford, Argyllshire, Scotland.* London: Institute of Geological Sciences.

Emsbo, P. 2000. Gold in Sedex deposits. In: Hagemann, S. and Brown, P. ed(s). *Gold in 2000.* Society of Economic Geologists.

England, P.C. and Thompson, A.B. 1984. Pressure–temperature–time paths of regional metamorphism. Heat transfer during the evolution of regions of thickened continental crust. *Journal of Petrology*, **25**, pp.894-928.

Erdmann, S., Wodicka, N., Jackson, S. E. and Corrigan, D. 2013. Zircon textures and composition: refractory recorders of magmatic volatile evolution? *Contributions to Mineralogy and Petrology*, **165**(1), pp.45-71.

Esri. 2022. ArcGIS (2022). [Software]. [Accessed 30 March – 15 April 2022].

Etheridge, M.A., Wall, V.J. and Vernon, R.H. 1983. The role of the fluid phase during regional metamorphism and deformation. *Journal of Metamorphic Geology*, **1**, pp.205-226.

Etheridge, M. 1986. On the reactivation of extensional fault systems. *Philosophical Transactions of the Royal Society of London. Series A, Mathematical and Physical Sciences*, **317**(1539), pp.179-194.

Evans, J.W. and Stubblefield, C.J. 1929. *Handbook of the geology of Great Britain*. London: Murby.

Evans, K.A. 2010. A test of the viability of fluid–wall rock interaction mechanisms for changes in opaque phase assemblage in metasedimentary rocks in the Kambalda-St. Ives goldfield, Western Australia. *Mineralium Deposita*, **45**(2), pp.207-213.

Ewing, R.C. 2003. Radiation Effects in Zircon. Reviews in Mineralogy and Geochemistry, **53**(1), pp.387-425.

Fallick, A.E., Ashton, J.H., Boyce, A.J., Ellam, R.M. and Russell, M.J. 2001. Bacteria were responsible for the magnitude of the world-class hydrothermal base metal sulfide orebody at Navan, Ireland. *Economic Geology*, **96**(4), pp.885-890.

Farquhar, R.M. and Haynes, S.J. 1986. Lead isotope data for gold-bearing veins and their host metasedimentary rocks of the Goldenville Formation, eastern Nova Scotia. *Atlantic Geology*, **22**(1), pp.89-99.

Faure, G. 1986. *Principles of Isotope Geology*. 2nd edition. New York: John Wiley and Sons.

Faure, G. and Mensing, T.M. 2005. *Isotopes: Principles and Applications*. New York: John Wiley & Sons, Inc.

Fedorowich, J.S., Stauffer, M.R. and Kerrich, R. 1991. Structural setting and fluid characteristics of the Proterozoic Tartan Lake gold deposit, Trans-Hudson Orogen, northern Manitoba. *Economic Geology*, **86**(7), pp.1434-1467.

Fettes, D.J. 1970. The structural and metamorphic state of the Dalradian rocks and their bearing on the age of emplacement of the basic sheet. *Scottish Journal of Geology*, **6**(1), pp.108-118.

Fettes, D.J. 1979. A metamorphic map of the British and Irish Caledonides. *Geological Society, London, Special Publications*, **8**(1), pp.305-321

Fettes, D.J., Macdonald, R., Fitton, J.G., Stephenson, D. and Cooper, M.R. 2011. Geochemical evolution of Dalradian metavolcanic rocks: implications for the break-up of the Rodinia supercontinent. *Journal of the Geological Society*, **168**(5), pp.1133-1146.

Field, C.W. and Fifarek, R.H. 1985. Light stable isotope systematics in epithermal systems. In: Berger, B. and Bethke, P. *Reviews in Economic Geology.* 2nd edition. Society of Economic Geologists.

Field, J.D., Appold, M.S., Renson, V. and Coveney, R.M. 2018. Lead and sulfur isotope composition of trace occurrences of Mississippi Valley-type mineralization in the U.S. midcontinent. *Journal of Geochemical Exploration*, **184**, pp.66-81.

Fisher, G.W. 1978. Rate laws in metamorphism. *Geochimica et Cosmochimica Acta*, **42**, pp.1035-1050.

Flowerdew, M.J., Daly, J.S., Guise, P.G. and Rex, D.C. 2000. Isotopic dating of overthrusting, collapse and related granitoid intrusion in the Grampian orogenic belt, northwestern Ireland. *Geological Magazine*, **137**, pp.419-435.

Flowers, R.M., Bowring, S.A., Tulloch, A.J. and Klepeis, K.A. 2005. Tempo of burial and exhumation within the deep roots of a magmatic arc, Fiordland, New Zealand. *Geology*, **33**(1), pp.17-20.

Foley, N.K. and Ayuso, R.A. 1994. Lead isotope compositions as guides to early gold mineralizations; the North Amethyst vein system, Creede District, Colorado. *Economic Geology*, **89**(8), pp.1842-1859.

Fortey, N.J. and Smith, C.G. 1986. Stratabound mineralisation in Dalradian rocks near Tyndrum, Perthshire. *Scottish Journal of Geology*, **22**(3), pp.377-393.

Fortey, N.J., Coats, J.S., Gallagher, M.J., Smith, C.G. and Greenwood, P.G. 1993. New strata-bound barite and base metals in Middle Dalradian rocks near Braemar, northeast Scotland. *Transactions of the Institutions of Mining and Metallurgy, Section B: Applied Earth Science*, **102**, pp.55-64.

Fougerouse, D., Micklethwaite, S., Tomkins, A.G., Mei, Y., Kilburn, M., Guagliardo, P., Fisher, L. A., Halfpenny, A., Gee, M., Paterson, D. and Howard, D.L. 2016. Gold remobilisation and formation of high-grade ore shoots driven by dissolution-reprecipitation replacement and Ni substitution into auriferous arsenopyrite. *Geochimica et Cosmochimica Acta*, **178**, pp.143-159.

Fougerouse, D., Reddy, S.M., Aylmore, M., Yang, L., Guagliardo, P., Saxey, D.W., Rickard, W.D. A. and Timms, N. 2021. A new kind of invisible gold in pyrite hosted in deformation-related dislocations. *Geology*, **49**(10), pp.1225-1229.

Foulger, G., Natland, J. and Anderson, D. 2005. A source for Icelandic magmas in remelted Iapetus crust. *Journal of Volcanology and Geothermal Research*, **141**(1-2), pp.23-44.

Fowler, M., Henney, P., Darbyshire, D. and Greenwood, P. 2001. Petrogenesis of high Ba–Sr granites: the Rogart pluton, Sutherland. *Journal of the Geological Society*, **158**(3), pp.521-534.

Fowler, A., Prokoph, A., Stern, R. and Dupuis, C. 2002. Organization of oscillatory zoning in zircon: analysis, scaling, geochemistry, and model of a zircon from Kipawa, Quebec, Canada. *Geochimica et Cosmochimica Acta*, **66**(2), pp.311-328.

Fraser, G.L., Pattison, D.R.M. and Heaman, L.M. 2004. Age of the Ballachulish and Glencoe Igneous Complexes (Scottish Highlands), and paragenesis of zircon, monazite and baddeleyite in the Ballachulish Aureole. *Journal of the Geological Society, London*, **161**, pp.447-462.

Freeman, B., Klemperer, S.L., Hobbs, R.W. 1988. The deep structure of northern England and the Iapetus Suture zone from BIRPS deep seismic reflection profiles. *Journal of the Geological Society*, **145**, pp.727-740.

Frelinger, S.N., Ledvina, M.D., Kyle, J.R. and Zhao, D. 2015. Scanning electron microscopy cathodoluminescence of quartz: Principles, techniques and applications in ore geology. *Ore Geology Reviews*, **65**, pp.840-852.

Friedrich, A.M., Bowring, S.A., Martin, M.W. and Hodges, K.V. 1999a. Short-lived continental magmatic arc at Connemara, western Ireland Caledonides: implications for the age of the Grampian orogeny. *Geology*, **27**, pp.27-30.

Friedrich, A.M., Hodges, K.V., Bowring, S.A. and Martin, M.W. 1999b. Geochronological constraints on the magmatic, metamorphic and thermal evolution of the Connemara Caledonides, western Ireland. *Journal of the Geological Society*, **156**, pp. 1217-1230.

Friend, P.F., Williams, B.P.J., Ford, M. and Williams, E.A. 2000. Kinematics and dynamics of Old Red Sandstone basins. *Geological Society, London, Special Publications*, **180**(1), pp.29-60.

Frondel, C. 1938. Stability of colloidal gold under hydrothermal conditions. *Economic Geology*, 33(1), pp.1-20.

Frost, B., Chamberlain, K. and Schumacher, J. 2001. Sphene (titanite): phase relations and role as a geochronometer. *Chemical Geology*, **172**(1-2), pp.131-148.

Frost, B.R., Mavrogenes, J.A., and Tomkins, A.G. 2002. Partial melting of sulphide ore deposits during medium- and high-grade metamorphism. *The Canadian Mineralogist*, **40**, pp. 1-18.

Fu, B., Kendrick, M.A., Fairmaid, A.M., Phillips, D., Wilson, C.J.L. and Mernagh, T.P. 2012. New constraints on fluid sources in orogenic gold deposits, Victoria, Australia. *Contributions to Mineralogy and Petrology*, **163**(3), pp.427-447.

Fyfe, W.S. and Henley, R.W. 1973. Some thoughts on chemical transport processes, with particular reference to gold. *Mineral Science and Engineering*, **5**(4), pp.275-303.

Gaboury, D. 2013. Does gold in orogenic deposits come from pyrite in deeply buried carbon-rich sediments?: Insight from volatiles in fluid inclusions. *Geology,* **41**(12), pp. 1207-1210.

Gaboury, D. 2019. Parameters for the formation of orogenic gold deposits. *Applied Earth Science*, **128**(3), pp.124-133.

Gaboury, D., MacKenzie, D. and Craw, D. 2021. Fluid volatile composition associated with orogenic gold mineralization, Otago Schist, New Zealand: Implications of H2 and C2H6 for fluid evolution and gold source. *Ore Geology Reviews*, **133**, p.104086.

Gagnevin, D., Daly, J.S. and Kronz, A. 2010. Zircon texture and chemical composition as a guide to magmatic processes and mixing in a granitic environment and coeval volcanic system. *Contributions to Mineralogy and Petrology*, **159**(4), pp. 579-596.

Gammons, C.H. and Williams-Jones, A.E. 1997. Chemical mobility of gold in the porphyry-epithermal environment. *Economic Geology*, **92**(1), pp.45-59.

Gamo, T., Okamura, K., Charlou, J.L., Urabe, T., Auzende, J.M., Ishibashi, J., Shitashima, K. and Chiba, H. 1997. Acidic and sulfate-rich hydrothermal fluids from the Manus back-arc basin, Papua New Guinea. *Geology*, **25**(2), pp.139-142.

Gardés, E. and Montel, J.-M. 2009. Opening and resetting temperatures in heating geochronological systems. *Contributions to Mineralogy and Petrology*, **158**(2), pp.185-195.

Garofalo, P., Fricker, M., Günther, D., Bersani, D. and Paolo Lottici, P. 2014. Physical-chemical properties and metal budget of Au-transporting hydrothermal fluids in orogenic deposits. *Geological Society, London, Special Publications*, **402**(1), pp.71-102.

Gartman, A., Hannington, M., Jamieson, J.W., Peterkin, B., Garbe-Schönberg, D., Findlay, A.J., Fuchs, S. and Kwasnitschka, T. 2018. Boiling-induced formation of colloidal gold in black smoker hydrothermal fluids. *Geology*, **46**(1), pp.39-42.

Gavelin, S., Parwel, A. and Ryhage, R. 1960. Sulfur isotope fractionation in sulfide mineralization. *Economic Geology*, **55**(3), pp.510-530.

Gaynor, S.P., Svensen, H.H., Polteau, S. and Schaltegger, U. 2022. Local melt contamination and global climate impact: Dating the emplacement of Karoo LIP sills into organic-rich shale. *Earth and Planetary Science Letters*, 579, article no: 117371 [no pagination]

Gehrels, G. 2011. Detrital Zircon U-Pb Geochronology: Current Methods and New Opportunities. In: Busby, C. and Azor, A. Tectonics of Sedimentary Basins. Wiley, pp.45-62.

Geiger, H. and Nuttall, J.M. 1911. LVII. The ranges of the α particles from various radioactive substances and a relation between range and period of transformation. *The London, Edinburgh, and Dublin Philosophical Magazine and Journal of Science*, **22**(130), pp.613-621.

Geisler, T., Rashwan, A.A., Rahn, M.K.W., Poller, U., Zwingmann, H., Pidgeon, R.T., Schleicher, H. and Tomaschek, F. 2003. Low-temperature hydrothermal alteration of natural metamict zircons from the Eastern Desert, Egypt. *Mineralogical Magazine*, **67**(3), pp.485-508.

George, T.N. 1960. The stratigraphical evolution of the Midland Valley. *Transactions of the Geological Society of Glasgow*, **24**, pp.32-107.

Gibert, F., Moine, B., Schott, J. and Dandurand, J.L. 1992. Modeling of the transport and deposition of tungsten in the scheelite-bearing calc-silicate gneisses of the Montagne Noire, France. *Contributions to Mineralogy and Petrology*, **112**(2-3), pp.371-384.

Giese, U., Katzung, G., Walter, R. and Weber, J. 1997. The Caledonian deformation of the Brabant Massif and the Early Palaeozoic in northeast Germany: compared. *Geological Magazine*, **134**(5), pp.637-652.

Giggenbach, W.F. 1984. Mass transfer in hydrothermal alteration systems—A conceptual approach. *Geochimica et Cosmochimica Acta*, **48**(12), pp.2693-2711.

Giggenbach, W.F. 1992. Magma degassing and mineral deposition in hydrothermal systems along convergent plate boundaries. *Economic Geology*, **87**, pp. 1927-1944.

Giggenbach, W.F. 1997. The origin and evolution of fluids in magmatic-hydrothermal systems. In: Barnes, H.L. ed. *Geochemistry of hydrothermal ore deposits*. 3rd edition. New York: John Wiley & Sons, pp.737-796.

Gillen. C. 1982. *Metamorphic Geology: An Introduction to Tectonic and Metamorphic Processes*. London: George, Allen and Unwin.

GlobaLID Core Team. 2021. GlobaLID web application V. 1.0, database status: 2023-11-19.

Glover, B. and Winchester, J. 1989. The Grampian Group: a major Late Proterozoic clastic sequence in the Central Highlands of Scotland. *Journal of the Geological Society*, **146**(1), pp.85-96.

Glover, B., Key, R., May, F., Clark, G., Phillips, E. and Chacksfield, B. 1995. A Neoproterozoic multi-phase rift sequence: the Grampian and Appin groups of the southwestern Monadhliath Mountains of Scotland. *Journal of the Geological Society*, **152**(2), pp.391-406.

Godwin, C.I., Gabites, J.E. and Andrew, A. 1988. Leadtable. *A galena lead isotope data base for the Canadian Cordillera, with a guide to its use by explorationists.* British Columbia Geological Survey Branch, Mineral Resources Division.

Goldfarb, R.J., Leach, D.L., Pickthorn, W.J. and Paterson, C.J. 1988. Origin of lode-gold deposits of the Juneau gold deposit, southeast Alaska. *Geology,* **16**, pp.440-443.

Goldfarb, R.J., Leach, D.L., Rose, S.C. and Landis, G.P. 1989. Fluid Inclusion Geochemistry of Gold-Bearing Quartz Veins of the Juneau Gold Belt, Southeastern Alaska: Implications for Ore Genesis. *Economic Geology Monograph*, **6**, pp.363-375.

Goldfarb, R.J., Snee, L.W. and Miller, L.D. 1991. Rapid dewatering of the crust deduced from ages of mesothermal gold deposits. *Nature*, **354**, pp. 296-298.

Goldfarb, R., Miller, D., Leach, D. and Snee, L. Gold Deposits in Metamorphic Rocks of Alaska. 1997. In: Goldfarb, R. and Miller, L. *Mineral Deposits of Alaska*. Society of Economic Geologists, pp. 151-190.

Goldfarb, R., Groves, D. and Gardoll, S. 2001. Orogenic gold and geologic time: a global synthesis. *Ore Geology Reviews*, **18**(1-2), pp.1-75.

Goldfarb, R.J., Ayuso, R., Miller, M.L., Ebert, S.W., Marsh, E.E., Petsel, S.A., Miller, L.D., Bradley, D., Johnson, C. and McClelland, W. 2004. The Late Cretaceous Donlin Creek Gold Deposit, Southwestern Alaska: Controls on Epizonal Ore Formation. *Economic Geology*, **99**(4), pp.643-671.

Goldfarb, R.J., Baker, T., Dube, B., Groves, D.I., Hart, C.J. and Gosselin, P. 2005. Distribution, character, and genesis of gold deposits in metamorphic terranes. *Economic Geology,* **100**, pp.407-450.

Goldfarb, R.J., and Santosh, M. 2014. The dilemma of the Jiaodong gold deposits: Are they unique?. *Geoscience Frontiers*, **5**(2), pp. 139-153.

Goldfarb, R. and Groves, D. 2015. Orogenic gold: Common or evolving fluid and metal sources through time. *Lithos*, **233**, pp.2-26.

Goldfarb, R.J. and Pitcairn, I. 2023. Orogenic gold: is a genetic association with magmatism realistic?. *Mineralium Deposita*, **58**(1), pp.5-35.

Goldhaber, M.B., Church, S.E., Doe, B.R., Aleinikoff, J.N., Brannon, J.C., Podosek, F.A., Mosier, E.L., Taylor, C.D. and Gent, C.A. 1995. Lead and sulfur isotope investigation of Paleozoic sedimentary rocks from the southern Midcontinent of the United States; implications for paleohydrology and ore genesis of the Southeast Missouri lead belts. *Economic Geology*, **90(**7), pp.1875-1910.

Goodman, S. and Winchester, J.A. 1993. Geochemical variations within metavolcanic rocks of the Dalradian Farragon Beds and adjacent formations. *Scottish Journal of Geology*, **29**(2), pp.131-141.

Goodman, S., Crane, A., Krabbendam, M., Leslie, A.G. and Ruffell, A. 1996. Correlation of depositional sequences in a structurally complex area: the Dalradian of Glenn Fearnach to Glen Shee, Scotland. *Earth and Environmental Science Transactions of The Royal Society of Edinburgh*, **87**(4), pp.503-513.

Google Earth. 2024. [Online]. [Accessed 26 February 2024].

Google Maps. 2024. [Online]. [Accessed 26 February 2024].

Gosselin, J.M., Audet, P., Estève, C., McLellan, M., Mosher, S.G. and Schaeffer, A.J. 2020. Seismic evidence for megathrust fault-valve behavior during episodic tremor and slip. *Science Advances*, **6**(4), article no: eaay5174 [no pagination]

Götze, J., Plötze, M. and Habermann, D. 2001. Origin, spectral characteristics and practical applications of the cathodoluminescence (CL) of quartz – a review. *Mineralogy and Petrology*, **71**, pp.225-250.

Götze, J. 2009. Chemistry, textures and physical properties of quartz — geological interpretation and technical application. *Mineralogical Magazine*, **73**, pp.645-671.

Götze, J. and Kempe, U. 2009. Physical Principles of Cathodoluminescence (CL) and its Applications in Geosciences. In: Gucsik, A. ed. *Cathodoluminescence and its Application in the Planetary Sciences*. Berlin: Springer.

Götze, J. and Möckel, R. 2012. *Quartz: Deposits, Mineralogy and Analytic*s. Heidelberg: Springer Berlin.

Gow, P.A. and Walshe, J.L. 2005. The role of preexisting geologic architecture in the formation of giant porphyry-related Cu ± Au deposits: Examples from New Guinea and Chile. *Economic Geology*, **100**, pp.819-833.

Graham, C.M. 1974. Metabasite amphiboles of the Scottish Dalradian. *Contributions to mineralogy and petrology*, **47**, pp.165-185.

Graham, C.M. 1976. Petrochemistry and tectonic significance of Dalradian metabasaltic rocks of the SW. Scottish Highlands. *Journal of the Geological Society*, **132**(1), pp.61-84.

Graham, C.M. and Bradbury, H.J. 1981. Cambrian and late Precambrian basaltic igneous activity in the Scottish Dalradian: a review. *Geological Magazine*, **118**(1), pp.27-37.

Graham, C.M. and Borradaile, G.J. 1984. The petrology and structure of Dalradian metabasaltic dykes of Jura: implications for early Dalradian evolution. *Scottish Journal of Geology*, **20**(2), pp.257-270.

Graham, S., Holwell, D., McDonald, I., Jenkin, G., Hill, N., Boyce, A., Smith, J. and Sangster, C. 2017. Magmatic Cu-Ni-PGE-Au sulfide mineralisation in alkaline igneous systems: An example from the Sron Garbh intrusion, Tyndrum, Scotland. *Ore Geology Reviews*, **80**, pp.961-984.

Gramlich, J.W., Murphy, T.J., Garner, E.L. and Shields, W.R. 1973. Absolute isotopic abundance ratio and atomic weight of a reference sample of rhenium. *Journal of Research of the National Institute of Standards and Technology*, **77**, pp.691-698.

Grammatikopoulos, T.A. and Clark, A.H. 2006. A comparative study of wollastonite skarn genesis in the Central Metasedimentary Belt, southeastern Ontario, Canada. *Ore Geology Reviews*, **29**(2), pp.146-161.

Graupner, T., Niedermann, S., Kempe, U., Klemd, R. and Bechtel, A. 2006. Origin of ore fluids in the Muruntau gold system: Constraints from noble gas, carbon isotope and halogen data. *Geochimica et Cosmochimica Acta*, **70**(21), pp.5356-5370.

Green Glen Minerals. 2021. Annual report and financial statements for the period ended 31st December 2021. [online]. Green Glen Minerals [25 February 2024]. Available from: https://greenglenminerals.com/investors/investor-documents

Grimshaw, M.R. 2018. *Gold mineralisation in the Lone Star area of the Klondike gold District, Yukon, Canada.* Ph.D. thesis, University of Leeds.

Groch, M.W. 1998. Radioactive decay. *RadioGraphics*, **18**(5), pp.1247-1256.

Grootenboer, J. and Schwarcz, H.P. 1969. Experimentally determined sulfur isotope fractionations between sulfide minerals. *Earth and Planetary Science Letters*, **7**(2), pp.162-166.

Groves, D.I. 1993. The crustal continuum model for late-Archaean lode-gold deposits of the Yilgarn Block, Western Australia. *Mineralium Deposita*, **28**, pp.366-374.

Groves, D.I., Goldfarb, R.J., Gebre-Mariam, M., Hagemann, S.G. and Robert, F. 1998. Orogenic gold deposits: a proposed classification in the context of their crustal distribution and relationship to other gold deposit types. *Ore geology2 reviews*, **13**(1-5), pp.7-27.

Groves, D.I., Goldfarb, R.J., Robert, F. and Hart, C.J.R. 2003. Gold Deposits in Metamorphic Belts: Overview of Current Understanding, Outstanding Problems, Future Research, and Exploration Significance. *Economic Geology*, **98**(1), pp.1-29.

Groves, D.I. and Santosh, M. 2015. Province-scale commonalities of some world-class gold deposits: Implications for mineral exploration. *Geoscience Frontiers*, **6**(3), pp.389-399.

Groves, D.I. and Santosh, M. 2016. The giant Jiaodong gold province: The key to a unified model for orogenic gold deposits? *Geoscience Frontiers*, **7**(3), pp.409-417.

Groves, D., Santosh, M., Deng, J., Wang, Q., Yang, L. and Zhang, L. 2020a. A holistic model for the origin of orogenic gold deposits and its implications for exploration. *Mineralium Deposita*, **55**(2), pp.275-292.

Groves, D.I., Santosh, M. and Zhang, L., 2020b. A scale-integrated exploration model for orogenic gold deposits based on a mineral system approach. *Geoscience Frontiers*, **11**(3), pp.719-738.

Guha, J., Lu, H.-Z., and Gagnon, M. 1990. Gas composition of fluid inclusions using solid probe mass spectrometry and its application to study of mineralizing processes. *Geochimica et Cosmochimica Acta*, **54**(3), pp.553-558.

Guitreau, M. and Flahaut, J. 2019. Record of low-temperature aqueous alteration of Martian zircon during the late Amazonian. *Nature Communications*, **10**(1), article no: 2457 [no pagination]

Gunn, A.G., Shaw, M.H., Rollin, K.E., Styles, M.T. 1996. *Gold mineralisation in the Dalradian rocks of Knapdale-Kintyre, south-west Highlands, Scotland*. Keyworth: British Geological Survey.

Gustafson, L.B. and Hunt, J.P. 1975. The porphyry copper deposit at El Salvador, Chile. *Economic Geology*, **70**(5), pp.857-912.

Hall, A.J., Boyce, A.J. and Fallick A.E. 1987. Iron sulphides in metasediments: isotopic support for a retrogressive pyrrhotite to pyrite reaction. Chemical Geology (Isotope Geoscience Section), **65**, pp.305-310.

Hall, A.J., Boyce, A.J. and Fallick, A.E. 1988. A sulphur isotope study of iron sulphides in the Late Precambrian Dalradian Easdale Slate Formation, Argyll, Scotland. *Mineralogical Magazine*, **52**(367), pp.483-490.

Hall, L. and Roberts, D. 1988. Timing of Ordovician deformation in the Caledonian-Appalachian orogen. *Geological Society, London, Special Publications*, **38**(1), pp.291-309.

Hall, A.J., Boyce, A.J. and Fallick, A.E. 1994a. A sulphur isotope study of iron sulphides in the late Precambrian Dalradian Ardrishaig Phyllite Formation, Knapdale, Argyll. *Scottish Journal of Geology*, **30**(1), pp.63-71.

Hall, A.J., McConville, P., Boyce, A.J. and Fallick, A.E., 1994b. Sulphides with high δ34S from the Late Precambrian Bonahaven Dolomite, Argyll, Scotland. Mineralogical Magazine, **58**(392), pp.486-490.

Halliday, A. and Stephens, W. 1984. Crustal controls on the genesis of the 400 Ma old Caledonian granites. *Physics of the Earth and Planetary Interiors*, **35**(1-3), pp.89-104.

Halliday, A., Stephens, W., Hunter, R., Menzies, M., Dickin, A. and Hamilton, P. 1985. Isotopic and chemical constraints on the building of the deep Scottish lithosphere. *Scottish Journal of Geology*, **21**(4), pp.465-491.

Halliday, A., Aftalion, M., Parsons, I., Dickin, A. and Johnson, M. 1987. Syn-orogenic alkaline magmatism and its relationship to the Moine Thrust Zone and the thermal state of the lithosphere in Northwest Scotland. *Journal of the Geological Society, London*, **144**, pp.611-617.

Halliday, A., Graham, C., Aftalion, M. and Dymoke, P. 1989. Short paper: the depositional age of the Dalradian Supergroup: U-Pb and Sm-Nd isotopic studies of the Tayvallich Volcanics, Scotland. *Journal of the Geological Society*, **146**(1), pp.3-6.

Halls, C. and Zhao, R. 1995. Listvenite and related rocks: perspectives on terminology and mineralogy with reference to an occurrence at Cregganbaun, Co. Mayo, Republic of Ireland. *Mineralium Deposita*, 30(3-4), pp.303-313.

Hamilton, P., Evensen, N., O'Nions, R. and Tarney, J. 1979. Sm—Nd systematics of Lewisian gneisses: implications for the origin of granulites. *Nature*, **277**(5691), pp.25-28.

Hanchar, J. M. and Rudnick, R. L. 1995. Revealing hidden structures: The application of cathodoluminescence and back-scattered electron imaging to dating zircons from lower crustal xenoliths. *Lithos*, **36**(3-4), pp.289-303.

Harmon, R., Halliday, A., Clayburn, J. and Stephens, W. 1984. Chemical and isotopic systematics of the Caledonian intrusions of Scotland and Northern England: a guide to magma source region and magma-crust interaction. *Philosophical Transactions of the Royal Society of London. Series A, Mathematical and Physical Sciences*, **310**(1514), pp.709-742.

Harris, A.L. and Pitcher, W.S. 1975. A Correlation of Precambrian Rocks in the British Isles. *Special Reports of the Geological Society, London*, **6**, pp.52-75

Harris, A.L., Baldwin, C.T., Bradbury, H.J., Johnson, H.D. and Smith, R.A. 1978. Ensialic basin sedimentation: the Dalradian Supergroup. In: Bowes, D.R. and Leake, B.E. ed(s). *Crustal Evolution in North-western Britain and adjacent regions*. London: Geological Society, pp. 115-138.

Harris, A.L., Haselock, P.J., Kennedy, M.J., Mendum, J.R., Long, C.B., Winchester, J.A. and Tanner, P.W.G., 1994. The Dalradian Supergroup in Scotland, Shetland and Ireland. In: Gibbons, W.E. and Harris, A.L. ed(s). *A revised correlation of Precambrian rocks in the British Isles*. London: Geological Society.

Harris, A.C. and Golding, S.D. 2002. New evidence of magmatic-fluid–related phyllic alteration: Implications for the genesis of porphyry Cu deposits. *Geology*, **30**(4), pp.335-338.

Harrison, T., Catlos, E. and Montel, J. 2002. U-Th-Pb Dating of Phosphate Minerals. *Reviews in Mineralogy and Geochemistry*, **48**(1), pp.524-558.

Harrison, T. and Zeitler, P. 2005. Fundamentals of Noble Gas Thermochronometry. *Reviews in Mineralogy and Geochemistry*, **58**(1), pp.123-149.

Hart, S.R., Shimizu, N., and Sverjensky, D.A. 1981. Lead isotope zoning in galena; an ion microprobe study of a galena crystal from the Buick Mine, Southeast Missouri. *Economic Geology*, **76**(7), pp.1873-1878.

Hart, C.J. 2007. Reduced intrusion-related gold systems. Mineral Deposits of Canada: A synthesis of Major deposit types, district metallogeny, the Evolution of geological provinces, and exploration methods: Geological Association of Canada, Mineral Deposits Division, Special Publication, pp.95-112.

Harte, B. and Hudson, N.F. 1979. Pelite facies series and the temperatures and pressures of Dalradian metamorphism in E Scotland. *Geological Society, London, Special Publications*, **8**(1), pp.323-337.

Hastie, E., Kontak, D. and Lafrance, B. 2020. Gold Remobilization: Insights from Gold Deposits in the Archean Swayze Greenstone Belt, Abitibi Subprovince, Canada. *Economic Geology*, **115**(2), pp.241-277.

Hastie, E., Schindler, M., Kontak, D. and Lafrance, B. 2021. Transport and coarsening of gold nanoparticles in an orogenic deposit by dissolution–reprecipitation and Ostwald ripening. *Nature Communications Earth & Environment,* **2**(1), article no: 57 (2021) [no pagination]

Haughton, P., Rogers, G. and Halliday, A. 1990. Provenance of Lower Old Red Sandstone conglomerates, SE Kincardineshire: evidence for the timing of Caledonian terrane accretion in central Scotland. *Journal of the Geological Society*, **147**(1), pp.105-120.

Hayba, D. 1997. Environment of ore deposition in the Creede mining district, San Juan Mountains, Colorado; Part V, Epithermal mineralization from fluid mixing in the OH Vein. *Economic Geology*, **92**(1), pp.29-44.

He, T., Corso, J.D., Newton, R.U., Wignall, P.B., Mills, B.J.W., Todaro, S., Di Stefano, P., Turner, E. C., Jamieson, R.A., Randazzo, V., Rigo, M., Jones, R.E. and Dunhill, A.M. 2020. An enormous sulphur isotope excursion indicates marine anoxia during the end-Triassic mass extinction. *Science Advances*, **6**(37).

Heaman, L.M. and LeCheminant, A.N. 1993. Paragenesis and U-Pb systematics of baddeleyite (ZrO2). *Chemical Geology*, **110**(1-3), pp.95-126.

Heaman, L.M. 2009. The application of U–Pb geochronology to mafic, ultramafic and alkaline rocks: An evaluation of three mineral standards. *Chemical Geology*, **261**(1-2), pp.43-52.

Hedenquist, J. and M. Aoki. 1991. Meteoric interaction with magmatic discharges in Japan and the significance for mineralization. *Geology*, **19**(10), pp.1041-1044.

Hedenquist, J.W., Simmons, S.F., Giggenbach, W.F. and Eldridge, C.S. 1993. White Island, New Zealand, volcanic-hydrothermal system represents the geo-chemical environment of high-sulphidation Cu and Au ore deposition. *Geology*, **21**, pp.731-734.

Hedenquist, J. and Lowenstern, J. 1994. The role of magmas in the formation of hydrothermal ore deposits. *Nature*, **370**(1), pp.519-527.

Hedenquist, J.W., Matsuhisa, Y., Izawa, E., White, N.C., Giggenbach, W. F. and Aoki, M. 1994. Geology, geochemistry, and origin of high sulphidation Cu-Au mineralization in the Nansatsu district, Japan. *Economic Geology*, **89**, pp.1-30.

Hedenquist, J.W., Arribas, A., Jr. and Reynolds, T.J. 1998. Evolution of an intrusion-centered hydrothermal system: Far Southeast-Lepanto porphyry and epithermal Cu-Au deposits, Philippines. *Economic Geology*, **93**, pp.373-405.2

Hedenquist, J.W. Aribas A.R., Golzalez-Urien, E., 2000a. Exploration for epithermal gold deposits. In: Hagemann, S. and Brown, P. *Gold in 2000.* Society of Economic Geologists, pp.245-277.

Hedenquist, J., Arribas, A. and Gonzalez-Urien. 2000b. Exploration for Epithermal Gold Deposits. In: Hagemann, S. and Brown, P. eds. *Gold in 2000*. Society of Economic Geologists, pp.245-276.

Hedenquist, J.W. and Arribas, A. 2022. Exploration Implications of Multiple Formation Environments of Advanced Argillic Minerals. *Economic Geology*, **117**(3), 609-643.

Heinrich, C.A., Driesner, T., Stefánsson, A. and Seward, T.M. 2004. Magmatic vapor contraction and the transport of gold from the porphyry environment to epithermal ore deposits. *Geology*, **32**(9), pp.761-764.

Henderson, W.T. and Robertson, A.H.F. 1982. The Highland Border rocks and their relation to marginal basin development in the Scottish Caledonides. *Journal of the Geological Society*, **139**(4), pp.433-450.

Henley, R.W., Norris, R.J. and Paterson, C.J. 1976. Multistage ore genesis in the New Zealand geosyncline a history of post-metamorphic lode emplacement. *Mineralium deposita*, **11**, pp.180-196.

Henley, R. 1985. The Geothermal Framework of Epithermal Deposits. In: Berger, B. and Bethke, P. ed(s). *Geology and Geochemistry of Epithermal Systems*. Society of Economic Geologists.

Henwood, W.J. 1871. Notes on the Molybdenite of Tomnadashan in Perthshire. In: Henwood, W.J. ed. *Observations on Metalliferous Deposits and Subterranean Temperature*. Royal Geological Society of Cornwall (Transactions of the Royal Geological Society of Cornwall), pp.650-654.

Herrington, R.J. and Wilkinson, J.J. 1993. Colloidal gold and silica in mesothermal vein systems. *Geology*, **21(**6), pp.539-542.

Herzig, P.M., Hannington, M.D., Fouquet, Y., von Stackelberg, U. and Petersen, S. 1993. Gold-rich polymetallic sulfides from the Lau back arc and implications for the geochemistry of gold in sea-floor hydrothermal systems of the Southwest Pacific. *Economic Geology*, **88**(8), pp.2182-2209.

Hiess, J., Condon, D.J., McLean, N., Noble, S.R. 2012. 238U/235U systematics in terrestrial uranium-bearing minerals. *Science*, **335** (6076), pp.1610-1614.

Higgins, A., Gilotti, J. and Smith, M. 2008. *The Greenland Caledonides.* Boulder: Geological Society of America.

Hill, N., Jenkin, G., Boyce, A., Sangster, C., Catterall, D., Holwell, D., Naden, J. and Rice, C. 2013. How the Neoproterozoic S-isotope record illuminates the genesis of vein gold systems: an example from the Dalradian Supergroup in Scotland. *Geological Society, London, Special Publications*, **393**(1), pp.213-247.

Hill., N. 2014. Development of a genetic model for targeting gold mineralisation in the Dalradian Supergroup, Scotland. Ph.D. thesis, University of Leicester.

Hirata, T. 1996. Lead isotopic analyses of NIST standard reference materials using multiple collector inductively coupled plasma mass spectrometry coupled with a modified external correction method for mass discrimination effect. *Analyst*, **121**(10), pp.1407-1411.

Hnatyshin, D., Creaser, R.A., Wilkinson, J.J. and Gleeson, S.A. 2015. Re-Os dating of pyrite confirms an early diagenetic onset and extended duration of mineralization in the Irish Zn-Pb ore field. *Geology*, **43**(2), pp.143-146.

Hoefs, J. 2009. *Stable Isotope Geochemistry*. Sixth edition. Berlin: SpringerVerlag.

Hodgson, C.J., and MacGeehan, P.J., 1982, Geological characteristics of gold deposts in the Superior Province of the Canadian Shield. In: Hodder, R.W., and Petruk, W. Ed(s). *Geology of Canadian Gold Deposits, Proceedings of the CIM Gold Symposium*. Institute of Mining and Metallurgy, pp.211-229.

Hodgson, C.J. 1989. The structure of shear-related, vein-type gold deposits: a review. *Ore Geology Reviews*, **4**, pp.231-273.

Hodkiewicz, P., Weinberg, R., Gardoll, S. and Groves, D. 2005. Complexity gradients in the Yilgarn Craton: fundamental controls on crustal-scale fluid flow and the formation of world-class orogenic-gold deposits. *Australian Journal of Earth Sciences*, **52**, pp.831-841.

Hodkiewicz, P.F., Groves, D.I., Davidson, G.J., Weinberg, R.F. and Hagemann, S.G. 2009. Influence of structural setting on sulphur isotopes in Archean orogenic gold deposits, Eastern Goldfields Province, Yilgarn, Western Australia. *Mineralium Deposita*, **44**(2), pp.129-150.

Hofstra, A.H., Leventhal, J.S., Northrop, H.R., Landis, G.P., Rye, R.O., Birak, D.G. and Dahl, A.R. 1991. Genesis of sediment-hosted disseminated-gold deposits by fluid mixing and sulfidization: Chemical-reaction-path modeling of ore-depositional processes documented in the Jerritt Canyon district, Nevada. *Geology*, **19**(1), pp.36-40.

Hogmalm, K.J., Dahlgren, I., Fridolfsson, I. and Zack, T. 2019. First in situ Re-Os dating of molybdenite by LA-ICP-MS/MS. *Mineralium Deposita*, **54**(6), pp.821-828.

Holdsworth R.E. 1990. Progressive deformation structures associated with ductile thrusts in the Moine Nappe, Sutherland, N. Scotland. *Journal of Structural Geology*, **12**, pp.443-452.

Holland, H.D. 1965. Some applications of thermochemical data to problems of ore deposits; [Part] 2, Mineral assemblages and the composition of ore forming fluids. *Economic Geology*, **60**(6), pp.1101-1166.

Holland, H.D. 1972. Granites, Solutions, and Base Metal Deposits. *Economic Geology and the Bulletin of the Society of Economic Geologists,* **67**(3), pp.281-301.

Holmes, A. 1946. An estimate of the age of the earth. *Nature*, **157**, pp.680-684.

Holzheid, A. and Grove, T.L. 2002. Sulfur saturation limits in silicate melts and their implications for core formation scenarios for terrestrial planets. *American Mineralogist*, **87**(2-3), pp.227-237.

Horstwood, M.S.A., Foster, G.L., Parrish, R.R., Noble, S.R. and Nowell, G.M. 2003. Common-Pb corrected in situ U–Pb accessory mineral geochronology by LA-MC-ICP-MS. *Journal of Analytical Atomic Mass Spectrometry*, **18**(8), pp.837-846.

Hoskin, P.W. 2000. Patterns of chaos: Fractal statistics and the oscillatory chemistry of zircon. *Geochim Cosmochima Acta*, **64**, pp.1905-1923.

Hough, R.M., Noble, R.R.P. and Reich, M. 2011. Natural gold nanoparticles. *Ore Geology Reviews*, **42**(1), pp.55-61.

Hronsky, J.M., Groves, D.I., Loucks, R.R. and Begg, G.C. 2012. A unified model for gold mineralisation in accretionary orogens and implications for regional-scale exploration targeting methods. *Mineralium Deposita*, **47**, pp.339-358.

Hu, H., Li, J., Lentz, D., Ren, Z., Zhao, X., Deng, X. and Hall, D. 2014. Dissolution–reprecipitation process of magnetite from the Chengchao iron deposit: Insights into ore genesis and implication for in-situ chemical analysis of magnetite. *Ore Geology Reviews*, **57**, pp.393-405.

Hu, S., Evans, K., Craw, D., Rempel, K., Bourdet, J., Dick, J. and Grice, K. 2015. Raman characterization of carbonaceous material in the Macraes orogenic gold deposit and metasedimentary host rocks, New Zealand. *Ore Geology Reviews*, **70**, pp.80-95.

Huang, Y., Sun, X., Shi, G., Sa, R., Guan, Y., Jiang, X. and Que, H. 2015. Re–Os dating of sulphides from the Yushui Cu-polymetallic deposit in eastern Guangdong Province, South China. *Ore Geology Reviews*, **70**, pp.281-289.

Hubberten, H.W. 1980. Sulfur isotope fractionations in the Pb-S, Cu-S and Ag-S systems. *Geochemical Journal*, **14**(4), pp.177-184.

Hudson, N.F. 1980. Regional metamorphism of some Dalradian pelites in the Buchan area, NE Scotland. *Contributions to Mineralogy and Petrology*, **73**, pp.39-51.

Hudson, N.F. 1985. Conditions of Dalradian metamorphism in the Buchan area, NE Scotland. *Journal of the Geological Society*, **142**(1), pp.63-76.

Huestis, S.P. 2002. Understanding the Origin and Meaning of the Radioactive Decay Equation. *Journal of Geoscience Education*, **50**(5), 524-527.

Hulin, C.D. 1929. Structural control of ore deposition. *Economic Geology*, **24**(1), pp.15-49.

Hurtig, N.C. and Williams-Jones, A.E. 2015. Porphyry-epithermal Au-Ag-Mo ore formation by vapor-like fluids: New insights from geochemical modeling. *Geology*, **43**(7), pp.587-590.

Huston, D.L. 1997. Stable Isotopes and Their Significance for Understanding the Genesis of Volcanic-Hosted Massive Sulfide Deposits. In: Barrie, C.T.D. and Hannington, M.D. ed(s). *Volcanic Associated Massive Sulfide Deposits: Processes and Examples in Modern and Ancient Settings.* Society of Economic Geologists.

Huston, D.L., Champion, D.C., Morrison, G., Mass, R., Thorne, J.P., Carr, G., Beams, S., Bottrill, R., Chang, Z-S., Dhnaram, C., Downe, P.M., Forster, D.B., Gemmell, J.B., Lisitsin, V., McNeill, A. and Vicary, M. 2017. *Spatial variations in lead isotopes, Tasman Element, eastern Australia.* Townsville: James Cook University.

Huston, D.L. and Champion, D.C. 2023. Applications of Lead Isotopes to Ore Geology, Metallogenesis and Exploration. In: Huston, D. and Gutzmer, J. ed(s). *Isotopes in Economic Geology, Metallogenesis and Exploration*. Springer.

Huston, D.L., Trumbull, R.B, Beaudoin, G. and Ireland, T. 2023. Light Stable Isotopes (H, B, C, O and S) in Ore Studies—Methods, Theory, Applications and Uncertainties. In: Huston, D. and Gutzmer, J. ed(s). *Isotopes in Economic Geology, Metallogenesis and Exploration*. Springer.

Hutchison, W., Finch, A. and Boyce, A. 2020. The sulphur isotope evolution of magmatic-hydrothermal fluids: insights into ore-forming Schwprocesses. *Geochimica et Cosmochimica Acta*, **288**, pp.176-198.

Hutchison, W., Finch, A., Borst, A., Marks, M., Upton, B., Zerkle, A., Stüeken, E. and Boyce, A. 2021. Mantle sources and magma evolution in Europe's largest rare earth element belt (Gardar Province, SW Greenland): New insights from sulphur isotopes. *Earth and Planetary Science Letters*, **568**, article no: 117034 [no pagination]

Hutton, D.H.W. 1982. A tectonic model for the emplacement of the Main Donegal Granite, NW Ireland. *Journal of the Geological Society*, **139**(5), pp.615-631.

Hutton, D., Aftalion, M. and Halliday, A. 1985. An Ordovician ophiolite in County Tyrone, Ireland. *Nature*, **315**(6016), pp.210-212.

Hutton, D.H. 1988. Igneous emplacement in a shear-zone termination: the biotite granite at Strontian, Scotland. *Geological Society of America Bulletin*, **100**(9), pp.1392-1399.

Hutton, D.H.W. and McErlean, M. 1991. Silurian and early Devonian sinistral deformation of the Ratagain granite, Scotland: constraints on the age of Caledonian movements on the Great Glen fault system. *Journal of the Geological Society*, **148**(1), pp.1-4.

Hutton, D.H.W. and Reavy, R.J. 1992. Strike-slip tectonics and granite petrogenesis. *Tectonics*, **11**(5), pp.960-967.

Huyskens, M.H., Zink, S. and Amelin, Y. 2016. Evaluation of temperature-time conditions for the chemical abrasion treatment of single zircons for U–Pb geochronology. *Chemical Geology*, **438**, pp.25-35.

Hyndman, R.D., McCrory, P.A., Wech, A., Kao, H. and Ague, J. 2015. Cascadia subducting plate fluids channelled to fore-arc mantle corner: ETS and silica deposition. *Journal of Geophysical Research: Solid Earth*, **120**(6), pp.4344-4358.

Imai, A. 1999. Pyrite Disease in Luzonite from the Lepanto Cu-Au Deposit, Mankayan, Philippines: further example of disease texture and its origin. *Resource Geology*, **49**, pp.163-168.

Ingebritsen, S.E. and Manning, C.E. 2010. Permeability of the continental crust: dynamic variations inferred from seismicity and metamorphism. *Geofluids*, **10**(1-2), pp.193-205.

Inghram, M.G. 1954. Stable isotope dilution as an analytical tool. *Annual Review of Nuclear Science*, **4**(1), pp.81-92.

Ishihara, S., Jin, M. and Sasaki, A. 2000. Source Diversity of Ore Sulphur from Mesozoic-Cenozoic Mineral Deposits in the Korean Peninsula Region. *Resource Geology*, **50**(4), pp.203-212.

Ixer, R., Pattrick, R. and Stanley, C. 1997. Geology, mineralogy and genesis of gold mineralization at Calliachar-Urlar Burn, Scotland. *Transactions of the Institution of Mining and Metallurgy Section B-Applied Earth Science*, **106**, pp.99-108.

Jacques, J.M. and Reavy, R.J. 1994. Caledonian plutonism and major lineaments in the SW Scottish Highlands. *Journal of the Geological Society*, **151**(6), pp.955-969.

Jaffey, A.H., Flynn, K.F., Glendenin, L.E., Bentley, W.C. and Essling, A.M. 1971. Precision Measurement of Half-Lives and Specific Activities of 235U and 238U. *Physical Review C*, *4*(5), pp. 1889-1906.

Jäger, E. 1979. Introduction to Geochronology. In: Jäger E., Hunziker J.C. ed(s). *Lectures in Isotope Geology*. Berlin: Springer, pp.1-12.

Jamielita, R.A., Davis, D.W., Krough, T.E. 1990. U–Pb evidence for Abitibi gold mineralization postdating greenstone magmatism and metamorphism. *Nature,* **346**, pp.831-834.

Janots, E., Engi, M., Rubatto, D., Berger, A., Gregory, C. and Rahn, M. 2009. Metamorphic rates in collisional orogeny from in situ allanite and monazite dating. *Geology*, **37,** pp.11-14.

Jenkin, G.R.T., Craw, D. and Fallick, A.E. 1994. Stable isotopic and fluid inclusion evidence for meteoric fluid penetration into an active mountain belt; Alpine Schist, New Zealand. *Journal of Metamorphic Geology*, **12**(4), pp.429-444.

Jensen, M. 1959. Sulphur isotopes and hydrothermal mineral deposits. *Economic Geology*, **54**(3), pp.374-394.

Jia, Y., Kerrich, R. and Goldfarb, R. 2003. Metamorphic origin of ore-forming fluids for orogenic gold-bearing quartz vein systems in the North American cordillera: Constraints from a reconnaissance study of δ 15N, δ D, and δ 18O. *Economic Geology*, **98**(1), pp.109-123.

Johnson, J.W., Oelkers, E.H. and Helgeson, H.C. 1992. SUPCRT92: A software package for calculating the standard molal thermodynamic properties of minerals, gases, aqueous species, and reactions from 1 to 5000 bar and 0 to 1000°C. *Computers & Geosciences*, **18**(7), pp.899-947.

Johnson, C.C. and Breward, N., 2004. *G-BASE: geochemical baseline survey of the environment.* Keyworth: British Geological Survey.

Johnston, D.T., Farquhar, J. and Canfield, D.E. 2007. Sulfur isotope insights into microbial sulfate reduction: When microbes meet models. *Geochimica et Cosmochimica Acta*, **71**(16), pp.3929-3947.

Johnstone, G.S. and Smith, D.I. 1965. Geological observations concerning the Breadalbane Hydroelectric project, Perthshire. *Bulletin of the Geological Survey of Great Britain*, **22**, pp.1-52.

Joly, A., Porwal, A., McCuaig, T., Chudasama, B., Dentith, M. and Aitken, A. 2015. Mineral systems approach applied to GIS-based 2D-prospectivity modelling of geological regions: Insights from Western Australia. *Ore Geology Reviews*, **71**, pp.673-702.

Jones, R.R., Holdsworth, R.E. and Bailey, W. 1997. Lateral extrusion in transpression zones: the importance of boundary conditions. *Journal of Structural Geology*, **19**(9), pp.1201-1217.

Jowett, E.C., Roth, T., Rydzewski, A. and Oszczepalski, S. 1991. "Background" δ 34 S values of Kupferschiefer sulphides in Poland: pyrite-marcasite nodules. *Mineralium Deposita*, **26**, pp.89-98.

Kalsbeek, F., Thrane, K., Higgins, A.K., Jepsen, H.F., Leslie, A.G., Nutman, A.P., and Frei, R. 2008. Polyorogenic history of the East Greenland Caledonides. In: Higgins, A.K., Gilotti, J.A. and Smith, M.P. ed(s). *The Greenland Caledonides: Evolution of the Northeast Margin of Laurentia*. Geological Society of America, pp.55-72.

Kamilli, R.J. 1998. Paragenesis. In: Marshall, C.P. and Fairbridge, R.W. ed(s). *Encyclopedia of Geochemistry*. Dordrecht, Springer, pp.485-488.

Kajiwara, Y., Krouse, H.R. and Sasaki, A. 1969. Experimental study of sulphur isotope fractionation between coexistent sulfide minerals. *Earth and Planetary Science Letters*, **7**(3), pp.271-277.

Kajiwara, Y. and Krouse, H.R. 1971. Sulphur isotope partitioning in metallic sulfide systems. Canadian Journal of Earth Sciences, **8**, pp.1397-1408.

Keith, T.E.C. and Muffler, L.P.J. 1978. Minerals produced during cooling and hydrothermal alteration of ash flow tuff from Yellowstone drill hole Y-5. *Journal of Volcanology and Geothermal Research*, **3**, pp. 373-402.

Keller, C.B., Schoene, B. and Samperton, K.M. 2018. A stochastic sampling approach to zircon eruption age interpretation. *Geochemical Perspectives Letters*, pp.31-35.

Kelley, S.P. and Fallick, A.E. 1990. High precision spatially resolved analysis of δ34S in sulphides using a laser extraction technique. *Geochimica et Cosmochimica Acta*, **54**(3), pp.883-888.

Kelley, K., Spry, P., McLemore, V., Fey, D. and Anderson, E. 2020. *Alkalic-Type Epithermal Gold Deposit Model: Chapter R of Mineral Deposit Models for Resource Assessment*. Reston, VA: United States Geological Survey.

Kerrich, R. and Fyfe, W.S. 1981. The gold—carbonate association: Source of CO2, and CO2 fixation reactions in Archaean lode deposits. *Chemical Geology*, **33**(1-4), pp. 265-294.

Kerrich, R. 1989. Archean gold: Relation to granulite formation or felsic intrusions?. *Geology*, **17**(11), pp.1011-1015.

Kerrich, R., Jia, Y., Manikyamba, C., and Naqvi, S.M. 2006. Secular variations of N-isotopes in terrestrial reservoirs and ore deposits. In: Kesler, S. and Ohmoto, H. *Evolution of Early Earth's Atmosphere, Hydrosphere, and Biosphere - Constraints from Ore Deposits*. Geological Society of America.

Kesler, S.E., Jones, H.D., Furman, F.C., Sassen, R., Anderson, W.H. and Kyle, J.R. 1994. Role of crude oil in the genesis of Mississippi Valley-type deposits: Evidence from the Cincinnati arch. *Geology*, **22**(7), pp.609-612.

Kesler, S.E., Chryssoulis, S.L. and Simon, G. 2002. Gold in porphyry copper deposits: its abundance and fate. *Ore Geology Reviews*, **21**(1-2), pp.103-124.

Kesler, S. and Wilkinson, B. 2008. Earth's copper resources estimated from tectonic diffusion of porphyry copper deposits. *Geology*, **36**(3), p.255.

Ketcham, R.A., Donelick, R.A. and Carlson, W.D. 1999. Variability of apatite fission-track annealing kinetics; III, Extrapolation to geological time scales. *American Mineralogist*, **84**(9), pp.1235-1255.

Kinnaird, J.A., Ixer R.A., Barreiro B. and Nex P.A.M. 2002. Contrasting sources for lead in Cu-polymetallic and Zn-Pb mineralization in Ireland: constraints from lead isotopes. *Mineralium Deposita*, **37**, pp.495-511.

Kinny, P.D., Strachan, R.A., Friend, C.R.L., Kocks, H., Rogers, G. and Paterson, B.A. 2003a. U–Pb geochronology of deformed metagranites in central Sutherland, Scotland: evidence for a widespread late metamorphism and ductile deformation of the Moine Supergroup during the Caledonian orogeny. *Journal of the Geological Society, London*, **160**, pp.259-269.

Kinny, P.D., Strachan, R.A., Friend, C.R.L., Kocks, H., Rogers, G. and Paterson, B.A. 2003b. U–Pb geochronology of deformed metagranites in central Sutherland, Scotland: evidence for widespread late Silurian metamorphism and ductile deformation of the Moine Supergroup during the Caledonian orogeny. *Journal of the Geological Society*, **160**(2), pp.259-269.

Kirkland, C., Alsop, G., Daly, J., Whitehouse, M., Lam, R. and Clark, C. 2013. Constraints on the timing of Scandian deformation and the nature of a buried Grampian terrane under the Caledonides of northwestern Ireland. *Journal of the Geological Society*, **170**(4), pp.615-625.

Kirkwood, C., Everett, P., Ferreira, A. and Lister, B. 2016. Stream sediment geochemistry as a tool for enhancing geological understanding: An overview of new data from south west England. *Journal of Geochemical Exploration*, **163**, pp.28-40.

Kiyosu, Y. 1973. Sulfur isotopic fractionation among sphalerite, galena and sulfide ions. *Geochemical Journal*, **7**(4), pp.191-199.

Kiyosu, Y. 1980. Chemical reduction and sulfur-isotope effects of sulfate by organic matter under hydrothermal conditions. *Chemical Geology*, **30**(1-2), pp.47-56.

Klein, S., Rose, T., Westner, K. J. and Hsu, Y.-K. 2022. From OXALID to GlobaLID: Introducing a modern and FAIR lead isotope database with an interactive application. *Archaeometry*, **64**(4), 935-950.

Kneller, B. and Aftalion, M. 1987. The isotopic and structural age of the Aberdeen Granite. *Journal of the Geological Society*, **144**(5), pp.717-721.

Knesel, K.M. and Davidson, J.P. 1999. Sr isotope systematics during melt generation by intrusion of basalt into continental crust. *Contributions to Mineralogy and Petrology*, **136**(3), pp.285-295.

Kocks, H. and Strachan, R.A. 2006. Heterogeneous reworking of Grampian metamorphic complexes during Scandian thrusting in the Scottish Caledonides; insights from the structural setting and U–Pb geochronology of the Strath Halladale Granite. *Journal of the Geological Society, London*, **163**, pp.525-538.

Kogan, V.V., Hinds, M.W. and Ramendik, G.I. 1994. The direct determination of trace metals in gold and silver materials by laser ablation inductively coupled plasma mass spectrometry wit2hout matrix matched standards. *Spectrochimica Acta Part B: Atomic Spectroscopy*, **49**, pp.333-343.

Konopinski, E.J. 1943. Beta-decay. *Reviews of Modern Physics*, **15**(4).

Kontak, D.J. and Smith, P.K. 1989. Sulphur isotopic composition of sulphides from the Beaver Dam and other Meguma-Group-hosted gold deposits, Nova Scotia: implications for genetic models. *Canadian Journal of Earth Sciences*, **26(**8), pp.1617-1629.

Kouzmanov, K. and Pokrovski, G. 2012. Hydrothermal Controls on Metal Distribution in Porphyry Cu (-Mo-Au) Systems. In: Hedenquist, J., Harris, M. and Camus, F. Ed(s). *Geology and Genesis of Major Copper Deposits and Districts of the World: A Tribute to Richard H. Sillitoe*. Society of Economic Geologists.

Krabbendam, M., Leslie, A.G., Crane, A. and Goodman, S. 1997. Generation of the Tay Nappe, Scotland, by large-scale SE-directed shearing. *Journal of the Geological Society*, **154**(1), pp.15-24.

Kramers, J.D. and Tolstikhin, I.N. 1997. Two terrestrial lead isotope paradoxes, forward transport modelling, core formation and the history of the continental crust. *Chemical geology*, **139**(1-4), pp.75-110.

Krawczyk, C.M., McCann, T., Cocks, L.R.M., England, R.W., McBride, J.H. and Wybraniec, S. 2008. *Caledonian tectonics*. In: McCann, T. ed(s). *The Geology of Central Europe Volume 1: Precambrian and Palaeozoi*c. London: Geological Society, pp.303-381

Krogh, T.E. 1982. Improved accuracy of U-Pb zircon ages by the creation of more concordant systems using an air abrasion technique. *Geochimica et Cosmochimica Acta*, **46**(4), pp.637-649.

Krogh, T., Kamo, S., Robinson, P., Terry, M. and Kwok, K. 2011. U-Pb zircon geochronology of eclogites from the Scandian Orogen, Northern Western Gneiss Region, Norway: 14-20 million years between eclogite crystallization and return to amphibolite facies conditions. *Canadian Journal of Earth Sciences*, **48**, pp.441-472.

Labidi, J., Cartigny, P. and Moreira, M. 2013. Non-chondritic sulphur isotope composition of the terrestrial mantle. *Nature*, **501**(7466), pp.208-211.

Labuz, J.F. and Zang, A. 2014. Mohr–Coulomb failure criterion. In: Ulusay, R. ed. The ISRM Suggested Methods for Rock Characterization, Testing and Monitoring: 2007-2014. Springer International Publishing, pp.227-231.

LaFlamme, C., Sugiono, D., Thébaud, N., Caruso, S., Fiorentini, M., Selvaraja, V., Jeon, H., Voute, F. and Martin, L. 2018. Multiple sulfur isotopes monitor fluid evolution of an Archean orogenic gold deposit. *Geochimica et Cosmochimica Acta*, **222**, pp.436-446.

Lambert, R. and McKerrow, W. 1976. The Grampian Orogeny. *Scottish Journal of Geology*, **12**(4), pp.271-292.

Large, R.R., Danyushevsky, L., Hollit, C., Maslennikov, V., Meffre, S., Gilbert, S., Bull, S., Scott, R., Emsbo, P., Thomas, H., Singh, B. and Foster, J. 2009. Gold and Trace Element Zonation in Pyrite Using a Laser Imaging Technique: Implications for the Timing of Gold in Orogenic and Carlin-Style Sediment-Hosted Deposits. *Economic Geology*, **104**(5), pp.635-668.

Large, R.R., Bull, S.W. and Maslennikov, V.V. 2011. A carbonaceous sedimentary source-rock model for Carlin-type and orogenic gold deposits. *Economic Geology*, **106**, pp.331-358.

Large, R.R., Gregory, D.D., Steadman, J.A., Tomkins, A.G., Lounejeva, E., Danyushevsky, L.V., Halpin, J.A., Maslennikov, V., Sack, P.J., Mukherjee, I., Berry, R. and Hickman, A. 2015. Gold in the oceans through time. *Earth and Planetary Science Letter*s, **428**, pp.139-150.

Lavelle, A. 2020a. *Report on the Detailed Mapping of the Calliachar-Urlar Gold Prospect, Aberfeldy Scotland*. Erris Gold Resources.

Lavelle, A. 2020b. *Channel Sampling Results & Scout Drill Targets Lead Trial 2020-2021*. Erris Gold Resources.

Lawley, C. and Selby, D. 2012. Re-Os GEOCHRONOLOGY OF QUARTZ-ENCLOSED ULTRAFINE MOLYBDENITE: IMPLICATIONS FOR ORE GEOCHRONOLOGY. *Economic Geology*, **107**(7), pp.1499-1505.

Lawley, C., Selby, D. and Imber, J. 2013. Re-Os Molybdenite, Pyrite, and Chalcopyrite Geochronology, Lupa Goldfield, Southwestern Tanzania: Tracing Metallogenic Time Scales at Midcrustal Shear Zones Hosting Orogenic Au Deposits. *Economic Geology*, **108**(7), pp.1591-1613.

Lawley, C.J.M., Creaser, R.A., Jackson, S.E., Yang, Z., Davis, B.J., Pehrsson, S.J., Dubé, B., Mercier-Langevin, P. and Vaillancourt, D. 2015. Unraveling the Western Churchill Province Paleoproterozoic Gold Metallotect: Constraints from Re-Os Arsenopyrite and U-Pb Xenotime Geochronology and LA-ICP-MS Arsenopyrite Trace Element Chemistry at the BIF-Hosted Meliadine Gold District, Nunavut, Canada. *Economic Geology*, **110**(6), pp.1425-1454.

Lawrence, D.M., Treloar, P.J., Rankin, A.H., Boyce, A. and Harbidge, P. 2013. A Fluid Inclusion and Stable Isotope Study at the Loulo Mining District, Mali, West Africa: Implications for Multifluid Sources in the Generation of Orogenic Gold Deposits. *Economic Geology*, **108**(2), pp.229-257.

Le Huray, A.P., Caulfield, J.B.D., Rye, D.M. and Dixon, P.R. 1987. Basement controls on sediment-hosted Pb-Zn deposits: a lead isotope study of Carboniferous mineralization in Central Ireland. *Economic Geology*, **82**, pp.1695-1709.

Leach, D.L., Sangster, D.F., Kelley, K.D., Large, R.R., Garven, G., Allen, C.R., Gutzmer, J. and Walters, S. 2005. Sediment-hosted lead-zinc deposits: A global perspective. In: Hedenquist, J., Thompson, J., Goldfarb, R. and Richards, J. ed(s). *100th Anniversary Volume*. Society of Economic Geologists.

Leach, D., Macquar, J., Lagneau, V., Leventhal, J., Emsbo, P. and Premo, W. 2006. Precipitation of lead-zinc ores in the Mississippi Valley-type deposit at Treves, Cevennes region of southern France. *Geofluids*, **6**(1), pp.24-44.

Lee, J.K.W., Williams, I.S. and Ellis, D.J. 1997. Pb, U and Th diffusion in natural zircon. *Nature*, **390**(6656), pp.159-162.

Leng, C.-B., Zhang, X.-C., Huang, Z.-L., Huang, Q.-Y., Wang, S.-X., Ma, D.-Y., Luo, T.-Y., Li, C. and Li, W.-B. 2015. Geology, Re-Os ages, sulfur and lead isotopes of the Diyanqinamu Porphyry Mo Deposit, Inner Mongolia, NE China. *Economic Geology*, **110**(2), pp.557-574.

Leslie, A.G, Smith, M. and Soper, N.J. 2008. Laurentian margin evolution and the Caledonian orogeny–a template for Scotland and East Greenland. In: Higgins, A.K., Gilotti, J.A. and Smith, M.P. *The Greenland Caledonides: Evolution of the Northeast Margin of Laurentia*. Geological Society of America, pp.307-343.

Lever, M.A., Rouxel, O., Alt, J. C., Shimizu, N., Ono, S., Coggon, R. M., Shanks, W. C., Lapham, L., Elvert, M., Prieto-Mollar, X., Hinrichs, K.-U., Inagaki, F. and Teske, A. 2013. Evidence for Microbial Carbon and Sulphur Cycling in Deeply Buried Ridge Flank Basalt. *Science*, **339**(6125), pp.1305-1308.

Li, Z.K., Li, J.W., Cooke, D.R., Danyushevsky, L., Zhang, L., O'Brien, H., Lahaye, Y., Zhang, W. and Xu, H.J. 2016a. Textures, trace elements, and Pb isotopes of sulfides from the Haopinggou vein deposit, southern North China Craton: implications for discrete Au and Ag–Pb–Zn mineralization. *Contributions to Mineralogy and Petrology*, **171**, pp.1-26.

Li, Y., Selby, D., Feely, M., Costanzo, A. and Li, X. 2016b. Fluid inclusion characteristics and molybdenite Re-Os geochronology of the Qulong porphyry copper-molybdenum deposit, Tibet. *Mineralium Deposita*, **52**(2), pp.137-158.

Li, Y., Selby, D., Condon, D. and Tapster, S. 2017. Cyclic Magmatic-Hydrothermal Evolution in Porphyry Systems: High-Precision U-Pb and Re-Os Geochronology Constraints on the Tibetan Qulong Porphyry Cu-Mo Deposit. *Economic Geology*, **112**(6), pp.1419-1440.

Li, Y., Zhang, S., Hobbs, R., Caiado, C., Sproson, A.D., Selby, D. and Rooney, A.D. 2019. Monte Carlo sampling for error propagation in linear regression and applications in isochron geochronology. *Science Bulletin*, **64**(3), pp.189-197.

Li, R., Chen, H., Large, R., Zhao, L., Liu, Y., Jiao, J., Xia, X. and Yang, Q. 2020. Ore-forming fluid source of the orogenic gold deposit: Implications from a combined pyrite texture and geochemistry study. *Chemical Geology*, **552**, article no: 119781 [no pagination]

Li, H., Wang, Q., Yang, L., Dong, C., Weng, W. and Deng, J. 2022a. Alteration and mineralization patterns in orogenic gold deposits: Constraints from deposit observation and thermodynamic modeling. *Chemical Geology*, **607**, article no: 121012 [no pagination]

Li, H., Wang, Q., Wenig, W., Dong, C., Yang, L., Wang, X. and Deng, J. 2022b. Co-precipitation of gold and base metal sulfides during fluid boiling triggered by fault-valve processes in orogenic gold deposits. *Ore Geology Reviews*, **149**, article no: 105090 [no pagination]

Lindgren, W. 1933. *Mineral deposits.* New York: McGraw HillBook Co.

Lisle, R. and Srivastava, D. 2004. Test of the frictional reactivation theory for faults and validity of fault-slip analysis. *Geology*, **32**(7), pp.569-572.

Liu, J., Wang, A., Xia, H., Zhai, Y., Gao, L., Xiu, Q., Zhang, Z., Zhao, Z. and Cao, D. 2010. Cracking mechanisms during galena mineralization in a sandstone-hosted lead–zinc ore deposit: case study of the Jinding giant sulfide deposit, Yunnan, SW China. *Mineralium Deposita*, **45**(6), pp.567-582.

Liu, W., Etschmann, B., Testemale, D., Hazemann, J., Rempel, K., Müller, H. and Brugger, J. 2014. Gold transport in hydrothermal fluids: Competition among the Cl−, Br−, HS− and NH3(aq) ligands. *Chemical Geology*, **376**, pp.11-19.

Liu, W., Zhang, J. and Wang, J. 2017. Sulphur isotope analysis of carbonate-hosted Zn–Pb deposits in northwestern Guizhou Province, Southwest China: Implications for the source of reduced sulphur. *Journal of Geochemical Exploration*, **181**, pp.31-44.

Liu, W., Chen, M., Yang, Y., Mei, Y., Etschmann, B., Brugger, J. and Johannessen, B. 2019. Colloidal gold in sulphur and citrate-bearing hydrothermal fluids: An experimental study. *Ore Geology Reviews*, pp.114, article no: 103142 [no pagination]

Lorand, J.P. 1990. Are spinel Iherzolite xenoliths representative of the abundance of sulfur in the upper mantle?. *Geochimica et Cosmochimica Acta*, **54**(5), pp.1487-1492.

Lowell, J. and Guilbert, J. 1970. Lateral and vertical alteration-mineralization zoning in porphyry ore deposits. *Economic Geology*, **65**(4), pp.373-408.

Lowenstern, J.B., Mahood, G.A., Rivers, M.L. and Sutton, S.R. 1991. Evidence for Extreme Partitioning of Copper into a Magmatic Vapor Phase. *Science*, **252**(5011), pp.1405-1409.

Lowry, D. 1991. The genesis of Late Caledonian granitoid-related mineralisation in Northern Britain. Ph.D. thesis, University of St Andrews.

Lowry, D., Boyce, A.B., Fallick, A.E. and Stephens, W.E. 1995. Genesis of porphyry and plutonic mineralisation systems in metaluminous granitoids of the Grampian Terrane, Scotland. *Transactions of the Royal Society of Edinburgh: Earth Science*, **85**, pp. 221-237.

Lowry, D., Boyce, A.J., Fallick, A.E., Stephens, W.E. and Grassineau, N.V. 2005. Terrane and basement discrimination in northern Britain using sulphur isotopes and mineralogy of ore deposits. *Geological Society, London, Special Publications*, **248**(1), pp.264-264.

Lusk, J., Campbell, F.A. and Krouse, H.R. 1975. Application of sphalerite geobarometry and sulfur isotope geothermometry to ores of the Quemont Mine, Noranda, Quebec. *Economic Geology*, **70**(6), pp.1070-1083.

Lusty, P.A., Naden, J., Bouch, J.J., McKervey, J.A. and McFarlane, J.A. 2011. Atypical Gold Mineralization in an Orogenic Setting--The Bohaun Deposit, Western Irish Caledonides. *Economic Geology*, **106**(3), pp.359-380.

Lyubetskaya, T. and Ague, J.J. 2010a. Modeling metamorphism in collisional orogens intruded by magmas: I. Thermal evolution. *American Journal of Science*, **310**(6), pp.427-458.

Lyubetskaya, T. and Ague, J.J., 2010b. Modeling metamorphism in collisional orogens intruded by magmas: II. Fluid flow and implications for Barrovian and Buchan metamorphism, Scotland. *American Journal of Science*, **310**(6), pp.459-491.

Ma, Y., Jiang, S.-Y., Frimmel, H.E. and Zhu, L.-Y. 2022a. In situ chemical and isotopic analyses and element mapping of multiple-generation pyrite: Evidence of episodic gold mobilization and deposition for the Qiucun epithermal gold deposit in Southeast China. *American Mineralogist*, **107**(6), pp.1133-1148.

Ma, Y., Jiang, S.-Y. and Frimmel, H.E. 2022b. Metallogeny of the Late Jurassic Qiucun epithermal gold deposit in southeastern China: Constraints from geochronology, fluid inclusions, and H-O-C-Pb isotopes. *Ore Geology Reviews*, **142**, article no: 104688 [no pagination]

Macdonald, R., Fettes, D.J., Stephenson, D. and Graham, C.M. 2005. Basic and ultrabasic volcanic rocks from the Argyll Group (Dalradian) of NE Scotland. *Scottish Journal of Geology*, **41**(2), pp.159-174.

Macdonald, R. and Fettes, D.J. 2006. The tectonomagmatic evolution of Scotland. *Earth and Environmental Science Transactions of The Royal Society of Edinburgh*, **97**(3), pp.213-295.

Machel, H.G., Krouse, H.R. and Sassen, R. 1995. Products and distinguishing criteria of bacterial and thermochemical sulfate reduction. *Applied geochemistry*, **10**(4), pp.373-389.

MacKenzie, D., Craw, D. and Finnigan, C. 2015. Lithologically controlled invisible gold, Yukon, Canada. *Mineralium Deposita*, **50**, pp.141-157.

Mackinder, A., Cousens, B.L., Ernst, R.E. and Chamberlain, K.R. 2019. Geochemical, isotopic, and U–Pb zircon study of the central and southern portions of the 780 Ma Gunbarrel Large Igneous Province in western Laurentia. *Canadian Journal of Earth Sciences*, **56**(7), pp.738-755.

MacWilliam, K.R.G. 2018. The geology and genesis of the Coffee gold deposit in west-central Yukon, Canada: Implications for the structural, magmatic, and metallogenic evolution of the Dawson Range, and gold deposit models. Ph.D. thesis, University of British Columbia.

Majid, M. 1974. *Mineralogy and Petrology of the Comrie Diorite*. Ph.D. thesis, University of Manchester.

Maloof, T., Baker, T. and Thompson, J. 2001. The Dublin Gulch intrusion-hosted gold deposit, Tombstone plutonic suite, Yukon Territory, Canada. *Mineralium Deposita*, **36**(6), pp.583-593.

Maltese, A. and Mezger, K. 2020. The Pb isotope evolution of Bulk Silicate Earth: Constraints from its accretion and early differentiation history. *Geochimica et Cosmochimica acta*, **271**, pp.179-193.

Mang, H.J. 1964. Alpha decay. *Annual Review of Nuclear Science*, **14**(1), pp.1-26.

Manor, M.J., Piercey, S.J., Wall, C.J. and Denisová, N. 2022. High-Precision CA-ID-TIMS U-Pb Zircon Geochronology of Felsic Rocks in the Finlayson Lake VMS District, Yukon: Linking Paleozoic Basin-Scale Accumulation Rates to the Occurrence of Subseafloor Replacement-Style Mineralization. *Economic Geology,* **117**(5), pp.1173-1201.

Mao, J., Wang, Y., Li, H., Pirajno, F., Zhang, C. and Wang, R. 2008. The relationship of mantle-derived fluids to gold metallogenesis in the Jiaodong Peninsula: evidence from D–O–C–S isotope systematics. *Ore Geology Reviews*, **33**(3-4), pp.361-381.

Marcoux, E. and Milési, J.-P. 1994. Epithermal gold deposits in West Java, Indonesia: geology, age and crustal source. *Journal of Geochemical Exploration*, **50**(1-3), pp.393-408.

Marignac, C. 1989. Sphalerite stars in chalcopyrite: Are they always the result of an unmixing process? *Mineralium Deposita*, **24**, pp.176-182.

Marini, L., Chiappini, V., Cioni, R., Cortecci, G., Dinelli, E., Principe, C. and Ferrara, G. 1998. Effect of degassing on sulphur contents and δ34S values in Somma-Vesuvius magmas. *Bulletin of Volcanology*, **60**(3), pp.187-194.

Marini, L., Moretti, R. and Accornero, M. 2011. Sulphur Isotopes in Magmatic-Hydrothermal Systems, Melts, and Magmas. *Reviews in Mineralogy and Geochemistry*, **73**(1), pp.423-492.

Mark, D., Rice, C., Fallick, A., Trewin, N., Lee, M., Boyce, A. and Lee, J. 2011. $^{40}Ar/^{39}Ar$ dating of hydrothermal activity, biota and gold mineralization in the Rhynie hot-spring system, Aberdeenshire, Scotland. *Geochimica et Cosmochimica Acta*, **75**(2), pp.555-569.

Mark, D.F., Rice, C.M., Hole, M. and Condon, D. 2020. Multi-chronometer dating of the Souter Head complex: rapid exhumation terminates the Grampian Event of the Caledonian Orogeny. *Earth and Environmental Science Transactions of the Royal Society of Edinburgh*, pp.1-14.

Markey, R., Stein, H., Hannah, J., Zimmerman, A., Selby, D. and Creaser, R. 2007. Standardizing Re–Os geochronology: A new molybdenite Reference Material (Henderson, USA) and the stoichiometry of Os salts. *Chemical Geology*, **244**(1-2), pp.74-87.

Marshall, D.J. 1988. *Cathodoluminescence of geological materials*. Unwin Hyman, Boston, 146.

Marshall, J.E.A., Haughton, P.D.W. and Hillier, S.J. 1994. Vitrinite reflectivity and the structure and burial history of the Old Red Sandstone of the Midland Valley of Scotland. *Journal of the Geological Society, London*, **151**, pp.425-438.

Mathieu, L. 2018. Quantifying hydrothermal alteration: a review of methods. *Geosciences*, **8**, article no: 245 [no pagination]

Mathur, R., Ruiz, J., Titley, S., Gibbins, S. and Margotomo, W. 2000. Different crustal sources for Au-rich and Au-poor ores of the Grasberg Cu–Au porphyry deposit. *Earth and Planetary Science Letters*, **183**(1–2), pp.7-14.

Mattinson, J.M., 1973. Anomalous isotopic composition of lead in young zircons. *Carnegie Institute of Washington Yearbook*, **72**, p.613.

Mattinson, J.M. 2005. Zircon U-Pb chemical abrasion ("CA-TIMS") method: Combined annealing and multi-step partial dissolution analysis for improved precision and accuracy of zircon ages. *Chemical Geology*, **220**, pp.47-66.

Mattinson, J.M. 2010. Analysis of the relative decay constants of 235U and 238U by multi-step CA-TIMS measurements of closed-system natural zircon samples. *Chemical Geology*, **275**(3-4), pp.186-198.

Mattinson, J.M. 2011. Extending the Krogh legacy: development of the CA–TIMS method for zircon U–Pb geochronology. *Canadian Journal of Earth Sciences*, **48**(2), pp.95-105.

Matthews, A.D. and Riley, J.P. 1970. The determination of Rhenium in sea water. *Analytica Chimica Acta*, **51**(3), pp.483-488.

Mavrogenes, J.A. and O'Neill, H.S.C. 1999. The relative effects of pressure, temperature and oxygen fugacity on the solubility of sulfide in mafic magmas. *Geochimica et Cosmochimica Acta*, **63**(7-8), pp.1173-1180.

Mazur, S., Mikolajczak, M., Krzywiec, P., Malinowski, M., Lewandowski, M. and Buffenmyer, V. 2016. Pomeranian Caledonides, NW Poland – A collisional suture or thin-skinned fold-and-thrust belt? *Tectonophysics*, **692**, pp.29-43.

McClay, Norton, M. G., Coney, P. and Davis, G. H. 1986. Collapse of the Caledonian orogen and the Old Red Sandstone. *Nature*, **323**(6084), pp.147-149.

McCoy, D.T., Newberry, R.J., Layer, P.W., DiMarchi, J.J., Bakke, Arne, Masterman, J.S., and Minehane, D.L. 1997. Plutonic-related gold deposits of interior Alaska. *Economic Geology*, *Monograp*h, **9**, pp.191-241.

McCuaig, T.C. and Kerrich, R. 1998. P-T-t-deformation fluid characteristics of lode gold deposits: evidence from alteration systematics. *Ore Geology Reviews*, **12**, pp.381-453.

McCuaig, T.C., Beresford, S. and Hronsky, J. 2010. Translating the mineral systems approach into an effective exploration targeting system. *Ore Geology Reviews*, **38**(3), pp.128-138.

McCuaig, T. and Hronsky, J. 2014. The mineral systems concept: the key to exploration targeting. *Applied Earth Science*, **126**(2), pp.77-78.

McDonough, W.F. 2003. Compositional model for the Earth's core. *Treatise on geochemistry*, 2, p.568.

McKanna, A.J., Koran, I., Schoene, B. and Ketcham, R.A. 2022. Chemical abrasion: the mechanics of zircon dissolution. *Geochronology Discussions*, **2022**, pp.1-46.

McKay, L., Shipton, Z.K., Lunn, R.J., Andrews, B., Raub, T.D. and Boyce, A.J. 2020. Detailed internal structure and along-strike variability of the core of a plate boundary fault: the Highland Boundary fault, Scotland. *Journal of the Geological Society*, **177**(2), pp.283-296.

McKellar, Z., Hartley, A.J., Morton, A.C. and Frei, D. 2020. A multidisciplinary approach to sediment provenance analysis of the late Silurian–Devonian Lower Old Red Sandstone succession, northern Midland Valley Basin, Scotland. *Journal of the Geological Society*, **177**(2), pp.297-314.

McKellar, Z., Hartley, A.J., Macdonald, D.I.M., Morton, A. and Frei, D. 2021. Sedimentology and provenance of the Lower Old Red Sandstone Grampian outliers: implications for Caledonian orogenic basin development and the northward extension of the Midland Valley Basin. *Journal of the Geological Society*, **178**(2), article no: jgs2020-141 [no pagination]

McKerrow, W., Mac Niociall, C. and Dewey, J. 2000. The Caledonian Orogeny redefined. *Journal of the Geological Society*, **157**(6), pp.1149-1154.

McKibben, M.A. and Eldridge, C.S. 1990. Radical sulphur isotope zonation of pyrite accompanying boiling and epithermal gold deposition; a SHRIMP study of the Valles Caldera, New Mexico. *Economic Geology*, **85**(8), pp.1917-1925.

McKinney, C.R., McCrea, J.M., Epstein, S., Allen, H.A. and Urey, H.C. 1950. Improvements in Mass Spectrometers for the Measurement of Small Differences in Isotope Abundance Ratios. *Review of Scientific Instruments*, **21**(8), pp.724-730.

McLeish, D.F., Williams-Jones, A.E., Board, W.S. and Clark, J.R. 2018. Nature and origin of the Brucejack high-grade epithermal gold deposit, northwestern British Columbia (NTS 104B): 2017 update; in Geoscience BC Summary of Activities 2017: Minerals and Mining, Geoscience BC, Report 2018-1, pp.31-40.

Meinert, L.D., Dipple, G.M. and Nicolescu, S. 2005. World Skarn Deposits. In: Hedenquist, J., Thompson, J., Goldfarb, R., Richards, J. *One Hundredth Anniversary Volume*. Society of Economic Geologists.

Mendum, J.R. and Fettes, D.J. 1985. The Tay nappe and associated folding in the Ben Ledi–Loch Lomond area. *Scottish Journal of Geology*, **21**(1), pp.41-56.

Mendum, J.R. and Noble, S.R. 2010 Mid-Devonian sinistral transpressional movements on the Great Glen Fault: the rise of the Rosemarkie Inlier and the Acadian Event in Scotland. In: Law, R.D, Butler, R.,

Holdsworth, R.E., Krabbendam, M. and Strachan, R.A. ed(s). *Continental Tectonics and Mountain Building: the Legacy of Peach and Horne*. London: Geological Society Special Publications, pp.161-87.

Mendum, J.R. 2012. Late Caledonian (Scandian) and Proto-Variscan (Acadian) orogenic events in Scotland. *Journal of the Open University Geological Society*, **33**(1), pp.37-51.

Menzies, C.D., Teagle, D.A., Craw, D., Cox, S.C., Boyce, A.J., Barrie, C.D. and Roberts, S., 2014. Incursion of meteoric waters into the ductile regime in an active orogen. *Earth and Planetary Science Letters*, **399**, pp.1-13.

Mernagh, T.P. and Bastrakov, E.N. 2013. An evaluation of hydrogen sulfide in orogenic gold fluids and the uncertainties associated with vapor-rich inclusions. *Geofluids*, **13**(4), pp.494-505.

Mesquita, M.J., Samson, I., Hartmann, L.A., de Lima Picanço, J. and Gomes, M.E.B. 2021. Shearing and fluid evolution of the Porto Nacional orogenic gold district, western Brazil: microstructural, fluid inclusion, and CO isotopic evidence. *Ore Geology Reviews*, 136, article no: 104242 [no pagination]

Meyer, S. and Schweidler, E. 1927. Die Prozesse der radioaktiven Umwandlung. *Radioaktivität*, pp.23-67.

Meyer, C. and Hemley, J.J. 1967, Wall rock alteration. In: Barnes, H.L. ed. *Geochemistry of Hydrothermal Ore Deposits*. New York: Holt, Rinehart, and Winston, pp.166-235.

Meyer, F.M. 2023. Case Histories of Orogenic Gold Deposits. *Minerals*, **13**(3), article no: 369 [no pagination]

Mezger, K. and Krogstad, E.J. 1997. Interpretation of discordant U-Pb zircon ages: An evaluation. *Journal of Metamorphic Geology*, **15**(1), pp.127-140.

Migdisov, A., Bychkov, A., Williams-Jones, A.E. and van Hinsberg, V.J. 2014. A predictive model for the transport of copper by HCl-bearing water vapour in ore-forming magmatic-hydrothermal systems: Implications for copper porphyry ore formation. *Geochimica et Cosmochimica Acta*, **129**, pp.33-53.

Mikucki, E.J. 1998. Hydrothermal transport and depositional processes in Archean lode-gold systems: A review. *Ore Geology Reviews*, **13**(1-5), pp.307-321.

Miles, A.J., Graham, C.M., Hawkesworth, C.J., Gillespie, M.R. and Hinton, R.W. 2013. Evidence for distinct stages of magma history recorded by the compositions of accessory apatite and zircon. *Contributions to Mineralogy and Petrology*, **166**(1), pp.1-19.

Miles, A., Graham, C., Hawkesworth, C., Gillespie, M., Dhuime, B. and Hinton, R. 2014. Using Zircon Isotope Compositions to Constrain Crustal Structure and Pluton Evolution: the Iapetus Suture Zone Granites in Northern Britain. *Journal of Petrology*, **55**(1), pp.181-207.

Miles, A.J., Woodcock, N.H. and Hawkesworth, C.J. 2016. Tectonic controls on post-subduction granite genesis and emplacement: The late Caledonian suite of Britain and Ireland. *Gondwana Research*, **39**, pp.250-260.

Miller, R. and O'Nions, R. 1984. The provenance and crustal residence ages of British sediments in relation to palaeogeographic reconstructions. *Earth and Planetary Science Letters*, **68**(3), pp.459-470.

Milot, J., Blichert-Toft, J., Sanz, M.A., Fetter, N., Télouk, P. and Albarède, F. 2021. The significance of galena Pb model ages and the formation of large Pb-Zn sedimentary deposits. *Chemical Geology*, **583**, article no: 120444 [no pagination]

Mitchell, A.H.G. 1978. The Grampian orogeny in Scotland: arc-continent collision and polarity reversal. *The Journal of Geology*, **86**(5), pp.643-646.

Moles, N.R. 1985. Metamorphic conditions and uplift history in central Perthshire: evidence from mineral equilibria in the Foss celsian–barite–sulphide deposit, Aberfeldy. *Journal of the Geological Society*, **142**(1), pp.39-52.

Moles, N., Boyce, A. and Fallick, A. 2014. Abundant sulphate in the Neoproterozoic ocean: implications of constant δ34S of barite in the Aberfeldy SEDEX deposits, Scottish Dalradian. *Geological Society, London, Special Publications*, **393**(1), pp.189-212.

Moles, N. and Selby, D. 2023. Implications of new geochronological constraints on the Aberfeldy stratiform barite deposits, Scotland, for the depositional continuity and global correlation of the Neoproterozoic Dalradian Supergroup. *Precambrian Research*, **384,** article no: 106925 [no pagination]

Moorbath, S. 1962. Lead isotope abundance studies on mineral occurrences in the British Isles and their geological significance. *Philosophical Transactions of the Royal Society of London. Series A, Mathematical and Physical Sciences*, **254**(1042), pp.295-360.

Morelli, R., Creaser, R.A., Seltmann, R., Stuart, F.M., Selby, D. and Graupner, T. 2007. Age and source constraints for the giant Muruntau gold deposit, Uzbekistan, from coupled Re-Os-He isotopes in arsenopyrite. *Geology*, **35**(9), pp.795-798.

Morency, C. and Doin, M.P., 2004. Numerical simulations of the mantle lithosphere delamination. *Journal of Geophysical Research: Solid Earth*, **109**(B3), article no: B03410 [no pagination]

Morgan, J.W., Golightly, D.W. and Dorrzapf, A.F. 1991. Methods for the separation of rhenium, osmium and molybdenum applicable to isotope geochemistry. *Talanta*, **38**, pp.259-265.

Morley, C. K., Haranya, C., Phoosongsee, W., Pongwapee, S., Kornsawan, A. and Wonganan, N. 2004. Activation of rift oblique and rift parallel pre-existing fabrics during extension and their effect on deformation style: examples from the rifts of Thailand. *Journal of Structural Geology*, **26**(10), pp.1803-1829.

Morris, G.A. and Page, L. 2005. New dates (415 Ma) for the Etive dyke swarm and the end of the Caledonian Orogeny in the SW Grampian Highlands of Scotland. *Journal of the Geological Society, London*, **162**, pp.741-744.

Morse, J.W. and Arvidson, R.S. 2002. The dissolution kinetics of major sedimentary carbonate minerals. *Earth-Science Reviews*, **58**(1-2), pp.51-84.

Mortensen, J., Craw, D., MacKenzie, D. and Gabites, J. 2010. Lead isotope constraints on the origin of Cenozoic orogenic gold systems in the Southern Alps and northwestern Otago, South Island, New Zealand. *New Zealand Journal of Geology and Geophysics*, **53**(4), pp.295-305.

Mortensen, J.K., Liverton, T. and Dodd, K. 2019. Chemostratigraphic constraints on the nature and origin of felsic schist units hosting stratabound and orogenic vein gold on Lone Star Ridge, Klondike Gold District, Yukon. *Journal of Geochemical Exploration*, **204**, pp.112-130.

Mortensen, J., Craw, D. and MacKenzie, D. 2022. Concepts and revised models for Phanerozoic orogenic gold deposits. In: Torvela, T., Lambert-Smith, J. and Chapman, R. ed(s). *Recent Advances in Understanding Gold Deposits: from Orogeny to Alluvium*. London: Geological Society Special Publications.

Morton, D.J. 1979. Palaeogeographical evolution of the Lower Old Red Sandstone basin in the western Midland Valley. *Scottish Journal of Geology*, **15**(2), pp.97-116.

Mountain, B. and Seward, T. 2003. Hydrosulfide/sulfide complexes of copper(I). *Geochimica et Cosmochimica Acta*, **67**(16), pp.3005-3014.

Moussa, N., Rouxel, O., Grassineau, N.V., Ponzevera, E., Nonnotte, P., Fouquet, Y. and le Gall, B. 2017. Sulfur and strontium isotopic study of epithermal mineralization: A case study from the SE Afar Rift, Djibouti. *Ore Geology Reviews*, **81**, pp.358-368.

Mousuf, A.K. 1952. K 40 Radioactive Decay: Its Branching Ratio and Its Use in Geological Age Determinations. *Physical Review*, **88**(1), p.150.

Mühe, R., Peucker-Ehrenbrink, B., Devey, C. W. and Garbe-Schönberg, D. 1997. On the redistribution of Pb in the oceanic crust during hydrothermal alteration. *Chemical Geology*, **137**(1-2), pp.67-77.

Mundil, R., Ludwig, K.R., Metcalfe, I. and Renne, P.R., 2004. Age and timing of the Permian mass extinctions: U/Pb dating of closed-system zircons. Science**, 305**(5691), pp.1760-1763.

Muth, K.G., Arth, J.G. and Reed Jr, J.C. 1979. A minimum age for high-grade metamorphism and granite intrusion in the Piedmont of the Potomac River gorge near Washington, DC. *Geology*, **7**(7), pp.349-350.

Myint, A., Li, H., Mitchell, A., Selby, D. and Wagner, T. 2021. Geology, mineralogy, ore paragenesis, and molybdenite Re-Os geochronology of Sn-W (-Mo) mineralization in Padatgyaung and Dawei, Myanmar: Implications for timing of mineralization and tectonic setting. *Journal of Asian Earth Sciences*, **212**, pp.581-593.

Naden, J, Gunn, A.G. and Shephard, T.J. 2010. *Fluids and mineralisation in the Scottish Dalradian*. Keyworth: British Geological Survey.

Neall, F.B. and Phillips, G.N. 1987. Fluid–wallrock interaction around Archean hydrothermal gold deposits: a thermodynamic model. *Economic Geology*, **82**, pp.1679-1694.

Nielsen, H. 1979. Sulfur Isotopes. In: Jäger, E., Hunziker, J.C. ed(s). Lectures in Isotope Geology. Berlin: Springer. https://doi.org/10.1007/978-3-642-67161-6_24

Nesbitt, B.E. 1991. Phanerozoic gold deposits in tectonically active continental margins. In: Foster, R. ed. Gold metallogeny and exploration. Springer US, pp.104-132.

Neumayr, P. and Hagemann, S.G. 2002. Hydrothermal Fluid Evolution within the Cadillac Tectonic Zone, Abitibi Greenstone Belt, Canada: Relationship to Auriferous Fluids in Adjacent Second- and Third-Order Shear Zones. *Economic Geology*, **97**(6), pp.1203-1225.

Neumayr, P., Walshe, J., Hagemann, S., Petersen, K., Roache, A., Frikken, P., Horn, L. and Halley, S. 2007. Oxidized and reduced mineral assemblages in greenstone belt rocks of the St. Ives gold camp, Western Australia: vectors to high-grade ore bodies in Archaean gold deposits? *Mineralium Deposita*, **43**(3), pp.363-371.

Nicholson, K. and Anderton, R. 1989. The Dalradian rocks of the Lecht, NE Scotland: stratigraphy, faulting, geochemistry and mineralisation. *Earth and Environmental Science Transactions of The Royal Society of Edinburgh*, **80**(2), pp.143-157.

Niedrig, H. 1978. Physical background of electron backscattering. *The Journal of Scanning Microscopies*, **1**, pp.17-34.

Nier, A.O. 1950. A redetermination of the relative abundances of the isotopes of carbon, nitrogen, oxygen, argon, and potassium. *Physical Review*, **77**, p.789.

Neilson, J., Kokelaar, P. and Crowley, Q. 2009. Timing, relations and cause of plutonic and volcanic activity of the Siluro-Devonian post-collision magmatic episode in the Grampian Terrane, Scotland. *Journal of the Geological Society of London*, **166**, 3, pp.545-562.

Norman, D.K., Parry, W.T. and Bowman, J.R. 1991. Petrology and geochemistry of propylitic alteration at Southwest Tintic, Utah. *Economic Geology*, **86**(1), pp.13-28.

Norris, R.J. and Henley, R.W. 1976. Dewatering of a metamorphic pile. *Geology*, **4**(6), pp.333-336.

Odling, N.E. 1997. Fluid flow in fractured rocks at shallow levels in the Earth's crust: an overview. In: Holness, M.B. Ed. *Deformation-enhanced Fluid Transport in the Earth's Crust and Mantle*. Chapman and Hall, pp.289-98.

Ogawa, M. 2018. Magmatic differentiation and convective stirring of the mantle in early planets: the effects of the magmatism-mantle upwelling feedback. *Geophysical Journal International*, **215**(3), pp.2144-2155.

Ohmoto, H. 1972. Systematics of Sulphur and Carbon Isotopes in Hydrothermal Ore Deposits. *Economic Geology*, **67**(5), pp.551-578.

Ohmoto, H. and Rye R.O. 1979. Isotopes of sulfur and carbon. In: Barnes HL. Ed. *Geochemistry of Hydrothermal Ore Deposits*. John Wiley and Sons, pp.509-567.

Ohmoto, H. and Lasaga, A.C. 1982. Kinetics of reactions between aqueous sulfates and sulfides in hydrothermal systems. *Geochimica et Cosmochimica Acta*, **46**(10), pp.1727-1745.

Ohmoto, H. 1986. Stable isotope geochemistry of ore deposits. *Reviews in Mineralogy and Geochemistry*, **16**(1), pp.491-559.

Ohmoto, H. and Goldhaber, M.B. 1997. Sulfur and carbon isotopes. In: Barnes, H.L. ed. *Geochemistry of Hydrothermal Ore Deposits*. John Wiley and Sons, pp.517-611.

O'Keefe, W.G. 1987, A regional lead isotope investigation of mineralization in Ireland. Ph.D. thesis, University College Dublin.

Olierook, H.K.H., Kirkland, C.L., Barham, M., Daggitt, M.L., Hollis, J. and Hartnady, M. 2021. Extracting meaningful U-Pb ages from core–rim mixtures. *Gondwana Research*, **92**, pp.102-112.

Oliver, G., Corfu, F. and Krogh, T. 1993. U-Pb ages from SW Poland: evidence for a Caledonian suture zone between Baltica and Gondwana. *Journal of the Geological Society*, **150**(2), pp.355-369.

Oliver, G., Chen, F., Buchwaldt, R. and Hegner, E. 2000. Fast tectonometamorphism and exhumation in the type area of the Barrovian and Buchan zones. *Geology*, **28**(5), pp.459-462.

Oliver, G. 2001. Reconstruction of the Grampian episode in Scotland: its place in the Caledonian Orogeny. *Tectonophysics*, **332**(1-2), pp.23-49.

Oliver, G., Wilde, S. and Wan, Y. 2008. Geochronology and geodynamics of Scottish granitoids from the late Neoproterozoic break-up of Rodinia to Palaeozoic collision. *Journal of the Geological Society*, **165**(3), pp.661-674.

O'Neil, J.R. 1986. Theoretical and experimental aspects of isotopic fractionation. *Reviews in Mineralogy*, **16**, pp.1-40.

O'Nions, R., Hamilton, P. and Hooker, P. 1983. A Nd isotope investigation of sediments related to crustal development in the British Isles. *Earth and Planetary Science Letters*, **63**(2), pp.229-240.

Ootes, L., Lentz, D., Creaser, R., Ketchum, J. and Falck, H. 2007. Re-Os MOLYBDENITE AGES FROM THE ARCHEAN YELLOWKNIFE GREENSTONE BELT: COMPARISON TO U-Pb AGES AND EVIDENCE FOR METAL INTRODUCTION AT 2675 Ma. *Economic Geology*, **102**(3), pp.511-518.

Oreskes, N. and Einaudi, M.T. 1992. Origin of hydrothermal fluids at Olympic Dam; preliminary results from fluid inclusions and stable isotopes. *Economic Geology*, **87**(1), pp.64-90.

Ordernheimer, F. 1840. *Report of the trials at Ardtalnaig, and of new appearances in this district*. GD112/18/4/1/25. Edinburgh: National Records of Scotland.

Ordnance Survey. 2016. Outline Map of the United Kingdom. [online]. Accessed 25 January 2024. Available from: https://www.ordnancesurvey.co.uk/documents/resources/uk-outline-admin-maps.pdf

O'Reilly, B.M., Hauser, F. and Readman, P.W. 2012. The fine-scale seismic structure of the upper lithosphere within accreted Caledonian lithosphere: implications for the origins of the 'Newer Granites'. *Journal of the Geological Society*, **169**(5), pp.561-573.

Orr, W.L. 1974. Changes in sulfur content and isotopic ratios of sulfur during petroleum maturation—study of Big Horn basin Paleozoic oils. *AAPG bulletin*, **58**(11), pp.2295-2318.

Pacey, A., Wilkinson, J.J., Boyce, A.J. and Cooke, D.R. 2016. Propylitic alteration and metal mobility in porphyry systems: a case study of the Northparkes Cu-Au deposits, NSW, Australia. *Applied Earth Science*, **125**(2), pp.93-93.

Palme, H. and O'Neill, H. 2003. Cosmochemical estimates of mantle composition. *Treatise on Geochemistry*, **2**, pp.1-38.

Pankhurst, R. 1970. The geochronology of the basic igneous complexes. *Scottish Journal of Geology*, **6**(1), pp.83-107.

Paquette, J.L., Monchoux, P. and Couturier, M. 1995. Geochemical and isotopic study of a norite-eclogite transition in the European Variscan belt: Implications for U-Pb zircon systematics in metabasic rocks. *Geochimica et Cosmochimica Acta*, **59**(8), pp.1611-1622.

Parat, F., Holtz, F. and Streck, M. J. 2011. Sulphur-bearing Magmatic Accessory Minerals. Reviews in Mineralogy and Geochemistry, **73**(1), pp.285-314.

Park, J., Campbell, I., Chiaradia, M., Hao, H. and Lee, C. 2021. Crustal magmatic controls on the formation of porphyry copper deposits. *Nature Reviews Earth & Environment*, **2**(8), pp.542-557.

Parker, R. and Pearson, N. 2012. TECHNICAL REPORT ON THE OMAGH GOLD PROJECT, COUNTIES TYRONE AND FERMANAGH, NORTHERN IRELAND. [Online]. Beckhamsted, UK: ACA HOWE INTERNATIONAL LIMITED. [16th February 2024]. Available from: https://galantas.com/site/assets/files/8081/galantas-gold-corp-ni-43-101-technical-report-10august2012.pdf

Parnell, J., Earls, G., Wilkinson, J.J., Hutton, D. HW., Boyce, AJ., Fallick, A. E., Ellam, R.M., Gleeson, S.A., Moles, N.R., Carey, P.F., Legg, I., and Carey, P.F. 2000. Regional Fluid Flow and Gold Mineralization in the Dalradian of the Sperrin Mountains, Northern Ireland. *Economic Geology*, **95**(7), pp. 1389-1416.

Parnell, J., Perez, M., Armstrong, J., Bullock, L., Feldmann, J. and Boyce, A. 2017. A black shale protolith for gold-tellurium mineralisation in the Dalradian Supergroup (Neoproterozoic) of Britain and Ireland. *Applied Earth Science*, **126**(4), pp.161-175.

Parrish, R. R. 1990. U–Pb dating of monazite and its application to geological problems. *Canadian Journal of Earth Sciences*, **27**(11), pp.1431-1450.

Parrish, R. 2003. Zircon U-Th-Pb Geochronology by Isotope Dilution -- Thermal Ionization Mass Spectrometry (ID-TIMS). *Reviews in Mineralogy and Geochemistry*, **53**(1), pp.183-213.

Parry, W.T., Jasumback, M., and Wilson, P.N. 2002. Clay Mineralogy of Phyllic and Intermediate Argillic Alteration at Bingham, Utah. *Economic Geology*, **97**(2), pp.221-239.

Paterson, B.A., Rogers, G., Stephens, W.E.S. and Hinton, R.W. 1992. The longevity of acid–basic magmatism associated with a major transcurrent fault. Geological Society of America, Abstracts with Programs, 25, A42.

Pattison, D.R.M. and Goldsmith, S.A. 2022. Metamorphism of the Buchan type-area, NE Scotland and its relation to the adjacent Barrovian domain. *Journal of the Geological Society*, **179**(1).

Pattrick, R.A.D., Coleman, M.L. and Russell, M.J. 1983. Sulphur isotopic investigation of vein lead-zinc mineralization at Tyndrum, Scotland. *Mineralium Deposita*, **18**, pp.477-485.

Pattrick, R. 1984. Sulphide mineralogy of the Tomnadashan copper deposit and the Corrie Buie lead veins, south Loch Tayside, Scotland. *Mineralogical Magazine*, **48**(346), pp.85-91.

Pattrick, R., Boyce, A. and MacIntyre, R. 1988. Gold-Silver vein mineralization at Tyndrum, Scotland. *Mineralogy and Petrology*, **38**(1), pp.61-76.

Peacock, S.M., Christensen, N.I., Bostock, M.G. and Audet, P. 2011. High pore pressures and porosity at 35 km depth in the Cascadia subduction zone. *Geology*, **39**(5), pp.471-474.

Pearson, R.G. 1963. Hard and soft acids and bases, *Journal of the American Chemical Society*, **85**, pp.3533-3539.

Pedersen, M. 2000. Lead isotope signatures of sedimentary rocks as a tool for tracing ore lead sources: a study of base-metal and barite occurrences in Jameson Land Basin, central East Greenland. *Applied Earth Science*, **109**(1), pp.49-59.

Peevler, J., Fayek, M., Misra, K.C. and Riciputi, L.R. 2003. Sulfur isotope microanalysis of sphalerite by SIMS: constraints on the genesis of Mississippi valley-type mineralization, from the Mascot-Jefferson City district, East Tennessee. *Journal of Geochemical Exploration*, **80**(2-3), pp.277-296.

Peng, J., Zhou, M.-F., Hu, R., Shen, N., Yuan, S., Bi, X., Du, A. and Qu, W. 2006. Precise molybdenite Re–Os and mica Ar–Ar dating of the Mesozoic Yaogangxian tungsten deposit, central Nanling district, South China. *Mineralium Deposita*, **41**(7), pp.661-669.

Penniston-Dorland, S.C. 2001. Illumination of vein quartz textures in a porphyry copper ore deposit using scanned cathodoluminescence: Grasberg Igneous Complex, Irian Jaya, Indonesia. *American Mineralogist*, **86**(5–6), pp.652-666.

Petrella, L., Thébaud, N., Fougerouse, D., Evans, K., Quadir, Z. and Laflamme, C. 2020. Colloidal gold transport: a key to high-grade gold mineralization? *Mineralium Deposita*, **55**(7), pp.1247-1254.

Petrella, L., Thébaud, N., Evans, K., LaFlamme, C. and. Occhipinti, S. 2021. The role of competitive fluid-rock interaction processes in the formation of high-grade gold deposits. *Geochimica et Cosmochimica Acta*, **313**, pp.38-54.

Pettke, T., Oberli, F. and Heinrich, C.A. 2010. The magma and metal source of giant porphyry-type ore deposits, based on lead isotope microanalysis of individual fluid inclusions. *Earth and Planetary Science Letters*, **296**(3-4), pp.267-277.

Phillips, G.N. and Groves, D.I. 1983. The nature of Archaean gold-bearing fluids as deduced from gold deposits of Western Australia. *Journal Geological Society Australia*, **30**, pp.25-39.

Phillips, G.N., Groves, D.I. and Brown, I.J. 1987. Source requirements for the Golden Mile, Kalgoorlie: significance to the metamorphic replacement model for Archean gold deposits. Canadian Journal of Earth Sciences, **24**(8), pp.1643-1651.

Phillips, E.R., and Aitken, A.M. 1998. *The petrology and composition of the Lower Old Red Sandstone exposed in the Aberfoyle area (Sheet 38E), central Scotland*. Keyworth: British Geological Survey.

Phillips, G.N. 1993. Metamorphic fluids and gold. *Mineralogical Magazine*, **57**, pp.365-365.

Phillips, G.N. and Powell, R. 1993. Link between gold provinces. *Economic Geology*, **88**(5),

Phillips, G.N. and Evans, K.A. 2004. Role of CO2 in the formation of gold deposits. *Nature*, **429**(6994), pp.860-863.

Phillips, G. and Powell, R. 2010. Formation of gold deposits: a metamorphic devolatilization model. *Journal of Metamorphic Geology*, **28**(6), pp.689-718.

Pickett, E., Hyslop, E. and Petterson, M. 2006. The Green Beds of the SW Highlands: deposition and origin of a basic igneous-rich sedimentary sequence in the Dalradian Supergroup of Scotland. *Scottish Journal of Geology*, **42**(1), pp.43-57.

Pidgeon, R.T., O'Neil, J.R. and Silver, L.T. 1966. Uranium and Lead Isotopic Stability in a Metamict Zircon under Experimental Hydrothermal Conditions. *Science*, **154**(3756), pp.1538-1540.

Pietras, J., Dennett, A., Selby, D. and Birdwell, J. 2022. The role of organic matter diversity on the Re-Os systematics of organic-rich sedimentary units: Insights into the controls of isochron age determinations from the lacustrine Green River Formation. *Chemical Geology*, **604**, article no: 120939 [no pagination]

Pitcairn, I., Teagle, D.A.H., Craw, D., Olivo, G.R., Kerrich, R. and Brewer, T.S. 2006. Sources of metals and fluids in orogenic gold deposits: insights from the Otago and Alpine schists, New Zealand. *Economic Geology*, **101** (8), pp.1525-1546.

Pitcairn, I., Skelton, A. and Wohlgemuth-Ueberwasser, C. 2015. Mobility of gold during metamorphism of the Dalradian in Scotland. *Lithos*, **233**, pp.69-88.

Plant, J.A., Watson, J.V. and Green, P.M. 1984. Moine– Dalradian relationships and their palaeotectonic significance. Proceedings of the Royal Society of London. A. *Mathematical and Physical Sciences*, **395**(1809), pp.185-202.

Plant, J., Breward, N., Simpson, P. and Slater, D. 1990. Regional geochemistry and the identification of metallogenic provinces: examples from lead-zinc-barium, tin-uranium and gold deposits. *Journal of Geochemical Exploration*, **39**(1-2), pp.195-224.

Plant, J., Stone, P. and Mendum, J. 1999. Regional geochemistry, terrane analysis and metallogeny in the British Caledonides. *Geological Society, London, Special Publications*, **164**(1), pp.109-125.

Plotinskaya, O.Y., Chugaev, A.V. and Seltmann, R. 2017. Lead isotope systematics of porphyry–epithermal spectrum of the Birgilda–Tomino ore cluster in the South Urals, Russia. *Ore Geology Reviews*, **85**, pp.204-215.

Pointon, M.A., Chew, D.M., Ovtcharova, M., Sevastopulo, G.D. and Delcambre, B. 2014. High-precision U–Pb zircon CA-ID-TIMS dates from western European late Viséan bentonites. *Journal of the Geological Society*, **171**(5), pp.649-658.

Pokrovski, G.S., Tagirov, B.R., Schott, J., Bazarkina, E.F., Hazemann, J.-L. and Proux, O. 2009. An in situ X-ray absorption spectroscopy study of gold-chloride complexing in hydrothermal fluids. *Chemical Geology*, **259**(1-2), pp.17-29.

Pokrovski, G.S., Akinfiev, N.N., Borisova, A.Y., Zotov, A. v. and Kouzmanov, K. 2014. Gold speciation and transport in geological fluids: insights from experiments and physical-chemical modelling. *Geological Society, London, Special Publications*, **402**(1), pp.9-70.

Pokrovski, G., Kokh, M., Guillaume, D., Borisova, A., Gisquet, P., Hazemann, J., Lahera, E., Del Net, W., Proux, O., Testemale, D., Haigis, V., Jonchière, R., Seitsonen, A., Ferlat, G., Vuilleumier, R., Saitta, A., Boiron, M. and Dubessy, J. 2015. Sulphur radical species form gold deposits on Earth. *Proceedings of the National Academy of Sciences*, **112**(44), pp.13484-13489.

Polya, D.A., Pattrick, R.A.D., Marsh, D.J. and Bao, J.J. 1995. Silver and base metal dispersion in stream sediments and waters around an epithermal Ag-Au-Cu prospect at Lagalochan, western Scotland. *Exploration and Mining Geology*, **3**(4), pp.271-284.

Porter, S. and Selby, D. 2010. Rhenium–Osmium (Re–Os) molybdenite systematics and geochronology of the Cruachan Granite skarn mineralization, Etive Complex: implications for emplacement chronology. *Scottish Journal of Geology*, **46**(1), pp.17-21.

Potra, A. and Macfarlane, A.W. 2014. Lead isotope studies of the Guerrero composite terrane, west-central Mexico: implications for ore genesis. *Mineralium Deposita*, **49**(1), pp.101-117.

Potra, A. and Moyers, A. 2017. Constraints on the sources of ore metals in Mississippi Valley-type deposits in central and east Tennessee, USA, using Pb isotopes. *Ore Geology Reviews*, **81**, pp.201-210.

Power, M.R. and Pirrie, D. 2000. Platinum-group element mineralization within ultramafic rocks at Corrycharmaig, Perthshire: implications for the origin of the complex. *Scottish Journal of Geology*, **36**(2), pp.143-150.

Proffett, J.M. 2009. High Cu grades in porphyry Cu deposits and their relationship to emplacement depth of magmatic sources. *Geology*, **37**(8), pp.675-678.

Prokofiev, V.Y. and Naumov, V.B. 2020a. Physicochemical Parameters and Geochemical Features of Ore-Forming Fluids for Orogenic Gold Deposits Throughout Geological Time. *Minerals*, **10**(1), article no: 50 [no pagination]

Prokofiev, V.Y., Banks, D.A., Lobanov, K.V., Selektor, S.L., Milichko, V.A., Akinfiev, N.N., Borovikov, A.A., Lüders, V. and Chicherov, M.V. 2020b. Exceptional concentrations of gold nanoparticles in 1, 7 Ga fluid inclusions from the Kola superdeep Borehole, Northwest Russia. *Scientific Reports*, **10**(1), p.1108.

Prokofiev, V.Y. and Naumov, V.B. 2022. Ranges of Physical Parameters and Geochemical Features of Mineralizing Fluids at Porphyry Deposits of Various Types of the Cu− Mo− Au System: Evidence from Fluid Inclusions Data. *Minerals*, **12**(5), pp.1-23.

Qiu, K.-F., Marsh, E., Yu, H.-C., Pfaff, K., Gulbransen, C., Gou, Z.-Y. and Li, N. 2017. Fluid and metal sources of the Wenquan porphyry molybdenum deposit, Western Qinling, NW China. *Ore Geology Reviews*, **86**, pp.459-473.

Qiu, K., Goldfarb, R., Deng, J., Yu, H., Gou, Z., Ding, Z., Wang, Z. and Li, D. 2020. Gold Deposits of the Jiaodong Peninsula, Eastern China. In: Sillitoe, R., Goldfarb, R., Robert, F. and Simmons, S. ed(s). *Geology of the World's Major Gold Deposits and Provinces*. Society of Economic Geologists, pp. 753-773.

Qu, X., Hou, Z. and Li, Y. 2004. Melt components derived from a subducted slab in late orogenic ore-bearing porphyries in the Gangdese copper belt, southern Tibetan plateau. *Lithos*, **74**(3-4), pp.131-148.

Quesnel, B., Scheffer, C. and Beaudoin, G. 2023. The Light Stable Isotope (Hydrogen, Boron, Carbon, Nitrogen, Oxygen, Silicon, Sulfur) Composition of Orogenic Gold Deposits. In: Huston, D. and Gutzmer, Jens. ed(s). *Isotopes in Economic Geology, Metallogenesis and Exploration*. Springer International Publishing, pp.283-328.

Ramezani, J., Schmitz, M.D., Davydov, V.I., Bowring, S.A., Snyder, W.S. and Northrup, C.J. 2007. High-precision U–Pb zircon age constraints on the Carboniferous–Permian boundary in the southern Urals stratotype. *Earth and Planetary Science Letters*, **256**(1-2), pp.244-257.

Ramsay, D.M. 1964. Deformation of pebbles in Lower Old Red Sandstone conglomerates adjacent to the Highland Boundary Fault. *Geological Magazine*, **101**, pp.228-248.

Ramsay, W.R.H., Bierlein, F.P., Arne, D.C. and VandenBerg, A.H.M. 1998. Turbidite-hosted gold deposits of Central Victoria, Australia: their regional setting, mineralising styles, and some genetic constraints. *Ore Geology Reviews*, **13**(1-5), pp.131-151.

Rasmussen, J.O. 1968. Alpha-decay. In: Siegbahn, K. *Alpha-, beta-and gamma-ray spectroscopy.* Elsevier, pp.701-743.

Rasmussen, D.J., Plank, T.A., Roman, D.C. and Zimmer, M.M. 2022. Magmatic water content controls the pre-eruptive depth of arc magmas. *Science*, **375**(6585), pp.1169-1172.

Rast, N. 1958. The tectonics of the Schichallion complex. *Quarterly Journal of the Geological Society*, **114**(1-4), pp.25-46.

Rathkopf, C., Mazdab, F., Barton, I. and Barton, M.D. 2017. Grain-scale and deposit-scale heterogeneity of Re distribution in molybdenite at the Bagdad porphyry Cu-Mo deposit, Arizona. *Journal of Geochemical Exploration*, **178**, pp.45-54.

Rauchenstein-Martinek, K., Wagner, T., Wälle, M., and Heinrich, C.A. 2014. Gold concentrations in metamorphic fluids: A LA-ICPMS study of fluid inclusions from the Alpine orogenic belt. *Chemical Geology*, **385**, pp.70-83.

Rayleigh, L. 1896. L. Theoretical considerations respecting the separation of gases by diffusion and similar processes. *The London, Edinburgh, and Dublin Philosophical Magazine and Journal of Science*, **42**(259), pp.493-498.

Read, H.H. 1952. Metamorphism and migmatisation in the Ythan Valley, Aberdeenshire. *Transactions of the Edinburgh Geological Society*, **15**(1), pp.265-279.

Reed, M.H. 1997. Hydrothermal alteration and its relationship to ore fluid composition. In: H.L. Barnes. ed. *Geochemistry of Hydrothermal Ore Deposits*. John Wiley, pp.303-366.

Reiners, P.W., Carlson, R.W., Renne, P.R., Cooper, K.M., Granger, D.E., McLean, N.M. and Schoene, B. 2017. *Geochronology and thermochronology*. John Wiley & Sons.

Rice, C.M., Trewin, N.H. and Anderson, L.I., 2002. Geological setting of the Early Devonian Rhynie cherts, Aberdeenshire, Scotland: an early terrestrial hot spring system. *Journal of the Geological Society*, **159**(2), pp.203-214.

Rice, C., Mark, D., Selby, D. and Hill, N. 2012. Dating vein-hosted Au deposits in the Caledonides of N. Britain. *Transactions of the Institute of Mining and Metallurgy (Sect B. Appl Earth Sci)*, **121**, pp.199-200.

Rice, C., Mark, D., Selby, D., Neilson, J. and Davidheiser-Kroll, B. 2016. Age and Geologic Setting of Quartz Vein-Hosted Gold Mineralization at Curraghinalt, Northern Ireland: Implications for Genesis and Classification. *Economic Geology*, **111**(1), pp.127-150.

Rice, S., Cuthbert, S. and Hursthouse, A. 2018. Tectono-magmatic controls of post-subduction gold mineralisation during late Caledonian soft continental collision in the Southern Uplands-Down-Longford Terrane, Britain and Ireland: A review. *Ore Geology Reviews*, **101**, pp.74-104.

Richard, P. and Krantz, R.W. 1991. Experiments on fault reactivation in strike-slip mode. *Tectonophysics*, **188**(1-2), pp.117-131.

Richards, J. 2003. Tectono-Magmatic Precursors for Porphyry Cu-(Mo-Au) Deposit Formation. *Economic Geology*, **98**(8), pp.1515-1533.

Richards, J. 2009. Postsubduction porphyry Cu-Au and epithermal Au deposits: Products of remelting of subduction-modified lithosphere. *Geology*, **37**(3), pp.247-250.

Richardson, S. and Powell, R. 1976. Thermal causes of the Dalradian metamorphism in the central Highlands of Scotland. *Scottish Journal of Geology*, **12**(3), pp.237-268.

Ridley, J.R. 1993. The relationship between mean rock stress and fluid flow in the crust: with reference to vein- and lode-style deposits. *Ore Geology Reviews*, **8**, pp.23-37.

Ridley, J.R. and Diamond, L.W. 2000. Fluid Chemistry of Orogenic Lode Gold Deposits and Implications for Genetic Models. In: Hagemann, S. and Brown, P. *Gold in 2000*. Society of Economic Geologists, pp.141-162.

Ripley E.M, Park Y-R, Li C. and Naldrett A.J. 1999. Sulfur and oxygen isotope evidence of country rock contamination in the Voisey's Bay Ni-Cu-Co deposit, Labrador, Canada. *Lithos,* **47**, pp.53-56.

Ripley, E. M. and Li, C. 2003. Sulfur Isotope Exchange and Metal enrichment in the formation of magmatic Cu-Ni (PGE) deposits. *Economic Geology*, **98**(3), pp.635-641.

Robb, L. 2005. *Introduction to ore-forming processes.* Oxford: Blackwell Publishing.

Robert, F. 2001, Syenite-associated disseminated gold deposits in the Abitibi greenstone belt, Canada, *Mineralium Deposita*, **36**, pp.503-516.

Roberts J.L. 1974. The structure of the Dalradian rocks in the SW Highlands of Scotland. *Journal of the Geological Society, London*, **130**, pp.93-124.

Roberts, J.L. and Treagus, J.E. 1977. Polyphase generation of nappe structures in the Dalradian rocks of the southwest Highlands of Scotland. *Scottish Journal of Geology,* **13**, pp.237-254.

Roberts, J.L. and Treagus, J.E. 1979. Stratigraphical and structural correlation between the Dalradian rocks of the SW and Central Highlands of Scotland. *Geological Society, London, Special Publications*, **8**(1), pp.199-204.

Rogers, G. and Dunning, G.R. 1991. Geochronology of appinitic and related granite magmatism in the W Highlands of Scotland: constraints on the timing of transcurrent fault movements. *Journal of the Geological Society, London*, **148**, pp.17-27.

Rogers, G., Paterson, B.A., Dempster, T.L., Redwood, S.D. 1994. *U±Pb geochronology of the Newer gabbros, NE Grampians. Caledonian Terrane Relationships in Britain*. Keyworth: British Geological Survey.

Roberts, S., Sanderson, D.J. and Gumiel, P. 1998. Fractal analysis of Sn-W mineralization from central Iberia; insights into the role of fracture connectivity in the formation of an ore deposit. *Economic Geology*, **93**(3), pp.360-365.

Rogowitz, A., Zaefferer, S. and Dubosq, R. 2018. Direct observation of dislocation nucleation in pyrite using combined electron channelling contrast imaging and electron backscatter diffraction. *Terra Nova*, **30**, pp.423-430.

Rollinson, H.R. 2014. *Using Geochemical Data*. Routledge.

Romero, J., Lafon, J., Nogueira, A. and Soares, J. 2013. Sr isotope geochemistry and Pb–Pb geochronology of the Neoproterozoic cap carbonates, Tangará da Serra, Brazil. *International Geology Review*, **55**(2), pp.185-203.

Rose, P.T.S. and Harris, A.L. 2000. Evidence for the Lower Palaeozoic age of the Tay Nappe: the timing and nature of Grampian events in the Scottish Highland sector of the Laurentian Margin. *Journal of the Geological Society*, **157**(2), pp.381-391.

Rossi, G., Pastorutti, A., Nagy, I., Braitenberg, C. and Parolai, S. 2021. Recurrence of Fault Valve Behavior in a Continental Collision Area: Evidence From Tilt/Strain Measurements in Northern Adria. *Frontiers in Earth Science*, **9**, article no: 641416 [no pagination]

Roy-Barman, M. 1993, Mesure du rapport ^{187}Os-^{186}Os dans les basaltes et les péridotites: contribution à la systématique ^{187}Re-^{187}Os dans le manteau. Ph.D. thesis, Université Paris Diderot (Paris 7).

Rudnick, R.L. and Gao, S., 2003. Composition of the continental crust. In: Rudnick, R.L. ed. *Treatise on Geochemistry*.

Ruffell, A., Moles, N. and Parnell, J. 1998. Characterisation and prediction of sediment-hosted ore deposits using sequence stratigraphy. *Ore Geology Reviews*, **12**(4), pp.207-223.

Russell, R. and Farquhar, R. 1960. Dating galenas by means of their isotopic constitutions—II. *Geochimica et Cosmochimica Acta*, **19**(1), pp.41-52.

Russell, M. 1985. The evolution of the Scottish mineral sub-province. *Scottish Journal of Geology*, **21**(4), pp.513-545.

Rusk, B. 2012. Cathodoluminescent Textures and Trace Elements in Hydrothermal Quartz. In: Götze, J. and Möckel, R. ed(s). *Quartz: Deposits, Mineralogy and Analytics*. Berlin: Springer, pp.307-329.

Rhys, D., DiMarchi, J., Smith, M., Friesen, R. and Rombach, C. 2003. Structural setting, style and timing of vein-hosted gold mineralization at the Pogo deposit, east central Alaska. *Mineralium Deposita,* **38**, pp.863-875.

Ryan, P.D., Soper, N.J., Snyder, D.B., England, R.W. and Hutton, D.H.W. 1995. The Antrim–Galway Line: a resolution of the Highland Border Fault enigma of the Caledonides of Britain and Ireland. *Geological Magazine*, **132**, pp.171-184.

Rye, R.O. and Czamanske, G.K. 1969. Experimental determination of sphalerite-galena sulfur isotope fractionation and application to ores at Providencia, Mexico. *Geological Society of America Abstracts*, **7**, pp. 195-196.

Rye, R.O., Bethke, P.M. and Wasserman, M.D. 1992. The stable isotope geochemistry of acid sulfate alteration. *Economic Geology*, **87**(2), pp.225-262.

Rye, R.O. 1993. The evolution of magmatic fluids in the epithermal environment; the stable isotope perspective. *Economic Geology*, **88**(3), pp.733-752.

Rye, R.O. 2005. A review of the stable-isotope geochemistry of sulfate minerals in selected igneous environments and related hydrothermal systems. *Chemical Geology*, **215**, pp.5-36.

Sabeva, R., Mladenova, V. and Mogessie, A. 2017. Ore petrology, hydrothermal alteration, fluid inclusions, and sulfur stable isotopes of the Milin Kamak intermediate sulphidation epithermal Au-Ag deposit in Western Srednogorie, Bulgaria. *Ore Geology Reviews*, **88**, pp.400-415.

Sahimi, M. 1994. *Applications of Percolation Theory*. London: Taylor & Francis.

Sahoo, A.K., Krishnamurthi, R. and Varghese, S. 2015. Phase separation of ore forming fluid related to gold mineralization in Wynad Gold Field, Southern Granulite Terrain, India: Evidences from fluid inclusion studies. *Geology of Ore Deposits*, **57**(6), pp.522-535.

Sakai, H. 1968. Isotopic properties of sulphur compounds in hydrothermal processes. *GEOCHEMICAL JOURNAL*, **2**(1), pp.29-49.

Sakai, H., Takenaka, T., Kishima, N. 1980. Experimental study of the rate and isotope effect in sulfate reduction by ferrous oxides and silicates under hydrothermal conditions. *Proceedings of the Third International Symposium on Water-Rock Interactions*, Edmonton, Alberta, pp.75-76.

Salomons, W. 1971. Isotope fractionation between galena and pyrite and between pyrite and elemental sulfur. *Earth and Planetary Science Letters*, **11**(1-5), pp.236-238.

Sánchez, M.G., Allan, M.M., Hart, C.J.R. and Mortensen, J.K. 2014. Extracting ore-deposit-controlling structures from aeromagnetic, gravimetric, topographic, and regional geologic data in western Yukon and eastern Alaska. *Interpretation*, **2**(4), pp.75-102.

Sangster, D. 2001. The role of dense brines in the formation of vent-distal sedimentary-exhalative (SEDEX) lead–zinc deposits: field and laboratory evidence. *Mineralium Deposita*, **37**(2), pp.149-157.

Sangster, D. 2018. Toward an integrated genetic model for vent-distal SEDEX deposits. *Mineralium Deposita*, **53**(4), pp.509-527.

Saunders, J.A. 1990. Colloidal transport of gold and silica in epithermal precious-metal systems: Evidence from the Sleeper deposit, Nevada. *Geology*, **18**(8), pp.757-760.

Saunders, J. and Schoenly, P. 1995. Boiling, colloid nucleation and aggregation, and the genesis of bonanza Au-Ag ores of the sleeper deposit, Nevada. *Mineralium Deposita*, **30**(3-4), pp.199-210.

Saunders, J.A., Mathur, R., Kamenov, G.D., Shimizu, T. and Brueseke, M.E. 2016. New isotopic evidence bearing on bonanza (Au-Ag) epithermal ore-forming processes. *Mineralium Deposita*, 51(1), pp.1-11.

Saunders, J.E., Pearson, N.J., O'Reilly, S.Y. and Griffin, W.L. 2018. Gold in the mantle: A global assessment of abundance and redistribution processes. *Lithos*, **322**, pp.376-391.

Savastano, L., Chapman, R., and Torvela, T. 2023. Metallogeny of gold (from in-situ to placer) in the Loch Tay area of Central Scotland. 17th SGA Biennial Meeting: Zurich, ETH Zurich.

Savastano, L., 2024. Metallogeny of the Loch Tay area (Central Scotland) from gold compositional variations, vein parageneses and structural constraints. Unpublished PhD thesis.

Scaillet, B., Pichavant, M. and Roux, J. 1995. Experimental crystallization of leucogranite magmas. *Journal of Petrology*, **36**(3), pp.663-705.

Schaltegger, U. 2007. Hydrothermal Zircon. *Elements*, **3**(1), pp.51-79.

Schaltegger, U., Ovtcharova, M., Gaynor, S.P., Schoene, B., Wotzlaw, J.F., Davies, J.F., Farina, F., Greber, N.D., Szymanowski, D. and Chelle-Michou, C. 2021. Long-term repeatability and interlaboratory reproducibility of high-precision ID-TIMS U–Pb geochronology. *Journal of analytical atomic spectrometry*, **36**(7), pp.1466-1477.

Schenberger, D.M. and Barnes, H.L. 1989. Solubility of gold in aqueous sulfide solutions from 150 to 350°C. *Geochimica et Cosmochimica Acta*, **53**(2), pp.269-278.

Schiller, W.R. and Neilsen, H. 1970. Hydrothermal exchange and fractionation of sulfur isotopes in synthesized ZnS and PbS. *Economic Geology*, **65**(3), pp.350-352.

Schoene, B. and Bowring, S.A. 2006. U–Pb systematics of the McClure Mountain syenite: thermochronological constraints on the age of the 40Ar/39Ar standard MMhb. *Contributions to Mineralogy and Petrology*, **151**(5), pp.615-630.

Schoene, B., Crowley, J.L., Condon, D.J., Schmitz, M.D. and Bowring, S.A. 2006. Reassessing the uranium decay constants for geochronology using ID-TIMS U–Pb data. *Geochimica et Cosmochimica Acta*, **70**(2), pp.426-445.

Schoene, B., Guex, J., Bartolini, A., Schaltegger, U. and Blackburn, T.J. 2010. Correlating the end-Triassic mass extinction and flood basalt volcanism at the 100 ka level. *Geology*, **38**(5), pp.387-390.

Schoene, B., Condon, D., Morgan, L. and McLean, N. 2013. Precision and Accuracy in Geochronology. *Elements*, **9**(1), pp.19-24.

Schoene, B. 2014. U–Th–Pb Geochronology. In: Turekian, K. and Holland, H. ed(s). *Treatise on Geochemistry*. 2nd edition. Amsterdam: Elsevier, pp.341-378.

Schmitz, M.D. and Schoene, B. 2007. Derivation of isotope ratios, errors, and error correlations for U-Pb geochronology using 205Pb-235U-(233U)-spiked isotope dilution thermal ionization mass spectrometric data. *Geochemistry, Geophysics, and Geosystems*, **8**, pp.1525-2027.

Schmitz, M., Singer, B. and Rooney, A. 2020. Radioisotope Geochronology. In: F. Gradstein, J. Ogg, M. Schmitz and G. Ogg. Ed(s). *Geologic Time Scale 2020*, First edition. [online] Elsevier. Available at: <https://doi.org/10.1016/B978-0-12-824360-2.00006-1> [Accessed 16 August 2022].

Schwartz, G. 1959. Hydrothermal alteration. *Economic Geology*, **54**, pp.161-183.

Scotgold. 2022. Annual Report 2022. [Online]. Tyndrum, UK: Scotgold. [16th February 2024]. Available from: https://www.scotgoldresources.com/wp-content/uploads/2022/12/Scotgold-AR-2022.pdf

Scotgold. 2023. News Release November 2023. [Online]. Tyndrum, UK: Scotgold. [16th February 2024]. Available from: https://www.scotgoldresources.com/wp-content/uploads/2023/11/SGZ-Potential-Administration-Appointment-06.11.pdf

Scott, R.A., Pattrick, R.A.D. and Polya, D.A. 1987. *S isotopic and related studies on Dalradian stratabound mineralisation in the Tyndrum region, Scotland*. Keyworth: British Geological Survey.

Scott, R.A., Pattrick, R.A.D. and Polya, D.A. 1991. Origin of sulphur in metamorphosed stratabound mineralisation from the Argyll Group Dalradian of Scotland. *Earth and Environmental Science Transactions of The Royal Society of Edinburg*h, **82**(2), pp.91-98.

Seal, R.R., Alpers, C.N. and Rye, R.O. 2000. Stable isotope systematics of sulfate minerals. *Reviews in Mineralogy and Geochemistry*, **40**(1), pp.541-602.

Seal, R.R. and Wandless, G.A., 2003. Sulfur isotope evidence for sea-floor mineralizing processes at the Bald Mountain and Mount Chase massive sulfide deposits, northern Maine. *Economic Geology Monograph Series*, **11**, pp.567-587.

Seal, R. 2006. Sulphur Isotope Geochemistry of Sulfide Minerals. *Reviews in Mineralogy and Geochemistry*, **61**(1), pp.633-677.

Searle, M.P. 2021. Tectonic evolution of the Caledonian orogeny in Scotland: a review based on the timing of magmatism, metamorphism and deformation. *Geological Magazine*, **159**(1), pp.124-152.

Seedorff, E. and Einaudi, M.T. 2004. Henderson Porphyry Molybdenum System, Colorado: II. Decoupling of Introduction and Deposition of Metals during Geochemical Evolution of Hydrothermal Fluids. *Economic Geology*, **99**(1), pp.39-72.

Seedorff, E., Dilles, J., Proffett Jr, J., Einaudi, M., Zurcher, L., Stavast, W., Johnson, D. and Barton., M. 2005. *Porphyry deposits: Characteristics and origin of hypogene features.* Economic Geology, 100th Anniversary Volume, pp.251-298.

Selby, D. and Creaser, R. 2001. Re-Os Geochronology and Systematics in Molybdenite from the Endako Porphyry Molybdenum Deposit, British Columbia, Canada. *Economic Geology*, **96**(1), pp.197-204.

Selby, D. and Creaser, R. A. 2004. Macroscale NTIMS and microscale LA-MC-ICP-MS Re-Os isotopic analysis of molybdenite: Testing spatial restrictions for reliable Re-Os age determinations, and implications for the decoupling of Re and Os within molybdenite. *Geochimica et Cosmochimica Acta*, **68**(19), pp.3897-3908.

Selby, D., Kelley, K., Hitzman, M. and Zieg, J. 2009. Re-Os sulfide (bornite, chalcopyrite, and pyrite) systematics of the carbonate-hosted copper deposits at Ruby Creek, Southern Brooks Range, Alaska. *Economic Geology*, **104**(3), pp.437-444.

Seno, T. and Kirby, S.H. 2014. Formation of plate boundaries: The role of mantle volatilization. *Earth-Science Reviews*, **129**, pp.85-99.

Seward, T.M. 1973. Thio – complexes of gold and the transport of gold in hydrothermal ore solutions. *Geochimica et Cosmochimica Acta*, **37**, pp.379-399.

Seward, T.M. 1981. Metal complex formation in aqueous solutions at elevated temperatures and pressures. *Physics and Chemistry of the Earth*, **13-14**, pp.113-132.

Seward, T.M. 1988. The Hydrothermal Chemistry of Gold and Its Implications for Ore Formation: Boiling and Conductive Cooling as Examples. (1989). In: Keays, R., Ramsay, W.R.H. and Groves, D. ed(s). *The Geology of Gold Deposits: The Perspective in 1988*. Society of Economic Geologists, pp.398-404.

Shackleton, R.M. 1958. Downward-facing structures of the Highland Border. *Quarterly Journal of the Geological Society*, **113**(1-4), pp.361-392.

Shahabpour, J. and Kramers, J.D. 1987. Lead isotope data from the Sar-Cheshmeh porphyry copper deposit, Iran. *Mineralium Deposita*, **22**, pp.278-281.

Shanks, W.C., Bischoff, J.L., and Rosenbauer, R.J. 1981. Seawater sulfate reduction and sulfur isotope fractionation in basaltic systems: Interaction of seawater with fayalite and magnetite at 200–350°C. *Geochimica et Cosmochimica Acta*, **45**(11), pp.1977-1995.

Sharp, Z. 2017. *Principles of Stable Isotope Geochemistry*. 2nd edition. University of New Mexico.

Sharpe, R. and Fayek, M. 2016. Mass bias corrections for U-Pb isotopic analysis by secondary ion mass spectrometry: Implications for U-Pb dating of uraninite. *Rapid Communications in Mass Spectrometry*, **30**(13), pp.1601-1611.

Shaw, J., Torvela, T., Cooper, M., Leslie, G. and Chapman, R. 2022. A progressive model for the development of the Cavanacaw Au–Ag–Pb vein deposit, Northern Ireland, and implications for the evolution and metallogeny of the Grampian Terrane. *Journal of Structural Geology,* **161***,* article no: 104637 [no pagination]

Shaw, J. 2023. Integration of local and regional structural data with gold microchemistry in the Sperrin Mountains of Northern Ireland and implications for regional exploration models. Ph.D. thesis, University of Leeds.

Shea, J. 2001. Teaching the Mathematics of Radiometric Dating. *Journal of Geoscience Education*, **49**(1), pp.22-24.

Shen, J.J., Papanastassiou, D.A. and Wasserburg, G.J. 1996. Precise Re-Os determinations and systematics of iron meteorites. *Geochimica et Cosmochimica Acta*, **60**(15), pp.2887-2900.

Sheppard, S.M.F. 1977. Identification of the origin of oreforming solutions by the use of stable isotopes. *Geological Society, London, Special Publications*, **7**(1), pp.25-41.

Sheppard, S.M.F. 1981. Stable isotope geochemistry of fluids. *Physics and Chemistry of the Earth*, **13**, pp.419-445.

Shirey, S.B. and Walker, R.J. 1995. Carius Tube Digestion for Low-Blank Rhenium-Osmium Analysis. *Analytical Chemistry*, **67**(13), pp.2136-2141.

Sibson, R.H., Moore, J.M. and Rankin, A.H. 1975. Seismic pumping: a hydrothermal fluid transport mechanism. *Journal of the Geological Society London*, **131**, pp. 653-659.

Sibson, R.H. 1981. Fluid flow accompanying faulting: field evidence and models. *Earthquake prediction: an international review*, **4**, pp.593-603.

Sibson, R. 1987. Earthquake rupturing as a mineralizing agent in hydrothermal systems. *Geology*, **15**, pp.701-704.

Sibson, R., Robert, F. and Poulsen, K. 1988. High-angle reverse faults, fluid-pressure cycling, and mesothermal gold-quartz deposits. *Geology*, **16**(6), pp.551-555.

Sibson, R.H. 1992. Fault-valve behavior and the hydrostatic-lithostatic fluid pressure interface. *Earth-Science Reviews*, **32**(1-2), pp.141-144.

Sibson, R.H. 1994. Crustal stress, faulting and fluid flow. *Geological Society, London, Special Publications*, **78**(1), pp.69-84.

Sibson, R.H. 1996. Structural permeability of fluid-driven fault-fracture meshes. *Journal of Structural Geology*, **18**, pp. 1031-1042.

Sibson, R.H. 2000. A brittle failure mode plot defining conditions for high-flux flow. *Economic Geology*, **95**, pp.41-48.

Sibson, R.H. 2004. Controls on maximum fluid overpressure defining conditions for mesozonal mineralisation. *Journal of Structural Geology*, **26**, pp.1127-1136.

Sibson, R.H. 2013. Stress switching in subduction forearcs: Implications for overpressure containment and strength cycling on megathrusts. *Tectonophysics*, **600**, pp.142-152.

Sibson, R.H. 2020. Preparation zones for large crustal earthquakes consequent on fault-valve action. *Earth, Planets and Space*, **72**, pp.1-20.

Sillitoe, R. 1972. A Plate Tectonic Model for the Origin of Porphyry Copper Deposits. *Economic Geology*, **67**(2), pp.184-197.

Sillitoe, R.H. 1973. The tops and bottoms of porphyry copper deposits. *Economic Geology*, **68**(6), pp.799-815.

Sillitoe, R.H. and Hart, S.R. 1984. Lead-isotopic signatures of porphyry copper deposits in oceanic and continental settings, Colombian Andes. *Geochimica et Cosmochimica Acta*, **48**(10), pp.2135-2142.

Sillitoe, R.H. 1997. Characteristics and controls of the largest porphyry copper-gold and epithermal gold deposits in the circum-Pacific region. *Australian Journal of Earth Sciences*, **44**(3), pp.373-388.

Sillitoe, R.H. and Thompson, J.F.H. 1998. Intrusion–Related Vein Gold Deposits: Types, Tectono-Magmatic Settings and Difficulties of Distinction from Orogenic Gold Deposits. *Resource Geology*, **48**(4), pp.237-250.

Sillitoe, R. 2000. Gold-Rich Porphyry Deposits. In: Hagemann., S. and Brown., P. ed(s). *Gold in 2000*. Society of Economic Geologists, pp.315-345.

Sillitoe, R. 2010. Porphyry Copper Systems. *Economic Geology*, **105**(1), pp.3-41.

Sillitoe, R. 2015. Epithermal paleosurfaces. *Mineralium Deposita*, **50**(7), pp.767-793.

Silver, L.T. and Deutsch, S. 1963. Uranium-lead isotopic variations in zircons: A case study: The *Journal of Geology*, **71**, pp.721-758.

Simmons, S.F., Sawkins, F.J. and Schlutter, D.J. 1987. Mantle-derived helium in two Peruvian hydrothermal ore deposits. *Nature*, **329**(6138) pp.429-432.

Simmons, S., White, N. and John, D. 2005. Geological Characteristics of Epithermal Precious and Base Metal Deposits. *Economic Geology*, **100**, pp.485-522.

Simmons, S.F., Brown, K.L. and Tutolo, B.M. 2016. Hydrothermal Transport of Ag, Au, Cu, Pb, Te, Zn, and Other Metals and Metalloids in New Zealand Geothermal Systems: Spatial Patterns, Fluid-Mineral Equilibria, and Implications for Epithermal Mineralization. *Economic Geology,* **111**(3), pp.589-618.

Simpson, P.R., Gallagher, M.J., Green, P.M., Middleton, R.S., Raiswell, R. and Williams, R.A.C. 1989. Gold mineralization in relation to the evolution of extensional volcano-sedimentary basins in the Scottish Dalradian and Abitibi belt, Canada. *Transactions of the Institution of Mining and Metallurgy Section B-Applied Earth Science*, **98**, pp.102-117.

Slater, C., Preston, T. and Weaver, L.T. 2001. Stable isotopes and the international system of units. *Rapid Communications in Mass Spectrometry*, **15**(15), pp.1270-1273.

Slobodník, M., Jacher-Śliwczyńska, K., Taylor, M.C., Schneider, J. and Dolníček, Z. 2008. Plumbotectonic aspects of polymetallic vein mineralization in Paleozoic sediments and Proterozoic basement of Moravia (Czech Republic). *International Journal of Earth Sciences*, **97**, pp.1-18.

Smith, J.W., Doolan, S. and McFarlane, E.F. 1977. A sulphur isotope geothermometer for the trisulfide system galena-sphalerite-pyrite. *Chemical Geology*, **19**(1-4), pp.83-90.

Smith, D.G. 1996. Fractures and mineralisation in the Scottish Dalradian. Ph.D. Thesis, University of Manchester.

Smith, M., Robertson, S. and Rollin, K. 1999. Rift basin architecture and stratigraphical implications for basement-cover relationships in the Neoproterozoic Grampian Group of the Scottish Caledonides. *Journal of the Geological Society*, **156**(6), pp.1163-1173.

Smith, R.A. and Krabbendam, M. 2003. Lithostratigraphy and structure along the Boundary Slide Corridor: background, problems and strategy. Edinburgh: British Geological Survey.

Smith, C.G, Gunn, A.G, Shepherd, T.J, Coats, J.S. and Wiggans, G.N. 2003. Gold in the Dalradian terrane: a review of previous work. Keyworth: British Geological Survey.

Smith, C.G., Livingstone, A. and Highton, A.J. 2022. Chapter 4 Scottish mineral Geological Conservation Review sites – Magmatic and skarn minerals. *Proceedings of the Geologists' Association*, **133**(4-5), pp.350-366.

Smoliar, M., Walker, R. and Morgan, J. 1996. Re-Os Ages of Group IIA, IIIA, IVA, and IVB Iron Meteorites. *Science*, **271**(5252), pp.1099-1102.

Soloviev, S.G., Kryazhev, S.G., Dvurechenskaya, S.S. and Trushin, S.I. 2020. The large Bakyrchik orogenic gold deposit, eastern Kazakhstan: Geology, mineralization, fluid inclusion, and stable isotope characteristics. *Ore Geology Reviews*, **127**, article no: 103863 [no pagination]

Soper, N. J., Webb, B. C. and Woodcock, N. H. 1987. Late Caledonian (Acadian) transpression in north-west England: timing, geometry and geotectonic significance. *Proceedings of the Yorkshire Geological Society*, **46**(3), pp.175-192.

Soper, N.J., England, R.W., Snyder, D.B. and Ryan, P.D. 1992a. The Iapetus suture zone in England, Scotland and eastern Ireland: a reconciliation of geological and deep seismic data. *Journal of the Geological Society*, **149**(5), pp.697-700.

Soper, N., Strachan, R., Holdsworth, R., Gayer, R. and Greiling, R. 1992b. Sinistral transpression and the Silurian closure of Iapetus. *Journal of the Geological Society*, **149**(6), pp.871-880.

Soper, N., Ryan, P. and Dewey, J. 1999. Age of the Grampian orogeny in Scotland and Ireland. *Journal of the Geological Society*, **156**(6), pp.1231-1236.

Soper, N.J. and Woodcock, N.H. 2003. The lost Lower Old Red Sandstone of England and Wales: a record of post-Iapetan flexure or Early Devonian transtension? *Geological Magazine*, **140**, pp.627-647.

Southam, G. and Saunders, J.A. 2005. The Geomicrobiology of Ore Deposits. *Economic Geology*, **100**(6), pp.1067-1084.

Spence-Jones, C.P., Jenkin, G.R.T., Boyce, A.J., Hill, N.J. and Sangster, C.J.S. 2018. Tellurium, magmatic fluids and orogenic gold: An early magmatic fluid pulse at Cononish Gold Deposit, Scotland. *Ore Geology Reviews*, **102**, pp.894-905.

Spilliaert, N., Allard, P., Métrich, N. and Sobolev, A.V. 2006. Melt inclusion record of the conditions of ascent, degassing, and extrusion of volatile-rich alkali basalt during the powerful 2002 flank eruption of Mount Etna (Italy). *Journal of Geophysical Research: Solid Earth*, **111,** article no: B04203 [no pagination]

Sporli, K. and Cargill, H. 2011. Structural Evolution of a World-Class Epithermal Orebody: The Martha Hill Deposit, Waihi, New Zealand. *Economic Geology*, **106**(6), pp.975-998.

Squire, R.J., Herrmann, W., Pape, D. and Chalmers, D.I. 2007. Evolution of the Peak Hill high-sulphidation epithermal Au–Cu deposit, eastern Australia. *Mineralium Deposita*, **42**(5), pp.489-503.

Stacey, J.S. and Kramers, J.D. 1975. Approximation of terrestrial lead isotope evolution by a two-stage model. *Earth and Planetary Science Letters*, **26**(2), pp.207-221.

Standish, C., Dhuime, B., Chapman, R., Hawkesworth, C. and Pike, A. 2014. The genesis of gold mineralisation hosted by orogenic belts: A lead isotope investigation of Irish gold deposits. *Chemical Geology*, **378-379**, pp.40-51.

Stanton, R. 1955. Lower Paleozoic mineralization near Bathurst, New South Wales. *Economic Geology*, **50**(7), pp.681-714.

Stanton, R. and Russell, R. 1959. Anomalous leads and the emplacement of lead sulfide ores. *Economic Geology*, **54**(4), pp.588-607.

Steadman, J.A., Large, R.R., Meffre, S. and Bull, S.W. 2013. Age, origin and significance of nodular sulfides in 2680 Ma carbonaceous black shale of the Eastern Goldfields Superterrane, Yilgarn Craton, Western Australia. *Precambrian Research*, **230**, pp.227-247.

Stefánsson, A. and Seward, T. 2003. Experimental determination of the stability and stoichiometry of sulphide complexes of silver(I) in hydrothermal solutions to 400°C. *Geochimica et Cosmochimica Acta*, **67**(7), pp.1395-1413.

Stefánsson, A. and Seward, T. 2004. Gold(I) complexing in aqueous sulphide solutions to 500°C at 500 bar. *Geochimica et Cosmochimica Acta*, **68**(20), pp.4121-4143.

Stein, H.J., Morgan, J. W., Markey, R.J. and Hannah, J.L. 1998a. An Introduction to Re-Os what's in it for the mineral industry? *SEG Discovery*, **32**, pp.1-15.

Stein, H., Sundblad, K., Markey, R., Morgan, J. and Motuza, G. 1998b. Re-Os ages for Archean molybdenite and pyrite, Kuittila-Kivisuo, Finland and Proterozoic molybdenite, Kabeliai, Lithuania: testing the chronometer in a metamorphic and metasomatic setting. *Mineralium Deposita*, **33**(4), pp.329-345.

Stein, H.J., Morgan, J.W. and Schersten, A. 2000. Re-Os Dating of Low-Level Highly Radiogenic (LLHR) Sulfides: The Harnas Gold Deposit, Southwest Sweden, Records Continental-Scale Tectonic Events. *Economic Geology*, **95**(8), pp.1657-1671.

Stein, H., Markey, R., Morgan, J., Hannah, J. and Schersten, A. 2001. The remarkable Re-Os chronometer in molybdenite: how and why it works. *Terra Nova*, **13**(6), pp.479-486.

Stein, H.J. and Bingen, B. 2002. 1.05–1.01 Ga Sveconorwegian metamorphism and deformation of the supracrustal sequence at Sæsvatn, south Norway: Re-Os dating of Cu-Mo mineral occurrences. *Geological Society, London, Special Publications*, **204**(1), pp.319-335.

Stein, H., Scherstén, A., Hannah, J., and Markey, R. 2003. Subgrain-scale decoupling of Re and 187Os and assessment of laser ablation ICP-MS spot dating in molybdenite. *Geochimica et Cosmochimica Acta*, **67**, pp.3673-3686

Steno, N. 1669. De solido intra solidum naturaliter contento Dissertationis prodromus. Ex typographia sub signo Stellae.

Stephens, W.E. and Halliday, A.N. 1979. Compositional variation in the Galloway plutons. In Origin of Granite Batholiths: Geochemical Evidence Based on a meeting of the Geochemistry Group of the Mineralogical Society. Boston, MA: Birkhäuser Boston, pp. 9-17

Stephens, W.E.S. and Halliday, A.N. 1984. Geochemical contrasts between late Scottish granitoids between 600 and 390 Ma Caledonian granitoid plutons of northern, central and southern Scotland. *Transactions of the Royal Society of Edinburgh: Earth Sciences*, **75**, pp.259-273.

Stephens, W. 1988. Granitoid plutonism in the Caledonian orogen of Europe. *Geological Society, London, Special Publications*, **38**(1), pp.389-403.

Stephenson, D. and Gould, D. 1995. British Regional Geology, the Grampian Highlands. London: HMSO.

Stephenson, D., Mendum, J., Fettes, D. and Leslie, A. 2013a. The Dalradian rocks of Scotland: an introduction. *Proceedings of the Geologists' Association*, **124**(1-2), pp.3-82.

Stephenson, D., Mendum, J.R., Fettes, D.J., Smith, C.G., Gould, D., Tanner, P.G. and Smith, R.A. 2013b. The Dalradian rocks of the north-east Grampian Highlands of Scotland. *Proceedings of the Geologists' Association*, **124**(1-2), pp.318-392.

Stern, R.A., Bodorkos, S., Kamo, S.L., Hickman, A.H. and Corfu, F. 2009. Measurement of SIMS Instrumental Mass Fractionation of Pb Isotopes During Zircon Dating. *Geostandards and Geoanalytical Research*, **33**(2), pp.145-168.

Stern, R. 2020. The Mesoproterozoic Single-Lid Tectonic Episode: Prelude to Modern Plate Tectonics. GSA Today, **30**(12), pp.4-10.

Stevens-Kalceff, M. 2009. Cathodoluminescence microcharacterization of point defects in α-quartz. *Mineralogical Magazine*, **73**, pp.585-605.

Stewart, M., Strachan, R.A. and Holdsworth, R.E. 1999. Structure and early kinematic history of the Great Glen Fault Zone, Scotland. *Tectonics*, **18**(2), pp.326-342.

Stewart, M, Strachan, R.A, Martin, M.W. and Holdsworth, R.E. 2001. Dating early sinistral displacements along the Great Glen Fault, Scotland: structural setting, emplacement and U–Pb geochronology of the syn-tectonic Clunes Tonalite. *Journal of the Geological Society, London* **158,** pp.821-830.

Stille, H., 1924. *Grundfragen der vergleichenden Tektonik*. Gebrüder Borntraeger.

Stoffregen, R.E. 1987. Genesis of acid-sulfate alteration and Au-Cu-Ag mineralization at Summitville, Colorado. *Economic Geology*, **82**(6), pp.1575-1591.

Stone P., McMillan A.A., Floyd J.D., Barnes R.P. and Phillips E.R. 2012. *British Regional Geology: South of Scotland*. Keyworth: British Geological Survey.

Strachan, R.A., Holdsworth, R.E., Friderichsen, J.D. and Jepsen, H.F. 1992. Regional Caledonian structure within an oblique convergence zone, Dronning Louise Land, NE Greenland. *Journal of the Geological Society*, **149**(3), pp.359-371.

Strachan, R.A. 2002. The Northern Highland and Grampian terranes. In: Strachan, R.A., Smith, M., Harris, A.L., Fettes, D.J. and Trewin, N.H. ed(s). *The Geology of Scotland*. The Geological Society of London, pp.81-1247.

Strachan, R.A., Alsop, G.I., Ramezani, J., Frazer, R.E., Burns, I.M. and Holdsworth, R.E. 2020. Patterns of Silurian deformation and magmatism during sinistral oblique convergence, northern Scottish Caledonides. *Journal of the Geological Society*, **177**(5), pp.893-910.

Stracke, A., Scherer, E.E., Reynolds, B.C., 2014. 15.4 - Application of Isotope Dilution in Geochemistry. In: Holland, H.D. and Turekian, K.K. ed(s). *Treatise on Geochemistry*. Second Edition. Oxford: Elsevier, pp.71-86.

Strauss, H. 2004. *4 Ga of seawater evolution: Evidence from the sulfur isotopic composition of sulfate. In Sulfur Biogeochemistry - Past and Present*. Geological Society of America.

Sturt, B.A. 1961. The geological structure of the area south of Loch Tummel. *Quarterly Journal of the Geological Society*, **117**(1-4), pp.131-156.

Stüwe, K., Will, T.M. and Zhou, S. 1993. On the timing relationship between fluid production and metamorphism in metamorphic piles: Some implications for the origin of post-metamorphic gold mineralisation. *Earth and Planetary Science Letters*, **114**(4), pp.417-430.

Stüwe, K. 1998. Tectonic constraints on the timing relationships of metamorphism, fluid production and gold-bearing quartz vein emplacement. *Ore Geology Reviews*, **13**(1-5), pp.219-228.

Suess, E. 1906. *The face of the earth 2*, Translated by H.B.C. Sollas, Oxford.

Sun, S.S., Carr, G.R. and Page, R.W. 1996. A continued effort to improve lead-isotope model ages. *AGSO Research Newsletter*, **24**, pp.19-20.

Sun, W., Huang, R.F., Li, H., Hu, Y.B., Zhang, C.C., Sun, S.J., Zhang, L.P., Ding, X., Li, C.Y., Zartman, R.E. and Ling, M.X. 2015. Porphyry deposits and oxidized magmas. *Ore Geology Reviews*, **65**, pp.97-131.

Sun, W., Wang, J., Zhang, L., Zhang, C., Li, H., Ling, M., Ding, X., Li, C. and Liang, H. 2017. The formation of porphyry copper deposits. *Acta Geochimica*, **36**(1), pp.9–15.

Sun, S.-C., Zhang, L., Li, R.-H., Wen, T., Xu, H., Wang, J.-Y., Li, Z.-Q., Zhang, F., Zhang, X.-J. and Guo, H. 2019. Process and Mechanism of Gold Mineralization at the Zhengchong Gold Deposit, Jiangnan Orogenic Belt: Evidence from the Arsenopyrite and Chlorite Mineral Thermometers. *Minerals*, **9**(2), article no: 133 [no pagination]

Sun, G., Zeng, Q., Zhou, J.-X., Zhou, L. and Chen, P. 2021. Genesis of the Xinling vein-type Ag-Pb-Zn deposit, Liaodong Peninsula, China: Evidence from texture, composition and in situ S-Pb isotopes. *Ore Geology Reviews*, **133**, article no: 104120 [no pagination]

Sundblad, K., Cumming, G.L. and Krstic, D. 1991. Lead isotope evidence for the formation of epithermal gold quartz veins in the Chortis Block, Nicaragua. *Economic Geology*, **86**(5), pp.944-959.

Suzuki, K., Shimizu, H. and Masuda, A. 1996. ReOs dating of molybdenites from ore deposits in Japan: Implication for the closure temperature of the ReOs system for molybdenite and the cooling history of molybdenum ore deposits. *Geochimica et Cosmochimica Acta*, **60**(16), pp.3151-3159.

Swainbank, I.G., Fortey, N.J. and Boast, A.M., 1981. Lead-Isotope ratios of galena from stratabound mineralization in the Scottish Dalradian. *In:Caledonian-Appalachian Stratabound Sulphides—Symposium Volume. Meeting at University of Strathclyde, Glasgow* (pp.20-23).

Szaran, J., 1996. Experimental investigation of sulphur isotopic fractionation between dissolved and gaseous H2S. *Chemical geology*, **127**(1-3), pp.223-228.

Takahashi, Y., Uruga, T., Suzuki, K., Tanida, H., Terada, Y. and Hattori, K. 2007. An atomic level study of rhenium and radiogenic osmium in molybdenite. *Geochimica et Cosmochimica Acta*, **71**(21), pp.5180-5190.

Tanner, P.G. and Pringle, M.S. 1999. Testing for the presence of a terrane boundary within Neoproterozoic (Dalradian) to Cambrian siliceous turbidites at Callander, Perthshire, Scotland. *Journal of the Geological Society*, **156**(6), pp.1205-1216.

Tanner, P.W.G. 2007a. The role of the Highland Border ophiolite in the∼ 470 Ma Grampian event, Scotland. *Geological Magazine*, **144(**3), pp.597-602.

Tanner, P.G. and Sutherland, S. 2007b. The Highland Border Complex, Scotland: a paradox resolved. *Journal of the Geological Society*, **164**(1), pp.111-116.

Tanner, G., 2008. Tectonic significance of the highland boundary fault, Scotland. *Journal of the Geological Society*, **165**(5), pp.915-921.

Tanner, P.G. 2012. The giant quartz-breccia veins of the Tyndrum–Dalmally area, Grampian Highlands, Scotland: their geometry, origin and relationship to the Cononish gold–silver deposit. *Earth and Environmental Science Transactions of the Royal Society of Edinburgh*, **103**(1), pp.51-76.

Tanner, P.G., Thomas, C.W., Harris, A.L., Gould, D., Harte, B., Treagus, J.E. and Stephenson, D., 2013. The Dalradian rocks of the Highland Border region of Scotland. *Proceedings of the Geologists' Association*, **124**(1-2), pp.215-262.

Tanner, P. 2014a. Structural controls and origin of gold–silver mineralization in the Grampian Terrane of Scotland and Ireland. *Geological Magazine*, **151**(6), pp.1072-1094.

Tanner, P.W.G. 2014b. A kinematic model for the Grampian Orogeny, Scotland. Geological Society, London, Special Publications, **390**(1), pp.467-511.

Tanner, D., Henley, R.W., Mavrogenes, J.A. and Holden, P. 2016. Sulfur isotope and trace element systematics of zoned pyrite crystals from the El Indio Au–Cu–Ag deposit, Chile. *Contributions to Mineralogy and Petrology*, **171**, pp.1-17.

Tarasova, Y., Budyak, A., Chugaev, A., Goryachev, N., Tauson, V., Skuzovatov, S., Reutsky, V., Abramova, V., Gareev, B., Bryukhanova, N. and Parshin, A. 2020. Mineralogical and isotope-geochemical (δ13C, δ34S and Pb-Pb) characteristics of the Krasniy gold mine (Baikal-Patom Highlands): Constraining ore-forming mechanisms and the model for Sukhoi Log-type deposits. *Ore Geology Reviews*, **119,** article no: 103365 [no pagination]

Tarney, J. and Jones, C. 1994. Trace element geochemistry of orogenic igneous rocks and crustal growth models. *Journal of the Geological Society*, **151**(5), pp.855-868.

Tassara, S. and Ague, J.J. 2022. A Role for Crustal Assimilation in the Formation of Copper-Rich Reservoirs at the Base of Continental Arcs. *Economic Geology*, **117**(7), pp.1481-1496.

Tatsumoto, M., Knight, R.J. and Allegre, C.J. 1973. Time Differences in the Formation of Meteorites as Determined from the Ratio of Lead-207 to Lead-206. **180**(4092), pp.1279-1283.

Taylor, H.P. 1974. The application of oxygen and hydrogen isotope studies to problems of hydrothermal alteration and ore deposition. *Economic Geology*, **69**, pp.843-883.

Taylor, B.E. 2007. Epithermal gold deposits. In: Goodfellow, W.D. ed. *Mineral Deposits of Canada: A Synthesis of Major Deposit-Types, District Metallogeny, the Evolution of Geological Provinces, and Exploration Methods*. Geological Association of Canada, pp. 113-139.

Taylor, R.D., Monecke, T., Reynolds, T.J. and Monecke, J. 2021. Paragenesis of an Orogenic Gold Deposit: New Insights on Mineralizing Processes at the Grass Valley District, California. *Economic Geology*, **116**(2), pp.323-356.

Tera, F. and Wasserburg, G.J. 1972. U-Th-Pb systematics in lunar highland samples from the Luna 20 and Apollo 16 missions. *Earth and Planetary Science Letters*, **17**(1), pp.36-51.

Tera, F. and Carlson, R.W. 1999. Assessment of the Pb–Pb and U–Pb chronometry of the early solar system. *Geochimica et Cosmochimica Acta*, **63**(11-12), pp.1877-1889.

Terzaghi, K. 1923. Die Berechnung der Durchlässigkeit des Tones aus dem Verlauf der hydromechanischen Spannungserscheinungen. Sitzungsberichte der Kaiserlichen Akademie der Wissenschaften (Wien), *Mathematisch-Naturwissenschaftliche Klasse*, **132**, pp.125-38.

Tilton, G. R., Pollak, R. J., Clark, A. H. and Robertson, R.C.R. 1981. Isotopic composition of Pb in Central Andean ore deposits. In: Kulme, L., Dymond, J., Dasch, J., Hussong, D. and Roderick, R. eds. *Nazca Plate: Crustal Formation and Andean Convergence*. Geological Society of America, pp. 791-816.

Thirlwall, M.F. 1981. Implications for Caledonian plate tectonic models of chemical data from volcanic rocks of the British Old Red Sandstone. *Journal of the Geological Society, London*, **138**, pp.123-138.

Thirlwall, M. 1982. Systematic variation in chemistry and Nd-Sr isotopes across a Caledonian calc-alkaline volcanic arc: implications for source materials. *Earth and Planetary Science Letters*, **58**(1), pp.27-50.

Thirlwall, M. 1983. Isotope geochemistry and origin of calc alkaline lavas from a Caledonian continental margin volcanic arc. *Journal of Volcanology and Geothermal Research*, **18**, pp.589-631.

Thirlwall, M.F. 1986. Lead isotope evidence for the nature of the mantle beneath Caledonian Scotland. *Earth and Planetary Science Letters*, **80**, pp.55-70.

Thirlwall, M. 1988. Geochronology of Late Caledonian magmatism in northern Britain. *Journal of the Geological Society*, **145**(6), pp.951-967.

Thirwall, M.F. 2002. Multicollector ICP-MS analysis of Pb isotopes, using a (207)Pb-(204)Pb double spike, demonstrates up to 400ppm/amu systematic errors in Tl normalization. *Chemical Geology*, **184** (3-4), pp.255-279.

Thode, H.G., Ding, T. and Crocket, J.H. 1991. Sulphur-isotope and elemental geochemistry studies of the Hemlo gold mineralization, Ontario: sources of sulphur and implications for the mineralization process. *Canadian Journal of Earth Sciences*, **28**(1), pp.13-25.

Thomas, P.R. 1979. New evidence for a Central Highland root zone. *Geological Society, London, Special Publications*, **8**(1), pp.205-211.

Thompson, J., Sillitoe, R., Baker, T., Lang, J. and Mortensen, J. 1999. Intrusion-related gold deposits associated with tungsten-tin provinces. *Mineralium Deposita*, **34**(4), pp.323-334.

Thompson, J.F.H. and Newberry, R.J. 2000. Gold deposits related to reduced granitic intrusions. *Reviews in Economic Geology*, **13**, pp. 377-400.

Thorpe, R.I. 2008. Release of lead isotope data in 4 databases: Canadian, Western Superior, foreign, and whole rock and feldspar. https://doi.org/10.4095/224837

Thost, C. 1860. On the Rocks, Ores, and other Minerals on the Property of the Marquess of Breadalbane in the Highlands of Scotland. *Quarterly Journal of the Geological Society*, **16**(1-2), pp.421-428.

Tom, E.M., Mark, E.B. and Joaquin, R. 1997. Trace Element Analysis of Natural Gold by Laser Ablation ICP-MS: A Combined External/Internal Standardisation Approach. *Geostandards Newsletter*, **21**, pp.271-278.

Tomkins, A.G., Pattison, D.R.M., and Frost, B.R. 2007. On the initiation of metamorphic sulfide anatexis. *Journal of Petrology*, **48,** pp.511–535.

Tomkins, A.G. 2013. On the source of orogenic gold. *Geology*, **41**, pp.1255-1256.

Tornos, F., Spiro, B.F., Shepherd, T.J. and Ribera, F. 1997. Sandstone-hosted gold lodes of the southern West Asturian Leonese zone (NW Spain). C*hronique de la recherche minière*, **528**, pp.71-86.
Torvela. 2020. *Geological Map of Loch Tay*. 1:250,000.

Torvela. 2021. *Photographs of the core retrieved from Boreholes EGR-001 and EGR-002*. [Photograph]. At: Leeds: School of Earth and Environment.

Torvela, T., Chapman, R. and Lambert-Smith, J. 2022. An introduction to Recent Advances in Understanding Gold Deposits: from Orogeny to Alluvium: the importance of multi-method approaches and developing a characterization. *Geological Society, London, Special Publications*, **516**(1), pp.1-14.

Tosdal, R.M., Wooden, J.L. and Bouse, R.M., 1999. Pb isotopes, ore deposits, and metallogenic terranes. In: Lambert, D. and Ruiz, J. ed(s). *Application of Radiogenic Isotopes to Ore Deposit Research and Exploration*. Society of Economic Geologists.

Tosdal, R.M. and Richards, J.P. 2001, Magmatic and structural controls on the development of porphyry Cu ± Mo ± Au deposits: *Reviews in Economic Geology*, **14**, pp. 157-181.

Tosdal, R., Dilles, J. and Cooke, D. 2009. From Source to Sinks in Auriferous Magmatic-Hydrothermal Porphyry and Epithermal Deposits. *Elements*, **5**(5), pp.289-295.

Townley, B.K. and Godwin, C.I. 2001. Isotope characterization of lead in galena from ore deposits of the Aysén Region, southern Chile. *Mineralium Deposita*, **36**(1), pp.45-57.

Townsend, A., Yu, Z., Mcgoldrick, P. and Hutton, J. 1998. Precise lead isotope ratios in Australian galena samples by high resolution inductively coupled plasma mass spectrometry. *Journal of Analytical Atomic Spectrometry*, **13**(8), pp.809-813.

Treagus, J.E. and King, G. 1978. A complete Lower Dalradian succession in the Schiehallion district, Central Perthshire. *Scottish Journal of Geology*, **14**(2), pp.157-166.

Treagus, J.E. 1991. Fault displacements in the Dalradian of the Central Highlands. *Scottish Journal of Geology,* **27**, pp.135-45

Treagus, J.E. 1999. A structural reinterpretation of the Tummel Belt and a transpressional model for evolution of the Tay Nappe in the Central Highlands of Scotland. *Geological Magazine*, 136(6), pp.643-660.

Treagus, J.E., Pattrick, R.A.D. and Curtis, S.F. 1999. Movement and mineralization in the Tyndrum fault zone, Scotland and its regional significance. *Journal of the Geological Society*, **156**, pp.591-604.

Treagus, J.E., 2000. Solid Geology of the Schiehallion District: Memoir for 1: 50000 Geological Sheet 55W (Scotland). Stationery Office.

Treagus, J. 2003. The Loch Tay Fault: type section geometry and kinematics. *Scottish Journal of Geology*, **39**(2), pp.135-144.

Trewin, N.H. and Rollin, K.E. 2002. Geological history and structure of Scotland. In: Trewin, N.H. ed. *Geology of Scotland*. London: Geological Society, pp.1-25.

Trewin, N.H. and Thirlwall, M.F. 2002. Old Red Sandstone. In: Trewin, N.H. ed. *The Geology of Scotland*. Fourth edition. London: The Geological Society, pp.213-249.

Tsunogae, T. and Dubessy, J. 2009. Ethane-and hydrogen-bearing carbonic fluid inclusions in a high-grade metamorphic rock. *Journal of mineralogical and petrological sciences,* **104**(5), pp.324-329.

Turnell, H.B. 1985. Palaeomagnetism and Rb-Sr ages of the Ratagan and Comrie intrusions. *Geophysical Journal International*, **83**(2), pp.363-378.

Ueda, K., Gerya, T.V. and Burg, J.P. 2012. Delamination in collisional orogens: Thermomechanical modeling. *Journal of Geophysical Research: Solid Earth*, **117**, article no: B08202 [no pagination]

Urey, H. 1947. The thermodynamic properties of isotopic substances. *Journal of the Chemical Society (Resumed)*, p.562.

Vallance, J., Boiron, M.C., Cathelineau, M., Fourcade, S., Varlet, M. and Marignac, C. 2004. The granite hosted gold deposit of Moulin de Cheni (Saint-Yrieix district, Massif Central, France): petrographic, structural, fluid inclusion and oxygen isotope constraints. *Mineralium Deposita*, **39**, pp.265-281.

Van Breemen, O., Aftalion, M., Pankhurst, R.J. and Richardson, S.W. 1979. Age of the Glen Dessary syenite, Inverness-shire: diachronous Palaeozoic metamorphism across the Great Glen. *Scottish Journal of Geology*, **25**, pp.49-62.

van Hinsbergen, D.J.J., Kaymakci, N., Spakman, W. and Torsvik, T.H. 2010. Reconciling the geological history of western Turkey with plate circuits and mantle tomography. *Earth and Planetary Science Letters*, **297**(3-4), pp.674-686.

van Staal, C.R. and Dewey, J.F. 2023. A review and tectonic interpretation of the Taconian–Grampian tract between Newfoundland and Scotland: diachronous accretion of an extensive forearc–arc–backarc system to a hyperextended Laurentian margin and subsequent subduction polarity reversal. In: Hynes, A.J. and Murphy, J.B. ed(s). *The Consummate Geoscientist: A Celebration of the Career of Maarten de Wit*. London: Geological Society.

Vermeesch, P. 2017. *Chapter 5 The U-Pb system*. [online]. [26 April 2024]. Available from: https://www.ucl.ac.uk/~ucfbpve/geotopes/indexch5.html

Vermeesch, P. 2018. IsoplotR: A free and open toolbox for geochronology. *Geoscience Frontiers*, **9**(5), pp.1479-1493.

Viete, D., Richards, S., Lister, G., Oliver, G. and Banks, G. 2010. Lithospheric-scale extension during Grampian orogenesis in Scotland. *Geological Society, London, Special Publications*, **335**(1), pp.121-160.

Viete, D.R., Forster, M.A. and Lister, G.S. 2011. The nature and origin of the Barrovian metamorphism, Scotland: 40 Ar/ 39 Ar apparent age patterns and the duration of metamorphism in the biotite zone. *Journal of the Geological Society*, **168**(1), pp.133-146.

Viete, D.R., Oliver, G.J.H., Fraser, G.L., Forster, M.A. and Lister, G.S. 2013. Timing and heat sources for the Barrovian metamorphism, Scotland. Lithos, **177**, pp.148-163.

Villa, I.M. and Hanchar, J.M. 2017. Age discordance and mineralogy. *American Mineralogist*, **102**(12), pp.2422-2439.

Völkening, J., Walczyk, T. and Heumann, K.G. 1991, Osmium isotope ratio determinations by negative thermal ionization mass spectrometry. *International Journal of Mass Spectrometry and Ion Processes*, **105**, pp.147-159.

von Quadt, A., Erni, M., Martinek, K., Moll, M., Peytcheva, I. and Heinrich, C.A. 2011. Zircon crystallization and the lifetimes of ore-forming magmatic-hydrothermal systems. *Geology*, **39**(8), pp.731-734.

Voute, F., Hagemann, S.G., Evans, N.J. and Villanes, C. 2019. Sulfur isotopes, trace element, and textural analyses of pyrite, arsenopyrite and base metal sulfides associated with gold mineralization in the Pataz-Parcoy district, Peru: implication for paragenesis, fluid source, and gold deposition mechanisms. *Mineralium Deposita*, **54**(7), pp.1077-1100.

Wagner, T., Boyce, A.J. and Fallick, A.E. 2002. Laser combustion analysis of δ34S of sulfosalt minerals: determination of the fractionation systematics and some crystal-chemical considerations. *Geochimica et Cosmochimica Acta*, **66**(16), pp.2855-2863.

Wagner, T., Fusswinkel, T., Wälle, M. and Heinrich, C.A. 2016. Microanalysis of Fluid Inclusions in Crustal Hydrothermal Systems using Laser Ablation Methods. *Elements*, **12**(5), pp.323-328.

Wallace, C. and Maher, K. 2019. Phyllic alteration and the implications of fluid composition at the Copper Flat hydrothermal System, New Mexico, USA. *Ore Geology Reviews*, **104**, pp.273-293.

Walther, J.V. and Orville, P.M. 1982. Volatile production and transport in regional metamorphism. *Contributions to Mineralogy and Petrology*, **79**, pp.252-257.

Wang, Y., Zeng, Q., Zhou, L., Chu, S. and Guo, Y. 2016. The sources of ore-forming material in the low-sulphidation epithermal Wulaga gold deposit, NE China: Constraints from S, Pb isotopes and REE pattern. *Ore Geology Reviews*, 76, pp.140-151.

Wang, J., Wen, H., Li, C., Zhang, J. and Ding, W. 2019. Age and metal source of orogenic gold deposits in Southeast Guizhou Province, China: Constraints from Re–Os and He–Ar isotopic evidence. *Geoscience Frontiers*, **10**(2), pp.581-593.

Wang, L., Kusky, T., Zhang, Y., Lentz, D., Zhong, Y., Ding, W., Deng, H., Giddens, R. and Peng, S. 2021. Extreme sulfur isotope fractionation of hydrothermal auriferous pyrites from the SW fringe of the Taupo Volcanic Zone, New Zealand: Implications for epithermal gold exploration. *Results in Geochemistry,* **3**, article no: 100009 [no pagination]

Wang, Q., Yang, L., Zhao, H., Groves, D.I., Weng, W., Xue, S., Li, H., Dong, C., Yang, L., Li, D. and Deng, J. 2022. Towards a universal model for orogenic gold systems: A perspective based on Chinese examples with geodynamic, temporal, and deposit-scale structural and geochemical diversity. *Earth-Science Reviews*, **224**, article no: 103861 [no pagination]

Wang, Q., Liu, X., Yin, R., Weng, W., Zhao, H., Yang, L., Zhai, D., Li, D., Ma, Y., Groves, D.I. and Deng, J. 2024. Metasomatized mantle sources for orogenic gold deposits hosted in high-grade metamorphic rocks: Evidence from Hg isotopes. *Geology*, **52**(2), pp.115-119.

Ward, J., Mavrogenes, J., Murray, A. and Holden, P. 2017. Trace element and sulfur isotopic evidence for redox changes during formation of the Wallaby Gold Deposit, Western Australia. *Ore Geology Reviews*, **82**, pp.31-48.

Warr, L.N. 2021. IMA–CNMNC approved mineral symbols. *Mineralogical Magazine*, **85**(3), pp. 291-320.

Watanabe, Y. and Hedenquist, J.W. 2001. Mineralogic and stable isotope zonation at the surface over the El Salvador porphyry copper deposit, Chile. *Economic Geology*, **96**(8), pp.1775-1797.

Watanabe, Y., Sato, R. and Sulaksono, A. 2018. Role of Potassic Alteration for Porphyry Cu Mineralization: Implication for the Absence of Porphyry Cu Deposits in Japan. *Resource Geology*, **68**(2), pp.195-207.

Watkins, K.P. 1983. Petrogenesis of Dalradian albite porphyroblast schists. *Journal of the Geological Society*, **140**(4), pp.601-618.

Watkins, K.P. 1987. Biotite- and garnet-forming reactions in inverted metamorphic zones in the Balquhidder region of the Scottish Dalradian. *Scottish Journal of Geology*, **23**(1), pp.105-127.

Wasserburg, G.J. 1963. Diffusion processes in lead-uranium systems. *Journal of Geophysical Research*, **68**(16), pp.4823-4846.

Wayne, D.M., Sinha, A.K. and Hewitt, D.A. 1992. Differential response of zircon U− Pb isotopic systematics to metamorphism across a lithologic boundary: an example from the Hope Valley Shear Zone, southeastern Massachusetts, USA. *Contributions to Mineralogy and Petrology*, **109(**3), pp.408-420.

Weatherley, D. and Henley, R. 2013. Flash vaporization during earthquakes evidenced by gold deposits. *Nature Geoscience*, **6**(4), pp.294-298.

Webb, S., Torvela, T., Chapman, R., Selby, D. and Gooday, R. 2023. An integrated approach towards unravelling the gold mineralisation processes around Ardtalnaig, Scotland. ETH Zürich, 1 September. Zurich: Society for Geology Applied to Mineral Deposits, extended abstracts.

Webb, S., Torvela, T., Chapman, R. and Savastano, L. 2024a. Textural mapping and building a paragenetic interpretation of hydrothermal veins. *Geological Society, London, Special Publications*, **541**(1).

Webb, S., Torvela, T., Chapman, R., Selby, D. and Gooday, R. 2024b. A reinterpretation of the mineralisation processes involved in the formation of the Tomnadashan sulphide deposit, Loch Tay, Scotland, UK. *Scottish Journal of Geology,* **60**.

Webster, R.K. 1959. Isotope dilution analysis. In: Waldron, J. ed. *Advances in mass spectrometry*. Pergamon, pp.103-119.

Wedepohl, K. and Hartmann, G. 1994. The composition of the primitive upper earth's mantle. In: Meyer HOA, Leonardos OH. eds. *Kimberlites, related rocks and mantle xenoliths*. Companhia de Pesquisa de Recursos Minerais, Rio de Janeiro, pp.486-495.

Weinberg, R.F. 2016. Himalayan leucogranites and migmatites: nature, timing and duration of anatexis. *Journal of Metamorphic Geology*, **34**(8), pp.821-843.

Wen, B.-J., Fan, H.-R., Santosh, M., Hu, F.-F., Pirajno, F. and Yang, K.-F. 2015. Genesis of two different types of gold mineralization in the Linglong gold field, China: Constrains from geology, fluid inclusions and stable isotopes. *Ore Geology Reviews*, **65**, pp.643-658.

Wendt, I. 1984. A three-dimensional U-Pb discordia plane to evaluate samples with common lead of unknown isotopic composition. Chemical Geology, **46**(1), pp.1-12.

Wendt, I. and Carl, C. 1991. The statistical distribution of the mean squared weighted deviation. *Chemical Geology: Isotope Geoscience Section*, **86**(4), pp.275-285.

Wesnousky, S.G. 2005. The San Andreas and Walker Lane fault systems, western North America: transpression, transtension, cumulative slip and the structural evolution of a major transform plate boundary. *Journal of Structural Geology*, **27**(8), pp.1505-1512.

Westner, J., Rose, T., Klein, S. and Hsu, Y. 2021. GlobaLID – Global Lead Isotope Database. V. 1.0. GFZ Data Services. https://doi.org/10.5880/fidgeo.2021.031

Westra, G. and Keith, S.B. 1981. Classification and genesis of stockwork molybdenum deposits. *Economic Geology*, 76(4), pp.844-873.

Wetherill, G. 1956. Discordant uranium-lead ages. Transactions, *American Geophysical Union*, **37**(3).

White, A.J.R., Waters, D.J., and Robb, L.J. 2015. Exhumation-Driven Devolatilization as a Fluid Source for Orogenic Gold Mineralization at the Damang Deposit, Ghana. *Economic Geology*, 110(4), pp.1009-1025.

Widmann, P., Davies, J.H.F.L. and Schaltegger, U. 2019. Calibrating chemical abrasion: Its effects on zircon crystal structure, chemical composition and U-Pb age. *Chemical Geology*, **511**, pp.1-10.

Wilke, M., Klimm, K. and Kohn, S. 2011. Spectroscopic studies on sulphur speciation in synthetic and natural glasses. *Reviews in Mineral Geochemistry*, **73**, pp.41-78.

Wilkinson, J.J. and Johnston, J.D. 1996. Pressure fluctuations, phase separation, and gold precipitation during seismic fracture propagation. *Geology*, **24**, pp.395-398.

Wilkinson, J., Boyce, A., Earls, G. and Fallick, A. 1999. Gold remobilization by low-temperature brines; evidence from the Curraghinalt gold deposit, Northern Ireland. *Economic Geology*, **94**(2), pp.289-296.

Wilkinson, J.J., Eyre, S.L. and Boyce, A.J. 2005. Ore-forming processes in Irish-type carbonate-hosted Zn-Pb deposits: Evidence from mineralogy, chemistry, and isotopic composition of sulfides at the Lisheen mine. *Economic Geology*, **100**(1), pp.63-86.

Wilkinson, J.J. 2013. Triggers for the formation of porphyry ore deposits in magmatic arcs. *Nature Geoscience*, **6**(11), pp.917-925.

Willan, R.C.R. and Coleman, M.L. 1983. S-isotope study of the Aberfeldy barite, zinc, lead deposit and minor sulfide mineralisation in the Dalradian metamorphic terrain, Scotland. Economic *Geology*, **78**, pp.1619-1656.

Winchester, J.A. 1974. The zonal pattern of regional metamorphism in the Scottish Caledonides. *Journal of the Geological Society*, **130**(6), pp.509-524.

Wilson, J.S.G. and Cadell, M. 1884. The Breadalbane Mines. *Royal Physics Society of Edinburgh*, 8, pp.189-207.

Wilson, C. 1994. Crystal growth during a single-stage opening event and its implications for syntectonic veins. *Journal of Structural Geology*, **16**, pp.1283-1296.

Wilson, A., Cooke, D. and Harper, B. 2003. The Ridgeway Gold-Copper Deposit: A High-Grade Alkalic Porphyry Deposit in the Lachlan Fold Belt, New South Wales, Australia. *Economic Geology*, **98**(8), pp.1637-1666.

Wood, S.A. and Samson, I.M. 1998. Solubility of ore minerals and complexation of ore metals in hydrothermal solutions. *Reviews in Economic Geology*, **10**, pp.33-80.

Woodcock, N.H. and Strachan, R.A. 2000. The Caledonian Orogeny: a multiple plate collision. In: Woodcock, N.H. & Strachan, R.A. ed(s). *Geological History of Britain and Ireland*. Blackwell Science, Oxford, pp.187-206.

Woodcock, N., Soper, N. and Strachan, R. 2007. A Rheic cause for the Acadian deformation in Europe. *Journal of the Geological Society*, **164**(5), pp.1023-1036.

Woodhead, J. and Hergt, J. 2000. Pb-isotope analyses of USGS reference materials. *Geostandards Newsletter*, **24**(1), pp.33-38.

Woodhead, J. 2002. A simple method for obtaining highly accurate Pb isotope data by MC-ICP-MS. *Journal of Analytical Atomic Spectrometry*, **17**(10), pp.1381-1385.

Wortmann, U.G., Bernasconi, S.M. and Böttcher, M.E. 2001. Hypersulfidic deep biosphere indicates extreme sulfur isotope fractionation during single-step microbial sulfate reduction. *Geology*, **29**(7), pp.647-650.

Wotzlaw, J.-F., Buret, Y., Large, S. J.E., Szymanowski, D. and von Quadt, A. 2017. ID-TIMS U–Pb geochronology at the 0.1‰ level using 10 13 Ω resistors and simultaneous U and 18 O/ 16 O isotope ratio determination for accurate UO 2 interference correction. *Journal of Analytical Atomic Spectrometry*, **32**(3), pp.579-586.

Wu, Y.-F., Evans, K., Li, J.-W., Fougerouse, D., Large, R.R. and Guagliardo, P. 2019. Metal remobilization and ore-fluid perturbation during episodic replacement of auriferous pyrite from an epizonal orogenic gold deposit. *Geochimica et Cosmochimica Acta,* 245, pp.98-117.

Wyman, D. A., O'Neill, C. and Ayer, J. A. 2008. Evidence for modern-style subduction to 3.1 Ga: A plateau–adakite–gold (diamond) association. In: Condie, K.C., Pease, V. ed(s). *When Did Plate Tectonics Begin on Planet Earth?* Geological Society of America, pp.129-148

Wyman, D. A., Cassidy, K. F., and Hollings, P. 2016. Orogenic gold and the mineral systems approach: Resolving fact, fiction and fantasy. *Ore Geology Reviews,* **78**, pp.322-335.

Xiao, B., Chen, H., Hollings, P., Wang, Y., Yang, J. and Wang, F. 2018. Element transport and enrichment during propylitic alteration in Paleozoic porphyry Cu mineralization systems: Insights from chlorite chemistry. *Ore Geology Reviews*, **102**, pp.437-448.

Xiong, Y., Zuo, R. and Miller, S.A., 2023. The behavior of hydrothermal mineralization with spatial variations of fluid pressure. Journal of Geophysical Research: *Solid Earth*, **128**(2), article no: JB025255 [no pagination]

Yang, F., Li, W., Zhu, X., Liu, J., Jiang, X., Yang, H. and Li, Y. 2022. Origin of the Bada porphyry Cu–Au deposit, eastern Tibet: Geology and isotope geochemistry (C–O–S–Pb) constraints. *Ore Geology Reviews*, **146**, article no: 104935 [no pagination]

Yardley, B.W.D. 1977. Nature and significance of the mechanism of sillimanite growth in the Connemara Schists, Ireland. *Contributions to Mineralogy and Petrology*, **65**, pp.53-58.

Yardley, B., Bottrell, S.H. and Cliff, R.A. 1991. Evidence for a regional-scale fluid loss event during mid-crustal metamorphism. *Nature*, **349**(6305), pp.151-154.

Yardley, B.W.D., Banks, D.A., Bottrell, S.H. and Diamond, L.W. 1993. Post-metamorphic gold-quartz veins from N.W. Italy: the composition and origin of the ore fluid. *Mineralogical Magazine*, **57**(388), pp.407-422.

Yardley, B.W.D. 2009. The role of water in the evolution of the continental crust. Journal of the Geological Society, **166**(4), pp.585-600.

Yardley, B. and Cleverley, J. 2013. The role of metamorphic fluids in the formation of ore deposits. *Geological Society, London, Special Publications*, **393**(1), pp.117-134.

Yesares, L., Drummond, D.A., Hollis, S.P., Doran, A.L., Menuge, J.F., Boyce, A.J., Blakeman, R.J. and Ashton, J.H. 2019. Coupling Mineralogy, Textures, Stable and Radiogenic Isotopes in Identifying Ore-Forming Processes in Irish-Type Carbonate-Hosted Zn–Pb Deposits. *Minerals*, **9**(6), pp.335.

Yue, S., Deng, X., and Lin, Z. 2022. Direct Re–Os dating of pyrite from the Jianchaling Au deposit, West Qinling, China. *Acta Geochimica*, **41**(2), pp.275-287.

Zachariáš, J., Žák, K., Pudilová, M. and Snee, L. W. 2013. Multiple fluid sources/pathways and severe thermal gradients during formation of the Jílové orogenic gold deposit, Bohemian Massif, Czech Republic. *Ore Geology Reviews*, **54**, pp.81-109.

Zack, T., Stockli, D.F., Luvizotto, G.L., Barth, M.G., Belousova, E., Wolfe, M.R. and Hinton, R.W., 2011. In situ U–Pb rutile dating by LA-ICP-MS: 208 Pb correction and prospects for geological applications. *Contributions to Mineralogy and Petrology*, **162**, pp.515-530.

Zartman, R.E. and Doe, B.R. 1981. Plumbotectonics—the model. *Tectonophysics*, **75**(1-2), pp.135-162.

Zartman, R.E. and Haines, S.M. 1988. The plumbotectonic model for Pb isotopic systematics among major terrestrial reservoirs-A case for bi-directional transport. *Geochimica et Cosmochimica Acta*, **52**(6), pp.1327-1339.

Zhai, D., Williams-Jones, A., Liu, J., Selby, D., Li, C., Huang, X., Qi, L. and Guo, D. 2019. Evaluating the Use of the Molybdenite Re-Os Chronometer in Dating Gold Mineralization: Evidence from the Haigou Deposit, Northeastern China. *Economic Geology*, **114**(5), pp.897-915.

Zhai, D., Williams-Jones, A.E., Liu, J., Selby, D., Voudouris, P.C., Tombros, S., Li, K., Li, P. and Sun, H. 2020. The Genesis of the Giant Shuangjianzishan Epithermal Ag-Pb-Zn Deposit, Inner Mongolia, Northeastern China. *Economic Geology*, **115**(1), pp.101-128.

Zhang, S., Cox, S.F. and Paterson, M.S. 1994. The influence of room temperature deformation on porosity and permeability in calcite aggregates. *Journal of Geophysical Research*, **99**, pp.761-775.

Zhang, S.B., Zheng, Y.F., Wu, Y.B., Zhao, Z.F., Gao, S. and Wu, F.Y. 2006. Zircon U–Pb age and Hf isotope evidence for 3.8 Ga crustal remnant and episodic reworking of Archean crust in South China. *Earth and Planetary Science Letters*, **252**(1-2), pp.56-71.

Zhang, J.Y., Qiu, K.F., Yin, R., Long, Z.Y., Feng, Y.C., Yu, H.C., Gao, Z.Y. and Deng, J., 2024. Lithospheric mantle as a metal storage reservoir for orogenic gold deposits in active continental margins: Evidence from Hg isotopes. *Geology*.

Zhao, H., Wang, Q., Groves, D. I., Santosh, M., Zhang, J. and Fan, T. 2022a. Genesis of orogenic gold systems in the Daduhe belt: Evidence of long-lived fertile mantle lithosphere as a source of diverse metallogeny on the western margin of the Yangtze Craton, China. *Ore Geology Reviews*, **145**.

Zhao, H., Wang, Q., Kendrick, M. A., Groves, D.I., Fan, T. and Deng, J. 2022b. Metasomatized mantle lithosphere and altered ocean crust as a fluid source for orogenic gold deposits. *Geochimica et Cosmochimica Acta*, **334**, pp.316-337.

Zheng, Y. 1992. The three-dimensional U-Pb method: Generalized models and implications for U-Pb two-stage systematics. *Chemical Geology*, **100**(1-2), pp.3-18.

Zheng, Y., Wu, Y., Yu, P., Hu, Z. and Chen, Y. 2021. Gold accumulation in the metavolcanic-hosted orogenic gold deposit constrained by pyrite paragenesis coupled with in-situ trace elements and sulfur isotope: The Sarekuobu example in the Chinese Altay Orogen. *Ore Geology Reviews*, **138**, article no: 104387 [no pagination]

Zhimin, Z. and Yali, S. 2013. DIRECT Re-Os DATING OF CHALCOPYRITE FROM THE LALA IOCG DEPOSIT IN THE KANGDIAN COPPER BELT, CHINA. *Economic Geology*, **108**(4), pp.871-882.

Zhong, Y.-T., Luo, Z.-Y., Mundil, R., Wei, X., Liu, H.-Q., He, B., Huang, X.-L., Tian, W. and Xu, Y.-G. 2022. Constraining the duration of the Tarim flood basalts (northwestern China): CA-TIMS zircon U-Pb dating of tuffs. *GSA Bulletin*, **134**(1-2), pp.325-334.

Zhou, J.X. 1987. An occurrence of shoshonites near Kilmelford in the Scottish Caledonides and its tectonic implications. *Journal of the Geological Society*, **144**(5), pp.699-706.

Zhou, J. 1988. A gold and silver-bearing subvolcanic centre in the Scottish Caledonides near Lagalochan, Argyllshire. *Journal of the Geological Society*, **145**(2), pp.225-234.

Zhou, Y.-X., Li, B., Zhu, Z.-Y. and Zhao, H.-X. 2023. Fe and S isotopes variation of pyrite from hydrothermal mineralization in the Zijinshan region in Fujian Province, SE China. *Geochemistry*, article no: 126047 [no pagination]

Zhu, D., Li, H., Algeo, T., Jiang, W. and Wang, C. 2021. The prograde-to-retrograde evolution of the Huangshaping skarn deposit (Nanling Range, South China). *Mineralium Deposita*, **56**, pp.1087-1110.

Ziegler, P.A. 1987. Compressional intra-plate deformations in the Alpine foreland—an introduction. *Tectonophysics*, **137**(1-4), pp.1-5.

Zoheir, B., Akawy, A. and Hassan, I. 2008. Role of fluid mixing and wallrock sulphidation in gold mineralization at the Semna mine area, central Eastern Desert of Egypt: Evidence from hydrothermal alteration, fluid inclusions and stable isotope data. *Ore Geology Reviews*, **34**(4), pp.580-596.

Zotov, A.V. 1991. The solubility of gold in aqueous chloride fluids at 350-550°C and 500-1500 atm: Thermodynamic parameters of AuCl_2-(aq) up to 750°C and 5000 atm. *Geochemistry International*, **28**, pp.63-71.

Appendix A: Table of samples and specimens

Table A.1. List of samples utilised throughout the course of this study (the 'ID' field), presented alongside the location of sampling, grid reference (GR) and a brief description. An indication of the type of analysis (e.g. petrographic, isotopic, or both) the sample was used in has also been provided.

Location	ID	GR	Description	Analysis
Ardtalnaig	ARD_1	NN 72677 38540	Boulder float >1 m in diameter; Gn in vuggy Qz; Green Glen Minerals reported gold grades of 17.5 g/t from a grab sample	$\delta^{34}S$, Pb
	ARD_FELS_1	NN 71934 38596	Fine-grained, reddish grey granitoid	CA-ID-TIMS
	ARD_FELS_2	NN 71042 38636	Tan brown outcrop of granitoid; heavily altered by many Qz veinlets (< 5 mm wide)	SEM
	RX2959KA	NN 71577 38887	Discarded rock chip from boulder float, contains trace amounts of Ccp; Green Glen Minerals reported gold grades of 11.5 g/t from a grab sample	SEM, Pb
Calliachar	LSCV1	NN 84157 45411	V3 outcrop sample; Gn chunks (>0.5 cm) set in vuggy Qz matrix	$\delta^{34}S$
	SW3	NN 84219 45455	Porphyritic felsite located in the Calliachar Burn; collected by Green Glen Minerals in Spring of 2021	CA-ID-TIMS
	CAL_GN	NN 8414 4547	Lump of galena float (>10 cm) collected close to V3	$\delta^{34}S$
	CAL_PY	NN 83555 45659	Crushed Py panned by Dr Rob Chapman from V7 in field campaigns before 2020	$\delta^{34}S$
	65004	NN 83522 45612	Hand specimen with pyrite and visible gold from V6	In-situ $\delta^{34}S$
	2003.1G.M.604 a-p	NN 83522 45612	Sample collected from opencast workings at V6 during exploration programmes conducted by Colby Gold plc, supplied by NMW; high-grade (>150 g/t) Py-Gn ore; abundant microscopic electrum; Py has experienced cataclasis	$\delta^{34}S$, Pb
	2003.1G.M.626 a-v	NN 83555 45659	V7; high-grade sulphide, Au grade of 100 g/t, contains Py and Gn; supplied by NMW, collected during Colby Gold plc exploration campaigns	$\delta^{34}S$, Pb
	2003.1G.M.627	NN 84002 45175	Discovery Vein (V1); euhedral Py and Apy in quartz; Au grade of >50 g/t; supplied by NMW; collected during Colby Gold plc exploration campaigns	$\delta^{34}S$

	2003.1G.M.630	NN 83594 45139	V5; Py-Gn-Ccp assemblage in Qz; Au grade of <1.7 g/t; Py too fine-grained to sample, only Gn could be supplied by NNW; collected during Colby Gold plc exploration campaigns	$\delta^{34}S$, Pb
Coire Buidhe	CB1, CB2, CB3, CB4	NN 68932 34597	Samples from Spoil Heap, which is located at the bottom of Meall nan Oighreag, with Apy, Ccp, Py, and Gn hosted in a coarse-grained (>1 cm) Qz matrix	$\delta^{34}S$, in-situ $\delta^{34}S$, Pb.
	CB_FELS_2	NN 70616 33673	Tan grey, very fine-grained granitoid hand specimens collected near Coire Buidhe	CA-ID-TIMS
	CB_GAL	NN 70423 34047	Hand specimens from the disused tips around the mine entrance at the peak of Meall nan Oighreag; contain voluminous Gn and Qz	$\delta^{34}S$, Pb
Comrie Pluton	CMRIE4	NN 77839 25474	Pink rhyolite with Ccp and Py	$\delta^{34}S$
	CMRIE7	NN 77947 25521	Potassic alteration zone in the granite of the Comrie Pluton with Py and Ccp mineralisation	
Glen Almond	GAV_PCa	NN 72983 32822	Py crystals retrieved from crushing the GAV; contained trace amounts of Gn	$\delta^{34}S$
	GAV_PCb	NN 72983 32822		$\delta^{34}S$, Pb
	GAV_GN	NN 72983 32822	Gn separated from crushed fragments of the GAV	$\delta^{34}S$
	RC1, RC2, RC3, RC4, RC5, AVRE, AVRE(2)	NN 72983 32822	Polished blocks and thin sections (AVRE) of the GAV, which contain gold, Gn, Sp, Ccp, Py and arsenian Py; used in Webb *et al.* 2024a	$\delta^{34}S$, in-situ $\delta^{34}S$, (AVRE = thin sections)
Lead Trial	LDT_CO	NN 70839 39258	Crushed Gn retrieved from the disused tips around Lead Trial	$\delta^{34}S$
	19882	NN 71391 39089	'Channel Sample' investigated by Green Glen Minerals; some visible Gn chunks	$\delta^{34}S$, Pb
	LDT_LSa, LDT_LSb, LDT_LSc, LDT_LSD, LDT_LSDb	NN 70833 39255	Samples containing Gn and Sp collected from the disused tips around Lead Trial	$\delta^{34}S$

	LDT1, LDT2	NN 70839 39260	Vein at Lead Trial crosscutting pelites of the Southern Highland Group (Fig. 5.4.a.); brecciated, vuggy Qz, repeated Qz generations observed across the width of the vein; Sp dominant, Gn relatively uncommon	SEM
	LDT4	NN 70836 39285	Vein at Lead Trial outcropping at top of hill and crosscutting rhyolites (Fig. 5.4.b.); brecciated, vuggy Qz, some Gn mineralisation	SEM
	RX2990KA, RX2991KA	NN 71135 39067	KA sample; boulder from Lead Trial; rhyolite-hosted vein with visible sulphide blebs; vuggy Qz	Pb
	RX2963KA, RX2964KA	NN 70835 39267	Outcrop at Lead Trial; schist and rhyolite breccia, contains sulphide blebs	Pb
	RX2996AKA, RX2996BKA	NN 71185 39084, NN 71185 39085	Boulder float comprised of vuggy Qz found close to Lead Trial; contains sulphide blebs, visible gold	Pb
	RX2967KA	NN 70835 39268	Outcrop at Lead Trial comprised of schist and rhyolite breccia; contains sulphide blebs	SEM
Tombuie	2003.1G.M.637	NN 776 444	Boulder float containing Gn, Sp, Ccp, Py and Sd in Qz; Au grade of 6 g/t; sample supplied by NMW, collected during Colby Gold plc exploration programmes	$\delta^{34}S$, Pb
Tomnadashan	SW_TOM_PY	NN 69125 37914	Disseminated Py within a hand specimen of the granite collected at the disused tips outside the mine entrance	$\delta^{34}S$, in-situ $\delta^{34}S$
	TOM_FELS		Granitoid-hosted disseminated mineralisation (Py and Ccp) in pink rhyolites (potassic alteration); collected from the disused tips outside the mine	$\delta^{34}S$
	TOM_FELS_2	NN 69203 37775	In-situ pink rhyolite sampled from the southern wall of the mine; this intrusion is a different hue from the diorite and granodiorite	CA-ID-TIMS
	TOM_QTZ	NN 69168 37831	Qz ± Carb vein containing pyrite, chalcopyrite and sulfosalt mineralisation; sample found in a disused tip adjacent to the entrance of the mine	$\delta^{34}S$, in-situ $\delta^{34}S$

	TD-0	NN 69125 37914	Polished block loaned by the University of Edinburgh; described as being a sample of mineralisation from the 'epithermal quartz vein' at Tomnadashan; sample mostly comprised of Qz and Ttr, with small amounts of Gn also present.	RLM
	G.2019.101.7	NN 69125 37914	B0018 polished block supplied by NMS; lump of Gn (< 10 cm) with visible Ccp and Sp inclusions	$\delta^{34}S$, Pb
	MOLY_CONC	NN 69105 37924	~0.7 mm wide Mol chunk found as a result of panning in the stream leaving the mine	$\delta^{34}S$
	TOM_MOLY_SM	NN 687 377	Mol specimen supplied by Dr Stephen Moreton in November 2022; collected from the smelter mill where material from Tomnadashan was taken during artisanal mining	Re-Os
	G.1878.49.10.1	NN 69125 37914	Mol specimen supplied by NMS; collected from the disused tips outside the mine; fine-grained and disseminated Mol and Py in granitoid hand specimen	Re-Os, $\delta^{34}S$
	G.002.26.2417.2	NN 69125 37914	B001 and B003 polished blocks supplied by NMS; disseminated Mol, Py, and Ccp mineralisation in the granitoid	In-situ $\delta^{34}S$
	PA_MOLY	NN 68600 37725	Collected by Peder Aspen in April 2023; coarse Mol chunks (5-7 mm) were found in Qz stringers	Re-Os, $\delta^{34}S$
Urlar	UB_GAL	NN 82489 44909	Mineralised Qz vein float with visible Gn chunks found in the Urlar Burn during panning prior to 2020	$\delta^{34}S$
	UB_VEINa	NN 82486 44911	Found by Dr Taija Torvela and Dr Rob Chapman during fieldwork in June of 2023; an in-situ Qz vein with large amounts of coarse-grained (>1 cm) Gn crystals, trace Py and Mlc; sulphides flow throughout cracks in the Qz	$\delta^{34}S$, Pb
	UV_SHa	NN 82320 44917	Visible Py and Gn; samples retrieved from the disused tips on the bank of the Urlar Burn.	$\delta^{34}S$, Pb
	UV_SHa			$\delta^{34}S$, Pb
	UB_VEINb	NN 82536 44954	Found by Dr Taija Torvela and Dr Rob Chapman during fieldwork in 2023; mineralogically similar to the material from the disused tips around the Urlar Burn	$\delta^{34}S$, Pb

Appendix B: Sample preparation and analytical procedures

B.1. Introduction

In this Appendix, a detailed explanation regarding each of the methods utilised to prepare and analyse the samples pertaining to this study (SEM microscopy, CA-ID-TIMS, Re-Os, $\delta^{34}S$, and Pb isotopes) is provided.

B.2. Petrographic characterisation

Throughout the course of this study, a variety of techniques involving microscopy (e.g. SEM, RLM and the use of optical microscopes) were used to describe the characteristics of both the veins and the granitoids around Loch Tay. However, the standard approach involved the implementation of SEM; for this task, it was necessary to produce polished thin sections of the rock samples that were collected during fieldwork.

Preparation of thin sections and polished blocks was conducted in the Rock Polishing Laboratory at the University of Leeds. This process involved cutting hand specimens with Logitech GTS1 and Buehler™ 2diamond saws into smaller chips measuring 50 x 25 mm. These fragments were initially polished using a manually operated Ecomet 250 Polisher Grinder (i.e. to smoothen the surface of the rock chip). Regarding the preparation of thin sections, the next step involved mounting the rock chips on slides of glass; this task was achieved by using a Logitech LP 50 lapping machine, which bathed the slides in a paste comprised of aluminium for intervals ranging between 5 and 15 seconds. EpoThin 2 Resin was then used to stick the slide of glass onto the rock sections, which were subsequently positioned with the glass slide facing downwards on a hot plate. Heating of the thin sections lasted for between 2 and 5 hours. The next step in the preparation of the thin sections was the use of the PetroThin Gravity-fed Precision Sectioning Machine (also manufactured by Buehler) to cut the portion of the thin section comprised by rock to thicknesses of 50 µm. The thin sections were then polished again using the Automat 250, a process that was completed over intervals lasting for less than 20 minutes. Regarding the preparation of polished blocks, the process differed in that smaller rock chips (i.e. < 2.5 cm) were required during the initial cutting stage; these smaller chips were placed into plastic capsules and filled with EpoThin 2 Resin and a hardener supplied by Buehler in a ratio of 2:1.

SEM characterisation of petrographic features was undertaken at the University of Leeds (Leeds electron microscopy and spectroscopy centre) using an FEI Quanta 650 FEG and a Tescan VEGA3 XM equipped with the following components and functions; X-max 150 SDD Energy Dispersive Spectroscopy (EDS), Aztec 3.3 software, and an RGB filtered CL system (Webb *et al.*, 2024a, b). Similar studies were also carried out at NMS using a Tescan CLARA Variable-Pressure Field Emission Gun SEM (VP-FEG-SEM), which came equipped with an Oxford Instruments Ultim Max 100 mm^2 EDS detector. The main approach to SEM imaging taken in

this study was therefore the dual application of SEM-BSE and EDS on thin sections and polished blocks. Following electron bombardment, the BSE detector tracks emitted electrons; these backscattered electrons are then used to create high-resolution images showing the distribution of different elements (Niedrig, 1978; Webb *et al.*, 2024a). The rate at which backscattered electrons are produced is dependent on the atomic number of the element being analysed. Denser elements produce a more pronounced electron deflection, resulting in brighter images (Niedrig, 1978). In addition to the SEM work, some limited RLM petrographic studies were also conducted at NMS using a GX Microscope POLTEC-1 fitted with a GXCAM-U23PRO-12 camera.

However, the use of SEM-CL in petrographic characterisation can assist in providing more information on specific phases and their precipitation history (Webb *et al.*, 2024a). The underpinning principle of SEM-CL is that following electron bombardment, a luminescent mineral emits light (Marshall, 1988). In SEM-CL, electron stimulation is achieved by using a hot filament to accelerate the electrons towards an anode. The electron beam scans the sample and a CL detector housed within the SEM translates the light emitted from the sample into images (Götze and Kempe, 2009). Throughout the course of this study, SEM-CL was used for two purposes: 1) to characterise textures within zircons and 2) to image the different hydrothermal quartz generations. In terms of the latter, SEM-CL is particularly suitable for this task because variations in quartz composition are caused by impurities linked to trace element substitution into the mineral lattice, particularly aluminium (Götze *et al.*, 2001; Götze, 2009; Stevens-Kalceff, 2009; Frelinger *et al.*, 2015). The specific element substituted into the lattice is dependent upon several factors, including the rate of crystallisation, fluid composition, pressure, temperature, and post-mineralisation deformation (Götze and Möckel, 2012). In the context of hydrothermal systems, in which quartz veins typically form as a result of repeated fracturing and fluid flow events, each distinct fluid is likely to involve a different form of trace element substitution; for this reason, the different quartz generations within a hydrothermal vein often record a distinct response in SEM-CL (Webb *et al.*, 2024a).

B.3. CA-ID-TIMS

Fist-sized hand specimens of ARD_FELS_1, ARD_FELS_2, CB_FELS_2, TOM_FELS_2 and SW3 were sent to the geochronology facility at the BGS as part of NEIF application 2649.0423. The approach to CA-ID-TIMS analyses was adapted from Mattinson (2005) and paraphrased throughout the rest of this section.

Initially, the zircons were annealed at a temperature of 900 °C for 60 hours in crucibles comprised of quartz prior to the selection of individual crystals for subsequent U-Pb analyses. This process involved the use of transmitted light microscopy to evaluate the morphology of the zircon crystals and the presence of internal features indicative of primary growth (i.e. visible cores, oscillatory zonation; Corfu, 2003). The selected zircon crystals were refluxed in 4 M HNO_3 on a hotplate at 120 °C for > 2 hours prior to ultrasonic cleaning for durations of approximately 20 minutes. Each zircon crystal was cleaned with acetone and 4 M HNO_3 before being placed into singular 300 µl FEP Teflon microcapsules and leached in 29 M HF inside a Parr container for over 12 hours at 180 °C. The zircons were cleaned with 4 M HNO_3 and refluxed in 6 M HCl at 120 °C for 2-5 hours before conducting a final clean using 4 M HNO_3.

The selected zircon samples and blanks were spiked with ^{205}Pb–^{233}U–^{235}U (ET535) EARTHTIME tracer solution prior to dissolution in ~150 µl 29 M HF and trace HNO_3 in a Parr vessel at temperatures 220 °C for over 60 hours. To ensure that dissolution was complete, visual inspection of some of the larger crystals was conducted and assumed for grains that were smaller (implementing a procedure for dissolution at the National Environment Research Council Isotope Geosciences Laboratories). Each solution was dried down prior to dissolution through mixing with a solution comprised of 3 M HCl in a Parr vessel for 24 hours at a temperature of 180 °C. It was then possible to isolate U and Pb fractions through the implementation of a procedure involving HCL-based anion exchange using Bio-Rad AG-1 resin in Teflon columns. Following this, the Pb and U fractions were recombined and dried down with a solution of ~10 µl of H_3PO_4 before being placed into zone-refined Re filaments in a silica gel matrix to further augment ionisation.

Regarding the measurement of isotope ratios, this task was completed by using Thermo-Electron Triton Thermal Ion Mass Spectrometry (TIMS). Pb was quantified using the dynamic mode on a MassCom secondary electron multiplier, whilst mass corrections were conducted by assuming a fractionation factor of 0.14 ± 0.02 % amu-1 (1 sigma) for samples spiked using ET535. In terms of monitoring the dead-time and linearity of the secondary electron multiplier, this was achieved by conducting several repeat measurements on a series of standards (NBS 982, NBS 981 and U 500). Following this process, uranium oxide (UO_2) was measured and corrected for isobaric interferences through the use of an $^{18}O/^{16}O$ value of 0.00205 (the value used by the International Union of Pure and Applied Chemistry). As with Pb, uranium was measured in a dynamic mode, although the correction for mass bias induced fractionation was

calculated using the ^{233}U-^{235}U ratio of the ET535 tracer solutions. It was then possible to make corrections for the addition of Pb and U as a result of laboratory contamination using the measured isotope composition and variability of the blanks; this procedure involved the use of a quantity based on measurements from contemporary total procedural blanks. Each U/Pb ratio measured during the analyses was constrained using the principles of isotope dilution and the ET535 mixed ^{205}Pb-^{233}U-^{235}U tracer. In terms of the $^{238}U/^{235}U$ ratio that was assumed, this value was 137.818 (Hiess *et al.*, 2012) and implemented in the data reduction algorithm within the UPbR spreadsheet produced by Schmitz and Schoene (2007). To visualise the resulting U-Pb data, IsoplotR (an open access program for geochronology; Vermeesch, 2018) was used to create rank-order and concordia plots. For a full breakdown of how the code generates plots from this information, see Vermeesch (2018).

B.4. Re-Os

Re-Os dating of molybdenite involved the implementation of the same analytical procedure described by Li *et al.* 2017. As such, the method from this publication (which was based on previous studies; Selby and Creaser, 2001; Lawley and Selby, 2012) has been paraphrased here (similarly to Webb *et al.* 2024b). Fractions of the molybdenite samples were crushed with a pestle into chunks < 2 mm before using tweezers to remove other minerals (e.g. pyrite) from the concentrate. Following this, the mixture of molybdenite and quartz that could not be removed by eye was placed into a Teflon beaker filled with 10 ml 32N HF at room temperature for one night, which resulted in the dissolution of quartz (Lawley and Selby, 2012). The molybdenite crystals were then washed with Milli-Q water three times and washed again using ethanol prior to drying out the crystals at ~35 °C.

For the digestion, a known quantity of molybdenite (>20 mg) and tracer solution (^{185}Re and the isotopically normal osmium isotope; Selby and Creaser, 2001) were both loaded into a Carius tube (Shirey and Walker, 1995) with 3 ml 15.5N HCl and 6 ml 16N HNO_3; this tube was then sealed and wrapped in steel (Li *et al.*, 2017). Over the course of 24 hours, the tube was placed into an oven for digestion at 220 °C, enabling the development of isotopic equilibrium conditions in the rhenium and osmium isotopes between the tracer and sample (Selby and Creaser, 2001). Following this process, the tubes were cooled down (i.e. to room temperature), and their surfaces were washed with Milli-Q water to remove any particles. The bases of the Carius tubes were then frozen in ethanol and dried ice prior to opening them from the top using an H_2-O_2 flame in a fume hood (Li *et al.*, 2017). Isolation of osmium from the medium comprised of acid was achieved through the implementation of $CHCl_3$; 3 × 3 mL at room temperature (Shen *et al.*, 1996) prior to being extracted back into HBr (Cohen and Waters, 1996). The HBr solution, now containing osmium, was dried out with osmium that had been purified by microdistillation (Roy-Barman, 1993; Birck *et al.*, 1997). Following the extraction of Os, acidic medium (which contained Re) was dried and then segregated through solvent extraction involving NaOH-acetone (Matthews and Riley, 1970). Further purification of the Re was achieved by using standard anion column chromatography (Morgan *et al.*, 1991).

Following this process, Re and Os were placed onto Ni and Pt filaments that had previously been outgassed (Li *et al.*, 2017). The isotopic compositions of Re and Os were quantified using negative thermal ionization mass spectrometry as ReO_4 and OsO_3, respectively (Creaser *et al.*, 1991; Völkening *et al.*, 1991). The Re-Os analyses were performed using a Thermo Scientific Triton mass spectrometer at Durham University; Re and Os isotope compositions were measured using the static Faraday cups collection mode (Li *et al.*, 2017). Furthermore, the Re and Os isotope compositions that were measured were corrected using a $^{18}O/^{16}O$ value of 0.002045 and a $^{17}O/^{16}O$ value of 0.001113 (Nier, 1950; Li *et al.*, 2017). To correct for the isotopic composition of Re, this was achieved by quantifying the fractionation induced by the analytical equipment using factors that represent the variations between standard analyses for Re and the $^{185}Re/^{187}Re$ ratio

(0.59738; Gramlich *et al.*, 1973) prior to and following the measurement of the Re contents of the sample (Li *et al.*, 2017). Mass induced fractionation of Os was measured by continually assessing the Os isotope composition of the isotopic tracer and corrected by implementing a $^{192}Os/^{188}Os$ value of 3.08761 (Li *et al.*, 2017). However, there were a number of uncertainties pertaining to the measurements of the Re and Os isotope contents of each sample, calibrating the tracer, and the weighing of the tracer and sample. The blanks utilised for this study for Re and Os were 2 and 0.5 pg respectively (Li *et al.*, 2017). Furthermore, a $^{187}Os/^{188}Os$ value of 0.24 ± 0.01 (n = 6, 2σ) was also used. To derive an age for each molybdenite sample, Equation 7 was implemented.

B.5. $\delta^{34}S$ methods

As explained in Chapter 4, two categories of $\delta^{34}S$ analyses were utilised throughout this study: in-situ and those without paragenetic context. Both methods are summarised in the subsections below.

B.5.1. $\delta^{34}S$ analyses (University of Leeds)

Sulphide powders were produced by using a Dremel to drill visible sulphide mineralisation in hand specimens, prior to storing the powders in vials. The $\delta^{34}S$ analyses that lack petrographic context were performed in the Cohen Geochemistry Laboratory at the University of Leeds using an Elementar PYRO cube attached to an IsoPrime continuous flow mass spectrometer in accordance with the methodology described by He *et al.* 2020, which is paraphrased in the rest of this subsection. The sulphides were weighed into tin capsules (measuring 8 x 5mm) and combusted at 1150 °C in a flow of helium (CP grade) and pure oxygen (N5.0) (He *et al.*, 2020). It was possible to achieve total combustion of each sample by moving gas through tungsten oxide at this temperatur2e. Furthermore, oxygen was extracted from the stream of gas through the use of copper wires heated to 850 °C; SICAPENT® was used to remove the water. Following this procedure, SO_2 was partitioned from N_2 and CO_2 through the use of adsorption and desorption columns that were sensitive to temperature. Each $\delta^{34}S$ datapoint was obtained by using mass 64 and 66 signals from the sample relative to those in the SO_2 reference gas (termed 'N3.0'). Following analysis, the raw values were calibrated to the international V-CDT scale by applying a standard comprised of barium sulphate (termed 'SWS-3') that had been measured against the internationally accepted standards of NBS-127 (+20.3 ‰), NBS-123 (+17.01 ‰), IAEA S-1 (−0.30 ‰), and IAEA S-3 (−32.06 ‰) and given a $\delta^{34}S$ value of +20.3 ‰ (He *et al.*, 2020). The raw values were also compared against the chalcopyrite standard CP-1, which had been given a value of −4.56 ‰ (He *et al.*, 2020). In terms of precision, repeat analyses of a laboratory standard comprised of $BaSO_4$ were within ± 0.3 ‰ (within 1 SD) of each other.

B.5.2. In-situ $\delta^{34}S$ analyses (SUERC)

The method implemented in the in-situ $\delta^{34}S$ analyses at SUERC was originally developed by Kelley and Fallick (1990). The laser sulphur system was developed in-house and consists of three key systems; the laser system (i.e. the laser, microscope, motorised X-Y-Z stage, imaging system and the vacuum chamber), a vacuum line to purify the gas, and a mass spectrometer to perform the measurement. The polished blocks were placed into a vacuum chamber, which was evacuated to around 1E-3 millibar via the gas extraction line. The vacuum chamber was then mounted on the X-Y-Z stage of a modified Lietz Mettalux 3 containing a coated mirror mounted at 45 ° (incident to the laser beam). The laser was a CGI Laser FL-1064-CW 30-Watt diode with pumped neodymium-doped yttrium aluminium garnet (Nd: YAG), which provided a 1064 nm beam focused to a spot size of ~80 μm.

To produce a gas sample, the vacuum chamber was isolated from the extraction line and filled with high-purity oxygen to a pressure of around 150-190 mbar. The X-Y stage was then moved to select laser targets. The laser power was set t2o 33 % and fired across a 0.25 mm^2 portion of the sample to combust the sulphide and produce SO_2. The gas sample was then transferred to the gas extraction line, which is comprised of borosilicate glass and has a rotary pump coupled with a liquid nitrogen in-line trap to create a vacuum of 1E-3 mbar.

Upon generation, the gas was passed through a spiral trap submerged in dry ice mixed with propan-2-ol to form a slurry at a temperature of ~-78 °C. Condensible gases produced in the laser chamber were trapped in a second spiral trap submerged in liquid nitrogen at -196 °C. The residual oxygen was then removed by the vacuum pump, leaving the condensible gases in the second spiral trap. The liquid nitrogen was removed from the trap, which was heated to room temperature. Liquid nitrogen was then applied to an n-pentane jacket trap and the gas was transferred here until it was frozen. The liquid nitrogen was then removed from this trap, enabling the n-pentane to warm to the freezing point of -130 °C. The CO_2 was trapped in a separate finger submerged in liquid nitrogen, leaving the SO_2 in the n-pentane jacket trap. The two traps were then isolated from each other prior to measuring the CO_2 pressure and removing the CO_2 via vacuum pump. The SO_2 was then transferred to the finger by warming up the n-pentane to room temperature; the pressure was then measured before transferring the gas directly from the extraction line to the mass spectrometer, which contained an inlet fitted with a cryogenic trap for cooling the liquid nitrogen to -196 °C. This trap was used to transfer the SO_2 gas sample to the mass spectrometer inlet, which was performed automatically by custom software scripts.

The mass spectrometer used for the ^{34}S measurement was a VG Isotech Optima (a gas source mass spectrometer with a Nier type source, a small radius analyser and three fixed faraday cups) configured to measure masses 64 and 66. The signals from the faraday cups were measured and used to calculate the $^{66}SO_2/^{64}SO_2$ ratio for both the sample gas and a reference gas of known composition over a series of

alternate measurements, which were combined to give a final value representing the isotopic difference between the sample gas and reference gas. This value and the known value of the reference gas were combined to calculate a final $\delta^{34SV\text{-}CDT}$ value for the sample gas. There is a small isotopic fractionation (associated with the laser combustion of sulphide minerals) that is applied to this value, enabling the mineral $\delta^{34SV\text{-}CDT}$ to be calculated.

In this paragraph, the approach taken to sulphur isotope geothermometry is briefly summarised, although the principles of sulphur isotope geothermometry were previously outlined in Section 2.8.3.d. Sulfur isotope fractionation is a temperature dependent process, meaning it may be possible to use $\delta^{34}S$ measurements to calculate the temperature recorded by a cogenetic pair of minerals, provided that they grew in equilibrium and the fractionation factor between the two minerals is known (Seal, 2006). In this study, Equation 14 was used to calculate temperatures from localities where data from two sulphide species are available (where datapoints are available for the same hand specimen); unfortunately, this was not the case at Lead Trial, the Comrie Pluton, Coire Buidhe and several of the veins in the Calliachar Burn. Furthermore, at the GAV, where pyrite and galena pairs are available (Appendix A), the paragenetic interpretation (Fig. 6.1.c.) clearly demonstrated that these sulphides did not coprecipitate, and hence a calculated temperature is not worthy of presentation.

B.6. Pb isotopes

The approach to Pb isotope analyses was originally developed by Thirlwall (2002) and is summarised in detail throughout the rest of this section. A Dremel drill was used to extract powders of galena from hand specimens of the LTVS before placing the powders into over 20 vials, which were dispatched to the Geochronology and Tracers Facility at the BGS. A small amount of each sample was placed into a Savillex vial that had previously been cleaned. 1ml 2M Teflon distilled HNO_3 was inserted into each vial. Each sample was dissolved through heating to temperatures of >100 °C over a time period of 24 hours. Following evaporation, the samples were placed in 2% Teflon distilled HNO_3 prior to preparation for analysis via Multi Collector Inductively Coupled Plasma Mass Spectrometry (MC-ICP-MS).

Regarding the analysis of Pb isotope ratios, this task was performed by using a Thermo Fisher Scientific Neptune Plus MC-ICP-MS. This mass spectrometer was coupled with a Jet Interface, which has a higher sensitivity as a result of using a large volume interface pump (Pfeiffer On-Tool Booster 150), a Jet sampler and X skimmer cones. Before each analysis, the samples were diluted by adding 2 % Teflon distilled HNO_3 and spiking them with a solution of Tl, which was added (in a ratio of ~1Tl:10Pb) to enable the correction of mass bias associated with the instrumentation. Each sample was placed into the instrument using a Savillex 50 µl/min PFA nebuliser connected to a unit with de-solvating capabilities (Cetac Aridus II). Each isotope of interest (^{202}Hg, ^{203}Tl, ^{204}Pb/Hg, ^{205}Tl, ^{206}Pb, ^{207}Pb and ^{208}Pb) was measured simultaneously. Every acquisition was comprised of 75 ratios retrieved at 4.2-second integrations after de-focusing of baseline measurements for 60 seconds. The precision of the method was evaluated using repeat analyses of NBS 981 Pb reference solution (which had been spiked with Tl). Average values derived for each of the NBS 981 ratios (previously corrected for mass bias) were then compared to the known values for this reference (double spike: $^{206}Pb/^{204}Pc$ = 16.9417, $^{207}Pb/^{204}Pb$ = 15.4996, $^{208}Pb/^{204}Pb$ = 36.724, $^{207}Pb/^{206}Pb$ = 0.91488, $^{208}Pb/^{206}Pb$ = 2.1677; Thirlwall, 2002). Following this, the sample data was normalised in accordance with the average relative deviation of measured reference values from the true value. Internal uncertainties (i.e. the reproducibility of the ratios that were measured) were propagated relative to uncertainties of external origin (i.e. the excess amounts of variance affiliated with the reproducibility of NBS 981 reference material).

Model Pb ages were calculated using the “Ll_model_age()” function in RStudio, which is an open-source code available from the Global Lead Isotope Database (Westner *et al.*, 2021; GlobalLID Core Team, 2021; Klein *et al.*, 2022). This code is capable of calculating model ages using the lead isotope growth models produced by Stacey and Kramers (1975), Cumming and Richards (1975), Albarède and Junteau (1984), and Albarède *et al.* 2012. These models all differ from one another because they involve different assumptions regarding the initial $^{206}Pb/^{204}Pb$, $^{207}Pb/^{204}Pb$, Mu, and Kappa values of the samples (Milot *et al.*, 2016), meaning that for a given batch of Pb isotope measurements, they yield different values (Milot *et al.*, 2016; Huston and Champion, 2023).

Appendix C: Lead Trial core-logs

C.1. Introduction

In this Appendix, summary logs for Boreholes EGR-001 and EGR-002 are presented. These summary logs were constructed using the logging sheets provided by Green Glen Minerals during the 2021 Field Campaign. A legend for the summary logs is presented below.

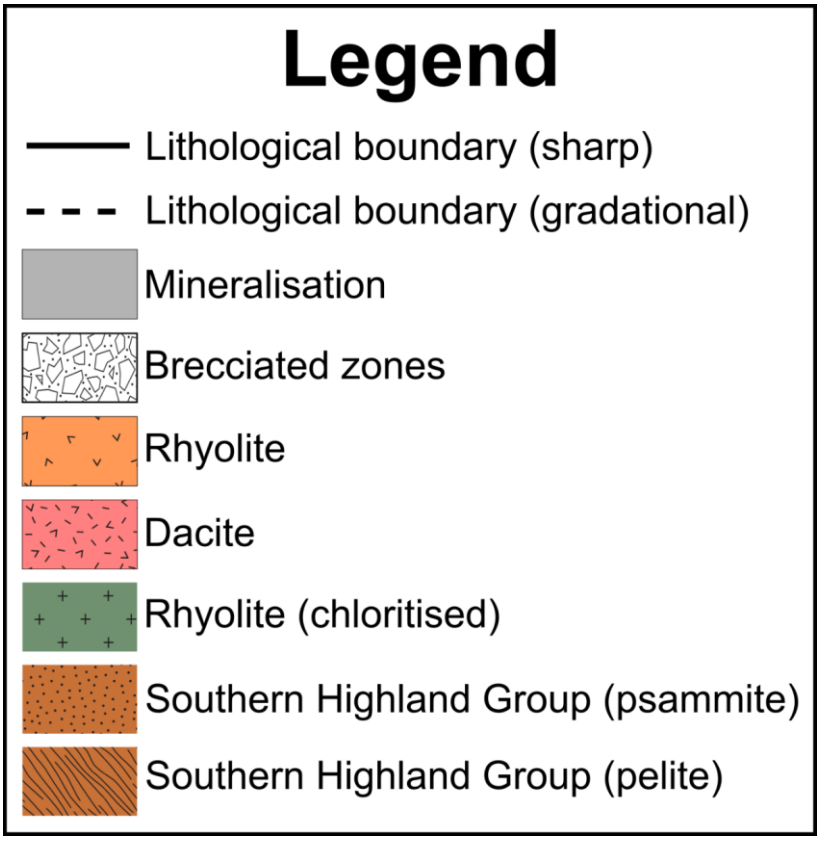

Figure C.1. Summary log for EGR-001, which was used to construct the Lead Trial cross-section (Fig. 5.7.)

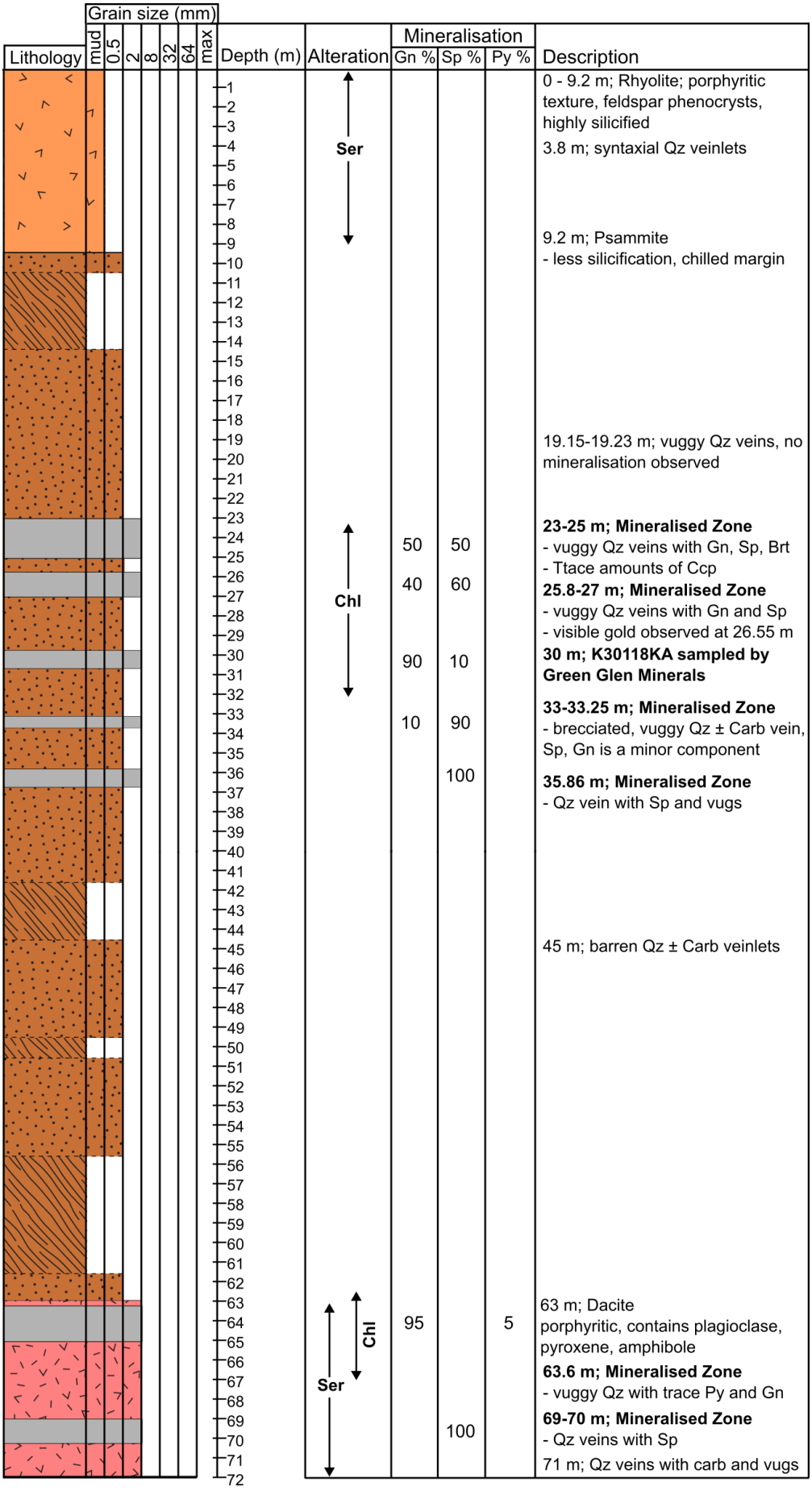

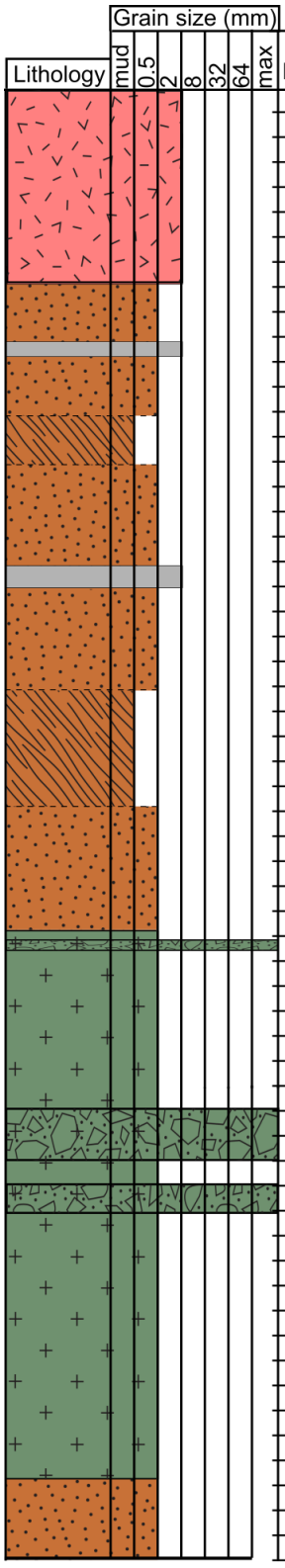

Alteration	Mineralisation			Description
	Gn %	Sp %	Py %	
Ser + Chl		100		**74 m; Mineralised Zone** - Qz veins with banded Chl, Sp in vugs
		100		**82 m; Mineralised Zone** - Qz veins with Sp in vugs
	50	50		**92-92.2 m; Mineralised Zone** - array of minor veins, Dol with Carb - Sp and Gn in equal proportions
Chl				105.8 m; Rhyolite heavily altered, hosts veins containing clays and Qz 106.2-106.5 m; minor brecciation
		50	50	112.85-115.4 m; brecciation with excessive veining; veins ~1-2 mm wide with coarse vugs; trace Sp and Py
				116.2-116.9 m; brecciation with pervasive and vuggy Qz veins and alteration; no mineralisation observed

Figure C.2. Summary log for EGR-002, which was used to construct the Lead Trial cross-section (Fig. 5.7.).

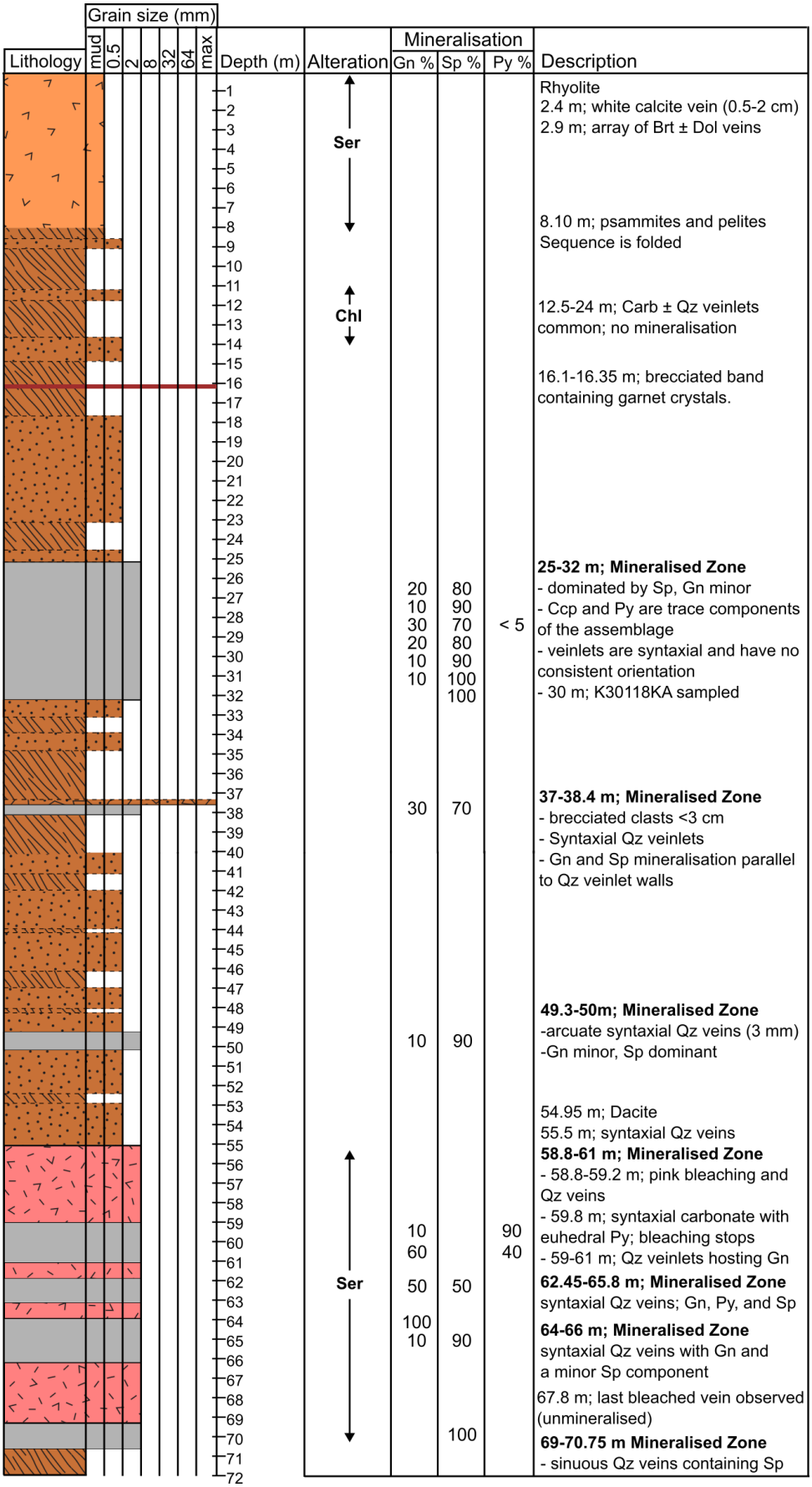

Appendix D: U-Pb data from the granitoids around Loch Tay

		Compositional Parameters						Radiogenic Isotope Ratios								Isotopic Ages					
	Fraction	Th/U	^{206}Pb* x10^{-13} mol	mol % ^{206}Pb*	Pb*/Pbc	Pbc (pg)	^{206}Pb/^{204}Pb	^{208}Pb/^{206}Pb	^{207}Pb/^{206}Pb	% err	^{207}Pb/^{235}U	% err	^{206}Pb/^{238}U	% err	corr. coef.	^{207}Pb/^{206}Pb	±	^{207}Pb/^{235}U	±	^{206}Pb/^{238}U	±
	(a)	(b)	(c)	(c)	(d)	(e)	(f)	(g)	(g)	(h)	(g)	(h)	(g)	(h)	(i)	(j)	(k)	(j)	(k)	(j)	(k)
ARD_FELS_2	z2	0.535	0.3007	98.08	16	0.49	949	0.168	0.055017	0.164	0.508294	0.279	0.067036	0.074	0.351	411.47	3.67	417.30	0.95	**418.36**	0.30
	z4	0.552	0.4006	98.70	23	0.44	1396	0.173	0.055093	0.394	0.509137	0.411	0.067055	0.095	0.289	414.56	8.81	417.87	1.41	**418.47**	0.39
	z3	0.539	0.2424	98.91	28	0.22	1667	0.169	0.055024	0.175	0.508794	0.197	0.067094	0.042	0.589	411.73	3.92	417.64	0.67	**418.71**	0.17
	z1	0.555	0.2926	98.71	23	0.32	1407	0.174	0.055218	0.440	0.510774	0.452	0.067119	0.119	0.231	419.59	9.83	418.97	1.55	**418.86**	0.48
CB_FELS_2	z4	0.611	0.0917	95.69	7	0.34	422	0.191	0.054933	1.405	0.507877	1.480	0.067084	0.340	0.329	408.05	31.43	417.02	5.06	**418.64**	1.38
	z2	0.572	0.2547	98.25	17	0.38	1042	0.180	0.055423	0.294	0.512558	0.371	0.067104	0.111	0.777	427.88	6.54	420.17	1.28	**418.76**	0.45
	z3	0.560	0.2769	98.59	21	0.33	1290	0.176	0.055235	0.288	0.512244	0.352	0.067291	0.110	0.685	420.28	6.44	419.96	1.21	**419.90**	0.45
	z1	0.535	0.1836	98.26	17	0.27	1047	0.168	0.055288	0.584	0.513395	0.632	0.067377	0.174	0.404	422.44	13.04	420.73	2.18	**420.42**	0.71
SW3	z1	0.570	0.7765	99.53	64	0.31	3836	0.179	0.055256	0.151	0.511388	0.220	0.067153	0.090	0.855	421.15	3.36	419.38	0.76	**419.06**	0.37
	z3	0.594	1.0009	99.67	94	0.27	5580	0.187	0.055193	0.114	0.510806	0.194	0.067153	0.097	0.910	418.61	2.54	418.99	0.67	**419.06**	0.39
	z4	0.709	0.3167	98.89%	28	0.30	1639	0.221	0.054780	0.264	0.507274	0.330	0.067191	0.096	0.761	401.85	5.92	416.61	1.13	**419.29**	0.39
	z5	0.676	0.7431	96.38%	8	2.32	499	0.211	0.054874	0.772	0.508487	0.852	0.067237	0.135	0.646	405.67	17.28	417.43	2.92	**419.56**	0.55
TOM_FELS_2	z1	0.749	4.4073	99.92%	402	0.29	22832	0.235	0.055161	0.111	0.509920	0.184	0.067076	0.093	0.878	417.32	2.49	418.40	0.63	**418.59**	0.38
	z2	0.814	4.5128	99.94%	527	0.23	29409	0.256	0.055313	0.125	0.511353	0.227	0.067079	0.153	0.853	423.50	2.79	419.36	0.78	**418.61**	0.62
	z5	0.808	3.5872	99.90%	326	0.30	18239	0.254	0.055245	0.141	0.510896	0.200	0.067101	0.091	0.787	420.76	3.14	419.05	0.69	**418.74**	0.37
	z4	0.794	14.7797	99.96%	853	0.47	47835	0.249	0.055189	0.084	0.510481	0.165	0.067115	0.086	0.976	418.50	1.88	418.77	0.57	**418.82**	0.35
	z3	0.826	2.4140	99.87%	248	0.26	13811	0.260	0.055212	0.020	0.510791	0.149	0.067127	0.084	0.861	419.44	0.46	418.98	0.51	**418.90**	0.34
	z6	1.112	7.5934	99.95%	763	0.29	39722	0.349	0.055207	0.102	0.510981	0.183	0.067159	0.102	0.897	419.29	2.27	419.11	0.63	**419.08**	0.42

Table D.1. CA-ID-TIMS data from the Loch Tay granitoids. The columns contain the following information: (a) Analysed zircon fraction. (b) Th contents calculated from radiogenic ^{208}Pb and the ^{207}Pb/^{206}Pb date of the sample, assuming concordance between U-Th and Pb systems. (c) ^{206}Pb concentration, also expressed as a molar percentage. (d) Ratio of radiogenic Pb (including ^{208}Pb) to common Pb. (e) Total mass of Pb. (f) Measured ratio corrected for fractionation and tracer contribution only. (g) Measured ratios corrected for fractionation, tracer, blank and, where applicable, initial common Pb. (h) Isotopic ratio uncertainty ±2 σ %. (i) The correlation coefficient is a measure for the degree of covariance between the uncertainties of the ^{206}Pb/^{238}U, ^{207}Pb/^{235}U and ^{207}Pb/^{206}Pb isotope ratios. (j) Isotopic dates calculated using the decay constants $\lambda^{238} = 1.55125^{E-10}$ and $\lambda^{235} = 9.8485^{E-10}$ (Jaffey *et al.* 1971). (k) Age uncertainty ±2 σ %.

Appendix E: $\delta^{34}S$ data from the LTVS

Table E.1. Compilation of $\delta^{34}S$ data from this study. More details on the samples used to derive this data can be found in Appendix A. Where an in-situ sample is described, the name of the polished block has also been added to the 'In-situ' column, as in some cases, this differs from the 'Sample ID.' Furthermore, occasionally a brief description of the original sample is given in this column because the in-situ descriptions do not always capture important observations at the hand-specimen scale. The 'No.' column represents the number that is referred to when the specific data point in question is discussed or described in the main text.

Locality	Sample code	In-situ?	Description	No.	Species	$\delta^{34}S$ (‰)	±
Tomnadashan	TOM_QTZ	No; from Qz±carb vein	Py, Ccp and Ttr coprecipitating in a Qz ± Carb vein	1	Py	+1.7	0.3
				2	Py	+1.8	0.3
		In-situ; Qz±carb vein (TOM_QTZ)	PyC (Stage 3) precipitating in the Qz ± Carb vein, Ttr inclusions are coeval with PyB	3	Py	+4.0	0.3
			PyC (Stage 3) precipitating in the Qz ± Carb vein, Trt inclusions are coeval with PyB	4	Py	+2.5	0.3
			PyC (Stage 3) precipitating in the Qz ± Carb vein, Trt inclusions are coeval with PyB	5	Py	+4.0	0.3
			The same region as No. 5 was targeted again to investigate the presence of intracrystal $\delta^{34}S$ variations	6	Py	+4.2	0.3
			PyC (Stage 3) being crosscut by Ccp veinlets	7	Py	+0.7	0.3
	SW_TOM_PY	No	Intergrowing Py and Ccp in sericitised and chloritised granitoid	8	Py	+2.4	0.3
				9	Py	+2.2	0.3
				10	Py	+1.7	0.3
				11	Py	+3.2	0.3
				12	Py	+2.9	0.3
				13	Py	+3.2	0.3

				14	Py	+3.2	0.3
				15	Py	+2.2	0.3
				16	Py	+2.3	0.3
		In-situ; disseminated in granitoid (SW_TOM_PYa)	PyA coprecipitating with BiTe inclusions	17	Py	+3.0	0.3
			PyA crosscut by Stage 3 Ttr	18	Py	+0.9	0.3
			PyA coprecipitating with BiTe inclusions	19	Py	+1.2	0.3
				20	Py	-0.1	0.3
	G.2002.26.2417.2	In-situ; disseminated in granitoid (B001)	Mol coprecipitating with PyA, which has also entrained Ilm fragments from the granitoid	21	Py	+3.3	0.3
	TOM_FELS	No	Disseminated Py and Ccp in granitoid	22	Py	+1.7	0.3
	G.2019.101.7	No	Fist-sized fragment of Gn with inclusions of Sp and Ccp	23	Gn	+4.7	0.3
				24	Gn	+5.5	0.3
				25	Gn	+5.3	0.3
		In-situ; B0018	Voluminous Stage 3 Gn, engulfs and brecciates previous Ccp mineralisation, observed to coprecipitate with minor Sp	26	Gn	+4.3	0.3
			Voluminous Stage 3 Gn, engulfs and brecciates previous Ccp mineralisation, observed to coprecipitate with minor Sp	27	Gn	+3.1	0.3
			This target focused on the Gn adjacent to the Stage 4 Qz veins	28	Gn	+2.7	0.3
			Zap 4, Position 4; Voluminous Stage 3 Gn, engulfs and brecciates previous Ccp mineralisation; was observed to coprecipitate with minor Sp	29	Gn	+3.8	0.3
	G.1878.49.10.1	No	Fine-grained (<1mm) flakes of Mol disseminated in granite; sample was loaded with pyrite	30	Mol	+1.8	0.3
				31	Mol	+2.5	0.3
	PA_MOLY	No	Mol fragment (1 cm) hosted in Qz veinlet crosscutting diorite	32	Mol	+2.5	0.3
				33	Mol	+2.6	0.3

	MOLY_CONC		Mol fragment (1 cm) retrieved by panning	34	Mol	+2.6	0.3
				35	Mol	+2.0	0.3
				36	Mol	+1.9	0.3
				37	Mol	+1.9	0.3
				38	Mol	+3.3	0.3
				39	Mol	+3.4	0.3
				40	Mol	+2.0	0.3
				41	Mol	+2.3	0.3
				42	Mol	+2.1	0.3
Ardtalnaig	ARD_1	No	Gn in vuggy Qz from the 'Schist Boulder', which yielded gold grades of 17.5 g/t	43	Gn	+1.8	0.2
	19882	No	Gn in vuggy Qz from the Green Glen Minerals 'Channel Sample'	44	Gn	+1.3	0.3
Lead Trial	LDT_LSa	No	Gn coprecipitating with Sp in vuggy Qz	45	Gn	+2.9	0.3
				46	Gn	+1.7	0.3
				47	Gn	+2.8	0.3
	LDT_LSb	No	Gn coprecipitating with Sp in vuggy Qz	48	Gn	+3.9	0.3
				49	Gn	+1.4	0.3
				50	Gn	+2.0	0.3
	LDT_CO	No	Panned concentrate collected from the disused tips next to the vein at Lead Trial	51	Gn	+2.3	0.2
	LDT_LSe	In-situ	Voluminous Gn coprecipitating with coarse Sp	52	Gn	-0.1	0.3
				53	Gn	-0.1	0.3
				54	Gn	-0.9	0.3
	LDT_LSa	In-situ	Voluminous Gn coprecipitating with coarse Sp	55	Gn	+0.6	0.3

				56	Gn	+0.5	0.3
Coire Buidhe	CB_GAL	No	Free-growing coarse Gn (<2 cm) in Qz	57	Gn	+5.7	0.3
				58	Gn	+5.3	0.3
				59	Gn	+4.7	0.3
		In-situ	Voluminous Gn stage coprecipitating with Sp	60	Gn	+0.1	0.3
				61	Gn	+0.8	0.3
				62	Gn	+0.6	0.3
Spoil Heap	CB3	No	Py intergrowing with Gn in Qz	63	Py	+7.4	0.2
	CB1			64	Py	+8.5	0.2
	CB1	In-situ	Py crosscut by Gn and sulfosalts;	65	Py	+8.7	0.3
			Py coprecipitating with CcpA	66	Py	+8.4	0.3
			Same position as No. 66, to investigate the presence of any zonation	67	Py	+8.4	0.3
			Py coprecipitating with Gn inclusions	68	Py	+10.0	0.3
			Same position as No. 69 to investigate the presence of any zonation	69	Py	+7.8	0.3
	CB3	No	Gn intergrowing with Py	70	Gn	+5.6	0.2
				71	Gn	+6.0	0.3
	CB1	No	Ccp intergrowing with Gn	72	Ccp	+7.3	0.2
				73	Ccp	+7.2	0.2
Glen Almond	GAV_PCa	No	Py retrieved from the vein after being crushed	74	Py	+10.5	0.3
				75	Py	+10.6	0.3
	GAV_PCb	No		76	Py	+9.6	0.3
	RC3	In-situ; RC3	Stage 2 PyB coprecipitating with Gn and Au; Py does not contain As	77	Py	+10.4	0.3

			Stage 3 PyC, which contains As, coprecipitating with Ccp and Gn	78	Py	+10.9	0.3
			Stage 3 PyC, which contains As, coprecipitating with Ccp and Gn	79	Py	+12.0	0.3
			Stage 2 PyB coprecipitating with Gn; Py noted to not contain As	80	Py	+11.7	0.3
			Stage 2 PyB coprecipitating with REE minerals; no other occurrences of REEs were observed in blocks from the GAV	81	Py	+11.0	0.3
			Stage 3 PyC, As detected via EDS here	82	Py	+10.6	0.3
	RC5	In-situ; RC5	Stage 2 PyB; close to rim of a coarse (>1 cm), euhedral crystal	83	Py	+11.0	0.3
			Stage 2 PyB; close to rim of a coarse (>1 cm), euhedral crystal	84	Py	+13.2	0.3
			Stage 2 PyB; close to the core of a coarse (>1 cm), euhedral crystal	85	Py	+10.7	0.3
			Stage 2 PyB; Ccp and Gn inclusions coeval, Stage 3 Au hosted in vug	86	Py	+10.2	0.3
			Stage 2 PyB, coeval Au and Ccp inclusions	87	Py	+10.4	0.3
			Stage 2 PyB, coeval Ccp inclusions	88	Py	+10.6	0.3
			Stage 2 PyB, coeval Ccp inclusions	89	Py	+11.1	0.3
			Stage 2 PyB, coeval Ccp and Gn inclusions	90	Py	+10.6	0.3
			Stage 2 PyB, coeval Ccp/Au inclusions	91	Py	+10.8	0.3
			Stage 2 PyB; returned to No.84 and ablated the adjacent region of the pyrite crystal	92	Py	+11.3	0.3
	GAV_GN	No	Gn chunks retrieved from the river (Glen Almond) by panning next to the vein	93	Gn	+6.0	0.3
				94	Gn	+7.5	0.3
				95	Gn	+7.3	0.3
				96	Gn	+7.8	0.3

				97	Gn	+8.3	0.3
				98	Gn	+7.9	0.3
				99	Gn	+7.9	0.3
				100	Gn	+7.8	0.3
	RC1	In-situ	Stage 5 GnE infilling cracks in Qz	101	Gn	+5.1	0.3
Comrie Pluton	CMRIE4	No	Disseminated Py and Ccp in the potassic alteration zone of the Comrie Pluton	102	Py	+4.9	0.3
	CMRIE7			103	Py	+5.3	0.3
Tombuie	2003.1G.M.637	No	Py intergrowing with Sp, Ccp, and Gn in Qz	104	Py	+12.4	0.3
				105	Py	+11.8	0.3
				106	Py	+12.4	0.3
			Ga intergrowing with Sp, Ccp, and Py in Qz	107	Gn	+12.3	0.3
				108	Gn	+12.3	0.3
Calliachar (Discovery Vein)	2003.1G.M.627	No	Coarse Py crystals (>1 cm)occurring in Qz vugs; decaying to goethite in places	109	Py	+7.8	0.3
Calliachar (V3)	LSCV1	No	Coarse Gn (0.5 cm) growing in Qz vugs; Py was present but has decayed	110	Gn	+6.5	0.3
				111	Gn	+6.4	0.3
				112	Gn	+6.3	0.3
	CAL_GN	No	Native Gn fragment (>10 cm) found near V3; broken into pieces	113	Gn	+5.9	0.3
				114	Gn	+6.0	0.3
				115	Gn	+5.0	0.3
				116	Gn	+5.4	0.3
Calliachar (V5)	2003.1G.M.630	No	Py and Gn are spatially associated in the Qz vugs	117	Gn	+7.2	0.3
Calliachar (V6)	2003.1G.M.604 a-p	No		118	Py	+9.1	0.3
	DISC_004	In-situ		119	Py	+8.3	0.3

			Coarse Py crystal; same area measured twice to investigate the presence of zonation	120	Py	+7.5	0.3
			Coarse Py, which does not contain As, coprecipitating with Gn	121	Py	+8.2	0.3
			same area measured twice to investigate the presence of zonation	122	Py	+7.5	0.3
	2003.1G.M.604 a-p	No	Py and Gn are spatially associated in the Qz vugs	123	Gn	+6.0	0.3
	DISC_004	In-situ; DISC_004	Uncertain whether Py or Apy; given the occurrence of Apy in V6 (Ixer *et al.*, 1997), it is likely to be the latter, although when corrected for Py the $\delta^{34}S$ value is +7.88 ‰	124	Apy	+7.9	0.3
			Rhombic shape and occurrence in V6 mean this is likely Apy, although the $\delta^{34}S$ value corrected for Py is +8.38 ‰	125	Apy	+8.4	0.3
Calliachar (V7)	CAL_PY	No	Pyrite particles previously separated from gossan during panning	126	Py	+8.3	0.3
				127	Py	+8.7	0.3
				128	Py	+8.8	0.3
				129	Py	+8.7	0.3
				130	Py	+8.8	0.3
				131	Py	+8.5	0.3
				132	Py	+8.8	0.3
				133	Py	+8.7	0.3
				134	Py	+9.0	0.3
	2003.1G.M.626 a-v	No	Gn spatially coincident with Py in Qz vugs	135	Gn	+5.9	0.3
Urlar	UV_SHa	No	Py, Ccp, and Gn spatially coincident in massive Qz	136	Py	+8.9	0.3
	UB_VEINb	No	Gn intergrowing with Py in Qz vein	137	Py	+10.8	0.3
	UV_SHb	No	Visible Py, Ccp and Gn in Qz vein	140	Py	+9.3	0.3
	UB_VEINa	No	Qz vein with large amounts of Gn, trace Py and Mlc	138	Gn	+9.5	0.3

	UB_GAL	No	Free-growing Gn in Qz vein with trace amounts of Ccp	139	Gn	+8.5	0.3
	UB_GAL	In-situ; UB_GAL	Gn veinlet infilling Qz cracks	141	Gn	+8.7	0.3
			Voluminous Gn stage displaying unusual ‘patchiness’	142	Gn	+7.3	0.3
			Gn veinlet infilling Qz cracks	143	Gn	+8.7	0.3
	UV_SHa	No	Visible Py, Ccp, and Gn in Qz vein	144	Ccp	+8.2	0.3

Table E.2. Compilation of mean $\delta^{34}S$ values from different localities in the LTVS with multiple $\delta^{34}S$ datapoints. At Tomnadashan and the Glen Almond Vein (GAV), mean values from samples in which the paragenetic context is uncertain are reported separately.

Locality	Sulphide	Description	Mean $\delta^{34}S$ (‰)	±
Tomnadashan	Py	Mean of Py values for which paragenetic context is unknown	+2.4	0.3
	Py	PyA; in-situ measurements targeted on Stage 1 of the paragenesis	+1.7	0.3
	Py	PyC; in-situ measurements on Py from Stage 3 of the paragenesis	+3.1	0.3
	Mol	Combined mean of $\delta^{34}S$ values of Mol (Stage 2 of the paragenesis)	+2.5	0.3
	Gn	GnC; all measurements pertain to the G.2019.101.7 sample (Stage 3 of the paragenesis)	+4.2	0.3
Ardtalnaig/Lead Trial	Gn	All samples from Lead Trial/ARD_1 pertain to GnC (Stage 3 of the paragenesis)	+1.4	0.3
Spoil Heap	Py	Mean of all $\delta^{34}S$ values from this locality	+8.5	0.3
	Gn	Gn is a minor phase at Spoil Heap, may coprecipitate with Py	+6.0	0.3
	Ccp	Chalcopyrite intergrows with Gn and Py at Spoil Heap	+7.2	0.3
Coire Buidhe	Gn	Combination of $\delta^{34}S$ measurements, which yielded a broad range in values (Table E.1.)	+2.9	0.3
Glen Almond Vein	Py	Paragenetic context is unknown	+10.2	0.3
	Py	PyB; Stage 2 in the paragenesis	+11.0	0.3
	Py	PyC; Stage 3 in the paragenesis	+11.2	0.3
	Gn	Voluminous Gn retrieved by crushing vein, likely to pertain to Stage 5	+7.2	0.3
Comrie Pluton	Py	Mean of measurements (not collected in-situ)	+5.1	0.3
Tombuie	Py	Mean of measurements (not collected in-situ)	+12.2	0.3
	Gn	Two measurements without paragenetic context yielded identical values	+12.3	0.3
Calliachar Burn V6	Py	Mean of $\delta^{34}S$ measurements	+8.0	0.3

	Apy	Two in-situ measurements, phase identification uncertain	+8.2	0.3
Calliachar Burn V7	Py	Mean values of Py flakes panned from gossan	+8.7	0.3
Urlar Burn	Py	Measurements from Py coprecipitating with Ccp and2 Gn	+9.7	0.3
	Gn	Mean of measurements from several hand specimens	+8.5	0.3

Appendix F: Pb data from the LTVS

Table F.1. Summary of the Pb isotope ratios derived from LTVS galena samples in this study. A detailed description of each sample can be found in Appendix A.

Locality	Sample ID	Total Pb/(V)	$^{206}Pb/^{204}Pb$	2SD %	$^{207}Pb/^{204}Pb$	2SD %	$^{208}Pb/^{204}Pb$	2SD %	$^{207}Pb/^{206}Pb$	2SD %	$^{208}Pb/^{206}Pb$	2SD %
Ardtalnaig	RX2959KA	19.9	17.4054	0.006	15.3930	0.007	37.551	0.008	0.88438	0.005	2.1574	0.006
Ardtalnaig	RX2959KA	20.8	17.4056	0.006	15.3932	0.007	37.552	0.008	0.88438	0.005	2.1575	0.006
Ardtalnaig	ARD_1	25.5	17.4042	0.006	15.3929	0.006	37.551	0.008	0.88444	0.005	2.1576	0.006
Lead Trial	RX2996AKA	19.6	17.4117	0.006	15.3937	0.006	37.554	0.008	0.88410	0.005	2.1568	0.006
Lead Trial	RX2991KA	21.0	17.4076	0.006	15.3936	0.006	37.552	0.008	0.88431	0.005	2.1572	0.006
Lead Trial	K30182KA	18.1	17.4117	0.006	15.3945	0.006	37.555	0.008	0.88415	0.005	2.1569	0.006
Lead Trial	K30118KA	16.6	17.4189	0.006	15.3946	0.006	37.557	0.008	0.88379	0.005	2.1562	0.006
Lead Trial	RX2963KA	20.1	17.4009	0.006	15.3912	0.007	37.546	0.008	0.88450	0.005	2.1578	0.006
Lead Trial	RX2963KA	20.7	17.4016	0.006	15.3916	0.007	37.548	0.009	0.88450	0.005	2.1578	0.006
Lead Trial	RX2990KA	15.6	17.4150	0.006	15.3935	0.007	37.552	0.009	0.88391	0.005	2.1563	0.006
Lead Trial	19882	23.5	17.4042	0.006	15.3929	0.007	37.552	0.008	0.88443	0.005	2.1577	0.006
Lead Trial	19882	24.0	17.4038	0.006	15.3925	0.006	37.550	0.008	0.88444	0.005	2.1576	0.006
Tomnadashan	G.2019.101.7	19.2	17.8158	0.006	15.4816	0.007	37.687	0.009	0.86898	0.005	2.1154	0.006
Coire Buidhe	CB_GAL_LS	12.0	17.7572	0.007	15.4598	0.007	37.676	0.009	0.87064	0.005	2.1217	0.006
Coire Buidhe	CB_GAL_LS	12.2	17.7564	0.007	15.4591	0.007	37.673	0.009	0.87062	0.005	2.1217	0.006
Coire Buidhe	CB_GAL_LS	11.7	17.7431	0.006	15.4575	0.007	37.667	0.008	0.87117	0.005	2.1230	0.006
Spoil Heap	CB3	12.2	17.6107	0.006	15.4335	0.007	37.592	0.008	0.87638	0.005	2.1346	0.006
Spoil Heap	CB3	16.7	17.6863	0.006	15.4464	0.007	37.641	0.009	0.87335	0.005	2.1283	0.006
Spoil Heap	CB3	18.8	17.6968	0.006	15.4480	0.007	37.648	0.009	0.87293	0.005	2.1274	0.006

Locality	Sample ID	Total Pb/(V)	$^{206}Pb/^{204}Pb$	2SD %	$^{207}Pb/^{204}Pb$	2SD %	$^{208}Pb/^{204}Pb$	2SD %	$^{207}Pb/^{206}Pb$	2SD %	$^{208}Pb/^{206}Pb$	2SD %
Glen Almond	GAV_PCb	10.1	17.5651	0.007	15.4208	0.007	37.572	0.009	0.87793	0.005	2.1391	0.006
Glen Almond	GAV_PCb	10.3	17.5647	0.007	15.4205	0.007	37.571	0.009	0.87792	0.005	2.1390	0.006
Calliachar V7	2003.1G.M.626 a-v	24.7	17.8630	0.006	15.4721	0.006	37.765	0.008	0.86615	0.005	2.1141	0.006
Calliachar V6	2003.1G.M.604 a-p	20.8	17.8078	0.006	15.4669	0.006	37.706	0.008	0.86855	0.005	2.1174	0.006
Calliachar V5	2003.1G.M.630	24.8	17.8561	0.006	15.4759	0.006	37.752	0.008	0.86670	0.005	2.1143	0.006
Urlar Burn	UV_SHa	16.0	17.7725	0.006	15.4667	0.007	37.685	0.009	0.87026	0.005	2.1205	0.006
Urlar Burn	UB_VEINb	12.6	17.8215	0.006	15.4806	0.007	37.719	0.008	0.86865	0.005	2.1165	0.006
Urlar Burn	UV_SHa	23.6	17.7730	0.006	15.4642	0.006	37.689	0.008	0.87010	0.005	2.1206	0.006
Urlar Burn	UV_SHa	23.8	17.7725	0.006	15.4636	0.006	37.688	0.008	0.87009	0.005	2.1206	0.006
Tombuie	Tombuie	23.7	17.7711	0.006	15.4588	0.006	37.670	0.008	0.86990	0.005	2.1198	0.006

ID	Locality	$^{206}Pb/^{204}Pb$	±	$^{207}Pb/^{204}Pb$	±	$^{208}Pb/^{204}Pb$	±
LS1	Lead Trial	17.3926	0.000118	15.3864	0.000121	37.5395	0.000349
LS2	Coire Buidhe	17.8342	0.000105	15.4736	0.000107	37.6987	0.000315
LS4a	Urlar Burn	17.7566	0.000101	15.4629	0.000106	37.6641	0.000294
LS4b	Urlar Burn	17.7560	0.000132	15.4624	0.000128	37.6627	0.000349
LS4c	Urlar Burn	17.7560	0.000125	15.4621	0.000120	37.6617	0.000339
LS4d	Urlar Burn	17.7562	0.000125	15.4626	0.000124	37.6630	0.000337
LS4x	Urlar Burn	17.7557	0.000167	15.4618	0.000159	37.6617	0.000430
LS4y	Urlar Burn	17.7566	0.000106	15.4626	0.000104	37.6637	0.000295
LS4z	Urlar Burn	17.7565	0.000139	15.4626	0.000144	37.6638	0.000394
LS5	Urlar Burn	17.7743	0.000112	15.4680	0.000118	37.6806	0.000326
LS6	Calliachar Burn	17.8732	0.000110	15.4721	0.000115	37.7642	0.000328
LS7	Urlar Burn	17.7555	0.000128	15.4597	0.000123	37.6663	0.000335
LS8	Urlar Burn	17.6874	0.000112	15.4470	0.000114	37.6108	0.000316

Table F.2. Pb isotope values derived by Savastano (2024) from galena samples associated with the LTVS.

Table F.3. Model Pb ages (Ma) calculated for LTVS galena samples. Ages were calculated using the following lead evolution models: SK_1975 (Stacey and Kramers, 1975), CR_1975 (Cumming and Richards, 1975), AJ_1984 (Albarède and Junteau, 1984) and A_2012 (Albarède *et al.*, 2012). The calculations were performed using the "Ll_model_age()" function on the Global Lead Isotope Database (Westner *et al.*, 2021). * indicates a Savastano (2024) sample.

Locality	Sample	Model Age (SK_1975)	Mu	Kappa	Model Age (CR_1975)	Mu	Kappa	Model Age (AJ_1984)	Mu	Kappa	Model Age (A_2012)	Mu	Kappa
Ardtalnaig	RX2959KA	507.456	9.018	3.995	821.761	10.302	3.882	574.803	9.034	4.032	681.21	9.354	4.034
	RX2959KA	506.647	9.018	3.995	821.21	10.302	3.882	574.007	9.034	4.032	680.499	9.354	4.034
	ARD_1	508.265	9.018	3.996	822.311	10.302	3.882	575.598	9.035	4.033	681.922	9.354	4.034
Lead Trial	RX2996AKA	503.906	9.02	3.992	817.857	10.304	3.882	571.159	9.036	4.029	677.356	9.355	4.031
	RX2991KA	507.141	9.022	3.993	820.059	10.303	3.882	574.34	9.038	4.031	680.2	9.356	4.033
	K30182KA	503.906	9.02	3.992	817.857	10.304	3.882	571.159	9.036	4.029	677.356	9.355	4.032
	K30118KA	500.359	9.023	3.988	813.951	10.306	3.882	567.518	9.038	4.025	673.501	9.356	4.029
	RX2963KA	506.467	9.01	3.994	824.063	10.301	3.882	574.136	9.027	4.031	681.81	9.35	4.033
	RX2963KA	507.771	9.014	3.995	823.462	10.301	3.882	575.266	9.031	4.032	682.221	9.352	4.034
	RX2990KA	499.364	9.015	3.988	816.254	10.305	3.882	566.846	9.031	4.025	674.098	9.352	4.028
	19882	508.265	9.018	3.996	822.311	10.302	3.882	575.598	9.035	4.033	681.922	9.354	4.035
	19882	508.265	9.018	3.995	822.311	10.302	3.882	575.598	9.035	4.032	681.922	9.354	4.034
	LS1*	502.363	8.99	3.995	828.717	10.298	3.883	570.871	9.009	4.032	681.887	9.454	4.034
Tomnadashan	G.2019.101.7	367.534	9.299	3.804	588.717	10.427	3.870	423.43	9.282	3.841	490.539	9.473	3.873
	Moorbath (1962)	222.401	8.648	3.670	743.362	10.344	3.878	307.042	8.698	3.714	489.796	9.182	3.78
Coire Buidhe	CB_GAL_LS	367.517	9.217	3.831	622.863	10.409	3.872	426.737	9.208	3.869	507.049	9.437	3.897
	CB_GAL_LS	366.181	9.213	3.83	623.469	10.409	3.872	425.571	9.204	3.867	506.603	9.435	3.896
	CB_GAL_LS	374.375	9.212	3.835	630.813	10.405	3.872	433.808	9.204	3.873	514.711	9.435	3.901
	LS2*	336.356	9.258	3.795	578.902	10.433	3.869	393.849	9.245	3.833	468.42	9.454	3.867

Spoil Heap	CB3	428.566	9.142	3.878	705.711	10.364	3.876	490.891	9.142	3.916	581.112	9.405	3.937
	CB3	394.19	9.174	3.857	663.292	10.387	3.874	455.179	9.171	3.894	541.474	9.418	3.919
	CB3	389.681	9.18	3.854	657.045	10.391	3.873	450.428	9.176	3.891	535.941	9.421	3.916
Glen Almond	GAV_PCb	437.828	9.096	3.895	731.909	10.35	3.877	501.999	9.102	3.933	599.023	9.386	3.952
	GAV_PCb	435.701	9.092	3.894	731.956	10.35	3.877	500.059	9.098	3.932	597.883	9.384	3.951
Calliachar V7	2003.1G.M.626 a-v	309.105	9.242	3.813	562.601	10.441	3.868	367.249	9.229	3.850	445.365	9.446	3.881
Calliachar V6	2003.1G.M.604 a-p	341.993	9.234	3.815	593.862	10.424	3.87	400.481	9.223	3.853	478.809	9.444	3.884
Calliachar V5	2003.1G.M.630	323.23	9.261	3.811	566.392	10.439	3.869	380.583	9.247	3.849	455.056	9.455	3.88
Calliachar Burn	LS6	301.173	9.239	3.805	556.944	10.444	3.868	359.418	9.227	3.842	438.211	9.445	3.875
Urlar Burn	UV_SHa	369.717	9.244	3.828	613.567	10.414	3.871	427.845	9.232	3.865	503.758	9.448	3.894
	UB_VEINb	361.486	9.293	3.819	585.941	10.429	3.87	417.607	9.276	3.856	485.824	9.47	3.885
	UV_SHa	363.341	9.23	3.829	613.696	10.414	3.871	422.008	9.22	3.866	500.282	9.442	3.895
	UV_SHa	363.341	9.23	3.829	613.696	10.414	3.871	422.008	9.22	3.866	500.282	9.442	3.895
	LS4a*	373.897	9.23	3.825	622.733	10.409	3.872	432.576	9.22	3.863	510.522	9.443	3.892
	LS4b*	372.565	9.226	3.825	623.338	10.409	3.872	431.414	9.217	3.863	510.077	9.441	3.892
	LS4c*	372.565	9.226	3.825	623.338	10.409	3.872	431.414	9.217	3.862	510.077	9.441	3.892
	LS4d*	374.689	9.231	3.826	623.295	10.409	3.872	433.358	9.221	3.863	511.234	9.443	3.892
	LS4x*	372.565	9.226	3.825	623.338	10.409	3.872	431.414	9.217	3.862	510.077	9.441	3.892
	LS4y*	373.897	9.23	3.825	622.733	10.409	3.872	432.576	9.22	3.863	510.522	9.443	3.892
	LS4z*	373.897	9.23	3.825	622.733	10.409	3.872	432.576	9.22	3.863	510.522	9.443	3.892
	LS5*	371.047	9.248	3.825	612.961	10.414	3.871	429.007	9.236	3.862	504.203	9.45	3.891
	LS7*	368.311	9.217	3.826	623.425	10.409	3.872	427.52	9.208	3.864	507.762	9.437	3.893
	LS8*	395.52	9.178	3.838	662.687	10.388	3.874	456.337	9.174	3.876	541.913	9.42	3.904
Tombuie	2003.1G.M.637	354.264	9.208	3.817	615.036	10.413	3.871	413.814	9.2	3.855	495.904	9.433	3.886